

JSR A

E-ISSN: 2687-6167

NUMBER 52

MARCH 2023

JOURNAL OF SCIENTIFIC REPORTS A

JOURNAL OF SCIENTIFIC REPORTS-A-MARCH 2023 NUMBER 52



Kutahya Dumlupınar University Scientific Reports A
Evliya Çelebi Campus Tavşanlı Road 10 KM. 43270 Kutahya
Phone : (0274) 443 19 42
E-mail : journals@gmail.com
gjsra.com

Dumlupınar University Press

gate of
science



Owner

On Behalf of Kütahya Dumlupınar University
Prof. Dr. Kazım UYSAL (Rector),
On Behalf of Institute of Graduate Studies
Assoc. Prof. Dr. Arif KOLAY (Director)

Editorial Board

Prof. Dr. Önder UYSAL
Prof. Dr. Fatih ŞEN
Prof. Dr. Cemal PARLAK
Prof. Dr. Oktay ŞAHBAZ
Assoc. Prof. Nevzat BEYAZIT
Assoc. Prof. Onur KARAMAN
Assoc. Prof. Cafer ÖZKUL
Assoc. Prof. Levent URTEKİN
Assist. Prof. Ümrhan ERÇETİN
Dr. Ceren KARAMAN
Assist. Prof. Durmuş ÖZDEMİR

Kütahya Dumlupınar University/ Mining Engineering
Kütahya Dumlupınar University / Biochemistry
Ege University / Physics
Kütahya Dumlupınar University/ Mining Engineering
Ondokuz Mayıs University / Environmental Eng
Akdeniz University / Medical Services and Tech
Kütahya Dumlupınar University / Geological Eng.
Ahi Evran University / Mechanical Eng.
Kütahya Dumlupınar University / Mechanical Eng.
Akdeniz University / Electrical and Energy
Kütahya Dumlupınar University / Computer Eng.

Journal of Scientific Reports-A started its publication life in 2000 as name of Journal of Science and Technology of Dumlupınar University and is a national peer-reviewed journal published regularly twice a year in June and December. The language of the journal is English. Articles submitted to the journal are evaluated by at least two referees who are experts in the subject and selected by the editorial board. All articles submitted to the journal are evaluated by the double-blind method. Articles submitted to our journal for review should not be previously published, accepted for publication and in the process of being evaluated for publication in another journal. All responsibility for the articles published in the journal belongs to the author(s).

The journal aims to share scientific studies carried out in the fields of science and engineering at national and international level with scientists and the public. Original research articles, review articles and short notes in science and engineering disciplines are accepted for the journal. Original research articles are expected to contain theoretical and experimental results and should not be published in other journals. In the review articles, it is expected that scientific, technological and current developments on a specific subject are reflected by using an extensive bibliography and made a satisfying evaluation of these. Short notes should be brief writings prepared to announce the first findings of an original study.

Editorial Policy

The journal is open access and the article evaluation period is between 1-2 months.

Correspondence Address: Kütahya Dumlupınar Üniversitesi Evliya Çelebi Yerleşkesi Fen Bilimleri Enstitüsü
43270 KÜTAHYA

E-mail: joursra@gmail.com

Phone: 0 274 443 19 42

Webpage: gsjsra.com

Fax: 0 274 265 20 60

Section Editors

Civil Engineering Prof. Dr. M. Çağatay KARABÖRK	Kütahya Dumlupınar University
Mechanical Engineering Prof. Dr. Ramazan KÖSE	Kütahya Dumlupınar University
Electrical-Electronics Engineering Assist. Prof. Kadir VARDAR	Kütahya Dumlupınar University
Computer Engineering Assoc. Prof. Doğan AYDIN	Kütahya Dumlupınar University
Industrial Engineering Assist. Prof. Üyesi Kerem CİDDİ	Kütahya Dumlupınar University
Mining Engineering Assist. Prof. Uğur DEMİR	Kütahya Dumlupınar University
Geology Engineering Assist. Prof. Muzaffer ÖZBURAN	Kütahya Dumlupınar University
Metallurgical and Materials Engineering Prof. Dr. Güray KAYA	Kütahya Dumlupınar University
Food Engineering Prof. Dr. Muhammet DÖNMEZ	Kütahya Dumlupınar University
Environmental Engineering Doç. Dr. Nevzat BEYAZIT	Ondokuz Mayıs University
Mathematics Assist. Prof. Cansu KESKİN	Kütahya Dumlupınar University
Physics Assoc. Prof. Huriye Sanem AYDOĞU	Kütahya Dumlupınar University
Chemistry Assoc. Prof. Bülent ZEYBEK	Kütahya Dumlupınar University
Biology Assist. Prof. Nüket Akalın BİNGÖL	Kütahya Dumlupınar University
Biochemistry Assoc. Prof. Derya KOYUNCU ZEYBEK	Kütahya Dumlupınar University
Occupational Health and Safety Prof. Dr. Cem ŞENSÖĞÜT	Kütahya Dumlupınar University
Software Engineering Assist. Prof. Şerif Ali SADIK	Kütahya Dumlupınar University

Advisory Board

Prof. Dr. Sibel AKAR	Eskişehir Osmangazi University / Chemistry
Prof. Dr. Abdurrahman AKTÜMSEK	Selçuk University/ Biology
Prof. Dr. Mustafa ALTUNOK	Gazi University / Tree-Jobs Industrial Engineering
Prof. Dr. Uğur ARİFOĞLU	Sakarya University / Electrical and Electr. Engineering
Prof. Dr. Oktay ARSLAN	Balıkesir University / Chemistry
Prof. Dr. Şükrü ASLAN	Sivas Cumhuriyet University / Environmental Engineering
Prof. Dr. Ülfe ATAV	Selçuk University / Physics
Prof. Dr. Mustafa BAYRAKTAR	TOBB Ekonomi ve Teknoloji University / Mathematics
Prof. Dr. Niyazi BİLİM	Konya Technical University / Mining Engineering
Prof. Dr. İsmail BOZTOSUN	Akdeniz University / Physics
Prof. Dr. Erdal ÇELİK	Dokuz Eylül University / Metallurgical and Material Eng.
Prof. Dr. Hayri DAYIOĞLU	Kütahya Dumlupınar University / Biology
Prof. Dr. Muhammet DÖNMEZ	Kütahya Dumlupınar University / Food Engineering
Prof. Dr. Mehmet Ali EBEOĞLU	Kütahya Dumlupınar University / Elec.and Electr. Eng.
Prof. Dr. İsmail Göktay EDİZ	Kütahya Dumlupınar University / Mining Engineering
Prof. Dr. İsmail EKİNCİOĞLU	Kütahya Dumlupınar University / Mathematics
Prof. Dr. Kaan ERARSLAN	Kütahya Dumlupınar University / Mining Engineering
Prof. Dr. Zeynal Abiddin ERGÜLER	Kütahya Dumlupınar University / Geological Eng.
Prof. Dr. Seyhan FIRAT	Gazi University / Civil Engineering
Prof. Dr. Remzi GÖREN	Sakarya University / Metallurgical and Material Eng.
Prof. Dr. Rasim İPEK	Ege University / Mechanical Engineering
Prof. Dr. Refail KASIMBEYLİ	Eskişehir Technical University / Industrial Engineering
Prof. Dr. Hamdi Şükür KILIÇ	Selçuk University / Physics
Prof. Dr. Yaşar KİBİCİ	Bilecik Şeyh Edebali University / Geological Eng.
Prof. Dr. İsmail KOCAÇALIŞKAN	Yıldız Technical University / Molecular Bio. and Gen.
Prof. Dr. Mahmut KOÇAK	Eskişehir Osmangazi University / Math-Computer
Prof. Dr. Muhsin KONUK	Üsküdar University / Molecular Biology and Gen.
Prof. Dr. Mustafa KURU	Başkent University / Molecular Biology and Gen.
Prof. Dr. Ömer İrfan KÜFREVİOĞLU	Atatürk University / Biochemistry
Prof. Dr. Halim MUTLU	Ankara University / Geological Engineering
Prof. Dr. Ekrem SAVAŞ	İstanbul Ticaret University / Mathematics
Prof. Dr. Murat TANIŞLI	Eskişehir Technical University / Physics
Prof. Dr. Ali Rehber TÜRKER	Gazi University / Chemistry
Prof. Dr. Mustafa TÜRKMEN	Giresun University / Biology
Prof. Dr. Abdülmecit TÜRÜT	İstanbul Medeniyet University / Physics Engineering
Prof. Dr. Eşref ÜNLÜOĞLU	Eskişehir Osmangazi University / Civil Engineering
Prof. Dr. Nurettin YAYLI	Karadeniz Technical University / Pharmacy
Prof. Dr. Yusuf YAYLI	Ankara University / Mathematics
Prof. Dr. Elçin YUSUFOĞLU	Uşak University / Mathematics
Prof. Dr. Hüseyin Serdar YÜCESU	Gazi University / Automotive Engineering
Prof. Dr. Mehmet Tevfik ZEYREK	Middle East Technical University / Physics

JOURNAL OF SCIENTIFIC REPORTS-A
E-ISSN: 2687-6167

CONTENTS

RESEARCH ARTICLES

- Effects of Gravity's Rainbow on a Relativistic Spin-1 Oscillator* 1-18
Semra GÜRTAŞ DOĞAN*
- Inverse Neuro-Fuzzy Model Based Controller Design for a Ph Neutralization Process* 19-34
Talha Burak AKCA*, Cenk ULU, Salih OBUT
- Exergoeconomic Analysis of a Photovoltaic Array Affected by Dynamic Shading* 35-50
Vedat KESKİN*
- 285 Nm Algan-Based Deep-Ultraviolet Led with High Internal Quantum Efficiency: Computational Design* 51-64
İrem ÖNER ALP*, Bilgehan Barış ÖNER, Esra EROĞLU
- Mineralogy and Geochemistry of Coal-Bearing Tunçbilek Formation in the Tunçbilek-Tavşanlı Coalfield (Kütahya, W-Turkey)* 65-98
Selin KARADİREK*
- Optimal Design of Organic Rankine Cycle Power Plants for Efficient Utilization of Biomass Energy in Nigeria* 99-124
John Akpaduado FRIDAY, Joseph OYEKALE*
- Investigation of the Seasonality of Occupational Accidents in Mine Operations* 125-148
Sevda TURAN*, Muhammet Mustafa KAHRAMAN
- Design and Application of Ac/Dc Switching Power Supply with Half Bridge Dc/Dc Converter Topology for Battery Systems of Electrical Vehicle* 149-173
Celaletdin AKGÜL*, Yücel ÇETİNCEVİZ, Erdal ŞEHİRLİ
- Evaluation of Controller Parameters on the Twin Rotor Multiple Input Multiple Output System Using Butterfly-Based Particle Swarm Optimization* 174-189
Ali Can ÇUBUKER*, M.Nuri ALMALI, İshak PARLAR
- A Hybrid Modified Subgradient Algorithm That Self-Determines the Proper Parameter Values* 190-199
Tuğba SARAÇ, Büşra TUTUMLU*, Emine AKYOL ÖZER
- Insight into the Effect of Ti/Zr Oxide Hybrid Particles on Dental Composites: Particle* 200-219

Synthesis and Characterization and the Mechanical Behavior of Composites Zerrin YEŞİL ACAR*	
Betaine Supplementation Protects Rats Against Alcohol-Induced Hepatic and Duodenal Injury: An Histopathological Study Ayşe ÇAKIR GÜNDOĞDU*, Fatih KAR, Cansu ÖZBAYER	220-233
Facile and Controlled Synthesis of 2d Organometal Halide Perovskite Pure $Ba_2mapb_2i_7$ and Heterostructured $Ba_2pbi_4/Ba_2mapb_2i_7$ Single Crystals Alp YILMAZ*, Aydan YELTİK	234-246
Polydatin, a Herbal Bioflavonoid, is Protective Against Cerebral Ischemia-Reperfusion Injury: Molecular, Biochemical and Histological Data Saadet ÇELİKÖZLÜ*, Said ALTIKAT, Filiz ÖZYİĞİT, Sibel KÖKTÜRK, Halit ÇELİKÖZLÜ	247-265
Detection of Fetal Electrocardiogram Signals from Maternal Abdominal Ecg Recordings Ulvi BAŞPINAR*, Yasemin KÖYLÜ	266-278
A Kinetic Study of Thermochemically Borided AISI 316L Stainless Steel Gökhan BAŞMAN, Mustafa Merih ARIKAN*, C. Fahir ARISOY, M. Kelami ŞEŞEN	279-296
The Effect of Levothyroxine Treatment on Maternal and Perinatal Outcomes in Pregnant Women with Subclinical Hypothyroidism: A 5-Year Retrospective Study at a Tertiary Care Hospital in Turkey Halil İbrahiö ERBIYIK, Rabia Merve PALALIOĞLU*	297-310
An Efficient Calibration Process for the Prediction of Rock Strength Through Machine Learning Algorithms Şaziye Özge DİNÇ GÖĞÜŞ*	311-326
Chemical and Mineralogical Analyses of the Late Neolithic Ceramics from Şah Valley (Singuber), Turkey Murat Bayazıt*, Esra KAYNAK, Nilgün COŞKUN	327-351
Brain Tumor Detection and Brain Tumor Area Calculation with Matlab Burak KAPUSIZ*, Yusuf UZUN, Sabri KOÇER, Özgür DÜNDAR	352-364
Antimicrobial Activity of (E)-3-(4-Sulfamoylphenylcarbamoyl) Acrylic Acid Derivatives Halil İLKİMEN*, Cengiz YENİKAYA, Aysel GÜLBANDILAR	365-375
Investigation of Some Univariate Normality Tests in Terms of Type-I Errors and Test Power Sevda KORKMAZ, Yıldırım DEMİR*	376-395

Investigation of the Strain Rate Sensitivity of Mg-6sn and Mg-6sn-3y Alloys 396-406
Güven YARKADAŞ*

Design and Analysis of Multi-Band Compact Microstrip Antenna in Gsm1900/Wlan/Wimax/Dsrc/X-Band Frequency Bands for Vehicle Applications 407-418
Hüsnü YALDUZ*, Hüseyin ÇİZMECİ

Detection of Pneumonia from X-Ray Images Using Deep Learning Techniques 419-440
Halit BAKIR*, Semih OKTAY, Timuçin Emre TABARU

Ecological Evaluation of Uncommon Heavy Metals Contamination in the Soils of the Central Province of Uşak, Western Türkiye 441-456
Ümit YILDIZ*

REVIEW ARTICLE

Biosensors: Types, Applications, and Future Advantages 457-481
Aleyna GÜNDOĞDU, Gizem GAZOĞLU, Elif KAHRAMAN, Esmâ YILDIZ, Gıem CANDIR, Duygu YALÇIN, Atakan KOÇ, Fatih ŞEN*



RESEARCH ARTICLE

EFFECTS OF GRAVITY'S RAINBOW ON A RELATIVISTIC SPIN-1 OSCILLATOR

Semra GÜRTAŞ DOĞAN*¹

*¹Hakkari University, Department of Medical Imaging Techniques, Hakkari, semragurtasdogan@hakkari.edu.tr,
ORCID: <https://orcid.org/0000-0001-7345-3287>

Receive Date: 28.10.2022

Accepted Date: 04.01.2023

ABSTRACT

We consider a relativistic spin-1 particle with non-minimal coupling in the context of gravity's rainbow in the three dimensional background spacetime spanned by static cosmic string. In this context, we acquire an exact solution of the associated spin-1 equation in the modified three dimensional static cosmic string-spanned background spacetime. This relativistic wave equation includes a reducible spinor and this allows us to acquire a non-perturbative expression including the modification functions in the energy domain. In the low energy limit, our results agree well with current literature and provide a basis to discuss the fundamental features of the relativistic spin-1 oscillator. Afterwards, we try to discuss the effects of gravity rainbow functions on the considered spin-1 oscillator in three different scenarios for the modification functions.

Keywords: *Gravity rainbow, Spin-1 oscillator, Planck energy, Doubly special relativity, Cosmic string, Topological defect*

1. INTRODUCTION

A useful way to determine the effects of a curved space or a non-trivial topology on the relativistic dynamics of quantum mechanical systems (QMSs) is to solve the corresponding forms of the covariant wave equations such as Duffin Kemmer Petiau (DKP), Vector boson (VB), the generalized Klein Gordon (KG), Dirac and fully-covariant many-body equations. It was showed the relativistic wave equations describing the dynamics of spinning particles, such as spin-1/2, spin-1, spin-2 etc., can be derived from the canonical quantization of the action for spinning classical particles [1]. There is a unifying principle to derive the well-known relativistic wave equations. That is, these equations can be reproduced as different quantum states of the same classical system [1]. The well-known DKP equation's spin-1 sector in three dimensions corresponds to the spin-1 equation, which was obtained as an excited state of Zitterbewegung [2–5]. This spin-1 equation includes a reducible spinor and yields 3×3 dimensional matrix equation in any 2+1 dimensional spacetime [6, 7]. In the current literature, we see that relativistic dynamics of the spin-0 bosons are studied through solving the spin-0 sector of the DKP equation [8] and the KG equation [9]. Due to the relative complexity, there is not much research based on the dynamics of spin-1 bosons in curved spaces [4–7,10]. The announced results

have shown that the covariant VB equation can provide a strong basis to analyse the dynamics of relativistic spin-1 particles in any 2+1 dimensional spacetime [4–7, 10]. Furthermore, this equation was also used to analyse the quantum gravity effects on the Hawking temperature of three dimensional black holes [11, 12]. It is thought that studies focus on the relativistic quantum systems's (Qs) dynamics in curved spaces can serve to establish a complete theory combining the main areas of physics such as relativity (c), quantum theory (\hbar) and gravity (G) since we do not yet have a complete theory that merges these areas. A useful way to determine the influence of a curved space on the physical systems is to use the exactly soluble systems such as the relativistic quantum oscillators [6, 13–16] and Hydrogen or Positronium like low-energy bound state systems [17–19]. After the Dirac oscillator (DO) [20], describing the interaction of a changing (linearly) electric field with an anomalous magnetic moment, had been introduced, the KG oscillator [21], DKP oscillator [22] and VB oscillator [23, 24] were introduced through establishing an analogy to the DO. The relativistic oscillators describe real physical systems [25, 26] and have several applications [27–35] in many areas of modern physics. Furthermore, the relativistic oscillators are the most preferred systems to determine the effects of topological defects on the associated systems and one of the most famous topological defects is the cosmic string. The cosmic strings [36] were introduced first by one-body solution of Einstein field equations in three dimensions [37, 38] and the results naturally extended to 3+1 dimensions [39] where there is a dynamical symmetry [15,19]. These objects are stable one-dimensional topological defects that are thought to have formed at the early stages of the universe [36] and they may cause several interesting phenomena in the universe [19,36]. Moreover, it is also known that the spatial part of the line element representing the static cosmic string-spaced spacetime describes the topological defect appearing in materials backgrounds [15]. For this reason, exact results acquired for relativistic QMSs in topological defect-induced background spacetimes have great importance in modern physics and such investigations have attained great attention by many research groups. Moreover, we are aware of relationships between the topological characteristics of the space and local physical laws, such that the local intrinsic geometry of the space is insufficient to exactly describe the physics of any system. Therefore, it is crucial to look at how, for instance, a nontrivial topology affects a QS. Also, in addition to the use of QMSs to detect gravitational waves [40], the effect of gravitational fields produced by cosmic strings on QSs has long drawn significant interest [41-43]. In what follows, we will deal with a relativistic spin-1 oscillator in the three dimensional background geometry induced by static cosmic string (see also [44]) and will try to obtain non-perturbative results including the effects of gravity's rainbow functions on such a spin-1 oscillator.

On the other hand, some semi-classical approaches are thought as very helpful to investigate the affects of gravity on the dynamics of physical systems due to the fact that we have not a well-established or a fully-fledged theory to determine the influence of gravity on the QSs. One of these interesting semi-classical approaches is the context of the gravity's rainbow scenario called sometimes also as doubly general relativity [45–47]. This interesting semi-classical approach has been applied to determine the effects of gravity on the relativistic QMSs [48, 49]. Briefly, in this context, as a result of a nonlinear Lorentz transformation in momentum space, the metric describing the background spacetime becomes energy-dependent and accordingly the relativistic dispersion relation is modified [48, 49]. In this scenario, the test fields feel a different geometry for each different frequency and also Planck length (or energy) and speed of light remain observer-independent [50–52]. Hence, at very high energy, we may investigate the influence of gravity on the QSs by using the spacetime metrics

modified according to the modified relativistic dispersion relation [53, 54]. This is also suggested according to observational consequences [46, 47, 50, 54]. The gravity's rainbow approach was used to investigate black hole thermodynamics [55], casimir effect [56], spin-0 field in the Schwarzschild metric [57], relativistic spin-1/2 oscillator in a topological defect-generated background spacetime [48] relativistic spin-0 oscillator in a global monopole spacetime [49], wormhole geometry [58,59] and the massive scalar field with Casimir effect [60]. In addition to these works, a massless spin-1 field was studied in the cosmic string background spacetime in the context of gravity's rainbow [61]. In this contribution, we will use the gravity's rainbow approach to determine the effects of gravity on a relativistic spin-1 oscillator through obtaining an analytical solution of the associated covariant VB equation in the modified 2+1 dimensional spacetime generated by a static point source. Then, we will compare our results with the literature in the low energy limit (LEL) where gravity's rainbow corrections vanish.

We organized this contribution as follows: in the second section we give the mathematical procedure, in the third section we derive a 3×3 matrix equation for the considered test field and determine the corresponding solution function. Accordingly, we arrive at a nonperturbative energy expression including the gravity rainbow corrections in general form. Then, we analyse the results in both LEL and very high energy limit in three different scenarios for the modification functions. In sec. (4), we give a summary and discuss the findings in details.

2. MATHEMATICAL PROCEDURE

Here, we introduce the relativistic spin-1 equation for a general spin-1 field and derive its' associated form to analyse the dynamics of a VB particle in the point source-generated background spacetime (2+1 dimensional cosmic string spacetime) in the context of gravity's rainbow. In any three dimensional curved space, the spin-1 equation can be written as follows [1, 4–6]

$$\left\{ \frac{1}{2} [\gamma^\mu \otimes I_2 + I_2 \otimes \gamma^\mu] \nabla_\mu + i\mathcal{M}I_4 \right\} \Phi = 0, \quad (1)$$

$$\nabla_\mu = \partial_\mu - \Gamma_\mu \otimes I_2 - I_2 \otimes \Gamma_\mu, \quad \mu = 0,1,2.$$

In this equation, γ^μ stand for the space-free Dirac matrices (DMs), Γ_μ represent spinorial affine connections for a Dirac field, I_2 and I_4 are the 2×2 and 4×4 unit matrices and Φ is the relativistic spin-1 field with mass of M and we will use the units $\hbar = c = 1$. Now, we will try to obtain a matrix equation describing the dynamics of the system under scrutiny. To do this, we should obtain the associated operators such as the space-dependent DMs and the spinorial connections in the Eq. (1). These operators can be determined through the following relation [19]:

$$\Gamma_\xi^\alpha = \frac{1}{4} g_{\mu\alpha} \left[e_{\nu,\xi}^{(a)} e_{(a)}^\alpha - \Gamma_{\nu\xi}^\alpha \right] \gamma^\mu \gamma^\nu, \quad \xi, \mu, \nu, \alpha, a = 0,1,2. \quad (2)$$

Here, the $\Gamma_{\nu\xi}^\alpha$ are the Christoffel symbols that can be determined by [19],

$$\Gamma_{\nu\xi}^{\alpha} = \frac{1}{2}g^{\alpha\epsilon}\{\partial_{\nu}g_{\xi\alpha} + \partial_{\xi}g_{\epsilon\nu} - \partial_{\epsilon}g_{\nu\xi}\}, \quad (3)$$

and $g_{\mu\alpha}$ is the metric tensor in covariant form. Here, $g^{\alpha\epsilon}$ is inverse of the covariant metric tensor. It should also be noted that the Greek indices represent the curved spacetime's coordinates. To determine the spinorial affine connections, we need to construct the space dependent DMs, γ^{μ} . These matrices can be constructed through the relation: $\gamma^{\mu} = e_{(a)}^{\mu} \gamma^{(a)}$ where $e_{(a)}^{\mu}$ are the tetrads (inverse) and $\gamma^{(a)}$ indicate the flat DMs [19]. It is known that the flat DMs can be expressed in terms of the Pauli matrices in any 2+1 dimensional spacetime background. The tetrad fields, $e_{\mu}^{(a)}$, are obtained through the relation: $g_{\mu\tau} = e_{\mu}^{(a)} e_{\tau}^{(b)} \eta_{(a)(b)}$, where $\eta_{(a)(b)}$ represents the Minkowski metric tensor (flat). It should be noted that the tetrad choices are not unique. That is, other choices can be preferred as long as the orthonormality, orthogonality and Clifford-Dirac algebra requirements are satisfied [13, 15]. Here, we should underline that the Latin indices indicate the coordinates of the flat Minkowski spacetime while the Greek indices represent the curved background's coordinates. It is useful to mention that there is no consensus about the shape of the modification functions within the framework of the gravity rainbow. Hence, for each case the relativistic dispersion relation is modified differently [48, 49]. For the used three cases [48, 49], the momentum operators in the relativistic wave equations are altered and accordingly the total energy (at very high energies) is changed. Although, there are different suggestions on how to choose the modification functions [48, 49], for each choice the corresponding dispersion relation must result in the usual relativistic dispersion relation in the LEL. This means that the obtained results for QMSs in the context of gravity rainbow must give the usual results obtained in the usual relativistic framework. Now, we can write the modified relativistic dispersion relation and then give the static cosmic string-generated 2+1 dimensional background geometry in the context of the gravity's rainbow scenario. The rainbow gravity originates from deformations of the Lorentz symmetry. This deformation can be represented, formally, through the following relativistic dispersion relation [48, 49]

$$\mathcal{E}^2 \mathcal{G}_0(\mathcal{X})^2 - \mathcal{P}^2 \mathcal{G}_1(\mathcal{X})^2 = \mathcal{M}^2,$$

where, \mathcal{E} is energy of the VB in question and \mathcal{P} is momentum of this particle possessing mass of \mathcal{M} . The modification functions $\mathcal{G}_0(\mathcal{X})$ and $\mathcal{G}_1(\mathcal{X})$ are the rainbow functions in which the argument $\mathcal{X} = \mathcal{E} / \mathcal{E}_p$ and $\mathcal{E}_p \sim 1.22 \times 10^{19}$ GeV is the Planck energy. Here, it is very important that the gravity rainbow functions are reduced into 1 in the LEL where $\mathcal{E} / \mathcal{E}_p \rightarrow 0$. In this limit, it is clear that one can recover the usual relativistic dispersion relation. In this scenario, the 2+1 dimensional static cosmic string spacetime known also as point source-generated spacetime can be written, with negative signature (+, -, -) as follows [48]

$$dS^2 = \mathcal{G}_0(\mathcal{X})^{-2} dt^2 - \mathcal{G}_1(\mathcal{X})^{-2} [d\rho^2 + \eta^2 \rho^2 d\phi^2] \quad (4)$$

This metric describes the usual polar space when $\eta = 1$ in the LEL, $\mathcal{E} \rightarrow 0$ for which $\mathcal{G}_k(\mathcal{X}) \rightarrow 1$, ($k = 0, 1$). In the presence of the topological defect ($0 < \eta < 1$), the background cannot be flat globally even though it is flat locally. Thus, the topology and accordingly symmetry of the background geometry is altered by the string tension [19]. For more details about the 2+1 dimensional static

cosmic string (point source)-induced spacetime can be found in the Refs. [19, 37, 38]. Now, we can easily write the covariant ($g_{\mu\alpha}$) and contravariant ($g^{\mu\alpha}$) metric tensors

$$g_{\mu\alpha} = \text{diag}(\mathcal{G}_0(\mathcal{X})^{-2}, -\mathcal{G}_1(\mathcal{X})^{-2}, -\mathcal{G}_1(\mathcal{X})^{-2}\eta^2\rho^2)$$

$$g^{\mu\alpha} = \text{diag}(\mathcal{G}_0(\mathcal{X})^2, -\mathcal{G}_1(\mathcal{X})^2, -\mathcal{G}_1(\mathcal{X})^2\eta^{-2}\rho^{-2})$$

Through these expressions and Eq. (3), one can evaluate the components (non-vanishing) of the Christoffel symbols as follows, by using the relation given in [19],

$$\Gamma_{\phi\phi}^{\rho} = -\eta^2\rho, \quad \Gamma_{\rho\phi}^{\phi} = \frac{1}{\rho}. \quad (5)$$

It is also known that we can chose the space-free DMs by means of Pauli matrices and such a choice is not unique. So, different choices are acceptable provided that the signature in the Eq. (4) are satisfied. Here we choice the flat DMs as the following: $\gamma^0 = \sigma^3$, $\gamma^1 = i\sigma^1$, and $\gamma^2 = i\sigma^2$ [19]. To construct the space-dependent DMs we need to the tetrad fields. Through the mentioned procedure before, one can obtain the tetrad fields and can arrive at the following results

$$e^{(a)}_{\mu} = \text{diag}(\mathcal{G}_0(\mathcal{X})^{-1}, -\mathcal{G}_1(\mathcal{X})^{-1}, -\mathcal{G}_1(\mathcal{X})^{-1}\eta\rho)$$

$$e^{(\mu)}_a = \text{diag}(\mathcal{G}_0(\mathcal{X}), -\mathcal{G}_1(\mathcal{X}), -\mathcal{G}_1(\mathcal{X})\eta^{-1}\rho^{-1}). \quad (6)$$

Now, by using these expressions, we can construct the generalized DMs

$$\gamma^t = \mathcal{G}_0(\mathcal{X}) \begin{pmatrix} 1 & 0 \\ 0 & -1 \end{pmatrix}, \quad \gamma^{\rho} = i\mathcal{G}_1(\mathcal{X}) \begin{pmatrix} 0 & 1 \\ 1 & 0 \end{pmatrix}, \quad \gamma^{\phi} = \frac{\mathcal{G}_1(\mathcal{X})}{\eta\rho} \begin{pmatrix} 0 & 1 \\ -1 & 0 \end{pmatrix}. \quad (7)$$

Furthermore, by using the obtained results it can be found that the spinorial affine connections have only one non-vanishing component. This one is obtained as follows

$$\Gamma_{\phi} = \frac{i}{2}\eta \begin{pmatrix} 1 & 0 \\ 0 & -1 \end{pmatrix}. \quad (8)$$

In this manuscript, we interest in a spin-1 oscillator in the 2+1 dimensional spacetime generated by static cosmic string in the context of gravity's rainbow. To derive the corresponding matrix equation for the system in question, we need to introduce the oscillator coupling. The spin-1 oscillator [6, 10] is introduced by adding a non-minimal interaction term in such a way that $\partial_{\rho} \rightarrow \partial_{\rho} + \mathcal{M}\omega_0(\sigma_3 \otimes \sigma_3)\rho$ where ω_0 is oscillator frequency and $\sigma_3 \otimes \sigma_3 = \text{diag}(1, -1, -1, 1)$. For the considered system, the symmetric spinor Φ can be factorised as $\Phi = e^{-i\mathbf{E}t} e^{i\mathbf{s}\Phi} (\vartheta_1(\rho), \vartheta_2(\rho), \vartheta_3(\rho), \vartheta_4(\rho))^{\mathbf{T}}$, in which \mathbf{T} means transpose of the matrix, according to the line element given in the Eq. (4).

3. EFFECTS OF GRAVITY'S RAINBOW FUNCTIONS

Here, we obtain a matrix equation consisting of coupled equations and then try to solve this equation. By inserting the obtained results in the Eq. (7) and Eq. (8) into the Eq. (1), one obtains a 4×4 dimensional matrix equation in reducible form (see also [62]). This equation can be rewritten by defining a new dimensionless independent variable, $z = \kappa\rho^2$, as follows

$$\begin{pmatrix} \widehat{\mathcal{D}}^* & \widetilde{\mathcal{M}} & -\frac{\tilde{s}}{\sqrt{z/\kappa}} \\ \tilde{\mathcal{E}} & -\frac{\tilde{s}}{\sqrt{z/\kappa}} & -\widetilde{\mathcal{M}} \\ -\mathcal{M} & -\widehat{\mathcal{D}}^\dagger & \tilde{\mathcal{E}} \end{pmatrix} \begin{pmatrix} \vartheta_+(z) \\ \vartheta_0(z) \\ \vartheta_-(z) \end{pmatrix} = 0 \quad (9)$$

where

$$\widehat{\mathcal{D}}^* = 2\kappa\sqrt{\frac{z}{\kappa}}\left(\partial_z + \frac{1}{2} + \frac{1}{2z}\right), \quad \widehat{\mathcal{D}}^\dagger = 2\kappa\sqrt{\frac{z}{\kappa}}\left(\partial_z - \frac{1}{2}\right)$$

$$\widetilde{\mathcal{M}} = \frac{\mathcal{M}}{g_1(\mathcal{X})}, \quad \tilde{\mathcal{E}} = \varepsilon \frac{g_0(\mathcal{X})}{g_1(\mathcal{X})}, \quad \tilde{s} = \frac{s}{\eta},$$

$\vartheta_\pm(z) = \vartheta_1(z) \pm \vartheta_2(z)$ and $\vartheta_0(z) = 2\vartheta_2(z)$ since $\vartheta_2(z) = \vartheta_3(z)$. Under these definitions, one of these equations becomes algebraic and this allows us to derive a non-perturbative wave equation. That is, by solving this set of equations for the $\vartheta_0(z)$ one derives a second order differential equation and moreover the resulting equation can be reduced into the following familiar form

$$\left(\frac{d^2}{dz^2} - \frac{1}{4} + \frac{q}{z} + \frac{\frac{1}{4} - p^2}{z^2}\right)\vartheta(z) = 0, \quad (10)$$

by considering an ansatz function, $\vartheta_0(z) = \vartheta(z)/\sqrt{z}$. By this way we arrive at the Whittaker equation and its regular solution [26] can be expressed as $\vartheta(z) = C W_{q,p}(z)$ where

$$q = -\frac{1}{2} - \frac{(\widetilde{\mathcal{M}}^2 - \tilde{\mathcal{E}}^2)}{4\kappa} + \frac{2\tilde{\mathcal{E}}\tilde{s}}{4\widetilde{\mathcal{M}}}, \quad p = \frac{s}{2}.$$

and C is a normalization constant. This solution function can also be expressed by means of confluent hypergeometric function, ${}_1F_1$ and it diverges when $z \rightarrow \infty$. Thus, we need to impose the following condition: $\frac{1}{2} + p - q = -n$, in which $n = 0, 1, 2, \dots$ is the overtone number, to acquire polynomial solution [26]. At that rate, the solution function becomes well-behaved and this termination leads a non-perturbative expression in energy domain

$$\mathcal{E}_{n,s}(\mathcal{X}) = -\frac{s\omega_0 g_1(\mathcal{X})^2}{n g_0(\mathcal{X})} \pm \frac{\mathcal{M}}{g_0(\mathcal{X})} \sqrt{1 + \frac{4\omega_0 g_1(\mathcal{X})^2}{\mathcal{M}} \mathcal{N} + \frac{s^2 \omega_0^2 g_1(\mathcal{X})^4}{\eta^2 \mathcal{M}^2}}, \quad (11)$$

$$\mathcal{N} = \left(n + 1 + \frac{s}{2\eta}\right).$$

This energy spectrum becomes as follows

$$\mathcal{E}_{n,s} = -s\omega_0 \pm \mathcal{M} \sqrt{1 + \frac{4\omega_0}{\mathcal{M}} \left(n + 1 + \frac{s}{2}\right) + \frac{s^2\omega_0^2}{\mathcal{M}^2}}, \quad (12)$$

when $\eta=1$ in the LEL where $\lim_{\mathcal{X} \rightarrow 0} \mathcal{G}_k(\mathcal{X})$, $k = 0,1$. It can be important that the result given by Eq. (12) gives exact result for a composite structure holding together by DO coupling, when $s = 0$ [26], and it can be also seen that it agrees well with the result obtained for one dimensional DO [26]. In a three dimensional spacetime background there are two spatial degrees of freedom. Accordingly, any spectra obtained for Qs must include two quantum numbers. This is why our results give the previously obtained results for one dimensional systems when we ignore the spin contributions. Now, we can discuss the energy spectrum in the Eq. (11). At first look, we see that the oscillator frequency couples with the spin and this coupling is altered by the string tension ($\propto \eta$) since there exists $\frac{s\omega_0}{\eta}$ terms in the spectrum even in the LEL. Also, we see that relativistic energy ($\mathcal{E}_{n,s}$) becomes $\mathcal{E} \sim \pm \mathcal{M}$ when $\omega \rightarrow 0$ and $\mathcal{X} \rightarrow 0$. In the LEL, dependence of the relativistic energy levels on the oscillator frequency can be seen in the Figure (1). This also shows that the VB oscillator does not stop oscillating even in the ground state and positive-negative energy states never mix. Now, we can discuss the results in three different scenarios for the gravity rainbow functions. Let we start the first case where [48, 49]

$$\mathcal{G}_0(\mathcal{X}) = \frac{e^{\mathcal{X}} - 1}{\mathcal{X}}, \quad \mathcal{G}_1(\mathcal{X}) = 1. \quad (13)$$

This choice was proposed to describe gamma-ray burst phenomena in the universe [63–65]. In this case, the energy expression in the Eq. (11) can be written as the following

$$\mathcal{X} = -\frac{s\omega_0\mathcal{X}}{\eta\varepsilon_p(e^{\mathcal{X}}-1)} \pm \frac{\mathcal{M}\mathcal{X}}{\varepsilon_p(e^{\mathcal{X}}-1)} \sqrt{1 + \frac{4\omega_0}{\mathcal{M}} \mathcal{N} + \frac{s^2\omega_0^2}{\eta^2\mathcal{M}^2}}, \quad (14)$$

and by solving this expression for \mathcal{X} one can acquire the following expressions

$$\mathcal{X}_{1,2} = \ln \left[\pm 1 \mp \frac{s\omega_0}{\eta\varepsilon_p} \pm \frac{\mathcal{M}}{\varepsilon_p} \sqrt{1 + \frac{4\omega_0}{\mathcal{M}} \mathcal{N} + \frac{s^2\omega_0^2}{\eta^2\mathcal{M}^2}} \right]. \quad (15)$$

Here, it is clear that the energy of the considered system is altered by one of the gravity rainbow functions and this alterations on the relativistic energy levels can be seen in the Figure (2) and Figure (3). In this parts, we see that the magnitude of the relativistic energy levels is increased by the gravity rainbow effect according to the first scenario.

Also, we can choose the modification functions according to proposal of both non-commutative geometry and loop quantum gravity [56, 63]. In this case the modification functions were considered as $\mathcal{G}_0(\mathcal{X}) = 1$, $\mathcal{G}_1(\mathcal{X}) = \sqrt{1 - \gamma\mathcal{X}^2}$ for which the energy expression can be written as the following form

$$\mathcal{X} = -\frac{s}{\eta}\Omega(1 - \gamma\mathcal{X}^2) \pm m\sqrt{1 + \frac{4\Omega}{m}(1 - \gamma\mathcal{X}^2)\mathcal{N} + \frac{s^2\Omega^2}{\eta^2m^2}(1 - \gamma\mathcal{X}^2)^2}, \quad (16)$$

$$\Omega = \frac{\omega_0}{\varepsilon_p}, \quad m = \frac{\mathcal{M}}{\varepsilon_p}.$$

Here, it seems not possible to obtain an expression in closed form for \mathcal{X} except for $s = 0$. However, we can discuss the effects of gravity's rainbow functions on the corresponding wave function(s). In this second scenario, the altered wave function(s) can be seen in the Figure (4). In this figure, we can also see the low energy ("usual") case for $\gamma = 0$. The others include the effects of one of the gravity rainbow functions, $\mathcal{G}_1(\mathcal{X})$, since $\mathcal{G}_0(\mathcal{X}) = 1$. The Figure (4) shows that amplitude of the normalized wave function(s) increases as the energy of the VB oscillator increases. In the third scenario, stemming from the need for constant velocity of light, proposed for solve the horizon problem puzzle, the modification functions are $\mathcal{G}_0(\mathcal{X}) = \frac{1}{1-\gamma\mathcal{X}}$ and $\mathcal{G}_1(\mathcal{X}) = \frac{1}{1-\gamma\mathcal{X}}$. For this, the energy expression can be expressed as follows

$$\mathcal{X} = -\frac{s\Omega}{\eta(1-\gamma\mathcal{X})} \pm m(1 - \gamma\mathcal{X})\sqrt{1 + \frac{4\Omega}{m(1-\gamma\mathcal{X})^2} + \frac{s^2\Omega^2}{\eta^2m^2(1-\gamma\mathcal{X})^2}}. \quad (17)$$

For this latest case, one can arrive that it is not possible to obtain an expression in closed-form for \mathcal{X} . Hence, we cannot see clearly what the dependence of the energy levels on the modification functions. However, we have plotted the effects of modification functions on the wave function(s) in the Figure (5). In this figure, we see that amplitude of the wave functions decreases in the presence of gravity's rainbow effect. However, space-dependence of the normalized wave functions seems to be same whether $\gamma = 0.1$ or $\gamma = 0.9$.

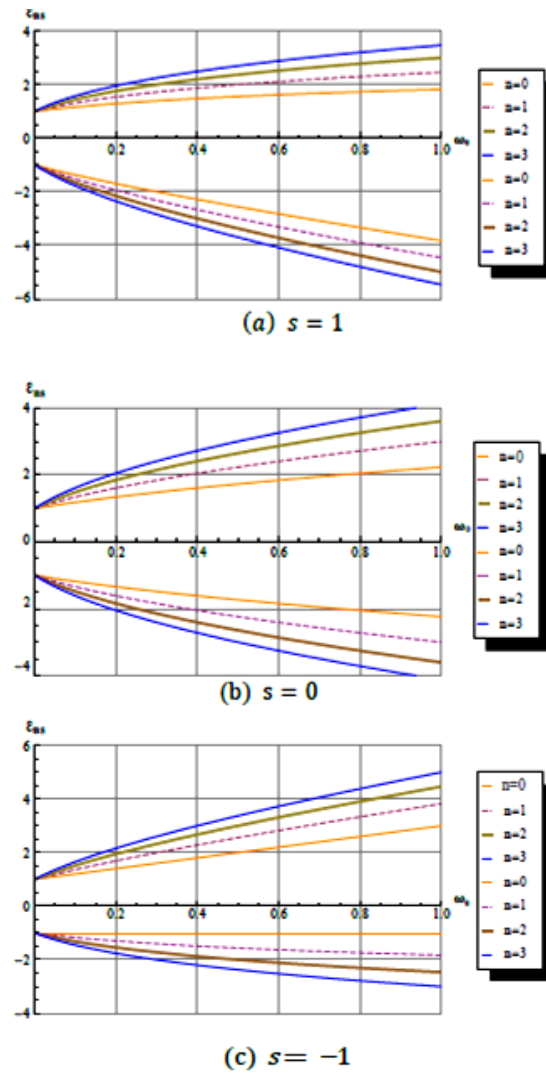
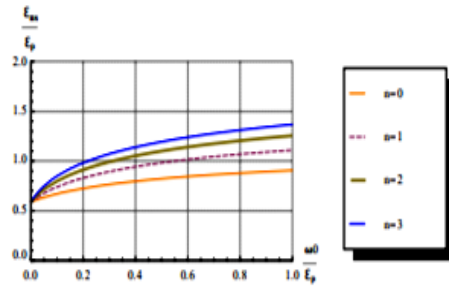
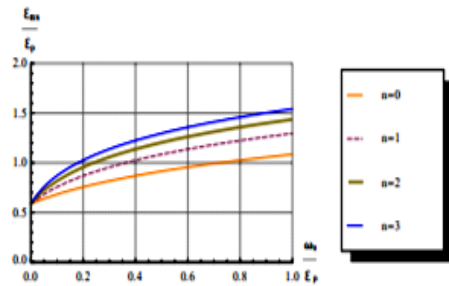


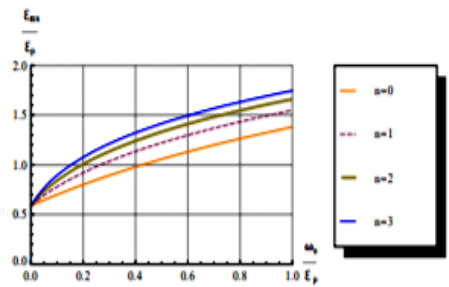
Figure 1. Behaviour of the relativistic energy levels with respect to the oscillator frequency in the LEL. Here, we get that $\mathcal{M} = 1$, $\eta = 1$.



(a) $s = 1.$



(b) $s = 0.$



(c) $s = -1.$

Figure 2. Alterations on the energy levels in high energy limit. Here, we get than $\frac{\mathcal{M}}{\varepsilon_p} = 0.8, \eta = 0.9.$

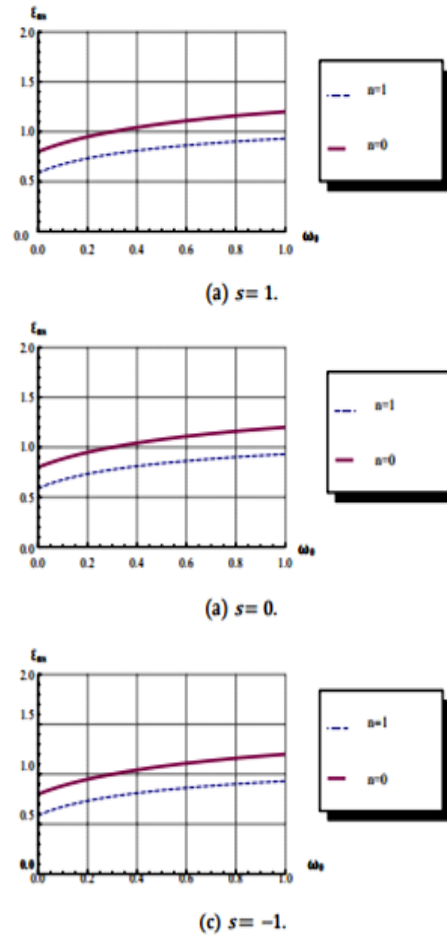


Figure 3. Effects of gravity's rainbow on the possible spin states for $\mathcal{M} = 0.8$, $\eta = 1$. Here, the dashed lines show the usual case and the others show the energy levels altered by the gravity rainbow effect if $\mathcal{G}_0(\mathcal{X}) = \frac{e^{\mathcal{X}} - 1}{\mathcal{X}}$, $\mathcal{G}_1(\mathcal{X}) = 1$.

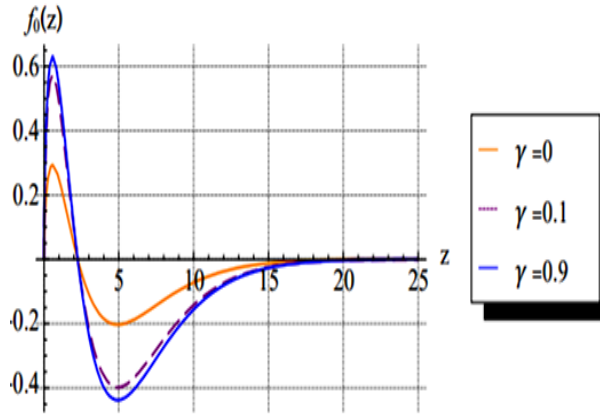


Figure 4. Space dependence of the wave functions (normalized) for different values of the parameter γ in the second scenario where $G_0(\mathcal{X}) = 1$, $G_1(\mathcal{X}) = \sqrt{1 - \gamma\mathcal{X}^2}$. Here, we get that $\mathcal{M} = 0.6$, $n = 1$, $\eta = 0.8$, $\omega = 0.6$, $s = 1$, $\mathcal{E}_p = 1$.

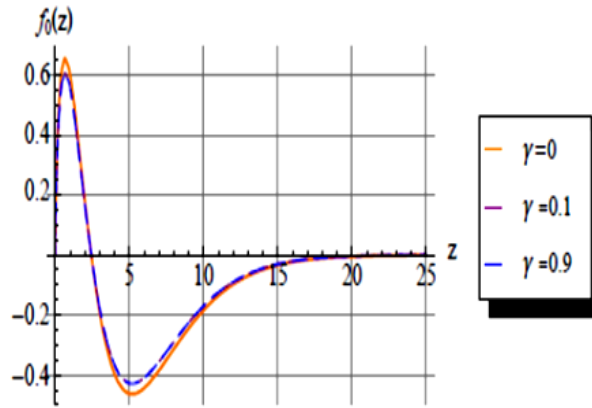


Figure 5. The normalized wave functions for the cases given in third case, according to the changing values of the parameter γ . Here, we get that $\mathcal{M} = 1$, $n = 1$, $\eta = 0.8$, $\omega = 0.6$, $s = 1$, $\mathcal{E}_p = 1$.

4. SUMMARY AND RESULTS

Here, we have interested in a relativistic VB oscillator in the context of gravity's rainbow in the 2+1 dimensional cosmic string-induced background geometry. According to the modified dispersion relation, by solving the fully covariant spin-1 equation in this background we have arrived at a non-perturbative energy expression including the modification functions. This expression is given in the

Eq. (11) and it can be reduced into the results in the Eq. (12) in the low energy limit (LEL) where relativistic energy (\mathcal{E}) of the particle is very small according to the Planck energy (\mathcal{E}_p) by assuming the background geometry is globally flat ($\eta = 1$). In the $\mathcal{E}/\mathcal{E}_p \rightarrow 0$ case, our results show that spin of the relativistic VB couples with the oscillator frequency and this influences the symmetry of the energy levels for particle-antiparticle states even when $\eta = 1$. For this usual case, behaviour of the energy levels according to the oscillator frequency (ω_0) is plotted in the Figure (1). This also shows that the VB oscillator does not stop oscillating even in the ground state and positive-negative energy states never mix. In this figure, one can see that magnitude of the energy levels increases for increasing values of the ω_0 and it can be seen also that $\mathcal{E} \sim \pm \mathcal{M}$, where \mathcal{M} is the rest mass of the VB particle, if $\omega_0 \rightarrow 0$. Here, we have observed that the effects of string tension ($\propto \eta$) on spin states ($s = 0, \pm 1$) of the spin-1 oscillator cannot be same due to the $\frac{s\omega_0}{\eta}$ terms in the energy spectrum. In the LEL, the resulting energy spectrum gives exact result obtained for a composite structure composed by a fermion-antifermion system holding together by DO interaction [26] if $s = 0$ when $\eta = 1$ and agrees well with the current literature (see also [10, 26]). That is, our results provide a strong basis for the effects of gravity's rainbow on the relativistic spin-1 oscillator. Here, it is very important to note that it may not be possible to show what the effect of the modification functions on the energy levels of the system in each shape of the modification functions even though the Eq. (11) is an algebraic equation. This is because the parameter \mathcal{X} depends explicitly on the energy of the system in question. According to the first scenario where the modification functions are $\mathcal{G}_0(\mathcal{X}) = \frac{e^{\mathcal{X}} - 1}{\mathcal{X}}$, $\mathcal{G}_1(\mathcal{X}) = 1$ and it is clear that the energy levels are altered by only one of these functions. For this, we have observed that the magnitude of the energy levels increases as oscillator frequency increases (see Figure 3). In the second scenario where $\mathcal{G}_0(\mathcal{X}) = 1$, $\mathcal{G}_1(\mathcal{X}) = \sqrt{1 - \gamma\mathcal{X}^2}$ we gave an expression including the effect of modification function in energy domain (see Eq. 16). In this case, we could not find any way to show what the dependence of the energy levels on the modification functions without loss of generality since the energy expression in the Eq. (16) do not allow to obtain an expression (in closed-form) that gives clearly the altered particle-antiparticle energy states. However, we showed the effects of the modification functions on the normalized wave functions with respect to the second scenario. In the Figure (4), one can see that magnitude of the normalized wave functions increases if the relativistic energy of the VB oscillator closes to Planck energy. In the latest case, the third case, we have encountered a similar technical problem. That is, we could not find explicit expressions showing the dependence of the particle-antiparticle energy levels on the modification functions even though we have arrived at a non-perturbative expression for the energy if $\mathcal{G}_0(\mathcal{X}) = \frac{1}{1 - \gamma\mathcal{X}}$ and $\mathcal{G}_1(\mathcal{X}) = \frac{1}{1 - \gamma\mathcal{X}}$. In this case, we have observed that amplitude of the normalized wave functions decreases for big values of the parameter and also we have seen that the amplitude seems not dramatically change whether the energy of the spin-one oscillator closes to Planck energy or very small with respect to it.

ACKNOWLEDGEMENTS

The author thanks the reviewers for important questions, valuable comments, careful reading and useful suggestions

REFERENCES

- [1] Barut, A. O. (1990). Excited states of zitterbewegung. *Physics Letters B*, 237, 436–439.
- [2] Unal, N. (1997). A simple model of the classical zitterbewegung: photon wave function. *Foundations of Physics*, 27, 731–746.
- [3] Unal, N. (1998). Path Integral Quantization of a Spinning Particle. *Foundations of Physics*, 28, 755–762.
- [4] Sucu, Y., Unal, N. (2005). Vector bosons in the expanding universe, *The European Physical Journal C*, 44, 287–291.
- [5] Sucu, Y., Tekincay, C. (2019). Photon in the Earth-ionosphere cavity: Schumann resonances. *Astrophysics and Space Science*, 364, 1–7.
- [6] Guvendi, A., Zare, S. and Hassanabadi, H. (2021). Vector boson oscillator in the spiral dislocation spacetime, *European Physical Journal A*, 57, 1–6..
- [7] Dogan, S.G. (2022). Landau Quantization for Relativistic Vector Bosons in a Gödel-Type Geometric Background. *Few-Body Systems*, 63, 1–10.
- [8] Hosseinpour, M., Hassanabadi, H., Kriz, J., Hassanabadi, S., Lutfuoğlu, B.C. (2021). Interaction of the generalized DKP equation with a non-minimal coupling under the cosmic rainbow gravity. *International Journal of Geometric Methods in Modern Physics*, 18, 2150224.
- [9] Zare, S., Hassanabadi, H., Guvendi, A., Chung, W.S. (2022). On the interaction of a Cornell-type nonminimal coupling with the scalar field under the background of topological defects. *International Journal of Modern Physics A*, 37, 2250033.
- [10] Guvendi, A. and Hassanabadi, H. (2021). Relativistic Vector Bosons with non-minimal coupling in the spinning cosmic string spacetime. *Few-Body Systems*, 62, 1–8.
- [11] Gecim, G., Sucu, Y. (2017). Massive vector bosons tunnelled from the (2+1)-dimensional Blackholes. *The European Physical Journal Plus*, 132, 1–8.
- [12] Gecim, G., Sucu, Y. (2018). The GUP effect on tunneling of massive vector bosons from the 2+1 dimensional blackhole, *Advances in High Energy Physics*, 2018.
- [13] Carvalho, J., Furtado, C., Moraes, F. (2011). Dirac oscillator interacting with a topological Defect. *Physical Review A*, 84, 032109.
- [14] Ahmed, F. (2019). The Klein-Gordon oscillator in (1+2)-dimensions Gurses space-time Backgrounds. *Annals of Physics*, 404, 1–9.

- [15] Guvendi, A. (2021). Dynamics of a composite system in a point source-induced spacetime. *International Journal of modern Physics A*, 36, 2150144.
- [16] Guvendi, A., Hassanabadi, H. (2021). Noninertial effects on a composite system. *International Journal of Modern Physics A*, 36, 2150253.
- [17] Marques, G. A., Bezerra, V. B. (2002). Hydrogen atom in the gravitational fields of topological Defects. *Physical Review D*, 66, 105011.
- [18] Guvendi, A., Sahin, R., Sucu, Y. (2021). Binding energy and decaytime of exciton in dielectric medium. *The European Physical Journal B*, 94, 1–7.
- [19] Guvendi, A., Sucu, Y. (2020). An interacting fermion-antifermion pair in the spacetime background generated by static cosmic string. *Physics Letters B*, 811, 135960.
- [20] Moshinsky, M., Szczepaniak, A. (1989). The Dirac oscillator. *Journal of Physics A: Mathematical and General*, 22, L817.
- [21] Bruce, S., Minning, P. (1993). The Klein Gordon oscillator. *Il Nuovo Cimento A*, (1965-1970), 106, 711–713.
- [22] Nedjadi, Y., Barrett, R.C. (1994). The Duffin-Kemmer-Petiau oscillator. *Journal of Physics A: Mathematical and General*, 27, 4301.
- [23] Guvendi, A. (2021). Effects of Rotating Frame on a Vector Boson Oscillator. *Sakarya University Journal of Science*, 25, 834–840.
- [24] Dogan, S.G. (2021). Two-Dimensional Vector Boson Oscillator. *Sakarya University Journal of Science*, 25, 1210–1217.
- [25] Bentez, J., y Romero, R.P.M., Nuez-Yepeç, H.N., Salas- Brito, A.L. (1990). Solution and hidden supersymmetry of a Dirac oscillator. *Physical Review Letters*, 64, 1643 6.
- [26] Guvendi, A. (2021). Relativistic Landau levels for a fermion-antifermion pair interacting through Dirac oscillator interaction. *The European Physical Journal C*, 81, 1–7.
- [27] Mandal, B. P., Verma, S. (2010). Path integral solution of noncentral potential. *Physics Letters A* 374, 1021– 1023.
- [28] Bakke, K. (2013). Rotating effects on the Dirac oscillator in the cosmic string spacetime. *General Relativity and Gravitation*, 45, 1847– 1859
- [29] Vitoria, R.L., Bakke, K. (2016). Relativistic quantum effects of confining potentials on the Klein Gordon oscillator. *The European Physical Journal Plus*, 131, 1–8.

- [30] Soares, A.R., Vitoria, R.L.L., Aounallah, H. (2021). On the Klein–Gordon oscillator in topological charged Ellis–Bronnikov-type wormhole spacetime. *The European Physical Journal Plus*, 136, 1–8.
- [31] Zare, S., Hassanabadi, H., de Montigny, M. (2020). Non-inertial effects on a generalized DKP oscillator in a cosmic string space-time. *General Relativity and Gravitation*, 52, 1–20.
- [32] Guvendi, A., Boumali, A. (2021). Superstatistical properties of a fermion-antifermion pair interacting via Dirac oscillator coupling in one-dimension. *The European Physical Journal Plus*, 136, 1–18.
- [33] Zare, S., Hassanabadi H., Guvendi, A. (2022). Relativistic Landau quantization for a composite system in the spiral dislocation spacetime, *The European Physical Journal Plus*, 137, 1–8.
- [34] Guvendi, A., Dogan, S. G. (2022). Effect of internal magnetic flux on a relativistic spin-1 Oscillator in the spinning point source-generated spacetime, arXiv preprint arXiv:2206.09898.
- [35] Franco-Villafane, J.A., Sadurni, E., Barkhofen, S., Kuhl, U., Mortessagne, F., Seligman, T.H. (2013). First Experimental Realization of the Dirac Oscillator, *Physical Review Letters*, 111, 170405.
- [36] Vilenkin, A. (1985). Cosmic strings and domain walls. *Physics Reports*, 121, 263–315.
- [37] Deser, S., Jackiw, R., Hoof, G. (1984). Three-dimensional Einstein gravity: dynamics of flat Space. *Annals of Physics*, 152, 220–235.
- [38] Clement, G. (1990). Rotating string sources in three-dimensional gravity. *Annals of Physics*, 201, 241–257.
- [39] Gott, J.R., Alpert, M. (1984). General relativity in a (2+1)-dimensional space-time. *General Relativity and Gravitation*, 16, 243–247.
- [40] Dogan, S.G., Sucu, Y. (2019). Quasinormal modes of dirac field in 2+1 dimensional gravitational wave background. *Physics Letters B*, 797, 134839
- [41] Yeşiltaş, Ö. (2015). Su (1,1) solutions for the relativistic quantum particle in cosmic string Spacetime. *The European Physical Journal Plus*, 130, 7, 128.
- [42] Bakke, K., Furtado, C. (2020). Bound states for neutral particles in a rotating frame in the cosmic string spacetime, *Physical Review D*, 82, 084025.
- [43] Huang, Z. (2020). Quantum entanglement of nontrivial spacetime topology. *The European Physical Journal C*, 8:2, 1–8.

- [44] Guvendi, A. (2022). Influence of spinning topological defect on the Landau levels of relativistic spin-0 particles. *Journal of Scientific Reports-A*, 050, 245–253.
- [45] Magueijo, J., Smolin, L. (2003). Generalized Lorentz invariance with an invariant energy scale. *Physical Review D*, 67, 044017.
- [46] Magueijo, J., Smolin, L. (2004). Gravity's Rainbow. *Classical and Quantum Gravity*, 21, 1725.
- [47] Amelino-Camelia, G. (2013). Quantum Spacetime Phenomenology. *Living Reviews in Relativity*, 16, 1–137..
- [48] Bakke, K., Mota, H. (2018). Dirac oscillator in the cosmic string spacetime in the context of gravity's rainbow. *The European Physical Journal Plus*, 133, 1–9.
- [49] de Montigny, M., Pinfeld, J., Zare, S., Hassanabadi, H. (2022). Klein–Gordon oscillator in a global monopole space–time with rainbow gravity. *The European Physical Journal Plus*, 137, 1–17.
- [50] Amelino-Camelia, G. (2002). Relativity in spacetimes with short-distance structure governed by an observer-independent (Planckian) length scale. *International Journal of Modern Physics D*, 11, 35–59.
- [51] Magueijo, J., Smolin, L. (2002). Lorentz Invariance with an Invariant Energy Scale. *Physical Review Letters*, 88, 190403.
- [52] Galan, P., Marugan, G.A.M. (2004). Quantum time uncertainty in a gravity's rainbow formalism. *Physical Review D*, 70, 124003.
- [53] Jacob, U., Mercati, F., Amelino-Camelia, G., Piran, T. (2010). Modifications to Lorentz invariant dispersion in relatively boosted frames. *Physical Review D*, 82, 084021.
- [54] Amelino-Camelia, G., Ellis, J., Mavromatos, N.E., Nanopoulos, D.V., Sarkar, S. (1998). Tests of quantum gravity from observations of γ -ray bursts. *Nature*, 393, 763–765.
- [55] Hendi, S.H., Panah, B.E., Panahiyan, S. (2017). Topological charged black holes in massive gravity's rainbow and their thermodynamical analysis through various approaches, *Physics Letters B*, 769, 191–201.
- [56] Bezerra, V.B., Mota, H.F., Muniz, C.R. (2017). Casimir effect in the rainbow Einstein's universe. *Europhysics Letters*, 120, 10005.
- [57] Bezerra, V.B., Christiansen, H.R., Cunha, M.S., Muniz, C.R. (2017). Exact solutions and phenomenological constraints from massive scalars in a gravity's rainbow spacetime, *Physical Review D*, 96, 024018.

- [58] Garattini, R. and Lobo, F. S. N. (2012). Self-sustained wormholes in modified dispersion relations. *Physical Review D*, 85, 024043.
- [59] Garattini, R. and Lobo, F. S. N. (2018). Gravity's Rainbow and traversable wormholes. In *Fourteenth Marcel Grossmann Meeting - MG14*, 1448–1453.
- [60] Bezerra, V.B., Mota, H.F., Muniz, C.R. (2017). Casimir effect in the rainbow Einstein's universe. *Europhysics Letters*, 120, 10005.
- [61] Sogut, K., Salti, M., Aydogdu, O. (2021). Quantum dynamics of photon in rainbow gravity. *Annals of Physics*, 431, 168556.
- [62] Dogan, S.G. (2022). Landau Quantization for Relativistic Vector Bosons in a Gödel-Type Geometric Background. *Few-Body Systems*, 63, 1–10.
- [63] Hendi, S. H. Momennia, M., Panah, B. E., Panahiyan, S. (2017). Nonsingular universe in massive gravity's rainbow. *Physics of the Dark Universe*, 16, 26–33.
- [64] Awad, A., Ali, A. F., Majumder, B. (2013). Nonsingular rainbow universes. *Journal of Cosmology and Astroparticle Physics*, 2013, 052.
- [65] Bezerra, V.B., Christiansen, H.R., Cunha, M.S., Muniz, C.R. (2017). Exact solutions and phenomenological constraints from massive scalars in a gravity's rainbow spacetime. *Physical Review D*, 96, 024018.



RESEARCH ARTICLE

**INVERSE NEURO-FUZZY MODEL BASED CONTROLLER DESIGN FOR A PH
NEUTRALIZATION PROCESS**

Talha Burak AKCA^{1*}, Cenk ULU², Salih OBUT³

^{1*} Yildiz Technical University, Faculty of Mechanical Engineering, Mechatronics Engineering, Istanbul, tbakca@yildiz.edu.tr,
ORCID: 0000-0001-8786-0326

² Yildiz Technical University, Faculty of Mechanical Engineering, Mechatronics Engineering, Istanbul, cenkulu@yildiz.edu.tr,
ORCID: 0000-0002-8588-6247

³ Yildiz Technical University, Faculty of Mechanical Engineering, Mechatronics Engineering, Istanbul, sobut@yildiz.edu.tr,
ORCID: 0000-0002-9833-8151

Receive Date: 01.11.2022

Accepted Date: 06.01.2023

ABSTRACT

Since pH neutralization processes have extremely nonlinear characteristics, controlling it might be difficult. Therefore, a special controller design is needed to handle the high nonlinearities of the process. In this study, an inverse neuro-fuzzy model-based controller (NFMBC) design is presented for control of a pH neutralization process (NP). Input-output (IO) data set of the process is collected by applying a proper excitation signal. Then, forward and inverse neuro-fuzzy models of the process are constructed by using this data set after a training process. In terms of design simplicity, a two-input-one-output model structure is chosen for both neuro-fuzzy models. These forward and inverse neuro-fuzzy models are used in a nonlinear internal model control (NIMC) structure in order to provide robustness against disturbances and model mismatches. To examine the proposed controller's performance, simulation studies are carried out under setpoint variation and disturbance conditions. Additionally, the performance of the inverse NFMBC is compared to that of a fuzzy proportional integral derivative (FPID) controller with a 7x7 rule base. The results demonstrate that the designed controller provides more effective control performance for setpoint variations and also exhibits higher robustness against disturbances in the acid flow rate than the FPID controller.

Keywords: *Fuzzy Model, Inverse Controller, Adaptive Network Based Fuzzy Inference System, pH Neutralization Process, Internal Model Control,*

1. INTRODUCTION

The problem of pH control is a widespread issue in sectors such as chemical processes, sewage treatment and wastewater management [1]. The safety and stability of the system operation directly depend on the performance of pH control. The aim of pH control in neutralization systems is to keep the pH value at a certain setpoint by regulating the neutralizing agent flow rate. However, the control

of pH NPs is a challenging task due to their extremely nonlinear characteristics [2]. The titration curve of a neutralization process, in general, is an S-shaped curve depending on both process and neutralization stream compositions. In some cases, process stream composition may change during the operation, making the control issue much more challenging [3]. Therefore, deriving an analytical model and also designing an effective controller are difficult tasks for pH processes.

In the literature, several linear and non-linear control approaches are proposed to solve the pH control problem. Classical linear PID controllers can hardly ever provide an efficient control performance for pH control applications [4]. Therefore, one way of applying the linear PID control approach to the pH control problem is to use a multi-model approach by linearizing the process model at a few operating points [5]. For instance, Nyström has successfully implemented the multi-model control technique to a pH NP [6]. There are some studies successfully applying linear model predictive control approach to pH neutralization processes [2], [7]. Despite the fact that linear controllers are simple to design, adaptive control or nonlinear control methods provide better control performance than the classical linear control methods [5], [8]. In [2], [9], nonlinear model predictive and adaptive control structures are proposed for the control of pH processes. Although all of these techniques are successful, it is still hard to obtain an adequate model representing the pH NP in any operating condition for practical applications [5].

Highly nonlinear systems can be modeled and controlled using fuzzy logic since fuzzy models are universal approximators and fuzzy controllers have a nonlinear structure [10]. Therefore, fuzzy models and controllers can effectively be used for pH neutralization processes. For example, a fuzzy PI controller design is presented by considering the titration curve in [5]. In [11], an adaptive fuzzy PI control structure with an online tuning mechanism is proposed for pH control. Similarly, there are some fuzzy model (FM) based control approaches proposed in literature such as fuzzy model predictive control [12].

One easy and effective way of controller design is to use an inverse model of a process as the main controller. But it is not an easy task to derive inverse definitions of analytical models of processes. However, there are various exact and approximate inversion methods for fuzzy models [13]–[16]. Therefore, inverse fuzzy model-based control approaches are effective alternatives to conventional control approaches since forward and inverse fuzzy models of nonlinear systems can be derived without the need for any mathematical model. Several inverse fuzzy model based control approaches are proposed and effectively applied to the control problem of pH processes [1], [13], [16].

The adaptive network-based fuzzy inference system (ANFIS) technique described by Jang makes it simple to construct forward and inverse fuzzy models of nonlinear systems [17]. ANFIS approach is widely used in various modeling and control applications [18]. Some studies about ANFIS-based modeling and also control of pH processes are presented in the literature [19-21]. In this study, an inverse NFMBC design for a pH NP is presented. Although the inverse controllers are able to provide perfect control in an open loop (OL) manner, they can show poor control performance or become unstable in case of sudden disturbances and in the presence of noises. Therefore, an internal model control (IMC) structure, which is a closed loop structure, is used in this study. A proper excitation signal is applied to the system for modeling purposes and the input and output data are collected.

Then, forward and inverse ANFIS models of the process are trained by using the collected IO data set. These forward and inverse models are used in the IMC structure to advance the robustness of the control system against disturbances and model mismatches. The effectiveness of the designed inverse model-based controller is demonstrated through simulations under setpoint variation and disturbance conditions and the performance of this controller is compared to that of an FPID controller. The main advantage of the designed inverse NFMBC compared to the existing approaches is that it provides an effective performance although it uses only simple forward and inverse fuzzy models with 2 inputs and 1 output.

This article is arranged as follows: the pH process model is presented in Section 2, the fuzzy model design is presented in Section 3. The inverse controller design technique is demonstrated in Section 4. Section 5 presents simulation studies to show the effectiveness of the constructed inverse controller. Finally, the conclusions are presented in Section 6.

2. pH PROCESS MODEL

pH neutralization is a process involving reactions between acids and bases. In this study, the neutralization reaction among strong acid and weak acid mixture and strong base is considered as a process model due to its non-linear characteristic. Figure 1 shows the NP in a continuous stirred tank reactor (CSTR). It is assumed that there is perfect mixing within the CSTR. Since the base concentration is relatively high compared to the acid concentrations, a constant liquid level is assumed in the CSTR. Accordingly, the model can be written as:

$$V \frac{dx_i}{dt} = F(c_i - x_i) + u(b_i - x_i) \text{ for } i = 1, \dots, n \quad (1)$$

where c_i , b_i , and x_i represent the total ion concentration of the species in the corresponding streams in Figure 1. Because of the assumption of a constant liquid level, here the constant for the volume of liquid inside CSTR is symbolized by V . The simulation parameters of the model given in Eqn. 1 are listed in Table 1.

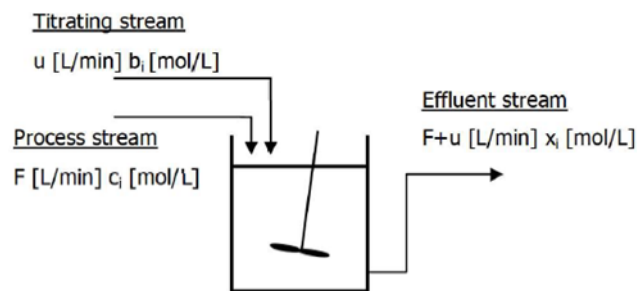


Figure 1. pH neutralization system.

Table 1. pH NP parameters.

Symbol	Process Parameters	Value
V	Volume of the reactor [L]	1
F	Flow rate of process stream [L/min]	1
u	Flow rate of titrating stream [L/min]	0-0.27
c_i	Total ion concentration vector of process stream $[C_{a1} C_{a2} C_b]$ [mol/L]	[0.001 0.001 0]
b_i	Total ion concentration vector of titrating stream $[C_{a1} C_{a2} C_b]$ [mol/L]	[0 0 0.1]

3. FUZZY MODELING of the pH PROCESS

An appropriate excitation signal is used to stimulate the system at each set-point to construct the forward FM of the NP. The uniform random signals plus constant values are used as the excitation signal and the corresponding output is obtained. Then, by using this input-output data set, the neuro-fuzzy based forward model of the system is obtained. In the data collection process, the sampling time is determined as 1 s, and the data is collected for 30000 seconds. The excitation signal and the corresponding output signal are demonstrated in Figure 2a and Figure 2b, respectively.

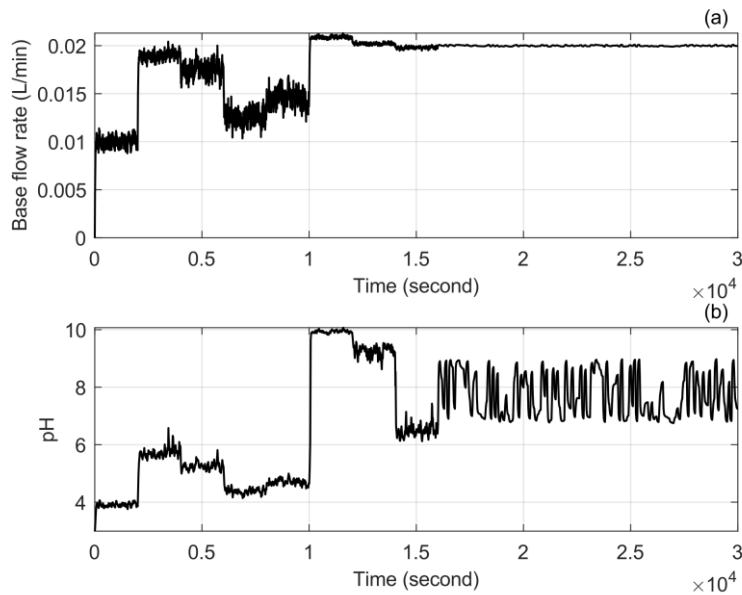


Figure 2. (a) Input signal (b) system output signal.

A two-input one-output Takagi-Sugeno (TS) FM structure is constructed as illustrated in Figure 3 since it provides an acceptable model approximation. The inputs of the FM are $y(k-1)$ and $u(k)$, and the output of the FM is $y(k)$. The input of $y(k-1)$ is expressed by 11 triangular membership functions (MFs), and the input of $u(k)$ is constructed by 3 triangular MFs. Here y denotes pH value and u denotes titrating stream flow rate. 33 singleton MFs are used to define the output $y(k)$. The training process uses the first 75% of the data and the validation process uses the remaining 25%. The rule base and MFs of the FM after training are represented in Table 2 and Figure 4, respectively.

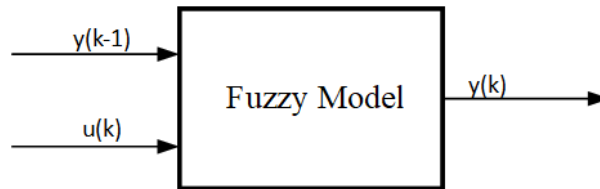


Figure 3. Input-output configuration of the fuzzy model.

Table 2. Rule base of the forward FM.

		u(k)		
		A1	A2	A3
y(k-1)	A1	2.989	3.032	0
	A2	3.163	3.718	3.837
	A3	4.244	4.387	4.493
	A4	0	5.044	5.169
	A5	0	5.582	5.886
	A6	0	5.084	6.772
	A7	0	-0.892	8.413
	A8	0	-6.014	9.889
	A9	0	4.698	9.182
	A10	0	8.399	9.467
	A11	0	9.785	10.07

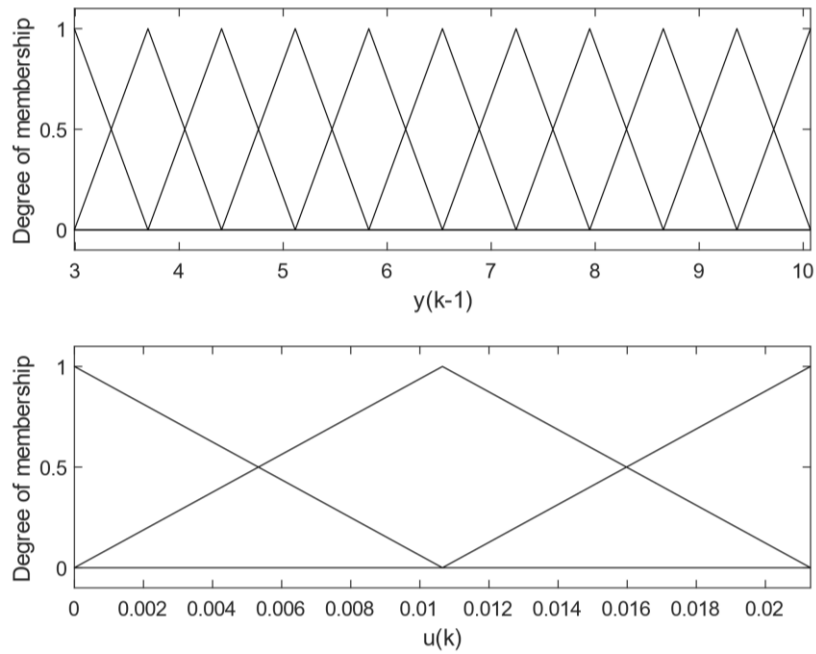


Figure 4. Antecedent membership functions of the trained FM.

The derived FM is compared with the neutralization system output for different setpoints. The forward FM response and the error between the system and the FM outputs are represented in Figure 5a and Figure 5b, respectively. The modeling performance of the derived fuzzy model is acceptable since it provides the root mean square error (RMSE) value of 4.8×10^{-3} .

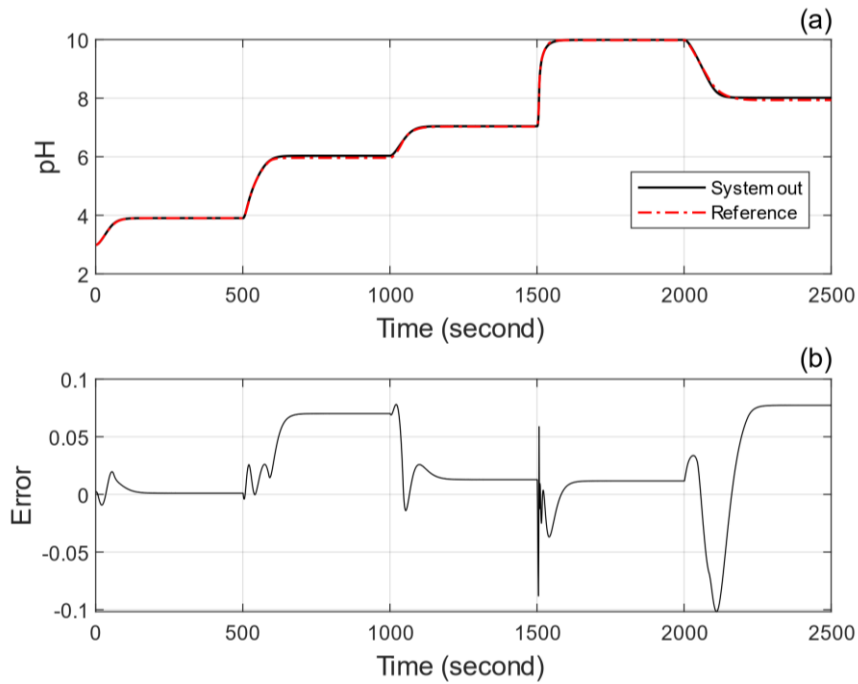


Figure 5. (a) Comparison of the system and the FM outputs (b) modeling error.

4. INVERSE NFMBC DESIGN

The inverse FM of the pH NP is designed by using ANFIS approach. Although the inverse controllers are able to provide perfect control in an OL manner, they can show poor control performance or become unstable in case of sudden disturbances and in the presence of noises. Therefore, the inverse FM of the pH NP is directly used as the main controller in the IMC structure shown in Figure 9 to increase robustness against disturbances and model mismatches.

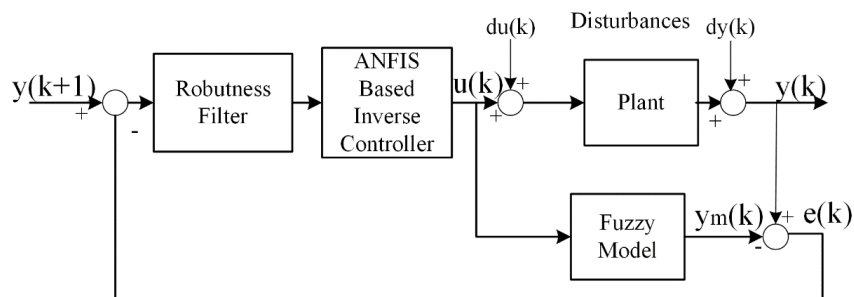


Figure 6. Proposed IMC structure.

$y(k)$ and $y(k-1)$ are used as inputs and $u(k)$ is used as the output by exchanging the IO data of the collected data set to derive the inverse FM of the pH NP. The IO configuration of the neuro-fuzzy based inverse controller is represented in Figure 6.



Figure 7. Input-output configuration of the neuro-fuzzy based inverse controller.

For inputs $y(k)$ and $y(k-1)$, 11 and 3 triangular MFs are used, respectively. 33 rule consequents are determined by using linear functions as shown in Table 3. The training process uses the first 75% of the data, while the validation process uses the remaining 25% of the data. The rule base and MFs of the trained inverse FM are represented in Table 3 and Figure 7, respectively.

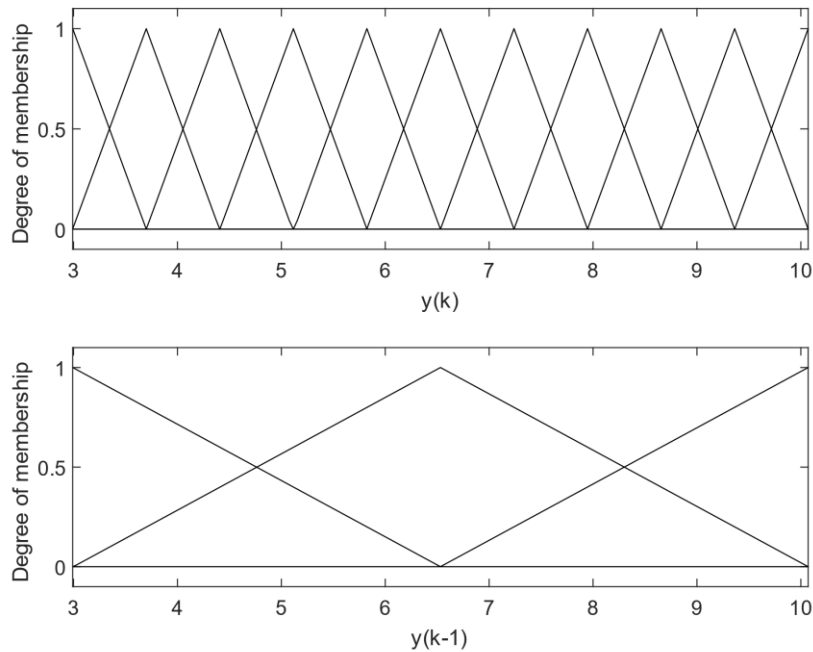


Figure 8. Antecedent MFs of the trained inverse FM.

Table 3. Rule base of the inverse FM.

		y(k-1)		
		A1	A2	A3
y(k)	A1	[0.34 -0.31 -0.11]	[-0.006 0.026 -0.17]	[0 0 0]
	A2	[0.11 -0.1 0.004]	[0.03 -0.02 -0.02]	[0 0 0]
	A3	[0.05 -0.04 0.004]	[0.14 -0.14 -0.03]	[0 0 0]
	A4	[0.14 -0.14 0.006]	[0.03 -0.03 -0.03]	[0 0 0]
	A5	[0.07 -0.07 0.02]	[0.02 -0.01 -0.02]	[-0.008 -0.009 -0.001]
	A6	[-0.001 0.002 0.03]	[0.009 -0.002 -0.02]	[-0.01 0.02 -0.02]
	A7	[0.02 0.01 0.002]	[0.005 -0.001 -0.009]	[-0.002 0.003 0.007]
	A8	[0 0 0]	[0.004 -0.0002 -0.01]	[0.0004 0.001 0.006]
	A9	[0 0 0]	[0.003 0.0008 -0.01]	[0.004 -0.002 0.006]
	A10	[0 0 0]	[-0.009 0.01 -0.009]	[0.01 -0.01 0.006]
	A11	[0 0 0]	[-0.08 0.08 0.004]	[0.04 -0.04 0.002]

In order to show the inverse FM validation, the output of the inverse controller is compared to the excitation signal in Figure 8a. The associated error signal is demonstrated in Figure 8b and the obtained RMSE value is 7.11×10^{-5} . As it is seen from Figure 8, the performance of the derived inverse FM is acceptable.

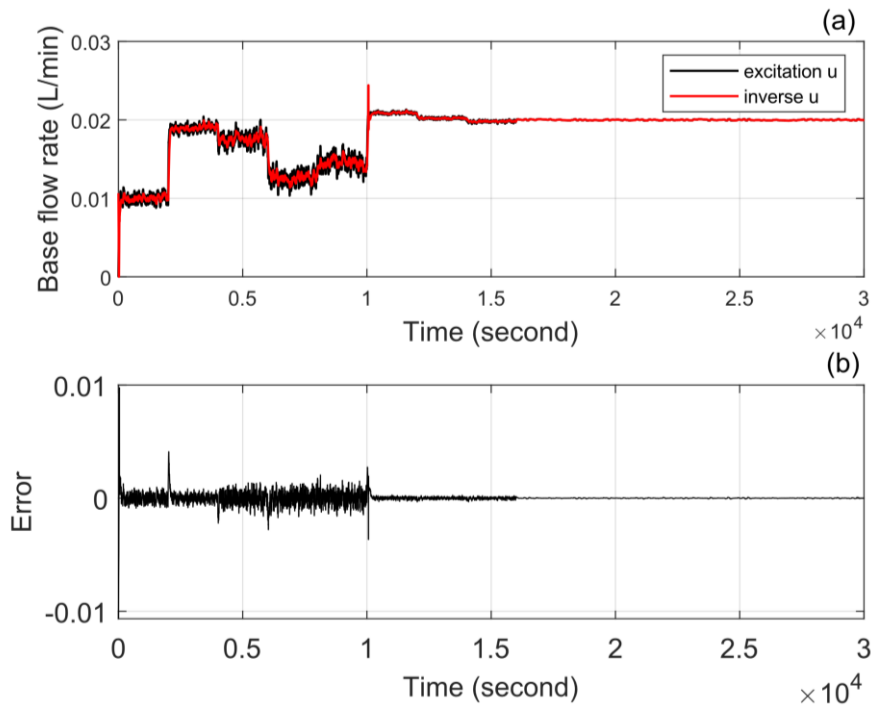


Figure 9. (a) Comparison of the excitation signal and the output of the inverse FM (b) the inversion error.

5. SIMULATION STUDIES

To demonstrate the performance of the proposed controller, simulation studies are performed under different setpoint and disturbance conditions. In the simulations, a FPID controller is also used for performance comparison. The block diagram of the FPID controller is demonstrated in Figure 10.

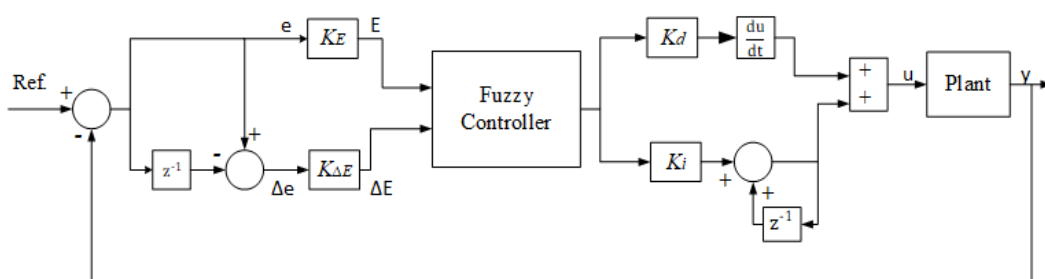


Figure 10. Block diagram of the FPID controller.

In order to design the FPID controller, TS fuzzy inference structure is chosen and a 7x7 symmetrical rule base is used. Triangular MFs are chosen for the definition of input variables E and ΔE as shown in Figure 11. Singleton MFs are defined for the control variable U. The parameters of the FPID controller are determined as $K_E=0.015$, $K_{\Delta E}=0.001$, $K_I=0.003$ and $K_d=0.95$.

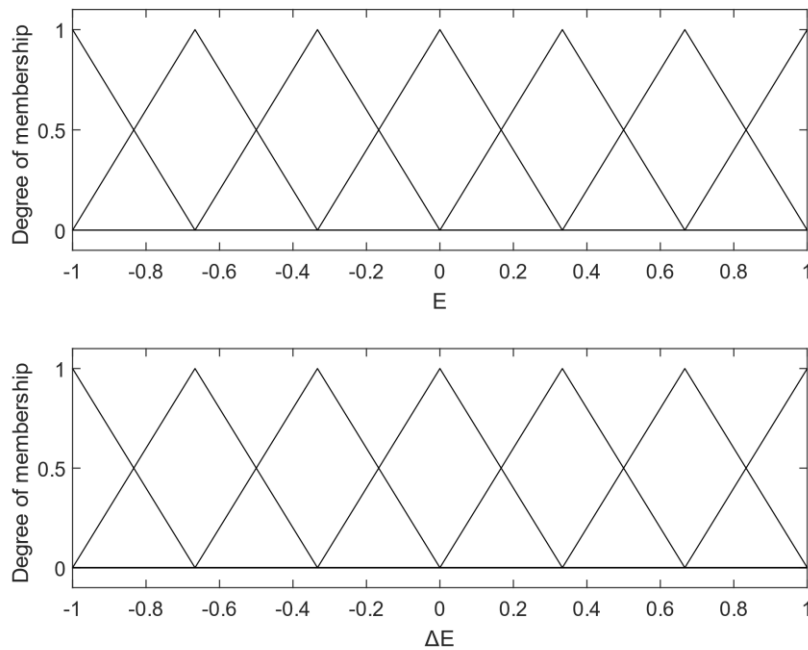


Figure 11. Antecedent MFs of the FPID controller.

The robustness filter in IMC structure is chosen as follows to provide a suitable control performance.

$$G_f(z) = \frac{0.09516}{z-0.9048} \quad (2)$$

In comparisons, the following integral square error (ISE) and integral absolute error (IAE) performance criteria are used.

$$\text{ISE: } \int e^2(t)dt \quad (3)$$

$$\text{IAE: } \int |e(t)|dt \quad (4)$$

The controller performances under setpoint variation are demonstrated in Figure 12 and performance results are compared in Table 4.

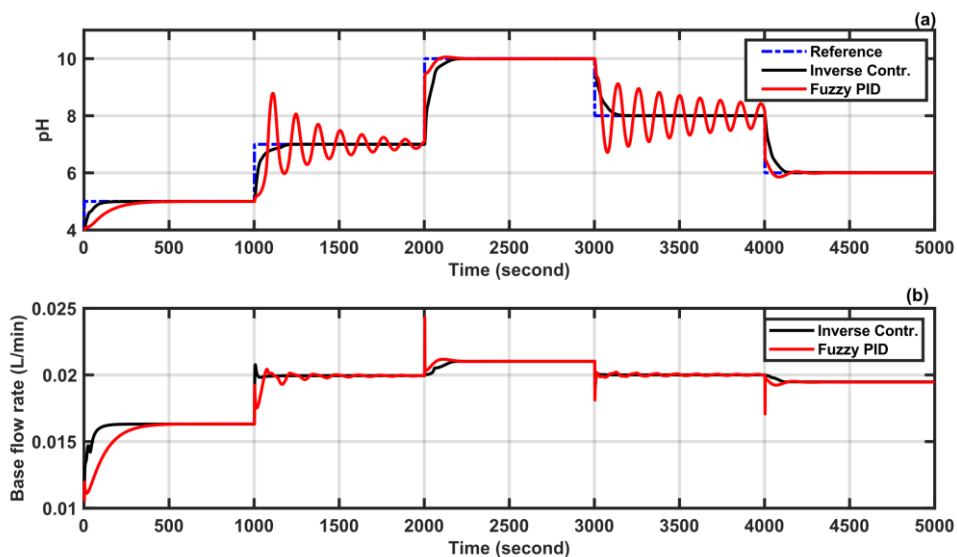


Figure 12. a) Comparison of the system responses under the setpoint variation b) control signals.

Table 4. Performance comparison under the setpoint variation.

Controller	IAE	ISE
FPID	1.392	1.072
Inverse Controller	0.4303	0.3601

As seen in Figure 12 and Table 4, the proposed inverse controller is able to provide significant control performance at all setpoint changes. On the other side, the FPID controller is able to provide satisfactory control performance only at certain pH values where the system gain is relatively low. For setpoint values where the system gain is high, the FPID controller gives oscillating system responses. In order to evaluate the control performances under disturbance conditions, change in acid flow rate is considered. The reference signal, applied disturbances, corresponding system responses, and control signals are represented in Figure 13. The performance criteria values are given in Table 5. As it is seen from Figure 13 and Table 5, the proposed controller exhibits superior robustness performance under disturbance conditions compared to the FPID controller.

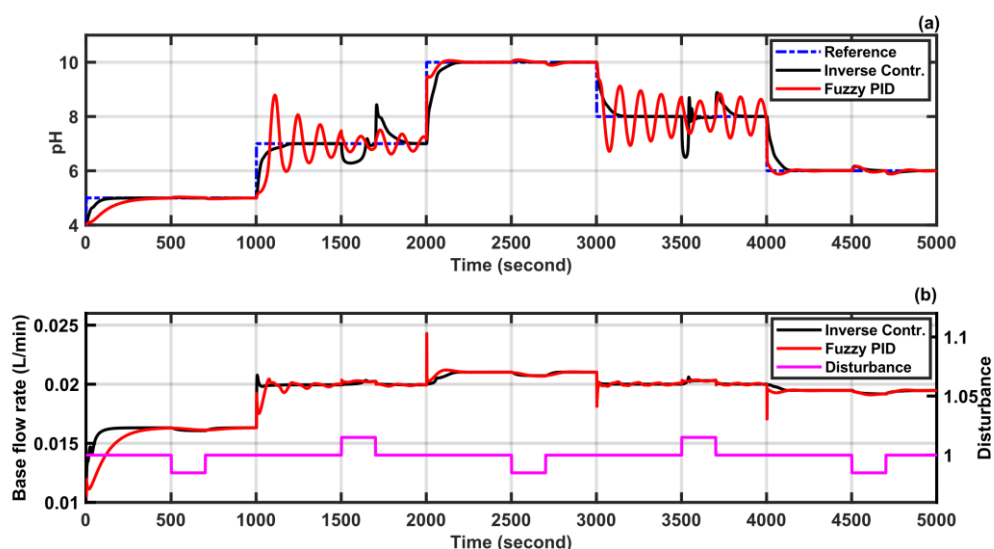


Figure 13. a) Comparison of the system responses under the input disturbance condition b) control signals.

Table 5. Performance comparison under the disturbance condition.

Controller	IAE	ISE
FPID	1.472	1.105
Inverse Controller	0.7168	0.5339

The pH NP is a highly nonlinear system depending on the nonlinear characteristic of its titration curve. The process has different process gains at different pH interval values. The process has lower gains for the pH intervals of [3-6] and [9-12] whereas it has higher gains for the pH intervals of [6-9]. Since the inverse controller is the inverse definition of the fuzzy model of the pH NP, it inherently possesses the process gain information and exhibits significant control performance for different pH levels. However, the conventional FPID controller with the symmetrical rule base is not able to handle these system gain variations as much as the inverse controller. Additionally, since the inverse controller is used in the IMC structure, it has the capability of handling disturbances. On the other hand, the conventional FPID controller has no special configuration to handle disturbances. Therefore, the inverse NFMBC provides superior robustness performance against disturbances compared to the conventional FPID controller. Consequently, the superior pH control performance is obtained by using the inverse NFMBC having only simple forward and inverse fuzzy models with 2 inputs and 1 output as compared to the conventional FPID controller.

6. CONCLUSION

In this study, an inverse NFMBC design is presented for a pH NP. An NIMC structure is used to provide robustness against disturbances and model mismatches. The forward and inverse fuzzy models of the pH NP are represented by simple fuzzy models with two inputs and one output. The training procedures of the fuzzy models are performed by using an input-output data set collected from the pH NP. The effectiveness of the designed inverse NFMBC is demonstrated through simulations under setpoint variation and disturbance conditions. The simulation results illustrate that the inverse NFMBC exhibits superior control performance compared to the FPID controller with a 7x7 rule base.

The forward and inverse fuzzy models of the pH NP used in the design procedure are in a basic structure with 2 inputs and 1 output, which makes the approach very suitable for real-time control applications. Additionally, these fuzzy models are obtained automatically based on the ANFIS approach without the need for any expert knowledge or tuning. Thanks to these properties, simple but effective controllers can be designed for highly nonlinear systems by using the proposed approach.

ACKNOWLEDGMENT

This research has not received any grants.

REFERENCES

- [1] Kumbasar, T., Eksin, I., Guzelkaya, M., and Yesil, E. (2012). Type-2 fuzzy model based controller design for neutralization processes. *ISA transactions*, 51(2), 277-287.
- [2] Estofanero, L., Edwin, R., and Claudio, G. (2019). Predictive controller applied to a pH neutralization process. *IFAC-PapersOnLine*, 52(1), 202-206.
- [3] Rose, T. P., and Devadhas, G. G. (2020). Detection of pH neutralization technique in multiple tanks using ANFIS controller. *Microprocessors and Microsystems*, 72, 102845.
- [4] Hall, R. C., and Seborg, D. E. (1989). Modelling and self-tuning control of a multivariable ph neutralization process part i: Modelling and multiloop control. In *1989 American Control Conference* (pp. 1822-1827). IEEE.
- [5] Fuente, M. J., Robles, C., Casado, O., Syafiie, S., and Tadeo, F. (2006). Fuzzy control of a neutralization process. *Engineering Applications of Artificial Intelligence*, 19(8), 905-914.
- [6] Nyström, R. H., Sandström, K. V., Gustafsson, T. K., and Toivonen, H. T. (1998). Multimodel robust control applied to a pH neutralization process. *Computers & chemical engineering*, 22, S467-S474.

- [7] Gu, B., and Gupta, Y. P. (2008). Control of nonlinear processes by using linear model predictive control algorithms. *ISA transactions*, 47(2), 211-216.
- [8] Wright R. A., and Soroush M. (1991). Strong Acid Equivalent Control of pH Processes: An Experimental Study. *Industrial & engineering chemistry research*, 30(11), 2437-2444.
- [9] Obut, S., and Özgen, C. (2008). Online identification and control of pH in a neutralization system. *Industrial & engineering chemistry research*, 47(13), 4394-4404.
- [10] Wang, L. X., and Mendel, J. M. (1992). Fuzzy basis functions, universal approximation, and orthogonal least-squares learning. *IEEE transactions on Neural Networks*, 3(5), 807-814.
- [11] Babuska, R., Oosterhoff, J., Oudshoorn, A., and Bruijn, P. M. (2002). Fuzzy self-tuning PI control of pH in fermentation. *Engineering Applications of Artificial Intelligence*, 15(1), 3-15.
- [12] Nascimento Lima, N. M., Manenti, F., Filho, R. M., Embiruçu, M., and Wolf Maciel, M. R. (2009). Fuzzy model-based predictive hybrid control of polymerization processes. *Industrial & Engineering Chemistry Research*, 48(18), 8542-8550.
- [13] Babuška, R., Sousa, J. M., and Verbruggen, H. B. (1998). Inverse fuzzy model based predictive control. In *Advances in fuzzy control* (pp. 129-154). Physica, Heidelberg.
- [14] Ulu, C. (2014). Exact analytical inverse mapping of decomposable TS fuzzy systems with singleton and linear consequents. *Applied Soft Computing*, 23, 202-214..
- [15] Ulu, C. (2015). Exact analytical inversion of interval type-2 TSK fuzzy logic systems with closed form inference methods. *Applied Soft Computing*, 37, 60-70.
- [16] Kumbasar, T., Eksin, I., Guzelkaya, M., and Yesil, E. (2011). Adaptive fuzzy model based inverse controller design using BB-BC optimization algorithm. *Expert Systems with Applications*, 38(10), 12356-12364.
- [17] Jang, J. S. (1993). ANFIS: adaptive-network-based fuzzy inference system. *IEEE transactions on systems, man, and cybernetics*, 23(3), 665-685..
- [18] Kampouropoulos, K., Andrade Rengifo, F., García Espinosa, A., and Romeral Martínez, J. L. (2014). A combined methodology of adaptive neuro-fuzzy inference system and genetic algorithm for short-term energy forecasting. *Advances in Electrical and Computer Engineering*, 14(1), 9-14.
- [19] Mota, A. S., Menezes, M. R., Schmitz, J. E., da Costa, T. V., da Silva, F. V., and Franco, I. C. (2016). Identification and online validation of a ph neutralization process using an adaptive network-based fuzzy inference system. *Chemical Engineering Communications*, 203(4), 516-526.

- [20] Sreekumar, S., Kallingal, A., and Mundakkal Lakshmanan, V. (2021). Adaptive neuro-fuzzy approach to sodium chlorate cell modeling to predict cell pH for energy-efficient chlorate production. *Chemical Engineering Communications*, 208(2), 256-270.
- [21] Sunori, S. K., Negi, P. B., Arora, S., Khan, F., Maurya, S., Juneja, P., ... and Ghai, K. (2022). Neuro-fuzzy Controller Design for pH Control in Sugar Refineries. 8th International Conference on Advanced Computing and Communication Systems (ICACCS) (Vol. 1, pp. 197-202). IEEE.



RESEARCH ARTICLE

**EXERGOECONOMIC ANALYSIS OF A PHOTOVOLTAIC ARRAY AFFECTED BY
DYNAMIC SHADING**

Vedat KESKİN¹

¹Samsun University, Civil Aviation College, Samsun, vedat.keskin@samsun.edu.tr, ORCID: 0000-0002-8084-4224

Receive Date: 02.11.2022

Accepted Date: 14.01.2023

ABSTRACT

Photovoltaic (PV) panels are affected by undesirable elements that exist around them, trees, structures, clouds, etc., as well as natural dirt, and dust accumulation on the PV surfaces. Unfortunately, partial shading falling on top of the PV panels may affect badly the output of photovoltaic arrays. In this study, an exergoeconomic analysis has been performed on the impact of dynamic partial shading created by a mislocated building on a photovoltaic array. Both experimental and theoretical results of this study have been compared on ambient temperature, solar radiation intensity, and shading ratio. The observations have been carried out on clear days starting in June 2018 to Mai 2019. According to the results, the shaded PV exergy efficiency (6.87%) and exergoeconomic parameter ($R_{ex} = 0.18508$ W/\$) are maxima in June and minimum in February ($E_x = 4.76\%$, $R_{ex} = 0.12228$ W/\$). As a result of this study, it can be said that the PV array exposed to long-term shading will seriously affect the service life of the PV array.

Keywords: *Photovoltaics, Exergy, Exergoeconomic, Dynamic Shading*

1. INTRODUCTION

The growth and development of the human population, and in turn the demand-based energy requirement is increasing exponentially. In addition, environmental and climate problems caused by unconscious consumption have made it necessary to switch to sustainable, clean, and cheap energy. To provide a sustainable life for people and living things, cheaper and unlimited renewable energy sources have become more and more popular in the ever-increasing and so expensive electricity production. The energy produced from photovoltaic panels is becoming more and more popular because of this feature and because it is powered by the sun, which is clean, free, and inexhaustible. Photovoltaic panels, which are the basic components of solar power plants, are the most basic component that converts the energy from the sun as electricity that is usable energy everywhere. The photovoltaic power system is different from other renewable power generation systems and is more attractive because it has fewer moving parts in its structure. Unfortunately, photovoltaic panels are adversely affected by factors such as clouds, nearby trees, neighboring structures, dirt, misdirection, and slopes that cause partial shading on their front surfaces [1]. The shading falling on the PV array

surface for different reasons may cause a decrease in the power production, but may also cause hot spots on the PV cells and even damage and so shortening their service life. The effect of shading by different obstacles and conditions on PV systems has been studied by many researchers [2-6].

Here are some well-known studies on shading and its effect, in chronological order; Bidram et al. [2] examined the negative effects of different PV array configurations, different PV system architectures, PV circuit topologies, reducing of electrical characteristics and hot spot events under partial shading. Dollar et al. [3] carried out experiments with PV modules produced from two different materials, on clear and sunny days, by creating graphs with the created current, voltage, and power parameters. He suggested that experimental analyzes with mathematical models are applied to estimate the lost power of the photovoltaic arrays. Chepp et al. [4] created a straightforward approach to assess how PV systems and modules perform when partially shaded. The proposed method's accuracy was contrasted with the approaches they selected, and I-V and performance values were examined. The variations between the results from the measurements and the models are quite close to 5%. A numerical and experimental study on partial shading detection was conducted by Khodapanah et al. [5]. It is feasible to discern between temporary and permanent shade conditions, the severity of the shading level, and, consequently, the time at which hot spots emerge using the technique they offer. The results of their investigation support their assertion that they can give partial shading detection without adding additional cells or modules to the system.

Recently, applying thermodynamics and environmental and economic analysis methods such as exergy and exergoeconomic analysis has been increasing. Mostly, the performance evaluations of PV power systems are made with the energy analysis method. Moreover, the exergy analysis method is more detailed, it is used to determine from which part of the system the losses originate [6-8].

Some of these studies are: There are some additional studies on shading effect and exergoeconomic analysis; Bayrak et al. [9], in their study, made an experimental setup to create shading at different positions and rates on the photovoltaic panel surface and calculated the efficiency of energy and exergy of the PV system. As a result, they found in the case of horizontal shading a significant loss of the efficiency of energy and exergy of about 99.98%. Bayrak and Öztop [10] investigated the effect of diagonal shading on the performance of PV via energy and exergy efficiency analysis under the same solar radiation. The PV array was left in the natural environment for 30 days for the shading effect of dust accumulation. In their experiment, an artificial shading was created of the triangle-like shape of different shadings. Experimental results showed that the reference panel with the efficiency of highest was only about 0.90% higher than the dusty panel. Variable values were observed for the dynamic shading panel.

It is seen that the energy analysis method is used in experimental and theoretical works on solar power plants and the shading falling on the panel surface and its effects. In addition, when the literature is searched, there is a few scientific research on the dynamic shading on the surface of the PV panel, which occurs in undesirable situations, and only the thermodynamic (exergy) analysis method was used in these studies. Differently, in this study, the exergy and exergoeconomic analysis of the effect of dynamic partial shading on the PV performance caused by an incorrectly positioned structure to the

PV array surface in a solar power plant established in the province Samsun was examined by recording the required data and shading ratio calculations for one consecutive year, 12 months.

2. MATERIALS AND METHODS

In this study, the effects of shading were investigated, starting from the morning until certain hours, caused by the transformer building of a grid-connected power plant capacity of 480 kW in the province of Samsun. You can find detailed technical specifications of the plant in ref. [11].

2.1. PV Array Power Plant

A shading-affected PV string controlled by the inverter (13) and another PV string without shading were selected for reference, inverter (16).



Figure 1. Image of the partially shaded PV array.

2.2. Methods

Sunny and clear days were preferred to get good data from the PV power generation plant. Calculations were made by recording the weather conditions parameters such as the temperature (T_a), the wind speed (v), and the solar radiation intensity (I_s) of the environment where the PV panels were installed.

The area (A) of the shaded PV surface, at 15-minute time intervals starting from sunrise until it left, was recorded with photographs as well as the current, voltage, and power values from the inverter. Evaluation processes of the effect of dynamic partial shading on PV performance were carried out by exergoeconomic analysis method as follows;

- The instantaneous solar radiation hitting the surface of the PV modules was determined by calculating the Liu and Jordan method [12] and measuring the solar radiation.
- Electrical efficiency calculations of shading-affected and unaffected PV arrays have been discussed in the previous publication [11].
- For economic calculations, instantaneous/average values are used instead of annual electricity generation.

- Net present value (NPV) is calculated. The operating and maintenance cost of the PV plant is taken as 10% and the salvage value as 5% of the current capital cost (P). The interest rate is taken as 8%.
- The energy loss rate and exergy loss rate of the shaded and un-shaded PV arrays were calculated.
- Related to the previous step the R_{en} and R_{ex} have also been calculated for the shaded and un-shaded PV arrays.

2.3. Analysis of the PV System

In this section, the calculations of energy, exergy, and exergoeconomic analysis, which are the performance and economic parameters of the PV system, shortly will be explained respectively.

2.3.1. Energy analysis

The main energy source of the universe is the sun. Therefore, the radiation of the sun striking the photovoltaic surface will create power named input energy to the PV system which is the basis of the first law of thermodynamics and is expressed as below;

$$P_s = I_s \times A \quad (1)$$

where P_s , I_s and A indicates the sun's radiation power, the intensity of solar radiation, and the area where the sun strikes, respectively.

As it is known, when solar radiation hits the PV panels, the available electricity is converted by the PV device. The maximum current (I_m), voltage (V_m), and power (P_m) equation of the converted useful electricity by the PV array are simply as follows;

$$P_m = I_m \times V_m \quad (2)$$

where V_m and I_m express maximum values of voltage and current, respectively.

The evaluation of the energy systems was made by taking into account the principles of the 1st law of thermodynamics, the efficiency and transformation of energy comparison of the PV power plant system were made with the equation given below [13]:

$$\eta = \frac{V_m \cdot I_m}{I_s \cdot A} \quad (3)$$

As understood from the equation, the energy efficiency of a PV system is given as the ratio between the maximum current (I_m) at maximum the power point and the maximum voltage (V_m) value at the maximum power point, and the intensity of solar irradiation (I_s) striking to the surface area (A) of the photovoltaic panel.

2.3.2. Exergy analysis

In thermodynamic (exergy) calculations of a PV power system, it is important to determine the exergy components of the parts that make up the system. The limitations of the Carnot cycle and other thermodynamic parameters such as enthalpy, entropy, and energy conversion, and physical and chemical exergy expressions of a power system have been clarified in the previous discussions [13]. Therefore, these concepts will not be considered in this part of this study. Therefore, electrical and thermal exergy parameters, which are the two main exergy components of this study, will be analyzed [14].

The following equation represents the total exergy balances of PV power systems:

$$\sum Ex_{in} = \sum Ex_{out} + \sum Ex_{loss} + \text{Irreversibility} \quad (4)$$

As it is known, the photovoltaic power system converts the electrical energy or exergy that comes from the sun into useful energy. In more details, detail, exergy analysis of a power system determines to do work, that is, the quality of energy. However, there is always a degradation of some of the energy gained by the power system, in other words, exergy loss. This loss is not recoverable, that is exergy loss also called irreversibility. In order to facilitate the calculations and comparisons, the exergy efficiency of a power system PV module is defined as the ratio of the total output exergy to the total input exergy;

$$\Psi_{PV} = \frac{Ex_{out}}{Ex_{in}} \quad (5)$$

The PV array produces energy or exergy input (Petalá's solar exergy model) due to the sun's radiation that strikes the PV surface and is expressed as follows [15]:

$$Ex_{in} = A \cdot I_s \left(1 - \frac{4}{3} \left(\frac{T_a}{T_s} \right) + \frac{1}{3} \left(\frac{T_a}{T_s} \right)^4 \right) \quad (6)$$

Or

$$Ex_{in} = A \cdot I_s \left(1 - \left(\frac{T_a}{T_s} \right) \right) \quad (7)$$

Where A shows the surface area of the PV module and T_a and T_s demonstrate ambient and sun temperatures respectively which $T_s = 5777$ K.

The PV modules' exergy output is expressed by [16]:

$$Ex_{out} = Ex_{el} - Ex_{th} \quad (8)$$

As we see from eq. 8, the PV modules' exergy output consists of two basic parameters; heat dissipated to the environment so-called thermal exergy (E_{x-th}), and the useful exergy named electrical exergy (E_{x-el}).

When sunlight strikes the PV array it produces useful electricity and it can be expressed as (Note that electrical exergy equals the electrical energy):

$$E_{X,el} = I_m \times V_m \quad (9)$$

Some of the energy coming from the sun causes the upper surface of the PV to heat up. In this case, the surface temperature of the PV panel consisting of cells will increase and thermal energy/exergy losses will occur as waste to the environment, called thermal exergy and its expression is as follows:

$$Ex_{th} = Q \left(1 - \left(\frac{T_a}{T_c}\right)\right) \quad (10)$$

Where

$$Q = h_{ca} A (T_c - T_a) \quad (11)$$

And

$$h_{ca} = 5.7 + 3.8v \quad (12)$$

$$T_{cell} = T_a + (T_{NOCT} - 20) \left(\frac{G}{800}\right) \quad (13)$$

Where T_{cell} is the temperature of the cell, the coefficient of the heat transfer is h_{ca} , the velocity of wind is v , and the temperature of the cell operating at nominal T_{NOCT} is usually at about 45 °C.

When equations (9) and (10) are inserted to write the equation of production exergy ($E_{x,out}$) in the exergy balance of the PV array, it can be expressed as follows:

$$E_{x,out} = I_m \cdot V_m - \left(1 - \left(\frac{T_a}{T_c}\right)\right) h_{ca} \cdot A (T_a - T_c) \quad (14)$$

If Equations (7) and (14) are replaced in Eq. (5), the exergy ratio was calculated as:

$$\Psi_{PV} = \frac{I_m V_m - \left(1 - \left(\frac{T_a}{T_c}\right)\right) h_{ca} A (T_a - T_c)}{AG \left(1 - \left(\frac{T_a}{T_s}\right)\right)} \quad (15)$$

2.3.3. Exergoeconomic analysis

Unfortunately, PV power generating systems, which consist of many components, undergo energy and exergy losses due to different reasons during the power generation process. It is 'exergoeconomic', which is a method of analysis that examines the cost or watt-dollar cost together, which uses the collaboration of economic and thermodynamic analysis together to understand and avoid these unwanted losses. For these reasons, first of all, analyses of energy and exergy main parameters that

express the quality of the PV power system will be completed, and then after exergoeconomic analysis is done [12].

The exergoeconomic parameter R_{ex} (or R_{en}) is the ratio of exergy loss per annual cost to minimize exergy loss. The exergoeconomic analysis is done together with exergy and economic analysis methods. As a result, cost and exergy disciplines should be discussed together to perform the optimum design of energy-generating systems. According to the generally known definition, according to the first law of thermodynamics, energy as in nature, that is, a change from one form to another, but it cannot be created or destroyed. By contrast, exergy, which is the expression of the second law of thermodynamics, will be exhausted in any action due to irreversibility and is therefore subject to a nonconservative law. For these reasons, the general equilibrium equation can be written as [14];

$$E_{acc} = E_{in} - E_{out} \quad (16)$$

$$E_{x,acc} = E_{x,in} - E_{x,out} - E_{x,cons} \quad (17)$$

The output terms can be rewritten as

$$E_{out} = E_{in} - E_{acc} \quad (18)$$

$$E_{x,out} = E_{x,in} - E_{x,cons} - E_{x,acc} \quad (19)$$

Where, $E_{x,out}$ is overall exergy gain, $E_{x,cons}$ is exergy consumption, and $E_{x,acc}$ is exergy accumulation. To simplify the calculations, two types of thermodynamic losses (L_{en} and L_{ex}) will be considered. Here, L_{en} and L_{ex} are represented as energy-based loss and exergy-based loss, respectively. Starting from the energy balance equation of a thermodynamic system, the energy loss ratio (L_{en}) calculations of the shaded and unshaded PV array can be written as follows [14]:

$$L_{en} = \sum_{in} Energy - \sum_{out} Energy \quad (20)$$

$$L_{ex} = \sum_{in} Exergy - \sum_{out} Exergy \quad (21)$$

As in most exergoeconomic studies, inspired by Rosen and Dincer [16], the definition of the exergoeconomic parameter 'R' is loss of energy to exergy ratio. First, the loss of energy rate,

$$R_{en} = \frac{L_{en}}{NPV} \quad (22)$$

For exergy loss rates,

$$R_{ex} = \frac{L_{ex}}{NPV} \quad (23)$$

As it is known, there are four common financial analysis methods applied in research on the cost and profitability of PV power systems; net present value (NPV), Profitability Index, Internal Rate of

Return, and Discounted Payback Period. In this study, NPV, which is one of the four analysis methods, was chosen and can be calculated as follows [16]. Findings and details of net present value (NPV) calculations are made in the 'Conclusions and Discussions' section.

3. RESULTS AND DISCUSSIONS

This section covers the energy, exergy, and exergoeconomic analysis of the adverse effects of shading caused by the power control unit building of a grid-connected PV power plant. This study continued for 12 months, from June 2018 to May 2019. Two equal numbers of PV arrays each controlled by separate inverters, one cleaned and the other not cleaned, were chosen to make controlled experimental observations. To get better results measurements were taken on cloudless and sunny days. Experimental data were recorded and calculations related to the data were made. Technical details of this research are available in the literature [11].

The exergy efficiency of the shaded and un-shaded PV string is discussed in Figures 2-4 correlated to solar irradiation, ambient temperature, and shading ratio parameters versus time. In the exergoeconomic analysis section, 'Operation and Maintenance Costs' and 'NPV Calculations' are given in tables 1 and 2. Then, the changes in the energy (L_{en}) and exergy loss (L_{ex}) ratios and the exergoeconomic parameters R_{en} and R_{ex} , and the shading ratio versus time are presented in figures 5-8.

3.1. Exergy Analysis

As can be seen in Figure 1, analyzes were made depending on the temperature of the environment where the photovoltaic power plant is installed. The ambient temperature for the province of Samsun varies between 9 and 25 degrees Celcius on average during the year.

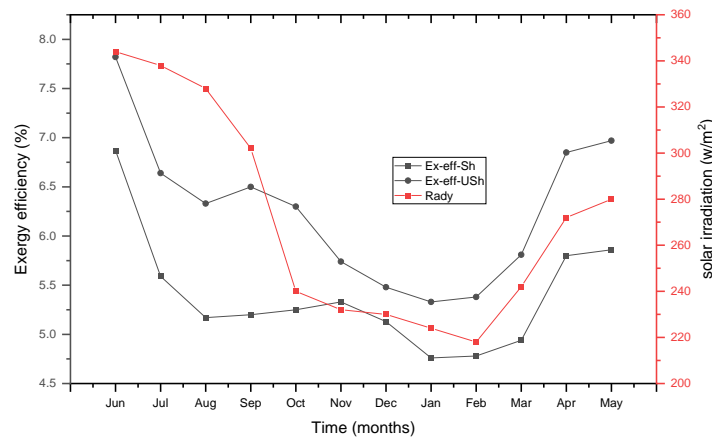


Figure 2. Exergy efficiency (%) and solar irradiation (w/m^2) versus time.

The correlation of exergy efficiency of the 'Sh-Array' and 'UnSh-Array' PV strings are similar during the 12 months. While the calculated efficiency of exergy values of shaded and unshaded PV arrays was high in the first three months (first, second and third) when the observations started, and an inverse relationship was observed due to the heating of the PV cells due to the ambient temperature and so the increase in thermal loss, on the other hand, a linear relationship was observed in the next months of the year (Fig. 3).

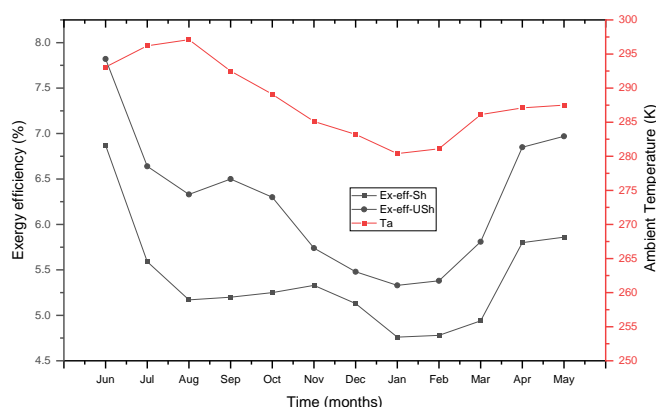


Figure 3. Exergy efficiency (%) and ambient temperature (K) versus time.

On the other hand, the exergy efficiency difference of 'Sh-array' and 'Un-Sh-array' in August, September, and October is about 1.4% maximum. According to these figures, the exergy efficiency of shaded and unshaded PV arrays showed a parallel variation during the 12 months. In terms of exergy efficiency is minimum in January and February in proportion to the ambient temperature and solar radiation, while it is maximum in June (see Figures 2, 3, and 4).

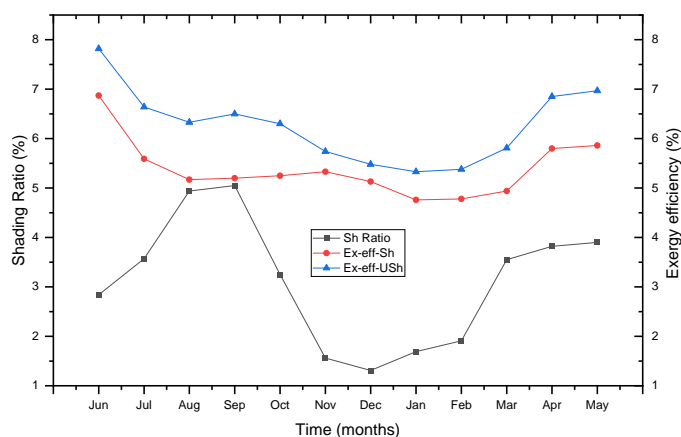


Figure 4. Exergy efficiency (%) and shading ratio (%) versus time.

In detail, while the exergy efficiency values of 'Sh-string' and 'UnSh-string' were the highest with 6.87% and 7.82%, respectively, in June, they were the lowest at about 4.76% and 5.33% in January. However, depending on the azimuth angle of the incoming solar irradiation, the shading ratio is the lowest at about 1.31% in December. In June, it is only about 2.84%, the highest is about 5.05% in September. According to the graphical analysis data, we can generalize that the exergy efficiency of shaded and non-shaded photovoltaic strings increases positively depending on the power source the sun's rays angle of hitting the PV surface, and the sunshine hours, see Figures 2, 3, and 4.

3.2. Exergoeconomic Analysis

Here, the results data of the exergoeconomic analysis of the impact of dynamic shading created by an undesired structure on the shaded and unshaded PV strings are discussed. Basic components for exergoeconomic analysis; L_{en} , L_{ex} , R_{en} , R_{ex} , and NPV were defined, and calculations and comparisons were made. The data necessary to make the calculations and comparisons were collected from the start of the experiment in June 2018 for 12 months.

Since the grid-connected PV power plant was established as part of an EU support program, estimated values were used to calculate the cost of the system's components. These i.e. 'Cost of capital', modules, stands, etc. design and construction, testing the functioning of the system's components, training of employees-technicians, and operating (maintenance) of the PV power system.

The costs of the components are given in Table 1 and 2. The inverter (ABB array) is about \$3900 and the cleaning and maintenance cost is about \$1000, 25 years 5×5000 \$(25000\$). The discount rate i , which includes inflation and interest rates, is assumed to be 10% on average. Finally, the NPV will be around \$100000.

Table 1. Operational and Maintenance Costs.

ABB inverter	2*34 kWe	3900 \$
Cleaning and Maintenance cost	5 years	1000 \$
Life cycle (25 years)		5*5000
		25000\$

Table 2. Calculations of the NPV of PV string system.

PV Module (95\$)	240*100	24000 \$
Support structure (\$)	25*240	6000 \$
Installation cost	2	5000 \$
Capital cost		35000 \$
Discount Rate (%)		10
Operational Cost for Each Year (\$)		1000 \$
NPV		100000 \$

In addition, in the calculations of the cost of the PV arrays, the PV modules and the stands, and all the other equipment used for the installation are included. Table 2 shows the costs of all major equipment of the PV system. To find $L_{en,loss}$, the difference between $E_{en,input}$, and $E_{en,output}$ is calculated. Similarly,

(since $L_{ex}=E_{ex}$) the exergy loss rate is calculated. Monthly variations in exergoeconomic parameters including R_{en} and $R_{ex:loss}$ are given in Figures 7 and 8. Losses of shaded and non-shaded PV strings peak in June, and then proportionally with T_a and I_s is lowest in December till February and increase again for the next months.

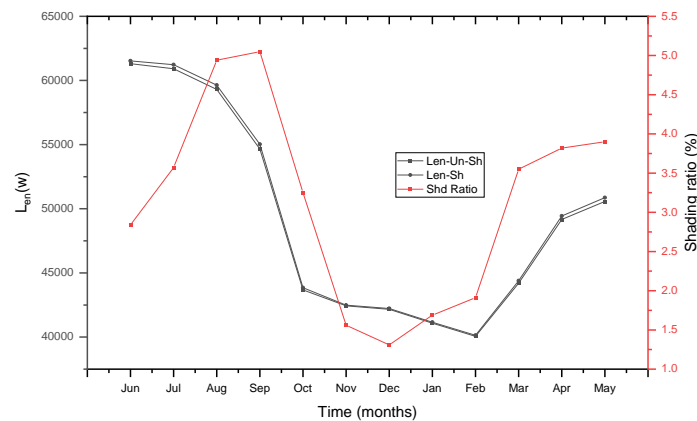


Figure 5. Variations of energy loss rates (L_{en}) and shading ratio versus time.

The energy loss rate of 'Un-Sh-Array' and 'Sh-Array' PV arrays is about 61308 w and 61529 w in June, while the lowest is about 40059 w and 40139 w in February. The variation of 'Un-Sh-Array' and 'Sh-Array' PV arrays examined varying in time (months), it can be seen that the thermodynamic loss rates vary between 55677 and 55524 W in the first month, June, and between 36761 and 36683 W, the lowest in February, the ninth month, see Fig. 5. It can be seen that the graphs of shaded and unshaded PV panels show similar characteristics, and the values of shaded PV arrays are smaller than those of unshaded ones. It can be said that the highest loss rates, starting in June and decreasing due to solar radiation, are the lowest in February, then increase again and shows seasonal characteristics. Details can be seen in figures 5 and 6.

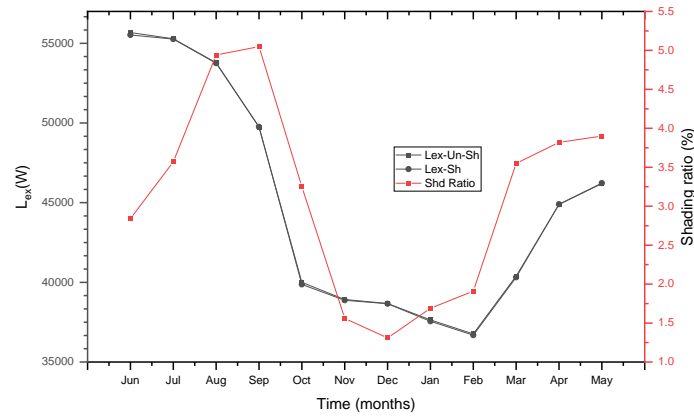


Figure 6. Variations of exergy loss rates and shading ratio versus time.

The correlations of R_{en} and R_{ex} and the shading ratio depending on time can be seen in Figures 7 and 8. R_{en} and R_{ex} values, which are exergoeconomic parameters of shaded and unshaded PV arrays, vary seasonally, depending on the months, that is on the ambient temperature and the angle of incidence of solar radiation. There is a small difference between them. Experimental observations starting from June, as the R_{en} (R_{ex}) values of the PV arrays, it is obvious that the values of the two PV strings (inv. 13 and 16) are at peak in proportion to the intensity of solar irradiation. Then, it starts to decrease slightly until December and is lowest up to February.

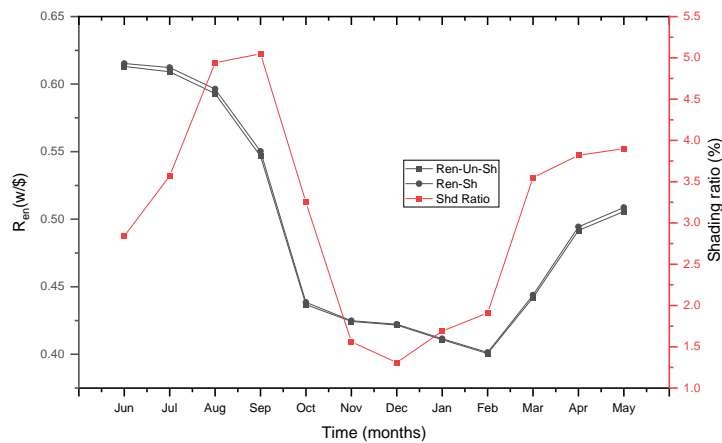


Figure 7. Variations of exergoeconomic parameter (R_{en}) and shading ratio versus time.

In details, R_{en} (R_{ex}) loss values for June were 0.615 (0.555) W/\$ for the ‘Sh’ PV string and 0.613 (0.557) W/\$ for the ‘Un-Sh’ string, then linearly it decreases to 0.401 (0.368) W/\$ and 0.401 (0.367) W/\$, respectively. In March it slightly increases linearly up to June.

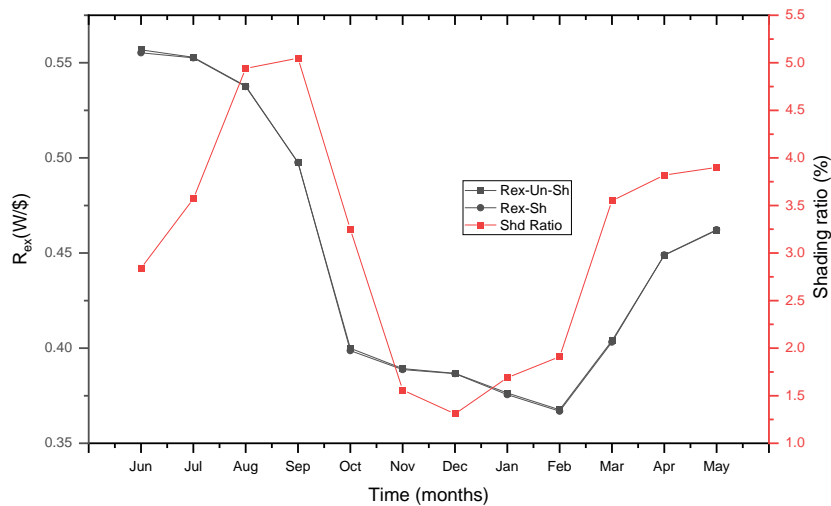


Figure 8. Variations of exergoeconomic parameter (R_{ex}) and shading ratio versus time.

As seen in Fig. 8, there is an increase and decrease observed of the exergoeconomic parameters, R_{en} (R_{ex}), of shaded and unshaded PV arrays in parallel with the solar radiation intensity, but it exhibits a more stable behavior for the T_a parameter of the environment where the PV system is installed. In other words, while the ambient temperature increases from June to the end of August, R_{en} (R_{ex}) values tend to decrease in reverse.

4. CONCLUSIONS

In this study, a comparative analysis was made on the impact of shading on a part of the front surface of a PV string, which was built without considering the angle of incidence of the sun's rays. The shading-affected PV string is controlled by the inverter (13) and the unaffected is controlled by the inverter (16), the observations continued from sunrise to the hours when the shading leaves. Findings and calculations were carried out with exergoeconomic parameters from June 2018 to May 2019. The measurements were conducted on cloudless and sunny days. These scientific observations are based on controlled experimental calculations and their findings can be briefly outlined as follows:

- For both shaded and unshaded PV strings, the meteorological and ecological details such as ambient temperature, sun's irradiation, and speed of the wind are the main factors that affect the production of the PV power plant.
- Since the high T_a causes the PV panels to heat up, there will be losses for both PV strings.
- The intensity of the sun's rays will affect it positively, but after a certain intensity, the value will affect it negatively.
- Positive contributions were observed when wind speed cooled the PV panel.

- As the dynamic partial shading ratio increases (the electric generating area of the panel surface will decrease), the electrical energy and exergy efficiency produced by the affected PV array decrease inversely compared to the unaffected.
- The energy (L_{en}) and exergy (L_{ex}) loss rate decrease slightly as the shading ratio increases.
- The exergoeconomic parameters R_{en} (R_{ex}) are maximum in June 0.615 (0.555) W/\$ of the 'Sh' PV string and 0.613 (0.557) W/\$ of the 'UnSh' string, then linearly it decreases to 0.401 (0.368)W/\$ and 0.401 (0.367) W/\$, respectively.
- The shading ratio is a maximum in September of about 5.05% and a minimum of about 1.31% in December, and R_{en} (R_{ex}) is about 0.550 (0.498) W/\$.

At the end of 12-month observations a year, undesirable structures built close to the PV arrays can create partial shading, and as a consequence, bad results can occur in electricity generation and cost problems in long service life. It was concluded that there may be a risk of damaging PV modules by creating hot spots on PV cells exposed to long-term undesirable shading. One of the results of this study is that the environmental factors of the structures that make up the PV power systems should be taken into account and it is important to manage the design phase correctly.

ACKNOWLEDGMENT

This scientific research did not receive any special assistance or support from any public or private institution, commercial enterprise, or financial institution in non-profit sectors.

REFERENCES

- [1] Gostein, M., Duster, T., and Thuman, C., (2015), Accurately measuring PV soiling losses with soiling station employing module power measurements. In: IEEE 42nd Photovoltaic Specialists Conference (PVSC), New Orleans, LA, pp. 1–4.
- [2] Bidram, A., Davoudi, A., and Balog, R. S., (2012), "Control and Circuit Techniques to Mitigate Partial Shading Effects in Photovoltaic Arrays," in IEEE Journal of Photovoltaics, vol. 2, no. 4, pp. 532-546, DOI: 10.1109/JPHOTOV.2012.2202879.
- [3] Dolara, A., Lazaroiu, G.C., Leva, S., Manzolini, G., (2013), Experimental investigation of partial shading scenarios on PV (photovoltaic) modules., Energy, 55, pp. 466-475, DOI:10.1016/j.energy.2013.04.009
- [4] Chepp, E. D., Gasparin, F. P., Krenzinger, A., (2022), Improvements in methods for analysis of partially shaded PV modules, Renewable Energy, 200, 900-910, <https://doi.org/10.1016/j.renene.2022.10.035>.
- [5] Khodapanah, M., Ghanbari, T., Moshksar, E., and Hosseini, Z., (2022), Partial shading detection and hotspot prediction in photovoltaic systems based on numerical differentiation and integration of the P – V curves, IET Renew. Power Gener.,1–17, <https://doi.org/10.1049/rpg2.12596>

- [6] Ceylan, İ., and Arslan, O., (2022), Performance evaluation of staged ORC power plant sourced by waste heat, *Journal of Scientific Reports-A, Number 50*, 1-19.
- [7] Duman, N., Buyruk, E., Acar, H.İ., Caner, M., Kiliç, F. and Can, A. (2021). Exergy Analysis of a Ground Source Heat Pump System for Cold Climatic Condition of Sivas, Turkey. *Transactions of FAMENA*, 45 (SI-1), 13-22. <https://doi.org/10.21278/TOF.SI1006321>
- [8] Mohammadi, B., Ranjbar, S. F., and Ajabshirchi, Y. (2021). Comprehensive evaluation of a semi-solar greenhouse:Energy, exergy, and economic analyses with experimental validation. *Scientia Iranica*, 28(5), 2613-2627. doi: 10.24200/sci.2021.53709.3375
- [9] Bayrak, F., Ertürk, G., Oztop, H.F., (2017), Effects of partial shading on energy and exergy efficiencies for photovoltaic panels., *J. Clean. Prod.*, 164, pp. 58-69, 10.1016/J.JCLEPRO.2017.06.108
- [10] Bayrak, F., Oztop, H.F., (2020), Effects of static and dynamic shading on thermodynamic and electrical performance for photovoltaic panels., *Appl. Therm. Eng.*, 169, Article 114900, 10.1016/j.applthermaleng.2020.114900
- [11] Keskin V., Pour Rahmati Khalejan S. H. and Çıkla R., (2021), “Investigation of the shading effect on the performance of a grid-connected PV plant in Samsun/Turkey”, *Politeknik Dergisi*, 24(2): 553-563.
- [12] Gaur, A., and Tewari, G.N., (2014), Exergoeconomic and enviroeconomic analysis of photovoltaic modules of different solar cells *J. Sol. Energy*, 8.
- [13] Sahin, A.D., Dincer, I., and Rosen, M .A., (2007), Thermodynamic analysis of solar photovoltaic cell systems, *Solar Energy Materials & Solar Cells*, 91, 153-159.
- [14] Bayat M., Ozalp M., (2018), Energy, exergy and exergoeconomic analysis of a solar photovoltaic module, *Exergetic, Energetic and Environmental Dimensions*, ed: Elsevier, pp. 383-402
- [15] Petela, R., (2003), Exergy of undiluted thermal radiation, *Solar Energy*, 74, 469-488.
- [16] Ozturk, M. and Dincer, I., (2020), Exergoeconomic analysis of a solar-assisted tea drying system, *Drying Technology*, 38:5-6, 655-662, DOI: 10.1080/07373937.2019.1669044

NOMENCLATURE

PV	:	Photovoltaic
R_{ex}	:	Exergoeconomic parameter, exergetic loss ratio
R_{en}	:	Exergoeconomic parameter, energetic loss ratio

E_{ex}	:	Exergy
E	:	Energy
T_a	:	ambient temperature
V	:	wind speed
I_S	:	solar radiation intensity
A	:	Area of the PV panels (m ²)
NPV	:	Net present value
I	:	Current
V	:	Voltage
P	:	Power

Greek letters

η_{pce}	:	efficiency
Ψ	:	Exergy efficiency



RESEARCH ARTICLE

285 nm AlGaIn-BASED DEEP-ULTRAVIOLET LED WITH HIGH INTERNAL QUANTUM EFFICIENCY: COMPUTATIONAL DESIGN

İrem ÖNER ALP^{1*}, Bilgehan Barış ÖNER², Esra EROĞLU³

^{1*}Gazi University, Faculty of Sciences, Department of Physics, Ankara, iremoner@gazi.edu.tr, ORCID: 0000-0002-6937-7864

²Gazi University, Faculty of Sciences, Department of Physics, Ankara, baris.oner@roketan.com.tr,
ORCID: 0000-0001-9440-2235

³METU, Faculty of Engineering, Department of Mechanical Engineering, Ankara, esraer@metu.edu.tr,
ORCID: 0000-0002-6848-5142

Receive Date: 26.10.2022

Accepted Date: 22.01.2023

ABSTRACT

In this paper, the systematic computational design process of AlGaIn-based multiple quantum-well (QW) deep-ultraviolet (DUV) light-emitting diode (LED) grown on sapphire (Al₂O₃) substrate was investigated. An optimization was held to increase internal quantum efficiency (IQE) handling the LED parameters such as doping percentage of the n- and the p-type layers of these devices. The structure parameters of the best design were determined through a customized genetic algorithm integrated into the nanostructure quantum electronic simulation (nextnano). As a determining factor, IQE was obtained to be 24% for the devised 285 nm LED. It has been demonstrated that this result can be increased up to a remarkably high value of 70% by a low threading dislocation density (TDD) and reduced Auger recombination. In addition, the operation input power and potential difference were successfully kept below 0.1 W/mm² and 5.05 V, respectively.

Keywords: *Deep-ultraviolet LED, UV-C LED, Quantum efficiency, Genetic algorithm*

1. INTRODUCTION

It is predicted that the biomedical application area of deep-ultraviolet (DUV) light-emitting diode (LED) systems will become widespread during and after the pandemic period [1-3]. However, the efficiencies of the devices with DUV radiation (20%) [4] have not yet reached the desired levels and are still a topic of current research. Deactivation of microorganisms such as viruses and bacteria is provided by irradiation in the UV-C range of 250 to 280 nm depending on their biological structures [5, 6]. Although the region where deactivation is most effective is below 265 nm, LED devices operating up to 300 nm can be preferred in order not to damage human cells [7]. Otherwise, UV-C LEDs have been extensively utilized in chemical detection through the fluorescence characteristics of some materials induced by UV-C light [8] and in drinking water decontamination due to the remarkable results achieved [9-12]. In this context, the selection criteria for the materials suitably

qualified depend on factors such as efficiency percentage, manufacturability, easy availability, and environmental friendliness (non-toxicity).

The AlGa_N alloy emits photons in the UV-C region, which can be controlled by adjusting the Al/Ga ratio and the other optoelectronic parameters. In addition, Al/In doped III-V compounds also play an important role in the determination of the operating wavelength and efficiency [13, 14]. At this point, the active region thickness and the concentrations in compounds predicted for a LED design are of crucial significance. For example, the higher the Al amount, the more dislocations appear in practice yielding adverse effects on the required optical properties [15]. Besides, low mismatch percent for the layers is important in crystal growth and the AlGa_N-based LED structure with the AlN buffer layer examined in this paper can be grown on sapphire (Al₂O₃) as it is often reported in the literature [16-20]. The various difficulties encountered during the production process apart from the ones mentioned, such as point defects, cracking issues, low hole concentration, junction heating effect, and low light extraction efficiency (LEE) should not be ignored as well [7]. Thus, high device efficiency will be obtained along with overcoming these handicaps.

Multiple research groups have carried out extensive examinations on DUV LED design and features of the constituent materials for several years yielding significant progress in performance [8, 21-27]. One of the most recent studies performed by Hirayama et al. have introduced an AlGa_N UV-C LED with high power in which a photonic crystal reflector was used [28]. Jain et al. proposed graded staircase quantum barriers against electron leakage problem for AlGa_N DUV LEDs [29]. A high LEE was measured by Zhang et al. for Ag-nanodots and Al electrodes adoption on AlGa_N LED operating at ~280 nm [30]. Itokazu et al. were previously able to establish an improvement in AlGa_N DUV LED performance via high-temperature annealing with an additional growth process for the AlN layer [31]. Shin et al. managed to get an enhanced LEE in a ~267 nm AlGa_N nanowire LED with photonic crystal [32]. Average package power values were obtained over 0.1 mW for AlGa_N UV-C LEDs emitting in the range of 230-240 nm by Moe et al. and the optical and electrical properties were characterized [33]. Chen et al. theoretically aimed to increase LEE choosing the contact layer as graphene in the deep UV LED block without p-GaN and have had a notable result [34].

The internal quantum efficiency (IQE), the enhancement of which is the subject of this study, is the other key factor that affects the LED efficiency and there have been significant attempts from researchers to improve IQE [35-39]. Shim et al. have proposed a method of temperature-independent measurement for IQE [40]. It is predicted that a very high-valued IQE for 284 nm InAlGa_N UV-C LED and have grown the DUV LEDs onto Al on sapphire operating at 222-282 nm [41]. By defect engineering, a similar result was obtained for IQE of 280 nm LED [42]. Hao et al. determined 267 nm LED IQE through a fitting method to electroluminescence data [43] and an increment on IQE value for AlGa_N-based DUV LED was observed by the use of nano patterned sapphire substrates yielding low dislocation density [44]. Guttman et al. have studied IQE of AlGa_N LEDs operating at 263 nm that has p-AlGa_N layers with different separate Al mole fractions [45].

In this paper, we have presented a systematic computational optimization process of DUV light-emitting devices to increase inner efficiency while minimizing the input power. IQE improvement of multi-layered quantum-well (QW) region including AlGa_N with AlN interlayer (IL) was addressed in

an algorithm which was developed by authors for the current study. The electron blocking layer (EBL) has been used because of the remarkable direct transition energy range in UV. In the next Section, the optimization method has been given. This step on IQE was performed by nanostructure quantum electronic simulation. Afterward, achieved results are reported for the LED structure with low-mismatch design and a discussion with the current literature is given. Finally, concluding remarks are written as a short summary.

2. MATERIAL AND METHOD

An ultraviolet multi-quantum well LED emitting under 300 nm wavelength has been aimed to design in this part of the study. An optoelectronic semiconductor nanodevice software package of nextnano was used [46, 47]. AlGa_N based LED devices have less lattice-mismatch issues due to the compatible lattice constants ($a_{\text{AlN}} = 4.38 \text{ \AA}$, $a_{\text{GaN}} = 4.50 \text{ \AA}$). Therefore, they constitute the basis of the device due to its above-mentioned superiorities over alternative UV materials. The main p-i-n layers of the LED are determined to be: an n-doped junction layer, 5 QW layers, a p-doped electron blocking layer (EBL) and finally a p-doped junction layer. QWs consist of a thinner Al_xGa_(1-x)N, a thicker Al_yGa_(1-y)N and an AlN interlayer (IL) between each quantum well. This brings 5 thickness, 3 doping and 6 alloy concentration degrees of freedom and therefore a total of 15 design parameters including input potential difference between p and n layers V_{pn} . These parameters are possible to be arranged such that a relatively high internal quantum efficiency value can be achieved for a low input power P_{in} for peak luminosity (λ_{PL}) wavelength under 300 nm. In order to construct such a design, here we utilize a conventional genetic algorithm as the optimization method which was written and developed by authors particularly for the current study. The main steps in the algorithm's cycle are given in Figure 1.

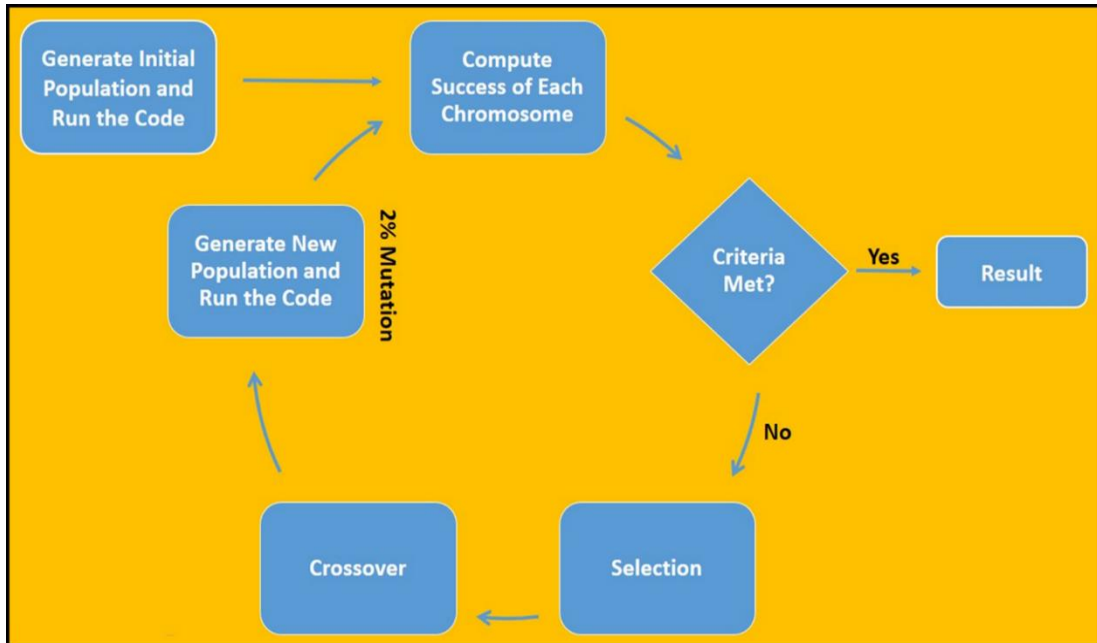


Figure 1. Flow chart of the utilized algorithm to generate highly efficient ultraviolet LED.

The number of chromosomes in each population was chosen as 75. Design parameters played the role of genes and V_{pn} was fixed at 5.00 V during the algorithm cycle. The first population was generated by a random selection (see the second column of Table 1). Success criteria of a chromosome are given by

$$s = \begin{cases} IQE, P_{in} < 10 \frac{W}{mm^2}, \lambda_{PL} < 300nm \\ 0, o.w. \end{cases} \quad (1)$$

Chromosomes were sorted after each computation considering their corresponding success rates and they were selected for the next crossover step such that each chromosome was coupled by the subsequent successful chromosome. Couplings began from the worst couples to the best ones. A final coupling was performed between the best and worst chromosomes. Therefore, the number of chromosomes in each population has been fixed. A new chromosome was generated at each crossover step with a 50% chance of getting genes from more and less successful chromosomes and a mutation chance of 2% was given at each turn.

3. RESULTS AND DISCUSSION

We share the results of the optimization via a customized genetic algorithm in Fig. 2 by a normalized success rate. The crossover phase given in the previous section keeps the average success rate low

while enabling a quick rise on each generation. By this means, the desired result (IQE value satisfying the success criteria) has been achieved within the seventh generation. The parameters related to the optoelectronic device design are listed in Table 1 and the third column shows the best results of the genetic algorithm optimization process. The reasonable initial ranges determined from the literature are also given in the second column.

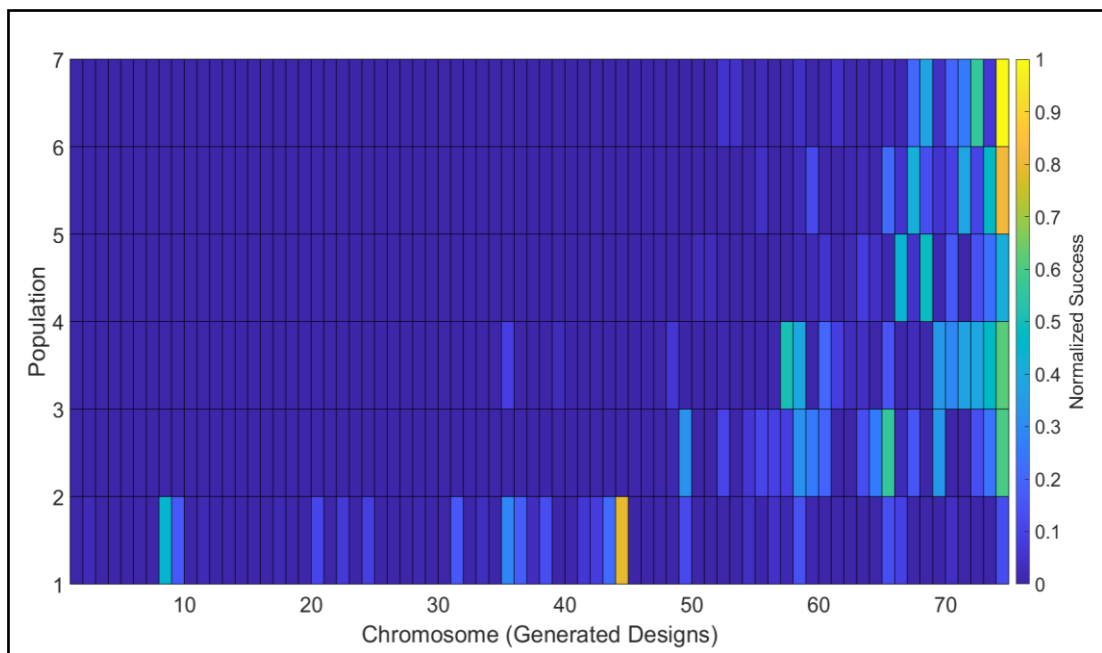


Figure 2. Normalized success rates of each chromosome.

The most effective decrease on the efficiency is due to radiative and nonradiative recombinations rates belonging to Auger and Shockley–Read–Hall (SRH) recombination modes. These phenomena are already known and there are several accepted recombination parameters within DUV region [43, 48]. There are no certain values, computations or direct experimental results standardized for the Auger recombination rate in AlGaIn alloys. Therefore, nonradiative-Auger and radiative recombination coefficients were determined to be $2.30 \times 10^{-30} \text{ cm}^6 \text{ s}^{-1}$ and $5.00 \times 10^{-11} \text{ cm}^3 \text{ s}^{-1}$, respectively [36, 49] and

Table 1. Design parameters of the optoelectronic device, initial population value windows of initial random generation and structure parameters of the best design.

Design Parameter	Parameter Window (if valid)	Best Design
Width of the n-doped layer	100 - 1000 nm	850 nm

Width of the QW 1st layer	10 - 15 nm	14.45 nm
Width of the QW 2nd layer	1 - 6 nm	2.66 nm
Width of the IL	0 - 2 nm	1.57 nm
Width of the EBL	15 - 60 nm	57.42 nm
Width of the p-doped layer	30 - 100 nm	95.47 nm
Al% of the n-doped layer	40% - 80%	66%
Al% of the QW 1st layer	40% - 80%	66%
Al% of the QW 2nd layer	30% - 70%	45%
Al% of the EBL	50% - 90%	50%
Al% of the p-doped layer	0 - 2.20e20 cm ⁻³	0
N_a of the n-doped layer	1.00e17 - 2.20e20 cm ⁻³	4.29e19 cm ⁻³
N_a of the QW 2nd layer	5.00e17 cm ⁻³	5.00e17 cm ⁻³
N_a of the EBL	1.00e17 - 2.20e20 cm ⁻³	6.39e17 cm ⁻³
N_a of the p-doped layer	1.00e17 - 2.20e20 cm ⁻³	1.13e19 cm ⁻³
V_{pn}	5.00 V	5.00 V
c_{Auger}	2.30e-30 cm ⁶ s ⁻¹	2.30e-30 cm ⁶ s ⁻¹
c_{recomb}	5.00e-11 cm ³ s ⁻¹	5.00e-11 cm ³ s ⁻¹
τ_n	1.00 e-9 s ⁻³	1.00 e-9 s ⁻³
τ_p	1.00 e-9 s ⁻³	1.00 e-9 s ⁻³
Size	1.00 mm × 1.00 mm	1.00 mm × 1.00 mm

τ_n and τ_p denote radiative lifetimes of free excitons. Another parameter important in the optimization process belongs to the electronic properties. Operating voltage difference between p-contact and n-

contact (V_{pn}) was kept fixed at 5.00 V at first since IQE saturates after a certain amount of V_{pn} increment.

The best design has an IQE of 24% when the forward voltage is 5.00 V. In this case, a 1.00 mm \times 1.00 mm LED requires an input power below 0.1 W and the LED structure formed according to Table 1 is demonstrated in Fig. 3. From hence, the block is going to be grown on a sapphire substrate and the active region consists of four sequential quantum-well (QW) regions. Each QW includes triple-layers, which are $Al_{0.66}Ga_{0.34}N$ (QW 1st), $Al_{0.45}Ga_{0.55}N$ (QW 2nd) and AlN (IL) from bottom to top with the widths of 14.45 nm, 2.66 nm, and 1.57 nm, respectively. Likewise, the width of the other layers and doping concentration values are presented once again in Fig. 3 so that the reader can follow more easily. The widths of the buffer layer and substrate were not included in the calculations. The attention should be paid that Al doping into the p-doped layer was not considered necessary according to the optimization results as can be seen in Table 1. In this manner, GaN has been specified as the p-layer (see Fig. 3). The next step of the V_{pn} adjustment was taken after getting the best results which includes operating voltage upper limit calculations.

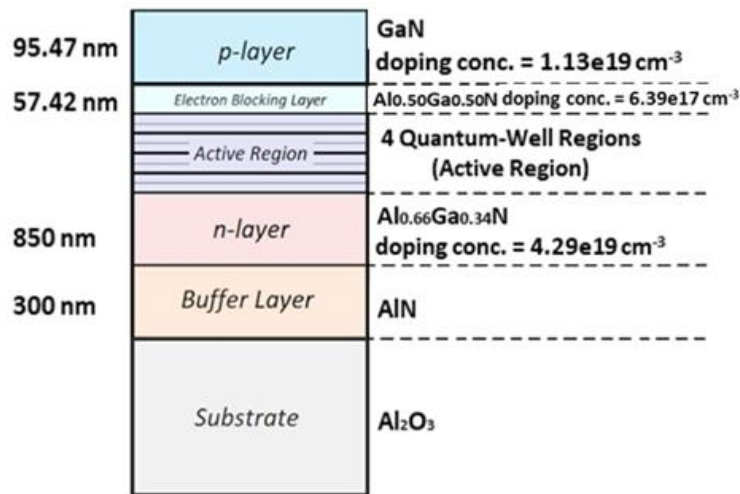


Figure 3. Schematics of the optimized multi QW UV-C AlGaIn-based LED.

In Fig. 4(a), the distribution of IQE and input power with respect to V_{pn} is plotted. The LED can operate up to 5.20 V where afterwards a breakdown occurs. Required input power also increases by V_{pn} which fails the success criteria over 5.05 V. Figure 4(b) shows emitted photon wavelength which reaches its peak intensity at 285 nm corresponding to UV-C region.

Efficiency improvement of III-V compound light emission mechanism mostly depends on threading dislocation densities (TDDs), low p-type concentrations, and the light extraction efficiency (LEE) [50]. Among these, the most efficient contribution comes from reduction of the TDD. In other words,

growing III-V compounds with a low threading dislocation density still continues to be main issues of experimental studies. In this regard, Hirayama et al. reported the highest relative IQE value of 86% predicted from a relation that assumes a 100% IQE at low temperature [41] and IQE was calculated as 85% by the same approach in a different study [42]. Hao et al. have achieved the value of 77% by reducing TDD [43] and a similar method has also been addressed by Dong et al. via a device based on nano patterned sapphire substrates. Increment on IQE values from 30% to 43% was achieved [44]. The authors of another study have achieved a quite well IQE value of 29% [45].

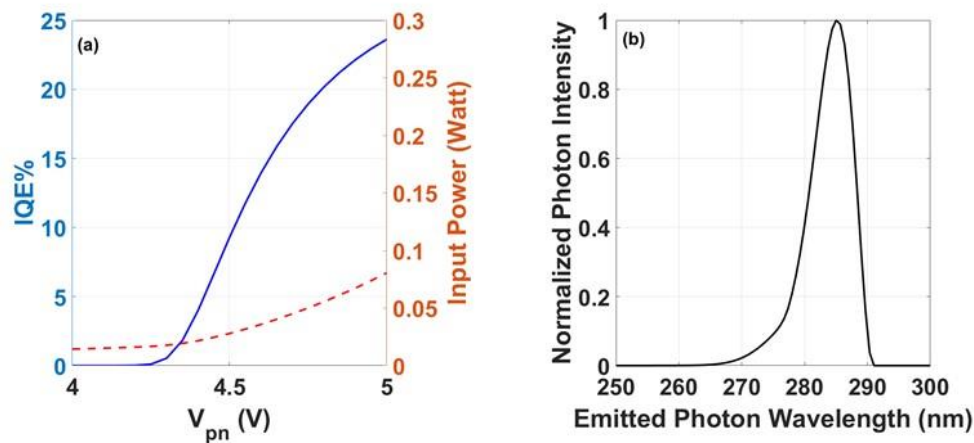


Figure 4. (a) V_{pn} dependence of internal quantum efficiency (solid line) and operating power (dashed line) were given. (b) Emitted light normalized intensity distribution was plotted (peak wavelength at 285 nm).

Besides, GaN based device efficiencies are addressed both theoretically and experimentally by dislocation density effects [51]. These researches clearly show that TDD should be considered to present more realistic results since it directly depends on the growth methods like MBE or MOCVD. TDD is still in improvement process by current experimental technology development studies.

Another effect arises because of nonradiative Auger recombination (c_{Auger}) as mentioned above. However; compounds do not have certain c_{Auger} values in the literature while they are usually accepted within an approximate range. One should note that, these parameters cannot be improved by design optimization. Nevertheless, these uncertainties necessitate an IQE scan of a parameter window constituted by c_{Auger} and c_{recomb} in order to include possible fabrication error and material effects. Therefore, IQE distribution was computed and plotted (see Figure 5) which covers a range of c_{Auger} between $10^{-30} - 10^{-32} \text{ cm}^6 \text{ s}^{-1}$. All other physical parameters are kept nominal as given in Table 1. The figure shows that especially c_{recomb} has a remarkable effect on the internal efficiency.

A final computation was done in order to find the LEE of the structure. The exact design given in Figure 3 was transferred to a finite-difference time-domain software package (MEEP) [52]. The result

shows that the deep UV LED design has a LEE value of 34% that leads an overall 8.2% external quantum efficiency (EQE). Huge part of the loss occurs due to non-negligible absorption coefficients of the semiconductor alloys. This situation directly implies a possible improvement by an optimization method on the extraction efficiency which was held out of the scope of this study.

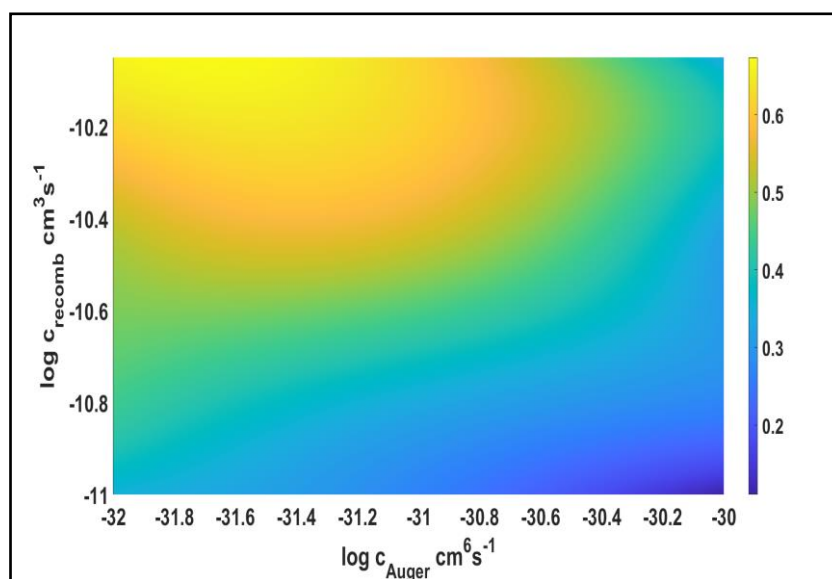


Figure 5. Radiative and nonradiative recombination dependence of IQE.

4. CONCLUSION

This research discusses the IQE improvement of DUV LED design. The analysis technique includes an implementation of a customized genetic algorithm on nanostructure quantum electronic simulations. The widths and doping concentrations of the constituents (EBL, QW, p- and n-doped layers) that gave the best results have been obtained. The main recombination parameters such as c_{Auger} , c_{recomb} , τ_n , and τ_p were taken into consideration in all simulations. Additionally, a parameter window of these recombinations have been presented to show the efficiency dependence. The AlGaIn UV-C LED addressed in the current study satisfies the success criteria determined up to 5.05 V according to the V_{pn} dependence of IQE. Standard design with 15 degrees of freedom let the IQE value to be 24% which can be increased over 50% by decreased TDD and up to 70% by an additional reduced Auger recombination. This result is remarkably high considering the output peak wavelength of 285 nm comparable to the prominent studies. Another advantage of the study lies beneath the low operation input power (below 0.1 W/mm²) requirement at room temperature. Although they are excluded from the scope of this study, LEE and EQE values, which can be further improved by optimization, have also been calculated to get a realistic idea about the device efficiency.

ACKNOWLEDGEMENT

The nanostructure quantum electronic simulation nextnano has been employed in the first optimization step on internal quantum efficiency. We would like to thank Dr. Stefan BIRNER and the team for their understanding and contribution in using the package.

Authors' Contribution

The first author contributed 40% to this study and remaining 60% has been shared as 35% and 25% by the second and third authors, respectively.

REFERENCES

- [1] Shur, M., (2021), Emerging applications of deep ultraviolet light emitting diodes, in UV and Higher Energy Photonics: From Materials to Applications 2021 Proceedings, International Society for Optics and Photonics, 11801, 1180105.
- [2] Li, J., Gao, N., Cai, D., Lin, W., Huang, K., Li, S., and Kang, J., (2021), Multiple fields manipulation on nitride material structures in ultraviolet light-emitting diodes, *Light: Science & Applications*, 10, 1-20.
- [3] Raeiszadeh, M. and Adeli, B., (2020), A critical review on ultraviolet disinfection systems against COVID-19 outbreak: Applicability, validation, and safety considerations, *ACS Photonics*, 7, 2941-2951.
- [4] Takano, T., Mino, T., Sakai, J., Noguchi, N., Tsubaki, K., and Hirayama, H., (2017), Deep-ultraviolet light-emitting diodes with external quantum efficiency higher than 20% at 275 nm achieved by improving light-extraction efficiency, *Applied Physics Express*, 10, 031002.
- [5] Chang, J.C., Ossoff, S.F., Lobe, D.C., Dorfman, M.H., Dumais, C.M., Qualls, R.G., and Johnson, J.D., (1985), UV inactivation of pathogenic and indicator microorganisms, *Applied and environmental microbiology*, 49, 1361-1365.
- [6] Kowalski, W., (2009), UVGI disinfection theory, in *Ultraviolet germicidal irradiation handbook*, Springer, Berlin, Heidelberg, 17-50.
- [7] Zollner, C.J., DenBaars, S.P., Speck, J., and Nakamura, S., (2021), Germicidal ultraviolet LEDs: a review of applications and semiconductor technologies, *Semiconductor Science and Technology*, 36, 123001.
- [8] SaifAddin, B.K., Almgobel, A.S., Zollner, C.J., Wu, F., Bonef, B., Iza, M., ... and Speck, J.S., (2020), AlGaIn deep-ultraviolet light-emitting diodes grown on SiC substrates, *ACS Photonics*, 7, 554-561.

- [9] Lui, G.Y., Roser, D., Corkish, R., Ashbolt, N.J., and Stuetz, R., (2016), Point-of-use water disinfection using ultraviolet and visible light-emitting diodes, *Science of the Total Environment*, 553, 626-635.
- [10] Song, K., Mohseni, M., and Taghipour, F., (2016), Application of ultraviolet light-emitting diodes (UV-LEDs) for water disinfection: A review, *Water Research*, 94, 341-349.
- [11] Kheyrandish, A., Mohseni, M., and Taghipour, F., (2017), Development of a method for the characterization and operation of UV-LED for water treatment, *Water Research*, 122, 570-579.
- [12] Vilhunen, S., Särkkä, H., and Sillanpää, M., (2009), Ultraviolet light-emitting diodes in water disinfection, *Environmental Science and Pollution Research*, 16, 439-442.
- [13] Nakamura, S., (1998), The roles of structural imperfections in InGaN-based blue light-emitting diodes and laser diodes, *Science*, 281, 956-961.
- [14] Kneissl, M., Seong, T.Y., Han, J., and Amano, H., (2019), The emergence and prospects of deep-ultraviolet light-emitting diode technologies, *Nature Photonics*, 13, 233-244.
- [15] Amano, H., Collazo, R., De Santi, C., Einfeldt, S., Funato, M., Glaab, J., ... and Zhang, Y., (2020), The 2020 UV emitter roadmap, *Journal of Physics D: Applied Physics*, 53, 503001.
- [16] Demir, İ., (2018), Growth temperature dependency of high Al content AlGa_N epilayers on AlN/Al₂O₃ templates, *Cumhuriyet Science Journal*, 39, 728-733.
- [17] Park, T.H., Lee, T.H., and Kim, T.G., (2019), Al₂O₃/AlN/Al-based backside diffuse reflector for high-brightness 370-nm AlGa_N ultraviolet light-emitting diodes, *Journal of Alloys and Compounds*, 776, 1009-1015.
- [18] Lim, S.H., Shin, E.J., Lee, H.S., Han, S.K., Le, D.D., and Hong, S.K., (2019), Effects of growth rate and III/V ratio on properties of AlN films grown on c-plane sapphire substrates by plasma-assisted molecular beam epitaxy, *Korean Journal of Materials Research*, 29, 579-585.
- [19] Nagasawa, Y. and Hirano, A., (2018), A review of AlGa_N-based deep-ultraviolet light-emitting diodes on sapphire, *Applied Sciences*, 8, 1264.
- [20] Park, K.W. and Yun, Y.H., (2020), Effects of AlN buffer layer on optical properties of epitaxial layer structure deposited on patterned sapphire substrate, *Journal of the Korean Crystal Growth and Crystal Technology*, 30, 1-6.
- [21] Ren, Z., Lu, Y., Yao, H.-H., Sun, H., Liao, C.-H., Dai, J., ..., and Li, X., (2019), III-nitride deep UV LED without electron blocking layer, *IEEE Photonics Journal*, 11, 1-11.

- [22] Acharya, J., Venkateshh, S., and Ghosh, K., (2021), Engineering the Active Region to Enhance the IQE by ~8% in AlGaIn/GaN based UV-C LED, in 2021 International Conference on Numerical Simulation of Optoelectronic Devices Proceedings, Institute of Electrical and Electronics Engineers, NUSOD 2021, 69-70.
- [23] Gao, N., Chen, J., Feng, X., Lu, S., Lin, W., Li, J., Chen, H., Huang, K., and Kang, J., (2021), Strain engineering of digitally alloyed AlN/GaN nanorods for far-UVC emission as short as 220 nm, *Optical Materials Express*, 11, 1282-1291.
- [24] Peng, Y., Guo, X., Liang, R., Cheng, H., and Chen, M., (2017), Enhanced light extraction from DUV-LEDs by AlN-doped fluoropolymer encapsulation, *IEEE Photonics Technology Letters*, 29, 1151-1154.
- [25] Liu, C., Melanson, B., and Zhang, J., (2020), AlGaIn-Delta-GaN quantum well for DUV LEDs, *Photonics*, 7, 87.
- [26] Zhuang, Z., Iida, D., and Ohkawa, K., (2020), Enhanced performance of N-polar AlGaIn-based deep-ultraviolet light-emitting diodes, *Optics Express*, 28, 30423-30431.
- [27] Tomson, R., Uhlin, F., and Fridolin, I., (2014), Urea Rebound Assessment Based on UV Absorbance in Spent Dialysate, *Asaio Journal*, 60, 459-465.
- [28] Hirayama, H., Kashima, Y., Matsuura, E., Maeda, N., and Jo, M., (2021), Progress on high-power UVC LEDs by increasing light-extraction efficiency, in *Light-Emitting Devices, Materials, and Applications XXV*, International Society for Optics and Photonics, 11706, 117060G.
- [29] Jain, B., Velpula, R.T., Patel, M., Sadaf, S.Md., and Nguyen, H.P.T., (2021), Improved performance of electron blocking layer free AlGaIn deep ultraviolet light-emitting diodes using graded staircase barriers, *Micromachines*, 12, 334.
- [30] Zhang, N., Xu, F.J., Lang, J., Wang, L.B., Wang, J.M., Sun, Y.H., ... and Shen, B., (2021), Improved light extraction efficiency of AlGaIn deep-ultraviolet light emitting diodes combining Ag-nanodots/Al reflective electrode with highly transparent p-type layer, *Optics Express*, 29, 2394-2401.
- [31] Itokazu, Y., Kuwaba, S., Jo, M., Kamata, N., and Hirayama, H., (2019), Influence of the nucleation conditions on the quality of AlN layers with high-temperature annealing and regrowth processes, *Japanese Journal of Applied Physics*, 58, SC1056.
- [32] Shin, W., Pandey, A., Liu, X., Sun, Y., and Mi, Z., (2019), Photonic crystal tunnel junction deep ultraviolet light emitting diodes with enhanced light extraction efficiency, *Optics Express*, 27, 38413-38420.

- [33] Moe, C.G., Sugiyama, S., Kasai, J., Grandusky, J.R., and Schowalter, L.J., (2018), AlGa_N Light- Emitting Diodes on AlN Substrates Emitting at 230 nm, *Physica Status Solidi (a)*, 215, 1700660.
- [34] Chen, X. and Wu, Y.R., (2015), Numerical study of current spreading and light extraction in deep UV light-emitting diode, in *Light-Emitting Diodes: Materials, Devices, and Applications for Solid State Lighting XIX*, International Society for Optics and Photonics, 9383, 93830Q.
- [35] Bhattacharyya, A., Moustakas, T.D., Zhou, L., Smith, D.J., and Hug, W., (2009), Deep ultraviolet emitting AlGa_N quantum wells with high internal quantum efficiency, *Applied Physics Letters*, 94, 181907.
- [36] Rudinsky, M.E. and Karpov, S.Y., (2020), Radiative and Auger recombination constants and internal quantum efficiency of (0001) AlGa_N deep- UV light- emitting diode structures, *Physica Status Solidi (a)*, 217, 1900878.
- [37] Bryan, Z., Bryan, I., Xie, J., Mita, S., Sitar, Z., and Collazo, R., (2015), High internal quantum efficiency in AlGa_N multiple quantum wells grown on bulk AlN substrates, *Applied Physics Letters*, 106, 142107.
- [38] Lobo-Ploch, N., Mehnke, F., Sulmoni, L., Cho, H.K., Guttman, M., Glaab, J., ... and Kneissl, M., (2020), Milliwatt power 233 nm AlGa_N-based deep UV-LEDs on sapphire substrates, *Applied Physics Letters*, 117, 111102.
- [39] Murotani, H., Tanabe, R., Hisanaga, K., Hamada, A., Beppu, K., Maeda, N., ... and Yamada, Y., (2020), High internal quantum efficiency and optically pumped stimulated emission in AlGa_N-based UV-C multiple quantum wells, *Applied Physics Letters*, 117, 162106.
- [40] Shim, J.I., Han, D.P., Oh, C.H., Jung, H., and Shin, D.S., (2018), Measuring the internal quantum efficiency of light-emitting diodes at an arbitrary temperature, *IEEE Journal of Quantum Electronics*, 54, 1-6.
- [41] Hirayama, H., Fujikawa, S., Noguchi, N., Norimatsu, J., Takano, T., Tsubaki, K., and Kamata, N., (2009), 222–282 nm AlGa_N and InAlGa_N- based deep- UV LEDs fabricated on high-quality AlN on sapphire, *Physica Status Solidi (a)*, 206, 1176-1182.
- [42] Wang, T.Y., Tasi, C.T., Lin, C.F., and Wu, D.S., (2017), 85% internal quantum efficiency of 280-nm AlGa_N multiple quantum wells by defect engineering, *Scientific Reports*, 7, 1-8.
- [43] Hao, G.D., Tamari, N., Obata, T., Kinoshita, T., and Inoue, S.I., (2017), Electrical determination of current injection and internal quantum efficiencies in AlGa_N-based deep-ultraviolet light-emitting diodes, *Optics Express*, 25, A639-A648.

- [44] Dong, P., Yan, J., Zhang, Y., Wang, J., Zeng, J., Geng, C., ... and Li, J., (2014), AlGaIn-based deep ultraviolet light-emitting diodes grown on nano-patterned sapphire substrates with significant improvement in internal quantum efficiency, *Journal of Crystal Growth*, 395, 9-13.
- [45] Guttman, M., Susilo, A., Sulmoni, L., Susilo, N., Ziffer, E., Wernicke, T., and Kneissl, M., (2021), Light extraction efficiency and internal quantum efficiency of fully UVC-transparent AlGaIn based LEDs, *Journal of Physics D: Applied Physics*, 54, 335101.
- [46] Trellakis, A., Zibold, T., Andlauer, T., Birner, S., Smith, R.K., Morschl, R., and Vogl, P., (2006), The 3D nanometer device project nextnano: Concepts, methods, results, *Journal of Computational Electronics*, 5, 285–289.
- [47] Birner, S., Zibold, T., Andlauer, T., Kubis, T., Sabathil, M., Trellakis, A., and Vogl, P., (2007), Nextnano: general purpose 3-D simulations, *IEEE Transactions on Electron Devices*, 54, 2137-2142.
- [48] Dmitriev, A. and Oruzhenikov, A., (1999), The rate of radiative recombination in the nitride semiconductors and alloys, *Journal of Applied Physics*, 86, 3241-3246.
- [49] Nippert, F., Tollabi Mazraehno, M., Davies, M.J., Hoffmann, M.P., Lugauer, H.J., Kure, T., ... and Wagner, M.R., (2018), Auger recombination in AlGaIn quantum wells for UV light-emitting diodes, *Applied Physics Letters*, 113, 071107.
- [50] Hirayama, H., Fujikawa, S., and Kamata, N., (2015), Recent progress in AlGaIn- based deep-UV LEDs, *Electronics and Communications in Japan*, 98, 1-8.
- [51] Yu, J., Hao, Z., Li, L., Wang, L., Luo, Y., Wang, J., and Li, H., (2017), Influence of dislocation density on internal quantum efficiency of GaIn-based semiconductors, *AIP Advances*, 7, 035321.
- [52] A. F. Oskooi, D. Roundy, M. Ibanescu, P. Ber-mel, J. D. Joannopoulos, and S. G. Johnson (2010), Meep: A flexible free-software package for electromagnetic simulations by the FDTD method, *Computer Physics Communications*, 181, 687-702.



RESEARCH ARTICLE

**MINERALOGY AND GEOCHEMISTRY OF COAL-BEARING TUNÇBİLEK FORMATION
İN THE TUNÇBİLEK-TAVŞANLI COALFIELD (KÜTAHYA, W-TURKEY)**

Selin KARADİREK^{1*}

^{1,*} Akdeniz University, Faculty of Engineering, Department of Geological Engineering, Antalya, selinhokerek@akdeniz.edu.tr,
ORCID: 0000-0003-4829-600X

Receive Date: 21.10.2022

Accepted Date: 22.01.2023

ABSTRACT

Tunçbilek-Tavşanlı (Kütahya) Basin is among the most important Neogene coal deposits of Turkey. This study aims to determine the mineralogical and geochemical properties of the rocks (coal, roof, floor and parting) in the Tunçbilek-Tavşanlı coal field. The main abundant minerals in Tunçbilek-Tavşanlı coals are quartz, kaolinite, illite-smectite and siderite. Dolomite, illite, smectite, mica, feldspar, pyrite, chlorite and jarosite are less abundant minerals. The mineralogy of non-coal rocks is similar to that of coals, but pyrite is absent. The most abundant major oxides in the studied samples are SiO₂, Al₂O₃ and Fe₂O₃, respectively. The SiO₂, Al₂O₃ and MgO are the most abundant major oxides, respectively, in the claystone samples representing partings. Trace element concentrations of Tunçbilek-Tavşanlı coal samples mostly showed higher concentrations (excluding Ba, Sr, Pr, Tb, Dy, Ho, Tm, As, Cd and Bi) compared to the world low-rank coal average. According to the relative enrichment of the elements, the concentration coefficients (CC) of the coal samples are generally in the range of slightly enriched-normal; The CC of the non-coal samples mainly indicate the normal. The average REY concentration in the studied samples is higher than the world low-rank coal concentration and mostly showed L-type enrichment. Moreover, the REY concentration of the supercritical groups constitutes a significant part of the REY_{total} concentration in the samples taken from the coal horizon. However, the studied samples are in the unpromising area according to the low cut-off grade value and the relationship between cut-off grade-C_{outl}. The high correlation coefficient between ash content and REY concentrations also indicates a mineral substance relationship. Al₂O₃/TiO₂ (between 12.5-31.7) ratios of Tunçbilek-Tavşanlı samples show intermediate and felsic source rocks.

Keywords: Coal, REE+Y (REY), Trace elements, Tunçbilek

1. INTRODUCTION

Coal, as an important energy source, consists of water, minerals, elements, rock fragments in addition to organic matter. Coal is still an important resource for many countries all around the world [1, 2]. Minerals and elements found in coal are more important than other side components. According to

numerous studies in this area, coal contains the greatest variety of minerals and elements existing in nature. From a scientific view of point, minerals and elements in coal are important parameters for determination of paleoenvironment-paleoclimate characteristics and geological evolution of coal, as they may include detailed records that occurred during peatification and subsequently changed during the coalification process [2-7].

Coal is used as an industrial raw material source in metallurgical processes, especially in electricity generation, in gasification, in cement industries, in the biological conversion process to high-value agricultural products. Furthermore, some coals contain Ge, Ga, U, V, Se, rare earth elements and Y (REE+Y or REY if Y is not included), some critical base metals such as Sc, Y, Au, Ag, Al and Mg [8]. Although the minerals and elements in coal are generally thought to have negative effects during the production, transportation and combustion of coal [9], they also have some beneficial aspects. Especially rare earth elements and some elements such as Y, Li, Ga, Se, Zr and Nb [8, 10-12] in coal attract attention as a potential raw material source, as they are used in the semiconductor industry. The concentrations of rare elements in coal ash are fairly high to make extraction in some countries [13-18]. Coals with high Al content have also attracted much attention in China in recent years because the coal ash has more than 50% wt. Al_2O_3 and has therefore been used for Al extraction [19, 20].

The Kütahya basin is an important basin with a variety of mineral deposits. There are also important coal deposits in the Tunçbilek-Tavşanlı basin. The first detailed geological study in the region was carried out by Arni in 1942 [21]. Afterwards, various studies on geology, tectonism and sedimentology of the basin have been carried out by many researchers [22-32]. With the understanding of the existence of economically important mineral deposits in the basin, studies have begun to be detailed in this direction [33-45]. This study is aimed to determine the major-trace element geochemistry and mineralogical composition of the coals and roof, parting, and floor associated with coal in the Tunçbilek coalfield, located in the west of Turkey, and to examine the usability as a by-product raw material in the industrial field based on these data.

2. GEOLOGICAL EVOLUTION AND STRATIGRAPHY OF THE STUDY AREA

The tectonic units forming the Anatolian plate were named by Ketin (1966) [46] for the first time as the Pontides in the north, Anatolides, Taurides and Border Folds towards the south. In later studies, it was distinguished from north to south as Rhodope-Istranca Zone, Istanbul Zone, Sakarya Zone, Anatolide-Tauride block (Tavşanlı Zone, Afyon Zone, Menderes Massif Kırşehir Massif, Arabian Platform by Okay and Tüysüz (1999) [47]. Figure 1 shows the location of study area that is placed in the north of Tunçbilek in Tavşanlı-Kütahya district.

Western Anatolia, in which the study area is located, contains several tectonostratigraphic units (Sakarya Zone and Anatolide-Tauride Block) from northern to southern [47, 48]. Around the study area, the Anatolide-Tauride Block consists of the Menderes Extensional Core Complex representing the metamorphic massif [49], the Afyon Zone metamorphic rocks [50] and the mélange units of the İzmir-Ankara Zone [51], together with the ophiolites and blueschist facies of the Tavşanlı Zone [39, 52]. The blueschist facies of the Tavşanlı Zone represent the Anatolide-Tauride Block subducting towards the north, under the Sakarya Zone during the Cretaceous-Paleocene [53]. Eocene-Oligocene

sedimentary units unconformably overlie these tectonic units [39]. All these units are covered by Neogene sedimentary units. E-W trending grabens (such as Bakırçay, Kütahya, Gediz, Simav, Küçük Menderes, Büyük Menderes) and NE-SW trending basins (such as Gördes, [54], Selendi [55], Emet [56], Uşak-Güre [57], Tunçbilek-Domaniç [22, 26, 58] and Seyitömer basins [26, 59]) in Western Anatolia are the basins that developed due to the extensional tectonic regime. The Kütahya Graben, which is divided into sub-basins namely Tavşanlı and Seyitömer. Tunçbilek-Tavşanlı coalfield is placed in Tavşanlı sub-basin [45].

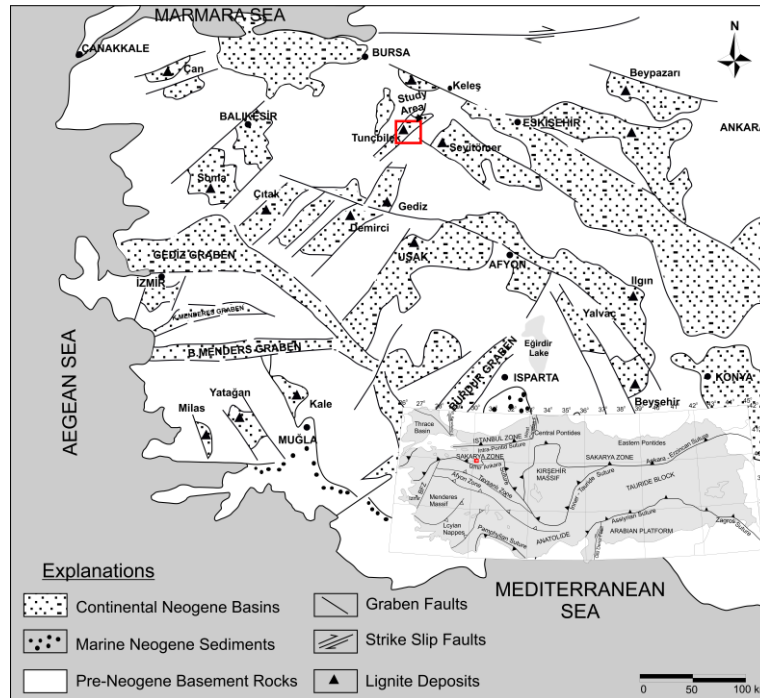


Figure 1. Tectonic setting of the Western Anatolian Neogene basin and location map of the study area (modified from [60] and [47]).

The basement rocks of the study area consist of metamorphic and ophiolitic rocks represented by Paleozoic and Mesozoic schist, quartzite, marble, serpentinite, peridotite, metaclastics and metacarbonates [26, 45]. In addition to other basement rock types, Eocene aged limestones (Oğulcaftepe Formation) exhibit a limited distribution [26, 39] (Fig. 2 and 3).

Beke Formation units (conglomerate, sandstone, claystone) are overlain on the basement rocks in Miocene. Baş (1986) [26] determined the age of Beke Formation as Middle Miocene based on pollen analysis. The coal-bearing Miocene Tunçbilek Formation, consisting of three members (Demirbilek, Güragaç and Yeldeğirmeni, respectively) is unconformably overlain on the Beke Formation. The Tunçbilek Formation shows lacustrine conditions. Demirbilek member of Tunçbilek formation

represents the coal-bearing marl, sandstone, and claystone. The Gurağaç member, which is gradually overlain by conglomerate, sandstone, and claystone intercalations, overlies the Demirbilek member, and the Tunçbilek Formation ends with the clayey-silicified limestones of the Yeldeğirmeni Member overlying the Gurağaç member [26, 39]. Common pyroclastic rocks in the basin are called Civanadagi tuffs [26].

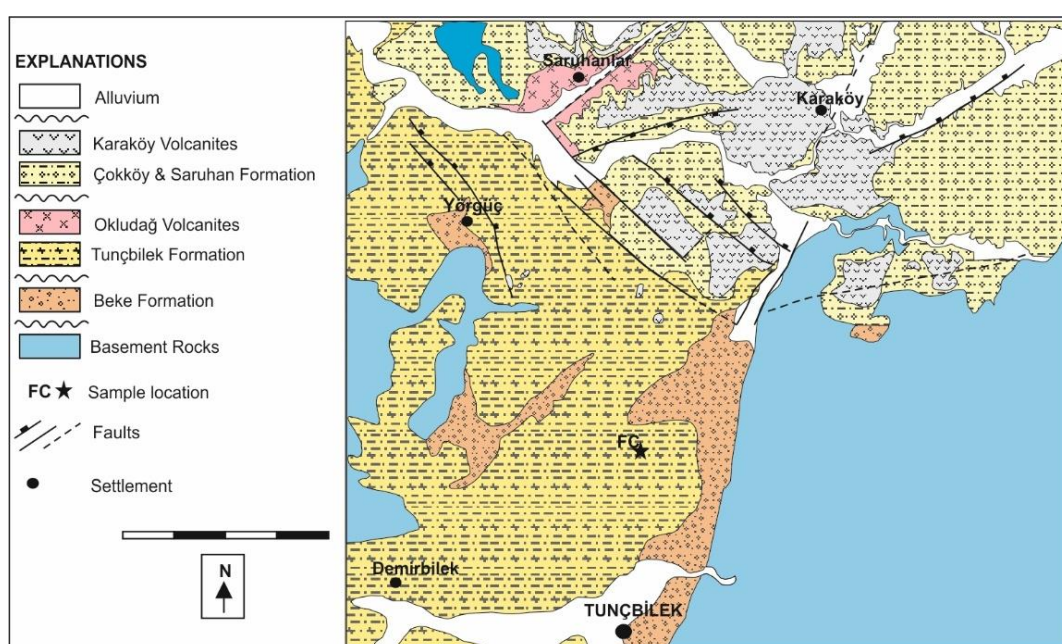


Figure 2. Geological map of the Tunçbilek-Tavşanlı basin (modified from [26], [39], [58] and [61]).

The Civanadağ tuffs conformably overlie the Tunçbilek Formation and are interbedded with the Oklukdağ Volcanites consisting of dyke, dome and lava flows [26]. The Saruhanlar Formation include conglomerate, sandstone, limestone and tuff layers and they are unconformably overlain on the Tunçbilek Formation during the Pliocene. Saruhanlar Formation is covered by andesitic-basaltic rocks called Pliocene Karaköy Volcanics and is vertically transitional to Çökköy Formation. The Çökköy Formation consists of conglomerate, claystone and marl. Due to the uplift and evaporation processes of the region in the Upper Pliocene, the lacustrine environment conditions have ended. The deposits overlying the Pliocene units are represented by Quaternary coarse-grained clastics, and travertines [26].

3. MATERIAL AND METHOD

The field studies were carried out in the open pit FC panel of the Garp Lignites Enterprise located in the Tunçbilek coal basin. Samples (total 25 samples including coal, clayey coal, carbonaceous shale,

and claystone) were taken from the open pit mine along the coal seam profile using the channel and representative sampling method.

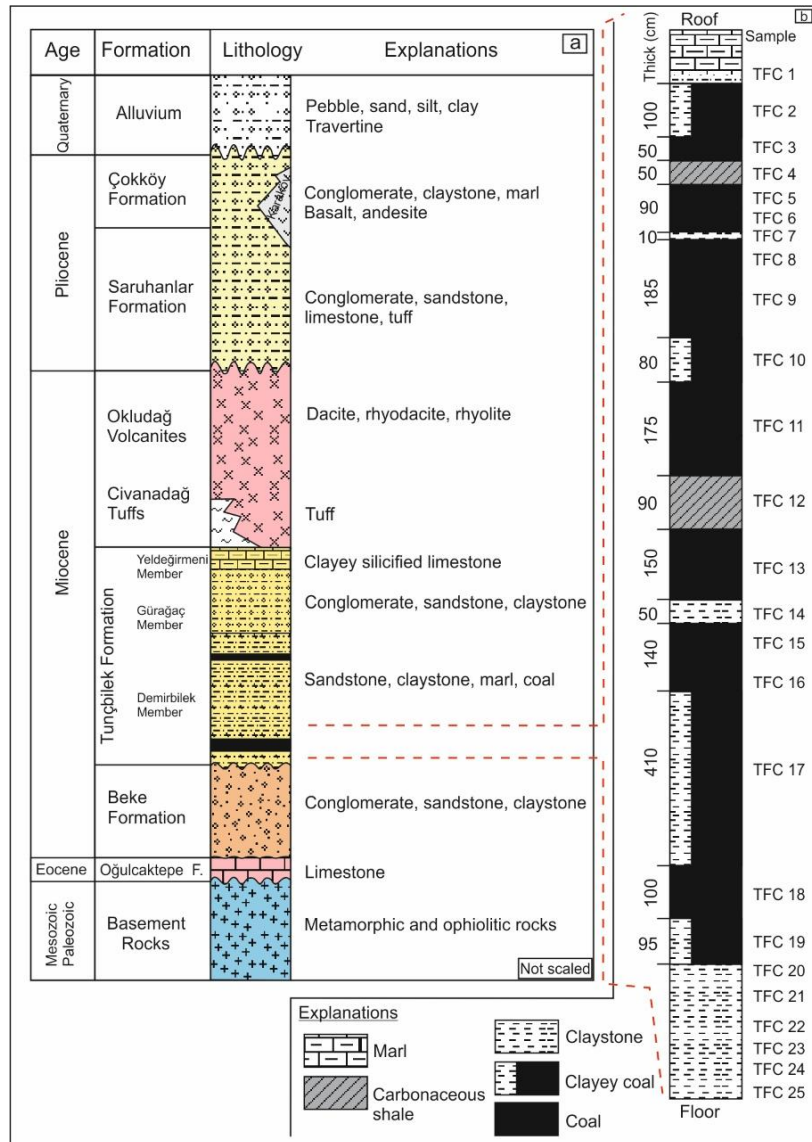


Figure 3. a) Stratigraphic column of Tunçbilek-Tavşanlı basin (modified from [26] and [39]) b) Coal seam profile of FC panel open pit.

Major and trace elements concentrations were determined using ICP-MS and ICP-AES at ACME Analytical Labs (Canada). Some trace elements such as Ni and Sc, and major oxide elements were determined by ICP-AES using LiBO₂ fusion method. Some of trace elements (Ba, Be, Co, Th, U, Sn, V) were determined by ICP-MS. Samples were decomposed by fusion with LiBO₂ before determining the total amounts of the elements. Other trace elements were also determined by ICP-MS based on the analysis of solutions (10 ml diluted fraction) obtained from 0.5 g samples.

There are some methods for detecting and identifying minerals in whole rock. Batch chemical analysis provides clues as to which minerals or mineral groups might be present in the sample. The mineralogical properties of the samples were determined by X-ray diffraction (XRD) analysis at the General Directorate of Mineral Research and Exploration (MTA) laboratory (Ankara, Turkey) using the Rigaku Geigerflex D-MaxII device. XRD analyzes were performed using copper [$\lambda(\text{CuK}\alpha) = 1.54056\text{\AA}$] radiation at scan rates of $2\theta=2-70^\circ$ per minute and $0.01^\circ/\text{minute}$. Samples for clay analyzes were prepared by separating the clay fraction using settling and centrifuging the suspension after dispersing in distilled water overnight. Clay particles were dispersed using ultrasonic vibration for about 15 minutes. Oriented samples of $<2\ \mu\text{m}$ fractions from each sample were prepared for analysis with normal spinning with air drying in the range of $2-30^\circ 2\theta$, with ethylene-glycol in the range of $2-20^\circ 2\theta$, with dissolving at 60°C for 2 hours, and with heating at 550°C for 2 hours in the range of $2-15^\circ 2\theta$. Mineral definitions on the obtained diffractoms were made using ASTM cards.

4. RESULTS AND DISCUSSION

4.1. Mineralogical Composition

The mineralogical composition of the samples determined by XRD whole rock and clay fraction analysis is given in Table 1. The non-clay minerals are, in order of abundance, quartz, siderite, dolomite, mica, K-feldspar, pyrite, and jarosite (Fig. 4). Since most of the samples examined are coal, organic materials are also present. Other samples are roof, floor and parting samples. The clay minerals are kaolinite, illite-smectite, illite, smectite, and chlorite (Fig. 5). It has been stated that quartz exhibits a distinct behavior at the time of coal formation as it has no significant relationship with other minerals and is predominantly of detrital origin [62]. However, it is rarely an authigenic (especially epigenetic) mineral in coal. [63]. Considering the previous studies, in the samples examined, it was determined that quartz was of clastic origin; it is thought to be originated from basement rocks (metamorphic) and volcanic materials. Epigenetic carbonate minerals (ankerite, calcite, dolomite, siderite) are commonly found as joint infillings in coal seams [64]. Cicioglu Sutcu et al. (2021) [45] determined that dolomite and siderite minerals in Tunçbilek coals are of syngenetic and epigenetic origin. Dolomite, siderite and calcite (only in one sample) minerals were detected in the examined samples. (Table 1).

The most abundant mineral in altered volcanic ash in coal horizon is kaolinite. However, an important amount of other clay minerals can exist in some cases [65]. Less stable primary minerals and alteration of volcanic glass can lead to the formation of kaolinite, smectite, illite, illite-smectite and chlorite [65] and may be transported into the basin by streams [24, 26, 66, 67]. The dominant clay minerals in the studied samples are kaolinite and illite-smectite. The accumulation of volcanogenic material in the peat bog environment of the Tunçbilek basin is formed by the transformation of

feldspar and mica group minerals into kaolinite and volcanic ash into tonsteins and overlain by coal seams in the basin [32].

Table 1. Mineral compositions of Tunçbilek-Tavşanlı samples (+++ dominant (>20%), ++ abundant (5-20%), + minor (<5%), Carb. shale : Carbonaceous shale).

Lithology	Sample No	Quartz	Dolomite	Siderite	Calcite	K-Felds.	Mica	Pyrite	Jarosite	Kaolinite	Chlorite	Illite	Illite-Sm.	Smectite
Claystone	TFC1	+++		++		+	+	+		+		++	+	
Clayey coal	TFC2	+++	+	++		+	+	+		++		++	+	
Coal	TFC3	++	++	+			+	+		++		+	+	+
Carb. shale	TFC4	+++	+	+	+		+	+		++		+	+	
Coal	TFC5	+++		+			+	+		++		+	+	
Coal	TFC6	++		+		+	+	+	+	++		+	+	
Claystone	TFC7	+++	+	+		+	+	+		++			++	+
Coal	TFC8	+++		+			+			++		+	+	
Coal	TFC9	+++		+		+	+			++		+	+	
Coal	TFC10	+++		+		+	+			++		+	+	+
Coal	TFC11	++	+	+			+	+	+	++	+		++	
Carb. shale	TFC12	+++	+	+			+	+	+	+++	+	+	+	
Coal	TFC13	++		+			+	+		++	+		+	
Claystone	TFC14	+++	+	++			+			++			+	
Coal	TFC15	+++		+			+		+	++			++	
Coal	TFC16	++	++	+			+			++		+	++	+
Clayey coal	TFC17	+++	+	+			+	+	+	+		+	+	
Coal	TFC18	++		+			+	+		++		+	++	
Coal	TFC19	++	+	+			+	+		++		+	+	
Claystone	TFC20	+++		+		+	+			++		++	+	
Claystone	TFC21	+++		+			+		+	++		++	+	
Claystone	TFC22	+++		+			+			++	+	++	+	
Claystone	TFC23	+++	+	++		+	+			+++	+	++	+	
Claystone	TFC24	+++	+	+						++		+	+	
Claystone	TFC25	+++	++	+			+			++		+	+	

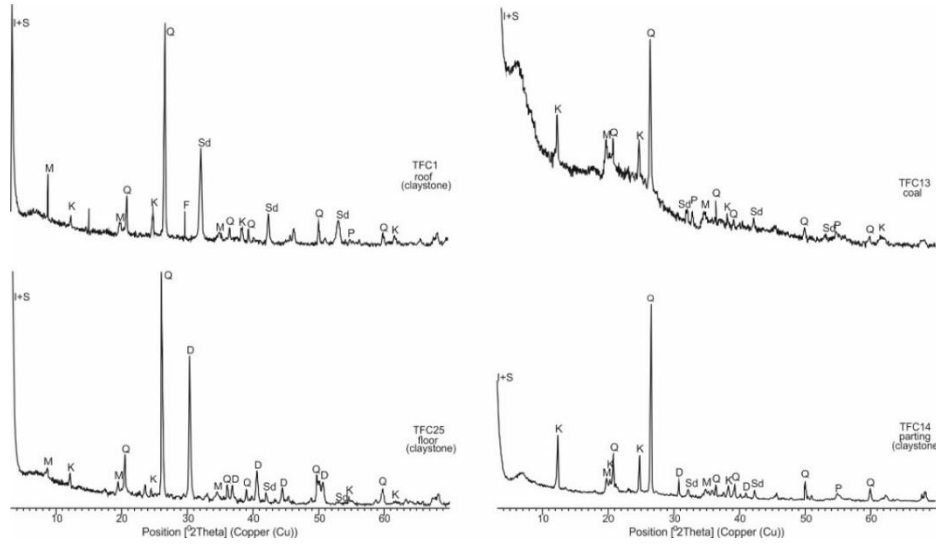


Figure 4. XRD patterns of specific samples. S= smectite, I= illite, K= kaolinite, M= mica, Q= quartz, D= dolomite, Sd= siderite, P= pyrite.

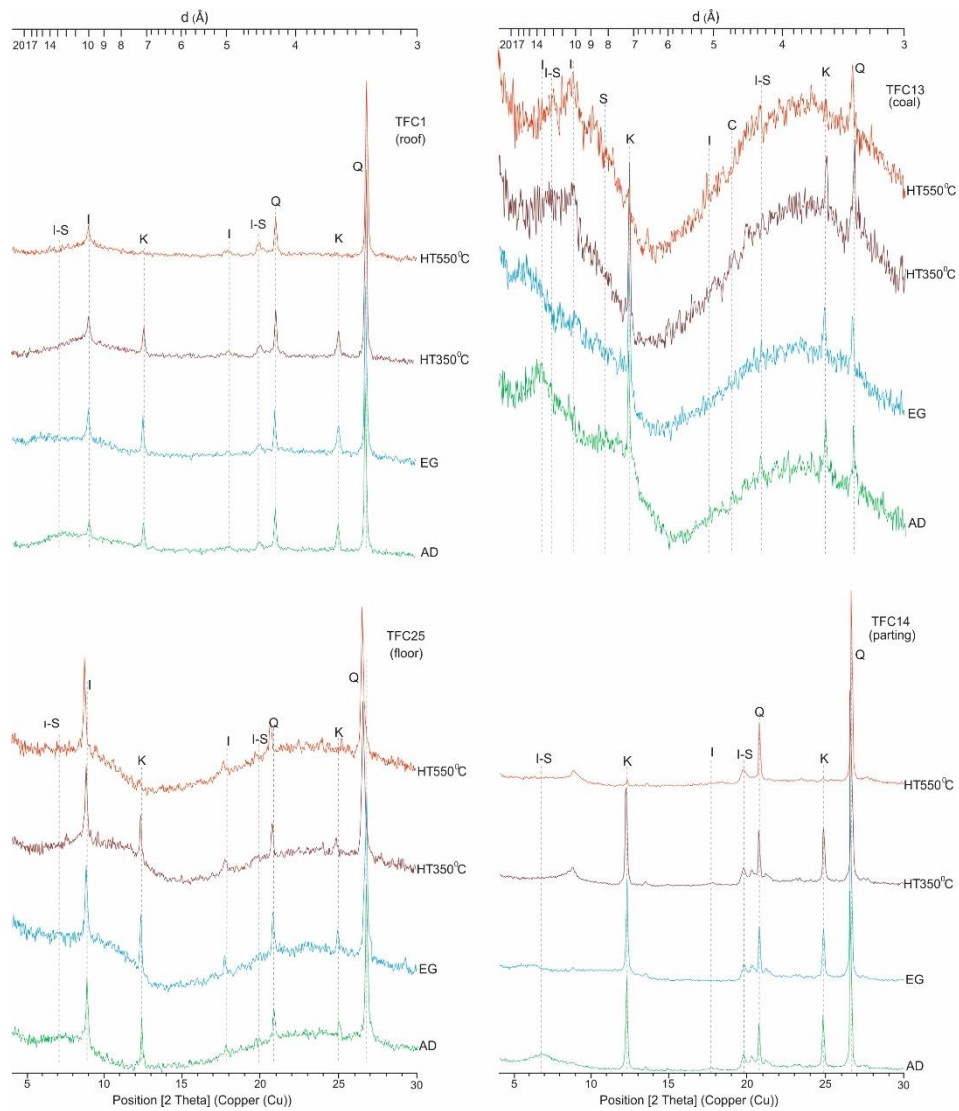


Figure 5. Detailed XRD patterns of specific samples. S= smectite, I= illite, K= kaolinite, Q= quartz, C= chlorite.

4.2. Chemical Composition

4.2.1. Major oxide elements

The concentrations of major oxides in the coal seam profile (coal, roof, parting, and floor) samples and the average values for world low-rank coals are given in Table 2. SiO₂, Al₂O₃ and Fe₂O₃ were found to be the most abundant major oxides in samples of coal, carbonaceous shale, and claystone

representing the roof and floor (except TFC24 and TFC25), whereas MgO, K₂O, CaO, TiO₂, Na₂O, P₂O₅ and MnO were found in smaller amounts. SiO₂, Al₂O₃ and MgO are the most abundant major oxides in the parting samples, while Fe₂O₃, K₂O, TiO₂, CaO, P₂O₅, Na₂O and MnO major oxides are present in smaller amounts. Major oxides are high in claystone and carbonaceous shale layers of profile samples. Concentrations of SiO₂ and Al₂O₃ in coal samples are quite low compared to other samples (Table 2).

Table 2. Major oxide and ash contents of FC panel samples of Tunçbilek-Tavşanlı.

Samples	SiO ₂	Al ₂ O ₃	Fe ₂ O ₃	MgO	CaO	Na ₂ O	K ₂ O	TiO ₂	P ₂ O ₅	MnO	LOI	Al ₂ O ₃ /TiO ₂	Ash
	%												
TFC1	47.43	11.31	10.66	5.13	1.00	0.08	1.25	0.62	0.12	0.24	21.7	18.2	80.0
TFC2	41.88	13.83	4.94	3.07	0.77	0.09	1.37	0.62	0.15	0.08	32.8	22.3	64.0
TFC3	6.36	2.52	1.65	0.95	0.97	0.00	0.15	0.11	0.00	0.03	87.2	22.9	19.5
TFC4	68.16	11.90	2.81	2.05	0.22	0.03	0.72	0.53	0.05	0.02	13.4	22.5	86.5
TFC5	34.93	5.20	0.78	0.58	0.14	0.02	0.27	0.29	0.03	0.00	57.6	17.9	28.6
TFC6	11.88	3.78	2.27	0.95	0.83	0.00	0.18	0.17	0.01	0.00	79.8	22.2	26.2
TFC7	48.05	26.29	2.45	3.18	0.31	0.06	0.86	0.83	0.21	0.00	17.3	31.7	83.2
TFC8	38.63	15.25	2.76	1.73	0.21	0.03	0.81	0.60	0.03	0.02	39.7	25.4	30.8
TFC9	27.34	9.82	2.86	1.57	0.38	0.02	0.65	0.44	0.02	0.02	56.6	22.3	40.9
TFC10	39.91	16.18	3.14	2.30	0.19	0.02	1.11	0.73	0.04	0.03	35.9	22.2	32.9
TFC11	25.83	11.00	3.06	1.50	0.19	0.02	0.66	0.41	0.04	0.02	57.0	26.8	15.6
TFC12	59.90	21.89	1.38	1.61	0.73	0.05	1.00	0.78	0.20	0.01	12.1	28.1	88.1
TFC13	11.27	4.41	2.97	0.74	0.19	0.01	0.30	0.25	0.03	0.02	79.6	17.6	12.6
TFC14	53.12	19.46	4.07	4.33	1.24	0.05	0.84	0.77	0.23	0.07	15.4	25.3	86.0
TFC15	49.61	17.63	4.77	3.27	0.46	0.03	1.57	0.90	0.22	0.05	20.9	19.6	52.8
TFC16	12.77	3.45	2.38	3.60	5.35	0.02	0.21	0.25	0.02	0.06	71.6	13.8	35.6
TFC17	36.30	13.15	3.81	2.57	0.31	0.03	1.10	0.65	0.09	0.04	41.4	20.2	66.8
TFC18	4.76	2.08	1.08	0.19	0.03	0.01	0.12	0.10	0.00	0.00	91.5	20.8	10.5
TFC19	6.37	2.26	0.68	0.28	0.12	0.01	0.15	0.12	0.00	0.00	90.0	18.8	8.2
TFC20	66.21	13.46	3.76	2.30	0.67	0.20	2.08	0.65	0.19	0.16	9.9	20.7	87.4
TFC21	66.43	13.09	3.70	2.24	0.95	0.20	2.01	0.62	0.18	0.13	10.0	21.1	90.8
TFC23	34.59	11.53	16.27	7.24	4.66	0.06	1.39	0.92	0.26	0.54	21.9	12.5	89.7
TFC24	65.79	2.95	7.33	6.52	0.55	0.06	0.31	0.16	0.06	0.56	15.5	18.4	90.5
TFC25	39.64	6.89	6.55	8.12	12.51	0.08	1.05	0.41	0.19	0.19	24.0	16.8	90.1

Contents of SiO₂ vary between 49.61% and 4.76% in coal samples and 17.63% and 2.08% in other samples. Similarly, contents of Al₂O₃ range from 17.63% to 2.08% in coal samples and from 26.29% to 6.89% in other samples. Samples with high Al₂O₃ content are rich in kaolinite. Fe₂O₃ concentration is more abundant in the other samples compared to the samples belonging to the partings (Table 2). Siderite and pyrite minerals are relatively abundant in the mineralogical composition of these samples. Samples with high MgO content are those abundant in dolomite minerals (Table 1). There is a positive correlation between major oxides (Table 3). Al₂O₃ shows high positive linear correlation with SiO₂, K₂O, TiO₂, P₂O₅, and MgO exhibits high positive correlation with Fe₂O₃, CaO and MnO and (Fig. 6) Silicates are the most abundant mineral group in coal. Silicate group minerals are associated with many elements found in coal, particularly SiO₂, Al₂O₃, and to a lesser extent MgO, K₂O, TiO and clastic minerals such as major oxides, quartz, and clay, including Na₂O, CaO and Fe₂O₃, indicating a mixed clay assemblage [7, 68]. Other important silicates are micas, analcime and various feldspars [69]. The origins of SiO₂ and Al₂O₃ in the examined samples are kaolinite and illite-smectite mixed bedded clays. Concentration of SiO₂ is partially related to quartz content (Table 1).

Table 3. Ash contents (wt.%, db) and element affinities calculated from Pearson correlation coefficients (correlation is significant at 0.01, correlation is significant at 0.05 “*”).

Correlation with ash (0.70 <r<1.0)	Ba, SiO ₂ , MgO, P ₂ O ₅
Correlation with ash (0.50 <r<0.69)	Ga, Sr, Ta, Th, U, Cu, Pb, Zn, V, Y, Eu, Gd, Tb, Dy, Ho, Er, Tm, Yb, Lu, Al ₂ O ₃ , Fe ₂ O ₃ , Na ₂ O, K ₂ O, TiO ₂ , MnO
Correlation with ash (0.49 <r<0.20)	Ni, Sc, Co, Cs, Hf, Nb, Sn, W, Zr, Rb, La, Ce, Pr, Nd, Sm, Cd, Bi, Sb, Cr, CaO
Negative correlation with ash (-0.90 <r<-0.4)	Mo
Correlation with SiO ₂	Ba, Cs, Ga, Rb, Ta, V, Y, La*, Ce*, Pr*, Nd*, Sm*, Eu*, Gd*, Tb*, Dy*, Ho*, Er, Tm, Yb, Lu, Pb*, Zn, Cd*, Bi*, Au
Correlation with Al ₂ O ₃ 0.5 <r<1.0	SiO ₂ , MgO, K ₂ O, TiO ₂ , P ₂ O ₅ , REE+Y (Y, La, Ce*, Pr, Nd, Sm, Eu, Gd, Tb, Dy, Ho, Er, Tm, Yb, Lu), Ba, Cs*, Ga, Hf, Rb, Sn, Sr, Ta, U, V, W, Zr, Pb, Zn, Bi, Au
Correlation with Fe ₂ O ₃ 0.5 <r<1.0	MgO, K ₂ O*, TiO ₂ *, MnO
Correlation with CaO	MgO (0.688)
Correlation with K ₂ O 0.5 <r<1.0	SiO ₂ , P ₂ O ₅ *
Correlation with TiO ₂	SiO ₂ , Al ₂ O ₃ , Fe ₂ O ₃ *, K ₂ O, P ₂ O ₅ , REE+Y
Correlation with MgO 0.5 <r<1.0	Fe ₂ O ₃ , CaO, P ₂ O ₅ *
Correlation with Na ₂ O 0.45 <r<1.0	SiO ₂ , K ₂ O, P ₂ O ₅ *
Negative correlation with TOTC	Al ₂ O ₃ , SiO ₂
Negative correlation with TOTS	SiO ₂ *

Samples containing abundant illite, illite-smectite and partially mica or feldspar have high K₂O concentration (Tables 1, 2). The source of MgO in low-rank coals is usually organic origin, calcite, and silicate minerals [70]. The source of MgO in the samples examined is dolomite, smectite and smectite-illite minerals. The source of Fe₂O₃ and CaO is usually dolomite, siderite, smectite and pyrite. MnO presented a positive correlation with MgO and Fe₂O₃ (Table 3). Therefore, MnO may be

of siderite origin. TiO_2 , P_2O_5 and NaO , which are less abundant in the samples, may be derived from clay and mica group minerals [45, 70]. The ratio of $\text{Al}_2\text{O}_3/\text{TiO}_2$ is stated to be a reliable indicator for the provenance of sedimentary rocks [71, 72, 73, 74]. The ratios of $\text{Al}_2\text{O}_3/\text{TiO}_2$ are 3-8, 8-21 and 21-70 for sediments derived from mafic, intermediate and felsic igneous rocks, respectively [71]. The ratios of $\text{Al}_2\text{O}_3/\text{TiO}_2$ of Tunçbilek-Tavşanlı samples vary between 12.5-31.7 (Table 2), showing intermediate- felsic rocks. The tuffs in the study area have been characterized as rhyolitic-rhyodacitic tuffs [32].

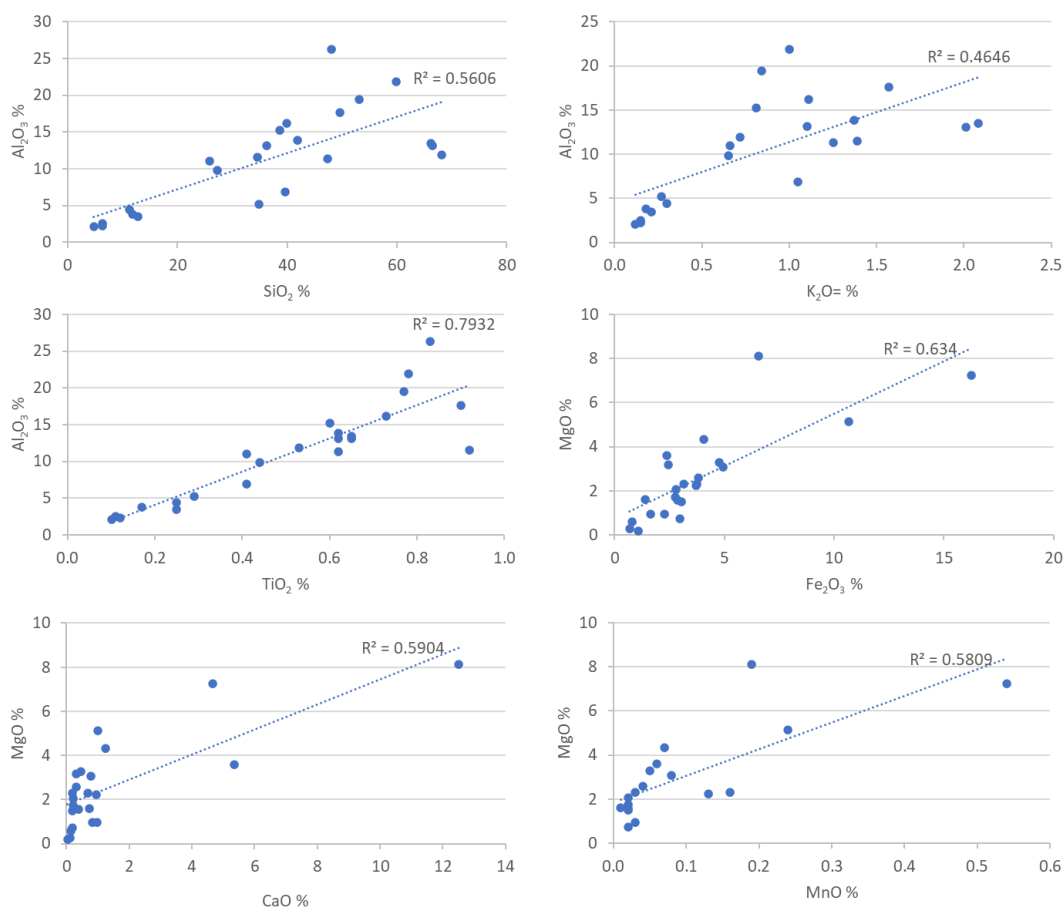


Figure 6. Plots showing relationship between some major oxides in all samples.

4.2.2. Trace elements

In this study, trace element values determined for studied coal samples were compared with the average values of world low-rank coals stated by Ketris and Yudovich (2009) [75] (Table 4). In the studied coal samples, Ni, Sc, Be, Co, Cs, Ga, Hf, Nb, Rb, Sn, Ta, Th, U, V, W, Zr, Y, La, Ce, Nd, Sm,

Eu, Gd, Mo, Cu, Pb, Zn and Hg elements presented higher concentrations compared to the world low-rank coal averages. The relative enrichment of trace elements is classified by Dai et al (2015a) [76]: “unusually enriched ($CC > 100$), significantly enriched ($10 < CC < 100$), enriched ($5 < CC < 10$), slightly enriched ($2 < CC < 5$), normal ($0.5 < CC < 2$) and depleted ($CC < 0.5$)”, where CC stands for concentration coefficient and is defined as the ratio of the concentration of trace elements in the samples studied to those in world coals). The CCs of studied coal samples are generally in the slightly enriched-normal range (Fig. 7a), whereas a normal enrichment ($0.5 < CC < 2$) is indicated according to the CC values of the non-coal samples (Fig. 7b).

Concentration of Ni (190–1960 $\mu\text{g/g}$, average 840 $\mu\text{g/g}$) in the samples of the Tunçbilek-Tavşanlı coal seam is much higher than the average value of world low-rank coals (9 $\mu\text{g/g}$; [75]) (Table 4) and concentration coefficients are much higher than 10 ($CC > 10$) (Fig. 7a). Finkelman (1981) [77] stated that significant amounts of Ni in coal may be organically related. Inorganically bound Ni can be largely associated with sulfides. Finkelman (1988) [78] stated that Ni in coal can also occur in clays. Finkelman (1994) [79] noted a low level of confidence in Ni formation patterns due to the lack of direct evidence and the contradictory available evidence. In the studied samples, Ni showed a weak positive correlation coefficient with ash (Table 3). Therefore, considering the lithology of the source region, which gives detritus to the coal-bearing succession, rocks such as serpentine and peridotite found in the basement rocks may be responsible for the enrichment of Ni. Trace elements with a CC of 5-10 include Cs, Co and Rb. The Cs concentrations in the Tunçbilek-Tavşanlı coal seam vary between 1.10 and 9.20 $\mu\text{g/g}$. The weighted average of the Cs concentrations (5.25 $\mu\text{g/g}$) are higher than the world's low-rank coals (0.98 $\mu\text{g/g}$; [75]). Cesium is predominantly associated with silicate minerals in low-rank coals [70]. Cobalt is enriched in the Tunçbilek-Tavşanlı coal seam with a concentration ranging from 4.8 to 96.7 $\mu\text{g/g}$. The average Co concentration of 41.4 $\mu\text{g/g}$ in the studied samples is much higher than the average Co concentration of the world's low-rank coals (4.2 $\mu\text{g/g}$) [75].

Cobalt in coal deposits generally occurs worldwide in an organic association or in Co-including minerals such as monosulfide, clay, and pyrite [70, 76]. Rubidium concentration in the studied samples ranges from 10.2 to 104.7 $\mu\text{g/g}$, presenting higher values compared to the average of world's low-rank coal and is associated with clay minerals (especially illite and mixed-layer clays). There is a weak positive correlation between Ce, Co and Rb and ash (Table 3) and shows the inorganic association. A series of trace elements including, Sc, Be, Hf, Nb, Ta, Th, V, W, Zr, Cu, Pb and Zn, are slightly enriched in Tunçbilek-Tavşanlı coals with CC values between 2 and 5. While Cd and Bi elements with concentration coefficients lower than 0.5 show depletion, other elements with CC from 0.5 to 2 have concentrations close to the world's low-rank coals average values.

Trace element concentrations of Tunçbilek-Tavşanlı coals present higher values for Ni, Co, Cs, Ga, Nb, Rb, Th, U, V, W, Zr, Cu, Pb and Hg elements comparing to USA and China coals. Moreover, Hf, Ta, Y and rare earth elements (REE) show higher concentrations than the USA coals. Compared to Chinese coals, the element As presents a higher concentration.

Parting, roof and floor samples, when compared with mean values for upper continental crust (UCC), only Ni ($CC > 10$) is significantly enriched element whereas Co, Th, U, Pb, As, Bi and Hg are slightly

enriched with CC between 2 and 5) (Fig. 7b). Moreover, the rest of trace elements have values close to the UCC averages with a concentration coefficient between 0.5 and 2.

Table 4. Trace elements concentrations ($\mu\text{g/g}$) and the loss on ignition (LOI, %) of Tunçbilek-Tavşanlı samples.

Sample	TFC1	TFC2	TFC3	TFC4	TFC5	TFC6	TFC7	TFC8	TFC9	TFC10	TFC11	TFC12	TFC13	TFC14	TFC15	TFC16	TFC17	TFC18	TFC19	TFC20	TFC21	TFC23	TFC24	TFC25	World [75]	Lignite [75]	UCC [80]	USA [81]	China [3,6,82]
LOI	21.7	32.8	87.2	13.4	57.6	79.8	17.3	39.7	56.6	35.9	57	12.1	79.6	15.4	20.9	71.6	41.4	91.5	90	9.9	10	21.9	15.5	24	-	-	-	-	-
Be	3	6	1	3	5	4	4	7	2	2	2	2	1	6	2	9	2	2	1	2	2	2	1	1	1.6	1.2	2.1	2.2	2.1
Se	17	15	4	8	5	6	2	12	11	15	7	8	5	6	14	7	13	5	4	16	14	23	7	11	3.9	4.1	14	4.2	4.4
V	107	124	24	49	70	41	104	103	81	90	48	98	40	104	92	101	92	40	23	127	123	123	38	75	25	22	97	22	35
Cr	0.08	0.05	0.02	0.03	0.02	0.02	0	0.04	0.06	0.07	0.04	0.02	0.03	0.02	0.09	0.03	0.07	0.02	0.01	0.05	0.05	0.09	0.02	0.04	17	15	0.01	0.001	-
Co	101	64.9	18.6	13.2	4.8	14	3	26.6	67.5	76.5	68	12.6	12.4	24.2	96.7	48.8	64.1	39.3	6.2	63.2	103.1	126.7	20.3	28.1	5.1	4.2	17.3	6.1	7.1
Ni	1335	1162	288	190	197	460	143	481	1064	1478	1128	199	638	367	1960	845	1923	477	309	914	1501	1477	316	505	13	9	47	14	13.7
Cu	60.7	75.3	10.7	29.2	16.7	13.5	9.4	50.7	33	61.7	42.2	22.7	29.6	22.5	63.3	34.5	55.7	26.5	11.6	53.2	60.5	89.9	16.9	32.7	46	15	28	16	17.5
Zn	88	79	14	38	16	22	107	48	43	78	66	106	22	96	62	25	43	11	18	98	87	77	18	41	23	18	67	53	41.4
Ga	13.4	15.5	2.2	14.8	6.7	4.6	25.9	15.3	10	17.1	9.9	22	4.5	20.1	18.9	4.5	14.2	2	2.3	15.5	15.4	12.1	3	8	5.8	5.5	17.5	5.7	6.6
As	47.6	8	3.2	0.8	1.7	10.7	4.8	2.1	4.1	1.9	32.1	2.1	3.8	4.1	2.6	6.5	1.8	2.9	6.2	10.2	18.6	29.1	27.9	10.7	8.3	7.6	4.8	24	3.8
Rb	66.9	78.1	10.2	63.3	23.8	14.1	25.4	87.2	74.7	94.2	57.4	53.9	20.2	37.3	104.7	15.3	86.3	9.3	9.2	90.3	88.6	53.9	14.3	44.8	14	10	84	21	9.3
Sr	83.7	113	31.7	85.6	65.7	55.4	815.2	97.2	62.8	94.6	84.1	435.1	110.1	550.1	125.9	75.8	101.5	16.4	25.3	243.4	188.7	302.9	33	150.2	110	120	320	130	140
Zr	118.3	154.1	29	153.4	385.9	141.2	520.8	151.2	142.1	136.4	69.6	245.8	48.7	356.1	136.9	103.6	143.7	73.1	30.5	115.1	99.6	137.1	33.5	64.1	36	35	193	27	89.5
Nb	14.3	12.9	2	22.6	39	9.9	12.8	16.6	10.1	15.3	5.1	13.1	4.3	19.4	23.2	16.9	11.5	3.2	3.1	11.8	11.3	17.4	3.4	7.7	3.7	3.3	12	2.9	9.4
Mo	1.1	3.7	2.6	0.4	2.5	3.5	1.4	3.1	2.9	1	4.6	0.4	1.6	2.4	1.2	6	1.3	3.3	1.3	0.5	0.4	0.7	0.8	0.4	2.2	2	1.1	3.3	3.1
Sn	1	2	1	2	1	1	6	2	1	3	2	7	1	5	3	1	2	1	1	2	2	1	1	1	1.1	0.79	2.1	1.3	2.11
Cs	7.9	8.4	1.9	8.1	3.5	1.9	3.6	9.2	6.2	8.9	6	6.1	3.4	2.6	8.9	2.4	7.3	1.1	1.5	9.1	8.9	4.2	2.2	10.3	1	0.98	4.9	1.1	1.13
Ba	208	183	21	114	63	31	387	123	78	103	65	378	139	306	234	34	495	14	19	468	437	211	204	217	150	150	624	170	159
Hf	3.3	3.5	0.8	3.4	4.6	3.2	15.1	4	3.3	4.1	2	8.8	1.2	9.7	4.6	2.2	4	1.6	0.9	3.2	2.8	3.4	0.8	1.7	1.2	1.2	5.3	0.7	3.7
Ta	0.7	0.9	0.1	0.8	0.3	0.3	2	0.9	0.5	1	0.4	1.6	0.3	1.5	1.7	0.5	0.9	0.2	0.1	0.9	0.7	1.1	0.2	0.4	0.28	0.26	0.9	0.22	0.62

W	2.2	2.8	1.4	3.6	2.3	1.7	3.7	7.8	1.5	2.7	1.9	7.2	0.6	4.1	2.9	4.3	1.8	0.7	1.8	2.6	2.6	3.6	1.3	1.3	1.1	1.2	1.9	1	1.1
Hg	0.16	0.13	0.07	0.05	0.1	0.29	0.16	0.11	0.19	0.31	0.5	0.15	0.28	0.11	0.23	0.16	0.2	0.17	0.12	0.11	0.15	0.33	0.06	0.04	0.1	0.1	0.05	0.17	0.16
Pb	29.3	31	4.6	22.5	7.9	19	120.3	20.9	19.8	19.2	30.1	78.2	7.7	82.5	23	9.4	20	8	4.1	28.7	30.3	30.2	5.3	15.7	7.8	6.6	17	11	15.1
Bi	0.4	0.4	0.1	0.4	0.3	0.1	1.2	0.4	0.2	0.4	0.5	1	0.1	0.9	0.5	0.1	0.4	0.1	0.1	0.3	0.3	0.2	0.1	0.1	0.97	0.84	0.16	<1	0.79
Th	13.7	18.9	3.3	23.7	13.1	7.1	100.6	22.6	16.6	24.3	18.7	73	7.1	66.1	26.6	7.4	23.7	6.2	2.9	14.2	12.7	9.3	3.4	6.3	3.3	3.3	10.5	3.2	5.8
U	2.6	7.9	1.4	7	5.9	2.1	29	6.4	3.9	4.5	4.1	21.8	0.8	20.7	5.5	3.9	6.1	1.7	0.4	2.9	2.4	2.1	1.6	1.5	2.4	2.9	2.7	2.1	2.4
V/Ni	0.08	0.11	0.08	0.26	0.36	0.09	0.73	0.21	0.08	0.06	0.04	0.49	0.06	0.28	0.05	0.12	0.05	0.08	0.07	0.14	0.08	0.08	0.12	0.15	-	-	-	-	-
V/(V+Ni)	0.07	0.10	0.08	0.21	0.26	0.08	0.42	0.18	0.07	0.06	0.04	0.33	0.06	0.22	0.04	0.11	0.05	0.08	0.07	0.12	0.08	0.08	0.11	0.13	-	-	-	-	-
Sr/Cu	1.38	1.50	2.96	2.93	3.93	4.10	86.72	1.92	1.90	1.53	1.99	19.17	3.72	24.45	1.99	2.20	1.82	0.62	2.18	4.58	3.12	3.37	1.95	4.59	-	-	-	-	-
Ga/Rb	0.20	0.20	0.22	0.23	0.28	0.33	1.02	0.18	0.13	0.18	0.17	0.41	0.22	0.54	0.18	0.29	0.16	0.22	0.25	0.17	0.17	0.22	0.21	0.18	-	-	-	-	-
U/Th	0.19	0.42	0.42	0.30	0.45	0.30	0.29	0.28	0.23	0.19	0.22	0.30	0.11	0.31	0.21	0.53	0.26	0.27	0.14	0.20	0.19	0.23	0.47	0.24	-	-	-	-	-

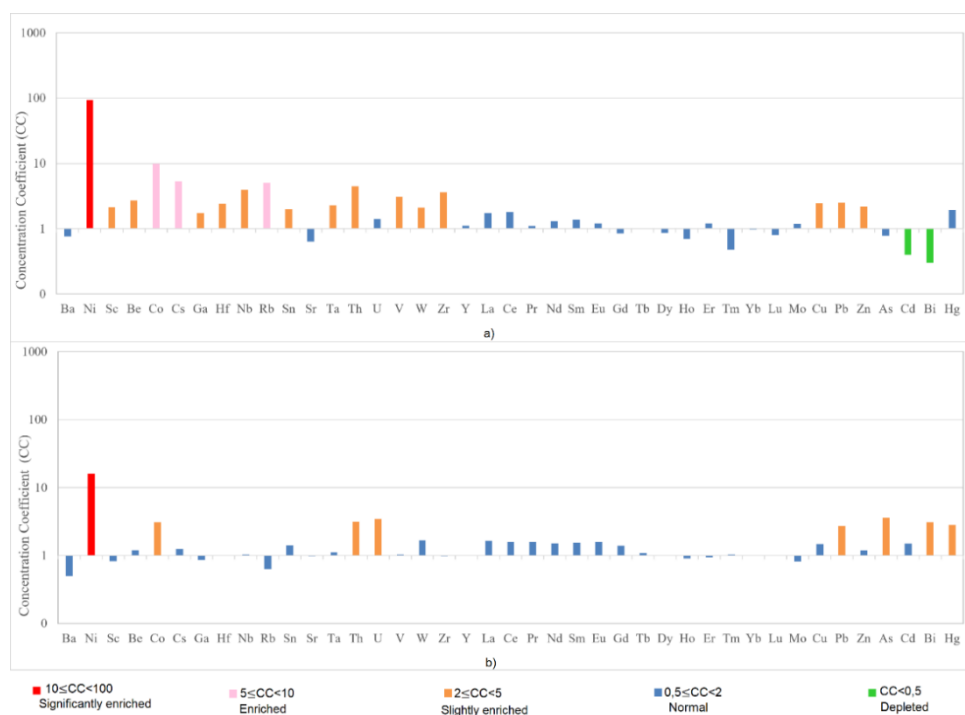


Figure 7. Concentration coefficients of trace elements of studied samples a) coal, b) parting, roof, and floor.

Several elements (e.g. S, B, U, Ba, Ni) and their ratios (e.g. Th/U, V/(V+Ni), Ni/Co, Sr/Cu) can be used as indicators (salinity, paleoredox conditions and paleoclimate) for the depositional environment during or after peat deposition. Especially when evaluating the formation environment of coal, the water chemistry of the sedimentation environment and the elemental chemistry of the coal may differ due to various effects in diagenetic or epigenetic processes. Therefore, elements with similar geochemical behavior or related element ratios should be used rather than a single element [81]. V/Ni, V/(V+Ni), which are redox sensitive geochemical indices, are widely used in sedimentary rocks rather than other trace element ratios [2, 82, 83]. A high V/Ni (>3) reducing environment indicates a V/Ni suboxic environment between 1.9-3, whereas a low (<1.9) V/Ni ratio indicates oxic environments [84]. Moreover, high (>1) V/Ni ratios indicate marine carbonates or siliciclastics, while low (<1) values indicate lacustrine or terrestrial origin [85]. (El-Sabagh et al., 2018). V/(V + Ni) ratios ≤ 0.46 , 0.46-0.60, 0.54-0.82 and >0.84 indicate oxic, dysoxic, suboxic-anoxic and euxinic environments, respectively [86]. Low V/Ni and V/(V + Ni) ratios in the studied samples indicate oxidizing conditions and lacustrine origin (Table 4) and are consistent with the sedimentation environment of coal. U/Th ratios are other redox sensitive ratios used to determine the depositional environment of organic matter-rich deposits [87]. U/Th ratio <0.75 indicates oxic, 0.75-1.25 indicates suboxic, >1.25 indicates suboxic-anoxic depositional environment [82]. Tunçbilek-Tavşanlı coal samples of roof,

parting and floor presented low (<0.84) values. Other ratios that provide information about the precipitation environment by using element ratios are Sr/Cu and Ga/Rb ratios. In particular, the Sr/Cu and Ga/Rb ratios of fine-grained sediments provide information about the climatic changes of the deposition environment. Sr/Cu ratios between 1.3–5.0 are associated with humidity, while values greater than 5.0 are associated with drought [88]. Ga/Rb ratios offer lower values as the temperature decreases [89]. Parting samples taken from the Tunçbilek-Tavşanlı field indicate arid climate, while other samples vary and indicate a humid climate.

4.2.3. Rare earth elements and yttrium (REE+Y or REY)

The total REE+Y concentration in the studied samples of Tunçbilek-Tavşanlı coal seam ranges between 25.77 and 167.26 µg/g (Table 5), with an average of 95.04 µg/g, which is higher than the average REE+Y concentration of world's low-rank coals (65.27 µg/g; [75]). This average value corresponds to 0.7 times the average REE+Y concentration (135.89 µg/g; [91, 3, 6]) of Chinese coals, and corresponds to 1.5 times the average REE+Y concentration (62.09 µg/g; [90]) of USA coals. REE+Y concentrations were normalized to UCC values to show the REE+Y distribution patterns of the studied samples (Fig. 8).

Correlation coefficient between ash content and REE+Y concentrations is high ($r=0.74$; Table 3). The coal sample with the highest ash content (TFC17) has the maximum REE+Y concentration (152.4 µg/g) and the minimum REE+Y value (25.8 µg/g) is the coal sample with the lowest ash content (TFC19; 8.2 µg/g), which is an indication of mineral matter association for REE+Y in Tunçbilek-Tavşanlı coal samples. It has been stated that REYs in low rank coals in Turkey are generally associated with tuff type, acid and alkaline volcanic ash and formed in the peat bog stage [92]

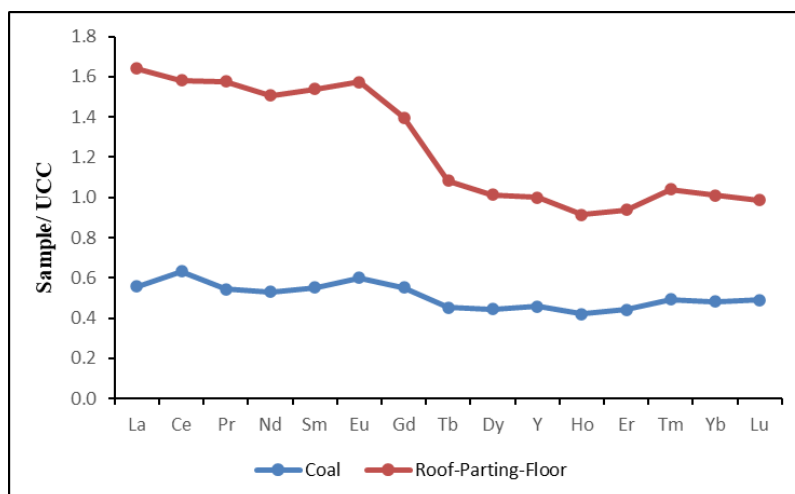


Figure 8. REE+Y distribution patterns of FC pano samples of Tunçbilek-Tavşanlı basin.

As suggested by Seredin and Dai (2012) [13], three enrichment phases of rare earth elements and yttrium in coal are adopted in this study:

- 1) “Light REE (La, Ce, Pr, Nd and Sm) enrichment (L-type; $La_N/Lu_N > 1$); N : REE+Y concentrations in the studied samples normalized by average values of UCC [93]”;
- 2) “Medium REE+Y (Eu, Gd, Tb, Dy and Y) enrichment (M-type; $La_N/Sm_N < 1$, $Gd_N/Lu_N > 1$)”;
- 3) “Heavy REE (Ho, Er, Tm, Yb and Lu) enrichment (H-type; $La_N/Lu_N < 1$).”

Table 5. REE+Y contents of studied samples of Tunçbilek -Tavşanlı coalfield.

Sample	La	Ce	Pr	Nd	Sm	Eu	Gd	Tb	Dy	Y	Ho	Er	Tm	Yb	Lu	REE+Y
TFC1	23.7	46.9	5.05	18.5	3.53	0.83	3.26	0.47	2.46	14.4	0.51	1.50	0.21	1.46	0.23	123.0
TFC2	30.2	67.9	6.90	26.1	4.85	1.17	4.40	0.62	3.32	17.1	0.66	1.83	0.27	1.68	0.26	167.3
TFC3	6.6	10.7	1.05	4.0	0.63	0.21	0.61	0.10	0.54	3.3	0.13	0.34	0.05	0.32	0.06	28.6
TFC4	22.3	51.8	5.43	20.2	3.43	0.80	2.76	0.39	2.16	12.1	0.41	1.18	0.17	1.13	0.17	124.4
TFC5	19.0	41.1	4.48	16.5	2.96	0.65	2.46	0.41	2.38	14.6	0.50	1.43	0.21	1.38	0.23	108.3
TFC6	12.9	24.9	2.77	10.0	1.94	0.42	1.58	0.24	1.42	10.6	0.34	1.04	0.16	1.18	0.22	69.7
TFC7	146.1	282.4	31.92	114.0	19.17	3.79	13.78	1.68	8.38	43.9	1.49	4.30	0.63	4.04	0.59	676.2
TFC8	23.6	59.4	5.37	20.6	3.79	0.86	3.11	0.43	2.50	12.8	0.47	1.50	0.22	1.48	0.22	136.4
TFC9	17.2	43.3	3.89	14.6	2.54	0.55	1.94	0.27	1.34	6.5	0.27	0.74	0.11	0.73	0.11	94.1
TFC10	22.8	49.6	5.09	18.9	3.30	0.81	2.89	0.42	2.19	11.7	0.45	1.33	0.19	1.19	0.19	121.1
TFC11	17.8	45.9	3.93	13.9	2.52	0.55	2.02	0.28	1.48	8.3	0.29	0.83	0.13	0.86	0.13	98.9
TFC12	91.2	185.0	21.06	75.3	13.13	2.75	8.83	1.14	5.58	26.0	0.96	2.60	0.38	2.35	0.34	436.6
TFC13	7.3	17.4	1.79	7.0	1.45	0.32	1.21	0.18	0.95	5.4	0.19	0.61	0.09	0.51	0.08	44.5
TFC14	91.9	175.7	20.26	73.8	12.63	2.77	9.00	1.20	6.27	33.0	1.16	3.21	0.47	2.97	0.46	434.8
TFC15	26.8	64.9	6.30	23.0	4.36	1.00	3.93	0.55	3.09	17.4	0.60	1.74	0.25	1.55	0.25	151.7
TFC16	6.9	15.6	1.42	4.8	0.94	0.23	0.81	0.13	0.74	4.2	0.13	0.42	0.06	0.41	0.06	36.9
TFC17	27.9	67.8	6.10	22.5	4.00	0.93	3.47	0.47	2.51	13.0	0.52	1.46	0.20	1.32	0.19	152.4
TFC18	11.8	27.4	2.64	9.7	1.60	0.37	1.35	0.18	0.90	4.5	0.18	0.50	0.07	0.44	0.06	61.7
TFC19	6.2	9.9	0.91	3.4	0.62	0.15	0.54	0.09	0.53	2.6	0.10	0.31	0.04	0.33	0.05	25.8
TFC20	29.9	57.2	6.47	23.3	4.58	1.04	3.88	0.58	3.20	17.5	0.68	2.00	0.29	1.88	0.28	152.8
TFC21	26.4	49.8	5.35	19.9	3.67	0.82	3.08	0.45	2.41	13.5	0.51	1.60	0.23	1.61	0.26	129.6
TFC23	21.6	49.6	5.36	21.8	4.56	1.18	4.77	0.73	4.12	21.2	0.83	2.27	0.33	2.12	0.32	140.8

TFC24	7.0	13.7	1.41	5.7	1.07	0.29	0.98	0.15	0.80	5.3	0.19	0.54	0.08	0.50	0.07	37.8
TFC25	19.8	36.1	3.88	13.7	2.71	0.69	2.71	0.42	2.33	14.1	0.49	1.41	0.19	1.28	0.20	100.0
World [75]	11	23	4.0	12	2.00	0.47	2.70	0.32	2.10	8.4	0.54	0.93	0.31	1.00	0.20	68.97
Lignite [75]	10	22	3.5	11	1.90	0.50	2.60	0.32	2.00	8.6	0.50	0.85	0.31	1.00	0.19	65.27
UCC [80]	31	63	7.1	27	4.70	1.00	4.00	0.70	3.90	21.0	0.83	2.30	0.30	2.00	0.31	169.14
USA [81]	12	21	2.4	9.5	1.70	0.40	1.80	0.30	1.90	8.5	0.35	1.00	0.15	0.95	0.14	62.09
China[3,6,82]	22.5	46.7	6.42	22.3	4.07	0.84	4.65	0.62	3.74	18.2	0.96	1.79	0.64	2.08	0.38	135.89

Coal is characterized by an L-type enrichment, except for TFC5, TFC6 samples with H-type enrichment and TFC12, TFC23, TFC24 samples with M-L type enrichment in the roof, floor, and parting samples, respectively (Table 6).

Since Ce, Eu and Gd anomalies occur only under certain geochemical conditions, they can be used as indicators to reflect the paleoenvironmental characteristic sediment-source region, and tectonic evolution [94]. However, Eu is inhibited by Ba concentrations in many cases, as stated by Dai et al. (2016) [94] and Yan et al. (2018, 2019) [95, 96]. The positive correlation between Ba and Eu concentrations in coal (Fig. 9a) and the Ba/Eu ratio, which ranged from 37.8 to 434.4 and averaged 148.6 in coal samples, was found by Yan et al. (2018) [95]. It clearly shows Ba interference on Eu, although it is lower than the interference threshold Ba/Eu=1000. Again, the weak correlation between Ba and Eu concentrations in non-coal samples (Fig. 9b) indicates that Ba do not interact with Eu in these samples despite low Ba/Eu ratios (ranging from 116 to 339). Therefore, no interpretation could be made for the samples.

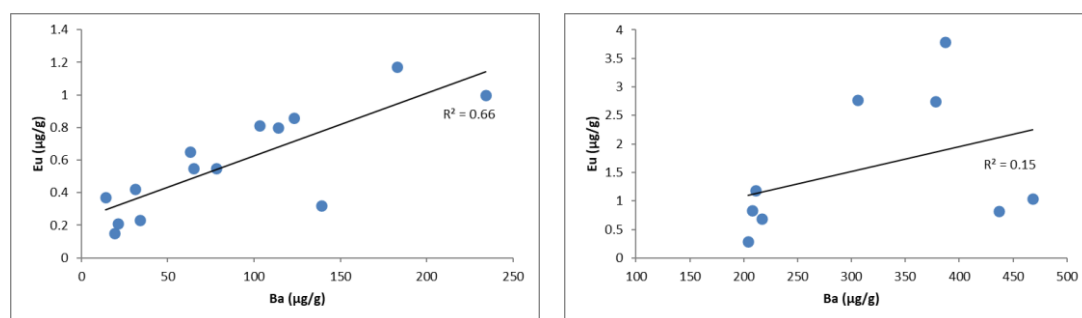


Figure 9. Relationship between Ba and Eu concentrations of studied samples a) coal samples; b) roof, floor, and parting.

Furthermore, redox-sensitive Ce and Eu anomalies (in non-coal samples) and in some cases, non-redox-sensitive La, Gd, and Y anomalies in coal may change under certain geochemical conditions [94]. In this study, the Eq. 1-3 were used to measure the separation of Ce, Eu and Gd concentrations from other REE+Y in dispersion models.

$$Eu_N/Eu_N^{\square} = Eu_N / [(Sm_N \times 0.67) + (Tb_N \times 0.33)] \quad (1)$$

$$Ce_N/Ce_N^{\square} = Ce_N / [(La_N \times 0.5) + (Pr_N \times 0.5)] \quad (2)$$

$$Gd_N/Gd_N^{\square} = Gd_N / [(Sm_N \times 0.33) + (Tb_N \times 0.67)] \quad (3)$$

Respectively, in the calculations of Gd_N/Gd_N^{\square} and Eu_N/Eu_N^{\square} , Tb is used instead of Eu to avoid confusion of Eu anomaly with Gd anomaly and in order to avoid confusion of the Gd anomaly with the Eu anomaly, Tb is used instead of Gd concentration. The Y_N/Ho_N ratio in coal is used to represent the divergence of geochemical twins Y and Ho, which produces Y anomalies in the REE+Y

classification. Values $Y_N/Ho_N < 1$ and > 1 represent negative and positive anomalies, respectively [94]. While Ce in the studied coal samples generally shows weak positive anomaly; Ce in the non-coal samples is generally characterized by negative anomaly (Table 6). Generally, groundwater or hydrothermal leak of roof, parting and floor can cause Ce anomalies in both coals and non-coal fractions. During non-coal leaching, Ce^{3+} can be converted to Ce^{4+} , which is preferentially precipitated in-situ[97]. Thus, non-coal fractions show Ce-depletion relative to coals, but cause leaks richer in REY, and it usually indicates oxidizing conditions for the leaching process [2]. In the studied samples, the REY values are higher, while the Ce anomaly in the roof and floor samples is lower than the coals. Eu element, another redox sensitive rare earth element, is not recommended to be used in coals[65]. Eu and Gd show weak positive anomalies in all samples (Table 6). Yttrium shows positive anomaly in coal samples except TFC7, TFC17 and TFC18 and in non-coal samples. If peat interacts with sea water, it generally shows positive anomalies for La, Gd and Y[98]. However, since coals are also affected by hydrothermal fluids during peat deposition, positive anomalies for La, Gd and Y may be under the combined influence of seawater and hydrothermal fluids [76]. Since the study area exhibits lacustrine environment characteristics, positive anomalies of La, Gd and Y can be attributed to hydrothermal fluids.

Table 6. Anomalies and enrichment patterns of Eu, Ce, Gd and Y of coal samples in Tunçbilek-Tavşanlı coal basin.

Sample	Eu_N/Eu_N^*	Ce_N/Ce_N^*	Gd_N/Gd_N^*	La_N/Lu_N	La_N/Sm_N	Gd_N/Lu_N	Y_N/Ho_N	ET	C_{out}	Critic REE+Y	Non-critic REE+Y	Super Critic REE+Y
TFC1	1.15	1.01	1.17	1.03	1.02	1.10	1.12	L	0.77	38.16	35.54	49.31
TFC2	1.19	1.11	1.18	1.16	0.94	1.31	1.02	L-M	0.71	50.14	46.35	70.77
TFC3	1.53	0.94	1.09	1.10	1.59	0.79	1.00	L	0.75	8.49	8.89	11.26
TFC4	1.19	1.11	1.12	1.31	0.99	1.26	1.17	L-M	0.69	36.83	33.92	53.68
TFC5	1.06	1.05	1.02	0.83	0.97	0.83	1.15	H	0.83	35.97	28.90	43.42
TFC6	1.08	0.98	1.08	0.59	1.01	0.56	1.23	H	0.89	23.72	19.19	26.80
TFC7	1.08	0.97	1.17	2.48	1.16	1.81	1.16	L	0.61	176.05	210.97	289.15
TFC8	1.16	1.24	1.15	1.07	0.94	1.10	1.08	L-M	0.63	38.69	35.87	61.79
TFC9	1.12	1.25	1.11	1.56	1.03	1.37	0.95	L	0.54	24.00	25.57	44.52
TFC10	1.21	1.08	1.14	1.20	1.05	1.18	1.03	L	0.68	35.35	34.08	51.62
TFC11	1.12	1.29	1.13	1.37	1.07	1.20	1.13	L	0.54	25.34	26.27	47.31
TFC12	1.14	0.99	1.10	2.68	1.05	2.01	1.07	L-M	0.60	113.37	134.22	189.03
TFC13	1.10	1.13	1.10	0.91	0.76	1.17	1.12	M	0.79	14.46	11.75	18.27
TFC14	1.17	0.96	1.11	2.00	1.10	1.52	1.12	L	0.67	120.25	133.79	180.76
TFC15	1.14	1.18	1.18	1.07	0.93	1.22	1.15	M	0.69	46.78	41.39	67.55
TFC16	1.18	1.17	1.06	1.15	1.11	1.05	1.28	L	0.65	10.52	10.07	16.26
TFC17	1.17	1.22	1.19	1.47	1.06	1.42	0.99	L	0.58	40.87	41.47	67.55
TFC18	1.18	1.16	1.19	1.97	1.12	1.74	0.99	L	0.57	16.15	17.39	28.15
TFC19	1.15	0.96	1.04	1.24	1.52	0.84	1.03	L	0.68	7.08	8.27	10.42

TFC20	1.12	0.97	1.11	1.07	1.00	1.07	1.02	L	0.79	47.62	44.83	60.33
TFC21	1.12	0.98	1.12	1.02	1.09	0.92	1.05	L	0.74	38.68	38.50	52.41
TFC23	1.19	1.08	1.17	0.68	0.72	1.16	1.01	M-H	0.96	51.30	36.29	53.20
TFC24	1.30	1.02	1.12	1.00	0.99	1.09	1.10	L-M	0.88	12.78	10.46	14.54
TFC25	1.18	0.97	1.14	0.99	1.11	1.05	1.14	L	0.85	32.65	29.10	38.26

Seredin and Dai (2012) [13] developed a new classification for the evaluation of REE+Y in coal as an economic raw material, which considers REE+Y degree, element composition, resources of rare metals, exploitable tonnage of coal, formation forms of rare metals in coal and coal burning production, extraction methods, environmental problems, supply and demand relationship of rare metals [65]. According to this classification, REE+Y is divided into three groups namely critical (Nd, Eu, Tb, Dy, Y and Er), non-critical (La, Pr, Sm ve Gd) and super critical (Ce, Ho, Tm, Yb and Lu). In the studied samples, the critical and non-critical groups present close values in the total REE+Y concentration, while the REE+Y concentration of the super critical groups constitutes a significant portion of the total REE+Y concentration in the coal, roof, floor and parting samples (Table 6).

Dai et al. (2017) [65] stated that REE+Y content greater than 1000 µg/g is considered as the cut-off grade for useful recovery, and the second criterion is REE+Y_{def}, rel-C_{outl} graph. Where REE+Y_{def} stands for the percentage of critical elements in total REE+Y, C_{outl} (outlook coefficient) is the ratio of relative amount of critical REE+Y metal in the total REE+Y. Excessive REE+Y is calculated by Eq. 4:

$$C_{outl} = (Nd + Eu + Tb + Dy + Er + Y / \Sigma REE+Y) / (Ce + Ho + Tm + Yb + Lu / \Sigma REE+Y) \quad (4)$$

REE+Y sources with $0.7 \leq C_{outl} \leq 1.9$ and $C_{outl} > 2.4$ are considered as promising and highly promising, respectively [65]. The C_{outl} values of Tunçbilek-Tavşanlı samples were calculated and given in Table 6. According to the relationship between the cut-off grade and C_{outl}, the coal, roof, floor and parting layers remain within the unpromising area (Fig. 10).

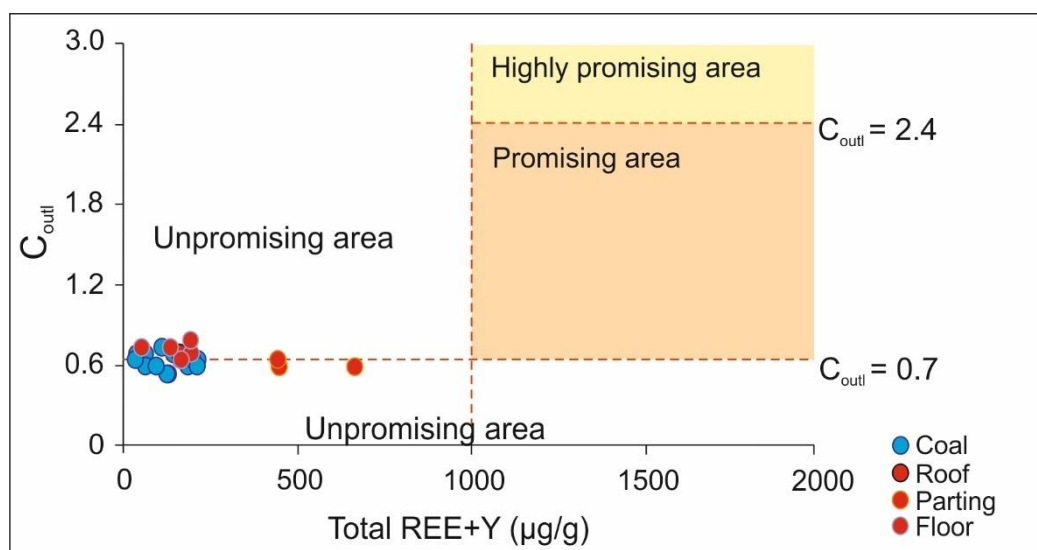


Figure 10. Evaluation of REE+Y in coal and host rock samples of Tunçbilek-Tavşanlı coal field [65].

5. CONCLUSION

The minerals in the studied coal samples are, in order of abundance, quartz, kaolinite, illite-smectite and siderite, dolomite, illite, smectite, mica, feldspar, pyrite, chlorite and jarosite. The mineral compositions of the samples taken from the roof-floor-parting showed similarities with the coal samples. SiO_2 , Al_2O_3 and Fe_2O_3 are generally the most abundant major oxides in the studied samples. The MgO , K_2O , CaO , TiO_2 , Na_2O , P_2O_5 and MnO were also detected in lesser amounts. Only in the parting samples, SiO_2 , Al_2O_3 and MgO are the most abundant major oxides whereas Fe_2O_3 , K_2O , TiO_2 , CaO , P_2O_5 , Na_2O and MnO were found to be in lesser amounts. It was observed that the major oxide contents were high in claystone and carbonaceous shale samples. Concentration of SiO_2 and Al_2O_3 in coal samples is quite low comparing to other samples and the main source of SiO_2 and Al_2O_3 is kaolinite and illite-smectite mixed-layer clays. Samples with high Al_2O_3 content are abundant in kaolinite, however, SiO_2 may be partially related to the quartz content. Siderite and pyrite minerals are relatively abundant in samples with high Fe_2O_3 . It was observed that dolomite minerals were more abundant in samples with high MgO .

The CC values of Tunçbilek-Tavşanlı coals are predominantly in the slightly enriched-normal ranges, whereas the CC values of the roof, floor and parting samples present normal values. According to the concentration coefficient, the Ni element in the coals is significantly enriched; Cs, Co and Rb elements are enriched and are of inorganic origin. REE+Y concentration (average 95.04 $\mu\text{g/g}$) is higher than the average REE+Y concentration of world's low-rank coals and USA coals. In samples with high ash content, REE+Y concentration is high, while relatively low concentration of REE+Y in samples with low ash content indicates mineral matter relationship. This shows that it may be related to the tuffy units in the coal basin. The Eu, Ce, Gd and Y values of coal seam samples of Tunçbilek

Formation show weak positive anomalies. This suggested that it may be related to hydrothermal fluids. Based on the Al_2O_3/TiO_2 ratio and the L-type enrichment of REE+Y, it can be concluded that the terrestrial materials around the coal basin in the early stage of peat deposition are mainly derived from intermediate-felsic tuffs. Element ratios (V/Ni, V/(V +Ni), U/Th) indicate oxidizing conditions and lacustrine origin. In addition, the Sr/Cu and Ga/Rb ratios of the roof, coal and floor strata samples indicate humid conditions, whereas the Sr/Cu and Ga/Rb ratios of parting strata samples indicate relatively arid climate. The usability of REE+Y in Tunçbilek-Tavşanlı coals as an industrial raw material source does not constitute a potential source according to the cut-off grade- C_{out} association, although the extremely critical groups (Ce, Ho, Tm, Yb and Lu) are dominant.

ACKNOWLEDGEMENT

This study was funded by Akdeniz University Research Coordination Unit (FYL-2019-5015). The author would like to thank Turkish Coal Enterprises for their support during field work and sampling, and all the reviewers for their valuable comments and contributions.

REFERENCES

- [1] Thurber, M.C., Morse, R.K., (2015), *The Global Coal Market: Supplying Major Fuel for Emerging Economies*, Cambridge University Press, Cambridge, 702 p.
- [2] Dai, S., Bechtel, A., Eble, C.F., Flores, R.M., French, D., Graham, I.T., Hood, M.M., Hower, J.C., Korasidis, V.A., Moore, T.A., Puttmann, W., Wei, Q., Zhao, L., O'Keefem, J.M.K., (2020), Recognition of peat depositional environments in coal: A review, *International Journal of Coal Geology*, 219, 103383.
- [3] Dai, S., Tian, L., Chou, C.L., Zhou, Y., Zhang, M., Zhao, L., Wang, J., Yang, Z., Cao, H., Ren, D., (2008a), Mineralogical and compositional characteristics of Late Permian coals from an area of high lung cancer rate in Xuan Wei, Yunnan, China: occurrence and origin of quartz and chamosite, *International Journal of Coal Geology*, 76, 318–327.
- [4] Dai, S., Ren, D., Zhou, Y., Chou, C.L., Wang, X., Zhao, L., Zhu, X., (2008b), Mineralogy and geochemistry of a superhigh-organic-sulfur coal, Yanshan Coalfield, Yunnan, China: evidence for a volcanic ash component and influence by submarine exhalation, *Chemical Geology*, 255, 182–194.
- [5] Dai, S., Wang, X., Chen, W., Li, D., Chou, C.L., Zhou, Y., Zhu, C., Li, H., Zhu, X., Xing, Y., Zhang, W., Zou, J., (2010), A high-pyrite semianthracite of Late Permian age in the Songzao Coalfield, southwestern China: mineralogical and geochemical relations with underlying mafic tuffs, *International Journal of Coal Geology*, 83, 430–445.

- [6] Dai, S., Ren, D., Chou, C.L., Finkelman, R.B., Seredin, V.V., Zhou, Y., (2012), Geochemistry of trace elements in Chinese coals: a review of abundances, genetic types, impacts on human health, and industrial utilization, *International Journal of Coal Geology*, 94, 3-21.
- [7] Finkelman, R.B., Dai, S., French, D., (2019), The importance of minerals in coal as the hosts of chemical elements, *International Journal of Coal Geology*, 212, 103251.
- [8] Dai, S., Finkelman, R.B., (2018), Coal as a promising source of critical elements: progress and future prospects, *International Journal of Coal Geology*, 186, 155–164.
- [9] Güllüdağ, C.B., Aksoy, E., Ünal, N., Özmen, S.F., (2020), Radioactivity concentrations and risk assessment of Tekirdağ lignites (case study of Malkara coalfield), *Acta Geophysica*, 68, 1411–1420.
- [10] Seredin, V.V., Finkelman, R.B., (2008), Metalliferous coals: A review of the main genetic and geochemical types, *International Journal of Coal Geology*, 76, 253–289.
- [11] Lin, R., Soong, Y., Granite, E.J., (2018b), Evaluation of trace elements in U.S. coals using the USGS COALQUAL database version 3.0. Part II: Non-REY critical elements, *International Journal of Coal Geology*, 192, 39–50.
- [12] Zhao, L., Ward, C.R., French, D., Graham, I.T., Dai, S., Yang, C., Xie, P., Zhang, S., (2018), Origin of a kaolinite-NH₄-illite-pyrophyllite-chlorite assemblage in a marine-influenced anthracite and associated strata from the Jincheng Coalfield, Qinshui Basin, Northern China, *International Journal of Coal Geology*, 185, 61–78.
- [13] Seredin, V.V., Dai, S., (2012), Coal deposits as potential alternative sources for lanthanides and yttrium, *International Journal of Coal Geology*, 94, 67–93.
- [14] Hower, J.C., Eble, C.F., Dai, S.F., Belkin, H.E., (2016), Distribution of rare earth elements in eastern Kentucky coals: indicators of multiple modes of enrichment?, *International Journal of Coal Geology*, 160, 73–81.
- [15] Kolker, A., Scott, C., Hower, J.C., Vazquez, J.A., Lopano, C.L., Dai, S., (2017), Distribution of rare earth elements in coal combustion fly ash, determined by SHRIMP-RG ion microprobe, *International Journal of Coal Geology*, 184, 1–10.
- [16] Laudal, D.A., Benson, S.A., Addleman, R.S., Palo, D., (2018), Leaching behavior of rare earth elements in Fort Union lignite coals of North America, *International Journal of Coal Geology*, 191, 112–124.
- [17] Lin, R., Soong, Y., Granite, E.J., (2018a), Evaluation of trace elements in U.S. coals using the USGS COALQUAL database version 3.0. Part I: rare earth elements and yttrium (REY), *International Journal of Coal Geology*, 192, 1–13.

- [18] Wagner, N.J., Matiane, A., (2018), Rare earth elements in select Main Karoo Basin (South Africa) coal and coal ash samples, *International Journal of Coal Geology*, 196, 82–92.
- [19] Seredin, V.V., (2012), From coal science to metal production and environmental protection: a new story of success, *International Journal of Coal Geology*, 90, 1–3.
- [20] Dai, S., Yan, X., Ward, C.R., Hower, J.C., Zhao, L., Wang, X., Zhao, L., Ren, D., Finkelman, R.B., (2018), Valuable elements in Chinese coals: a review, *International Geology Review*, 60, 590–620.
- [21] Arni, P., (1942), Anadolu ofiyolitlerinin yaşlarına mütedir malumat, *Bulletin of the Mineral Research and Exploration*, 28, 472-488.
- [22] Nebert, K., (1960), Tavşanlı'nın batı ve kuzeyindeki linyit ihtiva eden Neojen sahasının mukayeseli stratigrafisi ve tektoniği, *Bulletin of the Mineral Research and Exploration*, 54, 7-35.
- [23] Kalafatçıoğlu, A., (1962), A note on the geology of the region between Tavşanlı and Dağardı, and on the age of the serpentines and limestones, *Bulletin of the Mineral Research and Exploration*, 58, 38-46.
- [24] Okay, A.I., (1981), The geology and blueschist metamorphism of the ophiolites in Northwest Turkey (Tavşanlı-Kütahya), *Bulletin of the Geological Society of Turkey*, 24, 85-95.
- [25] Okay, A.I., (1984), Kuzeybatı Anadolu'da yer alan metamorfik kuşaklar, *Ketin Sempozyumu*, pp. 83-92.
- [26] Baş, H., (1986), Tertiary geology of the Domaniç-Tavşanlı-Kütahya-Gediz region, *Geological Engineering*, 11-18.
- [27] Helvacı, C., İnci, U., Yağmurlu, F., Yılmaz, H., (1987), Neogen stratigraphic and economic potential of Western Turkey, *Journal of Isparta Engineering Faculty of Akdeniz University*, 3, 31-45.
- [28] Kocuyigit, A., Bozkurt, E., (1997), Kütahya-Tavşanlı çöküntü alanının neotektonik özellikleri, TÜBİTAK Project No: YDABÇAG-126, 78 p.
- [29] Günal Türkmenoğlu, A., Yavuz-Işık, N., (2007), Mineralogy, chemistry and potential utilization of clays from coal deposits in the Kütahya province, Western Turkey, *Applied Clay Science*, 42, 63-73.
- [30] Özburan, M., (2009), Neotectonic investigation of Kütahya and Its surrounding, *Dissertation, Kocaeli University*, 209 p.

- [31] Göncüoğlu, M.C., (2011), Geology of the Kütahya-Bolkardağ belt, Bulletin of the Mineral Research and Exploration, 142, 223-277.
- [32] Erkoyun, H., Kadir, S., Huggett, J., (2019), Occurrence and genesis of tonsteins in the Miocene lignite, Tunçbilek Basin, Kütahya, western Turkey, International Journal of Coal Geology, 202, 46-68.
- [33] Soytürk, T., (1992), Tunçbilek kömürlerinin kendiliğinden yanmaya yatkınlıklarının araştırılması, Dissertation, Anadolu University, 76 p.
- [34] Yavuz, N., (1994). Palynology, petrography and chemistry of the Tavşanlı coals (Kütahya), Dissertation, Middle East Technical University, Ankara, , 90 p.
- [35] Bacak, G., (2003). Mineralogical, petrographical and petrogenetical study of Southern Dağardı (Tavşanlı-Kütahya) ophiolite, Dissertation, İstanbul Technical University, İstanbul, 284 p.
- [36] Karayigit, A.I., Celik, Y., (2003), Mineral matter and trace elements in Miocene coals of the Tuncbilek-Domanic Basin, Kutahya, Turkey, Energy Sources, 25, 339-355.
- [37] Parlak, A., (2010), Briquetting Tunçbilek lignites and retention of sulfur in ash during combustion, Dissertation, Gazi University, Ankara, 104 p.
- [38] Akkiraz, M.S., Akgün, F., Utescher, T., Wilde, V., Bruch, A.A., Mosbrugger, V., Üçbaş, S.D., (2012), Palaeoflora and climate of lignite-bearing lower-middle Miocene sediments in the Seyitömer and Tunçbilek sub-basins, Kütahya province, Northwest Turkey, Turkish Journal of Earth Sciences, 21, 213-235.
- [39] Helvacı, C., Ersoy, E.Y., Billor, M.Z., (2017), Stratigraphy and Ar/Ar geochronology of the Miocene lignite-bearing Tunçbilek-Domanic Basin, western Anatolia, International Journal of Earth Science, 106, 1797-1814.
- [40] Akçay, A., (2017), Neotectonic investigation of the coaly Neogene area between Kızılbük-Degirmisaz (Tavşanlı/Kütahya), Dissertation, Dumlupınar University, 67 p.
- [41] Emre, Ö., Duman, T.Y., Özalp, S., Şaroğlu, F., Olgun, Ş., Elmacı, H., Çan, T., (2018), Active fault database of Turkey, Bulletin of Earthquake Engineering, 16, 3229-3275.
- [42] Akgün, E., Özden, S., (2019), Plio-Quaternary stress states along the Kütahya Fault and surroundings, NW Turkey, Turkish Journal of Earth Sciences, 28, 671-686.
- [43] Kezer, Z., (2019), Tectonic geomorphology of the Kütahya Graben (Western Anatolia), Dissertation, Hacettepe University, 92 p.

- [44] Kazancı, C., (2019), Organic facies characteristics of FC pano opencast mine coals, Tunçbilek (Tavşanlı-Kütahya), Dissertation, Akdeniz University, Antalya, 67 p.
- [45] Cicioglu Sutcu, E., Şentürk, S., Kapıcı, K., Gökçe, N., (2021), Mineral and rare earth element distribution in the Tunçbilek coal seam, Kütahya, Turkey, *International Journal of Coal Geology*, 245, 103820.
- [46] Ketin, İ., (1966), Tectonic Units of Anatolia, *Bulletin of the Mineral Research and Exploration*, 66, 20-37.
- [47] Okay, A.I., Tüysüz, O., (1999), Tethyan sutures of northern Turkey, *Geological Society Special Publication*, 156 (1), 475–515.
- [48] Şengör, A.M.C., Yılmaz, Y., (1981), Tethyan evolution of Turkey: a plate tectonic approach, *Tectonophysics*, 75, 181-241.
- [49] Candan, O., Koralay, O.E., Akal, C., Kaya, O., Oberhänsli, R., Dora, O.Ö., Konak, N., Chen, F., (2011), Supra-Pan-African unconformity between core and cover series of the Menderes Massif/Turkey and its geological implications, *Precambrian Research*, 184, 1–23.
- [50] Candan, O., Çetinkaplan, M., Oberhänsli, R., Rimmelé, G., Akal, C., (2005), Alpine high-P/low-T metamorphism of the Afyon Zone and implications for the metamorphic evolution of Western Anatolia, Turkey, *Lithos*, 84, 102-124.
- [51] Göncüoğlu, M.C., Sayit, K., Tekin, U.K., (2010), Oceanization of the northern Neotethys: geochemical evidence from ophiolitic melange mélangé basalts within the İzmir-Ankara suture belt, NW Turkey, *Lithos*, 116, 175–187.
- [52] Okay, A.I., Harris, N.B.W., Kelley, S.P. (1998), Exhumation of blueschists along a Tethyan suture in northwest Turkey, *Tectonophysics*, 285, 275–299.
- [53] Okay, A.I., Tansel, I., Tüysüz, O., (2001), Obduction, subduction and collision as reflected in the Upper Cretaceous–Lower Eocene sedimentary record of Western Turkey, *Geological Magazine*, 138 (2), 117–142.
- [54] Yılmaz, Y., Genç, S.C., Gürer, F., Bozcu, M., Yılmaz, K., Karacık, Z., Altunkaynak, S., Elmas, A., (2000), When did the Western Anatolian grabens begin to develop? In: Bozkurt, E., Winchester, J.A., Piper, J.A.D. (eds) *Tectonics and magmatism in Turkey and the surrounding area*, *Journal of the Geological Society of London*, 173, 131–162.
- [55] Ersoy, Y., Helvacı, C., (2007), Stratigraphy and geochemical features of the Early Miocene bimodal (ultrapotassic and calc-alkaline) volcanic activity within the NE-trending Selendi basin, western Anatolia, Turkey, *Turkish Journal of Earth Sciences*, 16, 117–139.

- [56] Ersoy, E.Y., Helvacı, C., Palmer, M.R., (2011), Stratigraphic, structural and geochemical features of the NE-SW trending Neogene volcanosedimentary basins in western Anatolia: implications for associations of supradetachment and transtensional strike-slip basin formation in extensional tectonic setting, *Journal of Asian Earth Sciences*, 41, 159–183.
- [57] Seyitoğlu, G., Anderson, D., Nowell, G., Scott, B.C., (1997), The evolution from Miocene potassic to Quaternary sodic magmatism in western Turkey: implications for enrichment processes in the lithospheric mantle, *Journal of Volcanology and Geothermal Research*, 76, 127–147.
- [58] Çelik, Y., (1999), Sedimentology and coal-potential of the Domaniç (Kütahya) Neogene basin, Dissertation, İstanbul University, İstanbul, 205 p.
- [59] Özburan, M., Gürer, Ö.F., (2012), Late Cenozoic polyphase deformation and basin development, Kütahya region, western Turkey, *International Geology Review*, 54 (12), 1401-1418.
- [60] Yağmurlu, F., Inaner, H., Nakoman, E., Inci, U., (2004), Age, tectonic setting, and quality distribution of the Neogene lignite deposits of western Anatolia, *Geologica Belgica*, 7 (3), 251–258.
- [61] Ersoy, E.Y., Helvacı, C., (2016), Geochemistry and petrology of the lower Miocene bimodal volcanic units in the Tunçbilek–Domaniç basin, western Anatolia, *International Geology Review*, 58 (10), 1234-1252.
- [62] Vassilev, S.V., Vassileva, C.G., Baxter, D., Andersen, L.K., (2010), Relationships between chemical and mineral composition of coal and their potential applications as genetic indicators. Part 2. Mineral classes, groups and species, *Geologica Balcanica*, 39 (3), 43–67.
- [63] Vassilev, S., Vassileva, C., (1996), Mineralogy of combustion wastes from coal-fired power stations, *Fuel Processing Technology*, 47, 261–280.
- [64] Ward, C.R., (2016), Analysis, origin and significance of mineral matter in coal: an updated review, *International Journal of Coal Geology*, 165, 1–27.
- [65] Dai, S., Xie, P., Jia, S., Ward, C.R., Hower, H.C., Yan, X., French, D., (2017), Enrichment of U-Re-V-Cr-Se and rare earth elements in the Late Permian coals of the Moxinpo Coalfield, Chongqing, China: genetic implications from geochemical and mineralogical data, *Ore Geology Review*, 80, 1–17.
- [66] Baş, H., (1983), Domaniç-Tavşanlı-Kütahya-Gediz yörelerinin Tersiyer jeolojisi ve volkanitlerinin petrolojisi, MTA Report No. 7293, 86 p.

- [67] Türkmenoğlu, A.G., Yavuz-Işık, N., (2008), Mineralogy, chemistry and potential utilization of clays from coal deposits in the Kütahya province, Western Turkey, *Applied Clay Science*, 42, 63-73.
- [68] Fu, X., Wang, J., Tan, F., Feng, X., Zeng, S., (2013), Minerals and potentially hazardous trace elements in the late Triassic coals from the Qiangtang Basin, China, *International Journal of Coal Geology*, 116-117, 93-105.
- [69] Wang, X., Wang, X., Pan, S., Yang, Q., Hou, S., Jiao, Y., Zhang, W., (2018), Occurrence of analcime in the middle Jurassic coal from the Dongsheng Coalfield, northeastern Ordos Basin, China, *International Journal of Coal Geology*, 196, 126-138.
- [70] Finkelman, R.B., Palmer, C.A., Wang, P., (2018), Quantification of modes of occurrence of 42 elements in coal, *International Journal of Coal Geology*, 185, 138-160.
- [71] Hayashi, K.I., Fujisawa, H., Holland, H.D., Ohmoto, H., (1997), Geochemistry of ~1.9 Ga sedimentary rocks from northeastern Labrador, Canada, *Geochimica Cosmochimica Acta*, 61, 4115-4137.
- [72] He, B., Xu, Y.G., Zhong, Y.T., Guan, J.P., (2010), The Guadalupian-Lopingian boundary mudstones at Chaotian (SW China) are clastic rocks rather than acidic tuffs: implication for a temporal coincidence between the end-Guadalupian mass extinction and the Emeishan volcanism, *Lithos*, 119, 10-19.
- [73] Dai, S., Yang, J., Ward, C.R., Hower, J.C., Liu, H., Garrison, T.M., French, D., O'Keefe, J.M.K., (2015b), Geochemical and mineralogical evidence for a coal-hosted uranium deposit in the Yili Basin, Xinjiang, northwestern China, *Ore Geology Review*, 70, 1-30.
- [74] Dai, S., Seredin, V.V., Ward, C.R., Hower, J.C., Xing, Y., Zhang, W., Song, W., Wang, P., (2015c), Enrichment of U-Se-Mo-Re-V in coals preserved within marine carbonate successions: geochemical and mineralogical data from the Late Permian Guiding Coalfield, Guizhou, China, *Mineralium Deposita*, 50, 159-186.
- [75] Ketris, M.P., Yudovich, Y.E., (2009), Estimations of Clarkes for carbonaceous biolithes: world average for trace element contents in black shales and coals, *International Journal of Coal Geology*, 78, 135-148.
- [76] Dai, S., Wang, P., Ward, C.R., Tang, Y., Song, X., Jiang, J., Hower, J.C., Li, T., Seredin, V.V., Wagner, N.J., Jiang, Y., Wang, X., Liu, J., (2015a), Elemental and mineralogical anomalies in the coal-hosted Ge ore deposit of Lincang, Yunnan, southwestern China: key role of N₂-CO₂-mixed hydrothermal solutions, *International Journal of Coal Geology*, 152, 19-46.
- [77] Finkelman, R.B., (1981), Modes of occurrence of trace elements in coal: USGS Open-File Report No. OFR-81-99, 301 p.

- [78] Finkelman, R.B., (1988), The inorganic geochemistry of coal: a scanning electron microscopy view, *Scanning Microscopy*, 2 (1), 97-105.
- [79] Finkelman, R.B., (1994), Modes of occurrence of potentially hazardous elements in coal: levels of confidence, *Fuel Processing Technology*, 39, 21–34.
- [80] Rudnick, R.L., Gao, S. (2003), Treatise on geochemistry, volume 3, In: The Crust, Holland, H.D. and Turekian, K.K. (Eds), Elsevier-Pergamon, Oxford, 683 p.
- [81] Dai, S., Ji, D., Ward, C.R., French, D., Hower, J.C., Yan, X., Wei, Q., (2018b), Mississippian anthracites in Guangxi Province, southern China: Petrological, mineralogical, and rare earth element evidence for high-temperature solutions. *International Journal of Coal Geology*, 197, 84–114.
- [82] Jones, B., Manning, D.A.C., (1994), Comparison of geochemical indices used for the interpretation of palaeoredox conditions in ancient mudstones. *Chemical Geology*, 111, 111–129.
- [83] Karadirek, S., Altunsoy, M., (2022), Geochemical characteristics and paleodepositional setting of coal-bearing strata in Konya-Karapınar Basin, Central Anatolia, Turkey. *Journal of African Earth Sciences*, 186, 1-13.
- [84] Galarraga, F., Reategui, K., Martinez, A., Martinez, M., Llamas, J.F., Marquez, G., (2008), V/Ni ratio as a parameter in palaeoenvironmental characterisation of non-mature medium crude oils from several Latin American basins. *Journal of Petroleum Science and Engineering*, 61, 9–14.
- [85] El-Sabagh, S.M. Rashad, A.M. El-Naggar, A.Y. El Nady, M.M. Badr, I.A. Ebiad M.A., Abdullah E.S., (2018), API gravities, vanadium, nickel, sulfur, and their relation to gross composition: Implications for the origin and maturation of crude oils in Western Desert, Egypt, *Petroleum Science and Technology*, 36, 1-8.
- [86] Kimura, H., Watanabe, Y., (2001), Ocean anoxia at the Precambrian–Cambrian boundary. *Geology*, 29, 995–998.
- [87] Shi, L., Feng, Q.L., Shen, J., Ito, T., Chen, Z.Q., (2016), Proliferation of shallow-water radiolarians coinciding with enhanced oceanic productivity in reducing conditions during the Middle Permian, South China: evidence from the Gufeng Formation of western Hubei Province. *Paleogeography, Paleoclimatology, Paleoecology*, 444, 1–14.
- [88] Lerman, A., Imboden, D.M., Gat, J.R., (1995), *Physics and Chemistry of Lakes*. Springer, Berlin, Heidelberg.
- [89] Roy, D.K., Roser, B.P., (2013), Climatic control on the composition of Carboniferous–Permian Gondwana sediments, Khalaspir basin, Bangladesh. *Gondwana Research*, 23, 1163–1171.

- [90] Finkelman, R.B., (1993), Trace and minor elements in coal, In: Organic Geochemistry Engel, M.H., Macko, S.A. (Eds), Plenum, New York, pp. 593–607.
- [91] Dai, S., Zhou, Y., Ren, D., Wang, X., Li, D., Zhao, L., (2007), Geochemistry and mineralogy of the Late Permian coals from the Songzao Coalfield, Chongqing, southwestern China, Science In China Series D-Earth Sciences, 50, 678–688.
- [92] Yalçın Erik, N., (2022), A non-traditional resource for critical minerals; Rare Earths (REY+Sc) contents of some Turkish low rank coals, Kahramanmaraş Sutcu Imam University Journal of Engineering Sciences, 25, 155-172.
- [93] Taylor, S.R., McLennan, S.H., (1985), The continental crust: Its composition and evolution, Blackwell, Oxford, 312 p.
- [94] Dai, S., Graham, I.T., Ward, C.R., (2016), A review of anomalous rare earth elements and yttrium in coal, International Journal of Coal Geology, 159, 82–95.
- [95] Yan, X., Dai, S., Graham, I.T., He, X., Shan, K., Liu, X., (2018), Determination of Eu concentrations in coal, fly ash and sedimentary rocks using a cation exchange resin and inductively coupled plasma mass spectrometry (ICP-MS), International Journal of Coal Geology, 191, 152–156.
- [96] Yan, X., Dai, S., Graham, I.T., French, D., (2019), Mineralogy and geochemistry of the Palaeogene low-rank coal from the Baise Coalfield, Guangxi Province, China: Contributions from surrounding terrigenous lithologies and the depositional environment, International Journal of Coal Geology, 214, 103282.
- [97] Dai, S., Ren, D., Chou, C.-L., Li, S., Jiang, Y., (2006), Mineralogy and geochemistry of the No. 6 coal (Pennsylvanian) in the Junger Coalfield, Ordos Basin, China. International Journal of Coal Geology, 66, 253–270.
- [98] Bau, M., Koschinsky, A., Dulski, P., Hein, J.R., (1996), Comparison of the partitioning behaviours of yttrium, rare earth elements, and titanium between hydrogenetic marine ferromanganese crusts and seawater. Geochimica Cosmochimica Acta, 60, 1709–1725.



RESEARCH ARTICLE

OPTIMAL DESIGN OF ORGANIC RANKINE CYCLE POWER PLANTS FOR EFFICIENT UTILIZATION of BIOMASS ENERGY IN NIGERIA

John Akpaduado FRIDAY¹, Joseph OYEKALE^{2*}

¹Federal University of Petroleum Resources Effurun, Department of Mechanical Engineering, P.M.B. 1221 Effurun, Delta State, Nigeria, johnakpaduado909@gmail.com, ORCID: 0000-0002-8220-7093

^{2*}Federal University of Petroleum Resources Effurun, Department of Mechanical Engineering, P.M.B. 1221 Effurun, Delta State, Nigeria, oyekale.oyetola@fupre.edu.ng, ORCID: 0000-0003-4018-4660

Receive Date: 08.11.2022

Accepted Date: 02.02.2023

ABSTRACT

This study investigated the optimal design choice among four organic Rankine cycle (ORC) configurations for efficient utilization of solid biomass energy in Nigeria. Although vast opportunities exist for large-scale biomass power plants in the country, there has been little or no practical implementation yet, due to the limitation of technical know-how regarding thermodynamic conversion technologies. To bridge this gap, a thermodynamic optimization technique was applied in this study to the ORC. Specifically, the subcritical ORC (SUBORC), the regenerative subcritical ORC (SUBORC-REGEN), the supercritical ORC (SUPERORC), and the regenerative supercritical ORC (SUPERORC-REGEN) configurations were compared using established zero-dimensional optimization models implemented in MATLAB. Results showed that the SUPERORC-REGEN would be the most preferred choice amongst the options compared. Specifically, a palm kernel expeller (PKE) biomass fuel considered could yield about 1.98 MW of power at a thermal efficiency of about 28%. Additionally, it was obtained that the supercritical ORC would always outperform the subcritical types technically, with or without a regenerator. For the regenerative configurations, results showed that the supercritical ORC would generate 113 kW and 429 kW more net power than the subcritical ORC, respectively for n-pentane and n-butane working fluids. Similarly, the study reiterated that adopting a regenerative configuration would improve ORC performance. For instance, the SUPERORC-REGEN yielded 63% and 73% more power than the SUPERORC, respectively for n-pentane and n-butane working fluids. The practical economic implications of the different ORC configurations should be examined in future studies, alongside the investigation of exergy-based optimization potentials on component basis.

Keywords: *Organic Rankine Cycle, Biomass Energy, Renewable Power Plant, Sustainable Energy System, ORC Thermodynamic Optimization*

1. INTRODUCTION

The global energy scene has been saturated in recent times with debates on the need to transition from fossil-reliant infrastructure to systems that would use clean, renewable, and affordable energy sources. The reasons for these are not far-fetched; combustion of fossil fuels for energy generation is always associated with the emission of obnoxious gases into the atmosphere, which not only damages the ecosystem but also poses grave challenges to human health. Additionally, the non-renewable nature of most fossil fuels means that the reserves around the world would be depleted someday, even if it takes centuries. Thus, lots of scientific, socio-economic, political, and technical efforts are required worldwide to facilitate the practical deployment of renewable energy systems and to ameliorate the aforementioned consequences of conventional energy systems [1]. Additionally, although lots of research and practical activities have been carried out hitherto on modern energy systems powered by renewable resources [2], [3], [4], [5], [6], [7], [8], only a few of such systems are at commercial scale today.

Biomass is one renewable energy resource that has attracted unprecedented attention in the 21st century as a sustainable alternative to fossil fuels [9], [10]. It is formed from metabolic processes undergone by inanimate and animate living species [11]. Several resources are often referred to as biomass, but the main classes include forest biomass (woods and residues), agricultural biomass (energy crops, rotation crops, etc), and renewable wastes (industrial wastes and municipal wastes) [12], [13]. Depending on the sources of generation, biomass fuels can be solid, liquid, or gaseous in states. However, it is widely acknowledged that biomass fuels exist most abundantly as solids, which makes solid biomass the most commonly applied [14]. Several countries have formulated policies to identify and quantify biomass fuel reserves available locally and to promote their use for energy generation [15], [16], [17]. Additionally, similar efforts are currently being made at regional and global levels to campaign for the progressive use of biomass energy especially in energy-intensive sectors, such as the steel and cement industries, where low-temperature renewable sources might find limited or no relevance [18]. An example of such an international campaign effort is being made through the European Biomass Conference and Exhibition (EUBCE), an annual event that is currently in its 30th edition in the year 2022.

The research and practical efforts aimed at promoting energy generation from biomass fuels are not limited to developed countries. Several developing economies such as Nigeria have also acknowledged the potential roles of biomass in achieving the United Nation's Sustainable Development Goal (SDG) number 7 on clean and affordable energy. To justify this, a few of the many research on the assessment of biomass availability and potential usage for energy in Nigeria are summarized in this section. Olanrewaju et al. [19] assessed the potential of biomass energy in Nigeria and reported that more than 200 billion kg of biomass resources are available each year for energy generation in Nigeria, 80% of which are woody fuels and charcoals. Ben-Iwo et al. [20] corroborated the assertion that biomass resources are abundant in Nigeria, reporting specifically that it could contribute about 80% of the total energy consumed in the country. In a similar study, Ezealigo et al. [21] estimated that crop residues available in Nigeria could be processed into 8 Mtoe of cellulosic ethanol and 13 Mtoe of biogas each year, further reiterating the vast potential of biomass fuels for energy generation in the country. The same assertion was confirmed in the study by Jekayinfa et al.

[22] where bioenergy producible from several biomass resources in Nigeria was estimated at 2.3 EJ. However, the authors stated explicitly that despite the huge potential, little or nothing has been done towards the practical realization of large-scale bioenergy plants in the country. In the Southwestern part of the country alone, Elehinafe et al. [23] identified over 100 different types of woody/forest biomass which, if properly managed, could provide an inexhaustible biomass fuel reserve for powering thermal power plants in this region of the country. That is notwithstanding other aforementioned agricultural residues, municipal wastes, and industrial wastes which have been reported substantial in quantity in Nigeria [24]. Apart from the studies aimed at assessing biomass energy potential in Nigeria, other authors have focused on experimental characterization of different biomass fuels to facilitate their practical applications in biomass power plants [25], [26], [27]. The legal perspectives on the challenges and prospects of converting organic wastes to electrical energy in Nigeria were the focus of [28], where the authors remarked that a coherent and explicit legal framework is required to promote biomass energy in the country. Moreover, the life cycle assessment of selected Nbiomass fuels available abundantly in Nigeria has also been x-rayed in the literature [29], [30].

It is inferable from the foregoing literature review that huge potential exists for the generation of electricity from biomass in Nigeria. However, there is hardly one large-scale biomass thermal power plant existing in the country at the moment. Although all the studies reviewed above are congruent that biomass energy is sustainable in Nigeria, there is a lack of detailed technical information on the potential performance of power plants for the exploitation of Nigerian biomass fuels. To bridge this research gap, it is aimed in this study to assess different configurations of organic Rankine cycle (ORC) plants for optimal power generation from a typical biomass fuel in Nigeria. The choice of ORC technology is due to its global acceptance as a sustainable power conversion technology that is particularly suited for renewable energy resources [31], [32], [33], [34], [35], [36], including industrial waste heats [37], [38]. More so, several biomass-fired ORC plants have been installed in several countries already, most of which are currently running profitably [39], [40]. The specific objectives of this study are:

- To obtain optimal design configurations of ORC plant for efficient conversion of biomass to energy based on the features of a typical agricultural residue in Nigeria;
- To study the effects of the temperature at which the biomass fuel interacts with the ORC plant on system performance; and
- To analyze the sensitivity of system performance to the minimum cycle temperature.

The description of methods applied in the study, the main results obtained and their interpretation, and the summary of the entire study in the form of a conclusion, are presented in sections 2, 3, and 4 of this document, respectively.

2. METHODOLOGY

2.1. System Configurations

For the biomass section of the plant, a small-scale design is considered with a distinct zone for the combustion of biomass fuels, separated from the heater where hot flue combustion gases heat a heat transfer fluid (HTF) moving in cross flow to the gases. To achieve crossflow, a shell and tube heat exchanger configuration was employed with Therminol 66 considered as the HT flowing on the liquid side, interacting with the gases majorly by the convection heat transfer process. The combustion air is pre-heated at the entrance to the combustion chamber by the unused exhaust heat leaving the boiler with the high-temperature gases. It is possible to easily control the thermal capacity of this type of boiler, which makes it fit for this study. More details about the referenced biomass boiler can be found in the literature [41].

For the ORC section, four different configurations were compared for optimal exploitation of the biomass thermal energy produced by the furnace. The first configuration assumes a subcritical ORC type without regeneration, tagged here as SUBORC. It is subcritical because the maximum cycle pressure is below the critical pressure of the working fluid, and it is without regeneration because the working fluid leaving the turbine is condensed directly without recovering its heat within the cycle. In the second configuration, a subcritical ORC type is also assumed, but with the addition of a regenerator, tagged here as SUBORC-REGEN. In the regenerator, the heat content of the working fluid at the turbine exit is exploited within the cycle to pre-heat the liquid working fluid leaving the pump, before the external heat source is applied in the evaporator/pre-heater. The third configuration is considered a supercritical ORC type without a regenerator, tagged here as SUPERORC. In supercritical/transcritical ORC, the minimum cycle pressure is below the working fluid critical pressure but the maximum cycle pressure is greater than the working fluid critical pressure. Finally, the fourth configuration assumes a supercritical ORC type with a regenerator, tagged here as SUPERORC-REGEN. For each of the four ORC configurations, toluene, n-pentane, and n-butane were compared as working fluids. The choice of these working fluids is centered on their wide applications in real biomass ORC plants operating in different parts of the world [42], [43]. Air is considered as the heat sink for all the ORC configurations, so as not to mount additional pressure on water in the potential plant site, which is already inadequately supplied. Moreover, the biomass section interacts with the ORC plant mainly through the HTF for all configurations. At nominal conditions, the inlet temperature of the HTF leaving the boiler coincides with the ORC heat source temperature, while the temperature of the HTF exiting the ORC is the same as that entering the biomass boiler. Figure 1 illustrates the interactions of the biomass heat source with the ORC plant, based on a recuperative configuration.

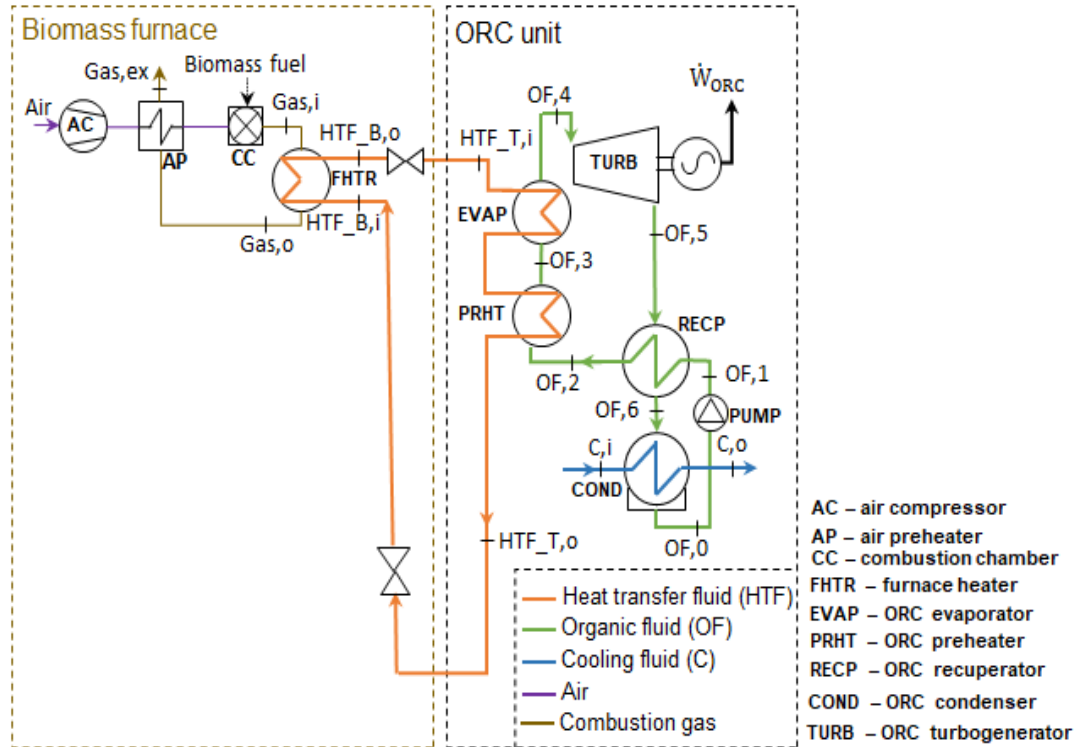


Figure 1. Interaction of the biomass heat source with the ORC unit.

2.2. Modeling of the Biomass and ORC Units

2.2.1. Biomass fuel and furnace modeling

The study employed an agricultural residue, palm kernel expeller (PKE), as the biomass fuel given its abundant availability in Nigeria and its favourable thermogravimetric characteristics for direct combustion [25]. A summary of the composition of the biomass fuel is highlighted in Table 1, in addition to the most relevant features of the combustion furnace. With an excess air value assumed to be 50%, the combustion gas temperature and mass flow rate were obtained by solving the combustion side balance equations for mass and energy, as follows:

$$\dot{m}_{Bio} + \dot{m}_{Air} = \dot{m}_{Gas} + \dot{m}_{Ash} + \dot{m}_{umb} \quad (1)$$

$$\dot{m}_{Bio}(LHV + h_{Bio}) + \dot{m}_{Air}h_{Air} = \dot{m}_{Gas}h_{Gas,i} + \dot{m}_{Ash}h_{Ash} + \dot{m}_{umb}LHV + \dot{Q}_{Loss} \quad (2)$$

The symbols \dot{m}_{Gas} , \dot{m}_{Air} , \dot{m}_{Bio} , and \dot{m}_{Ash} denote mass flow rates of combustion gases, air, biomass fuel, and ash residue from the combustion of the biomass fuel, respectively, while \dot{Q}_{Loss} and \dot{m}_{umb} represent the insulation-induced heat losses in the furnace and mass flow rate of the unburned fuel,

respectively. In this study, the sum of \dot{Q}_{Loss} and \dot{m}_{umb} was assumed equal to 1% of the useful part of the total biomass thermal energy.

It should be mentioned explicitly here that the aforementioned model-control mechanism of the biomass system means that the mass and energy balance equations of the combustion boiler are preserved not only at nominal conditions but also at off-design conditions. In this regard, the mass flow rate of biomass fuel consumed by the boiler is regulated depending on the thermal power required by the ORC per time. However, the temperature of the combustion gas is preserved by assuming the air-fuel ratio constant even under off-design conditions, to preserve the efficiency and other technical features of the modular biomass combustion boiler.

As stated earlier, the heat transfer side of the biomass boiler comprises a liquid-gas shell and tube heat exchanger configuration. The specific heat capacity of the HTF is obtained at the average temperature of the inlet and exit sides, and depending on the thermal duty required of the biomass system, the HTF mass flow rate is determined from the energy balance equation defined by the First Law of Thermodynamics. The effectiveness-NTU method is employed to simulate the behaviour of the liquid-gas heat exchanger under off-design conditions. Beginning with the thermal duty required of the biomass boiler, the change in the heat transfer by convection is computed based on the mass flow rate variation. Consequently, the real heat exchanger effectiveness and the temperature of the gas at the heat exchanger exit are determined.

2.2.2. ORC modeling

The ORC plant was designed to satisfy the zero-dimensional mass and energy balance models defined by the First Law of Thermodynamics. These models were implemented in MATLAB on a component basis for each of the ORC configurations studied. The mass and energy balance equations are defined respectively as follows:

$$\sum \dot{m}_i = \sum \dot{m}_o \quad (3)$$

$$\sum \dot{m}_i h_i + \dot{Q} = \sum \dot{m}_o h_o + \dot{W} \quad (4)$$

The symbol \dot{m} denotes the mass flow rate of a working substance (kg/s), h represents the specific enthalpy (kJ/kg), \dot{Q} is the flow of thermal energy, and \dot{W} denotes the flow of work. The subscript 'i' indicates a flow into a component/system, while 'o' indicates an outward flow. The mass balance equation applies to all the system components as shown in eq. 3. For the energy model in eq. 4, the term \dot{W} is null in all the heat exchangers, assuming zero pressure drop. In the pump, \dot{W} is at the inlet side of the equation, and \dot{Q} was taken as zero, assuming perfect thermal insulation of the component. Similarly, \dot{Q} is taken as zero in the turbine for the same reason (perfect thermal insulation), and \dot{W} is an outward flow representing the gross electrical power produced by the plant. Both \dot{W} and \dot{Q} were taken into account in the fan. The specific mathematical models applied to the plant components are exemplified in a previous study [44] for a regenerative subcritical ORC configuration. The net power output is obtained by subtracting the auxiliary power (for pump and fan) from the gross turbine power

obtainable directly from eq. 4. Additionally, thermal efficiency was computed for the different case studies, defined as follows:

$$\eta = \frac{W_{net}}{\dot{Q}_{ORC,in}} \quad (5)$$

2.3. Optimization Approach of the ORC Systems

The optimization models which were also programmed in MATLAB, defined as the objective function, the maximization of the net power output of the ORC plant. For each of the ORC configurations considered, the optimization tools require the following input parameters:

- The temperature of the HTF (heat source) leaving the ORC and entering the biomass boiler;
- The minimum cycle (condensation) temperature; and
- HTF mass flow rate at the ORC inlet.

Additionally, other cycle parameters were fixed in the optimization tools as independent variables, as follows:

- Pinch point temperatures of the heat exchangers (evaporator, pre-heater, condenser, and recuperator in the case of the SUBORC-REGEN and SUPERORC-REGEN);
- Isentropic and electromechanical efficiencies of the pump;
- Isentropic and electric generator efficiencies of the turbine; and
- Mechanical efficiency of the fan.

The values assigned to these fixed variables are highlighted in Table 1. The decision variables optimized by the tool to maximize net output power are as follows:

- Maximum pressure and temperature of the ORC;
- ORC working fluid mass flow rate;
- Degree of superheat; and
- Minimum cycle pressure.

Table 1. Characteristics of the biomass ORC plant.

Biomass combustion unit		ORC unit	
Furnace thermal duty	Decision variable	Working fluid	Toluene, n-Pentane, and n-Butane
Fuel composition (dry basis, % by weight)	53.6 % C, 5.1 % H, 0.5 % N ₂ , 40.8 % O ₂ ,	Heat sink	Air
Volatiles (dry basis, % by weight)	76.1	Net electrical power	Optimized
Ash (dry basis, % by weight)	2.6	Nominal input thermal power	Decision variable
Higher heating value (dry basis)	21 MJ/kg	Nominal HTF flow rate	Decision variable
Moisture content (after drying)	8.9 %	Isentropic efficiency - pump	0.80
Stoichiometric air-fuel ratio	5	Motor efficiency - pump	0.98
Excess air	150 %	Isentropic efficiency - turbine	0.85
		Electromechanical efficiency	0.92
		Mechanical efficiency – cooling fan	0.60
		Pinch point temperature difference	5 °C

2.4. Sensitivity Analyses

Sensitivities of the objective function (net output power) to inlet temperature of the biomass heat source and cycle minimum (condensation) temperature were also investigated in the study. Additionally, ORC thermal efficiency that corresponds to each output power was computed during the sensitivity analysis for all the ORC configurations. Suffice it to mention that the optimization models were used for the sensitivity analysis, such that the results obtained remain the optimal choices for each of the working fluids and ORC configurations.

3. RESULTS AND DISCUSSION

3.1. Optimal Parameters of The Biomass ORC Plant Based on The Different Configurations

The main results of the optimization studies are presented in this section for the different configurations and organic working fluids considered.

3.1.1. Subcritical ORC without regeneration (SUBORC)

Table 2 highlights the optimal design of subcritical ORC plants without regeneration for the three working fluids investigated in this study. As can be seen, n-pentane would yield about 1 MW of electrical power from the biomass SUBORC plant, the highest among the working fluids compared in this study. Specifically, results showed that toluene would yield about 0.16 MW less and n-butane

about 0.18 MW less, relative to n-pentane. The optimal thermal efficiency of the SUBORC plant followed a similar trend for the three working fluids; n-pentane showed the best performance at about 14%, followed by toluene at about 11.9%, and n-butane at about 11.6%. More so, the optimal parameters recorded for the auxiliary cycle power, ORC working fluid, minimum and maximum cycle temperature, and minimum and maximum cycle pressure follow different patterns for the different working fluids. For instance, for the n-pentane which recorded the highest net power and thermal efficiency, the evaporation temperature is only in the middle of the other two working fluids; greater than that of n-butane but less than that of toluene. The main significance of this is that the net power and thermal efficiency recorded by n-pentane take into account all the important cycle parameters highlighted in the table, rather than optimizing based on just a single or a few sets of parameters.

Table 2. Optimal parameters of the SUBORC plant utilizing biomass energy.

Parameter	Toluene	n-Pentane	n-Butane
Net Work (W)	8.3706e+05	1.0072e+06	8.1649e+05
Pump Work (W)	23398	44063	50081
Fan Work (W)	2.7001e+05	2.6339e+05	2.7238e+05
Max Pressure (Pa)	1.5625e+06	3.033e+06	3.4164e+06
Max Temperature (°C)	246.39	196.08	167.94
Min Pressure (Pa)	1e+05	1.1567e+05	3.7849e+05
Min Temperature (°C)	110.13	40	40
Superheat Degrees (°C)	1	6.3931	22.384
ORC WF mass flow rate (kg/s)	12.791	12.076	13.18
Thermal Efficiency (%)	11.91	14.33	11.62

3.1.2. Subcritical ORC with regeneration (SUBORC-REGEN)

Table 3 reports the optimal design of subcritical ORC plants with regeneration for the three working fluids. Here too, n-pentane would yield the highest net electrical power of about 1.9 MW. However, the use of a regenerator would shore up significantly the performance of n-butane, making it outperform toluene. Specifically, results showed that while toluene would yield just about 1 MW of net electrical power, n-butane would yield 50% more at about 1.5 MW. Moreover, juxtaposing the results of the SUBORC and the SUBORC-REGEN shows that the use of regeneration would increase net power production for all the working fluids employed, but at varying degrees. In this regard, results showed that toluene would yield about 21% more power with the use of a regenerator relative to the SUBORC configuration; n-pentane would yield about 86% more power, and n-butane about 89% more power. Additionally, the trend of thermal efficiency for the three working fluids is similar to that of the net power; n-pentane recorded the highest efficiency at about 27%, followed by n-butane at about 22% and toluene at about 14%. As would be expected, regeneration also increased significantly the thermal efficiency for all the working fluids analyzed in the study, also at varying degrees. Specifically, regeneration would improve the ORC thermal efficiency by only about 2.5 percentage points using toluene as the working fluid, followed by n-butane with an increase of about 10.4 percentage points, and n-pentane with an increase of about 12.3 percentage points.

Table 3. Optimal parameters of the SUBORC-REGEN plant utilizing biomass energy.

Parameter	Toluene	n-Pentane	n-Butane
Net Work (W)	1.0088e+06	1.8699e+06	1.5453e+06
Pump Work (W)	21291	49617	56236
Fan Work (W)	2.0067e+05	1.7217e+05	1.8366e+05
Max Pressure (Pa)	1.1833e+06	3.033e+06	3.4164e+06
Max Temperature (°C)	228.21	294	258.72
Min Pressure (Pa)	1e+05	1.1567e+05	3.7849e+05
Min Temperature (°C)	110.13	40	40
Superheat Degrees (°C)	1	104.31	113.17
ORC WF mass flow rate (kg/s)	15.714	13.598	14.8
Thermal Efficiency (%)	14.36	26.61	21.99

3.1.3. Supercritical ORC without regeneration (SUPERORC)

Results of the optimal design of the supercritical ORC plant without regeneration for biomass energy exploitation are highlighted in Table 4. In this case, toluene showed a high level of incompatibility with the characteristics of the biomass heat source under investigation, basically due to the need to increase the cycle maximum pressure beyond the critical pressure of the working fluid. Thus, only n-pentane and n-butane were assessed for the SUPERORC configuration as defined in this study. As can be seen, n-pentane would also outperform n-butane in this case study, yielding about 1.22 MW of electrical power from the biomass system as against about 1.14 MW achievable with the use of n-butane. Again, optimal thermal efficiencies of the SUBORC plant followed a trend similar to the net power output from the respective working fluids; n-pentane showed the best performance at about 17%, followed by n-butane at about 16%. Furthermore, results showed that increasing the cycle maximum pressure above the working fluid critical pressure would increase net output power and thermal efficiency for all working fluids. Results revealed specifically that for non-regenerated ORC configurations, SUPERORC increased net output power by about 210 kW for n-pentane and about 324 kW for n-butane, relative to the SUBORC case study.

Table 4. Optimal parameters of the SUPERORC plant utilizing biomass energy.

Parameter	n-Pentane	n-Butane
Net Work (W)	1.2172e+06	1.1409e+06
Pump Work (W)	1.2715e+05	1.288e+05
Fan Work (W)	2.563e+05	2.6056e+05
Max Pressure (Pa)	1.1e+07	1.1e+07
Max Temperature (°C)	295	273.73
Min Pressure (Pa)	1.1567e+05	3.7849e+05
Min Temperature (°C)	40	40
Superheat Degrees (°C)	98.45	121.75
ORC WF mass flow rate (kg/s)	9.3396	9.6956
Thermal Efficiency (%)	17.32	16.23

3.1.4. Supercritical ORC with regeneration (SUPERORC-REGEN)

Table 5 highlights the results of the optimal design of the supercritical ORC plant with regeneration with n-pentane and n-butane as working fluids. It was obtained that n-pentane for the SUPERORC-REGEN case study would yield the highest power among all the configurations compared in this study, at about 1.98 MW. However, its increase over output power with n-butane for the same case study is only marginal, estimated at slightly above 8 kW. Additionally, juxtaposing the results in Tables 4 and 5 corroborate the earlier analysis that the addition of a regenerator would increase net output power. Here, integration of a regenerator to the supercritical ORC plant would yield about 63% more net output power for n-pentane and about 73% more for n-butane. Similarly, comparing the regenerated ORC for the subcritical and supercritical configurations (SUBORC-REGEN vs. SUPERORC-REGEN) corroborate the earlier analysis that the application of maximum pressure higher than the working fluid critical pressure would increase performance. Here, about 113 kW more power is generated by n-pentane and about 429 kW by n-butane, when the supercritical configuration is adopted in place of the subcritical one for the regenerative ORC plant. Furthermore, the trend of thermal efficiency for the working fluids is equally similar to that of the net power under this case study; n-pentane recorded a thermal efficiency of about 28.22%, slightly higher than what obtains in n-butane, 28.10%. As would be expected, regeneration also increased significantly the thermal efficiency for the working fluids analyzed in the supercritical ORC configurations. Specifically, regeneration would improve the supercritical ORC thermal efficiency by about 11 percentage points using n-pentane as the working fluid, and by approximately 12 percentage points with n-butane as the working substance. Moreover, switching from subcritical to supercritical configuration for the regenerative ORC would also improve the thermal efficiency by 1.61 percentage points for n-pentane and 6.11 percentage points for n-butane working fluids.

Table 5. Optimal parameters of the SUPERORC-REGEN plant utilizing biomass energy.

Parameter	n-Pentane	n-Butane
Net Work (W)	1.983e+06	1.9746e+06
Pump Work (W)	1.0022e+05	1.7979e+05
Fan Work (W)	1.6939e+05	1.722e+05
Max Pressure (Pa)	6.1532e+06	1.1e+07
Max Temperature (°C)	295	295
Min Pressure (Pa)	1.1567e+05	3.7849e+05
Min Temperature (°C)	40	40
Superheat Degrees (°C)	98.45	143.02
ORC WF mass flow rate (kg/s)	13.272	13.533
Thermal Efficiency (%)	28.22	28.10

3.2. Sensitivity of the Optimal ORC Parameters to Biomass Inlet Temperature

3.2.1. Net power output and thermal efficiency variations for the SUBORC configuration

The effects of change in biomass temperature at the ORC inlet on the system performance are reported in this section for the SUBORC configuration. As can be seen in Fig. 2, net output power increases linearly with an increase in heat source inlet temperature for all the working fluids. The highest net power output is recorded by n-pentane over all the range of biomass inlet temperatures analyzed in this study. For n-butane and toluene, performance depends strongly on the exact biomass temperature at the ORC inlet. Specifically, results showed that n-butane outperforms toluene only at lower heat source temperatures. About equal net output power is produced by the two working fluids up to around 294 °C, beyond which toluene would yield higher net output power than n-butane. Additionally, thermal efficiencies of ORC using both n-pentane and n-butane are obtained to be insensitive to a change in biomass inlet temperature, while the efficiency increases also linearly with biomass inlet temperature for toluene.

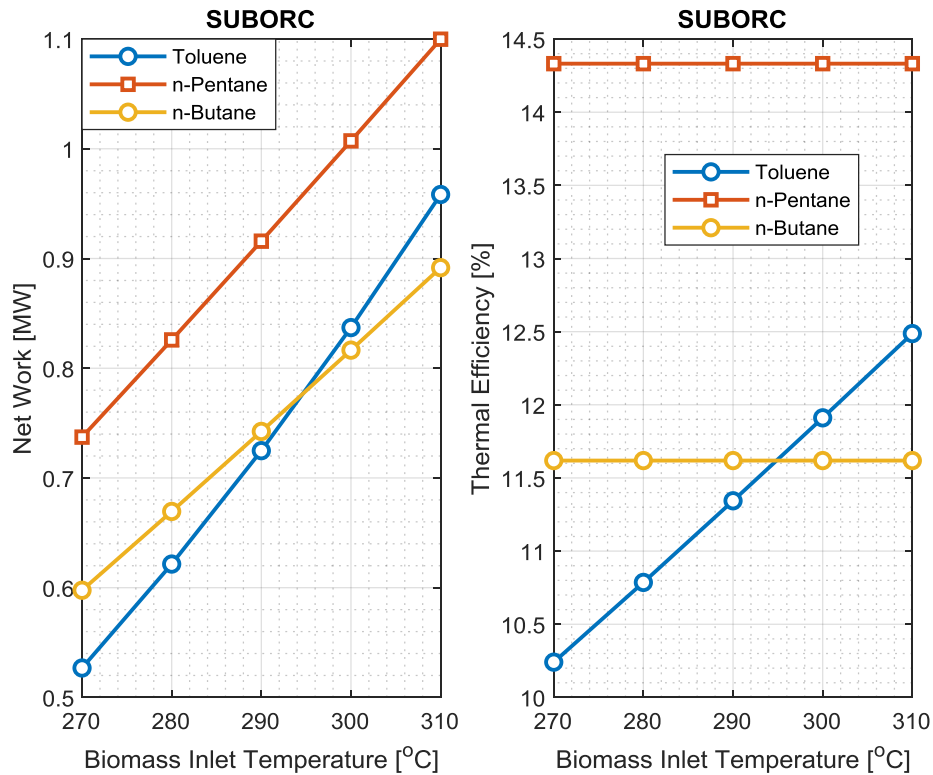


Figure 2. Variations of the net output power and thermal efficiency with heat source temperature for the SUBORC.

3.2.2. Net power output and thermal efficiency variations for the SUBORC-REGEN configuration

Sensitivity analysis results for the SUBORC-REGEN configuration (Fig. 3) also show that the high net output power recorded by n-pentane is across a wide range of biomass temperatures at the ORC inlet. Here too, the net output power increases linearly with an increase in the heat source temperature for all the working fluids considered. However, it is worth noting that there is no overlap of net output power in the case study as observed in the SUBORC; n-butane yielded more net power than toluene irrespective of the temperature of the heat source. Moreover, results showed that the plant thermal efficiency would increase initially with an increase in biomass inlet temperature up to around 300 °C for n-pentane, beyond which it remains fairly constant. Again, n-butane showed insensitivity to thermal efficiency with varying heat source temperatures, and toluene showed a linear increase in thermal efficiency as the biomass temperature increased.

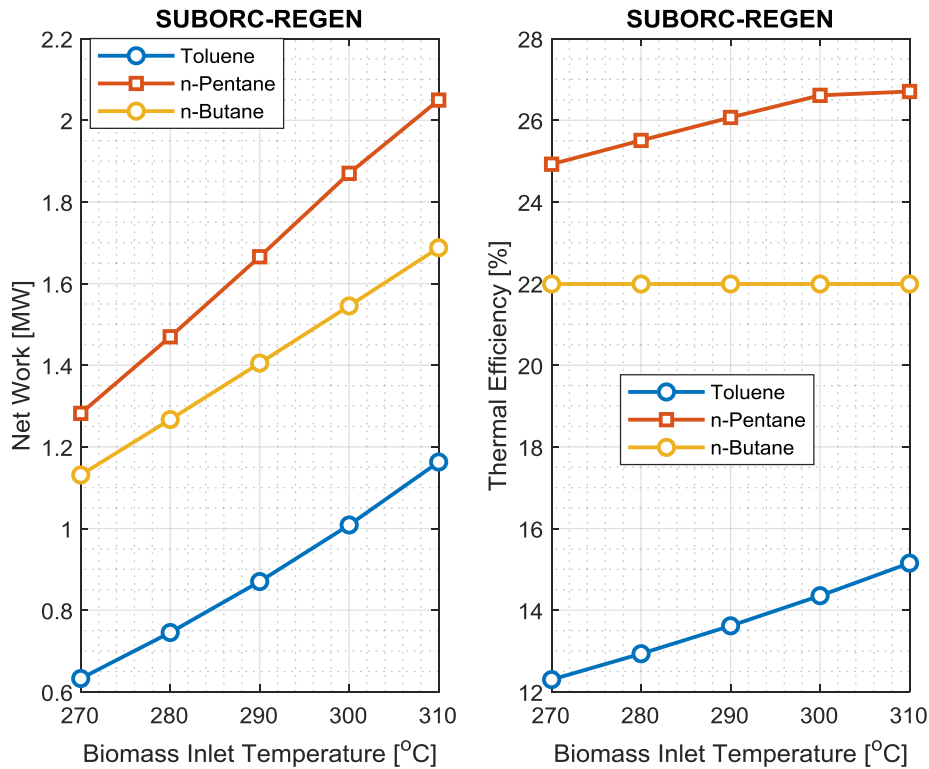


Figure 3. Variations of the net output power and thermal efficiency with heat source temperature for the SUBORC-REGEN.

3.2.3. Net power output and thermal efficiency variations for the SUPERORC configuration

The results of the sensitivity of net power output and thermal efficiency to variation in biomass inlet temperature are shown in Fig. 4 for the SUPERORC configuration. As can be seen, net output power increases with an increase in heat source temperature for the two working fluids. Also, n-pentane showed higher net power output than n-butane across the range of biomass temperature considered, although at a lower degree compared to the SUBORC configuration. Additionally, the thermal efficiency of the SUPERORC configuration increases non-uniformly with an increase in biomass temperature at the ORC inlet for n-pentane. For n-butane, there is only a slight increase in efficiency between 270 °C and 280 °C biomass temperature; thermal efficiency remains constant with a further increase in heat source temperature.

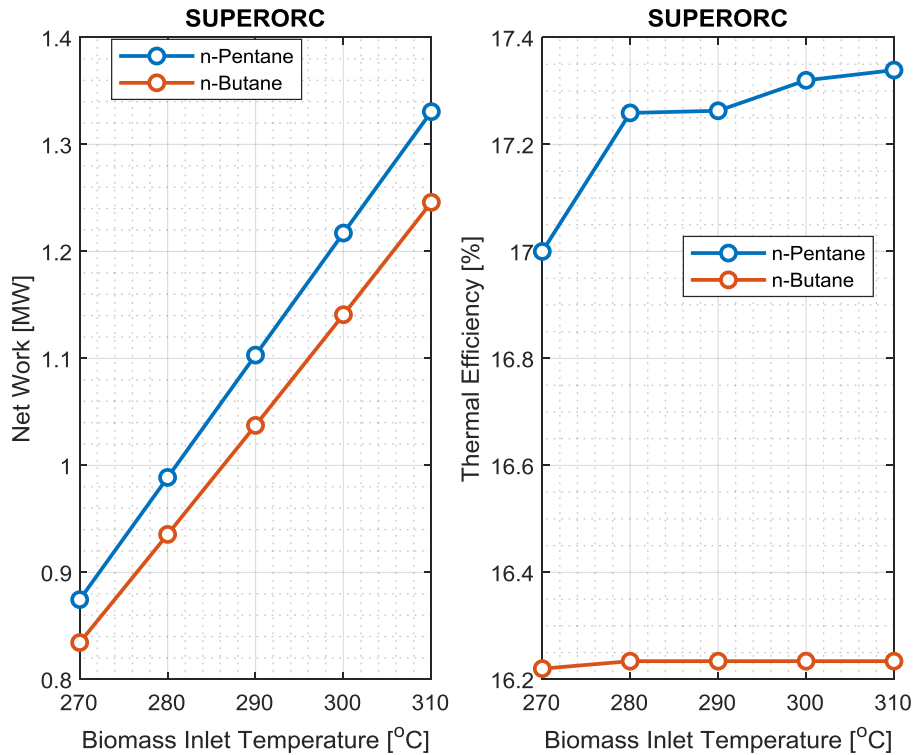


Figure 4. Variations of the net output power and thermal efficiency with heat source temperature for the SUPERORC.

3.2.4. Net power output and thermal efficiency variations for the SUPERORC-REGEN configuration

As can be seen in Fig. 5, net power output equally increases with an increase in biomass temperature for both n-pentane and n-butane. However, the margin of the net output power between n-pentane and n-butane is quite small throughout the range of temperatures investigated, implying that the two working fluids would perform at about the same level for the SUPERORC-REGEN configuration. In like manner, the thermal efficiency increases linearly with an increase in heat source temperature for the two working fluids.

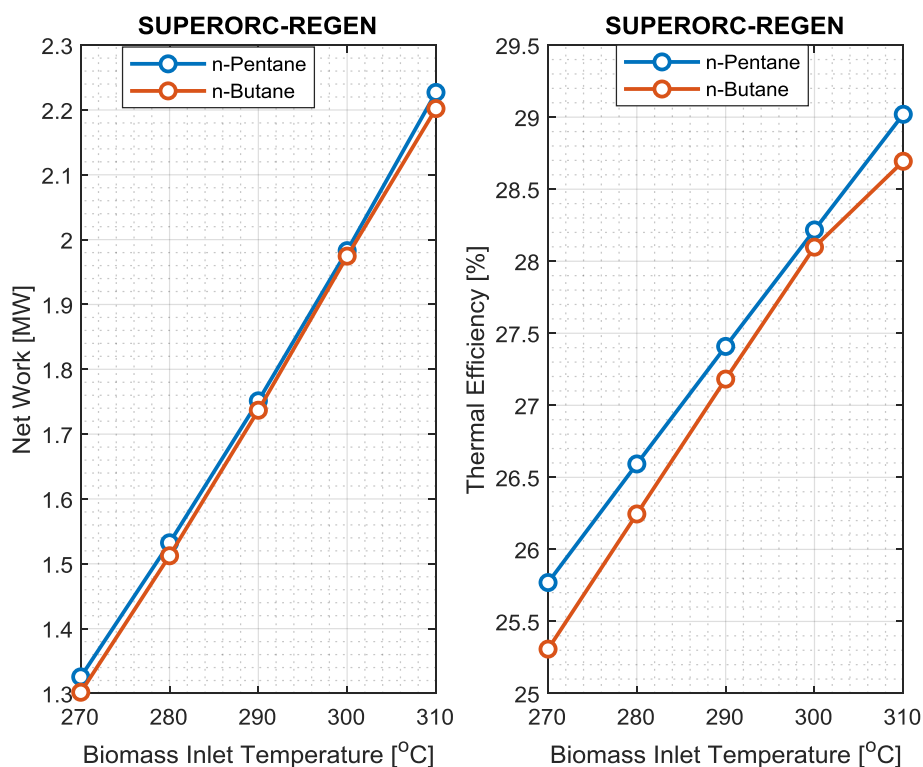


Figure 5. Variations of the net output power and thermal efficiency with heat source temperature for the SUPERORC-REGEN.

3.3. Sensitivity of the Optimal ORC Parameters to Minimum Cycle (Condenser) Temperature

3.3.1. Net power output and thermal efficiency variations for the SUBORC configuration

Effects of the cycle minimum temperature (condenser temperature) on net output power and thermal efficiency are reported here for the SUBORC. As can be seen in Fig. 6, increasing the condenser temperature led to a linear decrease in net output power for n-pentane and n-butane, while toluene showed no sensitivity to a change in condenser temperature. More so, the same trend was obtained for the thermal efficiency; an increase in condenser temperature decreases thermal efficiency linearly for n-pentane and n-butane, while toluene remains constant over the range of the condenser temperature considered.

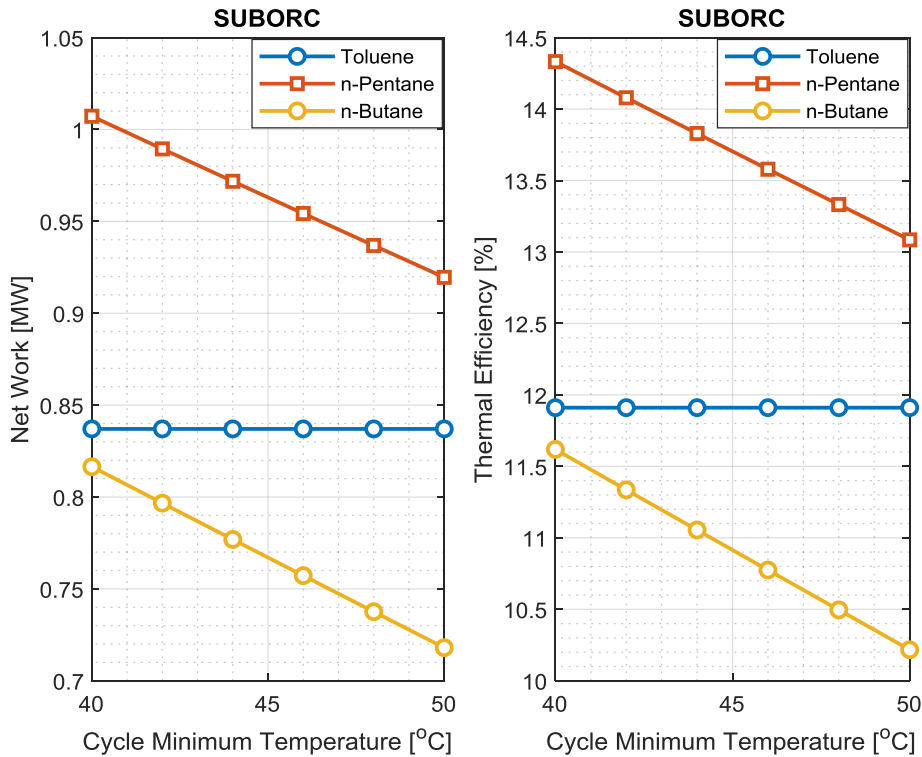


Figure 6. Variations of the net output power and thermal efficiency with condenser temperature for the SUBORC.

3.3.2. Net power output and thermal efficiency variations for the SUBORC-REGEN configuration

Furthermore, Fig. 7 shows that net power output and thermal efficiency decrease linearly with an increase in the cycle minimum temperature for n-pentane and n-butane, while toluene shows no sensitivity with a variation in condenser temperature.

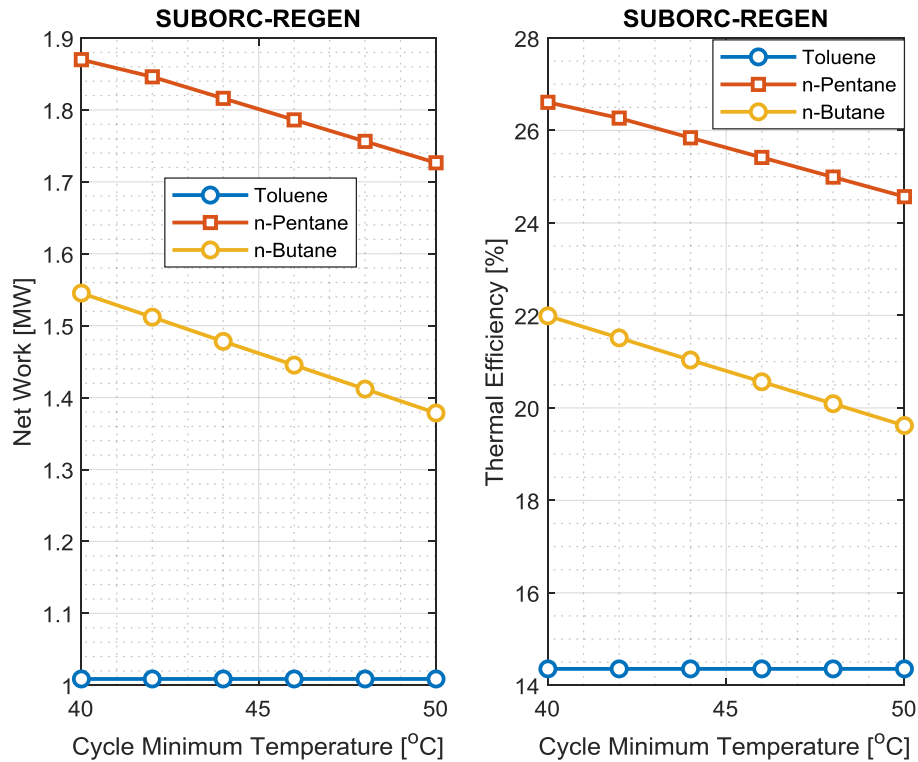


Figure 7. Variations of the net output power and thermal efficiency with condenser temperature for the SUBORC-REGEN.

3.3.3. Net power output and thermal efficiency variations for the SUPERORC configuration

For the supercritical ORC without regeneration, Fig. 8 shows that both n-pentane and n-butane resulted in a decrease in both the net power output and thermal efficiency with an increase in condenser temperature. However, n-pentane still showed a better performance across the range of condenser temperatures considered in the study.

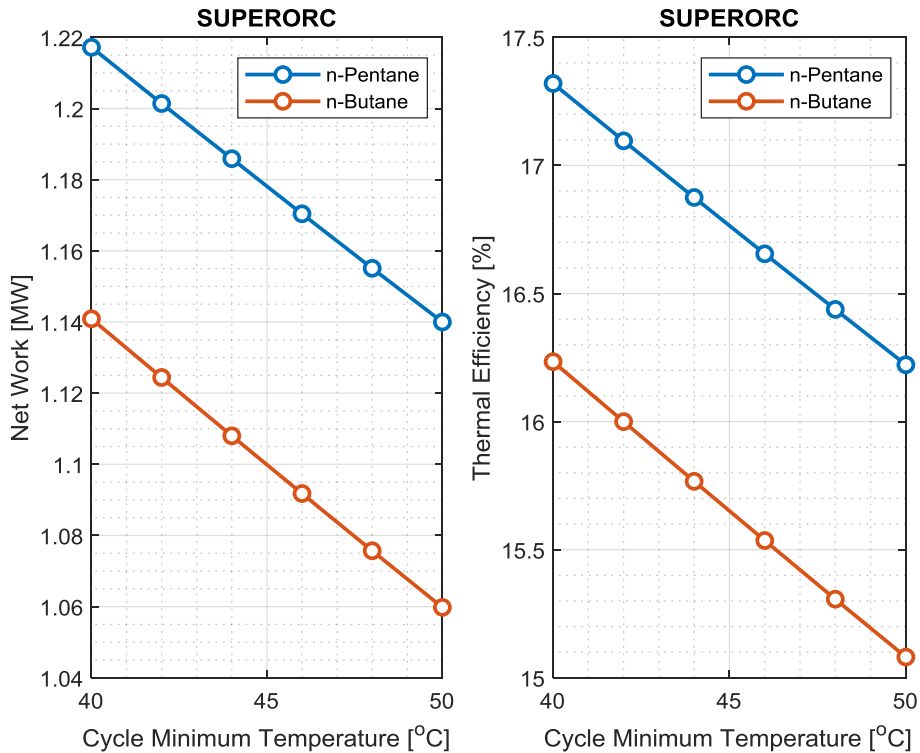


Figure 8. Variations of the net output power and thermal efficiency with condenser temperature for the SUPERORC.

3.3.4. Net power output and thermal efficiency variations for the SUPERORC-REGEN configuration

The sensitivity analysis results which are shown in Fig. 9 also revealed that the lower the cycle minimum temperature, the higher the net output power and thermal efficiency for both n-pentane and n-butane. It can however be seen here also that the magnitude of the difference between the two working fluids is quite marginal over the range of condenser temperatures considered, with both the net power and efficiency of n-butane almost matching those of n-pentane when the condenser temperature of around 50 °C is considered.

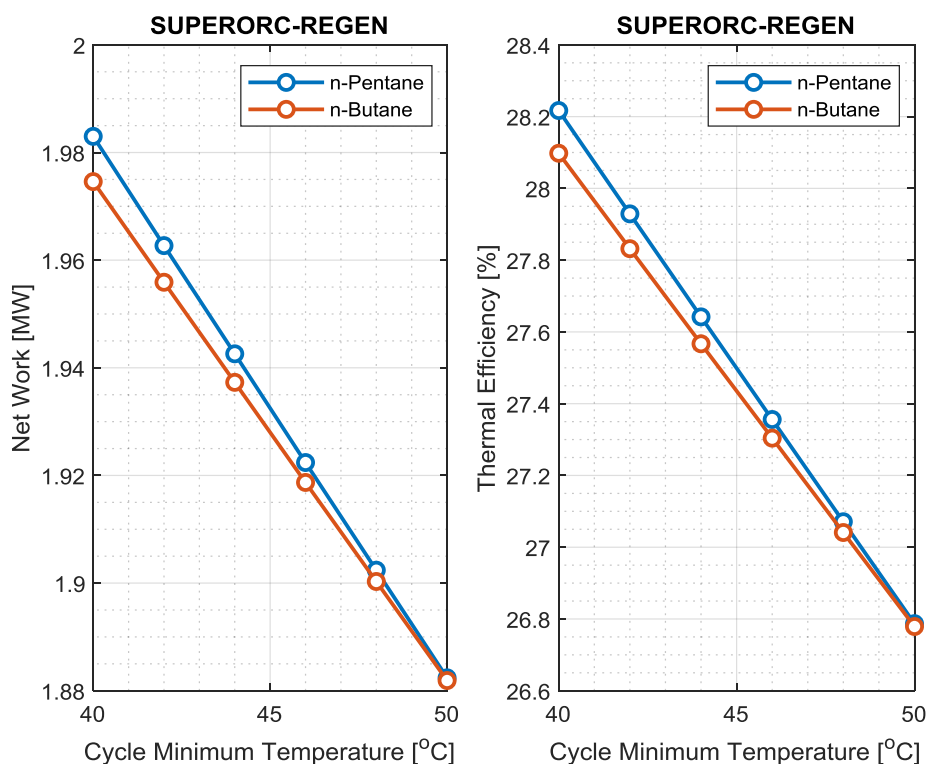


Figure 9. Variations of the net output power and thermal efficiency with condenser temperature for the SUPERORC-REGEN.

4. CONCLUSIONS

An attempt has been made in this study to investigate several ORC configurations to select one that would optimize electricity production from the combustion of a typical solid biomass fuel available abundantly in Nigeria. Although several authors have reported in the literature that there is vast potential for energy generation from biomass in Nigeria, no known large-scale biomass power plant exists in the country due to the limitation of technical know-how relating to conversion technologies. To bridge this gap, characteristics of a PKE, an agricultural waste available all over Nigeria, were employed in this study for the optimal design of ORC plants. A model-control biomass boiler was used to analyze the direct combustion of the solid biomass fuel to provide the thermal energy required for the ORC plant operation. For the ORC specifically, optimal designs of four different configurations were compared: the SUBORC, the SUBORC-REGEN, the SUPERORC, and the SUPERORC-REGEN. Furthermore, the effects of the temperature of the biomass heat source at the

ORC inlet and the minimum cycle temperature on the optimal performance of the various configurations were assessed. The main results obtained from the study are:

- The supercritical ORC type is capable of generating higher electrical power than the subcritical type. Taking for instance the regenerative ORC configuration, results showed that supercritical ORC would generate 113 kW and 429 kW more net power than the subcritical ORC, respectively for n-pentane and n-butane working fluids. Similarly, it was reiterated in the study that the adoption of regeneration improves ORC performance. Exemplarily, the SUPERORC-REGEN yielded 63% and 73% more power than the SUPERORC respectively for n-pentane and n-butane working fluids. Overall, it was obtained that the SUPERORC-REGEN would be the preferred choice amongst the options compared in this study for optimal exploitation of typical solid biomass in Nigeria;
- The working fluid n-pentane yielded the highest net power output and thermal efficiency for all the configurations examined. Specifically for the preferred SUPERORC-REGEN configuration, it yielded net power of about 1.98 MW and thermal efficiency of 28.22%;
- Increasing the biomass temperature at the ORC inlet led to an increase in net power output for all the configurations and working fluids considered in the study. Again, n-pentane outperformed n-butane and toluene across the range of heat source temperature considered, but only marginally concerning n-butane for the preferred SUPERORC-REGEN configuration;
- Increasing the minimum cycle temperature resulted in a linear decrease in net power output and thermal efficiency for n-pentane and n-butane working fluids in all the configurations considered, as would be expected.

In sum, deploying a supercritical ORC plant with regeneration portends an optimal choice for sustainable exploitation of solid biomass fuels which are abundant in Nigeria, for energy production. Future studies should focus on the economic assessment of the various ORC configurations to spur investment to achieve practical implementation of such plants in the country. Additionally, an exergy-based analysis should be conducted to investigate further optimization potentials of the ORC plant on a component basis.

ACKNOWLEDGEMENT

The authors gratefully acknowledge the reviewers for their scientific contributions to this article.

REFERENCES

- [1] Karabacak, K. (2022). Economic feasibility analysis of a grid-connected PV energy system: A case study of Kutahya Dumlupinar University, Türkiye. *Journal of Scientific Reports–A*, Number 50, 200-216.

- [2] Rajmohan, K. S., Ramya, C., and Varjani, S. (2019). Trends and advances in bioenergy production and sustainable solid waste management. *Energy and Environment*, 32(6), 1059–1085. <https://doi.org/10.1177/0958305X19882415>
- [3] Goyal, N., Aggarwal, A., and Kumar, A. (2022). Concentrated solar power plants: A critical review of regional dynamics and operational parameters. *Energy Research and Social Science*, 83(October 2021), 102331. <https://doi.org/10.1016/j.erss.2021.102331>
- [4] López-Manrique, L. M., Macias-Melo, E. V, Aguilar-Castro, K. M., Hernández-Pérez, I., and Díaz-Hernández, H. P. (2019). Review on methodological and normative advances in assessment and estimation of wind energy. *Energy and Environment*, 32(1), 25–61. <https://doi.org/10.1177/0958305X19893070>
- [5] Nourpour, M., Khoshgoftar Manesh, M. H., Pirozfar, A., and Delpisheh, M. (2021). Exergy, Exergoeconomic, Exergoenvironmental, Energy-based Assessment and Advanced Exergy-based Analysis of an Integrated Solar Combined Cycle Power Plant. *Energy and Environment*, 0958305X211063558. <https://doi.org/10.1177/0958305X211063558>
- [6] Guo, S., Liu, Q., Sun, J., and Jin, H. (2018). A review on the utilization of hybrid renewable energy. *Renewable and Sustainable Energy Reviews*, 91, 1121–1147. <https://doi.org/10.1016/J.RSER.2018.04.105>
- [7] Oyekale, J., Petrollese, M., Vittorio, T., and Cau, G. (2018). Conceptual design and preliminary analysis of a CSP-biomass organic Rankine cycle plant. In 31st International Conference on Efficiency, Cost, Optimization, Simulation and Environmental Impact of Energy Systems, ECOS 2018, Guimaraes; Portugal.
- [8] Ahmadi, M. H., Banihashem, S. A., Ghazvini, M., and Sadeghzadeh, M. (2018). Thermo-economic and exergy assessment and optimization of performance of a hydrogen production system by using geothermal energy. *Energy and Environment*, 29(8), 1373–1392. <https://doi.org/10.1177/0958305X18779573>
- [9] Mousa, E., Wang, C., Riesbeck, J., and Larsson, M. (2016). Biomass applications in iron and steel industry: An overview of challenges and opportunities. *Renewable and Sustainable Energy Reviews*, 65, 1247–1266. <https://doi.org/10.1016/J.RSER.2016.07.061>
- [10] Banja, M., Sikkema, R., Jégard, M., Motola, V., and Dallemand, J. F. (2019). Biomass for energy in the EU – The support framework. *Energy Policy*, 131(July 2018), 215–228. <https://doi.org/10.1016/j.enpol.2019.04.038>
- [11] Basu, P., and Basu, P. (2018). Introduction. *Biomass Gasification, Pyrolysis and Torrefaction*, 1–27. <https://doi.org/10.1016/B978-0-12-812992-0.00001-7>

- [12] Ashter, S. A., and Ashter, S. A. (2018). Biomass and its sources. *Technology and Applications of Polymers Derived from Biomass*, 11–36. <https://doi.org/10.1016/B978-0-323-51115-5.00002-5>
- [13] García, R., Pizarro, C., Lavín, A. G., and Bueno, J. L. (2017). Biomass sources for thermal conversion. *Techno-economical overview. Fuel*, 195, 182–189. <https://doi.org/10.1016/J.FUEL.2017.01.063>
- [14] Bajwa, D. S., Peterson, T., Sharma, N., Shojaeiarani, J., and Bajwa, S. G. (2018). A review of densified solid biomass for energy production. *Renewable and Sustainable Energy Reviews*, 96, 296–305. <https://doi.org/10.1016/J.RSER.2018.07.040>
- [15] Freitas, F. F., De Souza, S. S., Ferreira, L. R. A., Otto, R. B., Alessio, F. J., De Souza, S. N. M., ... Ando Junior, O. H. (2019). The Brazilian market of distributed biogas generation: Overview, technological development and case study. *Renewable and Sustainable Energy Reviews*, 101(October 2018), 146–157. <https://doi.org/10.1016/j.rser.2018.11.007>
- [16] Umar, M. S., Urmee, T., and Jennings, P. (2018). A policy framework and industry roadmap model for sustainable oil palm biomass electricity generation in Malaysia. *Renewable Energy*, 128(2018), 275–284. <https://doi.org/10.1016/j.renene.2017.12.060>
- [17] Scheftelowitz, M., Becker, R., and Thrän, D. (2018). Improved power provision from biomass: A retrospective on the impacts of German energy policy. *Biomass and Bioenergy*, 111(June 2017), 1–12. <https://doi.org/10.1016/j.biombioe.2018.01.010>
- [18] Malico, I., Nepomuceno Pereira, R., Gonçalves, A. C., and Sousa, A. M. O. (2019). Current status and future perspectives for energy production from solid biomass in the European industry. *Renewable and Sustainable Energy Reviews*, 112, 960–977. <https://doi.org/10.1016/J.RSER.2019.06.022>
- [19] Olanrewaju, F. O., Andrews, G. E., Li, H., and Phylaktou, H. N. (2019). Bioenergy potential in Nigeria. *Chemical Engineering Transactions*, 74(May), 61–66. <https://doi.org/10.3303/CET1974011>
- [20] Ben-Iwo, J., Manovic, V., and Longhurst, P. (2016). Biomass resources and biofuels potential for the production of transportation fuels in Nigeria. *Renewable and Sustainable Energy Reviews*, 63, 172–192. <https://doi.org/10.1016/j.rser.2016.05.050>
- [21] Ezealigo, U. S., Ezealigo, B. N., Kemausuor, F., Achenie, L. E. K., and Onwualu, A. P. (2021). Biomass valorization to bioenergy: Assessment of biomass residues' availability and bioenergy potential in Nigeria. *Sustainability (Switzerland)*, 13(24). <https://doi.org/10.3390/su132413806>
- [22] Jekayinfa, S. O., Orisaleye, J. I., and Pecenka, R. (2020). An assessment of potential resources for biomass energy in Nigeria. *Resources*, 9(8), 1–41. <https://doi.org/10.3390/resources9080092>

- [23] Elehinafe, F. B., Okedere, O. B., Sonibare, J. A., and Mamudu, A. O. (2021). Identification of the woody biomasses in Southwest, Nigeria as potential energy feedstocks in thermal power plants for air pollution control. *Cogent Engineering*, 8(1). <https://doi.org/10.1080/23311916.2020.1868146>
- [24] Odejobi, O. J., Ajala, O. O., and Osuolale, F. N. (2022). Review on potential of using agricultural, municipal solid and industrial wastes as substrates for biogas production in Nigeria. *Biomass Conversion and Biorefinery*, (0123456789). <https://doi.org/10.1007/s13399-022-02613-y>
- [25] Akinrinola, F. S., Darvell, L. I., Jones, J. M., Williams, A., and Fuwape, J. A. (2014). Characterization of selected nigerian biomass for combustion and pyrolysis applications. *Energy and Fuels*, 28(6), 3821–3832. <https://doi.org/10.1021/ef500278e>
- [26] Akinrinola, F. S., Ikechukwu, N., Darvell, L. I., Jones, J. M., and Williams, A. (2020). The potential use of torrefied Nigerian biomass for combustion applications. *Journal of the Energy Institute*, 93(4), 1726–1736. <https://doi.org/10.1016/j.joei.2020.03.003>
- [27] Awoyale, A. A., Lokhat, D., and Eloka-Eboka, A. C. (2021). Experimental characterization of selected Nigerian lignocellulosic biomasses in bioethanol production. *International Journal of Ambient Energy*, 42(12), 1343–1351. <https://doi.org/10.1080/01430750.2019.1594375>
- [28] Olujobi, O. J., Ufua, D. E., Olokundun, M., and Olujobi, O. M. (2022). Conversion of organic wastes to electricity in Nigeria: legal perspective on the challenges and prospects. *International Journal of Environmental Science and Technology*, 19(2), 939–950. <https://doi.org/10.1007/s13762-020-03059-3>
- [29] Anyaoha, K. E., and Zhang, L. (2021). Renewable energy for environmental protection: Life cycle inventory of Nigeria’s palm oil production. *Resources, Conservation and Recycling*, 174(March), 105797. <https://doi.org/10.1016/j.resconrec.2021.105797>
- [30] Anyaoha, K. E., and Zhang, L. (2022). Technology-based comparative life cycle assessment for palm oil industry: the case of Nigeria. *Environment, Development and Sustainability*, (0123456789). <https://doi.org/10.1007/s10668-022-02215-8>
- [31] Ennio, M., and Astolfi, M. (2016). *Organic Rankine Cycle (ORC) Power Systems: Technologies and Applications*.
- [32] Guodong, C., Wenxiong, W., Bin, D., Yunfeng, L., Hong, T., Jun, Z., and Yongge, L. (2022). Geothermal Energy Exploitation and Power Generation via a Single Vertical Well Combined with Hydraulic Fracturing. *Journal of Energy Engineering*, 148(1), 4021058. [https://doi.org/10.1061/\(ASCE\)EY.1943-7897.0000809](https://doi.org/10.1061/(ASCE)EY.1943-7897.0000809)

- [33] Raghuwanshi, S. S., and Arya, R. (2019). Renewable energy potential in India and future agenda of research. *International Journal of Sustainable Engineering*, 12(5), 291–302. <https://doi.org/10.1080/19397038.2019.1602174>
- [34] Alsagri, A. S., Chiasson, A., and Shahzad, M. W. (2022). Geothermal Energy Technologies for Cooling and Refrigeration Systems: An Overview. *Arabian Journal for Science and Engineering*, 47(7), 7859–7889. <https://doi.org/10.1007/s13369-021-06296-x>
- [35] Ust, Y., Ozsari, I., Arslan, F., and Safa, A. (2020). Thermodynamic Analysis and Multi-Objective Optimization of Solar Heat Engines. *Arabian Journal for Science and Engineering*, 45(11), 9669–9684. <https://doi.org/10.1007/s13369-020-04880-1>
- [36] Fangyong, H., Yumin, G., Weifeng, W., Zhequan, Y., and Jiangfeng, W. (2020). Thermodynamic Analysis and Optimization of a Solar-Powered Organic Rankine Cycle with Compound Parabolic Collectors. *Journal of Energy Engineering*, 146(6), 4020067. [https://doi.org/10.1061/\(ASCE\)EY.1943-7897.0000709](https://doi.org/10.1061/(ASCE)EY.1943-7897.0000709)
- [37] Ye, W., Liu, C., Liu, J., Wang, H., Yang, S., and Pan, X. (2022). Research on TEG–ORC Combined Bottom Cycle for Cascade Recovery from Various Vessel Waste heat Sources. *Arabian Journal for Science and Engineering*, 47(3), 3151–3161. <https://doi.org/10.1007/s13369-021-06050-3>
- [38] Ceylan, I., Arslan, O. (2022). PERFORMANCE EVALUATION of STAGED ORC POWER PLANT SOURCED by WASTE HEAT. *Journal of Scientific Reports-A*, (050), 1–19.
- [39] Tartièrre, T., and Astolfi, M. (2017). A World Overview of the Organic Rankine Cycle Market. *Energy Procedia*, 129, 2–9. <https://doi.org/10.1016/j.egypro.2017.09.159>
- [40] Kalina, J., and Mateusz, Ś. (2020). Operational experiences of municipal heating plants with biomass-fired ORC cogeneration units, 181(September 2018), 544–561. <https://doi.org/10.1016/j.enconman.2018.12.045>
- [41] Gölles, M., Reiter, S., Brunner, T., Dourdoumas, N., and Obernberger, I. (2014). Model based control of a small-scale biomass boiler. *Control Engineering Practice*, 22(1), 94–102. <https://doi.org/10.1016/j.conengprac.2013.09.012>
- [42] Maraver, D., Uche, J., and Royo, J. (2012). Assessment of high temperature organic Rankine cycle engine for polygeneration with MED desalination: A preliminary approach. *Energy Conversion and Management*, 53(1), 108–117. <https://doi.org/10.1016/J.ENCONMAN.2011.08.013>
- [43] Maraver, D., Sin, A., Royo, J., and Sebastián, F. (2013). Assessment of CCHP systems based on biomass combustion for small-scale applications through a review of the technology and analysis

of energy efficiency parameters. Applied Energy, 102, 1303–1313.
<https://doi.org/10.1016/j.apenergy.2012.07.012>

- [44] Petrollese, M., Oyekale, J., Tola, V., and Cocco, D. (2018). Optimal ORC configuration for the combined production of heat and power utilizing solar energy and biomass. In ECOS 2018 - Proceedings of the 31st International Conference on Efficiency, Cost, Optimization, Simulation and Environmental Impact of Energy Systems.



RESEARCH ARTICLE

INVESTIGATION OF THE SEASONALITY OF OCCUPATIONAL ACCIDENTS IN MINE OPERATIONS

Sevda TURAN^{1*}, Muhammet Mustafa KAHRAMAN²

¹Gumushane University, Faculty of Health Sciences, Department of Occupational Health and Safety, Gumushane, sevda_turan_960@outlook.com, ORCID: 0000-0002-1131-6380

²Istanbul Technical University, Faculty of Mines, Department of Mining Engineering, Istanbul, kahramanmm@itu.edu.tr, ORCID: 0000-0003-3792-1084

Receive Date: 28.10.2022

Accepted Date: 02.02.2023

ABSTRACT

Mine operations might be viewed as relatively risky in terms of worker safety when compared to other industries. Every year, there are a lot of occupational accidents and near-misses at mining sites. Most of the time, data from these circumstances are recorded, but they are typically not properly utilized. Information gathered from occurrences helps researchers understand how various conditions affect accidents and their frequency. The information obtained from such investigations may provide practical advice on how to prevent happening again. For instance, there are many studies in the literature that analyze mining accidents according to their countries, yearly frequency, work areas, and types of work; however, there isn't a single study that looks at the relationship between meteorological conditions and the seasonality of the accidents. The correlations between seasonal and regional variables, such as temperature, humidity, and pressure, and occupational accidents that occurred in mines with various climatic features, chosen from two different nations, were examined in this study. The findings indicate that there is a strong relationship between the frequency of accidents and the seasons, however this relationship would be weaker if incidents were looked into on a monthly basis. In conclusion, this article demonstrates that temperature and humidity in mining operations during severe weather conditions have a significant impact on occupational accidents.

Keywords: *Occupational accidents, Mining, Seasonality, Temperature, Humidity.*

1. INTRODUCTION

Mining is a very important sector for the development of humanity, which has shaped history since ancient times, from the industrial revolution to the present. Today, many products necessary for life are obtained as a result of mining activities [1]. With the spread of industrialization globally, occupational accidents have emerged in relation to the human-oriented working environment and the tools used, leading to economic losses [2]. Compared to developed countries, occupational accidents

with death, injury and property damage are at very high levels in Turkey [3]. Among the sectors in which these accidents occur, the mining sector has the highest death rate [4].

The human body is affected by the climatic conditions of the environment in which it lives [5]. Underground and surface workers in the mining sector are exposed to a wide variety of hazards, such as high heat and humidity, pressure, poor ventilation, poor lighting, falls, noise and vibration, tight openings, stress, and dust and gases generated during operation [6]. As a result of these effects, a decrease in the concentration of employees and work efficiency can occur. Many parameters that affect the performance of employees throughout their careers. With the effect of these factors, the performance and motivation of the employees can be adversely affected which can result in a higher number of occupational accidents.

One of the most important external factors in physical working conditions is climate and weather conditions. The temperature of the workplace is the first consideration when discussing weather conditions. Extremely hot or cold weather can adversely affect the workers and lead to a work accident. As a result of excessive heat, employees in the workplaces experience depressed mood, anxious mood, weakness, inattention, weakness and excessive sweating, resulting in muscle spasms and pains due to the salt excreted from the body [7]. Those who work in mines in hot and humid conditions take frequent breaks to reduce their body temperature and there is a decrease in productivity [5]. If the temperature is low or below normal, it becomes difficult for the employees to operate physically and mentally. In cold weather conditions, workers suffer from shivering, cold, frostbite in certain parts of the body and cold burns. As a result of working for extended durations under low temperatures, excessive fatigue can occur, and poor performance and focusing problems are experienced. This situation can lead to work accidents [7]. Another factor related to weather and climatic conditions is humidity. Extremely high or low humidity can adversely affect the health and productivity of employees [7]. High humidity makes it difficult to sweat, which makes various ailments including asthma, joint problems, cardiovascular disorders, and respiratory problems more likely to develop [8]. Employee performance suffers as a result of these disruptions, and workplace mishaps may happen.

2. PREVIOUS STUDIES

In literature, numerous studies have focused on mining accidents based on various factors such as their nations, frequency, job regions, and types of work. Köse et al., (1990) examined the occupational accidents that occurred between 1983-1988. As a result of the study, it was seen that the employees who started to work without training experienced accidents and this increased the number of accidents occurring in the enterprise. Additionally, it has been found that accidents tend to happen more frequently in the summer and on the first four days of the week than on any other days of the week. Further, it was noted that research conducted at the end of working hours revealed a higher rate of accidents [9].

According to Güyagüler and Bozkurt (1992), the expense of work-related accidents is more than the expense of taking preventative measures. It has been underlined that accidents have decreased as a result of the steps developed have to improve workplace health and safety [10].

Önder et al. (2005), found that the hot work environment had an impact on the physiological and psychological well-being of those who worked in underground mining. The study emphasizes the likelihood of workplace accidents as a result of these impacts. Computer algorithms may be used to assess the present level of heat stress and the effectiveness of the recommended solutions, according to researchers [5].

The impact of accidents on productivity between 1943 to 2009 was examined by Korkmaz (2011). According to the research, other employees suffered as a result of deadly workplace accidents. It has been stressed as a result that it impacts employees' performance and lowers their productivity [11].

Yaşar et al. (2015) discussed significant disasters that happened in Turkey and throughout the world throughout history. In the study, it was noted that multiple people were impacted whenever an occupational disaster happened and that mining, which resulted in the deaths of numerous employees, is in the "extremely risky" category [12].

Occupational incidents, according to Durşen (2016), are the main reason behind workplace accidents. These accidents can also be brought on by the physical impacts of the workplace or by psychological hazards like stress at work, a heavy workload, or irregular hours [13].

According to Turan (2019), when occupational accidents are evaluated according to months, departments, and accident types, usually are affected by seasonal factors like temperature, humidity, and pressure from two different nations' metal and coal mines [14].

In conclusion, while examining the influence of other factors on mining accidents, many subjects such as experience, stress, and efficiency were discussed and examined; however, it was concluded that sufficient research was done only in 2019 in on whether the effects of weather conditions (temperature and humidity) on the accidents occurring in underground and surface mines. In the study, the relationships between seasonal and geographical variables including temperature, humidity, and pressure, as well as occupational accidents that occurred in metal and coal mines chosen from two different nations, were explored. Additionally, based on the year and shift, it was established which period the accidents were concentrated in, and the reasons of the associated accidents were described [14]. The goal of this study is to determine whether there is a relevant correlation between occupational accidents and seasons in places with various climates by integrating weather data with the distribution of mining accidents throughout the year.

3. METHODOLOGY

In this study, occupational accident data of four different mines were collected and the relevant occupational health and safety data were collected. Meteorological data (temperature, humidity and pressure) of the periods in which the accidents occurred manually recorded. Figure 1 illustrates the approach taken in this study and the processes involved.

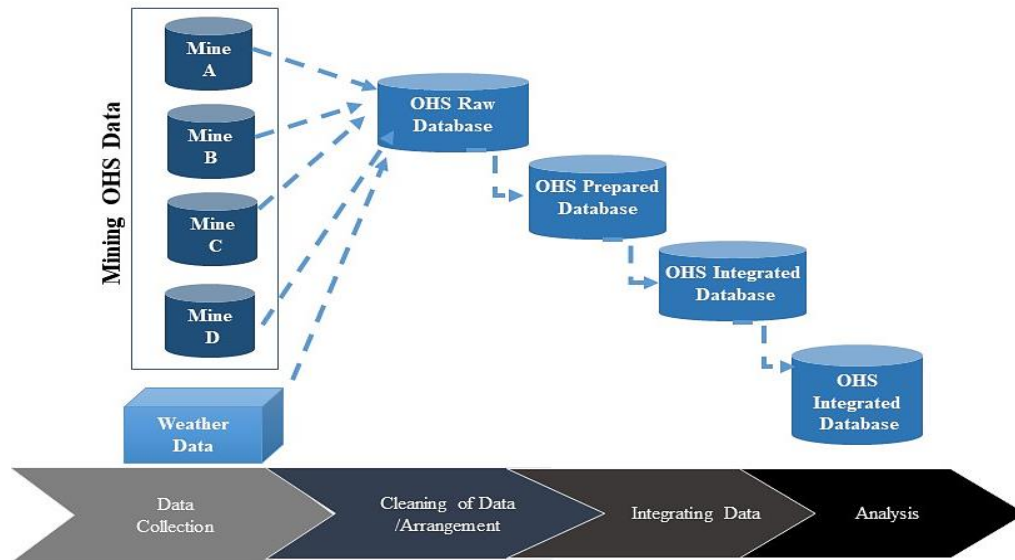


Figure 1. Stages of the method used in the study.

Data collection: incident data for two full years for each operation were collected from OHS systems and manually recorded files. The average maximum and lowest temperatures, humidity, and pressure for the and times when the incidents happened were carefully gathered from the web.

Cleaning and editing data: All of the accidents that occurred over the years were individually evaluated in the data collected from the mines. In the course of the year, the common data points in four mines were arranged, and irrelevant parameters were eliminated.

The following common information has been discovered when the data from the mines are examined:

- accident date
- accident time
- type of accident
- accident site
- accident department
- ore produced
- shift hour

Similarly, it was determined that the pressure did not significantly change throughout the year and would not contribute to the study when the characteristics relating to the weather conditions (temperature, humidity, and pressure) were studied.

Integration of data: The database was updated every day with information on accidents and the weather so that the records of accidents in mines from various eras can be compared and analyzed with meteorological data from mines (day, month, season, year).

Analysis of data: The final phase of the study used the business intelligence method to analyze the mine graphs on a monthly and seasonal basis (processing the raw data to make it more meaningful and useful). Monthly and seasonal averages were compared against annual accident shares per month or season. These analyses led to an investigation into whether the weather had a relation on the accidents.

4. BACKGROUND INFORMATION ABOUT THE MINES

Mine A is an open pit mine that produces copper and is located in the United States. The mine is in the southern region of the country. While the winters are warm, dry, and often clear throughout the year, the summer months are hot and steamy.

Mine B is a facility that produces metallic ore in Turkey. Mining techniques that combine open pit and underground methods. Blasting fragments the material. In open pits, truck and hydraulic excavators are used; underground, the standard cut-and-fill process is used. Rainfall in the area is heavy during the winter and spring.

Mine C is located in the northwest of the United States and produces potash as an open pit with truck-excavator production. The mine's location is in an area with a four-season climate, which has four distinct seasons. Winters are extremely cold, snowy, and partially overcast, whereas summers are brief, pleasant, dry, and clear.

Mine D is an open pit mine that produces coal in the western part of the United States. In the mining operation, trucks, and excavators are used. The climate of the area where the mine is located is hot, humid, and rainy in the summer; very cold, windy, and snowy in the winter; and typically partially overcast all year.

5. RESULTS

5.1. Weather Conditions of The Regions

Table 1 provides the yearly averages for temperature, humidity, and pressure for the locations where the mines are located.

Table 1. Annual average temperature, humidity and pressure averages of the regions where the mines are located.

Mines	Average Low Temperature	Average High Temperature	Average Humidity (%)	Average Pressure (Bar)

Mine A	20.2	32.1	29.8	1,011
Mine B	8.2	20.2	46.4	879
Mine C	0.6	12.5	66.7	1,015
Mine D	0.4	5.2	63.5	1,016

These facts indicate that Mine A is located in a hot, dry, and pressure-normal region. Mine B is situated in a region with a moderate climate, low humidity, and low pressure. Mines C and D are situated in chilly, somewhat humid, and pressure-normal locations.

5.1.1. Temperature-accident relationship

The data of the low and high-temperature averages measured in the regions where the mining operations are located are matched with the monthly and seasonal distributions of the accident shares in each mine.

Monthly basis

Monthly temperature accident distribution of Mine A is given in Figure 2.

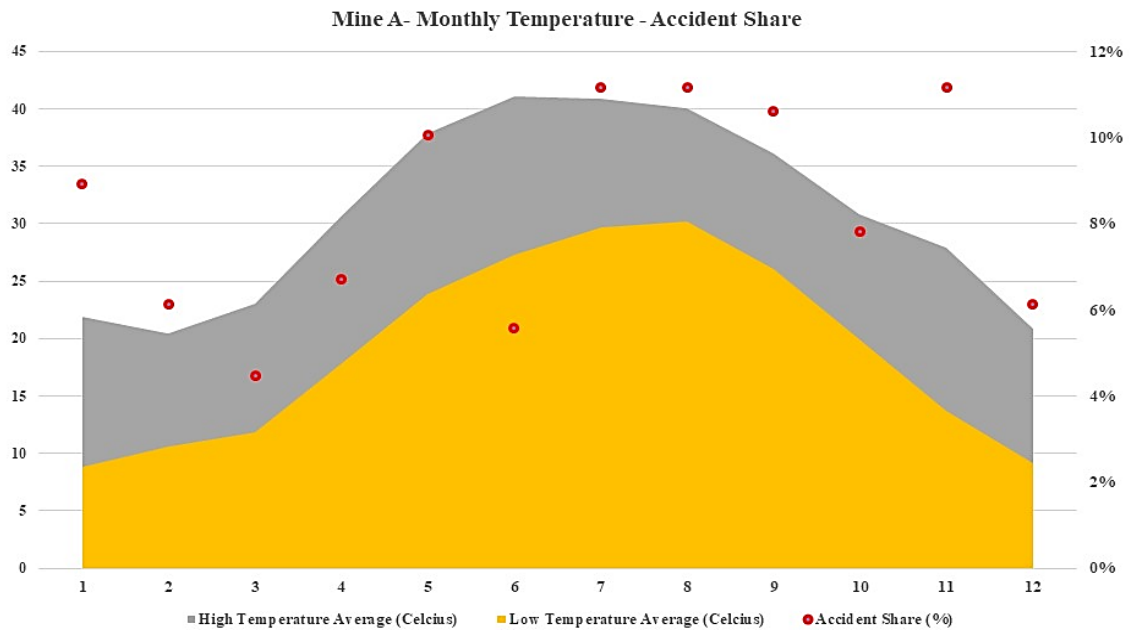


Figure 2. Monthly average temperature and accident share distribution of Mine A.

According to this distribution, accidents are intensified between the 5th-11th months; while between the 12th-4th months relatively few accidents occur. The correlation coefficient between the two series was found to be positive at 50%. It is possible to say that there is a moderate relationship.

In Figure 3, the monthly temperature accident distribution of Mine B is given. Accordingly, accidents are concentrated between the months 8th-12th of the year, and a relatively low number of accidents occur in the first 7 months of the year. The correlation coefficient between the two series was positive 49%. It is possible to say that there is a moderate relationship.

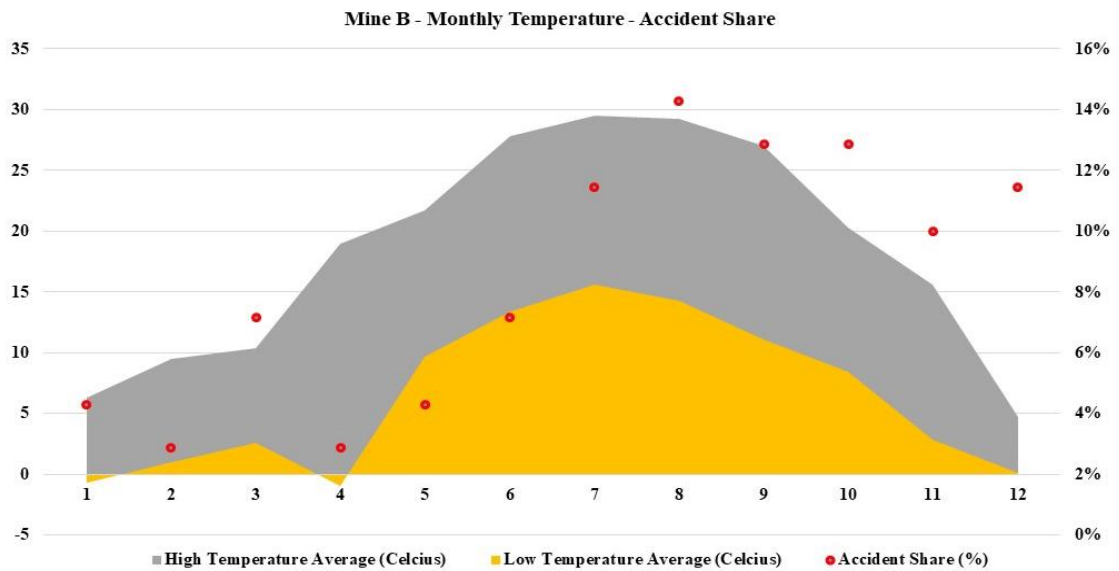


Figure 3. Monthly average temperature and accident share distribution of Mine B.

In Figure 4, monthly temperature accident distribution of Mine C is given. According to this figure, while the accidents are concentrated between the 10th-2nd months, relatively a smaller number of accidents occur between the 3rd-9th months. The correlation coefficient between the two series was calculated as negative 39%. It is possible to say that there is a moderate relationship.

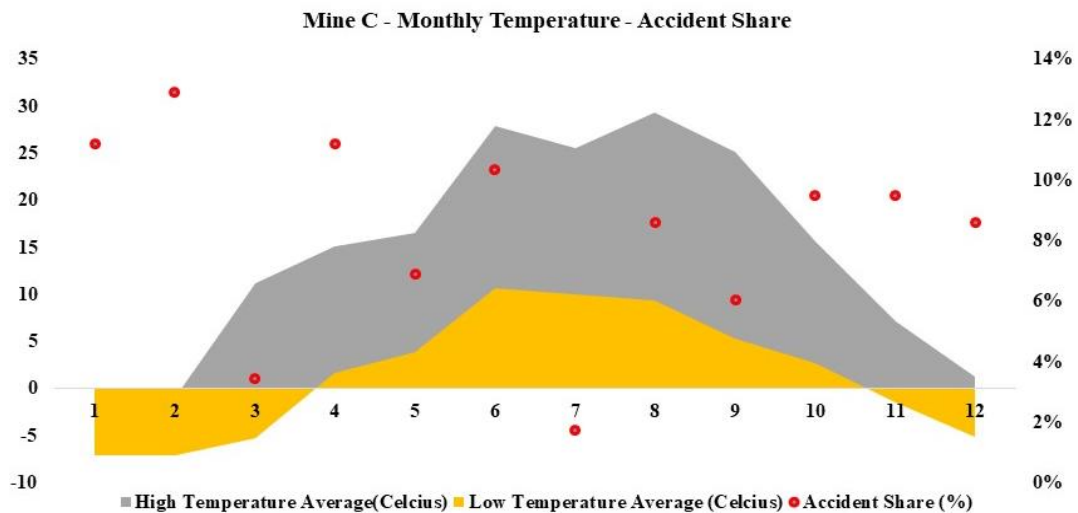


Figure 4. Monthly average temperature and accident share distribution of Mine C.

In Figure 5, the monthly temperature accident distribution of Mine D is given. According to this, while the accidents are concentrated between 12th-1st months, relatively less number of accidents occur between 2nd-11th months. The correlation coefficient between the two series was calculated as negative 38%. It is possible to say that there is a moderate relationship.

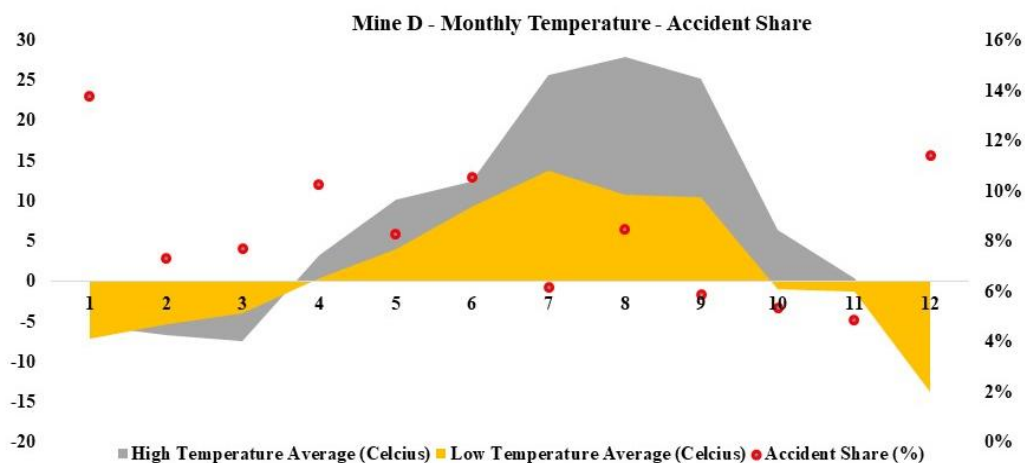


Figure 5. Monthly average temperature and accident share distribution of Mine D.

Season Basis

In Figure 6, the seasonal temperature accident distribution of Mine A is given. Accordingly, while accidents occur more intensely in summer and autumn, there are relatively fewer accidents in the winter and spring seasons. The correlation coefficient between the two series was found to be positive and 62%. It is possible to say that there is a moderate relationship.

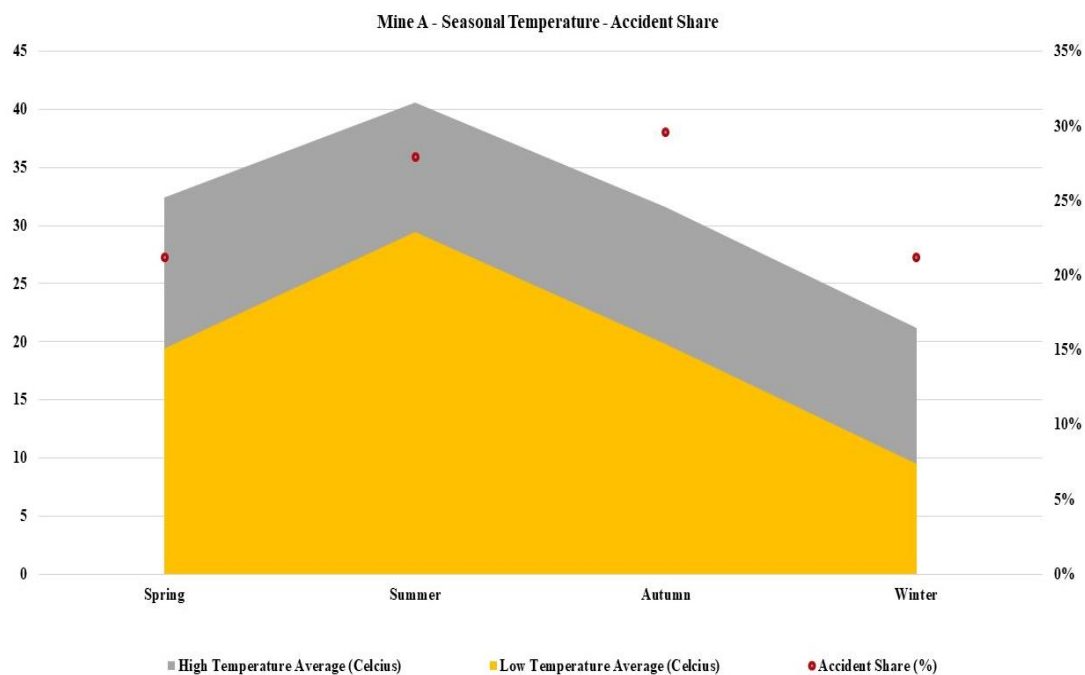


Figure 6. Distribution of seasonal average temperature and accident share of Mine A.

In Figure 7, the seasonal temperatures and accident distribution of Mine B are given. Accordingly, while accidents occur more intensely in summer and autumn, there are relatively fewer accidents in the winter and spring seasons. The correlation coefficient between the two series was positive and 72%. It is possible to say that there is a high degree of a positive relationship.

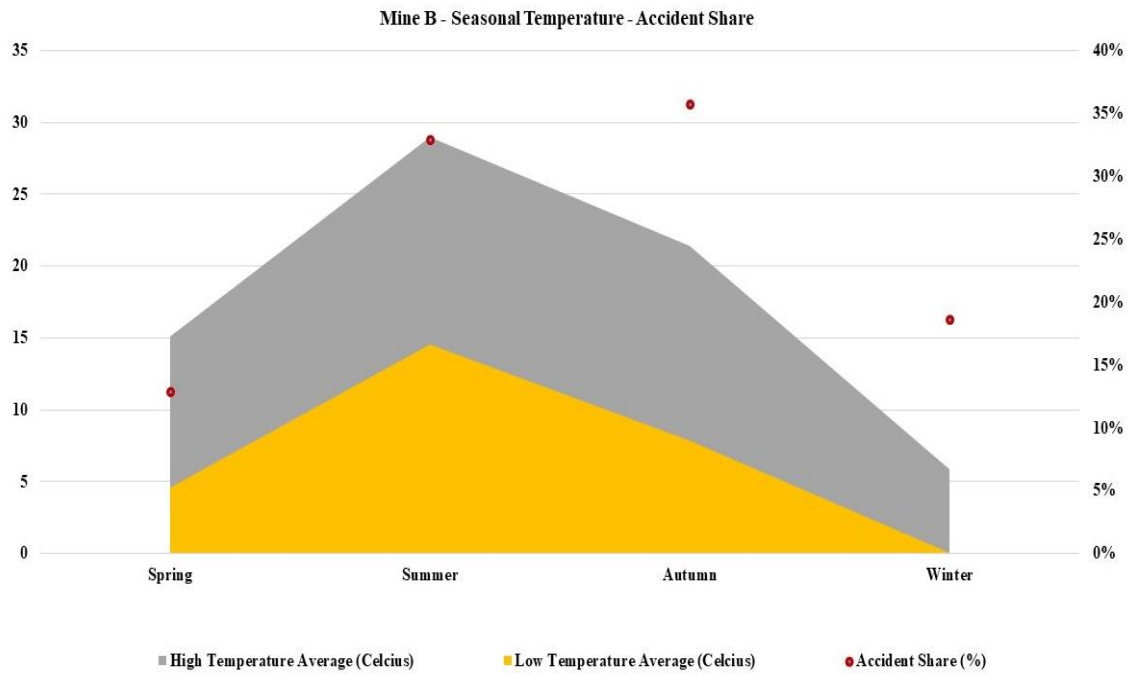


Figure 7. Distribution of seasonal average temperature and accident share of Mine B.

In Figure 8, seasonal temperature accident distribution of Mine C is given. Accordingly, while the accidents are more intense in the autumn and winter seasons, there are relatively fewer accidents in the spring and summer seasons. The correlation coefficient between the two series was negative and 90%. It is possible to say that there is a very high degree of a negative relationship.

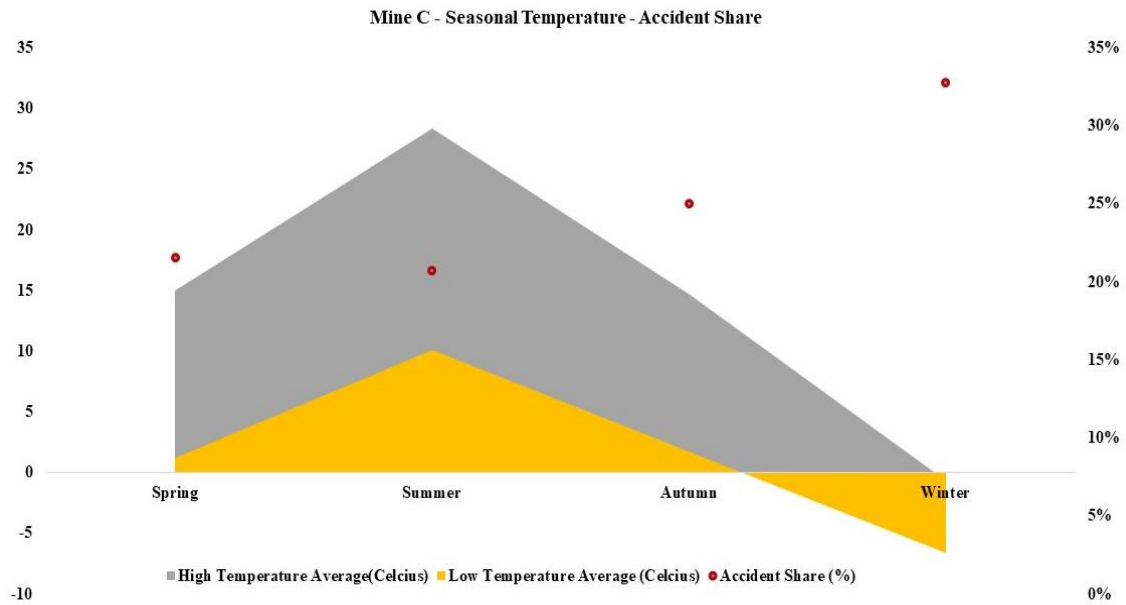


Figure 8. Distribution of seasonal average temperature and accident share of Mine C.

In Figure 9, the seasonal temperature accident distribution of Mine D is given. Accordingly, while the accidents are more intense in the winter and spring seasons, there are relatively fewer accidents in the summer and autumn seasons. The correlation coefficient between the two series was found to be negative and 59%. It is possible to say that there is a moderate negative relationship.

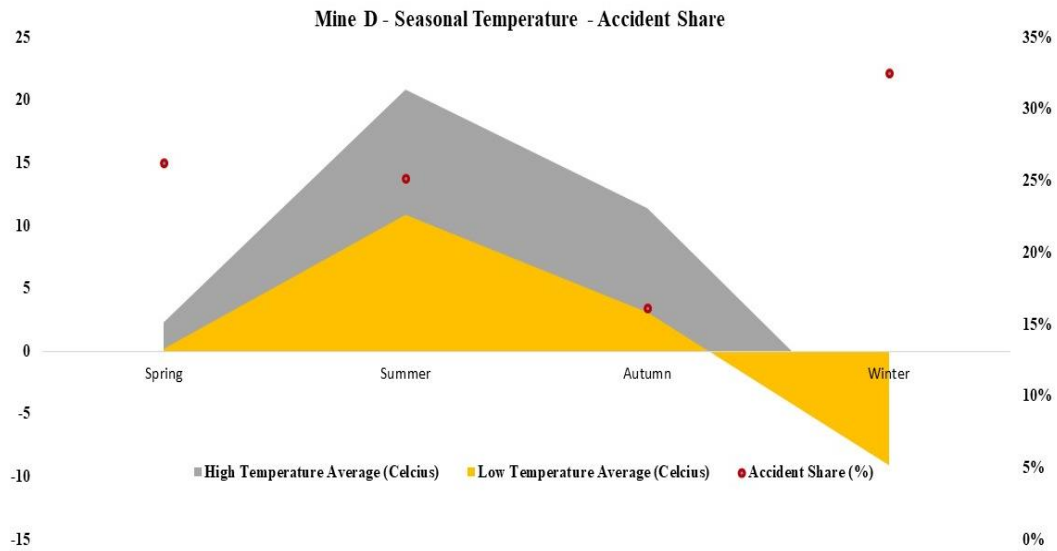


Figure 9. Distribution of seasonal average temperature and accident share of Mine D.

5.1.2. Humidity–accident relationship

In this section, the daily average humidity (%) data of the regions where the mining operations are located are matched with the monthly and seasonal distributions of the accident rates (monthly or seasonal accident number/total annual accident number) in each mine.

Monthly basis

Figure 10. It gives the moisture and accident distribution of Mine A on a monthly scale.

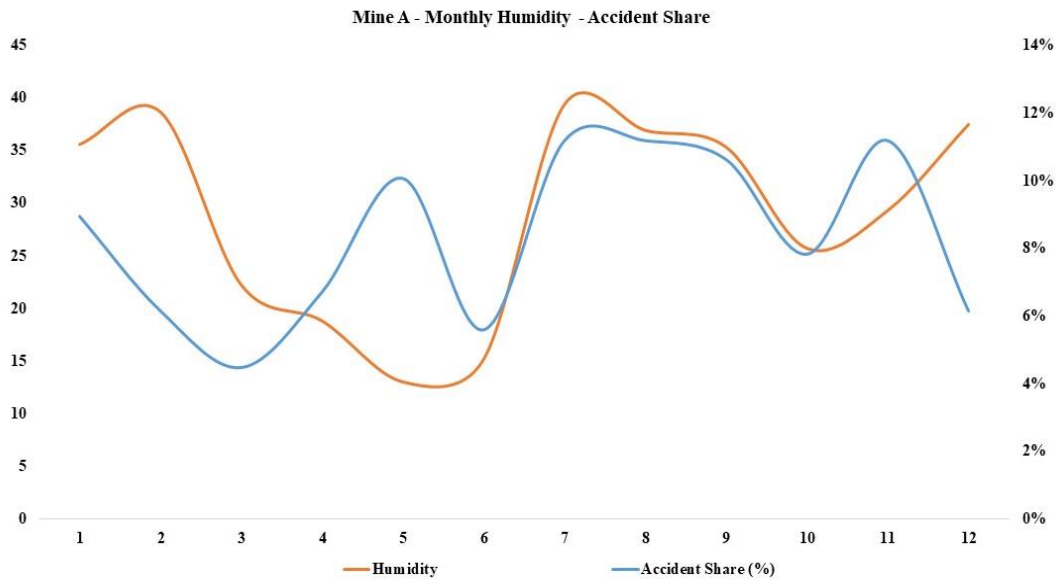


Figure 10. Monthly average humidity and accident share distribution of Mine A.

According to this distribution, the accidents are concentrated between the 5th-11th months, while the 12th-4th months are the periods when relatively few accidents occur. The correlation coefficient between the two series was found to be positive at 33%. It is possible to say that there is a low degree relationship.

In Figure 11, the monthly moisture and accident distribution of Mine B is given. According to this figure, while the accidents are concentrated between the 8th-12th months, in the first 7 months of the year, a relatively lower number of accidents occur. The correlation coefficient between the two series was positive at 10%. It is not possible to say that there is any relationship.

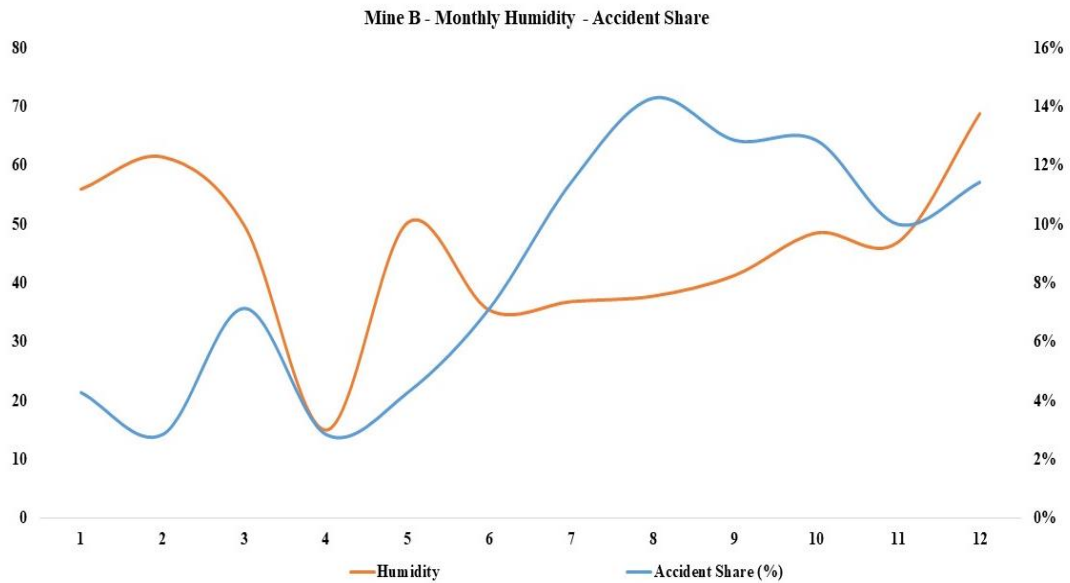


Figure 11. Monthly average humidity and accident share distribution of Mine B.

In Figure 12, the monthly moisture and accident distribution of Mine C is given. According to this figure, while the accidents are concentrated between the 10th-2th months, a relatively low number of accidents occur between the 3th-9th months. The correlation coefficient between the two series was calculated as positive 56%. It is possible to say that there is a moderate relationship.

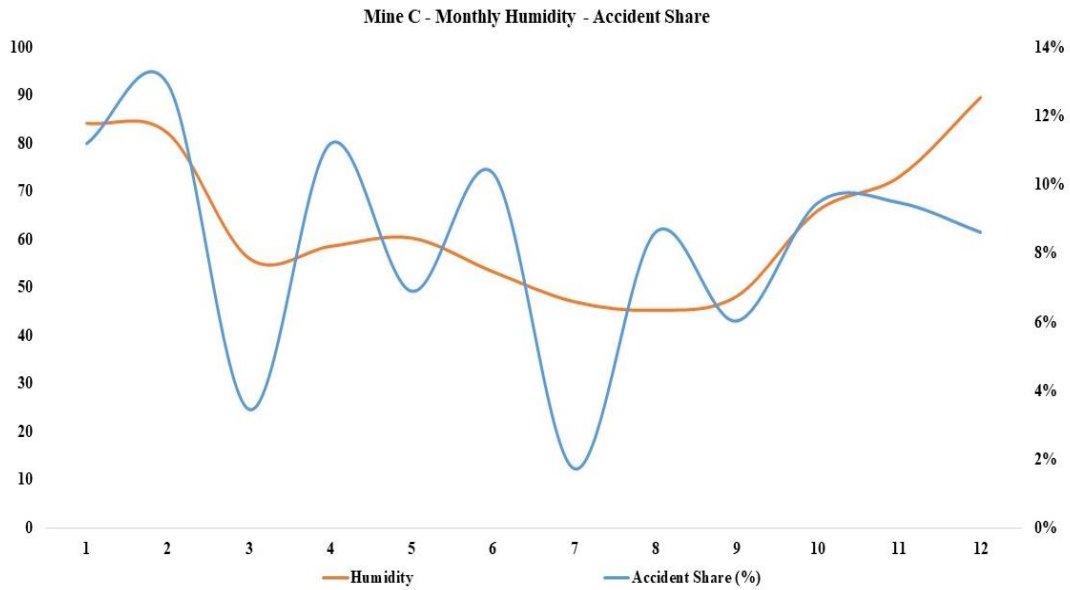


Figure 12. Monthly average humidity and accident margin distribution of Mine C.

In Figure 13, the monthly moisture and accident distribution of Mine D is given. According to this figure, while the accidents are concentrated between the 12th-1st months, relatively a smaller number of accidents occur between the 2th-11th months. The correlation coefficient between the two series was calculated as positive 34%. It is possible to say that there is a low degree of relationship.

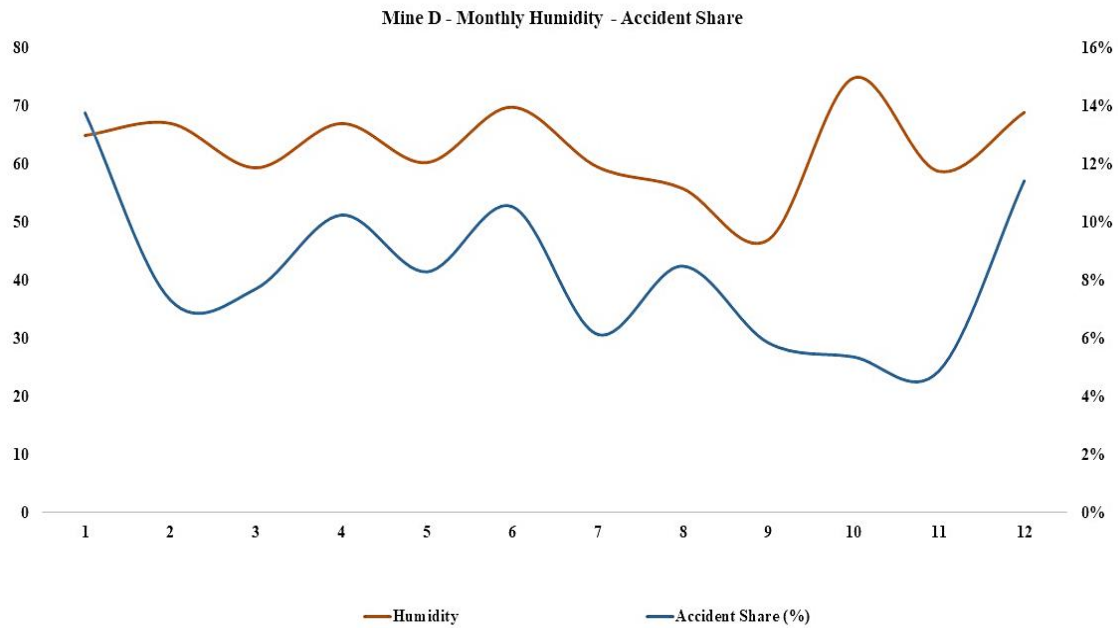


Figure 13. Monthly average humidity and accident share distribution of Mine D.

Season Basis

The seasonal humidity-accident distribution of Mine A is given in Figure 14. Accordingly, while accidents occur more intensely in summer and autumn, there are relatively fewer accidents in the winter and spring seasons. The correlation coefficient between the two series was found to be positive and 31%. It is possible to say that there is a low degree of relationship.

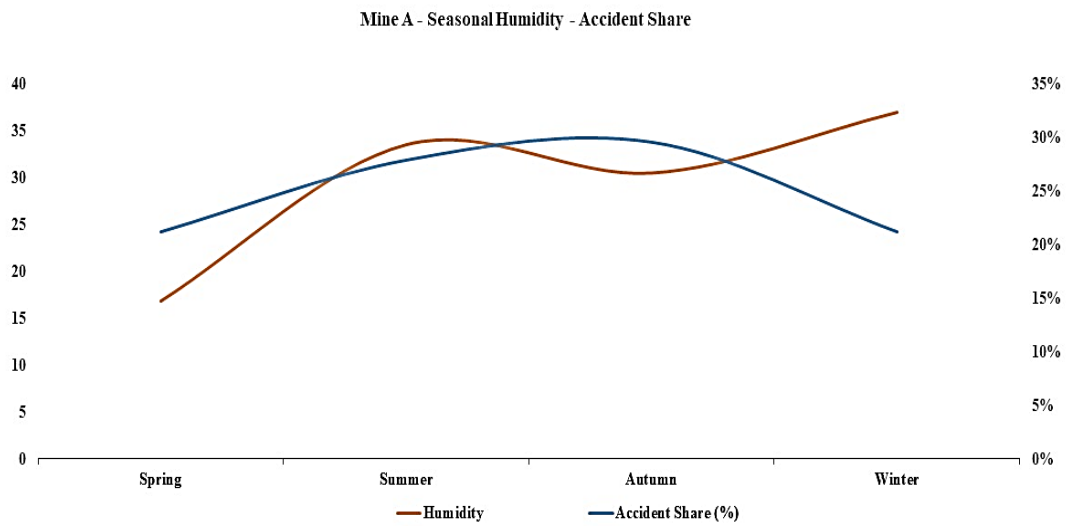


Figure 14. Distribution of seasonal average humidity and accident margin for Mine A.

The seasonal humidity and accident distribution of Mine B are given in Figure 15. Accordingly, while accidents occur more intensely in summer and autumn, there are relatively fewer accidents in the winter and spring seasons. The correlation coefficient between the two series was negative and 51%. It is possible to say that there is a moderate negative relationship.

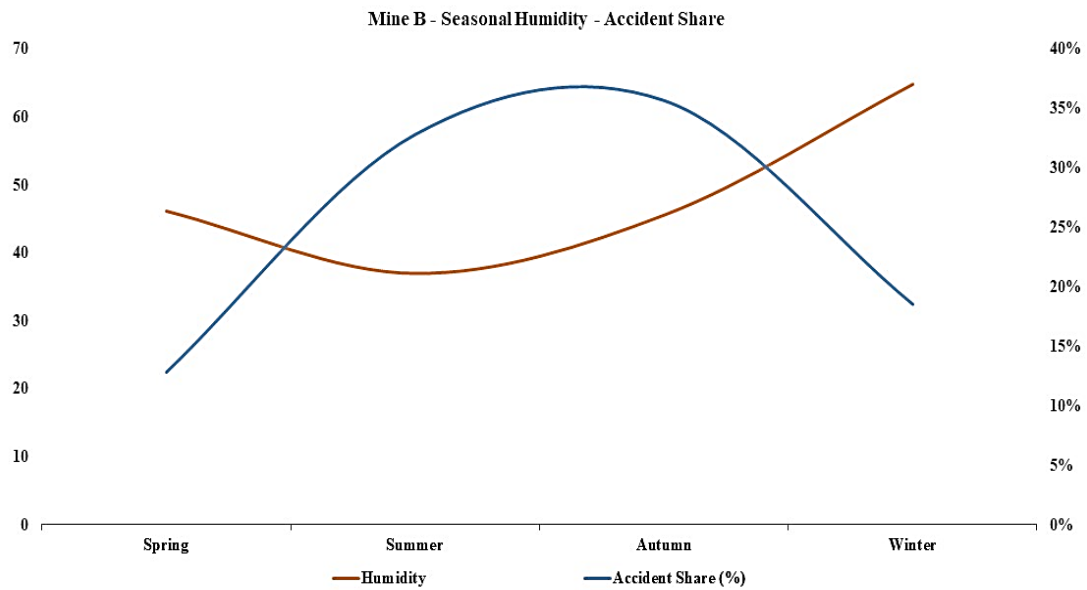


Figure 15. Distribution of seasonal average humidity and accident margin for Mine B.

The seasonal humidity accident distribution of Mine C is given in Figure 16. Accordingly, while the accidents are more intense in the autumn and winter seasons, there are relatively fewer accidents in the spring and summer seasons. The correlation coefficient between the two series was positive and 98%. It is possible to say that there is a very high degree of a positive relationship.

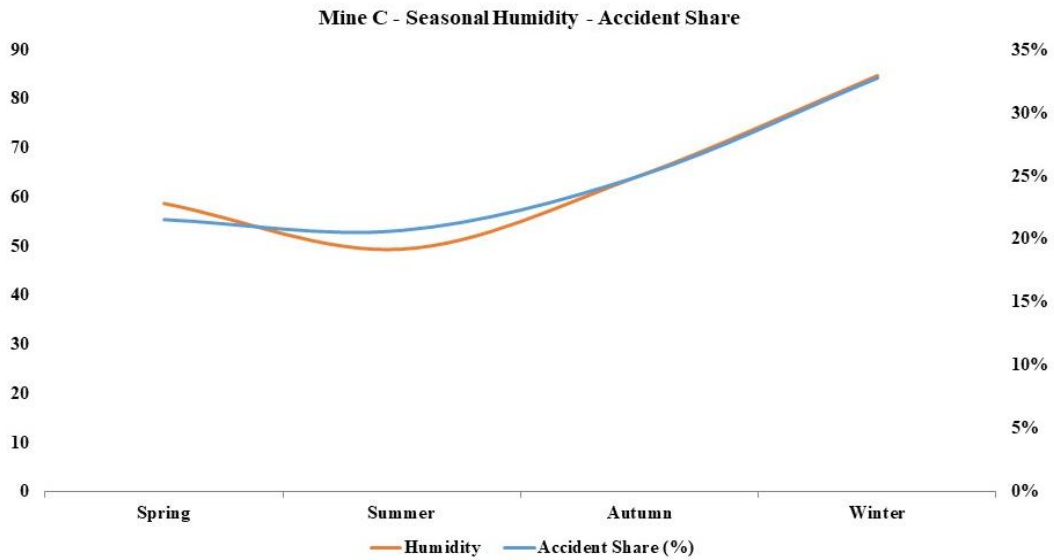


Figure 16. Distribution of seasonal average humidity and accident margin for Mine C.

The seasonal humidity accident distribution of Mine D is given in Figure 17. Accordingly, while the accidents are more intense in the winter and spring seasons, there are relatively fewer accidents in the summer and autumn seasons. The correlation coefficient between the two series was found to be positive and 96%. It is possible to say that there is a very high degree of a positive relationship.

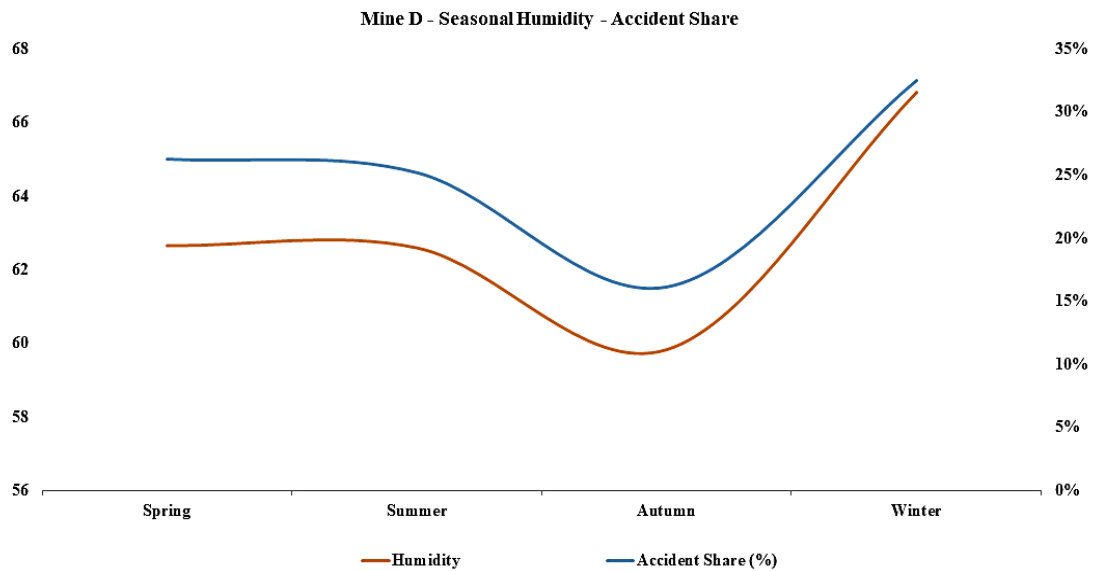


Figure 17. Seasonal average humidity and accident margin distribution of Mine D.

6. CONCLUSION

In this study, accident frequencies and weather conditions such as temperature and humidity were examined on a monthly and seasonal scale. It was found that while there is a positive and moderate correlation with temperature in Mines A and Mine B, which are located in relatively warm and temperate regions; a negative and low correlation with temperature was calculated in Mine C and Mine D, which are located in relatively colder and humid regions (Table 2). Although it is not possible to draw a strong conclusion from here; while there is a relatively significant and positive or negative relationship with temperature according to the region, a significant relationship with humidity appears to be a positive relationship only in Mine C on a monthly scale. This is evaluated as impact of thermal comfort and work schedules during warmer months.

Table 2. Table showing the relationship between the selected weather parameters and the accident monthly correlation (r values).

Parameter	Mine A	Mine B	Mine C	Mine D
Average Low Temperature & Accident	0.50	0.57	-0.34	-0.40
Average High Temperature & Accident	0.51	0.41	-0.44	-0.37
Average Humidity & Accident	0.33	0.10	0.56	0.34

As a result, Mine A and Mine B, which are located in relatively warm and temperate regions, showed a positive and moderately strong correlation with temperature. Mine C and Mine D, which are located in relatively colder and humid regions, showed a negative and low correlation with temperature (Table 2). Although it is difficult to make firm conclusions from this, it is possible to conclude that in regions with a colder climate, accidents tend to occur more frequently on periods when the temperature is low: while in hot regions, accidents tend to occur more frequently during times when the temperature is high. Only in Mine C does a significant and strong association with humidity seem to be positive on a monthly timeframe.

Results of correlation computations on a seasonal scale seem to show more favorable outcomes (Table 3). For Mines A and B, which are situated in warm and temperate regions, respectively, there is a positive medium to high degree link between seasonal temperature and accidents. It was determined that Mine C and Mine D had a strong to moderately strong negative connection with seasonal temperature and accidents. This leads to the conclusion that when the temperature rises, accidents occur more frequently in hotter places while they occur less frequently in colder regions. Mine managers can take this into account and make adjustments accordingly. While Mine C and Mine D appear to have a very high and positive connection with moisture, Mine A and Mine B show positive low and negative low correlations with moisture. It is possible to infer from this study that accidents happen more frequently in cold and humid areas at times of increased humidity.

In line with these results, for the control of work accidents; temperature and humidity levels should be taken into account and the awareness of employees should be increased during the periods of intense accident times. Although seasons, temperature, pressure and humidity are not the definitive causes of accidents, it is a fact that the number of accidents is related to them.

Table 3. Seasonal correlation (r values) in the table showing the relationship between the selected weather parameters and the accident.

Parameter	Mine A	Mine B	Mine C	Mine D
Average Low Temperature & Accident	0.64	0.71	-0.88	-0.56
Average High Temperature & Accident	0.59	0.73	-0.91	-0.62
Average Humidity & Accident	0.31	-0.51	0.98	0.96

These results provide a good starting point for discussion and further research. Seasonality, timing and location of occupational accidents are topics that have huge potential on understanding where occupational incidents are concentrated the most. Further studies should investigate the time of day, time of shift, daily weather conditions, activities, and locations impact on occupational accidents.

ACKNOWLEDGMENT

This study was prepared using the Master's Thesis titled "EXAMINATION OF SEASONALITY AND TIME OF ACCIDENTS OCCURRING IN MINES". I would like to thank all referees for their valuable contributions and advice during this study.

REFERENCES

- [1] Bilim, N., Dursun, A.E., ve Bilim, A. (2015). Maden ekipmanlarına bağlı iş kazalarının genel değerlendirmesi ve çözüm önerileri. Türkiye 5. Uluslararası Maden Makinaları Sempozyumu ve Sergisi, 1-2 Ekim, Eskişehir.
- [2] Durdu, H. İ. (2014). İş kazalarının ekonomik analizi ve bazı sektörler bazında değerlendirilmesi. Sosyal Güvence Dergisi, 5, 67-91.
- [3] Camkurt, M. Z. (2013, Mayıs - Ağustos – Kasım). Çalışanların kişisel özelliklerinin iş kazalarının meydana gelmesi üzerindeki etkisi. TÜHİS İş Hukuku ve İktisat Dergisi, 24(6) / 25(1-2), 70-101.
- [4] Tozman, B. (2010). Türkiye madencilik sektöründe iş kazalarının istatistiksel analizi. Eskişehir Osmangazi Üniversitesi, Fen Bilimleri Enstitüsü, Maden Mühendisliği Anabilim Dalı, Yüksek Lisans Tezi, Mayıs, 45s.
- [5] Önder, M., Saraç, S., ve Eren, N. (2005, Aralık). Yeraltı ocaklarında ısı stresinin etkileri ve analizi üzerine bir paket program. Madencilik, 44(4), 39-46.
- [6] Bhattacharjee, A., and Kunar, B. M. (2016). Miners' Return to Work Following Injuries in Coal Mines. Medycyna Pracy, 67(6), 729-742.
- [7] Camkurt, M. Z. (2007, Mayıs/Ağustos). İşyeri çalışma sistemi ve işyeri fiziksel faktörlerinin iş kazaları üzerindeki etkisi. TÜHİS İş Hukuku ve İktisat Dergisi, 20(6) / 21(1), 80-106.
- [8] Üçüncü, K., Aydın, A., ve Tiryaki, S. (2015). Kapalı mekanlarda insan faktörü ve odun esaslı malzemelerin havanın bağıl nemine etkisi. Mühendislik Bilimleri ve Tasarım Dergisi, 3(3), 533-540.
- [9] Köse, H., Şenkal, S., ve Aközel, A. (1990, 21-25 Mayıs.). "GLİ Tunçbilek Bölgesi yeraltı işletmelerindeki kaza istatistikleri". Türkiye 7. Kömür Kongresi Bildiriler Kitabı, Zonguldak, 363-381.
- [10] Güyagüler, T., ve Bozkurt, R. (1992). Kömür madenciliğinde meydana gelen iş kazalarının maliyetleri. Türkiye 8. Kömür Kongresi Bildiriler Kitabı, TMMOB, Zonguldak, 552, 331-343.

- [11] Korkmaz, O. (2011). İş kazaları ile verimlilik arasındaki ilişki: Türkiye Taşkömürü Kurumu örneği. *Journal of Yasar University*, 6(23), 3805-3813.
- [12] Yaşar, S., İnal, S., Yaşar, Ö., and Kaya, S. (2015). Big Mining Disasters From Past to Present, *Madencilik*, 54(2), 33-43.
- [13] Durşen, M. (2016). Yeraltı kömür işletmelerinde çalışanların psikososyal risklerinin değerlendirilmesi. T.C. Çalışma ve Sosyal Güvenlik Bakanlığı İş Sağlığı ve Güvenliği Genel Müdürlüğü, İş Sağlığı ve Güvenliği Uzmanlık Tezi, Ankara, 88s.
- [14] Turan, S. (2019). Madenlerde meydana gelen iş kazalarının mevsimselliğinin ve kaza zamanının incelenmesi. Gümüşhane Üniversitesi, Fen Bilimleri Enstitüsü, İş Sağlığı ve Güvenliği Anabilim Dalı, Yüksek Lisans Tezi, Temmuz, 79s.



RESEARCH ARTICLE

DESIGN AND APPLICATION OF AC/DC SWITCHING POWER SUPPLY WITH HALF BRIDGE DC/DC CONVERTER TOPOLOGY FOR BATTERY SYSTEMS of ELECTRICAL VEHICLE

Celaletdin AKGÜL^{1*}, Yücel ÇETİNCEVİZ², Erdal ŞEHİRLİ³

^{1*}Kastamonu University, Faculty of Engineering and Architecture, Electrical and Electronics Engineering, Kastamonu, em.celaleddinakgul@gmail.com, ORCID: 0000-0001-7214-9478

²Kastamonu University, Faculty of Engineering and Architecture, Electrical and Electronics Engineering, Kastamonu, yetcinceviz@kastamonu.edu.tr, ORCID: 0000-0001-6834-9442

³Kastamonu University, Faculty of Engineering and Architecture, Electrical and Electronics Engineering, Kastamonu, eshirli@kastamonu.edu.tr, ORCID: 0000-0003-0822-3201

Receive Date: 01.12.2022

Accepted Date: 02.03.2023

ABSTRACT

This study presents design, analysis and application details of electrical vehicle battery charge device based on half bridge DC-DC converter. Half bridge DC-DC converter in the paper has 620 W power, 25 kHz switching frequency and input DC voltage is obtained by uncontrolled bridge rectifier. In addition, information about the battery that is charged, and battery pack are given. Besides, a protection structure of battery is added by measuring both current and voltage of battery. Firstly, equations required for half bridge DC-DC converter is derived and simulation of battery charge circuit is realized by using PSIM and MATLAB/Simulink. Then, the results of the experimental study and the simulation results are given comparatively. The experimental results prove the accuracy of the simulation studies.

Keywords: *Half Bridge DC-DC Converter, Electrical Vehicle, Battery, MATLAB/Simulink, Application.*

1. INTRODUCTION

Nowadays, interest to the alternative and renewable energy sources has been increasing much because of decreasing fossil sources and fossil sources has negative factors such as climate change, increasing of carbon dioxide rate, decrease of oxygen, air pollution, global warming, negative effect to human health. Recently, the use and the tendency of using of renewable energy sources has increased much. Besides, due to the negative effect of the fossil sources, electrical vehicle has becoming more popular and in future it is assumed that the electrical vehicle will take place of fossil fuel-based vehicles. In addition, electrical vehicle consists of some key components including battery, battery charger, electrical motor, and motor driver. However, the most important part is battery and battery charger of

the electrical vehicle. To charge battery of electrical vehicle, DC power source is required. This DC source is provided by switching power supply [1, 2, 3].

As a battery type for electrical vehicle the best option for today is lead-acid, nickel-cadmium, nickel-metal, lithium-ion, and zinc-air [4, 5, 6]. Especially, lithium-ion batteries because of having higher power density are the most preferable battery type [7, 8, 9]. Operation and operation safety of lithium-ion batteries are so important for the use in electrical vehicle [10]. Also, lithium-ion batteries have higher reliability, higher power density, long lasting, lower discharge rate, and higher efficiency features [11]. To obtain higher power value with desired voltage levels, each battery cells are connected series and parallel [12]. On the other hand, the most important problem in electrical vehicle is the limitation of the battery such as weight, cost, limited charge capacity, short driving distance, long charge duration [13]. So, fast charging specification having different kind of DC-DC converter topology ensure the use of electrical vehicle for continuous driving [14].

Efficiency is so important topic for switching power supply. Higher efficiency can be obtained by optimum design of magnetic materials, lower switching losses at the switch on and off conditions. In addition, switching power supply can operate with higher switching frequency rate from kHz to MHz, higher switching frequency provides reducing the size of equipment used in the converter [15]. Also, switching power supply ensures wide input voltage range, lower loss, higher efficiency, weight, and size comparing to linear power supplies.

It is hard to choose switching power supply topologies for low or medium power level. For lower and medium power levels, push-pull and half bridge converter are more popular than full bridge converter [16]. For 200 W – 1000 W power level, generally half bridge topology is preferred, also in half bridge topology, a capacitor is added to primary winding [17]. The biggest disadvantage of push-pull converter is voltage stress which is twice of input voltage [17,18]. However, the main advantage of the half bridge converter regarding to push-pull converter is the construction of primary windings. In push pull converter, the primary should be wounded by two equally windings that causes design difficulty. In addition, half of dc source voltage is applied to the primary windings of half bridge converter but in push pull converter total dc source voltage is applied to half of primary windings. It is also mentioned in literature that the push-pull converter is more suitable for low voltage applications, and it has higher voltage stress on power switches. Nevertheless, push-pull converter has an easiness of driving power switches because it has two low side power switches which can be driving without the need of isolation or bootstrap driving principle. Advantage of half bridge converter comparing to push-pull converter is not having middle point of primary winding that provides easiness for applications [16]. In addition, comparing of full bridge converter, voltage stress of the half bridge converter is nearly half due to the splitted capacitor connection to the primary of transformer. Therefore, half bridge converter is preferable than push-pull and full bridge converters.

For power converter, to conduct their simulations there are a few software such as PSIM and MATLAB providing simulation capability of the converters with higher accuracy [19,20,21,22].

In this paper, by using half bridge DC-DC converter, for electrical vehicle design, simulation and application of batter charge device is realized. Modeling, control design and evaluation of the performance of charger device is conducted by PSIM and MATLAB/Simulink software. Half bridge

DC-DC converter-based battery charger is designed for 620 W power with 112 V output voltage. Design details are also given in this paper and measurements are conducted to validate the applications. In addition, battery back construction is included in the paper. Besides, a protection structure of battery is added by measuring both current and voltage of battery.

2. HALF BRIDGE DC-DC CONVERTER

Single phase AC is converter to DC by diode bridge circuit. Resulting DC is applied to the half bridge DC-DC converter. Half bridge DC-DC converter consists of two power switches, capacitors at input and output, high frequency transformer, high frequency rectifier circuit, and an inductor. After, applying DC, to the power switches, because the power switches are switched on one by one, a high frequency AC on the transformer is obtained. Resulting high frequency AC, is converter to DC by using high frequency diode rectifier. To avoid short circuits because of switch on and off condition of Q_1 and Q_2 , dead time is adjusted. During the dead time, energy for load is supplied by inductor L.

As shown in Fig. 1, there are four operation mode of the half bridge DC-DC converter.

1. Operation mode 1, Q_1 is switched on, Q_2 is switched off.
2. Operation mode 2, Q_1 and Q_2 are switched off.
3. Operation mode 3, Q_1 is switched off, Q_2 is switched on.
4. Operation mode 4, Q_1 and Q_2 are switched off.

Square wave AC voltage is occurred at primary windings after the operation of the Q_1 and Q_2 of half bridge DC-DC converter. The square waveform voltage at secondary of the transformer can be obtained lower or higher than primary winding voltage. AC square wave voltage at secondary winding is rectified by D_1 and D_2 diodes. After filtering of the secondary voltage, output voltage V_o is obtained. At Fig. 2., steady state wave forms of half bridge DC-DC converter are shown.

At mode 1, Q_1 is switched on, Q_2 is switched off, D_1 is switched on, D_2 is switched off. Primary winding of the high frequency transformer is connected to mid-point of the series connected capacitors. So, primary winding voltage is equal to $V_{dc}/2$.

When the Q_1 switch is on, there is a voltage drop on the primary winding resulting induced voltage on secondary winding. The induced secondary voltage is rectified by diode and after LC filtering transferred to R load. Secondary voltage can be calculated by (1).

$$V_{se} = \frac{N_s}{N_p} \left(\frac{V_{dc}}{2} \right) \quad \#(1)$$

Voltage at output inductor is calculated by (2).

$$V_{L1} = \frac{N_s}{N_p} \left(\frac{V_{dc}}{2} \right) - V_o \quad \#(2)$$

Current change of the inductor i_{L1} is equal to (3).

$$\frac{di_{L1}}{dt} = \frac{v_{L1}}{L1} = \frac{1}{L1} \left[\frac{N_s}{N_p} \left(\frac{V_{dc}}{2} \right) - V_o \right] \quad \#(3)$$

Peak inductor current $i_{L1}(pk)$ can be found at $t=kT$ by (4) [24].

$$I_{L1(pk)} = I_{L1}(0) + \frac{1}{L1} \left[\frac{N_{s1}}{N_p} \left(\frac{V_{dc}}{2} \right) - V_o \right] kT \quad \#(4)$$

At mode 2, Q_1 and Q_2 switches are off. So, $kT < t \leq T/2$ is valid. Diodes at secondary side are forced for conduction by magnetizing current. Decreasing rate of \dot{I}_{L1} can be found by (5) [24].

$$\frac{di_{L1}}{dt} = -\frac{V_o}{L_1} \quad 0 < t \leq (0.5 - k)T \quad \#(5)$$

Initial value of i_{L1} can be calculated by (6).

$$I_{L1}(0) = i_{L1} [t = (0.5 - k)T] = I_{L1(pk)} - \frac{V_o(0.5 - k)T}{L_1} \quad \#(6)$$

At mode 3, Q_1 is switched off, Q_2 is switched on, D_2 is switched on, D_1 is switched on. The voltage on primary winding is equal to $-V_{dc}/2$. Reverse operation of mode 1 is realized. V_o output voltage can be found by the integral in (7) [24].

$$V_o = 2 * \left[\int_0^{kT} \left(\frac{N_{s1}}{N_p} \left(\frac{V_{dc}}{2} \right) - V_o \right) dt + \int_k^{T/2} -V_o dt \right] \quad \#(7)$$

Output voltage can be calculated by (8).

$$V_o = \frac{N_{s1}}{N_p} V_{dc} k \quad \#(8)$$

Output power is calculated by (9).

$$P_o = V_o I_L = \eta P_i = \eta \frac{V_{dc} I_{p(avg)} k}{2} \quad \#(9)$$

$I_{p(avg)}$ average primary current can be calculated by (10).

$$I_{p(avg)} = \frac{2P_o}{\eta V_{dc} k_{max}} \tag{10}$$

Drain current of Q₁ and Q₂ is found by (11).

$$I_{d(max)} = I_{p(avg)} = \frac{2P_o}{\eta V_{dc} k_{max}} \tag{11}$$

Maximum voltage on switch is equals to (12).

$$V_{c(max)} = V_{dc(max)} \tag{12}$$

Maximum duty cycle k cannot be more than 50%. Half bridge DC-DC converter is generally used for medium power applications with the 350 W - 800 W power range [24].

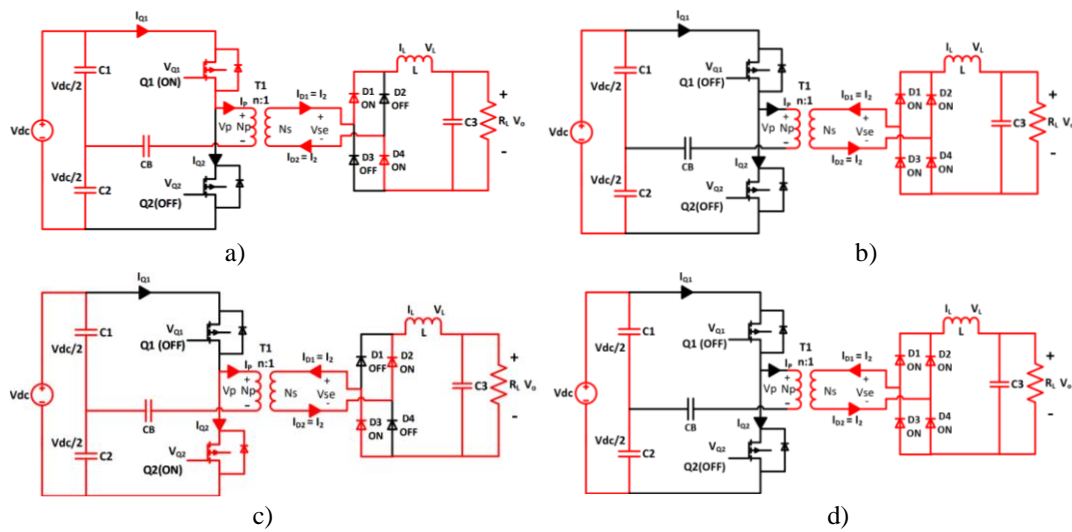


Figure 1. Operation modes of half bridge DC-DC converter, Mode 1, Q₁ is on Q₂ is off (a), Mode 2 (b), Q₁ and Q₂ is off, Mode 3 (c), Q₁ is off Q₂ is on, Mode 4, Q₁ and Q₂ is off (d).

In every operation mode, the $V_{Q1} + V_{Q2} = V_{dc}$ equation which is derived by Kirchoff voltage Law of closed loop regarding V_{dc} and both Q₁ and Q₂ switches voltages, should be verified. So, by neglecting the switch on state voltage drops, at Mode 1 $0 + V_{Q2} = V_{dc}$, at Mode 2 $V_{Q1} + V_{Q2} = V_{dc}$, at Mode 3 $V_{Q1} + 0 = V_{dc}$, at Mode 4 $V_{Q1} + V_{Q2} = V_{dc}$.

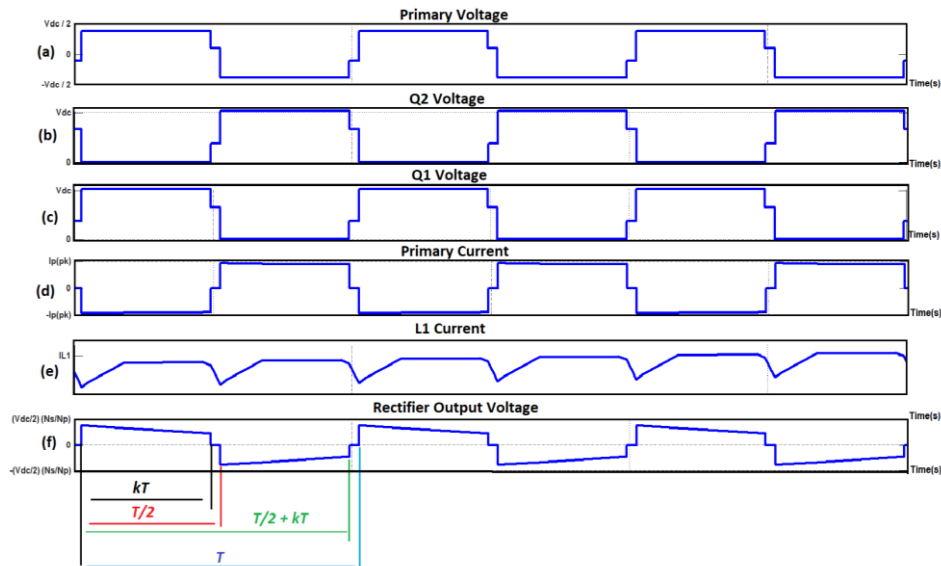


Figure 2. Steady-state wave form of half bridge converter at continuous conduction mode. Primary voltage (a), Q_2 voltage (b), Q_1 voltage (c), primary current (d), L_1 current (e), rectifier output voltage (f).

3. DESING OF HALF BRIDGE DC-DC CONVERTER

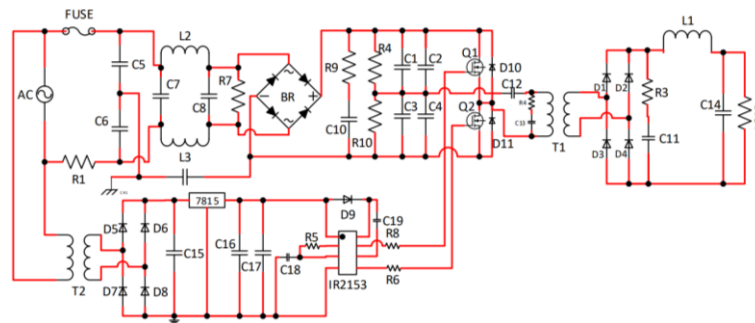


Figure 3. Half bridge DC-DC converter application circuit.

Application circuit of half bridge DC-DC converter is shown in Fig.3. In this circuit, IR2153 MOSFET driver integrated circuit is used. AC grid voltage is converted to DC voltage by diode bridge. Capacitors in parallel to each other are charged by half of DC voltage. High frequency transformer is connected between the midpoint of capacitors and power switches. To reduce the high frequency noise due to the power switches, a filter is added between AC grid and diode bridge. In addition, for protection of power switches, a parallel RC snubber circuit and diodes are used. For

powering of IR2153 IC with 15 V, second transformer and diode bridge are used. Applied converter parameters are defined as 25 kHz switching frequency, 750 W output power and 0.8 efficiency. In addition, for transformer, ETD 54 core with N87 material of EPCOS company is chosen. Besides, for output inductor, ETD39 core with N87 material of EPCOS company is used. Also, litz wire is employed both transformer and inductor.

3.1. Design of High Frequency Transformer

Require calculations for transformer is achieved by using (13-18).

$$V_{inmax} = V_{rms} * \sqrt{2} \quad \#(13)$$

$$P = V * I, \quad P_{out} = 700W, \quad V_{out} = 110V \Rightarrow I_{out} = 6,36A \quad \#(14)$$

$$P_{in} = P_{out}/\eta, \quad I_{in} = P_{out}/311 = 2,81A \quad \#(15)$$

Dead time is set as 1 μ s. Total period is 40 μ s because the switching frequency is 25 kHz. Voltage is occurred in primary 49% of total period, when it is thought that 2 μ s dead time each two-half period. Duty cycle and conduction time is as in (16).

$$D = (100 - 2)/2 = \%49, \quad t_{on} = \%49 * 40\mu s = 19.6\mu s \quad \#(16)$$

Primary turn number N_p can be calculated in (17) when magnetic flux density (B) is taken as 100 mT. A_e is cross sectional area of the core.

$$N_p = V_{in} * t_{on} / 2 * \Delta B * A_e \quad \#(17)$$

Secondary turn number can be calculated by (18).

$$N_s = N_p * V_{out} / 2 * D * V_{in} \quad \#(18)$$

Required conductor number of litz wire and cross-sectional area of the conductor can be calculated by (19-23). I_p primary current, S cross sectional area, J current density.

$$S = I_p / J \quad \#(19)$$

When the frequency of the current passing through the conductor is increased, current passes surface of h conductor. It is called as skin effect. In (20), skin depth that is the depth of the current passing from conductor while frequency change is given. In the application, operating frequency is 35 kHz, so skin depth is calculated as 0.45 mm.

$$\delta = \frac{72}{\sqrt{f}} \quad \#(20)$$

Transformer and inductor are wound by conductor having 0.3 mm diameter. For primary and secondary windings, parallel conductor number is calculated by using (19), (21), (22).

$$S = \pi r^2 \quad \#(21)$$

$$S = I_s / j \quad \#(22)$$

For output side inductor, required calculations are done by using (24). ΔI inductor ripple current, is taken as 20% of output current.

$$L_{out} = \frac{(V_{in} - V_{out}) * D * T}{2 * \Delta I} \quad \#(24)$$

In application, as a power switch IXTQ460P2 power MOSFET, as a parallel diode of MOSFET, MUR460, as rectifier diodes DSEP15-06A are used.

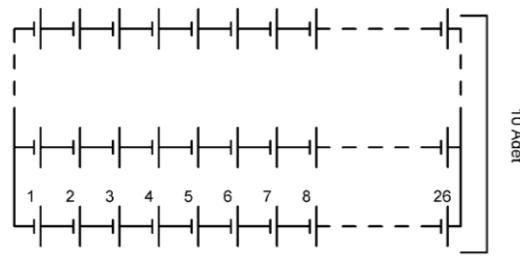
3.2. Battery Pack

Battery pack is obtained series and parallel combination of li-ion battery cell having 3,6 V value. Total parallel battery cell number is 10 and total series connected battery cell number is 26. Parameter of battery pack is given in Table 1.

Table 1. Battery pack parameters.

Parameter	Value
Battery Cell Capacity	3450 mAh
Battery Nominal Voltage	3,6 V
Parallel connection number	10
Battery capacity	34,5 Ah
Series connection number	26
Maximum Voltage	109,2 V

Each battery cell capacity is 3450 mAh and nominal voltage is 3.6 V. Battery pack structure and battery pack is shown in Fig. 4. As it is seen, there are 10 parallel connection and 26 series connection of each battery cell.



a)



b)

Figure 4. Battery pack connection circuit (a), battery pack (b).

3.3. Simulation Results

Before the applications of half bridge DC-DC converter-based battery charger, at first, simulation studies are conducted. To conduct simulations, Matlab/Simulink and PSIM software are used. Firstly, simulation study is realized by resistor as a load then battery in Matlab/Simulink. After that, for validation of the Matlab/Simulink, PSIM simulation is made via resistor as a load.

Firstly, simulation is conducted by using resistors as a load and its Matlab/Simulink circuit is given in Fig. 5. Protection circuit by measuring current and voltage of the battery is seen by the figure. Via protection logic, at the condition of higher current and voltage more than defined limit the converter stops its operation. Besides, required dead time between the operation of the switch is added in the simulations as it is seen by the figure.

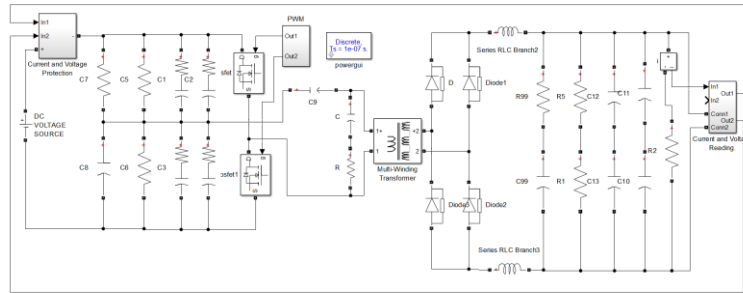


Figure 5. Matlab/Simulink simulation circuit resistor as a load.

In Fig. 6 switching signals of the switches are seen. Dead time between each switch can be observed easily by the figure and it is set as 1 μ s. After applying the signal in Fig. 6 to the switches, operation of the converter is realized.

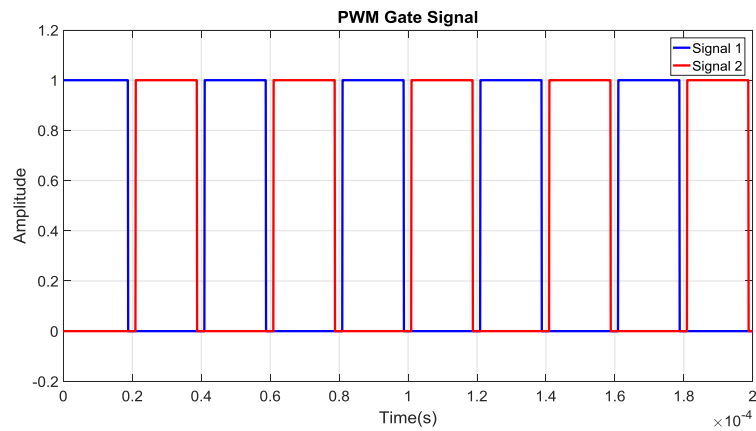


Figure 6. Switching signals of power switches.

After applying the signals in Fig. 6 to the power switches, high frequency AC voltage is induced at the secondary windings of the transformer as given in Fig. 7. Zero voltage values in the figure are because of the dead time between each switch.

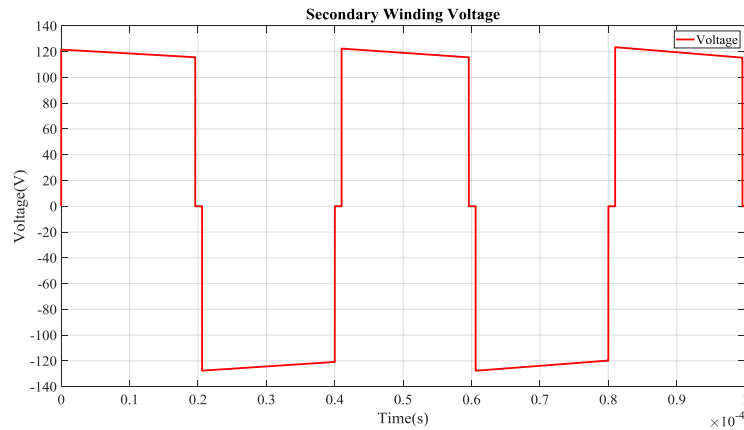


Figure 7. Voltage waveform of transformer secondary winding.

Switching signals in Fig. 6 results in drain-source voltages of power switches given in Fig. 8, after applying the power to the converter. It is seen that the drain-source voltage does not include peak values which is an advantage of the topology.

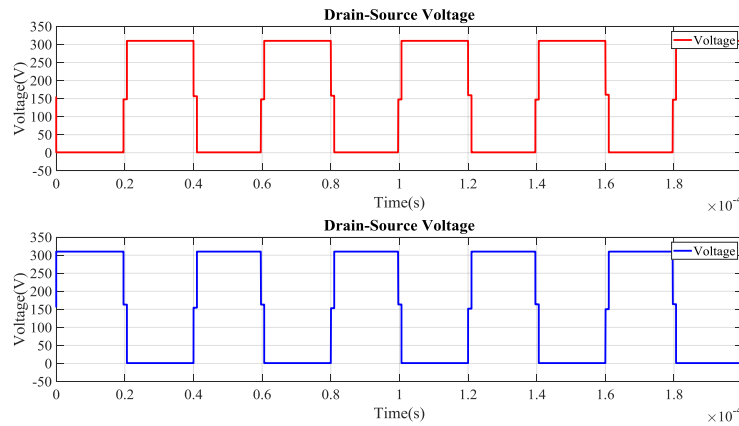


Figure 8. Drain source voltage of MOSFET 1 and MOSFET2.

After operation of each power switches, primary winding of the transformer has a voltage drop as given in Fig. 9. Also transferring energy to the secondary windings causes current drawn by primary winding that is given in Fig. 9. Because of the dead time between switches, both current and voltage has zero values.

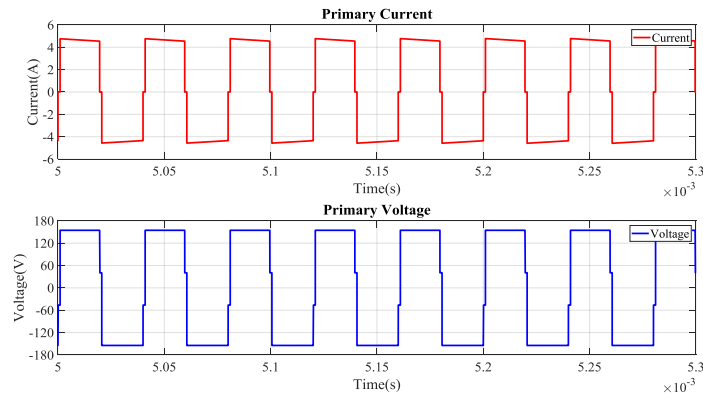


Figure 9. Transformer primary winding voltage and current.

After inducing voltage at secondary, high frequency AC voltage is rectified by the high frequency diode bridge and applied to the load via inductor. Therefore, resulting load voltage and current are given in Fig. 10. The load voltage is obtained as 113.6 V and load current is obtained as 5.6 A.

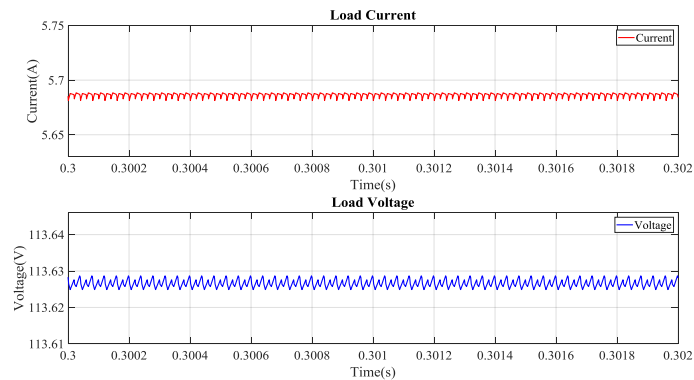


Figure 10. Load voltage and current.

Fig. 11. A graph of the V and I power waveforms of the MOSFET is shown.

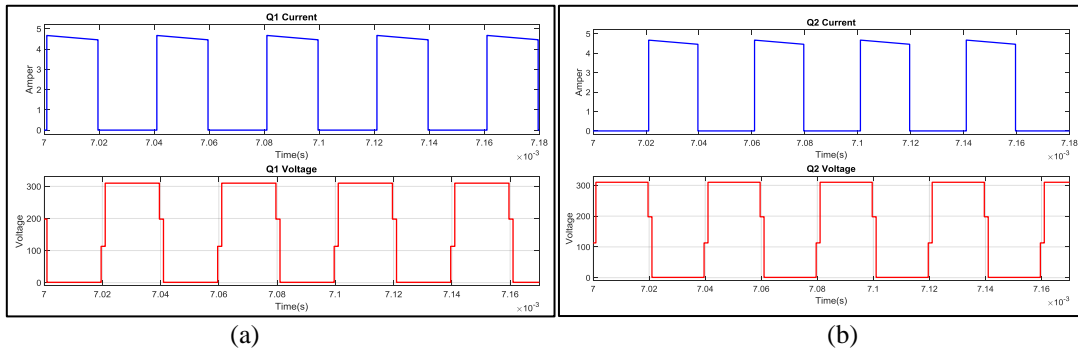


Figure 11. V and I waveforms of the MOSFET. (a) Q1 V and I waveforms, (b) Q2 V and I waveforms.

Simulation study in Matlab/Simulink is also carried out by using Li/Ion battery as a load and the simulation circuit is given in Fig. 12.

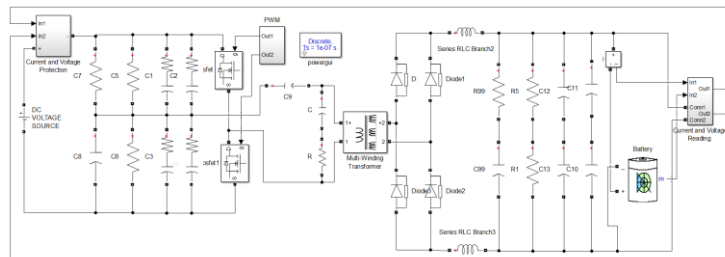


Figure 12. Matlab/Simulink simulation circuit Li/Ion battery as a load.

After the operation of the converter, the battery is charged. To observe the charging situation of the battery, SOC value is observed as given in Fig. 13. It is depicted that the SOC is increasing meaning that the batter is charging.

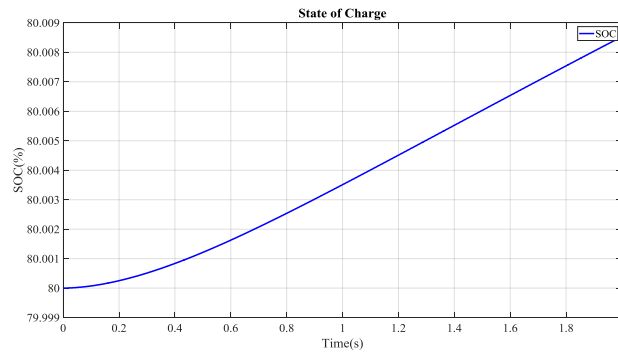


Figure 13. Li/Ion battery state of charge (SOC).

In order to provide charging of Li/Ion battery, there should be enough output voltage as given in Fig 14. In addition, while the charging process with the SOC in Fig 13., the battery draws current from the converter as shown in Fig. 14.

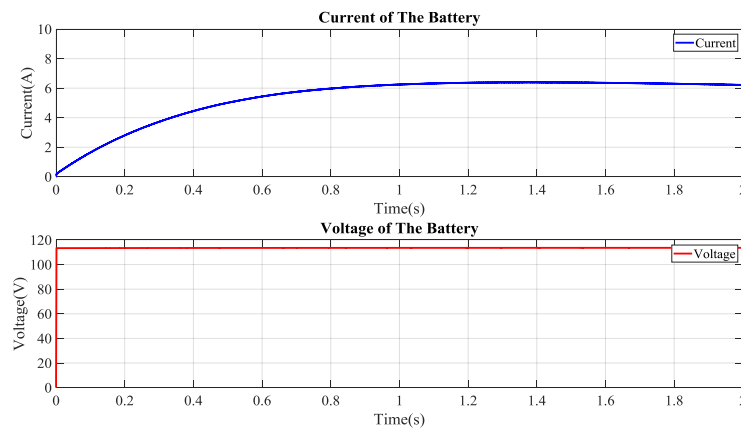


Figure 14. Li/Ion battery voltage and current.

To validate the results conducted with Matlab/Simulink, simulation study is conducted with PSIM software. The simulation circuit of PSIM is given in Fig. 15.

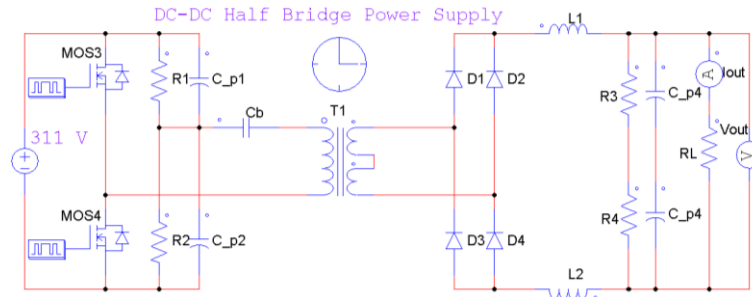


Figure 15. PSIM simulation circuit.

After operation of the converter with a resistor as load in PSIM, the output voltage and current are obtained as given in Fig. 16. It is observed by the simulation the output voltage is 110 V and output current is 6.2 A.

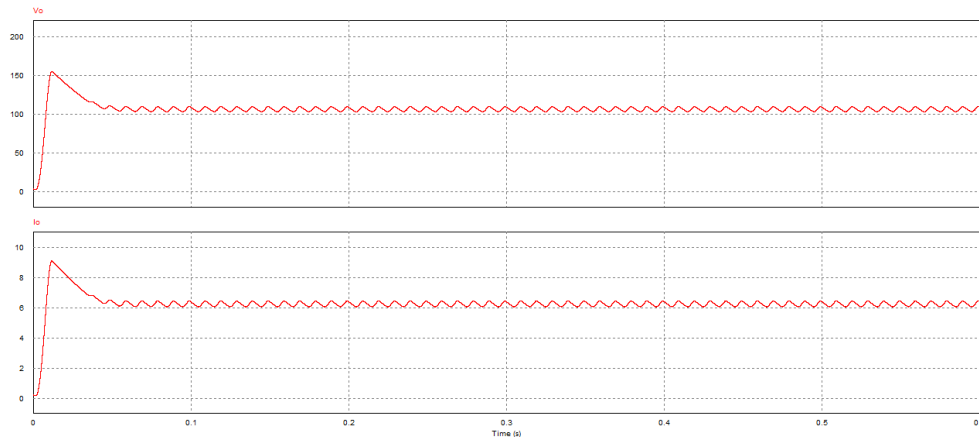


Figure 16. Output voltage and current of the PSIM simulation.

3.4. Material Selection

On the base of simulation studies, application of half bridge DC-DC converter is realized. For the converter, materials used in the application is selected as given in Table .2.

Table 2. Half bridge dc-dc converter material list.

Material	Part Number	Material Values	Size(mm)
C1 and C2	KENDEIL K054006810PM0E050	400V and 680 μ F -40°C-+105°C	(D x L) 35.00 x 50.00

C_B	FARATRONİC C42P2105KBSC400	275VAC and 1μF -40°C-+125°C	(W x H x T) 32.0 x 18.00 x 9.00
D1 and D2	IXYS DSEP15-06A	600V and 15A -55°C-+150°C	TO220AC PACKAGE
Q1 and Q2	IXYS IXTQ460P2	500V and 24A -55°C-+150°C	TO3P PACKAGE

4. EXPERIMENT

Circuit parameters of half bridge DC-DC converter for application are defined as follows.

$$V_{in} = 311V$$

$$V_{out} = 112V$$

$$I_o = 5.5A$$

$$f_s = 25 \text{ kHz}$$

$$\eta = (P_{out} / P_{in}) * 100 = (620.48/697.5) * 100 = \% 88.9$$

In addition, material values for half bridge DC-DC converter are given below.

Magnetic core= ETD54/28/19

Material = N87 EPCOS

Q1 – Q2: IXTQ460P2 - MOSFET DIS.24A 500V, $R_{DS(on)} \leq 270m\Omega$,

Diode: DSEP15-06A (15A 600V) -TO-220AC

Circuit connection diagram of the half bridge DC-DC converter-based battery charger is given in Fig. 17. Charging of the battery takes much time, therefore experiments are conducted by using resistive load and measurements are taken by using resistive load. However, the converter is tested with battery as well. The converter control is realized with open loop structure through IR2153 IC. Furthermore, the IC has dead time generator internally and dead time is set as 1 μs Besides, protection circuit is added with Arduino microcontroller by measuring current and voltage. As a current sensor ACS712 type sensor is used. Voltage is measured with voltage divider.

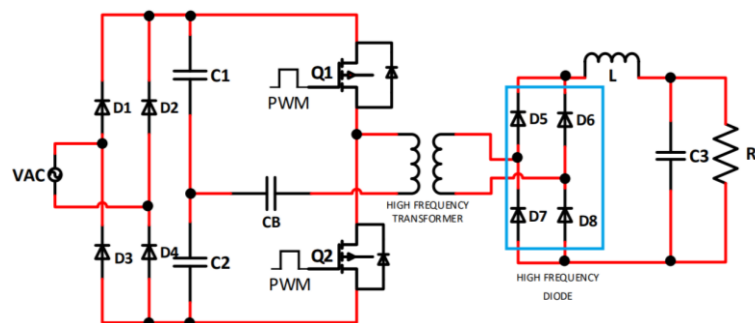


Figure 17. Half bridge DC-DC converter-based charger connections.

The battery charger is installed in the electrical vehicle as shown in Fig. 18, also protection circuit is given in the same figure. The battery pack is connected to the electrical motor of the vehicle in the figure.

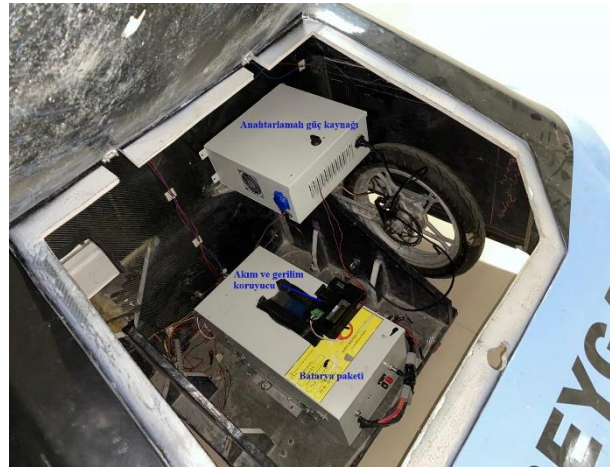


Figure 18. Installation of the battery charger to the electrical vehicle.

Fig. 19 shows the half bridge DC-DC converter-based battery charger circuit feeding resistive load and measurement units. Also, for protection of the battery and the charger, a protection circuit measuring battery current and voltage using Arduino Nano micro controller is done. In addition, an LCD screen is used to visualize battery voltage and current. Fig 19 also shows the measurement results that output voltage and current values of the load with multimeters as 5.54 A output current and 112 V output voltage.



Figure 19. Application setup and measurements.

Fig. 20 shows the output current of the load by oscilloscope. Output current is measured by ACS 712 current sensor and oscilloscope probe is connected to ACS 712 output to measure the output current

waveform. When it is calculated by the oscilloscope measurement results regarding to ACS712 output voltage, output current is approximately obtained as 5.54 A. Instead of using current probe, which is expensive, such way of current measurements is more practical and cheaper. However, in Fig. 20, ACS712 provides analog output as a voltage, this seems confusing. But after calculations regarding to ACS 712 output voltage, output current is found as approximately 5.54 A.

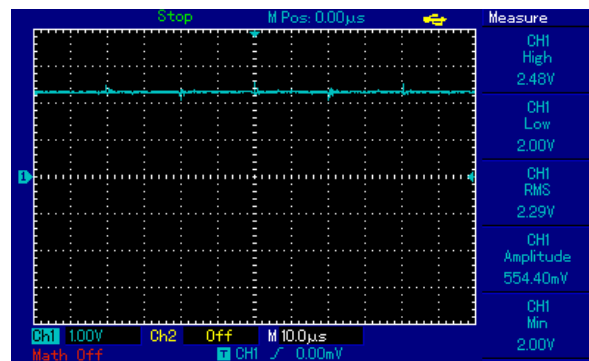
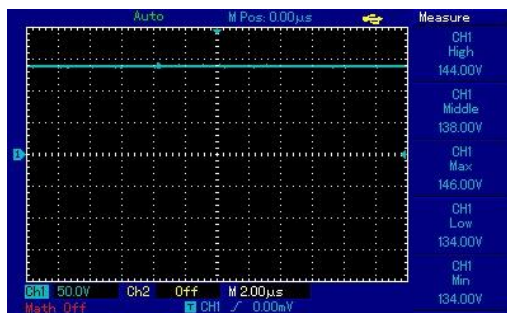
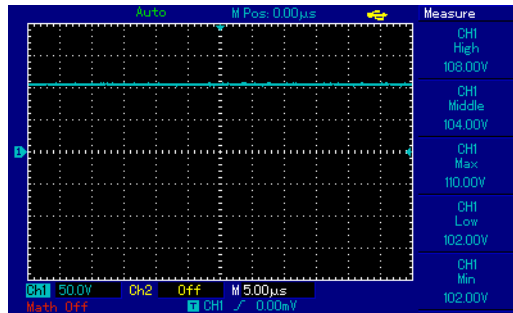


Figure 20. Load current as an output voltage of the ACS 712 current sensor.

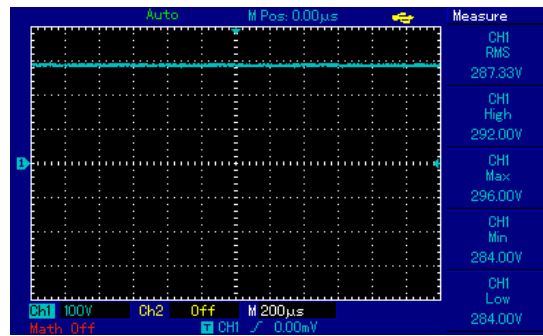
The waveform of the input, output and rectified input voltage of the converter is given in Figure 21. The input voltage is 146 V, the output voltage is 110V and the rectified input voltage is measured as 296 V.



(a)



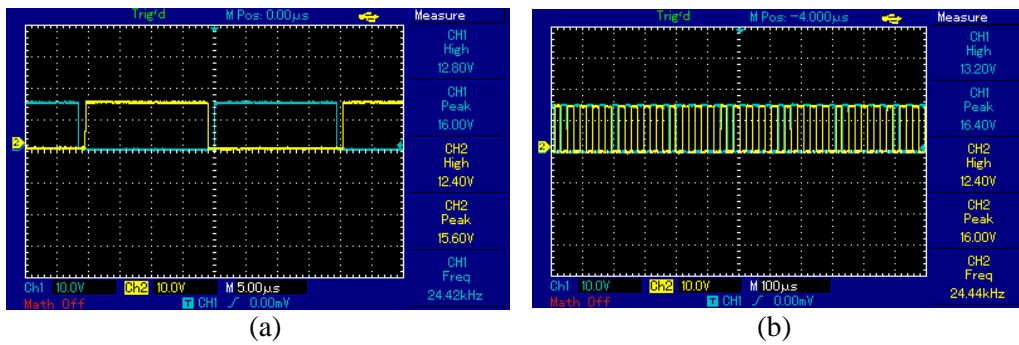
(b)



(c)

Figure 21. Voltage results of half bridge dc to dc converter. (a) Input voltage, (b) Output voltage, (c) Rectified input voltage.

Gate-source PWM signals of Q_1 - Q_2 power switches having $1 \mu\text{s}$ dead time is given in Fig. 22. Similar to the simulation results in Fig. 7, application has also the same waveform.



(a)

(b)

Figure 22. Switching signals of power switches, a) $5 \mu\text{s}$ time scale, b) $100 \mu\text{s}$ time scale.

After applying signals given in Fig 22, the voltage on primary winding is obtained as high frequency square wave and given in Fig. 23. IT is seen that there is no peak value on primary voltage, it is the same waveform as by the simulation results in Fig. 10. So, simulation results prove the application.

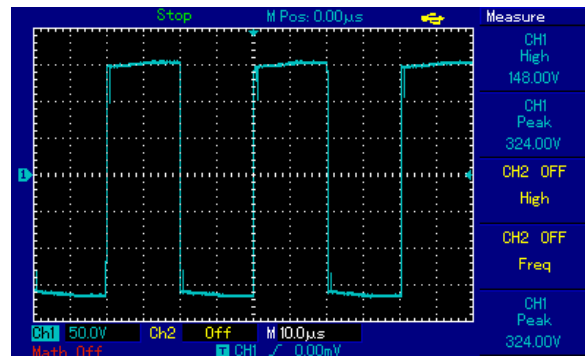


Figure 23. Primary voltage waveform of the converter.

Half bridge DC/DC converter is connected to the sinusoidal grid by diode bridge. The grid voltage and current is shown in Fig 24. It is seen that sinusoidal voltage is obtained, as 220 V. But the grid current is not sinusoidal because of the higher valued capacitor at the DC side.

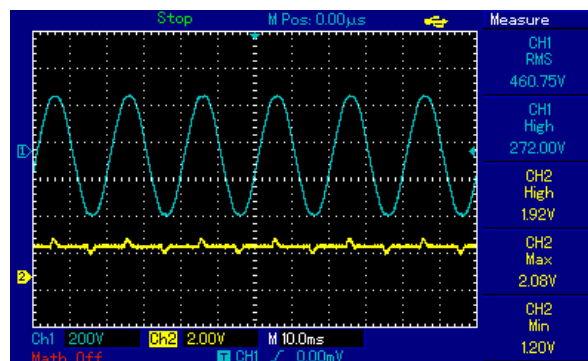


Figure 24. AC voltage and current of the converter under load.

5. DISCUSSION

Design, simulation, and application of battery charge device for electrical vehicle by using half bridge DC-DC converter topology for up to 620 W and its protection system including current and voltage protection is presented in the study. The half bridge DC-DC topology is one of the power converter topologies providing moderate or higher power conversion. By changing turns ratio of high frequency transformer, it ensures lower or higher output DC voltage. In addition, as an advantage of the topology, the converter has two power switches and lower voltage stress on the switches. So, the converter is very convenient as a battery charging device. Therefore, both application and simulations prove assumed results successfully that is charging the Li/Ion battery while ensuring protection. For the simulation, MATLAB/Simulink and PSIM software are used. Simulation results including protection structure approve the applications. [25] presents half bridge DC-DC converter focusing on

power factor correction for battery charging of the electrical vehicle but the protection of the battery is not covered as it presented in the paper. Although, full-bridge and DAB based electrical vehicle battery charger are presented in [26], [27] for higher power, number of switch and voltage stress on the power switches are higher than presented study. [28] presents electrical vehicle charger based on LLC converter, but it does not present battery package structure as it is given presented study and have higher number of power switches increasing cost. However, presented study includes just DC-DC conversion, power factor correction is not a scope of the study. To have higher power factor, another front-end converter is good to be added to have higher power factor as future work.

6. CONCLUSION

In this study, design, simulation, and application of battery charge device for electrical vehicle by using half bridge DC-DC converter topology is presented. Modeling of charge device its control scheme design and evaluation of its performance is conducted by MATLAB/Simulink and PSIM environment. Besides, battery pack consisting of 260 single battery cells used for charging is presented. In experimental study, current and voltage graphs of half bridge DC-DC converter at 620 W full load with 25 kHz switching frequency are obtained and it is observed that the charge device presents desired performance. Besides, protection of the battery pack is provided by using both current and voltage measurements. If the battery draws more than allowable current limit and battery voltage drop is more than maximum voltage, the battery charger stops its operation as a protection which is so important for increasing battery lifetime. Application results of charging and protection are also validated by simulation studies.

Closed loop application by using microcontroller and linear control techniques after modeling the converter is aimed to be conducted as a future study. In order to realize closed loop application, an isolated voltage measurement circuit will also be designed.

ACKNOWLEDGEMENT

This study is supported by the scientific research project entitled with ‘Tubitak Efficiency Challenge Yarış Aracı Atabey Gazi’nin modernizasyonu ve yerleşik şarj birimi tasarımı’ with the number Ü-BAP01/2021-55, by Kastamonu University.

REFERENCES

- [1] Collin, A. J., Djokic, S. Z., Thomas, H. F., and Meyer, J. (2011, October). Modelling of electric vehicle chargers for power system analysis. In *11th International Conference on Electrical Power Quality and Utilisation* (pp. 1-6). IEEE.
- [2] Safayatullah, M. D., Elrais, M. T., Ghosh, S. and Rezaii, R. (2022). A comprehensive review of power converter topologies and control methods for electric vehicle fast charging applications. *IEEE Access*, 10, 40754-40793.

- [3] Khalid, M., Ahmad, F., Panigrahi, B. J., and Al-fagih, L. (2022) A comprehensive review on advanced charging topologies and methodologies for electric vehicle battery. *Journal of Energy Storage*, 53, 105084.
- [4] Oman, H. (1998, November). On-board energy and power management on electric vehicles: effect of battery type. In *17th DASC. AIAA/IEEE/SAE. Digital Avionics Systems Conference. Proceedings (Cat. No. 98CH36267)* (Vol. 2, pp. 143-1). IEEE.
- [5] Martins, L. S., Guimares, L. F., Junior, A. B. B., Tenorio, J. A. S., and Espinoza, D. C. R. (2021) Electric car battery: An overview on global demand, recycling and future approaches towards sustainability. *Journal of Environmental Management*, 295(1), 113091.
- [6] Liaqat, M., Ghadi, Y. Y., Adnan, M. and Fazal, M. R. (2022). Multicriteria Evaluation of Portable Energy Storage Technologies for Electric Vehicles. *IEEE Access*, 10, 64890-64903.
- [7] Kim, T. H., Park, J. S., Chang, S. K., Choi, S., Ryu, J. H., and Song, H. K. (2012). The current move of lithium-ion batteries towards the next phase. *Advanced Energy Materials*, 2(7), 860-872.
- [8] Elmahallawy, M., Elfouly, T., Alouani, A. and Massoud, A. M. (2022). A Comprehensive Review of Lithium-Ion Batteries Modeling, and State of Health and Remaining Useful Lifetime Prediction. *IEEE Access*, 10, 119040-119070.
- [9] Chen, W., Liang, J., Yang, Z., and Li, G. (2021) A Review of Lithium-Ion Battery for Electric Vehicle Applications and Beyond. *Energy Procedia*, 158, 4363-4368.
- [10] Duan, J., Tang, X., Dai, H., Yang, Y., Wu, W., Wei, X., and Huang, Y. (2020). Building safe lithium-ion batteries for electric vehicles: a review. *Electrochemical Energy Reviews*, 3(1), 1-42.
- [11] Umair Ali, M., Hussain Nengroo, S., Adil Khan, M., Zeb, K., Ahmad Kamran, M., and Kim, H. J. (2018). A real-time simulink interfaced fast-charging methodology of lithium-ion batteries under temperature feedback with fuzzy logic control. *Energies*, 11(5), 1122.
- [12] Kılıc, E. (2019). Da-da yükselten dönüştürücü ile elektrikli araç batarya şarj cihazı tasarımı. *Kahramanmaraş Sütçü İmam Üniversitesi Mühendislik Bilimleri Dergisi*, 22(4), 281-287.
- [13] Chéron, E., and Zins, M. (1997). Electric vehicle purchasing intentions: The concern over battery charge duration. *Transportation Research Part A: Policy and Practice*, 31(3), 235-243.
- [14] LaMonaca, S., and Ryan, L. (2022). The state of play in electric vehicle charging services—A review of infrastructure provision, players, and policies. *Renewable and Sustainable Energy Reviews*, 154, 111733.

- [15] Majid, A. (2012). Analysis and implementation of switch mode power supplies in MHz frequency region (Doctoral dissertation, Mid Sweden University).
- [16] Hung, Y. C., Shyu, F. S., Lin, C. J., and Lai, Y. S. (2003, November). New voltage balance technique for capacitors of symmetrical half-bridge converter with current mode control. In *The Fifth International Conference on Power Electronics and Drive Systems, 2003. PEDS 2003.* (Vol. 1, pp. 365-369). IEEE.
- [17] Al-Badrani, H., Ameen, Y. M., and Kadir, M. N. A. (2021, October). An AC/DC switch mode power supply based on half bridge DC/DC converter for low power applications. In *2021 12th International Renewable Energy Congress (IREC)* (pp. 1-6). IEEE.
- [18] Hung, Y. C., Shyu, F. S., Lin, C. J., and Lai, Y. S. (2003, November). Design and implementation of symmetrical half-bridge DC-DC converter. In *The Fifth International Conference on Power Electronics and Drive Systems, 2003. PEDS 2003.* (Vol. 1, pp. 338-342). IEEE.
- [19] Randall Shafer, "Fundamentals of Power Electronics with Matlab", Charles River Media, 1st ed., 2007.
- [20] Armata J.M, Besrest B., Pauly R., "PSIM/MATLAB cosimulation for electrical architectures global models", AES 2005
- [21] Khader, S., Hadad, A., and Abu-Aisheh, A. A. (2011, April). The application of psim and matlab/simulink in power electronics courses. In *2011 IEEE Global Engineering Education Conference (EDUCON)* (pp. 118-121). IEEE.
- [22] Mehar, H. (2013). The case study of simulation of power converter circuits using Psim software in teaching. *American Journal of Educational Research*, 1(4), 137-142.
- [23] Asadi, F., and Eguchi, K. (2021). Power Electronics Circuit Analysis with PSIM®. In *Power Electronics Circuit Analysis with PSIM®*. De Gruyter.
- [24] Muhammad, R. H., Narendra, K., and Ashish, R. K. (2014). Power Electronics Devices, Circuits and Applications. *Pearson Education*.
- [25] Kushwaha, R., and Singh, B. (2022) A Bridgeless Isolated Half-Bridge Converter Based EV Charger With Power Factor Preregulation. *IEEE Transactions on Industry Applications* 58(3), 3967-3976.
- [26] Park, Y., Chakraborty, S. and Khaligh, A. (2022) DAB Converter for EV Onboard Chargers Using Bare-Die SiC MOSFETs and Leakage-Integrated Planar Transformer. *IEEE Transactions on Transportation Electrification* 8(1), 209-224.

- [27] Mendoza-Varela, I. A., Alvarez-Diazcomas, A., Rodriguez-Resendiz, J., and Martinez-Prado, M. A. (2021) Modeling and Control of a Phase-Shifted Full-Bridge Converter for a LiFePO4 Battery Charger. *MDPI Electronics* 10(21), 2568.
- [28] Al-Attar, H., Hamida, M. A., Ghanes, M., and Taleb, M. (2022) LLC DC-DC Converter Performances Improvement for Bidirectional Electric Vehicle Charger Application. *MDPI World Electric Vehicle Journal* 13(1), 2.

NOMENCLATURE

f_s	Switching frequency
P_{out}	Output power
V_{out}	Output voltage
I_{out}	Output current
P_{in}	Input power
I_{in}	Input Current
t_{on}	Conduction Time
A_e	Magnetic core window field
B	Magnetic flux density
S	Cross sectional area
J	Current density
δ	Skin depth
L_{out}	Output coil inductance
V_{dc}	Input voltage
V_o	Output voltage
$V_{c(max)}$	Maximum voltage on switch
$V_{in(max)}$	Maximum input voltage
V_{rms}	Stands for root-mean-square voltage
V_{L1}	Inductor output voltage.
I_p	Primary current
I_L	Inductor current
$I_{L1(pk)}$	Peak Inductor current
$I_{p(avg)}$	Average primary current
$I_{d(max)}$	Maximum drain current
t	Operating mode time
k	Duty cycle
k_{max}	Maximum duty cycle
N_s	Secondary turn number
N_p	Primary turn number
V_{se}	Secondary voltage
T	Period
ΔI	Output current swing difference.
D	Duty rate.
P_o	Output power

P_i	Input power
η	Efficiency
L	Inductor
C	Capacitor
R	Resistance
SOC	State of Charge
PWM	Pulse-Width Modulation
LCD	Liquid-Crystal Display



RESEARCH ARTICLE

**EVALUATION OF CONTROLLER PARAMETERS ON THE TWIN ROTOR MULTIPLE
INPUT MULTIPLE OUTPUT SYSTEM USING BUTTERFLY-BASED PARTICLE SWARM
OPTIMIZATION**

Ali Can ÇABUKER^{1,*}, M. Nuri ALMALI², İshak PARLAR³

¹Van Yuzuncu Yil University, Faculty of Engineering, Department of Electrical and Electronics Engineering, 65080, Van, alicancabuker@gmail.com, ORCID: 0000-0003-2011-2117

²Van Yuzuncu Yil University, Faculty of Engineering, Department of Electrical and Electronics Engineering, 65080, Van, mnal@yyu.edu.tr, ORCID: 0000-0003-2763-4452

³Van Yuzuncu Yil University, Faculty of Engineering, Department of Electrical and Electronics Engineering, 65080, Van, ishakparlar@yyu.edu.tr, ORCID: 0000-0002-3383-8091

Receive Date:02.11.2022

Accepted Date: 02.03.2023

ABSTRACT

Studies on the control of nonlinear systems with metaheuristic algorithms are increasing day by day. It is one of the nonlinear systems in the Twin rotor multiple input multiple output (TRMS) system, which emerged as a prototype of helicopters. This system has two control angles horizontally and vertically. In this study, the yaw and pitch angle control parameters of the TRMS system were found using both traditional and butterfly-based particle swarm optimization (BFPSO) method. In experimental studies, reference values of main propeller and tail propeller angles were tried to be reached in TRMS with fractional order proportional-integral-derivative (FOPID), proportional-integral-derivative (PID) and tilt-integral-derivative (TID) controllers.

Keywords: TRMS, Pitch Angle, Yaw Angle, BFPSO, PID, FOPID, TID.

1. INTRODUCTION

The use of metaheuristic algorithms for systems with nonlinear behavior to reach reference values is gaining momentum today. In the studies carried out, algorithms that give better results are developed, inspired by the behavior changes of animals. These algorithms can be based not only on the behavior of animals, but also on biologically based algorithms such as the immune system. Particle Swarm Optimization (PSO), which is one of the most basic types of swarm optimization, has also been developed over time and has allowed different types of optimization algorithms [1]. Another optimization type created using the PSO algorithm is BFPSO [2, 3]. These optimization types are used in many areas such as renewable energy applications and TRMS systems [4]. In addition to swarm-based optimizations, biological-based algorithms such as genetic algorithms are also used in the control of nonlinear systems [5, 6]. The aim of this study is to estimate the controller coefficients for

nonlinear systems of traditional controllers and metaheuristic optimization methods. Hybrid optimization types have been developed to improve the performance of the two optimization types, usually finding solutions using their populations. With the developed hybrid metaheuristic optimization types, coefficients can be found for control methods such as PID and FOPID. The coefficients obtained can provide a very effective success in the control of non-linear systems such as the twin rotor mimo system. Since non-linear systems are very sensitive, the control coefficient search range should also be found with precision [7, 8].

The remainder of the paper is arranged into several sections. Section 2 introduces configuration and theoretical analysis of the TRMS and BFPSO method. Experimental results of traditional control methods and BFPSO method-based controllers are shown in tables in section 3. Finally, in section 4 draws the main conclusions of the paper.

2. MATERIAL AND METHOD

2.1. TRMS

TRMS, which is produced as a prototype of helicopters, reaches the desired reference angle values with the speed of the DC motors fixed on the ground and on it, unlike the helicopter. When comparing TRMS to helicopter in general terms, TRMS is not capable of flying like a helicopter and does not include cyclic control. Also, in TRMS, a fixed beam determines the equilibrium position.

TRMS is a very difficult device to control due to the coupling dynamics that these angles create against each other, as well as the pitch and yaw angles [9-11]. The TRMS rotor aerodynamics have an angular velocity, which in turn turns the aerodynamic torques. Mechanical-electrical model and experimental setup of TRMS is given in Figure 1.

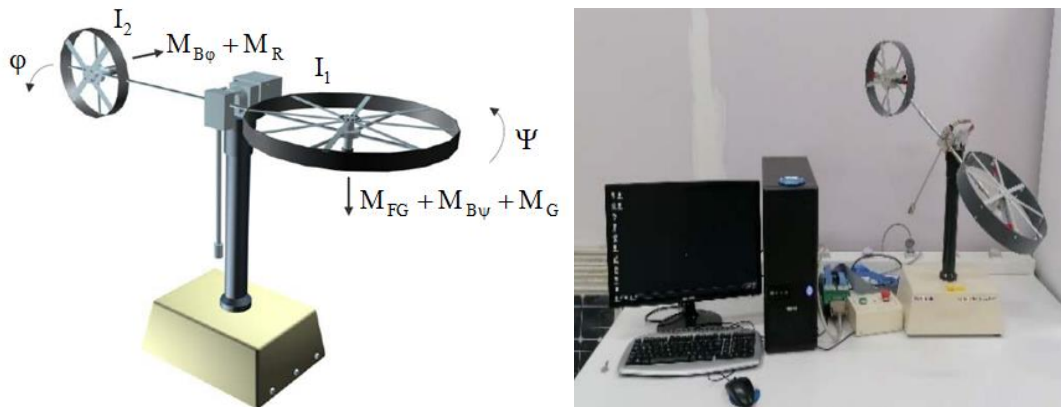


Figure 1. Mechanical-electrical model and experimental setup of TRMS.

The dynamical equations of TRMS are produced based on Newton's second law. The dynamic equation in the vertical plane is given in Eq.1.

$$M_v = J_v \frac{d^2 \alpha_v}{dt^2} \quad (1)$$

M_v is the sum of the moment components and J_v , is the sum of the moments of inertia about the horizontal axis. Moments of the repulsive forces in the horizontal plane as well as in the vertical plane can be expressed as in Eq.2.

$$M_{h1} = l_t F_h(w_t) \cos \alpha_v \quad (2)$$

In Figure 2, the blocks in the system structure of TRMS's main path pitch, main path yaw and coupling dynamics cross path from pitch and cross path from yaw, which are cross-connection dynamics are given [12].

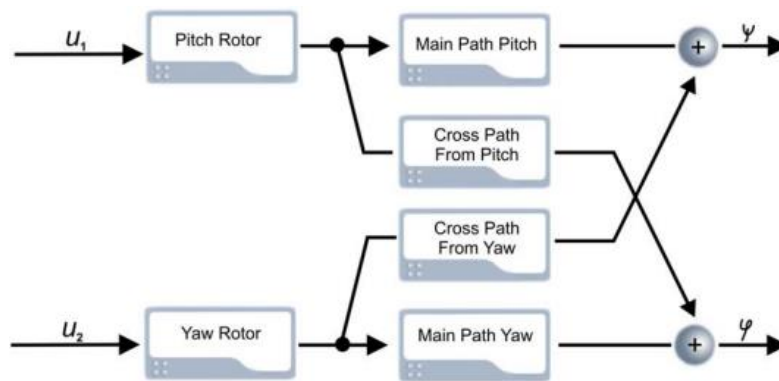


Figure 2. Decoupling Dynamics of TRMS.

The cross-link dynamics shown in Figure 2 cause control difficulties in TRMS, as Pitch and Yaw angles affect each other [13-14]. Transfer function of TRMS was given Eq. 3 and Eq. 4.

$$G_v = \frac{1.359}{s^3 + 0.997s^2 + 4.786s + 4.278} \quad (3)$$

$$G_h = \frac{3.6}{s^3 + 6s^2 + 5} \quad (4)$$

2.2. Particle Swarm Optimization

Particle swarm optimization algorithm is one of the oldest and basic algorithms based on swarm intelligence. It has been used in many applications since its first appearance in 1995. Particle swarm optimization method can be used to solve constrained, nonlinear and multi-objective optimization problems [15, 16]. The flowchart of PSO is given in Figure 3.

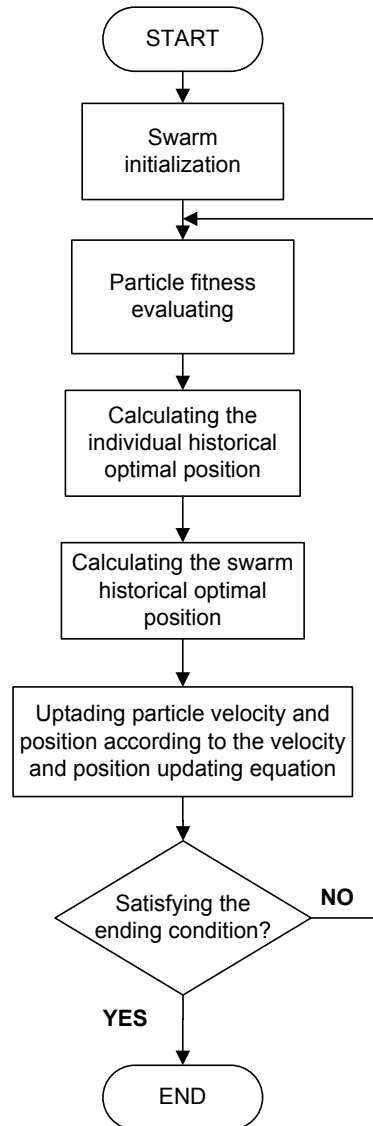


Figure 3. Flowchart of the particle swarm optimization algorithm.

The basic mathematical expressions of particle swarm optimization are given in equations 5 and 6. These equations will be rearranged later for butterfly-based particle swarm optimization;

$$v_{k+1} = w * v_k + c_1 r_1 (pbest_k - currentposition) + c_2 r_2 (gbest_k - currentposition) \quad (5)$$

$$x_{(k+1)} = x_k + V_{k+1} \tag{6}$$

2.3. Butterfly-Based Particle Swarm Optimization

In this study, we used butterfly-based particle swarm optimization, which was developed as a hybrid. Particle swarm optimization (PSO) consists of certain stages. The flow diagram of the BFPSO is given in Figure 4 [17-19].

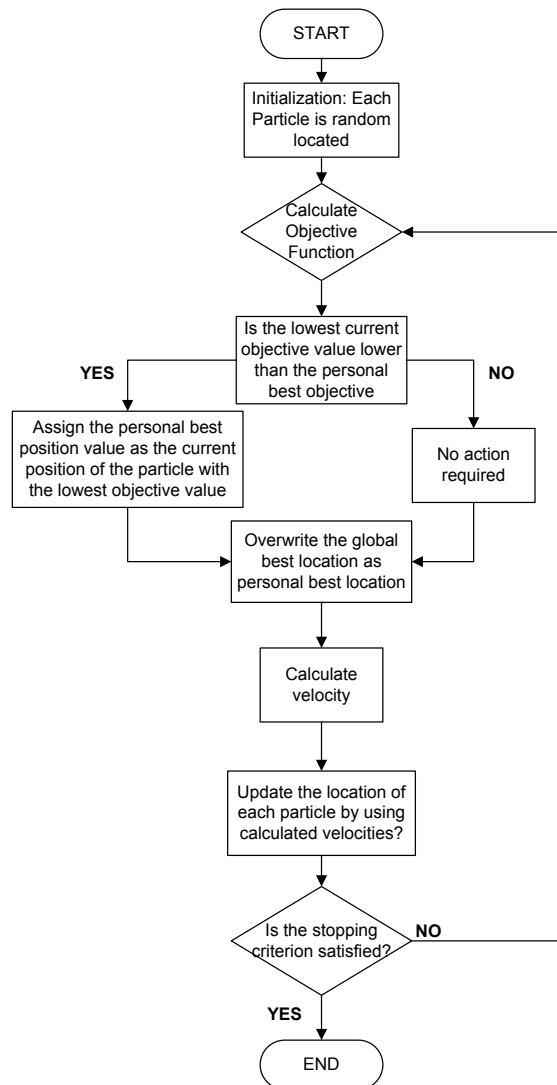


Figure 4. Flow Diagram of the BFPSO.

PSO phases begin by randomly placing each particle in the swarm. An objective function is then calculated for each part, comparing whether the calculated objective value is lower than the particle's personal best. If it is not lower and no action is taken, the personal best position value is assigned as the current position of the particle with the lowest objective value [20-22].

After these actions, the personal best position is updated by overwriting the global best position. Next; the velocity of each particle is calculated, the position of each particle is updated using the calculated velocity. Finally, it is questioned whether the obtained values are sufficient to stop the loop. The velocity and motion formulas of particle swarm optimization are given in Eq.5 and Eq.6.

In equations w is the inertia weight, r_1 and r_2 are two random numbers between (0, 1). c_1 and c_2 are the cognitive and social scaling parameters. However, in order to achieve butterfly-based particle swarm optimization, it is necessary to place the equations of butterfly optimization in the cycle of particle swarm optimization. The velocity equation of the particle swarm optimization is rewritten according to the butterfly optimization. The velocity equation for butterfly-based particle swarm optimization is given in Eq.7.

$$v_{k+1} = w * v_k + S_k(1 - P_k)c_1r_1(pb_{best_k}currentposition) + p_kc_2r_2(gbest_k - currentposition) \quad (7)$$

S_k and P_k are sensivity and probability in the velocity equation are given in Eq. 8 and Eq. 9 [2].

$$s_k = exp - (Iter_{max} - Iter_k)/Iter_{max} \quad (8)$$

$$P_k = FIT_{gbest,k}/-(FIT_{lbest,k}) \quad (9)$$

We choose parameters of BFPSO are $c_1=2$, $c_2=2$, $w=0.8$. $Iter_{max}$ in equation 8 indicates the maximum number of iterations, and $Iter_k$ indicates the number of iterations at the time of the loop and $Iter_{max} = 1000$. In equation 9, FIT_{best} =Fitness of local best solutions, FIT_{gbest} = Fitness of global best solutions [2].

2.4. TID (Tilt-Integral-Derivative) Controller

Introduced as a tilt controller (TID), it provides feedback gain as a function of frequency that is tilted or shaped by the gain frequency of a traditional balancing unit. For the tilt compensator, α is a real number, usually between 2 and 3. The α value in the TID controller optimizes the K_p value [17,24].

The traditional expression of the TID Controller is given in Eq. 10.

$$C(s) = T_iS^{-1} + T_tS^{-1/\alpha} + T_dS \quad (10)$$

The TID controller retains many of the advantages of the traditional PID controller due to its easy of adjustment. Also, the TID controller has three parallel paths with adjustable properties, just like the

general block diagram of the PID controller [25]. The general block diagram of the TID controller is given in Figure 5.

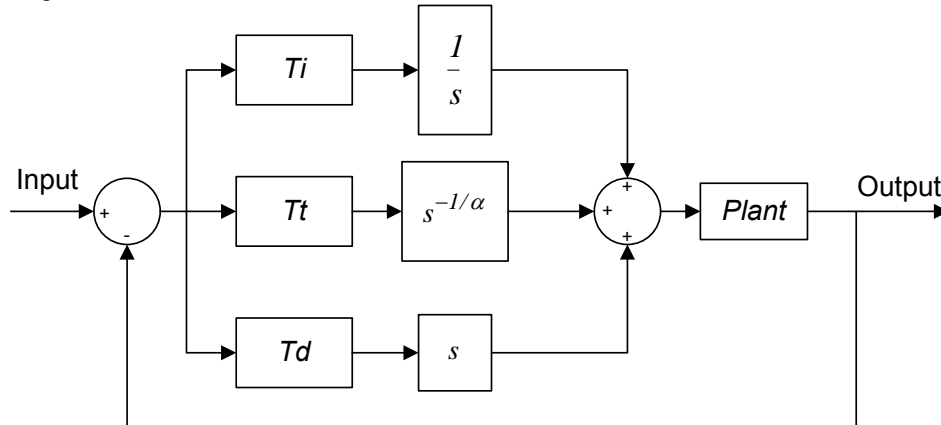


Figure 5. TID Controller general block diagram.

2.5. Fractional Order Proportional Integral Derivative (FOPID)

Fractional Proportional Differential Integral controller (FOPID), unlike classical PID controller, includes fractional degrees in its mathematical equation. Due to this feature, it provides a more effective control of the systems compared to the classical PID controller. Mathematical expression of fractional order PID controller is given in Eq.11.

$$FOPID = Kp + Ki. s^{-\lambda} + Kd. s^{\mu} \quad (11)$$

λ and μ in Eq. 11 represent the fractional power of integral and differential control.

2.6. IAE, ISE, ITAE and ITSE Error Performance

Specific tests are carried out to examine the fault performance of the twin rotor multi-input multi-output system. These tests are integral absolute error (IAE), integral squared error (ISE), integral time squared error (ITSE), and integral time absolute error (ITAE). Mathematical expressions of error performance measures are given in Eq.12-15 [26-28].

$$ISE = \int_0^{\infty} e^2(t)dt \quad (12)$$

$$ITSE = \int_0^{\infty} e^2(t)t dt \quad (13)$$

$$IAE = \int_0^{\infty} |e(t)|dt \quad (14)$$

$$ITAE = \int_0^{\infty} t|e(t)|dt \quad (15)$$

3. RESULTS

In this section, the effects of the coefficients obtained by using traditional control methods and BFPSO method on the controllers are discussed one by one. All experimental results are detailed. The rise time, settling time and overshoot times obtained from the graphs are calculated and presented in tables. Finally, the error performance analyzes between the results obtained with the traditional and BFPSO methods were evaluated. In this way, it can be easily seen how much performance is achieved with the traditional and BFPSO method.

PID, FOPID and TID controllers coefficients obtained by butterfly-based particle swarm optimization are given in Table 1-3.

Table 1. Coefficients of PID controller with BFPSO method.

BFPSO	Kp	Ki	Kd
PIDϕ	0.2354	0.4329	0.3250
PIDψ	0.2175	0.6207	0.3681

Table 2. Coefficients of FOPID controller with BFPSO method.

BFPSO	Kp	Ki	Kd	λ	μ
FOPIDϕ	0.3291	0.2397	0.2470	0.98	1.0295
FOPIDψ	0.1942	0.1563	0.1530	1.0125	0.9755

Table 3. Coefficients of TID controller with BFPSO method.

BFPSO	Kp	Ki	Kd	α
TIDϕ	0.1512	0.4898	0.2248	0.3179
TIDψ	0.1010	0.3838	0.1693	0.8936

PID, FOPID and TID controller coefficients obtained by trial and error method are given in Table 4-6. These coefficients are kept within the boundary conditions in which the TRMS system can operate.

Table 4. Coefficients of traditional PID controller.

Traditional	Kp	Ki	Kd
PIDϕ	3	2.5	1.5
PIDψ	2.5	7.5	10

Table 5. Coefficients of traditional FOPID controller.

Traditional	Kp	Ki	Kd	λ	μ
FOPIDϕ	0.25	0.10	0.05	1.2	1.90

FOPIDψ	0.20	0.10	0.05	1.2	1.8
-------------------------------	------	------	------	-----	-----

Table 6. Coefficients of traditional TID controller.

Traditional	Kp	Ki	Kd	α
TIDϕ	0.20	0.75	0.25	0.5
TIDψ	0.75	0.50	0.25	0.9

The pitch and yaw angles in TRMS were experimentally obtained using the coefficients of BFPSO. Pitch responses of PID, FOPID and TID controllers with BFPSO method and traditional method show in Figure 6.

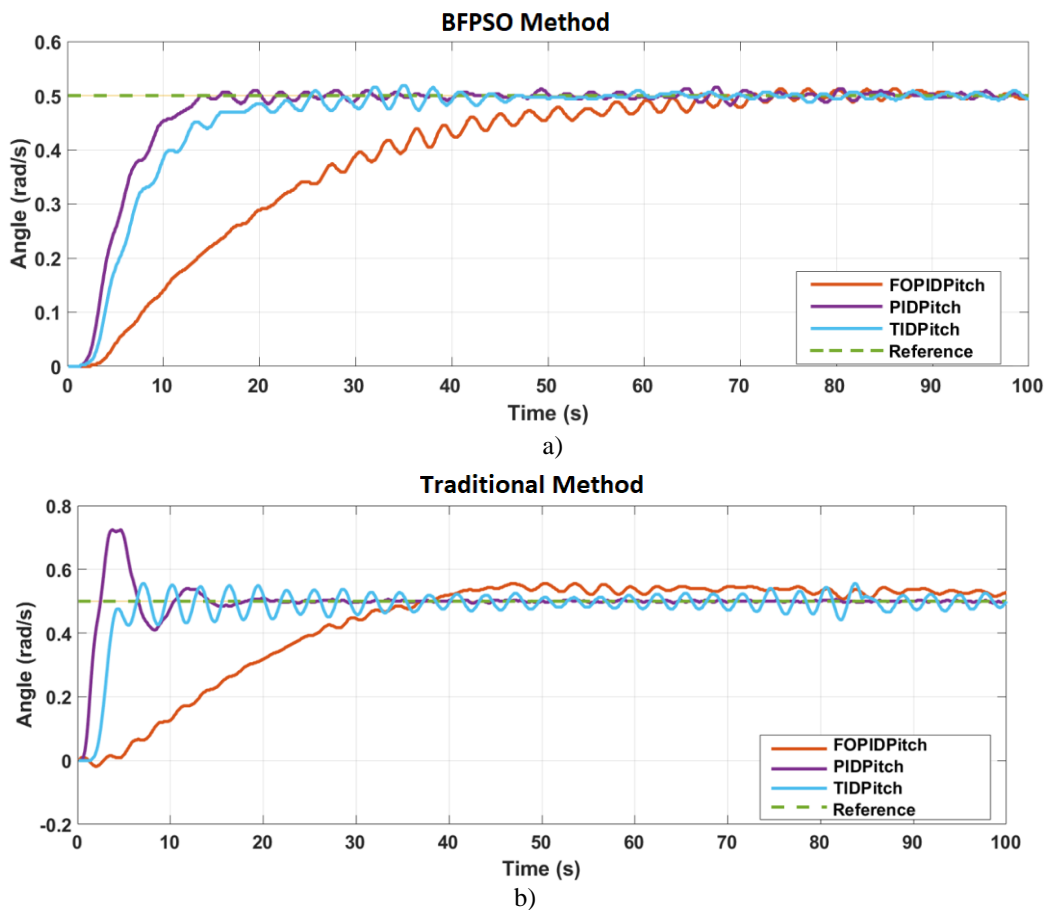


Figure 6. Pitch responses of PID, FOPID and TID controllers a) BFPSO method and b) traditional method.

As can be seen from the graphs obtained by using the coefficients obtained by the BFPSO method, it is seen that the pitch angles on all controllers have significantly improved in the amount of rise, settling and overshoot.

The pitch and yaw angles in TRMS were experimentally obtained using the traditional coefficients. Yaw responses of PID, FOPID and TID controllers with BFPSO method and traditional method show in Figure 7.

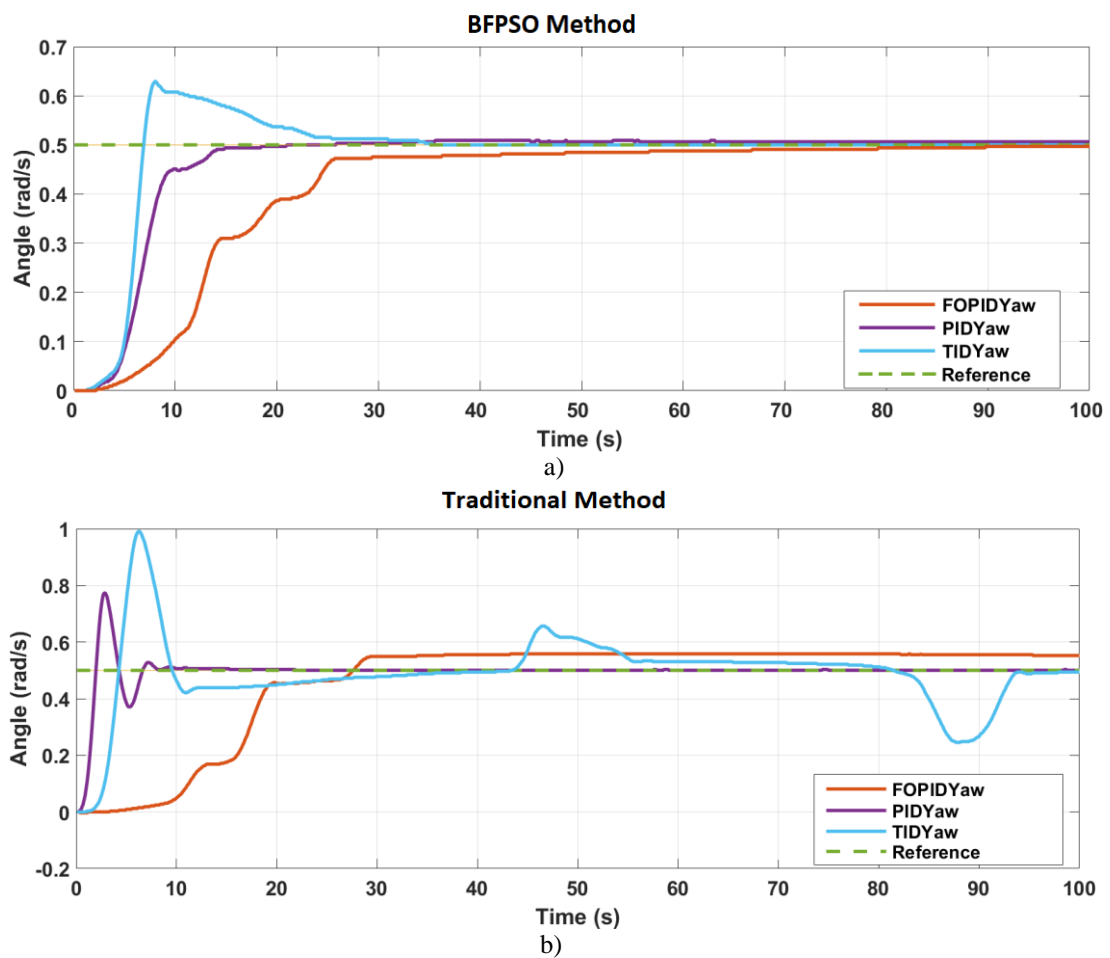


Figure 7. Yaw responses of PID, FOPID and TID controllers a) BFPSO method and b) traditional method.

As can be seen from the graphs obtained by using the coefficients obtained by the BFPSO method, it is seen that the yaw angles on all controllers have significantly improved in the amount of rise, settling and overshoot. It has also been observed that it prevents serious overshoots in yaw angles.

The error performance analyzes of pitch and yaw angles on the PID, FOPID and TID controllers of the coefficients obtained using the BFPSO and traditional method are given in Table 7-8.

Table 7. Error analyzes performance of PID, FOPID and TID controllers with BFPSO method.

BFPSO	ISE	ITAE	IAE	ITSE
PIDϕ	1.42	44.59	4.013	15.75
PIDψ	1.003	31.22	3.192	10.39
FOPIDϕ	2.842	113.8	8.376	113.8
FOPIDψ	3.218	192.1	10.85	175.9
TIDϕ	1.337	27.48	4.062	11.77
TIDψ	1.3	45.4	4.338	28.99

Table 8. Error analyzes performance of traditional PID, FOPID and TID controllers.

Traditional	ISE	ITAE	IAE	ITSE
PIDϕ	0.373	4.429	1.329	1.52
PIDψ	0.4107	14.78	1.796	0.4485
FOPIDϕ	3.49	326.9	11.89	191.7
FOPIDψ	4.26	463.6	16.22	463.5
TIDϕ	1.789	282.9	7.677	68.22
TIDψ	0.716	97.31	3.585	16.77

The rise time, settling time, overshoot and maximum values of the controllers in the yaw and pitch angles with the BFPSO and traditional method are given in Table 9-12.

Table 9. Rise time, settling time, overshoot and maximum values of yaw with BFPSO method.

BFPSO	Rise Time	Settling Time	Overshoot	Maximum Value
PIDϕ	8.4934	22.1729	0.1061	0.5093
FOPIDϕ	20.8403	68.0384	0	0.5000
TIDϕ	2.8283	37.1837	0.1289	0.6289

Table 10. Rise time, settling time, overshoot and maximum values of pitch with BFPSO method.

BFPSO	Rise Time	Settling Time	Overshoot	Maximum
--------------	------------------	----------------------	------------------	----------------

				Value
PID_ψ	8.3709	95.676	0.0154	0.5154
FOPID_ψ	43.4094	88.9760	0.0123	0.5123
TID_ψ	11.5126	99.0780	0.0185	0.5185

Table 11. Rise time, settling time, overshoot and maximum values of yaw angle with traditional method.

Traditional	Rise Time	Settling Time	Overshoot	Maximum Value
PID_φ	1.034	9.474	0.2731	0.7731
FOPID_φ	17.3	28.83	0.0584	0.5584
TID_φ	1.66	93.43	0.4910	0.9910

Table 12. Rise time, settling time, overshoot and maximum values of pitch angle with traditional method.

Traditional	Rise Time	Settling Time	Overshoot	Maximum Value
PID_ψ	1.321	16.87	0.2240	0.7240
FOPID_ψ	27.92	99.04	0.0553	0.5553
TID_ψ	1.71	99.77	0.0553	0.5553

4. CONCLUSION

The computer on which applications are performed on TRMS has i3 2nd generation 8 GB ram and used the TRMS owned by the university and the estimated budget of the TRMS is 250.000 Turkish liras. When the times to reach the reference values are compared; In yaw angles, the rise time was improved with the TID controller 2.8283 seconds, the PID controller 8.4934 seconds, and the FOPID controller 20.84 seconds. While there is a difference of about 6 seconds between the PID controller and the TID controller, the TID controller provides an advantage in rising time and a disadvantage in settling time. The TID controller has a high overshoot, while the PID controller settles to the reference value about 15 seconds ago. For the pitch angle, the PID controller responded faster than the TID controller for about 8 seconds at rise time and 4 seconds at settling time. On the contrary, in terms of overshoot, the FOPID controller performed faster than the other controllers with almost zero overshoot in yaw angle and 0.0123 seconds overshoot in pitch angle despite the slow response.

In the light of the obtained data, it has been observed that the PID controller gives better results than the FOPID and TID controllers for the pitch and yaw angle. In the graph obtained for the pitch angle, it was observed that the controllers could not provide sufficient resistance against the gravity and therefore experienced oscillations while reaching the reference value. It was seen that the most successful response against gravity was obtained with the PID controller. Among the control methods, FOPID was determined to be the controller that gave the slowest response in reaching the reference

value that is why error performance is high and the TID controller responds quickly at rise time, it makes a very slow movement at settling time. Butterfly-based particle swarm optimization gives better results than classical particle swarm optimization in terms of sensitivity and possibilities. High sensitivity prevents overshoot and deterioration in the control of TRMS. Because of that BFPSO was selected for the simulation of TRMS.

ACKNOWLEDGEMENTS

The authors thank the TRMS Application Unit at Van Yuzuncu Yil University Electronics Laboratory for some of the data presented in this article.

REFERENCES

- [1] Kennedy, J. and Eberhart, R. (1995). Particle swarm optimization. In Proceedings of ICNN'95-international conference on neural networks, 4, 1942-1948.
- [2] Bohre, A. K. Agnihotri, G. and Dubey, M. (2014). Hybrid butterfly based particle swarm optimization for optimization problems. In 2014 First International Conference on Networks & Soft Computing, 172-177.
- [3] Bohre, A. K. Agnihotri, G. and Dubey, M. (2015). The butterfly-particle swarm optimization (Butterfly-PSO/BF-PSO) technique and its variables. International Journal of Soft Computing, Mathematics and Control, IJSCMC, 4, 3.
- [4] Mathi, D. K. and Chinthamalla, R. (2020). A hybrid global maximum power point tracking method based on butterfly particle swarm optimization and perturb and observe algorithms for a photovoltaic system under partially shaded conditions. International Transactions on Electrical Energy Systems, 30, 10.
- [5] Agrawal, A. K. (2013). Optimal Controller Design for Twin Rotor MIMO System, Doctoral dissertation.
- [6] Mustapha, S. Fayçal, K. M. and Mohammed, S. (2015). Application of artificial immune algorithm-based optimisation in tuning a PID controller for nonlinear systems. International Journal of Automation and Control, 9, 3, 186-200.
- [7] Ting, T. O. Yang, X. S. Cheng, S. Huang, K. (2015). Hybrid metaheuristic algorithms: past, present, and future. Recent advances in swarm intelligence and evolutionary computation, 71-83.
- [8] Khanduja, N. Bhushan, B. (2021). Optimal design of FOPID Controller for the control of CSTR by using a novel hybrid metaheuristic algorithm. Sādhanā, 46, 2, 1-12.

- [9] TRMS, T. R. M. (2010). System Control Experiments Manuel. 33-949S: Feedback Instruments Ltd. Sussex, UK.
- [10] Tiwalkar, R. G. Vanamane, S. S. Karvekar, S. S. and Velhal, S. B. (2017). Model predictive controller for position control of twin rotor MIMO system. In 2017 IEEE International Conference on Power, Control, Signals and Instrumentation Engineering, ICPCSI, 952-957.
- [11] Chalupa, P. Přikryl, J. and Novák, J. (2015). Modelling of twin rotor MIMO system. Procedia Engineering, 100, 249-258.
- [12] Wijekoon, J. Liyanage, Y. Welikala, S. and Samaranyake, L. (2017). Yaw and pitch control of a twin rotor MIMO system. In 2017 IEEE International Conference on Industrial and Information Systems, ICIIS, 1-6.
- [13] Chaudhary, S. and Kumar, A. (2019). Control of Twin Rotor MIMO system using 1-degree-of-freedom PID, 2-degree-of-freedom PID and fractional order PID controller. In 2019 3rd International conference on Electronics, Communication and Aerospace Technology, ICECA, 746-751.
- [14] Katoch, S. Chauhan, S. S. and Kumar, V. (2021). A review on genetic algorithm: past, present, and future. Multimedia Tools and Applications, 80, 5, 8091-8126.
- [15] Wang, D. Tan, D. and Liu, L. (2018). Particle swarm optimization algorithm: an overview. Soft computing, 22, 2, 387-408.
- [16] El-Shorbagy, M. A. Hassanien, A. E. (2018). Particle swarm optimization from theory to applications. International Journal of Rough Sets and Data Analysis, IJRSDA, 5, 2, 1-24.
- [17] Jaen-Cuellar, A. Y. de J. Romero-Troncoso, R. Morales-Velazquez, L. and Osornio-Rios, R. A. (2013). PID-controller tuning optimization with genetic algorithms in servo systems. International Journal of Advanced Robotic Systems, 10, 9, 324.
- [18] Meena, D. C. and Devanshu, A. (2017). Genetic algorithm tuned PID controller for process control. In 2017 International Conference on Inventive Systems and Control, ICISC, 1-6.
- [19] Khuwaja, K. Tarca, I. C. and Tarca, R. C. (2018). PID controller tuning optimization with genetic algorithms for a quadcopter. Recent Innovations in Mechatronics, 5, 1, 1-7.
- [20] Abukan, Y. Almalı, M. N. Çabuker, A. C. and Parlar, İ. (2022). Determining The PID Parameters of The TRMS System Using PSO. 1ST INTERNATIONAL CONFERENCE ON ENGINEERING AND APPLIED NATURAL SCIENCES, Konya, Türkiye, 10 - 13 Mayıs 2022, 97-102.

- [21] Abdulhussein, K. G. Yasin, N. M. Hasan, I. J. (2021). Comparison between butterfly optimization algorithm and particle swarm optimization for tuning cascade PID control system of PMDC motor. *International Journal of Power Electronics and Drive Systems*, 12, 2, 736.
- [22] El Hajjami, L. Mellouli, E. M. Berrada, M. (2019). Optimal PID control of an autonomous vehicle using Butterfly Optimization Algorithm BOA. In *Proceedings of the 4th international conference on big data and internet of things*, 1-5.
- [23] Esgandanian, A. and Daneshvar, S. (2016). A comparative study on a tilt-integral-derivative controller with proportional-integral-derivative controller for a pacemaker. *International Journal of Advanced Biotechnology and Research, IJBR*, 7, 3, 645-650.
- [24] Aidoud, M. Feliu-Battle, V. Sebbagh, A. Sedraoui, M. (2022). Small signal model designing and robust decentralized tilt integral derivative TID controller synthesizing for twin rotor MIMO system. *International Journal of Dynamics and Control*, 1-17.
- [25] Lurie, B. J. (1994). Three-parameter tunable tilt-integral-derivative (TID) controller.
- [26] Yusoff, W. A. W. Yahya, N. M. and Senawi, A. (2006). Tuning of Optimum PID Controller Parameter Using Particle Swarm Optimization Algorithm Approach. *Fakulti Kejuruteraan Mekanikal University Malaysia Pahang*.
- [27] Faisal, R. F. and Abdulwahhab, O. W. (2021). Design of an adaptive linear quadratic regulator for a twin rotor aerodynamic system. *Journal of Control, Automation and Electrical Systems*, 32, 2 404-415.
- [28] Bahramipour-Esfahani, R. Nasri, M. Tabatabaei, S. M. (2021). Designing a Metaheuristic Multi-objective Fractional-order PID Controller for TRMS system. *Computational Intelligence in Electrical Engineering*, 12, 2, 91-112.

APPENDIX I

Table 13. TRMS nonlinear model parameters [7].

Parameters	Value
I_1 - Moment of inertia of pitch rotor	$6,8 \cdot 10^{-2} kg \cdot m^2$
I_2 - Yaw rotor moment of inertia	$2 \cdot 10^{-2} kg \cdot m^2$
a_1 - Static characteristic parameter	0,0135
b_1 - Static characteristic parameter	0,0924
a_2 - Static characteristic parameter	0,02
b_2 - Static characteristic parameter	0,09
M_G - Gyroscope momentum	0,32 Nm
$B_{1\psi}$ - Friction momentum function parameter	$6 \cdot 10^{-3} Nm/rad$
$B_{2\psi}$ - Friction momentum function parameter	$1 \cdot 10^{-3} Nm/rad$
$B_{1\varphi}$ - Friction momentum function parameter	$1 \cdot 10^{-1} Nm/rad$

$B_{2\phi}$ - Friction momentum function parameter	$1 \cdot 10^{-2} Nm/rad$
K_{gy} - Gyroscope momentum parameter	$0,05 rad/s$
k_1 - 1. Engine gain	1,1
k_2 - 2. Engine gain	0,8
T_{11} - 1. Engine denominator parameter	1,1
T_{10} - 1. Engine denominator parameter	1
T_{21} - 2. Engine denominator parameter	1
T_{20} - 2. Engine denominator parameter	1
T_p - Cross-reaction momentum parameter	2
T_0 - Cross-reaction momentum parameter	3,5
k_c - Cross-reaction momentum gain	-0,2



RESEARCH ARTICLE

A HYBRID MODIFIED SUBGRADIENT ALGORITHM THAT SELF-DETERMINES THE PROPER PARAMETER VALUES

Tuğba SARAÇ¹, Büşra TUTUMLU^{2,*}, Emine AKYOL ÖZER³

¹Eskişehir Osmangazi University, Faculty of Engineering and Architecture, Industrial Engineering Department, Eskişehir, tsarac@ogu.edu.tr, ORCID: 0000-0002-8115-3206

^{2*}Kütahya Dumlupınar University, Faculty of Engineering, Industrial Engineering Department, Kütahya, busra.tutumlu@dpu.edu.tr, ORCID: 0000-0002-0662-8128

³Eskişehir Teknik University, Faculty of Engineering, Industrial Engineering Department, Eskişehir, emineakyol@eskisehir.edu.tr, ORCID: 0000-0002-9570-2886

Receive Date: 13.11.2022

Accepted Date: 10.03.2023

ABSTRACT

A successful solution algorithm for non-convex optimization problems is the Modified Subgradient Algorithm (MSGa), which solves dual problems based on the sharp augmented lagrangian function. However, its performance highly depends on its parameter values, and determining the appropriate parameter values is difficult as they can be completely different for each problem. In this study, a new hybrid solution approach that a tabu search algorithm to find the appropriate MSGa parameter values and the MSGa algorithm run together is proposed. Although it seems like a contradiction to use an algorithm that also has its parameters to determine the most appropriate parameter values of an algorithm, this contradiction is eliminated by fixing the parameter values of the tabu search algorithm. The proposed algorithm does not need appropriate values of any algorithm parameter. It can find appropriate parameter values for each problem itself starting with the same fixed initial values. To show the success of the developed algorithm, especially on 0-1 quadratic problems, it is compared with the classical MSGa algorithm by using the quadratic knapsack test instances taken in the literature. According to the obtained solutions, the superiority of the hybrid algorithm has been demonstrated.

Keywords: *Modified Subgradient Algorithm (MSGa), Tabu Search Algorithm, Quadratic Knapsack Problem.*

1. INTRODUCTION

Lagrangian relaxation and subgradient algorithms have been widely applied to integer or mixed integer programming problems. However, classic Lagrangian techniques often result in a duality gap and generally cannot determine the optimum value of the primal integer optimization problems, such as the quadratic 0-1 problems that are non-convex [1].

Recently, a considerable amount of literature has been published on different augmented Lagrangian duality methods that can eliminate the duality gap in most non-convex problems and obtain good solutions. The MSGA is developed by Gasimov [2], and then, a general version of the algorithm including generalized augmented Lagrangian dual problems is presented by Gasimov and Rubinov [3]. They applied this algorithm to a different kind of optimization problem. Gasimov and Ustun [4] demonstrated the performance of the MSGA for non-convex 0-1 quadratic assignment problems. Gasimov and Ustun [5] focussed on a generalized version of the algorithm to handle sharp augmented Lagrangian dual problems. In another study, Burachik et.al. [6] developed an inexact version of the algorithm that could obtain solutions to the problems with less computational time. Sipahioglu and Saraç [7] examined the algorithm's performance for QKP with an inequality constraint. To solve a general portfolio optimization problem, Ustun and Kasimbeyli [8] applied the feasible value-based modified subgradient (F-MSG) algorithm, which is a generalized version of the MSGA. Ulutas and Sarac [9], handled a multi-period facility layout problem where the sum of material handling and re-layout costs are minimized. They proposed the MSGA for this problem and determined its parameters of MSGA by using the design of the experiment. In another study, Ozcelik and Sarac [10] addressed the cell formation problem with alternative part routes to minimize the weighted sum of the voids and the exceptional elements. They proposed a hybrid genetic algorithm based on MSGA. Takan and Kasimbeyli [11] developed a new hybrid subgradient algorithm for solving the capacitated vehicle routing problem. In another recent study conducted by Bulbul and Kasimbeyli [12], a new version of the aircraft maintenance routing problem is addressed. The authors proposed a hybrid solution approach for this problem, which hybridized the F-MSGA and the ant colony optimization metaheuristic. As can be seen from these studies, MSGA is a successful solution method that is widely used in solving discrete problems with linear or quadratic objective functions. However, two difficulties can be encountered when using this algorithm. The first is that solving the dual problem can be very difficult. So, the studies on the MSGA in the literature in which the hybrid solution approach is suggested have generally focused on the solution of the dual problem and used metaheuristic algorithms to solve the dual problem. However, another important issue affecting the performance of the MSGA is the determination of appropriate parameter values. In the literature, only one study [9] has been accessed to determine the parameters of the MSGA by using the experimental design method.

The design of the experiment is usually used for determining the parameter sets of the algorithms to improve the solutions in the literature. However, it has two important disadvantages: (1) the success of the parameter set depends on the problem type so for each test instance the parameter sets must be redetermined by resolving it for each parameter combination in the experiment plan (2) in the design of experiment, parameter values are the factor levels so only a few predefined values are available for every parameter and combinations of these levels can be examined. In fact, the optimum values of the parameters may not be one of these levels.

In this study, a new hybrid solution approach that a tabu search algorithm (TSA) to find the appropriate MSGA parameter values and the MSGA run together is proposed. Although at first glance, it seems like a contradiction to use an algorithm with parameters to determine the most appropriate parameter values of an algorithm, this is eliminated by fixing the parameter values of TSA. Different from the design of the experiment, the developed algorithm has two significant

advantages: (1) The TSA searches the appropriate parameter values for each instance automatically, and (2) The parameter values are not selected among only a few predefined numbers, the algorithm searches the appropriate values in a very large set. So, the optimum values can be obtained. To show the performance of the hybrid algorithm, it is compared with the classical MSGA by using the quadratic knapsack problem instances taken from the literature.

The remainder of this study is organized as follows. In the following section, the hybrid solution approach is introduced. TSA and the proposed hybrid algorithm are explained, respectively. Quadratic knapsack problems which are used for testing the hybrid algorithm's performance and test results are given in the third section. In the last section, conclusions are presented.

2. HYBRID SOLUTION APPROACH

In this section, the proposed solution approach combining the MSGA and a TSA, to find the appropriate parameter values of the MSGA is explained in detail. Before the steps of the algorithm, MSGA and the TSA are explained in the following sub-sections.

2.1. Modified Subgradient Algorithm

The MSGA can be applied to non-convex problems with the equality constraint. For non-convex problems, using the classical Lagrangian method can result in a non-zero duality gap. However, this problem can be eliminated by using the sharp-augmented Lagrangean function. It is proven that when the objective and constraint functions are all Lipschitz then the sharp augmented Lagrangean guarantees the zero-duality gap [2]. The algorithm has many other remarkable features. In the primal problem, it is not required convexity or differentiability conditions and the penalty parameter. This means, when the parameters are selected accurately, the optimal value can be found with the MSGA. So, the success of the MSGA depends on the selection of parameter values. The MSGA is briefly as follows:

$$\min P = \min_{x \in S} f(x) \quad (1)$$

$$\text{subject to } g(x) = 0 \quad (2)$$

P represents the primary problem. ($f: X \rightarrow R$, $g: X \rightarrow R^n$) S is a compact subset of X . The sharp-augmented Lagrangean function (L) associated with P is given in Eq. (3) ($L: S \times R^n \times R_+ \rightarrow R$):

$$L(x, u, c) = f(x) + c \|g(x)\| - \langle g(x), u \rangle \quad (3)$$

Where, $\|g(x)\|$ is the Euclidean-Norm of $g(x)$. $\langle g(x), u \rangle$ is the Euclidean Inner-Product on R^n . c and u are the dual variables. $H(u, c)$ is the dual function. (P^*) dual the problem of (P).

$$H(u, c) = \min_{x \in S} L(x, u, c), \quad \text{for } u \in R^n, \text{ and } c \in R_+ \quad (4)$$

$$(P^*) \quad \max_{(u,c) \in R^n \times R_+} H(u, c) \quad (5)$$

The steps of the MSGA are given below:

Step 0. Select $(u_1, c_1) \in R^n \times R_+$ and $k=1$.

Step 1. Solve the sub-problem with Lagrange multipliers (u_k, c_k) .

$$(P) \quad \underset{x_k \in S}{\text{Minimize}} \quad f(x_k) + c_k \|g(x_k)\| - \langle u_k, g(x_k) \rangle \quad (6)$$

$$\text{subject to} \quad f(x_k) + c_k \|g(x_k)\| - \langle u_k, g(x_k) \rangle \leq \bar{H} \quad (7)$$

If $\|g(x_k)\| \neq 0$ for the obtained solution x_k , x_k is not a feasible solution for (P), go to *Step 2*, if $\|g(x_k)\| = 0$, x_k is a feasible solution for (P) and (u_k, c_k) is a solution to (P*) STOP.

Step 2. Calculate (u_{k+1}, c_{k+1}) values by using the formulas in Eq. (8) and go to *Step 1*.

$$u_{k+1} = u_k - \alpha s_k g(x_k), \quad c_{k+1} = c_k + (1 + \alpha) s_k \|g(x_k)\| \quad (8)$$

Here, s_k denote positive scalar step size and it can be calculated by the formula in Eq. (9).

$$s_k = \frac{\delta \alpha (\bar{H} - L(x_k, u_k, c_k))}{(\alpha^2 + (1 + \alpha)^2) \|g(x_k)\|^2} \quad (9)$$

Where, \bar{H} is an upper bound value in the (P*) and δ is a step size parameter. $\alpha > 0$ and $0 < \delta < 2$.

Parameters of step size formulation (9) are \bar{H} , α and δ . Selecting the values for these parameters is important for the success of the MSGA. In the following two sections, it is explained how the values of these parameters are determined.

2.2. Tabu Search Algorithm

The TSA is a metaheuristic originally developed by Glover, which has been successfully applied to a variety of combinatorial optimization problems [13]. In this algorithm, to escape from local optimal, it also accepts unimproved solutions when not all neighborhoods are improved. It is briefly a single-solution-based metaheuristic that is used to explore a search space beyond local optimization, guided by a local search algorithm. The feature that distinguishes it from other algorithms is that the successive moves are limited by keeping them in a list to prevent the algorithm from repeatedly visiting the same solutions. The list in which successive moves are kept is called the *Tabu List (TL)*. *TL* operates with short-term memory and this memory is updated in each iteration. It is very critical for the performance of the TSA. Another critical feature is the *aspiration criterion*. If a move leads to a better solution than the current solution, that is, if it is a good move, but it is available in the *TL*, this

move is removed from the TL and the move is allowed thanks to the aspiration criterion. For this reason, diversity is ensured in the algorithm by allowing previously the tabu moves.

In TSA, another important term is tabu list size. It determines how long a move will remain in the tabu list. Accordingly, when the number of tabu moves reaches the tabu list size, the oldest element in the tabu list is removed from the list. Thus, the tabu list has an innovative memory structure. The steps of the basic TSA are given below:

Step 1. Determine the TSA parameter values (Tabu list size (s), number of iterations(t), the structure of the neighborhood etc.)

Step 2. Generate a feasible initial solution (x). Define this solution as the best-obtained solution and an empty tabu list ($x^*=x, TL=\{\}$).

Step 3. Generate a feasible new solution (x') by applying a move that except the tabu move in the TL or ensure the aspiration criterion in the TL

Step 4. Update the TL and the current solution ($x=x', TL=\{move_{xt}\}$)

Step 5. If the tabu list size is equal to s , delete the oldest element from the tabu list.

Step 6. If the current solution is better than the best-obtained solution, update the best-obtained solution ($x^*=x$).

Step 7. If the termination criterion is met, stop. If not, update the t ($t=t+1$) and return to *Step 3*.

The parameters of the TSA are described and their fixed values are given below.

Neighbour generation scheme: There are 3 parameters we try to find their proper values. By adding a certain amount ($\Delta_1, \Delta_2, \Delta_3$) to the current parameter values (\bar{H}, α, δ) or by reducing a certain amount from the current parameter values, 6 neighbors ($\bar{H}-\Delta_1, \bar{H}+\Delta_1, \alpha-\Delta_2, \alpha+\Delta_2, \delta-\Delta_3, \delta+\Delta_3$) are obtained in each iteration.

Tabu list size: The tabu list size is fixed to six.

Termination criterion: This parameter decides how many iterations are allowed. It is fixed to 30.

2.3. Hybrid MSGA

In this section, the steps of the developed algorithm are given.

Step 0. Determine the maximum iterations number ($IMAX$). And select the maximum number of updates of the dual variables allowed ($KMAX$). Set the initial parameter values of MSGA as $\bar{H}=0, \alpha=5, \delta=1$ and set the certain amounts (adding to the parameters or reducing from the parameters) as ($\Delta_1=500, \Delta_2=1, \Delta_3=0.2$).

Step 1. Generate the 6 neighbors $(\bar{H} - \Delta_1, \bar{H} + \Delta_1, \alpha - \Delta_2, \alpha + \Delta_2, \delta - \Delta_3, \delta + \Delta_3)$ of the current parameter values. If $\delta - \Delta_3 \leq 0$ or $\delta + \Delta_3 \geq 2$ add this neighbor to the tabu list. If all generated neighbors are in the tabu list go to *Step 4*. Otherwise, compute the objective function for each neighbor, which is not in the tabu list, by using the MSGA. To solve the problem, repeat *Step 1.0-Step 1.2* for all neighbors.

Step 1.0. Select a vector (u_1, c_1) as zero vector. Let $k = 1$.

Step 1.1. Solve the sub-problem with Lagrange multipliers (u_k, c_k) .

$$\underset{x \in S}{\text{Minimize}} f(x) + c_k \|g(x)\| - \langle u_k, g(x) \rangle \quad (10)$$

$$\text{subject to } f(x) + c_k \|g(x)\| - \langle u_k, g(x) \rangle \leq \bar{H} \quad (11)$$

In this problem, x_k is the global solution. If $\|g(x_k)\| = 0$, or $k \geq KMAX$ then go to *step 2*. x_k is a solution to (P) and (u_k, c_k) is a solution to (P^*) . If $\|g(x_k)\| \neq 0$, go to *Step 1.2*.

Step 1.2. Calculate the dual variables u_{k+1} and c_{k+1} by using formulation (3) and calculate step size by using formulation (8). $k = k + 1$ and repeat *Step 1.1*.

Step 2. If $\|g(x_k)\| = 0$ for any neighbor, $f(S^*)$ and S^* are the objective function value and the relevant parameter values of the best neighbor and go to *Step 3*. If $\|g(x_k)\| \neq 0$, go to *Step 4*.

Step 3. Set the best neighbor (S^*) as move and memorize it ($S := S^*$) if $f(S^*) < f(S)$ and update the *TL* and go to *Step 5*.

Step 4. If $k \geq KMAX$ for all neighbors then $KMAX = KMAX + 10$. Divide all the Δ_i 's by 2 and then delete all the moves from the *TL*. Go to *Step 5*.

Step 5. If the number of iterations is equal to *IMAX*, stop and the best solution is S^* . If not equal, increase the number of iterations by 1 and go to *Step 1*.

3. COMPUTATIONAL RESULTS

Quadratic knapsack test problems, their optimal solutions are known, have been used to demonstrate the effectiveness of the hybrid algorithm. First, all test problems are solved with MSGA using the same initial parameter values for \bar{H} , α and δ . Then, the test problems have been also solved with the hybrid algorithm using the same initial parameter values. Thus, it is aimed to show how much the solution performance can be increased by intelligently determining the \bar{H} , α and δ parameters of the MSGA with the hybrid algorithm. Before discussing the computational results, the quadratic knapsack problem to be used in testing the algorithm is explained in the following sub-section.

3.1. Quadratic Knapsack Problem

The knapsack problem (KP) is one of the well-known combinatorial optimization problems. It consists of selecting from a finite set of given objects in such a way that a linear function of selected objects is maximized while a set of knapsack constraints are satisfied.

The Quadratic Knapsack Problem (QKP) is given as follows:

$$(QKP) \quad \max z = \sum_{i=1}^n p_i x_i + \sum_{i=1}^{n-1} \sum_{j=i+1}^n p_{ij} x_i x_j \quad (12)$$

$$\text{subject to } \sum_{i=1}^n w_i x_i \leq a \quad (13)$$

$$x_i, x_j \in \{0,1\}, i, j = 1, \dots, n \quad (14)$$

Objective (12) is maximizing the total profit. If object i is chosen to knapsack, its profit (p_i), and if object j is also selected with it, additional profit (p_{ij}) is also earned. Total profit contains both kinds of profits. Constraint (13) guarantees that the total weights of the selected objects do not exceed the knapsack capacity. Constraint (14) is the sign constraint of decision variables.

In the first step of the hybrid solution approach, QKP should be transformed into a continuous form. The continuous nonlinear formulation of the problem with equality constraints (CNP) is given in below:

$$(CNP) \quad \min z = -\sum_{i=1}^n p_i x_i - \sum_{i=1}^{n-1} \sum_{j=i+1}^n p_{ij} x_i x_j \quad (15)$$

$$\text{subject to } \sum_{i=1}^n w_i x_i + \text{slack} - a = 0 \quad (16)$$

$$\sum_{i=1}^n (x_i - x_i^2) = 0 \quad (17)$$

$$0 \leq x_i \leq 1 \quad i = 1, \dots, n, \quad \text{slack} \geq 0 \quad (18)$$

The maximization objective function was transformed to the minimization which is given in equation (15). Capacity constraint (16) was converted to equality constraint with the help of a slack variable. To transform binary variables into a continuous form, a specific constraint (17) which was developed by Li [14] is used. Constraint (18), is the sign constraint of decision variables.

3.2. Test Results

In this section, ten QKP examples in the literature are used to compare the proposed hybrid algorithm with the classical MSGA. All instances have been solved using MSGA parameters and GAMS solver Minos on the HP6000 workstation. Obtained solutions and times are reported and compared. The n and d values are used to define the structure of the test problems. (n : The number of available objects, d : density or percentage of non-zero p_{ij}) The test instances have 100 objects with a density of 0.25.

The optimal solutions for these test instances have been known as all instances have been solved to optimal by Billionnet and Soutif [15] and the related website (<http://cedric.cnam.fr/~soutif/QKP/>) reports their optimum values.

The test problems have been solved with the parameter values given in Table 1.

Table 1. Test results.

Parameter	Value
s	6
$IMAX$	500
$KMAX$	30
$(\bar{H}, \alpha, \delta)$	(0, 5, 1)
$(\Delta_1, \Delta_2, \Delta_3)$	(500, 1, 0.2)

We solve all the test problems by using both MSGA and hybrid algorithm. To show the performance of the hybrid algorithm, we utilized percentage gap ($G\%$) which is indicate a gap between the optimal solution and solution of the MSGA/hybrid algorithm. The formulation of the gap is given in (19) and the results of test problems are given in Table 2.

$$Gap (G\%) = \frac{100 \times (value - opt.value)}{opt.value} \quad (19)$$

The optimum values of each instance are given in the first column. The second, third and fourth columns show the obtained objective value, gap ($G\%$) and solution time in seconds using the MSGA, respectively. Similarly, last three columns of the table represent obtained results by the hybrid algorithm. To solve the augmented Lagrangean function, Minos solver of the GAMS is used for both algorithms. According to the table, if appropriate values of MSGA parameters are not selected and if they are taken as $\Delta_1 = 500$, $\Delta_2 = 1$, and $\Delta_3 = 0.2$ for all test problems, MSGA has poor performance for solving QKP. Feasible solutions have been obtained for only three instances of ten by using the MSGA.

Table 2. Test results.

Instances	MSGA			Hybrid Algorithm		
	Value	G%	Time	Value	G%	Time
18558	-	-	-	18558	0.00	53.63
56525	56452	0.13	1.17	56452	0.13	0.82
3752	-	-	-	3717	0.93	32.31
50382	-	-	-	50382	0.00	43.93
61494	-	-	-	60955	0.88	3.00
36360	-	-	-	36137	0.61	2.73

14657	-	-	-	14657	0.00	9.00
20452	20452	0.00	0.56	20452	0.00	4.86
35438	35139	0.84	0.67	35325	0.32	0.47
24930	-	-	-	24748	0.73	2.37
				<i>mean</i>	0.36	56.84

As you can be seen from Table 2, the hybrid algorithm has high performance for solving QKP, even if it used the same initial parameter set ($\Delta_1 = 500$, $\Delta_2 = 1$, $\Delta_3 = 0.2$) with MSGA. It is a remarkable result because finding appropriate values of MSGA may not be easy for some test instances. Although the solution time of the hybrid algorithm is longer than MSGA, since the algorithm does not need a pre-successful parameter set and can determine the appropriate values of these parameters itself, this solution time can be considered reasonable.

4. CONCLUSION

Although the MSGA algorithm is successful in solving 0-1 quadratic programming problems, its performance largely depends on the correct determination of its parameter values. However, it is not easy to predict the values of MSGA parameters. Moreover, the appropriate values for each different problem can be very different. Therefore, in this study, a new hybrid solution approach that a TSA to find the appropriate MSGA parameter values and the MSGA algorithm run together. The proposed algorithm does not need appropriate parameter values of the MSGA or TSA. The proposed hybrid algorithm starts with the same fixed parameter values for all problems and the appropriate values of the parameters are determined dynamically by the algorithm. Computational results show great success in solving QKPs. Most of the problems were solved optimally. Even for problems that were not solved optimally, the solution was only 1% away from the optimal solution. In addition, a wide class of non-convex problems can be solved by using this proposed algorithm. In a further study, the performance of the hybrid algorithm may be demonstrated on the different types of non-convex problems.

ACKNOWLEDGMENT

There is no conflict of interest with any person/institution in the paper.

REFERENCES

- [1] Li, D., (1999), Zero duality gap in integer programming: p-norm surrogate constraint method, Operations Research Letters, 25, 89–96.
- [2] Gasimov, R., (2002), Augmented lagrangean duality and nondifferentiable optimization methods in non-convex programming, Journal of Global Optimization, 24, 187-203.

- [3] Gasimov, R.N. and Rubinov, A.M., (2004), On augmented lagrangeans for optimization problems with a single constraint, *Journal of Global Optimization*, 28, 153-173.
- [4] Gasimov, R.N. and Ustun, O., (2005), Solving the quadratic assignment problems using modified subgradient algorithm, *Proceedings of 35th International Conference on Computers & Industrial Engineering*, Istanbul, Turkey, 19-22 June 2012.
- [5] Gasimov, R.N. and Ustun, O., (2007), Solving the quadratic assignment problem using F-MSG algorithm, *Journal of Industrial and Management Optimization*, 3, 173-191.
- [6] Burachik, R.S., Kaya, C.Y. and Mammadov, M., (2010), An inexact modified subgradient algorithm for non-convex optimization, *Computational Optimization and Applications*, 45, 1-24.
- [7] Sipahioglu, A. and Saraç, T., (2009), The performance of the modified subgradient algorithm on solving the 0-1 quadratic knapsack problem, *INFORMATICA*, 20, 1-12.
- [8] Ustun, O. and Kasimbeyli, R., (2012), Combined forecasts in portfolio optimization: a generalized approach, *Computers & Operations Research*, 39, 805–819.
- [9] Ulutas, B. and Saraç, T., (2012), Determining the parameters of MSG algorithm for multi period layout problem, *Journal of Manufacturing Technology Management*, 7, 922–936.
- [10] Ozcelik, F. and Sarac, T., (2012), A genetic algorithm extended modified sub-gradient algorithm for cell formation problem with alternative routings, *International Journal of Production Research*, 15, 4025–4037.
- [11] Takan, M.A. and Kasimbeyli, R., (2020), A hybrid subgradient method for solving the capacitated vehicle routing problem, *Journal of Nonlinear and Convex Analysis*, 21, 413-423.
- [12] Bulbul, K.G. and Kasimbeyli, R., (2021), Augmented lagrangian based hybrid subgradient method for solving aircraft maintenance routing problem, *Computers & Operations Research*, 132.
- [13] Chelouah, R. and Siarry, P., (2000), Tabu search applied to global optimization, *European Journal of Operational Research*, 123, 256-270.
- [14] Li, H.L., (1992), An approximate method for local optima for nonlinear mixed integer programming problems, *Computers and Operations Research*, 19, 435-444.
- [15] Billionnet, A. and Soutif, E., (2004), An exact method based on lagrangean decomposition for the 0-1 quadratic knapsack problem, *European Journal of operational research*, 157, 565-575.



RESEARCH ARTICLE

INSIGHT INTO THE EFFECT OF TI/ZR OXIDE HYBRID PARTICLES ON DENTAL COMPOSITES: PARTICLE SYNTHESIS AND CHARACTERIZATION AND THE MECHANICAL BEHAVIOR OF COMPOSITES

Zerin YEŞİL ACAR^{1*}

^{1*}Burdur Mehmet Akif Ersoy University, Department of Dentistry Services, Vocational Schools, Burdur, zyacar@mehmetakif.edu.tr, ORCID: 0000-0002-1083-0222

Receive Date: 11.12.2022

Accepted Date: 10.03.2023

ABSTRACT

Hybrid particles were synthesized with sol–gel-based hydrothermal method using alkoxide precursors, and the usability of these particles in dental composites was investigated. First, the effects of varying Ti/Zr and $n_{\text{acid}}/n_{\text{alkoxide}}$ ratios on the crystal and microstructure of the synthesized particles (Ti, Zr) hybrids were investigated. X-ray diffraction (XRD), a particle size and a surface charge analyzer, thermogravimetric analysis (TGA), Brunauer–Emmett–Teller (BET) analysis, and Fourier transform infrared (FTIR) analysis were used to reveal the structural parameters. ZTit-1, ZTit-4, and ZTit-6 particles were crystalline, while ZTit-2, ZTit-3, and ZTit-5 particles were amorphous. The zeta potential of the most stable ZTit-4 particle was 43.33 mV. ZTit-3 particles had the highest surface area and ZTit-5 particles had the highest micropore area. The presence of Ti/Zr oxide and titanate structures was determined by FTIR analysis. In the next step of the study, the mechanical behavior of the synthesized Ti/Zr-based hybrid particles in the dental organic matrix was investigated. The flexural, compressive strengths, and microhardness of the ZTit-4 composite with optimal flowability were 175 ± 16.1 MPa, 242 ± 7.8 MPa, and 32.9 Hv.

Keywords: ZrO_2 - TiO_2 , Mixed oxide, Sol–gel, Composite, Flowability, Microhardness.

1. INTRODUCTION

Oral diseases negatively affect human health, well-being, and quality of life. Poor oral health linked to systemic bacterial and inflammatory sensitization can lead to adverse outcomes, including uncontrolled diabetes, cardiovascular disease, and respiratory disease [1]. A great majority of the world's population suffers from oral diseases, including caries, pulpitis, and periodontal disease, some of which can lead to defects in teeth and impaired function. Therefore, there is an urgent need for research on this subject. However, there is a significant challenge in rebuilding or reconstructing the heterogeneous and dynamic dental anatomical structure. To overcome these and similar problems, various dental materials are being studied and developed for use in reconstructing the curvature, color,

shape, and function of teeth [2]. An important particle used in materials studied and developed in dentistry is TiO₂. TiO₂ nanoparticles have been used to improve the fracture resistance of endodontically treated teeth, osseointegration of dental implants, antibacterial potential of a material, and adhesion to human teeth by incorporating them into adhesives [3]. Another important particle is ZrO₂, which is widely used in the production of dental prostheses, dental implants, and endodontic posts [3]. These applications have confirmed the potential use of TiO₂ and ZrO₂ nanoparticles in the development of materials used in the dental field.

TiO₂, a hard material with a high refractive index, is thermally stable, has superior mechanical properties, and is highly biocompatible. It exists in anatase, rutile, brookite (very rare), and amorphous forms [3,4]. ZrO₂ is naturally white, with high toughness, excellent strength, stable chemical properties, and good corrosion resistance, and is a biocompatible material that is a source of high-performance ceramic materials in terms of aesthetics and mechanical properties [2, 3, 5]. High-purity ZrO₂ exhibits three polymorphs depending on temperature: monoclinic, tetragonal, and cubic. Nanosized forms of TiO₂ and ZrO₂ particles, which are very popular in technological and scientific studies due to the aforementioned aspects, have recently been used more frequently in dental composites as they provide better dispersion, eliminate aggregation, and increase compatibility with organic polymers [6-8]. It was also reported that both ZrO₂ and TiO₂ nanoparticles are better than single additives due to the difference in the size of titanium and zirconium cations with the same stable oxidation state [6]. In the literature search, there are few studies in which TiO₂ and ZrO₂ particles are used together in dental composites, and the effects of these particles on the light transmittance and antibacterial effects of the composite were studied. There has been no discussion of the use of amorphous or crystalline TiZr hybrid oxides to strengthen the matrix.

With the continuous development of micro-/nanoscience and technology, it is possible to achieve practical functionalities such as desired mechanical properties, aesthetics, hardness, and fluidity (or viscosity) required for various clinical applications. Several factors, including the type of particle, its concentration by weight and volume, size, orientation, and distribution in the matrix, are critical in controlling the properties of designed dental composites. A strong matrix–particle interface is required to maximize the physical, mechanical, and biological performance of the resulting composites [9, 10]. The main aim in the present study was to synthesize particles using titanium and zirconium alkoxide precursors by polymeric sol–gel-based hydrothermal method and to investigate their usability in dental composites. On this basis, firstly, the effects of varying Ti/Zr and $n_{\text{acid}}/n_{\text{alkoxide}}$ ratios on the crystal structure and microstructure of hybrids of particles (Ti, Zr) with different crystallinity and content were investigated. The mechanical, flowability, and hardness behaviors of the synthesized pure ZrO₂, pure TiO₂ containing anatase–rutile crystal structures, and particles obtained in different phases including (Zr, Ti) oxide and (Zr, Ti) titanate in the dental matrix were determined.

2. MATERIAL AND METHOD

2.1. Chemicals and Apparatus

All chemicals were used at their commercially purchased purity without any purification. They comprised Zirconium (IV) n-propoxide (70 wt % in Propanol, Sigma-Aldrich, Zr(OPrⁿ)₄), Titanium (IV) isopropoxide (97 %, Sigma-Aldrich, Ti(OPrⁱ)₄) as alkoxide source, n-propanol (≥ 99.5 %, Sigma-

Aldrich, n-PrOH) as diluent/solvent, and hydrochloric acid (37 %, Sigma-Aldrich, HCl) as the catalyst. The crystalline phase was identified by Rigaku Geigerflex D Max/B model X-ray diffractometer. The size distribution and zeta potential of the particles were measured by a Malvern Zetasizer Nano series Nano-ZS model particle size analyzer. The alkoxide precursors remaining in the structure during the preparation of the particles were demonstrated using thermogravimetric analysis (TGA). An ASAP 2000 model Brunauer–Emmett–Teller (BET) analyzer was used to measure the surface of the particles. The change in the chemical structure of the synthesized particles was investigated by Fourier transform infrared (FTIR) spectroscopy (Perkin Elmer).

In the preparation of composites, camphorquinone (CQ) (Esschem) was chosen as a photoinitiator and ethyl 4-dimethyl amino benzoate (EDMAB) (Alfa Aesar) as a co-initiator. Nano-sized Aerosil 200 (12 nm, Evonik), micron-sized M8000 (1.8 µm, Sibelco), and synthesized zirconium and titanium-based hybrid oxide particles were used to form the inorganic phase. Silane-based 3-methacryloxy propyl trimethoxysilane (MPTS) (Aldrich) and n-hexane (Tekkim) were used respectively as the coupling agent and solvent to hold the organic matrix and inorganic particle together. The organic matrix was prepared using urethane dimethacrylate (UDMA) (Esschem). Bisphenol A ethoxylate dimethacrylate (BISEMA) (m+n=3, Esschem) was the main monomer. Triethylene glycol dimethacrylate (TEGDMA) (Esschem) was used both as a crosslinking and diluting monomer. Since the materials used in the dental field should have the properties required for clinical applications, the selection of composites was based on three-point flexural strength. In the testing and evaluation of the specimens according to the BS EN ISO 4049 standard, samples were first prepared in Teflon molds 25 mm in length, 2 mm in width, and 2 mm in thickness. After being placed in water, the samples were kept in an oven at 37±1 °C for 24 hours and dimensional measurements (length, width, and thickness) were recorded to an accuracy of 0.01 mm. The distance between the supports was adjusted according to the standard and a maximum charge (F) was applied to the sample at three points at a speed of 0.75 mm per minute until breakage. The results were calculated in mg/mm³ using Equation 1.

$$\sigma = \frac{3xFxL}{2xbxh^2} \quad (1)$$

σ = Flexural strength, F = Maximum charge (N), L = Distance between supports (mm), b = Width (mm), h = Height (mm).

At least five samples were used to ensure meaningful and reliable test results. The three-point flexural strength values of the five samples were averaged and composites with average flexural strength values equal to or greater than 50 MPa were considered to have passed the test. According to clinical practice, composites must have compressive strength to resist intraoral forces (chewing) and flexural strength. For the testing and evaluation of the specimens, samples were prepared in Teflon molds 4 mm in thickness and 3 mm in diameter. A compressive force was applied to the sample from a single point perpendicularly at a rate of 0.5 mm/min until breakage. As a result of this force, the specimen fractured and the pressure applied at the moment of fracture was calculated in MPa. In order to ensure meaningful and reliable test results, at least five specimens were tested and the compressive strength values of the five tested specimens were averaged. Composites with average strength values equal to or greater than 100 MPa were considered to have passed the test. The surface hardness of the

composites was measured using a Vickers microhardness tester with a loading of 50 grams for 10 seconds. Samples for microhardness measurement were prepared in the form of coins (2 mm thickness \times 20 mm diameter) in Teflon molds. After soaking in distilled water at 37 °C for 1 day, the samples were tested. In order for the results to be reliable, measurements were taken by selecting three points at equal distances from the center of each specimen. The mean and standard deviation of the measurement results for each sample were calculated and used as the final result.

2.2. Methods

2.2.1. Preparation of particles

Particles with different crystallinity and content were prepared by varying the Ti/Zr and $n_{\text{acid}}/n_{\text{alkoxide}}$ ratios. The details of the synthesis conditions are given in Table 1 and the preparation of the particle named ZTit-1 is given as an example. Initially, 7.60 g of $\text{Zr}(\text{OPr}^i)_4$ was stirred in 100 ml of n-PrOH in a beaker until homogeneous. In another beaker, 1.43 g of $\text{Ti}(\text{OPr}^i)_4$ was dispersed in 70 ml of n-PrOH. The concentrated HCl calculated to give an $n_{\text{acid}}/n_{\text{alkoxide}}$ ratio of 0.464 was diluted in 4.389 ml of n-PrOH.

These two alkoxide sources dispersed in alcohol (molar Ti/Zr= 0.3) were brought together and diluted HCl was added dropwise. After acid addition, the alkoxide sol was transferred to the autoclave and placed in the hydrothermal unit at 250 °C. After the hydrothermal treatment, the autoclave cooled to room conditions and was removed from the unit. The resulting particles were centrifuged to precipitate and washed 3 times with n-PrOH. The particles were left to dry in a vacuum oven at 40 °C.

Table 1. Details of the synthesis conditions of the synthesized particles and naming of the samples.

Sample code	Ti/Zr ratio (mol)	Alcohol volume (ml)	Hydrothermal treatment (h)	Acid quantity (mol, 10^{-3})	$n_{\text{acid}}/n_{\text{alkoxide}}$ ratio
ZTit-1	0.3	180	12-14	9.74	0.46
ZTit-2	0.5	180	12-14	9.74	0.40
ZTit-3	0.8	180	12-14	9.74	0.33
ZTit-4	0.8	180	12-14	12.99	0.89
ZTit-5	1	180	12-14	9.74	0.30
ZTit-6	1	180	12-14	32.47	1.00

2.2.2. Preparation of composites

Modification of particle surfaces with coupling agents

In the modification of particle surfaces with silane-based coupling agents, all particle modifications were conducted in the same way, and the preparation of M8000 particles modified by 1.5% by weight is given as an example. After the MPTS required for the particle was placed in the container, n-hexane was added. In a separate container, diluted MPTS was added to the particle soaked in a certain amount of n-hexane with stirring. The particle-agent mixture was stirred at room conditions until the solvent evaporated. It was then dried at 60 °C to completely remove the solvent.

Preparation of composites containing particles modified with coupling agents

Composites were prepared by adding Nano-sized A200 particles and hybrid particles synthesized in half the amount by weight, provided that the ratio of micron-sized M8000 silica particles to the matrix was constant. In the studies on the preparation of composites, all mixtures were prepared in the same way, and the preparation of 15 g of composite containing (A200:ZTit-1):M8000 particle mixture with a composition of (1.00:1.00):4.44 at 40% and (UDMA:BISEMA3):TEGDMA monomer triplet with a composition of (80:10):10 at 60% is given as an example. First 0.045 g of CQ and 0.0225 g of EDMAB were completely dissolved in 0.9 g of TEGDMA. Then UDMA:BISEMA3 was added at a ratio of 8:1 and mixed in a mixer at 3600 rpm for 15 seconds. A mixture of 6.0 g of (A200:ZTit):M8000 particles was added to the prepared organic matrix. After the mixture was injected into the molds, light was applied for 20 seconds at the appropriate wavelength with a dental radiation probe. The effects of the synthesized zirconium- and titanium-based particles (ZTit-1 to ZTit-6) on the properties of the final product when added to the matrix with A200 at a ratio of 1:1 were investigated by a systematic approach (Figure 1). Detailed information on the particle contents of the prepared systems is given in Table 2.

Table 2. Coding of prepared composites and naming of nano- and micron-sized silica particles and synthesized hybrid particles used in the preparation of these composites.

Composite code	Nanosized particle (mod. ratio 5%)	Synthesized particle (mod. ratio 5%)	Micron-sized particle (mod. ratio 1.5%)
ZTit-0		-	
ZTit-1		ZTit-1	
ZTit-2		ZTit-2	
ZTit-3	A200	ZTit-3	M8000
ZTit-4		ZTit-4	
ZTit-5		ZTit-5	
ZTit-6		ZTit-6	

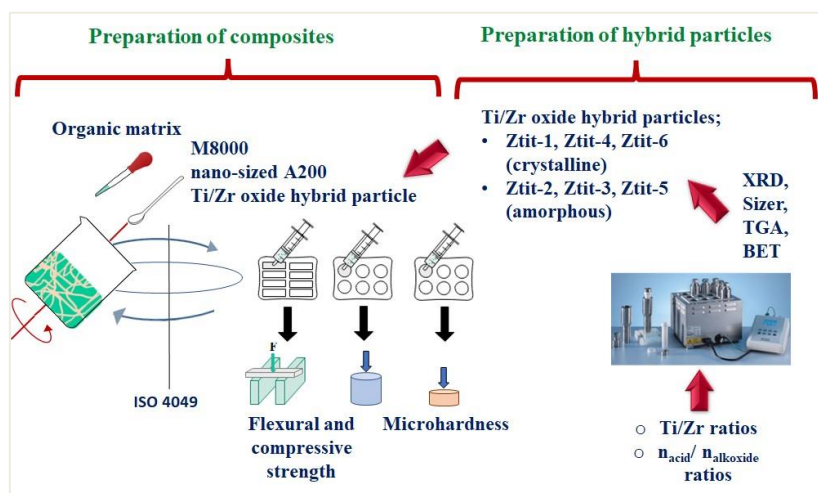


Figure 1. The experimental procedure of preparation of hybrid particles and composite.

3. RESULTS

Figure 2 and Figure 3 show the X-ray diffraction (XRD) patterns of the samples prepared by hydrothermal reaction at 250 °C for 12-14 h. Depending on the varying Ti/Zr and $n_{acid}/n_{alkoxide}$ ratios, nanoparticles in oxide form with different crystallinity and composition were obtained.

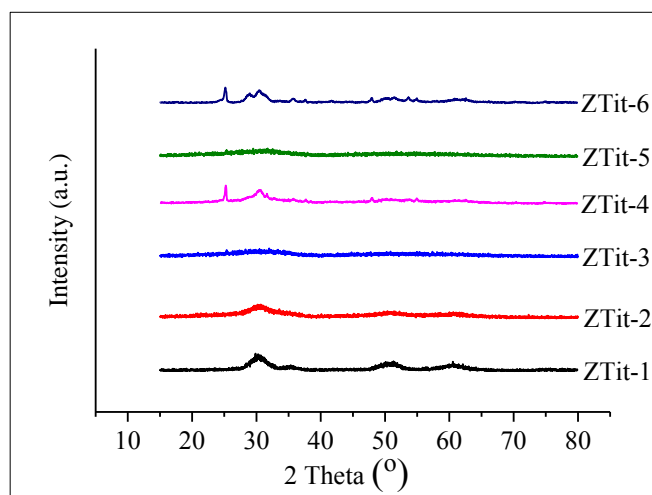


Figure 2. XRD patterns of synthesized zirconium- and titanium-based hybrid nanoparticles.

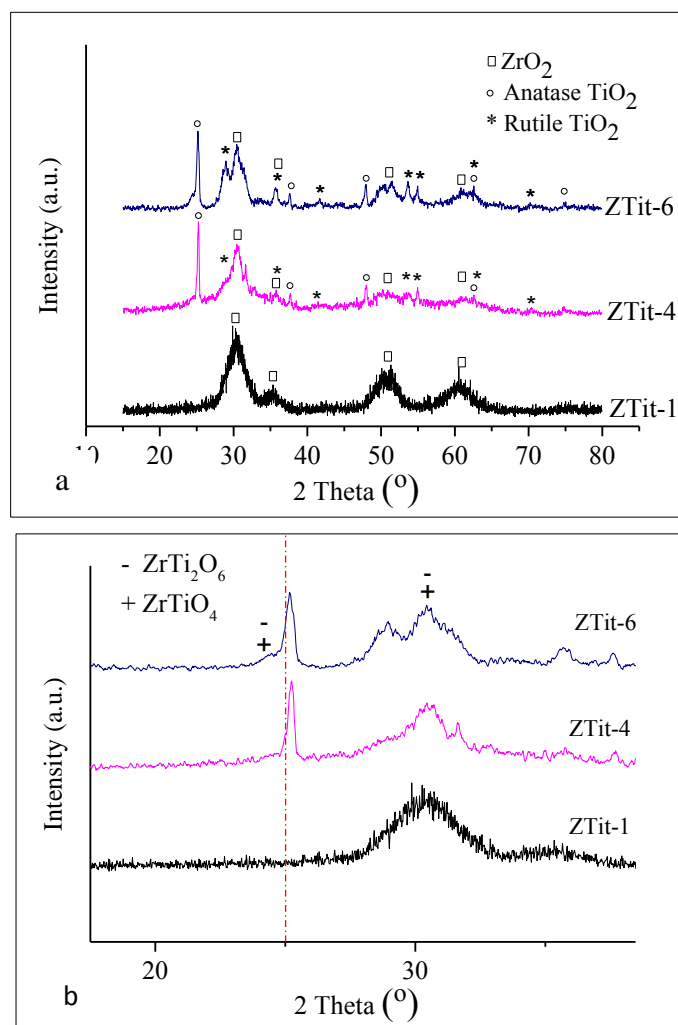


Figure 3. Characteristic XRD patterns of tetragonal ZrO₂, anatase, and rutile TiO₂ (a), triangular ZrTi₂O₆, and ZrTiO₄ species (b) in ZTit-1, ZTit-4, and ZTit-6 particles obtained in crystalline form.

The pattern seen at $2\theta = 30.22, 35.53, 50.65,$ and 60.73 and corresponding to (011), (002), (112), (103) reflections of the ZTit-1 particle with a Ti/Zr ratio of 0.3 and $n_{\text{acid}}/n_{\text{alkoxide}}$ ratio of 0.46 indicates a pure tetragonal ZrO₂ (t-ZrO₂ JCPDS 80-0965) structure [11, 12]. When the reactivity behaviors of tetravalent alkoxides of zirconium and titanium transition metals were compared, a TiO₂ structure could not be formed at a low Ti/Zr ratio due to the higher reactivity of zirconium alkoxide. No crystalline phase was obtained in ZTit-2 or ZTit-3 structures with Ti/Zr ratios of 0.5 and 0.8, respectively [13]. This result is directly related to the low $n_{\text{acid}}/n_{\text{alkoxide}}$ ratio (0.400 and 0.333,

respectively). It is thought that as the amount of acid, which plays a role in regulating the reaction rate and inorganic polymer network, decreases, the amount of water required for hydrolysis in the environment decreases, hydrolysis cannot be fully realized, and therefore crystal structures are not formed. This is supported by the formation of a crystalline structure in ZTit-4 particles obtained when the $n_{\text{acid}}/n_{\text{alkoxide}}$ ratio was increased from 0.333 to 0.89, provided that the Ti/Zr ratio remained constant at 0.8. When the reflections corresponding to 2θ angles in the pattern of ZTit-4 particles are examined comparatively, it is seen that ZrO_2 and anatase/rutile TiO_2 phases with a tetragonal crystal structure were formed. The patterns corresponding to the reflection at $2\theta = 25.25$ (101) and $2\theta = 27.42$ (110) were the main peaks of the anatase and rutile TiO_2 phases, respectively. The estimated anatase/rutile ratio was calculated based on the main peaks using the Spurr–Myers equation [14]:

$$X_A(\%) = \frac{100}{(1+1.265 \cdot \frac{I_R}{I_A})} \quad (2)$$

$$X_R(\%) = \frac{100}{(1+0.8 \cdot \frac{I_A}{I_R})} \quad (3)$$

Here, I_A is the anatase phase density at $2\theta = 25.25$, I_R is the rutile phase density at $2\theta = 27.42$, and X_R and X_A are the weight percentages of anatase and rutile phases in the sample. Using Equations 2 and 3 in the XRD spectrum of the mixed phase, it was determined that the crystal structure contains 53% anatase and 47% rutile.

When the patterns of ZTit-5 and ZTit-6 particles obtained when working with low (0.30) and high (1.00) acid amounts with a Ti/Zr ratio of 1.0 were examined, results similar to those from ZTit-3 and ZTit-4 were obtained. In the case of insufficient acid content, the ZTit-5 particle remained in the crystalline phase, while in the ZTit-6 sample prepared by increasing the acid content, tetragonal ZrO_2 , anatase/rutile TiO_2 structure, orthorhombic ZrTi_2O_6 , and ZrTiO_4 phases were observed. The characteristic XRD peaks at $2\theta = 24.87$ and $2\theta = 24.71$ indicate the ZrTi_2O_6 , and ZrTiO_4 phase in the hybrid particle. Reflections of the pure tetragonal ZrO_2 structure are given in Figure 2a. Moreover, XRD peaks at $2\theta = 25.24$ (101) and $2\theta = 47.79$ (101) indicate the presence of the anatase phase, while peaks at $2\theta = 27.42$ (110) and $2\theta = 54.5$ indicate rutile formation. According to the Spurr–Meyers equation, the crystal structure contains 78% anatase and 21% rutile by weight.

The dispersion behavior of the synthesized zirconium- and titanium-based hybrid nanoparticles is given in Figure 4.

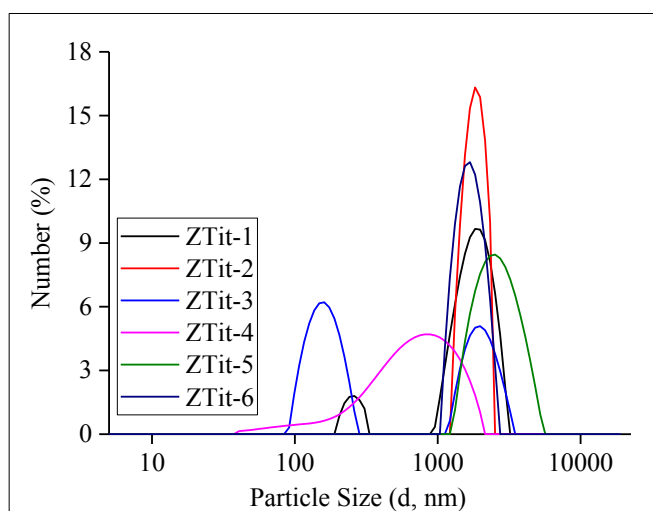


Figure 4. Particle size distributions of synthesized zirconium- and titanium-based hybrid nanoparticles.

ZTit-1 and ZTit-3 particles have bimodal distributions, while ZTit-2, ZTit-4, ZTit-5, and ZTit-6 particles have monomodal distributions. Except for ZTit-4, these synthesized hybrid particles exhibited a monodisperse distribution. Recent studies show that polydispersity characterization has become essential in nanoparticle applications, because it is difficult to control homogeneity in the size distribution of the sample and aggregation of nanoparticles is often a possible behavior [15]. ZTit-1 with the lowest titanium alkoxide ratio (low $n_{\text{acid}}/n_{\text{alkoxide}}$ ratio) exhibited an increasing bimodal distribution in parallel with the increase in the condensation reaction. At low acid and hence water contents, hydrolysis is slower than condensation and the excess of zirconium alkoxide in the solvent promotes the development of Zr-O-Zr chains through alcoholization, resulting in the formation of particles with relatively large sizes [16]. In ZTit-4 obtained by increasing the amount of titanium precursor (Ti/Zr= 0.8), the expected formation of larger polydisperse crystallites took place, as more alkoxide was available for growth on each crystal after nucleation. They exhibited monomodal and monodisperse distribution in high acid ZTit-6 with a Ti/Zr ratio of 1.0. A larger amount of water suppresses the growth of Zr-O-Zr chains by oxolation, resulting in smaller particles. An increase in the amount of water leads to an increase in the number of n in Zr(OH)_n formation, resulting in the formation of more reactive species that can contribute to the development of new species. The formation of the Zr-O-Zr network proceeds through oxolation and leads to even larger particles [16]. As a result, increasing the acid content of the medium in the synthesis of ZTit-6, which exhibits a slightly narrower particle size distribution, led to the formation of finer crystallites, which is in qualitative agreement with the reports of supporting studies [17].

Zeta potential values, which give information about the distribution of hybrid particles obtained at different alkoxide and acid ratios in a solvent, are presented in Table 3.

Table 3. Zeta potentials of synthesized zirconium- and titanium-based hybrid nanoparticles.

Sample Code	Zeta Potential (mV)
ZTit-1	13.97
ZTit-2	18.91
ZTit-3	31.02
ZTit-4	43.33
ZTit-5	6.60
ZTit-6	8.29

The synthesized hybrid particles may have -OH functional groups on their surfaces that are not incorporated into the metal oxide network, resulting in a positive surface charge. The surface charge of ZTit-4 particles dominated by the TiO₂ crystalline phase is high compared to the others, with a high positive zeta potential value (≥ 30 mV) indicating high stability. Dispersions of ZTit-3 and ZTit-4 particles in water with zeta potentials ≥ 30 mV are stable due to the dominant repulsive forces. In the structures where ZrO₂ and its derivative crystal phases are formed (ZTit-1, ZTit-5, and ZTit-6), the surface charges are low. The variation in particle surface charges depending on the reaction kinetics requires further investigation. As a result, during the synthesis, the difference in the Ti/Zr and $n_{\text{acid}}/n_{\text{alkoxide}}$ ratios not only led to amorphous and crystalline particles, but these variables also led to differences in the positive surface charges of the final structure.

TGA thermograms of particles obtained at different Ti/Zr and $n_{\text{acid}}/n_{\text{alkoxide}}$ ratios are given in Figure 5.

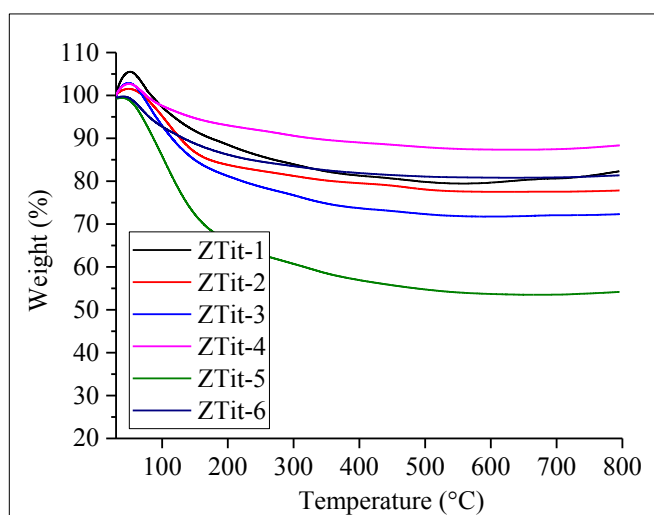


Figure 5. TGA thermogram of synthesized zirconium- and titanium-based hybrid nanoparticles.

The first noticeable feature in the thermograms is the higher mass losses in the amorphous ZTit-2, ZTit-3, and ZTit-5 structures that failed to transition to the crystalline phase. This is directly related to the increasing amount of alkoxide precursors that remain in the structure without participating in hydrolysis/condensation reactions due to the low $n_{\text{acid}}/n_{\text{alkoxide}}$ ratio. The aggressive loss from 70 to 150 °C is due to water and solvent remaining in the particle pores. The relatively gentle second curve from 200 to 400 °C is due to the removal of alkoxides.

The BET surface area, micropore area and external surface area, and micropore volume values of the synthesized nanoparticles differing according to the varying Ti/Zr and $n_{\text{acid}}/n_{\text{alkoxide}}$ ratios are given in Table 4.

Table 4. BET surface area, micropore area and external surface area, and micropore volume values.

	BET surface area (m ² /g)	Micropore area (A, m ² /g)	External surface area (mesopore area) (B, m ² /g)	A/B	Micropore volume (cm ³ /g), 10 ⁻²
ZTit-1	60.21	57.99	2.22	26.12	2.99
ZTit-2	172.98	98.70	74.28	1.33	5.18
ZTit-3	310.37	183.89	126.48	1.45	9.83
ZTit-4	155.48	-32.71	188.19	-	-1.97
ZTit-5	288.76	206.34	82.42	2.50	10.71
ZTit-6	74.17	-8.41	82.58	-	-0.52

The BET results show that ZTit-3 and ZTit-5 had the highest surface areas. In general, ZTit-2, ZTit-3, and ZTit-5 with amorphous structures were found to have high surface areas compared to the others. The surface areas of crystalline ZTit-1, ZTit-4, and ZTit-6 particles were lower. Negative micropore area and volume values were observed for ZTit-4 and ZTit-6 particles. This was due to the inadequacy of the t-plot equation for calculating pore size and other related properties in microporous and/or mesoporous structures [18].

The FTIR spectra of the particles obtained at different Ti/Zr and $n_{\text{acid}}/n_{\text{alkoxide}}$ ratios in the wavelength range from 4000 cm⁻¹ to 400 cm⁻¹ are given in Figures 6a-6b.

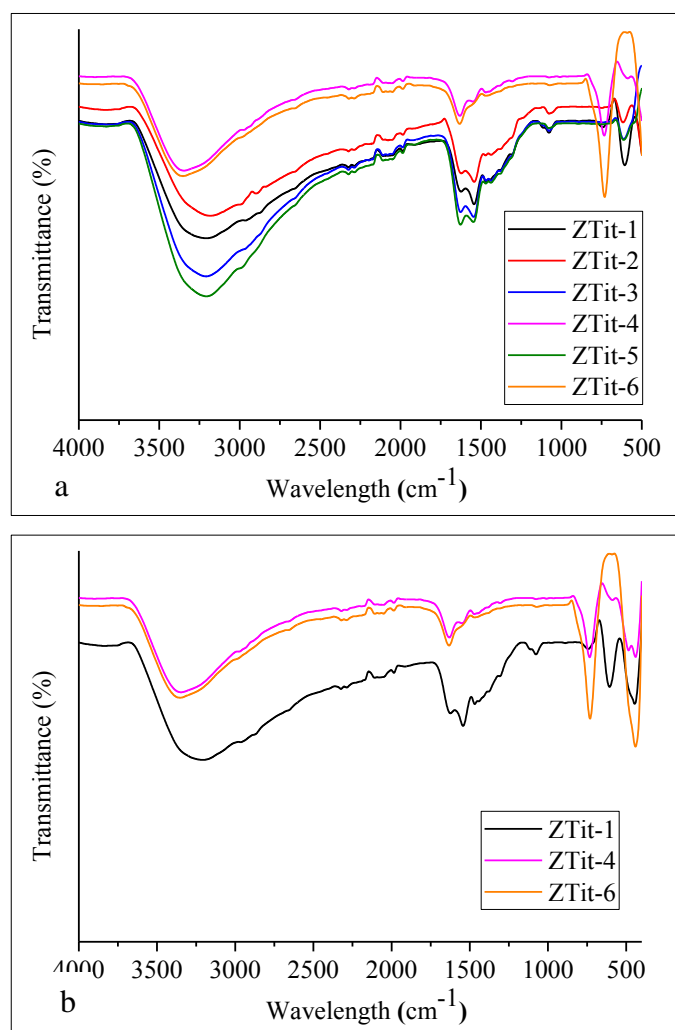


Figure 6. FTIR spectrum of synthesized zirconium- and titanium-based hybrid nanoparticles (a), magnified FTIR spectrum of particles obtained in crystalline form (b).

The broad absorption band around 3400 cm^{-1} in the FTIR spectrum in Figure 4a corresponds to -OH stretching vibrations indicating the presence of molecular water in the structure. The spectrum of ZTit-1 shows characteristic bands localized at approximately 1540 cm^{-1} and 450 cm^{-1} . These bands overlap with the reflections of the tetragonal ZrO_2 particle ([19, 20]. The peaks and bands seen in the FTIR spectrum of the ZTit-4 particle are consistent with the data reported in the literature for anatase and rutile crystal forms. The reported data show that the broad and intense bands at 520 cm^{-1} and between 900 and 400 cm^{-1} pertain to Ti-O stretching and bending vibrations in the anatase crystal

phase [21, 22]. The peaks at 464 cm^{-1} and 530 cm^{-1} are characteristic stretching vibrations of the Ti-O-Ti network in anatase TiO_2 [23]. When the fingerprint region of ZTit-4 is observed in more detail in Figure 4b, it is seen that the peaks and bands overlap with the peaks of pure ZrO_2 and anatase and rutile TiO_2 phases. The observed shifts are within acceptable limits for the interpretation of FTIR spectra. As seen in Figure 4-b, the stretching and bending vibrations of the Ti-O bond appeared at 593 cm^{-1} and the characteristic stretching vibration of the Ti-O-Ti network appeared at 485 cm^{-1} . The FTIR spectrum of the rutile form of TiO_2 is largely similar to that of anatase. For the particle in question, the maximum band at 680 cm^{-1} and the intense band at 536 cm^{-1} in the range of $830\text{-}400\text{ cm}^{-1}$ are specific to the pure rutile Ti-O vibration with a high transmittance value [21]. The stresses of this vibration are seen at around 736 cm^{-1} and 593 cm^{-1} in the spectrum. According to the studies in the literature, in the FTIR spectrum of the anatase/rutile mixture, the maximum of the main band due to the vibrations of Ti-O bonds and the Ti-O-Ti network is expected to be in the 576 cm^{-1} range [21]. The peak at 593 cm^{-1} in the spectrum of the synthesized ZTit-4 particle is the maximum of the main band. In the spectrum of ZTit-6, vibrational peaks pertaining to anatase TiO_2 , rutile TiO_2 , and tetragonal ZrO_2 were observed and these are consistent with the literature. Peaks between 500 cm^{-1} and 710 cm^{-1} are related to Ti-O and Zr-O-Ti vibrations [24].

In order to provide both aesthetic and mechanical properties such as translucency, antibacterial, flowability, biocompatibility and opacity in dental composites, particles with different ratios and sizes by weight are doped [10, 25]. Accordingly, composites were prepared by adding the synthesized hybrid particles with varying Ti/Zr and $n_{\text{acid}}/n_{\text{alkoxide}}$ ratios into the organic matrix with a replacement of 50% of A200. Of these particles; ZTit-1, ZTit-4, and ZTit-6 particles were crystalline, while ZTit-2, ZTit-3, and ZTit-5 particles were amorphous. Yield behavior is considered the main feature in evaluating the usability of dental composites developed for clinical applications [26]. The yield behavior of composites doped with $\text{TiO}_2\text{-ZrO}_2$ mixed oxides with different crystalline phases and the change in flexural strengths are given in Figure 7.

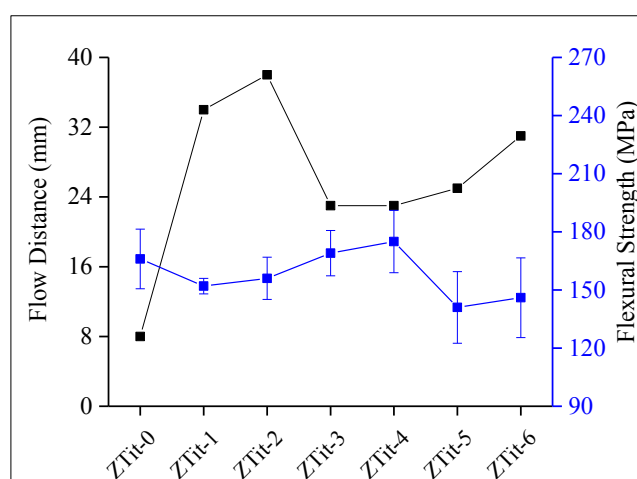


Figure 7. Flow distance and flexural strength graph of composites prepared by using hybrid particles.

The yield values of the composites were higher compared to those of ZTit-0 without hybrid particles. This was directly related to the larger particle size of amorphous and crystalline ZTit particles compared to A200. Due to their low surface area/volume ratio, the volume of the organic matrix per unit area in the composite was higher [27, 28]. The yield behavior of the crystal particles was ZTit-1>ZTit-6>ZTit-4 with yield distances of 34 mm, 31 mm, and 23 mm, respectively. The flowability of the composites in which they were used varied due to the fact that the three particles were modified with a constant amount of coupling agent without regard to their size-dependent surface areas. Mechanical characterization is an important phenomenon in the development of dental composite materials. Inorganic filler particles have a significant effect on the mechanical characterization of dental composite materials. In general, the strengthening of inorganic filler particles can be attributed to two aspects: (i) the binding force between the dental polymer matrix and inorganic particles, the interface, and (ii) the particle size distribution [29]. The flexural strengths of composites containing crystalline particles exhibited behavior of ZTit-4>ZTit-1>ZTit-6. The highest flexural strength value belonged to the ZTit-4 composite (175±16.1 MPa) and a significant increase was observed compared to the ZTit-0 composite: 166±15.4 MPa. This result is directly related to its lower flowability compared to ZTit-1 and ZTit-6. Optimal flowability in the molding of composites prevents undesirable conditions such as air bubbles that can cause microcracks in the structure. The flexural strengths of the more flowable ZTit-1 and ZTit-6 composites were 152±4.0 MPa and 146±20.6 MPa. According to the pure system, the decrease in strength is directly related to the composites moving away from optimal flowability. Composites using amorphous ZTit-2, ZTit-3, and ZTit-5 particles did not show a linear change at a low $n_{acid}/n_{alkoxide}$ ratio. With increasing alkoxide, their flowabilities decreased from 38 mm to 23 mm. ZTit-3 with the lowest flowability showed a strength of 169±11.7 MPa, while ZTit-5 composite with almost similar flowability showed a strength of 141±18.5 MPa. This result is closely related to the surface charges of the particles. The homogeneous distribution of the ZTit-3 particle with 31.01 mV zeta potential in the matrix resulted in an improvement in flexural strength. The surface charge-dependent zeta potential of the ZTit-5 particle of similar flowability was 6.59 mV, which did not exhibit a homogeneous distribution in the matrix and negatively affected the flexural strength.

A compressive strength test was used in laboratory experiments to simulate the chewing forces that stress composites used in the dental field [6]. The change in compressive strength versus yield behavior of composites containing the synthesized hybrid particles is shown in Figure 8.

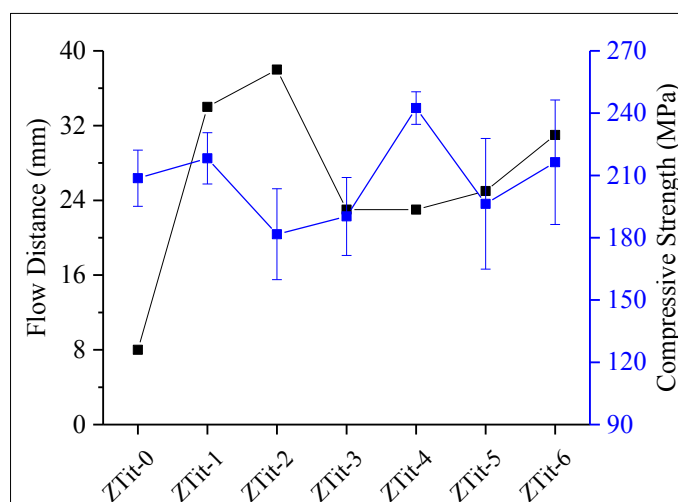


Figure 8. Flow distance and compressive strength graph of composites prepared using hybrid particles.

The compressive strength of the composites using hybrid particles did not exhibit a linear change compared to the pure composite. The compressive strengths of composites containing crystalline ZTit-1, ZTit-4, and ZTit-6 particles were 218 ± 12.3 MPa, 242 ± 7.8 MPa, and 218 ± 29.9 MPa, respectively. Their compressive strength was higher compared to that of the pure ZTit-0 composite (208 ± 13.5 MPa). Due to the optimal surface charge and homogeneous distribution of ZTit-4 particles in the matrix, the composite obtained with optimal flowability exhibited the highest strength. While the compressive strength values of the ZTit-1 and ZTit-6 composites based on their close flowability were similar, their standard deviation varied. This difference in standard deviation arose from the surface charges affecting their distribution in the matrix. The standard deviation of the compressive strength of ZTit-1, which had a slightly more positive surface charge, was lower, as expected. The flowability of the composites using amorphous ZTit-2, ZTit-3, and ZTit-5 particles decreased at a low $n_{\text{acid}}/n_{\text{alkoxide}}$ rate. The compressive strengths were 181 ± 21.9 MPa, 190 ± 18.8 MPa, and 196 ± 31.4 MPa, respectively. The optimal system in terms of flowability and zeta potential was the composite prepared with ZTit-3 particles and the standard deviation in compressive strength was slightly lower than the others. The standard deviation of the ZTit-6 composite, which exhibited the highest compressive strength, was also quite high. This result shows the importance of composite flowability and particle surface charge as a factor in particle distribution in the matrix. It is also evidence that they may be in competition.

Another test that provides information about the mechanical properties of the material is the microhardness test. The clinical significance of hardness is related to aesthetic restorations (discoloration and erosion), medical consequences of periodontal disease, and the development of secondary caries due to increased plaque accumulation [30]. This behavior of the composite can be

influenced by monomer type, filler type, morphology, volume, and weight. In particular, the type and size of inorganic particles and the extent of particle loading can lead to significant differences in the microhardness of these materials [31]. On this basis, the change in the microhardness values of the synthesized composites containing hybrid particles of different crystallinity and microstructure is shown in Figure 9.

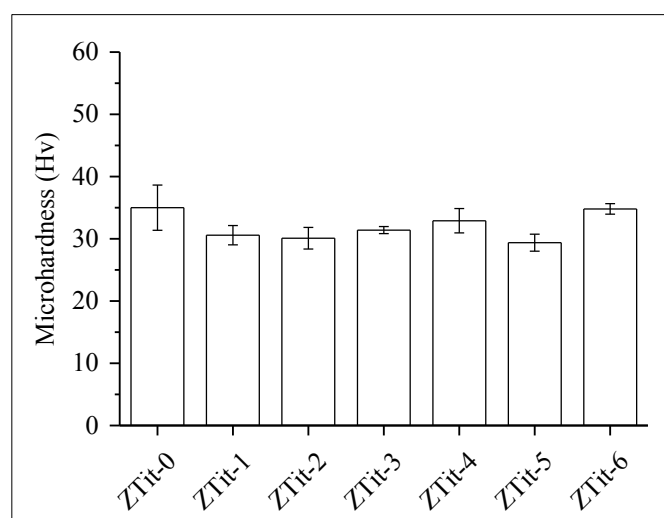


Figure 9. Microhardness graph of composites prepared using synthesized hybrid particles.

When the microhardness of the composites was analyzed, the microhardness of all composites except ZTit-2 was lower compared to ZTit-0. This decrease was related to the decrease in surface area due to increasing particle size. An important parameter affecting the microhardness of composites is the distribution of particles in the matrix. Therefore, as the particle size increases, the amount of particles per unit area loaded into the matrix decreases, leading to the formation of inter-particle voids. This results in a decrease in surface resistance to the notch created in the composite surface for hardness measurement [32, 33]. The microhardness of the composites using hybrid particles with the crystalline structure was analyzed and the decrease in the microhardness values of the composites containing ZTit-4 and ZTit-6 was less compared to ZTit-1. The formation of hybrid (Zr, Ti) and oxide structures during the synthesis of ZTit-4 and ZTit-6 particles enabled them to be obtained in smaller sizes. This resulted in higher microhardness values in the composites in which they were doped [32].

4. CONCLUSION AND COMMENT

In order to obtain high purity and more homogeneous titanium and/or zirconium oxide particles, a solvent-based wet chemical synthesis method has been developed as an alternative to the traditional solid-state reaction route. Within the scope of the method, the variation in Ti/Zr and $n_{\text{acid}}/n_{\text{alkoxide}}$ ratios resulted in particles with different crystal phases and microstructures. The most important conclusion

based on the synthesis/characterization of the particles was that by improving the synthesis conditions of the particles obtained in amorphous form (increasing the amount of acid, increasing the synthesis temperature) transition to the crystalline form with optional composition can be achieved. Accordingly, particle sizes, surface charges, and the presence/amount of alkoxide precursors that may remain in the structure can be controlled. Another important aspect of the study was to investigate the behavior of the synthesized Ti/Zr-based hybrid particles in the selected dental organic matrix. The flexural, compressive strengths, and microhardness of the composite containing ZTit-4 particles with optimal flowability were 175 ± 16.1 MPa, 242 ± 7.8 MPa, and 32.9 Hv, respectively. As a result, the mechanical behavior of the dental composite is influenced by the type, size, weight/volume, and surface properties of the particles forming the filler phase.

ACKNOWLEDGMENTS

I would like to thank Prof. Dr. Meltem ASİLTÜRK for allowing me to benefit from the laboratory facilities.

AUTHOR STATEMENT

Zerin YEŞİL ACAR: Methodology, Investigation, Original Draft Writing, Review and Editing

CONFLICT OF INTEREST

As the authors of this study, we declare that we do not have any conflict of interest statement.

ETHICS COMMITTEE APPROVAL AND INFORMED CONSENT

As the author of this study, we declare that we do not have any ethics committee approval and/or informed consent statement.

REFERENCES

- [1] Aminoroaya, A., Neisiany, R.E., Khorasani, S.N., Panahi, P., Das, O., Madry, H., Cucchiarini, M., Ramakrishna, S., (2021), A review of dental composites: Challenges, chemistry aspects, filler influences, and future insights, *Composites Part B: Engineering*, 216, 108852.
- [2] Hu, C., Sun, J., Long, C., Wu, L., Zhou, C., Zhang, X., (2019), Synthesis of nano zirconium oxide and its application in dentistry, *Nanotechnology Reviews*, 8(1), 396-404.
- [3] Al-Saleh, S., Alateeq, A., Alshaya, A.H., Al-Qahtani, A.S., Tulbah, H.I., Binhasan, M., Shabib, S., Farooq, I., Vohra, F., Abduljabbar, T., (2021), Influence of TiO₂ and ZrO₂ nanoparticles on adhesive bond strength and viscosity of dentin polymer: A physical and chemical evaluation, *Polymers*, 13(21), 3794.

- [4] Haas, K., Azhar, G., Wood, D.J., Moharamzadeh, K., Van Noort, R., (2017), The effects of different opacifiers on the translucency of experimental dental composite resins, *Dental Materials*, 33(8), e310-e316.
- [5] Hafizoğlu, M.A., Boyraz, T., Akkuş, A., The effect of mullite addition on wear properties of titania doped zirconia ceramics, *Dicle Üniversitesi Mühendislik Fakültesi Mühendislik Dergisi*, 13(1), 43-50.
- [6] Felemban, N.H., Ebrahim, M.I., (2017), The influence of adding modified zirconium oxide-titanium dioxide nano-particles on mechanical properties of orthodontic adhesive: an in vitro study, *BMC Oral Health*, 17(1) 1-8.
- [7] Sakhno, O. , Goldenberg, L., Stumpe, J., Smirnova, T., (2007), Surface modified ZrO₂ and TiO₂ nanoparticles embedded in organic photopolymers for highly effective and UV-stable volume holograms, *Nanotechnology*, 18(10), 105704.
- [8] Cazan, C., Enesca, A., Andronic, L., (2021), Synergic effect of TiO₂ filler on the mechanical properties of polymer nanocomposites, *Polymers*, 13(12), 2017.
- [9] Fu, S.-Y., Feng, X.-Q., Lauke, B., Mai, Y.-W., (2008), Effects of particle size, particle/matrix interface adhesion and particle loading on mechanical properties of particulate-polymer composites, *Composites Part B: Engineering*, 39(6), 933-961.
- [10] Cho, K., Rajan, G., Farrar, P., Prentice, L., Prusty, B.G., (2022), Dental resin composites: A review on materials to product realizations, *Composites Part B: Engineering*, 230, 109495.
- [11] Wang, J., Yin, W., He, X., Wang, Q., Guo, M., Chen, S., (2016), Good biocompatibility and sintering properties of zirconia nanoparticles synthesized via vapor-phase hydrolysis, *Scientific reports*, 6(1), 1-9.
- [12] Li, W., Zhao, Z., (2016), Hierarchically structured tetragonal zirconia as a promising support for robust Ni based catalysts for dry reforming of methane, *RSC advances*, 6(77), 72942-72951.
- [13] Tran, T.T.H., Bui, T.T.H., Nguyen, T.L, Man, H.N., Tran, T.K.C., (2019), Phase-pure brookite TiO₂ as a highly active photocatalyst for the degradation of pharmaceutical pollutants, *Journal of Electronic Materials*, 48(12), 7846-7861.
- [14] El-Sherbiny, S., Morsy, F., Samir, M., Fouad, O.A., (2014), Synthesis, characterization and application of TiO₂ nanopowders as special paper coating pigment, *Applied Nanoscience*, 4(3), 305-313.

- [15] Clayton, K.N., Salameh, J.W., Wereley, S.T., Kinzer-Ursem, T.L., (2016), Physical characterization of nanoparticle size and surface modification using particle scattering diffusometry, *Biomicrofluidics*, 10(5), 054107.
- [16] Marchisio, D.L., Omegna, F., Barresi, A.A., Bowen, P., (2008), Effect of mixing and other operating parameters in sol– gel processes, *Industrial & engineering chemistry research*, 47(19), 7202-7210.
- [17] Wahi, R.K., Liu, Y., Falkner, J.C., Colvin, V.L., (2006), Solvothermal synthesis and characterization of anatase TiO₂ nanocrystals with ultrahigh surface area, *Journal of colloid and interface science*, 302(2), 530-536.
- [18] Galarneau, A., Mehlhorn, D., Guenneau, F., Coasne, B., Villemot, F., Minoux, D., Aquino, C., Dath, J.-P., (2018), Specific surface area determination for microporous/mesoporous materials: The case of mesoporous FAU-Y zeolites, *Langmuir*, 34(47), 14134-14142.
- [19] Bermúdez-Reyes, B., Contreras-García, M., Almaral-Sánchez, J., Espitia-Cabrera, I., Espinoza-Beltrán, F., (2012), Chemical anchorage of Hydroxyapatite on 316LSS using a ZrO₂ interlayer for orthopedic prosthesis applications, *Superficies y vacío*, 25(3), 150-156.
- [20] Chandradass, J., Balasubramanian, M., Hyeon Kim, K., (2011), Solution phase synthesis of t-ZrO₂ nanoparticles in ZrO₂–SiO₂ mixed oxide, *Journal of Experimental Nanoscience*, 6(1), 38-48.
- [21] Johnson, M.S., Ates, M., Arslan, Z., Farah, I.O., Bogatu, C., (2017), Assessment of crystal morphology on uptake, particle dissolution, and toxicity of nanoscale titanium dioxide on *Artemia salina*, *Journal of Nanotoxicology and Nanomedicine*, 2(1), 11-27.
- [22] Al-Taweel, S.S., Saud, H.R., (2016), New route for synthesis of pure anatase TiO₂ nanoparticles via ultrasound-assisted sol-gel method, *J. Chem. Pharm. Res*, 8(2), 620-626.
- [23] Liu, K., Zhu, L., Jiang, T., Sun, Y., Li, H., Wang, D., (2012), Mesoporous micro-nanometer composite structure: synthesis, optoelectric properties, and photocatalytic selectivity, *International Journal of Photoenergy*, 2012.
- [24] Bavya Devi, K., Singh, K., Rajendran, N., (2011), Sol–gel synthesis and characterisation of nanoporous zirconium titanate coated on 316L SS for biomedical applications, *Journal of sol-gel science and technology*, 59(3), 513-520.
- [25] Elfakhri, F., Alkahtani, R., Li, C., Khaliq, J., (2022), Influence of filler characteristics on the performance of dental composites: A comprehensive review, *Ceramics International*.
- [26] Baroudi, K., Rodrigues, J.C., (2015), Flowable resin composites: a systematic review and clinical considerations, *Journal of clinical and diagnostic research*, 9(6), ZE18.

- [27] Wang, Y., (2007), High elastic modulus nanopowder reinforced resin composites for dental applications, University of Maryland, College Park.
- [28] Özak, Ş., (2012), Farkli yapıdaki yapay dişlerin mikrosertlik, yüzey pürüzlülüğü ve renk stabilitesi üzerinde değişik sıvı ortamlarının etkisinin değerlendirilmesi, Ankara Üniversitesi Sağlık Bilimleri Enstitüsü, Doktora tezi.
- [29] Yadav, R., Meena, A., (2022), Effect of aluminium oxide, titanium oxide, hydroxyapatite filled dental restorative composite materials on physico-mechanical properties, *Ceramics International*, 48(14), 20306-20314.
- [30] Gurbuz, O., Cilingir, A., Dikmen, B., Özsoy, A., Meltem, M., (2020), Effect of surface sealant on the surface roughness of different composites and evaluation of their microhardness, *European oral research*, 54(1), 1-8.
- [31] Atabek, D., Bani, M., Öztaş, N., Ekçi, E.S., (2016), The effect of various polishing systems on the surface roughness of composite resins, *Acta Odontologica Turcica*, 33(2).
- [32] El-Nagar, H., El-sadek, A., Ezzeldien, M., (2020), Structural analysis, optical and mechanical properties of $Ti_xZr_{1-x}O_2$ nanoparticles synthesized by modified co-precipitation route, *Applied Physics A*, 126(2), 1-12.
- [33] Alrahlah, A., Khan, R., Vohra, F., Alqahtani, I.M., Alruhaymi, A.A., Haider, S., Al-Odayni, A.-B., Saeed, W.S., Murthy, H., Bautista, L.S., (2022), Influence of the Physical Inclusion of ZrO_2/TiO_2 Nanoparticles on Physical, Mechanical, and Morphological Characteristics of PMMA-Based Interim Restorative Material, *BioMed Research International* 2022.



RESEARCH ARTICLE

**BETAINE SUPPLEMENTATION PROTECTS RATS AGAINST ALCOHOL-INDUCED
HEPATIC AND DUODENAL INJURY: AN HISTOPATHOLOGICAL STUDY**

Ayşe ÇAKIR GÜNDOĞDU^{1,*}, Fatih KAR², Cansu ÖZBAYER³

^{1*}Kütahya Health Sciences University, Faculty of Medicine, Department of Histology and Embryology, Kütahya, ayse.cakirgundogdu@ksbu.edu.tr, ORCID: 0000-0002-2466-9417

²Kütahya Health Sciences University, Faculty of Medicine, Department of Medical Biochemistry, Kütahya, fatih.kar@ksbu.edu.tr, ORCID: 0000-0001-8356-9806

³Kütahya Health Sciences University, Faculty of Medicine, Department of Medical Biology, Kütahya, cansu.ozbayer@ksbu.edu.tr, ORCID: 0000-0002-1120-1874

Receive Date: 10.01.2023

Accepted Date: 15.03.2023

ABSTRACT

Betaine is a natural compound synthesized endogenously in animals, plants, and microorganisms and can be intaken by diet. There is a growing body of evidence that suggests betaine has properties that can protect against damage caused by oxidation, inflammation, and cell death in various human diseases. Additionally, recent studies suggest that betaine may help prevent and/or ameliorate tissue damage from alcohol consumption. In the present study, we evaluated histopathological changes in the liver and duodenum tissues stained with hematoxylin and eosin (H&E) in the four groups of twenty-eight *Wistar albino* rats: control group, betaine pre-treated group (250 mg/kg/bw, 21 days, i.g.), acute ethanol ingested group (75% ethanol, 4 ml/kg/bw, i.g.) and betaine+ethanol group (75% ethanol, 4 ml/kg/bw, following betaine 250 mg/kg/bw, i.g.). We found that betaine pre-treatment reduced significantly ethanol-induced hepatocyte degeneration, sinusoidal dilatation, hemorrhage, and inflammatory cell infiltration in the liver ($p < 0.05$). We also showed that betaine protects duodenal mucosa significantly against epithelial damage at the tips of villi and hemorrhage ($p < 0.001$). Collectively, this study indicated that betaine supplementation could protect against histopathological changes induced by ethanol in hepatic and duodenal tissues.

Keywords: *Betaine, Ethanol, Liver, Duodenum, Histopathological changes.*

1. INTRODUCTION

Alcohol is a water soluble toxic organic compound that causes damage to almost all tissues in the body, especially the liver. The impact alcohol has on a person's health can change based on the amount and duration of alcohol consumed. Both short-term and long-term alcohol consumption can lead to a condition called alcoholic liver disease (ALD), which is responsible for 5.3% of global fatalities [1]. ALD is a serious disease with a spectrum that can range from fatty liver to hepatitis and fibrosis, and ultimately to cirrhosis. Although the pathogenesis is not clearly known, it is thought that

ALD is mainly associated with oxidative stress, lipid peroxidation, and inflammation [2]. The process of ethanol metabolism, as catalyzed by the enzyme alcohol dehydrogenase (ADH) in the liver, results in the production of the cytotoxic compound acetaldehyde. This metabolism also leads to the release of reactive oxygen species (ROS) which subsequently causes lipid peroxidation, endoplasmic reticulum stress, and elicitation of an inflammatory response via the production of cytokines [3]. All these factors play a role in the initiation and progression of liver tissue damage and subsequent dysfunction.

Although the liver is the main organ where ethanol oxidation takes place, it is known that it is also oxidized in the gastrointestinal tract. These catabolism reactions, called first-pass metabolism of ethanol, are mediated by alcohol dehydrogenase (ADH) and aldehyde dehydrogenase (ALDH) in the gastric and intestinal mucosa and are observed even only in small doses of alcohol consumption. Gastrointestinal metabolism is lower than in the liver, but it could still cause tissue damage by local acetaldehyde production [4]. Although the first-pass metabolism of alcohol is thought to occur mainly in the stomach, it has been shown that the ethanol concentration similar to that of the beverages is only found in the upper small intestine. Due to this high concentration in the lumen of the gastrointestinal tract, ethanol is expected to cause mucosal damage in the duodenum and jejunum rather than the stomach. Indeed, acute alcohol exposure results in mucosal injury, and hemorrhagic damage in the mucosa in the small intestine, more specifically in the duodenum [5]. Though the underlying mechanisms are not fully elucidated, studies suggest that ethanol has a direct toxic effect on the mucosa by leading to ROS production.

Betaine (trimethylglycine) is a natural compound found in almost all organisms, from microorganisms to plants and animals. While betaine could be synthesized endogenously from choline in the liver and kidneys, dietary betaine from sources such as whole grains, beets, spinach, and various seafood has a crucial role in the total betaine content of the body. Essential functions of betaine include acting as a methyl donor in transmethylation reactions and protecting cells against environmental stress by serving as an osmolyte [6]. Studies have suggested that betaine is a potent protective and therapeutic agent against pathological conditions such as neurodegenerative, hepatic, renal, and cardiovascular diseases owing to its ability to scavenge free radicals, increase antioxidant capacity and reduce apoptosis [7]. In addition, *in vivo* studies under ethanol-induced stress conditions have shown that betaine protects the cerebellum and testes against oxidative stress, prevents gastric ulcers, and improves hepatic steatosis by reducing homocysteine levels [8-10]. Moreover, a reduction in hepatic tissue damage has been reported in mice treated with betaine simultaneously with acute alcohol [11]. Similarly, it has been revealed that betaine pre-treatment reduces oxidative stress by increasing the antioxidant level and reducing the oxidant level, thus protecting the gastric tissue from the detrimental influences of ethanol [12]. However, the prophylactic influences of betaine against ethanol-induced damage to the liver and duodenum still need to be clarified. In this study, we aimed to determine whether betaine supplementation could protect against histopathological alterations induced by ethanol ingestion in the hepatic and duodenal tissues of the rats.

2. MATERIALS AND METHODS

2.1. Animal treatment

This study was approved by the Animal Experiments Local Ethics Committee of Kütahya Health Sciences University (2021.02.07). The experiments were performed on 28 healthy adult female *Wistar albino* rats (average weight 250-300 g). Animals were housed in controlled laboratory conditions with a 12 h dark/light cycle. They were fed a standard diet throughout the experiment and water was accessed ad libitum. The rats were allocated into 4 experimental groups (n=7) namely control, betaine, ethanol, and betaine+ethanol groups. The rats in the control group received 4 ml/kg of distilled water, which is the solvent of betaine. 250 mg/kg/body weight (bw) betaine was ingested into the rats in the betaine group for consecutive 21 days. 75% ethanol (4 ml/kg/bw) was given as a single dose to the rats in the ethanol group. Finally, a single dose of 75% ethanol was administered to the betaine+ethanol group after 21 days of betaine treatment. All applications were done intragastrically. All rats were decapitated under ketamine/xylazine anesthesia (90/10 mg/kg, intraperitoneally) and liver and duodenum tissues were taken. There were no excluded animals during the experiments and data points during the analysis.

2.2. Histopathological Analysis

The liver and duodenal tissues of rats were fixed for 48 hours in 10% neutral buffered formaldehyde solution. At the end of the fixation process, the tissues were dehydrated in the increasing alcohol series of 80%, 95% and 100%, then cleared in xylene. Sections at 4µm thickness were cut with a microtome (Thermo Electron Corporation, Shandon Finesse E, Germany). Following deparaffinization in xylene, the sections were rehydrated in descending series of alcohols and in water, respectively. Afterward, the tissues were taken into hematoxylin solution for 5 minutes to stain the cell nuclei. To stain the cell nuclei, the tissues were then taken into hematoxylin solution for 3 minutes. Tissues immersed in acid-alcohol were kept in eosin for 3 minutes for cytoplasmic staining after washing with tap water. Stained sections were mounted with entellan after soaking in increased alcohol series and keeping in xylene [13]. The prepared slides were examined in a blind manner by a histopathologist under a Nikon Eclipse 80i light microscope (Nikon, Germany) at x200 magnification and photographed.

To quantify the severity of the hepatic injury, each H&E-stained cross-section was scored for evidence of hepatocyte damage (swollen hepatocytes, vacuolated cytoplasm, pyknotic nuclei), sinusoidal dilatation, hemorrhage, and inflammatory cell infiltration based on the report by Akbulut. et al. [14]. Scoring for these histopathological features was performed as follows: score 0-no injury (no lesion observed), score 1-mild injury (less than 10% of tissue was affected), score 2-moderate injury (less than 50% of tissue was affected), and score 3-severe injury (more than 50% of tissue was affected). Accordingly, the mean histopathological score was scored cumulatively for each section, with a maximum score of 12 for the most severe hepatic injury. Mucosal injury of the duodenum was graded according to Ewer et al., 2004 [15], as follows: score 1- no damage, score 2- mild damage (superficial mucosal erosion, patchy mucosal hemorrhage and acute inflammatory infiltrate within the lamina propria), score 3-moderate damage (mucosal ulceration, mucosal hemorrhage and intact muscularis propria), score 4- localized severe damage (ulceration of the mucosa and focal hemorrhage), score 5-generalized severe damage (ulceration of the mucosa and diffuse hemorrhage).

2.3. Statistical Analysis

Histopathological scores showing the severity of injuries in liver and duodenum tissues were evaluated using statistical techniques in SPSS 21. The normality of the data was checked using the Shapiro-Wilk test and then ANOVA and Tukey test were applied to those data which met the normality assumptions. The final results were presented as mean and standard deviation and any differences were determined to be statistically significant if the p -value was less than 0.05.

3. RESULTS

For histopathological analysis, liver and duodenum sections from all experimental groups were assessed by H&E staining. Morphological changes in liver tissues are shown in Figure 1. Microphotographs of the control group showed that the rats in this group had normal liver architecture with hepatocytes arrayed in cords around the normal central vein and had normal hepatic parenchyma. The cytoplasm of hepatocytes was well preserved, they had a clear nucleus and distinct cell borders (Fig. 1A). Liver tissues of betaine-treated rats contained normally located hepatocytes and regular parenchyma, similar to the control group. Some animals in the betaine group showed mild signs of degeneration, but these findings were not statistically significant when compared to the rats in the control group ($p = 0.1263$) (Fig. 1B). The livers of the ethanol-treated rats showed more severe histological changes than both control and betaine groups. The most prominent findings in this group were hepatocyte degeneration, sinusoidal dilatation, hemorrhage, and inflammatory cell infiltration around the central vein (Fig. 1C-E). The pathological alterations triggered by ethanol in the livers of rats given betaine+ethanol were remarkably improved. Sinusoidal dilatation and inflammatory cell infiltration were less in this group than the ethanol group, and hemorrhage was not observed (Fig. 1F). Accordingly, the histopathological score of the liver increased in the ethanol group compared to the control group ($p < 0.001$) and reduced significantly in the betaine+ethanol group versus the ethanol group ($p < 0.05$) (Fig. 2).

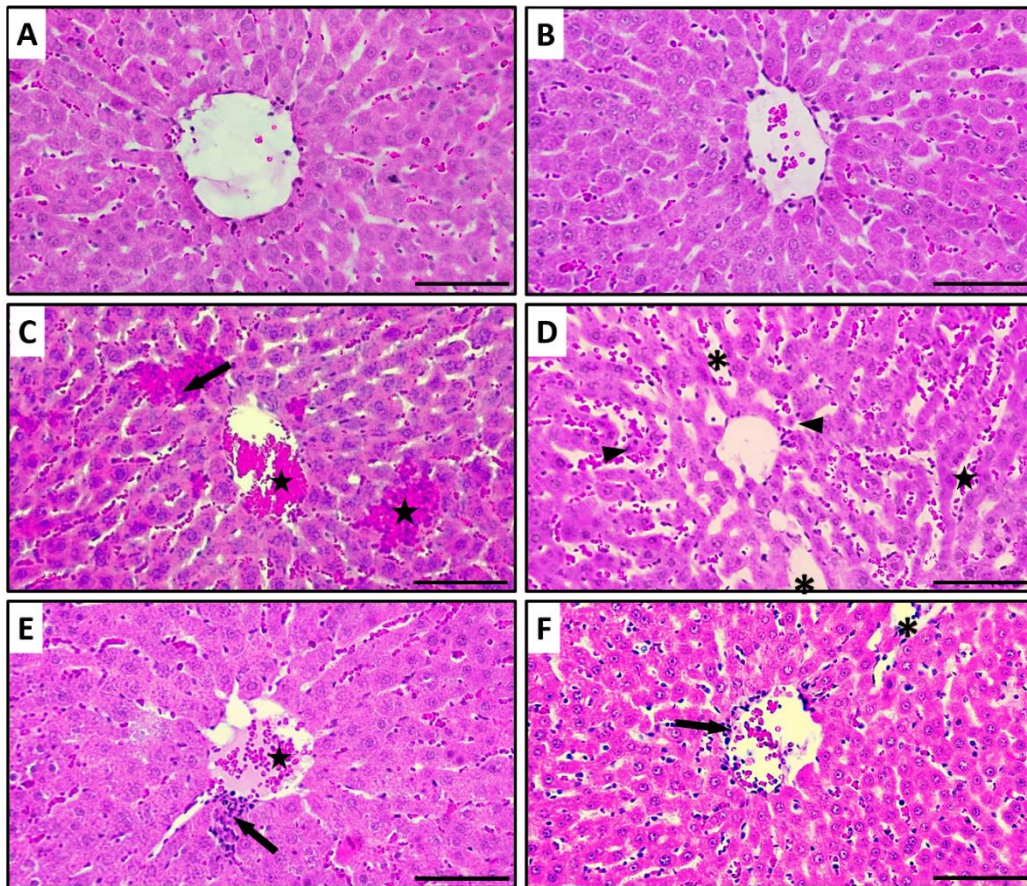


Figure 1. Histopathological evaluation of liver tissues. (A) Normal liver morphology in the control group. (B) Undamaged normal liver tissue in the betaine-treated group. (C-E) Hepatic injury characterized by hepatocyte damage (arrowheads), sinusoidal dilatation (asterisks), hemorrhage (stars), and inflammatory cell infiltration (arrows) in ethanol-administered rats. (F) Reduced hepatic injury with less inflammatory cell infiltration (arrow) and dilated sinusoids (asterisk) in the betaine+ethanol group. H&E staining, Scale bar=100 µm.

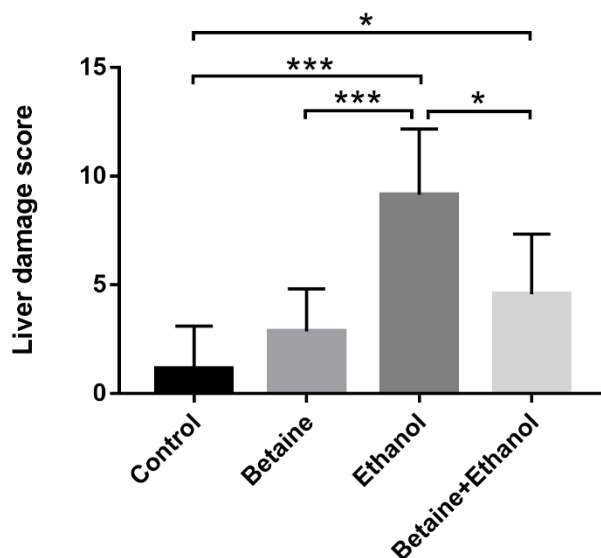


Figure 2. Comparison of histopathological scores of hepatic injury between groups. n=7, * $p < 0.05$, *** $p < 0.001$.

In the control group, the duodenum had a normal morphological appearance, the overlying epithelium of the villi was intact, crypts were spared, and lamina propria and lamina muscularis layers were regular (Fig. 3A, B). The histological structure of the duodenum in the betaine group was similar to that of the control group, only mildly sloughed epithelial cells were found in the tips of some villi, however, it did not cause a statistically significant difference when compared to the control group ($p = 0.1089$) (Fig. 3C, D). Ethanol ingestion caused severe mucosal damage characterized by the exfoliation of epithelial cells to the lumen and hemorrhage in the lamina propria (Fig. 3E, F). Betaine pre-treatment prevented ethanol-induced mucosal injury substantially. Both villous tip damage and hemorrhage were significantly less in the betaine+ethanol group than the ethanol group ($p < 0.001$) (Fig. 3G-H). Comparison of duodenal mucosal damage scores between groups is given in Figure 4.

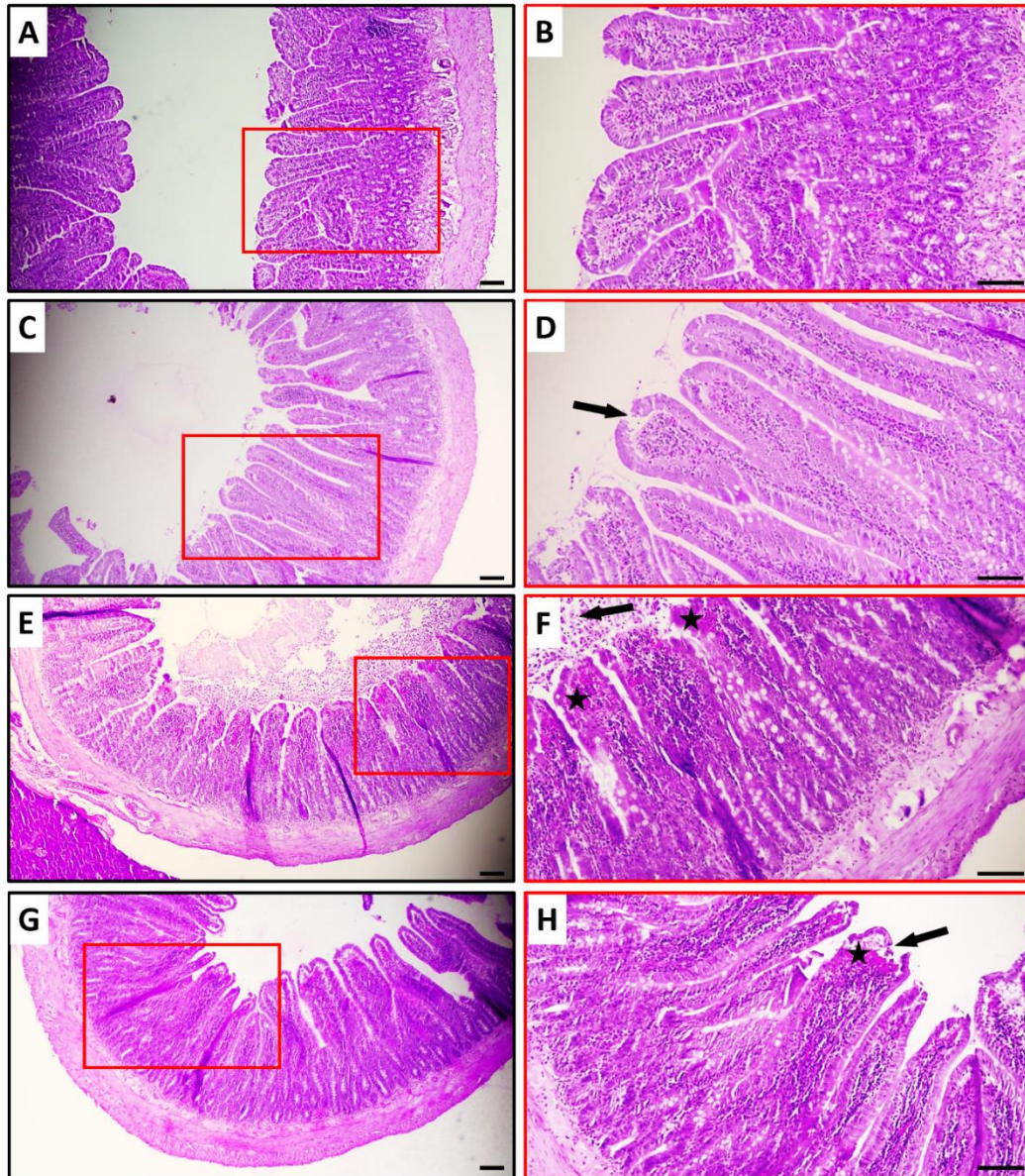


Figure 3. Histopathological evaluation of duodenum tissues. **(A-B)** Normal mucosa of the duodenum in the control group. **(C-D)** Nearly normal duodenal mucosa with only mildly sloughed epithelial cells (arrow) at the tips of some villi in the betaine-treated group. **(E-F)** Severe mucosal damage

characterized by exfoliation of epithelial cells to the lumen (arrow) and hemorrhage (stars) in the lamina propria in the ethanol-ingested group. (G-H) Reduced duodenal mucosal injury with villous tip damage (arrow) and hemorrhage (star) in the betaine+ethanol group. H&E staining, Scale bar=100 μ m.

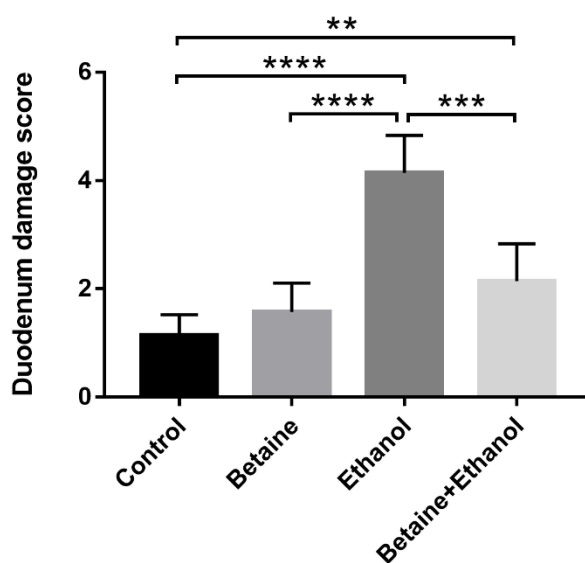


Figure 4. Comparison of histopathological scores of duodenal injury between groups. n=7, ** $p < 0.01$, *** $p < 0.001$, **** $p < 0.0001$.

4. DISCUSSION

Alcohol consumption is an important factor that threatens health and quality of life since it affects pathophysiological conditions in various organ systems including gastrointestinal, urinary, cardiovascular, and nervous systems [16-18]. ALD, which is the most crucial pathology related to alcohol, causes a series of liver disorders that might result in steatosis, fibrosis, cirrhosis, and even carcinoma and liver failure. The catabolism of ethanol to acetaldehyde, mediated by alcohol dehydrogenase (ADH) and cytochrome P450 2E1, takes place mainly in the liver. The gastrointestinal tract, where the first-pass metabolism of ethanol takes place, contains the organs that are most affected by the damage of alcohol after the liver. In this catabolic reaction of ethanol and acetaldehyde, ADH and aldehyde dehydrogenase (ALDH) of the gastric and intestinal mucosa are the main mediators [4]. Acetaldehyde produced in these reactions acts as an oxidative stress inducer by disrupting the balance of pro-oxidants and antioxidants and causes tissue damage by interacting with the proteins in the gastric and intestinal mucosa [19].

In our current study, consistent with previous studies, ingestion of rats with 75% ethanol caused hyperemia, dilatation of sinusoids, infiltration of mononuclear cells, and degeneration of hepatocytes.

When duodenal damage was examined, we showed that acute ethanol administration caused loss of epithelial cells in the villus tips and bleeding in the mucosa. Studies in rodents and humans have shown that the morphological changes induced by ethanol in the liver are characterized by steatosis, necrosis, fibrosis, mononuclear cell infiltration, hyperemia, dilatation of sinusoids, various degrees of degeneration of hepatocytes (swelling, vacuolization and hydropic degeneration), and Kupffer cell hyperplasia [20-23]. Moreover, morphological examinations in experimental animal models have reported that oral or intragastric ethanol intake poses a risk of bleeding in the gastric and duodenal mucosa. In addition, ethanol causes loss of epithelium at the tips of the villi in the duodenal mucosa, thus reducing the mucosal surface. It also leads to mononuclear cell infiltration to the epithelial layer and goblet cell hyperplasia [24-26]. In our study, the absence of changes such as steatosis, necrosis, and fibrosis in the liver is due to the fact that ethanol was not administered chronically, and only its acute effect was evaluated. Similarly, acute alcohol did not cause mononuclear cell infiltration and an increase in goblet cell count in duodenal mucosa as in chronic alcohol intake.

In the present study, in which we assessed the effects of pre-treatment of betaine for 21 days, we first showed that betaine exhibits hepatoprotection by reducing acute ethanol-induced hyperemia, sinusoidal dilatation, inflammatory cell infiltration, and hepatocyte degeneration. Next, we demonstrated that betaine also prevents the exfoliation of epithelial cells at the tips of the villi and hemorrhage in the lamina propria that is, it protects the duodenal mucosa from the toxic effects of ethanol. We speculate that this protective effect of betaine is related to the antioxidant, anti-apoptotic, and anti-inflammatory effects of this natural compound [27,28]. Previous studies investigating the effects of betaine against alcohol-induced tissue damage have shown that this natural compound provides protection through the methionine-homocysteine cycle [29]. In this cycle, betaine plays a role in converting homocysteine to methionine, thus enhancing the homocysteine level while decreasing the methionine concentration. Increased methionine is involved in antioxidation; it could be used in the synthesis of reduced glutathione (GSH) by hepatocytes as well as alleviate oxidative stress through chelation. In addition, betaine increases the level of GSH precursor S-adenosylmethionine (SAM) via sulfur-containing amino acid metabolism [29]. Betaine has also been shown to increase the activity of enzymatic antioxidants such as superoxide dismutase (SOD), catalase (CAT), and glutathione peroxidase (GPx) in the brain, testis and liver tissues [8,9,30]. Moreover, in our previous report, we showed that betaine improves total antioxidant status (TAS) and reduces total oxidant status (TOS) in betaine ethanol-treated rats [12].

It has been postulated that alcohol consumption causes an increase in the levels of S-adenosylhomocysteine (SAH), the metabolic precursor of homocysteine, in hepatocytes. SAH is produced in methyl transfer reactions, in which betaine is also involved, and is involved in the regulation of methylation reactions as a methyltransferase inhibitor [31]. Studies have shown that the increase in intracellular SAH is also associated with the induction of apoptosis [32,33]. Moreover, it has been reported that elevated SAH production is responsible for the increase in apoptosis observed following ethanol intake in hepatocytes [31]. It has been reported that betaine administration inhibits apoptosis by suppressing the increase in SAH in rat hepatocytes *in vivo* [34].

Ethanol-induced lesions in the gastrointestinal tract are closely associated with inflammation. Therefore, the use of agents with anti-inflammatory effects to protect tissues from ethanol damage is

considered a suitable approach [35]. Olli et al. showed that betaine reduces pro-inflammatory mediators interleukin-6 (IL-6) and tumor necrosis factor-alpha (TNF- α) mRNA levels in human adipocytes under hypoxia [36]. Similarly, Yang et al. reported that betaine supplementation decreases the levels of interleukin-1beta (IL-1 β), IL-6, TNF- α , and interferon-gamma (IFN- γ) in serum and increased the anti-inflammatory interleukin-10 (IL-10) in lipopolysaccharide-induced inflammation in rats [37]. Furthermore, Shi et al. proposed that betaine ameliorates ethanol-induced liver injury by reducing TNF- α , IFN- γ , and interleukin-18 (IL-18) levels [38]. These pieces of evidence suggest that the protective effect of betaine against tissue damage, which we observed in our study, is probably due to its ability to regulate inflammatory responses apart from its oxidative stress suppressor and apoptosis inhibitory features.

In conclusion, we demonstrated that betaine supplementation minimizes alcohol-induced injuries in hepatic and duodenal tissue in rats. These findings suggest the potential prophylactic value of betaine in preventing liver and duodenal damage caused by acute alcohol intake and warrant further investigations to reveal precise mechanisms of its protective effects.

ACKNOWLEDGEMENTS

Declared none.

REFERENCES

- [1] WHO, (2018), Global Status Report on Alcohol and Health; World Health Organization: Geneva, Switzerland.
- [2] Yuan, R., Tao, X., Liang, S., Pan, Y., He, L., Sun, J., Wenbo, J., Li, X., Chen, J. and Wang, C., (2018), Protective effect of acidic polysaccharide from *Schisandra chinensis* on acute ethanol-induced liver injury through reducing CYP2E1-dependent oxidative stress, *Biomed Pharmacother*, 99, 537-542.
- [3] Qiao, J.Y., Li, H.W., Liu, F.G., Li, Y.C., Tian, S., Cao, L.H., Hu, K., Wu, X.X. and Miao, M.S., (2019), Effects of *Portulaca Oleracea* Extract on Acute Alcoholic Liver Injury of Rats, *Molecules*, 24(16), 2887.
- [4] Pronko, P., Bardina, L., Satanovskaya, V., Kuzmich, A. and Zimatkin, S., (2002), Effect of chronic alcohol consumption on the ethanol-and acetaldehyde-metabolizing systems in the rat gastrointestinal tract, *Alcohol and Alcoholism*, 37(3), 229-235.
- [5] Bode, C. and Bode, J.C., (2003), Effect of alcohol consumption on the gut, *Best practice & research Clinical gastroenterology*, 17(4), 575-592.
- [6] Day, C.R. and Kempson, S.A., (2016), Betaine chemistry, roles, and potential use in liver disease, *Biochimica et Biophysica Acta (BBA)-General Subjects*, 1860(6), 1098-1106.

- [7] Rosas-Rodríguez, J.A. and Valenzuela-Soto, E.M., (2021), The glycine betaine role in neurodegenerative, cardiovascular, hepatic, and renal diseases: Insights into disease and dysfunction networks, *Life Sciences*, 285, 119943.
- [8] Alirezaei, M., Jelodar, G., Niknam, P., Ghayemi, Z. and Nazifi, S., (2011), Betaine prevents ethanol-induced oxidative stress and reduces total homocysteine in the rat cerebellum, *Journal of physiology and biochemistry*, 67, 605-612.
- [9] Alirezaei, M., Jelodar, G. and Ghayemi, Z., (2012), Antioxidant defense of betaine against oxidative stress induced by ethanol in the rat testes, *International Journal of Peptide Research and Therapeutics*, 18, 239-247.
- [10] Rehman, A. and Mehta, K.J., (2022), Betaine in ameliorating alcohol-induced hepatic steatosis, *European Journal of Nutrition*, 61(3), 1167-1176.
- [11] Arumugam, M.K., Chava, S., Perumal, S.K., Paal, M.C., Rasineni, K., Ganesan, M., Donohue, T.M., Jr., Osna, N.A. and Kharbanda, K.K., (2022), Acute ethanol-induced liver injury is prevented by betaine administration, *Front Physiol*, 13, 940148.
- [12] Çakır Gündoğdu, A., Kar, F. and Özbayer, C., (2022), Investigation of the Gastroprotective Effect of Betaine-Homocysteine Homeostasis on Oxidative Stress, Inflammation and Apoptosis in Ethanol-Induced Ulcer Model, *Journal of Investigative Surgery*, 35(11-12), 1806-1817.
- [13] Ozlu, H., Cakir Gundogdu, A., Elmazoglu, Z., Take Kaplanoglu, G., Otkar, L. and Karasu, C., (2021), Bacopa monnieri protects the directly affected organ as well as distant organs against I/R injury by modulating anti-inflammatory and anti-nitrosative pathways in a rat model for infrarenal aortic occlusion, *Journal of Investigative Surgery*, 34(9), 935-946.
- [14] Akbulut, S., Elbe, H., Eris, C., Dogan, Z., Toprak, G., Otan, E., Erdemli, E. and Turkoz, Y., (2014), Cytoprotective effects of amifostine, ascorbic acid and N-acetylcysteine against methotrexate-induced hepatotoxicity in rats, *World journal of gastroenterology: WJG*, 20(29), 10158-10165.
- [15] Ewer, A.K., Al-Salti, W., Coney, A.M., Marshall, J.M., Ramani, P. and Booth, I.W., (2004), The role of platelet activating factor in a neonatal piglet model of necrotising enterocolitis, *Gut*, 53(2), 207-213.
- [16] Güney, T.G., Çalışkan, A., Kar, F., Çakır Gündoğdu, A. and Özbayer, C., (2022), Sıçan böbrek dokusunda etanolün akut toksisitesi ve borik asitin koruyucu rolü, *Biyolojik Çeşitlilik ve Koruma*, 15(1), 107-113.
- [17] Fernández-Solà, J., (2020), The effects of ethanol on the heart: alcoholic cardiomyopathy, *Nutrients*, 12(2), 572.

- [18] Ding, Y., Wu, Y., Chen, J., Zhou, Z., Zhao, B., Zhao, R., Cui, Y., Li, Q. and Cong, Y., (2022), Protective effect of *Eucommia ulmoides* Oliver male flowers on ethanol- induced DNA damage in mouse cerebellum and cerebral cortex, *Food Science & Nutrition*, 10(8), 2794-2803.
- [19] Stickel, F., Hoehn, B., Schuppan, D. and Seitz, H., (2003), Nutritional therapy in alcoholic liver disease, *Alimentary pharmacology & therapeutics*, 18(4), 357-373.
- [20] Ozdil, S., Bolkent, S., Yanardag, R. and Arda-Pirincci, P., (2004), Protective effects of ascorbic acid, dl-alpha-tocopherol acetate, and sodium selenate on ethanol-induced liver damage of rats, *Biol Trace Elem Res*, 97(2), 149-162.
- [21] Sathiavelu, J., Senapathy, G.J., Devaraj, R. and Namasivayam, N., (2009), Hepatoprotective effect of chrysin on prooxidant-antioxidant status during ethanol-induced toxicity in female albino rats, *J Pharm Pharmacol*, 61(6), 809-817.
- [22] Xiao, Q., Chen, Y.H., Pratama, S.A., Chen, Y.L., Shirakawa, H., Peng, H.C. and Yang, S.C., (2021), The Prophylactic Effects of Glutamine on Muscle Protein Synthesis and Degradation in Rats with Ethanol-Induced Liver Damage, *Nutrients*, 13(8), 2788.
- [23] Zhong, W., Zhao, Y., Sun, X., Song, Z., McClain, C.J. and Zhou, Z., (2013), Dietary zinc deficiency exaggerates ethanol-induced liver injury in mice: involvement of intrahepatic and extrahepatic factors, *PLoS One*, 8(10), e76522.
- [24] Bode, C. and Bode, J.C., (1997), Alcohol's role in gastrointestinal tract disorders, *Alcohol health and research world*, 21(1), 76-83.
- [25] Person, J., (1991), Alcohol and the small intestine, *Scandinavian journal of gastroenterology*, 26(1), 3-15.
- [26] Persson, J., Berg, N., Sjolund, K., Stenling, R. and Magnusson, P., (1990), Morphologic changes in the small intestine after chronic alcohol consumption, *Scandinavian journal of gastroenterology*, 25(2), 173-184.
- [27] Kar, F., Hacıoglu, C., Kacar, S., Sahinturk, V. and Kanbak, G., (2019), Betaine suppresses cell proliferation by increasing oxidative stress-mediated apoptosis and inflammation in DU-145 human prostate cancer cell line, *Cell Stress and Chaperones*, 24(5), 871-881.
- [28] Hagar, H. and Al Malki, W., (2014), Betaine supplementation protects against renal injury induced by cadmium intoxication in rats: role of oxidative stress and caspase-3, *Environ Toxicol Pharmacol*, 37(2), 803-811.

- [29] Zhang, M., Zhang, H., Li, H., Lai, F., Li, X., Tang, Y., Min, T. and Wu, H., (2016), Antioxidant mechanism of betaine without free radical scavenging ability, *Journal of agricultural and food chemistry*, 64(42), 7921-7930.
- [30] Ahn, M., Park, J.S., Chae, S., Kim, S., Moon, C., Hyun, J.W. and Shin, T., (2014), Hepatoprotective effects of *Lycium chinense* Miller fruit and its constituent betaine in CCl₄-induced hepatic damage in rats, *Acta histochemica*, 116(6), 1104-1112.
- [31] Kharbanda, K.K., Rogers II, D.D., Mailliard, M.E., Siford, G.L., Barak, A.J., Beckenhauer, H.C., Sorrell, M.F. and Tuma, D.J., (2005), Role of elevated S-adenosylhomocysteine in rat hepatocyte apoptosis: protection by betaine, *Biochemical pharmacology*, 70(12), 1883-1890.
- [32] Ratter, F., Germer, M., Fischbach, T., Schulze-Osthoff, K., Peter, M.E., Dröge, W., Krammer, P.H. and Lehmann, V., (1996), S-adenosylhomocysteine as a physiological modulator of Apo-1-mediated apoptosis, *International immunology*, 8(7), 1139-1147.
- [33] Bellas, R.E., Harrington, E.O., Sheahan, K.L., Newton, J., Marcus, C. and Rounds, S., (2002), FAK blunts adenosine-homocysteine-induced endothelial cell apoptosis: requirement for PI 3-kinase, *American Journal of Physiology-Lung Cellular and Molecular Physiology*, 282(5), L1135-L1142.
- [34] Barak, A.J., Beckenhauer, H.C., Mailliard, M.E., Kharbanda, K.K. and Tuma, D.J., (2003), Betaine lowers elevated S-adenosylhomocysteine levels in hepatocytes from ethanol-fed rats, *The Journal of nutrition*, 133(9), 2845-2848.
- [35] Zhao, G., He, F., Wu, C., Li, P., Li, N., Deng, J., Zhu, G., Ren, W. and Peng, Y., (2018), Betaine in Inflammation: Mechanistic Aspects and Applications, *Front Immunol*, 9, 1070.
- [36] Olli, K., Lahtinen, S., Rautonen, N. and Tiihonen, K., (2013), Betaine reduces the expression of inflammatory adipokines caused by hypoxia in human adipocytes, *British journal of nutrition*, 109(1), 43-49.
- [37] Yang, Z., Yang, J.J., Zhu, P.J., Han, H.M., Wan, X.L., Yang, H.M. and Wang, Z.Y., (2022), Effects of betaine on growth performance, intestinal health, and immune response of goslings challenged with lipopolysaccharide, *Poultry Science*, 101(11), 102153.
- [38] Shi, Q.Z., Wang, L.W., Zhang, W. and Gong, Z.J., (2010), Betaine inhibits toll-like receptor 4 expression in rats with ethanol-induced liver injury, *World Journal of Gastroenterology: WJG*, 16(7), 897-903.

APPENDIX

T.C.
KÜTAHYA SAĞLIK BİLİMLERİ ÜNİVERSİTESİ
HAYVAN DENEYLERİ YEREL ETİK KURULU
ARAŞTIRMA BAŞVURUSU ONAYI

BASVURU BİLGİLERİ	ARAŞTIRMANIN ADI	Deneysel Üşer Modelinde Retain ve Melatonin'in Gastroprotektif Etkinliğinin İn Vivo Olarak Araştırılması
	ARAŞTIRMA YÜRÜTÜCÜSÜ KURUMU	Doç. Dr. Cansu ÖZBAYER KSBÜ Tıp Fakültesi Tıbbi Biyoloji A.D.
	PROJE YÜRÜTÜCÜSÜ KURUMU	Doç. Dr. Cansu ÖZBAYER KSBÜ Tıp Fakültesi Tıbbi Biyoloji A.D.
	YARDIMCI ARAŞTIRICILAR	Arş. Gör. Dr. Ayşe ÇAKIR GÜNDOĞDU Öğr. Gör. Dr. Fatih KAR Dr. Öğr. Üyesi Rameysa ÖZYURT
	ARAŞTIRMANIN TAHMİNİ SÜRESİ	12 ay
	KULLANILACAK HAYVAN TÜRÜ VE SAYISI	Sprague Dawley (E) – 42 adet
DESTEKLEYİCİ KURULUŞ	-	

DEĞERLENDİRİLEN İLGİLİ BELGELER	Belge Adı	Tarih
	ARAŞTIRMA BAŞVURU FORMU	08.02.2021

KARAR BİLGİLERİ	Karar No : 2021.02.07	Tarih : 17.02.2021
	Yukarıda başvuru bilgileri verilen araştırma projesi, gerekeç, amaç ve yöntemler dikkate alınarak görüşüldü ve ilgili belgeler incelendi. Proje bütçesinin nasıl karşılanacağına detaylandırılması, tüm analizlerin nerede ve hangi cihazlarla yapılacağı ile ilgili detaylı bilgi verilmesi, %75 etanol uygulamasının 3 günde ülser oluşturmaya ilgili modelin detaylandırılması ve bu konuyla ilgili kurulumuza literatür sunulması/ilgili bölüme referans eklenmesi veya bir ön çalışma yapılarak modelin denenmesi-sonuçlarının sunulması kurulumuza uygun görülmüştür. Belirtilen düzeltmeler yapılarak düzeltme formu doldurulup makaleler eklenerek veya ön çalışma yapılacağına ön çalışma başvuru formu doldurularak tekrar başvuru olduğu takdirde kurulumuza yeniden değerlendirilmesine OY ÇOKLUGU ile karar verilmiştir.	

ETİK KURUL BİLGİLERİ

ÜYELER

Unvanı / Adı / Soyadı EK Üyeligi	Uzmanlık Dalı	Kurumu	İlişki (*)	İmza
Prof. Dr. Aynur GÜLCAN Başkan	Mikrobiyoloji ve Klinik Mikrobiyoloji Anabilim Dalı	Tıp Fakültesi	<input type="checkbox"/> E <input checked="" type="checkbox"/> H	
Vet. HEKİM Aydın AKCİLAR Üye	Veteriner HEKİM	Tıp Fakültesi DEHYUB	<input type="checkbox"/> E <input checked="" type="checkbox"/> H	
Doç. Dr. Sermet İNAL Başkan Vekili	Ortopedi ve Travmatoloji Anabilim Dalı	Tıp Fakültesi	<input type="checkbox"/> E <input checked="" type="checkbox"/> H	TOPLANTIYA KATILMADI
Doç. Dr. Fikriye Yasemin ÖZATIK Üye	Farmakoloji Anabilim Dalı	Tıp Fakültesi	<input type="checkbox"/> E <input checked="" type="checkbox"/> H	
Dr. Öğr. Üyesi Yasemin TEKŞEN Üye	Farmakoloji Anabilim Dalı	Tıp Fakültesi	<input type="checkbox"/> E <input checked="" type="checkbox"/> H	
Dr. Öğr. Üyesi Sezer AKCER Üye	Anatomi Anabilim Dalı	Tıp Fakültesi	<input type="checkbox"/> E <input checked="" type="checkbox"/> H	
Dr. Öğr. Üyesi Mehmet Fatih EKICI Üye	Genel Cerrahi Anabilim Dalı	Tıp Fakültesi	<input type="checkbox"/> E <input checked="" type="checkbox"/> H	
Vet. HEKİM Ali BILCAN Sivil Üye	Veteriner HEKİM	Kütahya Belediyesi	<input type="checkbox"/> E <input checked="" type="checkbox"/> H	
Mustafa ÖZÜNLÜ Sivil Üye, STK Temsilcisi	Öğretmen	Milli Eğitim Bakanlığı	<input type="checkbox"/> E <input checked="" type="checkbox"/> H	

* Araştırma ile ilişkisi



RESEARCH ARTICLE

**FACILE AND CONTROLLED SYNTHESIS OF 2D ORGANOMETAL HALIDE
PEROVSKITE PURE $BA_2MAPb_2I_7$ AND HETEROSTRUCTURED $BA_2PbI_4/BA_2MAPb_2I_7$
SINGLE CRYSTALS**

Alp YILMAZ^{1,*}, Aydan YELTİK²

^{1*}TOBB University of Economics and Technology, Department of Material Science and Nanotechnology Engineering, Ankara, alpyilmaz9898@gmail.com, ORCID: 0000-0002-5224-423X

²TOBB University of Economics and Technology, Department of Material Science and Nanotechnology Engineering, Ankara, ayeltik@etu.edu.tr, ORCID: 0000-0001-6976-4680

Receive Date: 17.02.2023

Accepted Date: 15.03.2023

ABSTRACT

Two dimensional (2D) organometal halide perovskites (OHPs) have attracted intensive interest for their diverse optoelectronic applications. However, a practical and controllable solution-based way particularly for the synthesis of pure $BA_2MAPb_2I_7$ and heterostructured $BA_2PbI_4/BA_2MAPb_2I_7$ single crystals, which are of great importance for high performance photodetectors, is still lacking. In this study, we report the efficient synthesis route of large-area high-quality $BA_2MAPb_2I_7$ and $BA_2PbI_4/BA_2MAPb_2I_7$ single crystals. We show that the combined method of solution temperature lowering and limiting reagent approaches yields rapid and controllable synthesis. In addition, the correct determination of the BAI:MAI:PbI₂ molarity ratios in the synthesis process was revealed to be highly significant. These results provide fundamental insight and useful guideline for obtaining the presented 2D OHPs with regard to high practicality and controllability.

Keywords: 2D Perovskite, Single crystal synthesis, Solution temperature lowering, Limiting reagent approach, Heterostructure.

1. INTRODUCTION

Among many prominent two dimensional (2D) materials such as graphene[1] and transition metal dichalcogenides (TMD)[2–4], 2D organometal halide perovskites (OHPs) are promising layered materials for optoelectronic applications owing to their favorable properties such as high carrier mobility, long diffusion length, high absorption coefficient, tunable optical bandgap, and ease of forming heterostructures with other materials[5,6]. 2D OHPs structures are generally defined by the chemical formula $(RNH_3)_2(A)_{n-1}MX_{3n+1}$, where RNH_3 is a long-chain organic group ($CH_3(CH_2)_3NH_3$, $C_6H_5C_2H_4NH_3$, etc.), A is an organic or inorganic cation ($CH_3NH_3^+$, Cs, etc.), M is a bivalent metal cation (mainly Pb^{+2} , Sn^{+2} , Ge^{+2} , etc.), X is a halogen anion (Cl⁻, Br⁻, I⁻). Here the n value represents the number of the inorganic octahedron layers, giving the inorganic layer thickness. In recent years, 2D

OHPs have been studied as solution-processable active and supporting components in photovoltaics, LEDs, and photodetectors due to the higher stability feature compared to 3D OHPs and other superior characteristics[7]. Particularly, long-chain hydrophobic organic groups increase the durability of 2D OHPs by protecting the inorganic octahedra layers[8,9]. Also, the optoelectronic properties of 2D OHPs are able to be adjusted by just varying the number of inorganic layers (n)[10,11]. Among the various applications of 2D OHP single crystals which yield high crystallinity and less number of grain boundaries, photodetectors stand out, providing superior responsivity and short response rate[12,13].

Heterostructures emerge as structures formed by the combination of two different semiconductor materials with different unique optoelectronic properties such as graphene, TMD, black phosphorus, and perovskite. Thus, heterostructures significantly increase the functionality of optoelectronic applications such as photodetectors, photovoltaics, and transistors[14]. In particular, the synthesis of two different perovskite structures with different compositions as a single crystal is very important in order to overcome the problems such as the requirement of matching the lattice constant, and the formation of interface defects at the boundaries of materials[15]. Nowadays, researchers have succeeded in synthesizing various 2D perovskite heterostructures such as $(\text{BA})_2\text{PbI}_4/(\text{BA})_2\text{PbBr}_4$, $(\text{PEA})_2\text{PbI}_4/(\text{PEA})_2\text{MAPb}_2\text{I}_7$, $(2\text{T})_2\text{PbI}_4/(2\text{T})_2\text{PbBr}_4$, $(2\text{T})_2\text{SnI}_4/(2\text{T})_2\text{PbI}_4$ [16]. Moreover, 2D OHP single-crystal heterostructures are of great importance for dual-band high-performance photodetectors due to the tunable optical bandgap allowing high absorption coefficients over multiple spectral regions[15,17]. It is of great importance to synthesize high-quality 2D OHP pure single crystals and their heterostructures instead of widely used polycrystalline films for higher detector performances[15]. However, there are still important issues that need to be addressed and researched in detail regarding the synthesis process in terms of practicality and controllability. In particular, the use of slow and complex vapor deposition processes in the synthesis of $\text{BA}_2\text{PbI}_4/\text{BA}_2\text{MAPb}_2\text{I}_7$ single crystal heterostructures is a major concern.[18,19].

Single crystals of 2D OHPs with diverse optoelectronic properties have been obtained using compositional engineering through various synthesis methods such as solution-based crystal growth, vapor-phase epitaxial growth, and top-down (slicing, mechanical peeling) methods[20–22]. Among them, the solution-based crystal growth method is ideal for synthesizing 2D OHP single crystals with ease, high-quality and controllability[23]. Solution-based crystal growth methods are also listed as inverse temperature crystallization, anti-solvent vapor assisted crystallization, slow evaporation crystallization and solution temperature lowering (STL). The STL method is an important route for the synthesis of high-quality 2D OHP single crystals with large grain sizes[24]. On the other hand, during STL synthesis of 2D OHP $\text{BA}_2\text{MAPb}_2\text{I}_7$ (n=2) single crystal materials, which are of great importance for photodetector applications, BA_2PbI_4 (n=1) crystals are inevitably synthesized as side product and cause contamination; therefore, the inability to obtain homogeneous $\text{BA}_2\text{MAPb}_2\text{I}_7$ structures emerges as a major challenge[15]. Furthermore, this hinders the controlled synthesis of 2D OHP $\text{BA}_2\text{PbI}_4/\text{BA}_2\text{MAPb}_2\text{I}_7$ single crystal heterostructures for use in dual-band photodetectors. Considering the slow and complex vapor deposition processes used in the synthesis of $\text{BA}_2\text{PbI}_4/\text{BA}_2\text{MAPb}_2\text{I}_7$ single crystal heterostructures, a rapid and simple STL method provides highly important advantages for the controlled synthesis of heterostructures.

In this study, high-quality, large-area, pure 2D OHP $\text{BA}_2\text{MAPb}_2\text{I}_7$ single crystals were synthesized within a few hours using a facile solution-based synthesis route. The high controllability of the used approach, which included STL and limiting reagent methods, was achieved by carefully varying the concentration ratios of n-butylamine (BA) and methylamine (MA) cations. 2D OHP $\text{BA}_2\text{PbI}_4/\text{BA}_2\text{MAPb}_2\text{I}_7$ single crystal heterostructures were also synthesized and investigated in detail. Structural and optical properties of the synthesized perovskites were examined using various characterization techniques including scanning electron microscopy/energy dispersive X-ray spectroscopy (SEM/EDX), X-ray diffractometry (XRD), UV-Vis absorption spectroscopy, and steady-state photoluminescence (PL) spectroscopy. Accordingly, the characteristic spectra of the $\text{BA}_2\text{MAPb}_2\text{I}_7$ and $\text{BA}_2\text{PbI}_4/\text{BA}_2\text{MAPb}_2\text{I}_7$ single crystals were obtained. The SEM images illustrated the synthesized single crystals having large-area and layered structures. The XRD pattern of $\text{BA}_2\text{PbI}_4/\text{BA}_2\text{MAPb}_2\text{I}_7$ single crystal heterostructures was obtained as a mixture of the patterns of $\text{BA}_2\text{MAPb}_2\text{I}_7$ and BA_2PbI_4 single crystals as targeted. This result was also obtained in the PL and UV-Vis absorption spectra.

2. EXPERIMENTAL SECTION

2.1. Chemicals

The chemicals used here in the synthesis of perovskites are lead(II) iodide (PbI_2), methylammonium iodide (MAI), n-butylamine (BA), 57% aqueous hydriodic acid (HI), 50% aqueous hypophosphorous acid (H_3PO_2). They were purchased from Sigma-Aldrich and used as received in high purity.

2.2. Growth of 2D OHP single crystals

STL and limiting reagent methods were utilized to synthesize 2D OHP $\text{BA}_2\text{MAPb}_2\text{I}_7$ single crystals. Schematics of the synthesis steps, including the parameters, are shown in Figure 1. Herein, the concentration ratio of BA cations has been limited in the synthesis process of pure $\text{BA}_2\text{MAPb}_2\text{I}_7$ 2D OHP single crystals. Accordingly, 1.32 M PbI_2 powder chemical was dissolved in 0.250 mL HI solvent (A solution). After stirring at 200 rpm for 10 minutes at the temperature of 90°C , a transparent yellow solution was obtained. After that, 0.66 M of MAI powder chemical was added to the solution and MAPbI_3 was formed, and the color of the solution turned dark black. After 10 minutes, 28 μL of H_3PO_2 was added to the solution, dissolved at 90°C under 150 rpm stirring for 2 hours and the color of the solution turned transparent yellow again.

In a separate flask placed in an ice bath, 0.86 M of n-BA was dissolved in 0.250 mL HI solvent to obtain BAI precursor solution (solution B). The n-BA was dropwise added and dissolved under stirring (200 rpm) at 0°C for 2 hours. An amount of solution B at 0°C was rapidly added to solution A at 90°C until observing red nuclei with hundreds of micron lateral areas. The temperature of the solution was increased to 100°C and stirred at 200 rpm for 15 minutes. The solution was cooled to 25°C at a cooling rate of $30^\circ\text{C}/\text{h}$ and $\text{BA}_2\text{MAPb}_2\text{I}_7$ 2D OHP single crystals were grown. After that, the single crystals were collected by vacuum filtration and taken into vacuum for drying at 25°C overnight.

Further, BA_2PbI_4 2D OHP single crystals were synthesized using the STL method aforementioned, except that the molar concentrations of solution A and B were adjusted to the BAI:MAI: PbI_2 ratio of

2:0:1. The synthesis of $\text{BA}_2\text{PbI}_4/\text{BA}_2\text{MAPb}_2\text{I}_7$ 2D OHP single crystal heterostructures was also carried out following the steps outlined above, but the concentrations of solution A and B were adjusted to the $\text{BAI}:\text{MAI}:\text{PbI}_2$ molarity ratios of 2:1:2, 2:2:2, 2:3:2 and 2:4:2.

2.3. Structural characterization

The basic properties of the materials such as crystal quality, surface morphology, lateral thickness and grain boundary identification of the materials were examined as preliminary characterization using an optical microscope (Nikon series Eclipse H600L). The XRD system (Bruker D8 Advance) operating at 40 kV and using $\text{Cu K}\alpha$ ($\lambda=1.5418\text{\AA}$) as X-ray source was employed to characterize the crystal structure of the materials and to determine the distance between the inorganic layers. The analysis was performed at room temperature and within the diffraction angle range of $\theta=4-60^\circ$, choosing 0.5 second/step and 0.01° step size. The SEM/EDX system (Phenom XL) was used to examine the material's morphology, grain orientation, grain size, layer thickness, chemical structure, different element maps on the surface, and element ratios in the materials. The SEM/EDX device was operated in point mode with 10 kV.

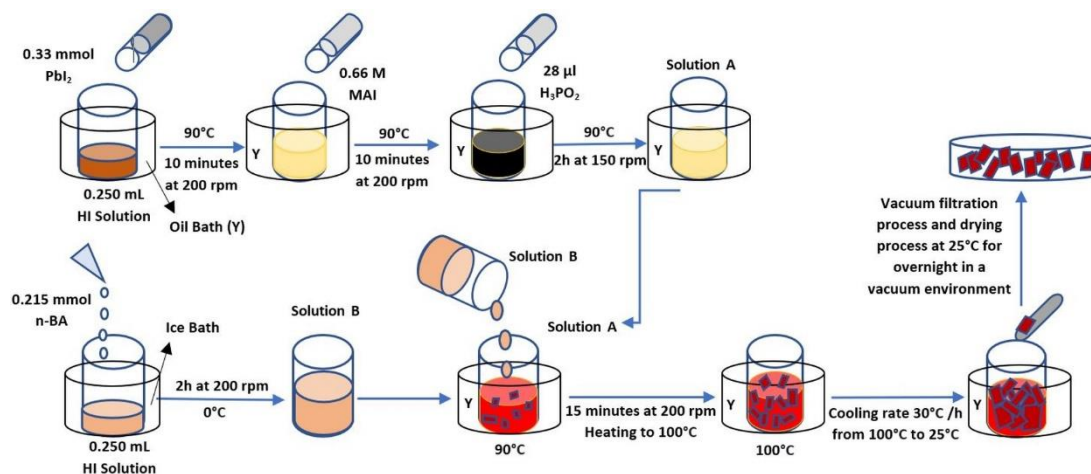


Figure 1. Schematic representation for the synthesis of 2D OHPs using STL method and limiting reagent approach.

2.4. Optical characterization

UV-Vis absorption spectroscopy was used to obtain the optical bandgap and absorption peak position of the synthesized materials. Hitachi U-5100 Spectrophotometer was operated in the wavelength range of 380-800 nm with a scanning speed of 100 nm/min. Cary Eclipse fluorescence spectrophotometer was used for the PL analyses to characterize the materials and reveal optical properties.

All the samples synthesized and investigated in this study were stored in Ar inert gas environment and all the characterization measurements were carried out at room temperature (25°C).

3. RESULTS AND DISCUSSIONS

High-quality $\text{BA}_2\text{MAPb}_2\text{I}_7$ 2D OHP single crystals with large surface area as shown in Figure 2(a-d) involving the SEM images with the corresponding EDX analyses were synthesized. The main principle of the utilized STL method is to obtain single crystals by gradually lowering the temperature. By this way, the solubility of perovskite decreases and a single crystal precipitate may form in saturated solution. The crystallization process takes place in two stages, nucleation, and crystal growth. The crystallization process begins with the formation of nucleation sites, which always occur in a supersaturated solution. The process can be controlled by adjusting the crystallization temperature and degree of saturation to maximize crystal growth and minimize co-nucleation to achieve the best single crystal quality. During the synthesis of $\text{BA}_2\text{MAPb}_2\text{I}_7$ 2D OHP single crystals, $n=1$ perovskites are synthesized as contamination[15]. This is because the solubility of perovskite single crystals in aqueous solution increases as the n value increases towards $n=\infty$ while transforming from 2D to 3D[15,25,26]. Hence, BA_2PbI_4 2D OHPs were synthesized as the growth rate of BA_2PbI_4 ($n=1$) single crystals was higher than that of $\text{BA}_2\text{MAPb}_2\text{I}_7$ ($n=2$) single crystals. In addition, due to the higher solubility of MA cations in aqueous solution than BA cations, the inability of MA cations to reach supersaturation in the prepared solution led to a further decrease in the growth rate of $\text{BA}_2\text{MAPb}_2\text{I}_7$ 2D OHP single crystals[27]. Therefore, solutions A and B were prepared with the molarity ratio of $\text{BAI}:\text{MAI}:\text{PbI}_2$ adjusted to be 0.86:0.33:0.66. Limited amounts of BA cations in solution B are added to solution A until the color turning point is reached where red nuclei are observed, which is called the limiting reagent approach.

Furthermore, BA_2PbI_4 2D OHP single crystals were synthesized by adjusting the $\text{BAI}:\text{MAI}:\text{PbI}_2$ molarity ratios to be 2:0:1 considering the stoichiometric ratio, as seen from Figure 2(e-h). When the $\text{BAI}:\text{MAI}:\text{PbI}_2$ molarity ratio was adjusted to 2:1:2 by increasing the MAI concentration, $\text{BA}_2\text{PbI}_4/\text{BA}_2\text{MAPb}_2\text{I}_7$ 2D OHP single crystal heterostructures were synthesized, as shown in Figure 2(i-k). In addition, $\text{BA}_2\text{PbI}_4/\text{BA}_2\text{MAPb}_2\text{I}_7$ heterostructures were synthesized also by adjusting the $\text{BAI}:\text{MAI}:\text{PbI}_2$ molar ratios to 2:2:2, 2:3:2 or 2:4:2 by increasing the concentration of MA cations. Due to the excess amount of MA concentration, $n=1$ perovskite structure was synthesized as contamination and prevented the synthesis of $n=2$ perovskite structure by acting as a kinetic barrier[26]. The lateral dimensions of the successfully synthesized 2D OHP single crystals ranged from tens of micrometers to a few millimeters. SEM images in Figure 2 show that perovskite single crystals have a layered structure stacked on top of each other with a smooth and homogeneous surface morphology free from grain boundaries or voids. In addition, it was observed that a small part of the red nuclei with a lateral area of hundreds of microns at the beginning of the cooling process was on the interface of the solution, and a large part was at the bottom of the solution. The reason for this is that the nucleation energy barrier, defined as the threshold energy value that must be exceeded for nucleation to occur, is significantly lower at the liquid-air interface than inside the solution. Therefore, the nucleation occurs much more easily at the interphase boundary[27]. Accordingly, it was stated that hydrophilic BA ($\text{C}_4\text{H}_9\text{NH}_3^+$) precursor cations align at the liquid-air interphase boundary, acting as a template for nucleation, rather than binding to water molecules in solution via static Coulomb interaction.

When the chemical analysis was made with the EDX method, the atomic concentration ratio of Pb:I in the structure of $\text{BA}_2\text{MAPb}_2\text{I}_7$ 2D OHP single crystals was found to be approximately 1:2, which is characteristic for the PbI_2 inorganic part of the perovskite structure. Moreover, while the weight concentrations of C and N atoms were found to be low, the weight concentrations of I and Pb atoms in the structure were found to be relatively high as shown in Figure 2(d). Previous studies have reported that perovskite structures are very sensitive to high-energy electron beams[28–32]. Therefore, these results are attributed to the increased temperature on the surface region in which high-energy electron beams are focused, causing the degradation of OHP single crystals. Accordingly, the organic part with higher volatility in the crystal structure is connected to the inorganic layers with weak van der Waals bonds. High thermal energy breaks the weak bonds and the organic volatile part splits from the structure. Owing to the same situation, similar results were observed for the BA_2PbI_4 and $\text{BA}_2\text{PbI}_4/\text{BA}_2\text{MAPb}_2\text{I}_7$ perovskites, as shown in Figure 2(h) and Figure 2(k), respectively.

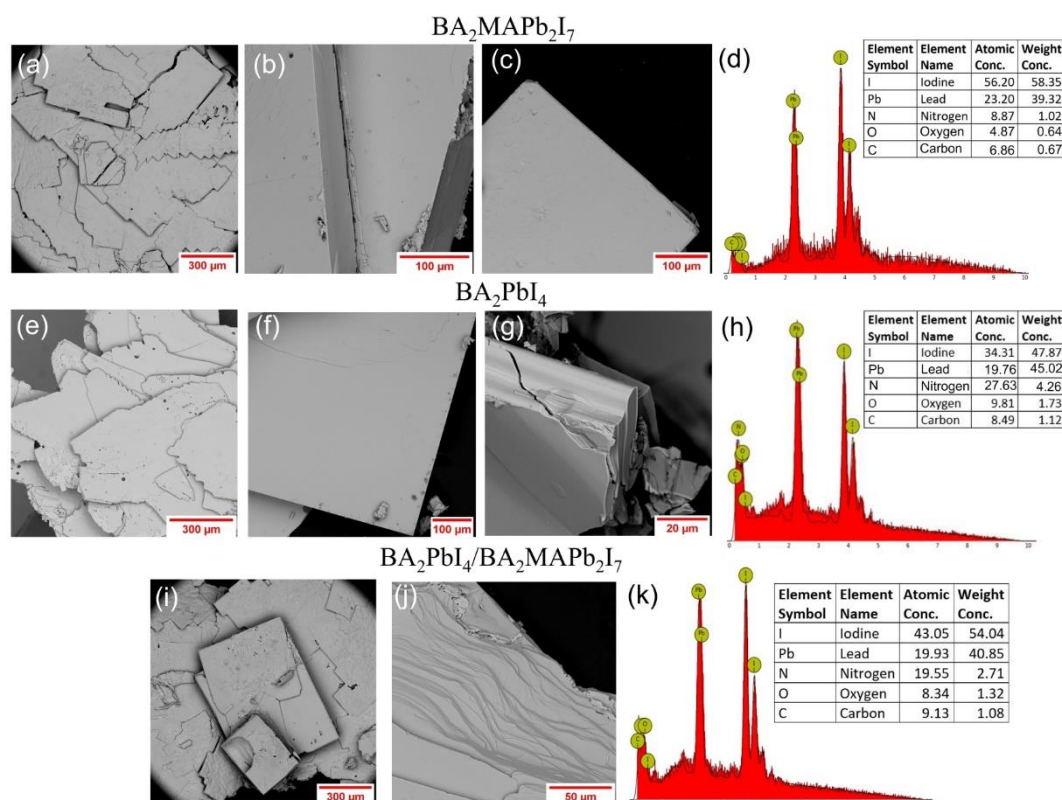


Figure 2. SEM images with the corresponding EDX spectra of the synthesized 2D OHP single crystals; **(a-d)** $\text{BA}_2\text{MAPb}_2\text{I}_7$, **(e-h)** BA_2PbI_4 , and **(i-k)** $\text{BA}_2\text{PbI}_4/\text{BA}_2\text{MAPb}_2\text{I}_7$ heterostructure.

Figure 3 shows comparative XRD patterns of BA_2PbI_4 , $\text{BA}_2\text{MAPb}_2\text{I}_7$ 2D OHP single crystals and $\text{BA}_2\text{PbI}_4/\text{BA}_2\text{MAPb}_2\text{I}_7$ 2D OHP single crystal heterostructures. The characteristic crystal planes for the crystal structure of $\text{BA}_2\text{MAPb}_2\text{I}_7$ 2D OHP single crystals was determined at diffraction peaks of 4.6° , 9.14° , 13.67° , 18.23° , 22.83° , 27.43° , 32.1° , 36.86° , respectively. In the literature, Zhou et al. reported that high intensity XRD peaks of $\text{BA}_2\text{MAPb}_2\text{I}_7$ crystals were obtained at the angles of 5.09° , 9.62° , 14.12° , 18.65° , 23.23° , 27.80° and 32.44° [33]. In addition, due to the continuity of the inorganic-organic-inorganic layer in the crystal structure of 2D OHP single crystals, the angle values at which XRD peaks increase regularly according to the d gap distance between the crystal planes[34–36]. Accordingly, the distance between the crystal planes of the synthesized 2D OHP single crystals was measured to be $d=1.964\text{nm}$ and, using the Bragg equation ($n\lambda = 2d\sin\theta$), it was calculated that the difference between the angle values between each peak should be approximately $2\theta=4.5^\circ$, which is consistent with the obtained results. XRD analysis demonstrates a single crystallinity of perovskite structures and confirms that the 2D OHPs were successfully synthesized according to the XRD results in previous studies[26,37]. Furthermore, XRD analysis identified the diffraction peaks corresponding to the characteristic crystal planes of the BA_2PbI_4 2D OHP single crystals as 6.48° , 12.94° , 19.35° , 25.89° , 32.5° , 39.22° , respectively. In the literature, Zhou et al. reported that high intensity diffraction peaks at the XRD analysis of BA_2PbI_4 crystals were obtained at the angles of 7.01° , 13.45° , 19.91° , 26.44° , 33.06° and 39.79° [25]. These results are in agreement with the results of XRD analysis in previous studies confirming the synthesis of BA_2PbI_4 2D OHP single crystals[33,37]. In addition, XRD analysis of $\text{BA}_2\text{PbI}_4/\text{BA}_2\text{MAPb}_2\text{I}_7$ 2D OHP single crystal heterostructures includes each of the diffraction peaks for characteristic planes of the crystal structures of BA_2PbI_4 and $\text{BA}_2\text{MAPb}_2\text{I}_7$ 2D OHP single crystals. These results are also consistent with the XRD results of BA_2PbI_4 and $\text{BA}_2\text{MAPb}_2\text{I}_7$ 2D OHP single crystals in the literature[15,33].

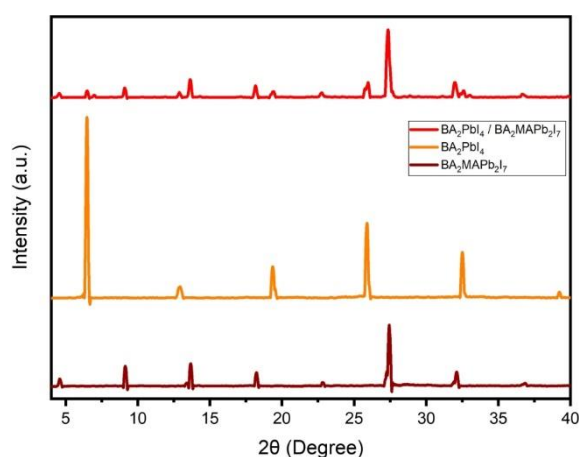


Figure 3. XRD patterns of the synthesized $\text{BA}_2\text{MAPb}_2\text{I}_7$, BA_2PbI_4 , and $\text{BA}_2\text{PbI}_4/\text{BA}_2\text{MAPb}_2\text{I}_7$ single crystals.

Absorption spectroscopy (UV-Vis) analysis was also performed to examine the optical properties of $\text{BA}_2\text{MAPb}_2\text{I}_7$ 2D OHP single crystals and showed the absorption peak at about 576 nm as shown in

Figure 4(a). Accordingly, there is a relationship between the photon energy $((\alpha h\nu)^{1/n} = \beta(h\nu - E_g))$ and the absorption coefficient $(\alpha = \beta/(h\nu) (h\nu - E_g)^n)$, and the band gap is determined by the straight line, which is drawn to the slope of the graph of $(\alpha h\nu)^{(1/2)}$ versus photon energy $(h\nu)$. The optical bandgap value was calculated as 2.04 eV by using the Tauc plot drawn in the inset figure.

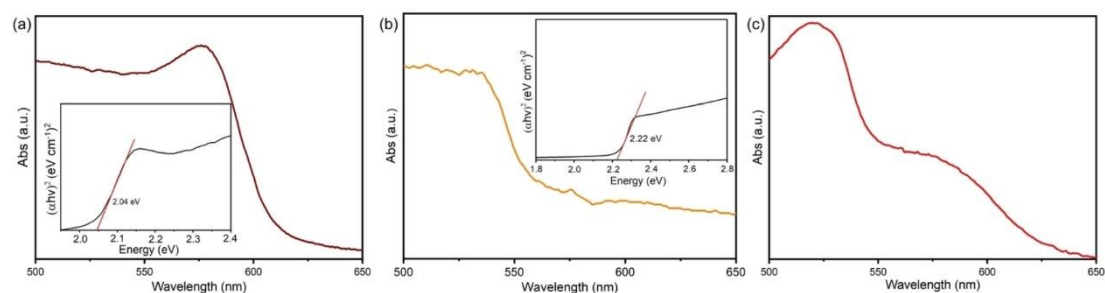


Figure 4. Absorption spectra of the synthesized single crystals; **(a)** $\text{BA}_2\text{MAPb}_2\text{I}_7$, **(b)** BA_2PbI_4 , and **(c)** $\text{BA}_2\text{PbI}_4/\text{BA}_2\text{MAPb}_2\text{I}_7$ heterostructure. Insets show the corresponding Tauc plots.

In addition, it was analyzed that the absorption onset value extends towards longer wavelengths due to the trap states of the 2D OHP single crystals[38]. BA_2PbI_4 2D OHP single crystals have an absorption peak at about 535 nm, an absorption onset value extending up to 700 nm due to the quantum confinement effect, and an optical bandgap value of 2.22 eV, as shown in Figure 4(b). When the optical properties of the heterostructure were examined by UV-Vis characterization method, it was observed that it had two absorption peaks at about 535 nm for the BA_2PbI_4 perovskite structure and at about 576 nm for the $\text{BA}_2\text{MAPb}_2\text{I}_7$ perovskite structure, as shown in Figure 4(c).

The optical properties of perovskite single crystals were investigated using the PL characterization method. In Figure 5(a), it is observed that the center of the emission peak for $\text{BA}_2\text{MAPb}_2\text{I}_7$ 2D OHP single crystal is at a wavelength of 584 nm. In addition, in the PL spectrum plot of Figure 5(b), it is observed that single crystals have a single luminescence peak at 520 nm wavelength for BA_2PbI_4 2D OHP single crystals. In Figure 5(c), $\text{BA}_2\text{PbI}_4/\text{BA}_2\text{MAPb}_2\text{I}_7$ 2D OHP single crystal heterostructure PL spectrum shows that one of the PL peaks is centered at about 588 nm for $\text{BA}_2\text{MAPb}_2\text{I}_7$ and the other PL peak is for BA_2PbI_4 2D OHP single crystals. The gray dashed line in this figure represents the data that could not be obtained experimentally due to the filtering constraint of the instrument and was plotted considering the PL spectrum of BA_2PbI_4 OHP in Figure 5 (b).

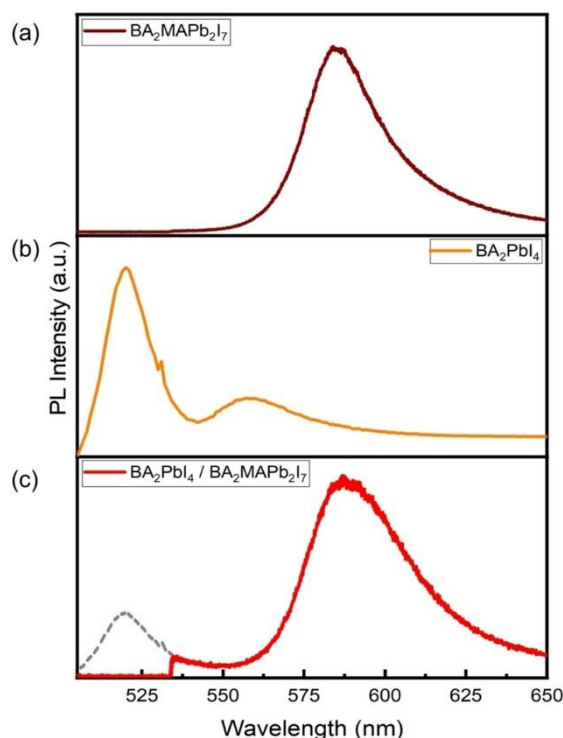


Figure 5. PL spectra of the synthesized single crystals; **(a)** $\text{BA}_2\text{MAPb}_2\text{I}_7$, **(b)** BA_2PbI_4 , and **(c)** $\text{BA}_2\text{PbI}_4/\text{BA}_2\text{MAPb}_2\text{I}_7$ heterostructure.

4. CONCLUSION

In summary, large-area high-quality $\text{BA}_2\text{MAPb}_2\text{I}_7$ 2D OHP single crystals were able to be synthesized within a few hours using solution-based STL method and limiting reagent approach. The concentration ratio of BA and MA cations was revealed to be significant for the synthesis of these crystals. Accordingly, the synthesis of $\text{BA}_2\text{PbI}_4/\text{BA}_2\text{MAPb}_2\text{I}_7$ 2D OHP single crystal heterostructures was carried out successfully. Herein, various characterization methods were utilized to investigate structural and optical properties of the synthesized 2D OHP single crystals. A novel pathway was introduced on rapid and controllable synthesis of large-area high-quality $\text{BA}_2\text{MAPb}_2\text{I}_7$ and $\text{BA}_2\text{PbI}_4/\text{BA}_2\text{MAPb}_2\text{I}_7$ 2D OHP single crystals. It is of great importance to carry out such studies in order to develop new synthesis approaches of 2D OHP materials with superior properties for use in optoelectronic applications.

ACKNOWLEDGEMENT

This work was supported by Scientific and Technological Research Council of Turkey. Project Number: TÜBİTAK 121M601.

REFERENCES

- [1] Tiwari, S.K., Sahoo, S., Wang, N. and Huczko, A., (2020), Graphene research and their outputs: status and prospect, *Journal of Science: Advanced Materials and Devices*, 5, 10–29.
- [2] Aras, F.G., Yılmaz, A., Tasdelen, H.G., Ozden, A., Ay, F., Perkgoz, N.K. and Yeltik, A., (2022), A review on recent advances of chemical vapor deposition technique for monolayer transition metal dichalcogenides (MX₂: Mo, W; S, Se, Te), *Materials Science in Semiconductor Processing*, 148, 106829.
- [3] Aras, F.G., Avad, J. and Yeltik, A., (2022), Glass- Assisted Chemical Vapor Deposition- Grown Monolayer MoS₂ : Effective Control of Size Distribution via Surface Patterning, *Physica Status Solidi (A)*, 219, 2200503.
- [4] Aras, F.G. and Yeltik, A., (2022), Role of gas flow direction on monolayer MoS₂ growth on patterned surfaces via CVD, *Semiconductor Science and Technology*, 38, 015013.
- [5] Hong, K., Le, Q. Van, Kim, S.Y. and Jang, H.W., (2018), Low-dimensional halide perovskites: review and issues, *Journal of Materials Chemistry C*, 6, 2189–2209.
- [6] Quan, L.N., Rand, B.P., Friend, R.H., Mhaisalkar, S.G., Lee, T.-W. and Sargent, E.H., (2019), Perovskites for next-generation optical sources, *Chemical Reviews*, 119, 7444–7477.
- [7] Chen, Y., Sun, Y., Peng, J., Tang, J., Zheng, K. and Liang, Z., (2018), 2D ruddlesden-popper perovskites for optoelectronics, *Advanced Materials*, 30, 1703487.
- [8] Smith, I.C., Hoke, E.T., Solis-Ibarra, D., McGehee, M.D. and Karunadasa, H.I., (2014), A layered hybrid perovskite solar-cell absorber with enhanced moisture stability, *Angewandte Chemie International Edition*, 53, 11232–11235.
- [9] Cao, D.H., Stoumpos, C.C., Farha, O.K., Hupp, J.T. and Kanatzidis, M.G., (2015), 2D homologous perovskites as light absorbing materials for solar cell applications, *Journal of the American Chemical Society*, 137, 7843–7850.
- [10] He, J., Fang, W.-H. and Long, R., (2020), Two-dimensional perovskite capping layer simultaneously improves the charge carriers lifetime and stability of MAPbI₃ perovskite: a time domain ab initio study, *The Journal of Physical Chemistry Letters*, 11, 5100–5107.

- [11] Krishna, A., Gottis, S., Nazeeruddin, M.K. and Sauvage, F., (2019), Mixed dimensional 2D/3D hybrid perovskite absorbers: the future of perovskite solar cells?, *Advanced Functional Materials*, 29, 1806482.
- [12] Zhang, Y., Lyu, M., Qiu, T., Han, E., Kim, I.K., Jung, M.-C., Ng, Y.H., Yun, J.-H. and Wang, L., (2020), Halide perovskite single crystals: optoelectronic applications and strategical approaches, *Energies*, 13, 4250.
- [13] Trivedi, S., Prochowicz, D., Parikh, N., Mahapatra, A., Pandey, M.K., Kalam, A., Tavakoli, M.M. and Yadav, P., (2021), Recent progress in growth of single-crystal perovskites for photovoltaic applications, *ACS Omega*, 6, 1030–1042.
- [14] Pham, P. V., Bodepudi, S.C., Shehzad, K., Liu, Y., Xu, Y., Yu, B. and Duan, X., (2022), 2D heterostructures for ubiquitous electronics and optoelectronics: principles, opportunities, and challenges, *Chemical Reviews*, 122, 6514–6613.
- [15] Wang, J., Li, J., Lan, S., Fang, C., Shen, H., Xiong, Q. and Li, D., (2019), Controllable growth of centimeter-sized 2D perovskite heterostructures for highly narrow dual-band photodetectors, *ACS Nano*, 13, 5473–5484.
- [16] Cheng, X., Han, Y. and Cui, B., (2022), Fabrication strategies and optoelectronic applications of perovskite heterostructures, *Advanced Optical Materials*, 10, 2102224.
- [17] Cao, F., Li, Z., Liu, X., Shi, Z. and Fang, X., (2022), Air induced formation of Cs₃Bi₂Br₉/Cs₃BiBr₆ bulk heterojunction and its dual-band photodetection abilities for light communication, *Advanced Functional Materials*, 32, 2206151.
- [18] Hwang, B. and Lee, J., (2019), 2D perovskite based self-aligned lateral heterostructure photodetectors utilizing vapor deposition, *Advanced Optical Materials*, 7, 1801356.
- [19] Wang, J., Li, J., Tan, Q., Li, L., Zhang, J., Zang, J., Tan, P., Zhang, J. and Li, D., (2017), Controllable synthesis of two-dimensional ruddlesden–popper type perovskite heterostructures, *The Journal of Physical Chemistry Letters*, 8, 6211–6219.
- [20] Li, J., Han, Z., Gu, Y., Yu, D., Liu, J., Hu, D., Xu, X. and Zeng, H., (2021), Perovskite single crystals: synthesis, optoelectronic properties, and application, *Advanced Functional Materials*, 31, 2008684.
- [21] Liu, J., Xue, Y., Wang, Z., Xu, Z.-Q., Zheng, C., Weber, B., Song, J., Wang, Y., Lu, Y., Zhang, Y. and Bao, Q., (2016), Two-dimensional CH₃NH₃PbI₃ perovskite: synthesis and optoelectronic application, *ACS Nano*, 10, 3536–3542.
- [22] Protesescu, L., Yakunin, S., Nazarenko, O., Dirin, D.N. and Kovalenko, M. V., (2018), Low-cost synthesis of highly luminescent colloidal lead halide perovskite nanocrystals by wet ball milling,

ACS Applied Nano Materials, 1, 1300–1308.

- [23] Zhu, T. and Gong, X., (2021), Low- dimensional perovskite materials and their optoelectronics, *InfoMat*, 3, 1039–1069.
- [24] Poglitsch, A. and Weber, D., (1987), Dynamic disorder in methylammoniumtrihalogenoplumbates (II) observed by millimeter- wave spectroscopy, *The Journal of Chemical Physics*, 87, 6373–6378.
- [25] Raghavan, C.M., Chen, T.-P., Li, S.-S., Chen, W.-L., Lo, C.-Y., Liao, Y.-M., Haider, G., Lin, C.-C., Chen, C.-C., Sankar, R., Chang, Y.-M., Chou, F.-C. and Chen, C.-W., (2018), Low-threshold lasing from 2D homologous organic–inorganic hybrid ruddlesden–popper perovskite single crystals, *Nano Letters*, 18, 3221–3228.
- [26] Stoumpos, C.C., Cao, D.H., Clark, D.J., Young, J., Rondinelli, J.M., Jang, J.I., Hupp, J.T. and Kanatzidis, M.G., (2016), Ruddlesden–popper hybrid lead iodide perovskite 2D homologous semiconductors, *Chemistry of Materials*, 28, 2852–2867.
- [27] Wang, K., Wu, C., Yang, D., Jiang, Y. and Priya, S., (2018), Quasi-two-dimensional halide perovskite single crystal photodetector, *ACS Nano*, 12, 4919–4929.
- [28] Klein-Kedem, N., Cahen, D. and Hodes, G., (2016), Effects of light and electron beam irradiation on halide perovskites and their solar cells, *Accounts of Chemical Research*, 49, 347–354.
- [29] Xiao, C., Li, Z., Guthrey, H., Moseley, J., Yang, Y., Wozny, S., Moutinho, H., To, B., Berry, J.J., Gorman, B., Yan, Y., Zhu, K. and Al-Jassim, M., (2015), Mechanisms of electron-beam-induced damage in perovskite thin films revealed by cathodoluminescence spectroscopy, *The Journal of Physical Chemistry C*, 119, 26904–26911.
- [30] Kim, T.W., Shibayama, N., Cojocaru, L., Uchida, S., Kondo, T. and Segawa, H., (2018), Real-time in situ observation of microstructural change in organometal halide perovskite induced by thermal degradation, *Advanced Functional Materials*, 28, 1804039.
- [31] Ran, J., Dyck, O., Wang, X., Yang, B., Geohegan, D.B. and Xiao, K., (2020), Electron beam related studies of halide perovskites: challenges and opportunities, *Advanced Energy Materials*, 10, 1903191.
- [32] Rothmann, M.U., Li, W., Zhu, Y., Liu, A., Ku, Z., Bach, U., Etheridge, J. and Cheng, Y., (2018), Structural and chemical changes to CH₃NH₃PbI₃ induced by electron and gallium ion beams, *Advanced Materials*, 30, 1800629.
- [33] Zhou, J., Chu, Y. and Huang, J., (2016), Photodetectors based on two-dimensional layer-structured hybrid lead iodide perovskite semiconductors, *ACS Applied Materials & Interfaces*, 8,

25660–25666.

- [34] Xu, Y., Li, Y., Wang, Q., Chen, H., Lei, Y., Feng, X., Ci, Z. and Jin, Z., (2022), Two-dimensional BA₂PbBr₄-based wafer for X-rays imaging application, *Materials Chemistry Frontiers*, 6, 1310–1316.
- [35] Lin, J., Chen, D., Wu, C., Hsu, C., Chien, C., Chen, H., Chou, P. and Chiu, C., (2021), A universal approach for controllable synthesis of n- specific layered 2D perovskite nanoplates, *Angewandte Chemie International Edition*, 60, 7866–7872.
- [36] Choi, E., Zhang, Y., Soufiani, A.M., Lee, M., Webster, R.F., Pollard, M.E., Reece, P.J., Lee, W., Seidel, J., Lim, J., Yun, J.-H. and Yun, J.S., (2022), Exploration of sub-bandgap states in 2D halide perovskite single-crystal photodetector, *Npj 2D Materials and Applications*, 6, 43.
- [37] Miao, Y., Xiao, Z., Zheng, Z., Lyu, D., Liu, Q., Wu, J., Wu, Y., Wen, X., Shui, L., Hu, X., Wang, K., Tang, Z. and Jiang, X., (2022), Designable layer edge states in quasi- 2D perovskites induced by femtosecond pulse laser, *Advanced Science*, 9, 2201046.
- [38] Du, Q., Zhu, C., Yin, Z., Na, G., Cheng, C., Han, Y., Liu, N., Niu, X., Zhou, H., Chen, H., Zhang, L., Jin, S. and Chen, Q., (2020), Stacking effects on electron–phonon coupling in layered hybrid perovskites via microstrain manipulation, *ACS Nano*, 14, 5806–5817.



RESEARCH ARTICLE

POLYDATIN, A HERBAL BIOFLAVONOID, IS PROTECTIVE AGAINST CEREBRAL ISCHEMIA-REPERFUSION INJURY: MOLECULAR, BIOCHEMICAL AND HISTOLOGICAL DATA

Saadet ÇELİKÖZLÜ^{1*}, Said ALTİKAT², Filiz ÖZYİĞİT³, Sibel KÖKTÜRK⁴, Halit ÇELİKÖZLÜ⁵

^{1*}Kütahya Dumlupınar University, Altıntaş Vocational School, Altıntaş, Kütahya, Turkey, saadet.celikozlu@du.edu.tr, ORCID: 0000-0001-9825-6458

²Kütahya Health Sciences University, Faculty of Medicine, Department of Biochemistry, Kütahya, Turkey, sayit.altikat@ksbu.edu.tr, ORCID: 0000-0002-5763-3787

³Bandırma On Yedi Eylül University, Faculty of Medicine, Department of Pharmacology, Bandırma, Balıkesir, Turkey, fozyigit@bandirma.edu.tr, ORCID: 0000-0002-0062-4281

⁴Istanbul University, Faculty of Medicine, Department of Histology and Embriology, İstanbul, Turkey, sibel.kokturk@istanbul.edu.tr, ORCID: 0000-0001-5636-3300

⁵Kütahya Health Sciences University, Faculty of Health Sciences, Kütahya, Turkey, halit.celikozlu@ksbu.edu.tr, ORCID: 0000-0002-0456-7077

Receive Date:02.12.2022

Accepted Date: 15.03.2023

ABSTRACT

This study aims to research the protective effects Polydatin have against cerebral ischemia/reperfusion damage. Polydatin is a natural polyphenic phytoalexin and which has strong antioxidant properties. In the present study, 5 groups were prepared as control, sham, ischemia/reperfusion (IR), Polydatin 30 (Pol 30), and Polydatin 60 (Pol 60). The four-vessel occlusion model was used to induce ischemia. Polydatin was injected intraperitoneally 30 minutes before ischemia. Hematoxylin Eosin staining were applied for histopathological study, SOD, CAT, and MDA levels determined, and TNF- α mRNA expression levels were measured by the RT-qPCR technique in brain tissue. According to the results, a serious loss of neurons in the CA 1 region of the hippocampus was observed in the IR group. Neuronal damage in the hippocampus decreased and the number of neurons increased significantly in the Pol 60 group compared to the IR group. CAT and SOD levels were reduced, and the MDA level rose in the IR group. In Pol 60 and Pol 30 groups, an increase was observed in the CAT and SOD levels, a decrease was observed in the MDA and total protein levels compared to the IR group. The amount of TNF- α mRNA expression in the brain tissues of the IR group was significantly higher compared to the control group. In the Pol 60 group, mRNA expression level decreased significantly compared to the IR group. In conclusion, the increase in MDA, decrease in SOD and CAT values, increase in TNF- α gene mRNA expression, and histological damage in the brain because of cerebral ischemia/reperfusion in rats were restored to normal levels with 30 and 60 mg/kg polydatin administration as protective before ischemia. Especially at 60 mg/kg polydatin supplementation with antioxidant properties has a neuroprotective effect against oxidative stress damage caused by cerebral ischemia/reperfusion.

Key Words: *Cerebral Ischemia, Reperfusion, Polydatin, Protective Effect.*

1. INTRODUCTION

Cerebral ischemia occurs with a temporary or permanent decrease in cerebral blood flow as a result of thrombotic or thromboembolic arterial occlusion. Currently, thrombolytic drugs are used to provide cerebral perfusion and there is no other approved treatment [1]. In general, thrombolytic therapy ameliorates the acute effect of ischemia by regulating blood flow, but this treatment does not provide a significant improvement in motor and cognitive impairments [2]. For this reason, it is necessary to investigate the mechanisms of cerebral ischemia formation and to identify potent neuroprotective agents that can be used after ischemia occurs.

Reperfusion occurs after thrombolytic therapy. Oxygen is restored by reperfusion, making this situation worse because a large amount of reactive oxygen species are formed with oxygen, and irreversible damage occurs in the cell [3]. Oxidative damage, inflammations, and apoptosis develop in cerebral ischemia/reperfusion damage. Therefore, previous research has indicated that antioxidant, anti-apoptotic, and anti-inflammatory agents can be used as a protective agent against cerebral ischemia/reperfusion injury [4]. In this study, we examined the protective effects of polydatin, which has a strong antioxidant effect, against cerebral ischemia/reperfusion injury.

Polydatin is a natural polyphenic phytoalexin derived from the roots of a Chinese plant called *Polygonum cuspidatum*. Polydatin is also found in foods we consume daily, such as grapes, peanuts, cocoa products, and chocolate [5-9]. Its chemical formula is C₂₀H₂₂O₈ (3, 4', 5 – trihydroxy stilbene – 3 – β – mono – D – glucoside). It is the glycoside form of resveratrol and is also known as Piceid. *Polygonum cuspidatum* has been used in Chinese medicine since ancient times as an antitussive, antiasthmatic, expectorant and for blood lipid improvement, high cholesterol, and hypertension [10-12]. However, with a detailed study of its chemical extraction, it has been found to have some important effects, such as antimicrobial [13], anti-inflammatory [14], antioxidative [15-18], hepatoprotective [19, 20], anticancer [21], antiapoptotic effect [22], scavenging free radical, increasing antioxidant production, regulating immune functions [23], healing ischemic damage in some organs such as the heart, lungs [24,25], kidneys [26], and brain [2, 14, 27].

Previous research showed that polydatin has a protective effect against injury caused by an acute shock in neurons, smooth muscle cells, and erythrocytes [28]. It has also been determined that polydatin prevents sepsis-induced multiple organ dysfunction syndrome which causes mitochondrial injury in the lung, liver, kidney, and intestines [29-31]. In a study, it was determined that polydatin can cross the blood-brain barrier [14]. With its feature to pass the blood-brain barrier, polydatin can prevent cerebral ischemia-reperfusion damage. In inflammation models in previous studies, it was indicated that polydatin inhibits some pro-inflammatory cytokines [32]. It also decreased MDA and increased SOD and CAT thus it improved oxidative stress parameters [33].

This study aimed to determine the effects of polydatin on the levels of MDA, SOD, and catalase, which are oxidative stress parameters in ischemia-reperfusion injury. We also investigated the mRNA expression level of the TNF-α gene.

MDA is a lipid peroxidation marker. The reperfusion process after ischemia is very favorable for lipid peroxidation and the formation of new free radicals. [34]. Due to lipid peroxidation, ATPase activity decreases and the synthesis of vital proteins is inhibited. As a result, proteolytic enzymes and mitochondrial matrix enzymes are released and cellular damage occurs. In this case, the antioxidant defense system (SOD, catalase) plays a very important role in preventing neuronal death. [35].

Studies show an increase in the synthesis of proinflammatory cytokines such as TNF- α , IL-1 β , and IL-6 after ischemia. There is a correlation between the increase in TNF- α , IL-1 β , and IL-6 levels as a result of ischemia/reperfusion, an increase in mortality, acute respiratory distress syndrome, and increased risk of multiple organ failure [36]. The pathological process driven by increased intracellular Ca⁺² during ischemia/reperfusion is the formation of calcium pyrophosphate and uric acid. This process sends signals that activate inflammatory agents such as TNF- α and IL-1 β (interleukin-1 β), which exacerbate ischemia-reperfusion injury. These cytokines in turn activate transcription factors such as NF- κ B to increase the expression of other cytokines and chemokines. Thus, it fires a cytokine storm that will trigger further cell damage with deep inflammation [37].

This study focuses on the free radical scavenging and inflammatory cytokine inhibitory effects of polydatin. For this purpose, we investigated the neuroprotective effects of polydatin, a new agent that can be used prophylactically against ischemia-reperfusion injury.

2. MATERIAL AND METHOD

Animal experiments of this study were conducted in the Kütahya Health Sciences University Faculty of Medicine Experimental Animal Breeding Research and Application Center laboratory. Ethical approval was token for animal experiments from the Animal Experiments Local Ethics Committee of Kütahya Health Sciences University Faculty of Medicine (No: 2019.03.04).

2.1. Experimental Groups

Control group (n=8): No treatment was applied to the rats in this group.

Sham group (n=8): Surgical procedure was applied to the rats in this group, but ischemia/reperfusion damage was not created. 1 ml of saline was given one hour before the surgical procedure.

Ischemia/reperfusion (IR) group (n=8): Half an hour of ischemia and half an hour of reperfusion were applied to the rats in this group.

Polydatin 30mg/kg + IR (Pol 30) group (n=8): 30mg/kg polydatin was injected intraperitoneally to the rats in this group one hour before the ischemia. (PD (C₂₀H₂₂O₈, MW: 390.38, purity \geq 95%), Pub Chem Substance ID 329750984, Sigma- Aldrich Co. LLC. St. Louis, MO, USA).

Polydatin 60 mg/kg + IR (Pol 60) group (n=8): 60mg/kg polydatin was injected intraperitoneally to the rats in this group one hour before the ischemia.

2.2. Experimental Procedure-Induction of Ischemia/Reperfusion

In our study, the four – vessels occlusion model was applied to induce ischemia. After anesthesia and analgesia, an incision was made in the midline of the dorsal of the neck, and both *Arteria vertebralis* were cauterized along the foramen alaris of C1 with bipolar electrocautery (Fig. 1). 24 hours after cautery application, midline incision of the neck was made. After superficial microdissection was performed, it was advanced towards the right and left carotid arteries (*Arteria carotis communis*, ACC) with deep microdissection. When the trachea was seen, the paratracheal muscles were dissected, and it was reached to ACC and both ACCs were kept closed for 30 minutes with the Vasco Bulldog clamp (Fig. 2). Then, the clamps were removed and reperfusion was applied for 30 minutes.



Figure 1. Electrocautery application (24 hour before ischemia).

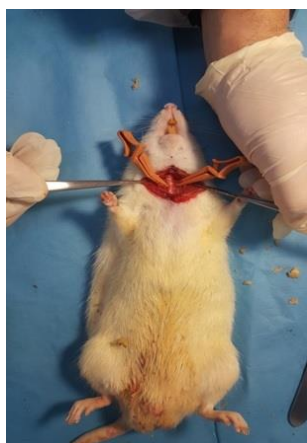


Figure 2. Ischemia application (ACCs were kept closed for 30 minutes with the Vasco Bulldog clamp).

After ischemia and reperfusion, the rats were sacrificed and brains were removed with craniectomy. Brain tissues were divided into three parts. The first piece was kept in a 10% formaldehyde for histological examination. The second and third pieces were kept at -80°C until biochemical and molecular examinations were performed.

2.3. Histopathological Examination

Brain tissues were fixed with 10% formaldehyde solution. Then brain tissues were embedded in paraffin after the routine tissue fixation process and sectioned at 5-10 μ m with a microtome. Hematoxylin Eosin (H&E) staining were applied to the tissues. Stains were examined under a microscope, the CA1 region of the hippocampus was photographed and analyzed with an image analysis program.

2.4. Biochemical Analyses

For biochemical analysis, brain parts that were properly extracted from rats were stored at -80°C. Before analyses, brain tissues were homogenized at 8000 rpm for 5 minutes with a homogenizer in a chilled sodium phosphate buffer at pH7.4, 50 μ M containing 0.25 M sucrose. The homogenates were precipitated by centrifugation at 10,000 rpm at +4°C for 30minutes and the supernatant was used to define SOD, CAT, and MDA levels, and protein quantification.

2.4.1. Determination of malondialdehyde (MDA) level

MDA levels were defined using the double heating method of Draper and Hadley [38]. In this method, thiobarbituric acid (TBA) reacts with MDA and a pink color is formed. This color was measured spectrophotometrically at 532 nm. MDA concentrations were calculated with the aid of the standard table of the MDA-TBA complex [39-42].

2.4.2. Determination of catalase (CAT) activity level

CAT activities were determined using the Aebi method [43]. CAT enzyme activities were measured spectrophotometrically by observing changes in sample and blank absorbance at 240 nm for one minute.

2.4.3. Determination of superoxide dismutase (SOD) activity level

SOD levels were detected depending on spectrophotometric measurement of the inhibitory effect of SOD on the autoxidation of 6-hydroxydopamine (6-OHDA) [44, 45]. Spectrophotometric measurements were made at 490nm until the 60th second of oxidation because the autoxidation rate curve is constant in the first minute. The results were calculated as U/mg protein.

2.4.4. Protein quantification

The protein concentration of tissue homogenates was calculated as mg/ml using bovine serum albumin by method of Lowry et al. [46].

2.4.5. Statistically analysis

The results obtained were analyzed using IBM SPSS 20 package program. While ANOVA test was used for intergroup comparisons, the Post hoc test was used for intragroup comparisons and $p < 0.05$ was statistically significant.

2.5. Molecular Analyses

For the molecular study, brain tissues were homogenized with a homogenizer before RNA isolation from the brain tissue stored at -80°C. Then the brain tissues were centrifuged, and mRNA was isolated

from the supernatant using the High Pure RNA Tissue Kit-Version09 (Roche). Subsequently, cDNA was obtained with Transcriptor First Strand cDNA Synthesis Kit-Version6.0 (Roche). Sample cDNAs were diluted 1 : 10 with PCR-grade water. The amount of mRNA expression of the TNF- α gene was determined by RT - qPCR using the FastStart Essential DNA Green Master (Roche) in accordance with the kit procedures, for which specially produced primers were used. The base sequence of the primers is given below. CP values and melting curves of the samples were determined by RT-qPCR analysis. The data obtained were analyzed using LightCycler480 Instrument Software Version1.5.1.

Rat TNF- α (Forward): 5' TGAACTTCGGGGTGATCG 3'
Rat TNF- α (Reverse): 5' GGGCTTGTCACCTCGAGTTTT 3'

2.5.1. Housekeeping gene

B-Actin gene was used as the housekeeping gene for normalization. The specific production primer sequences of the β -Actin gene used are given below.

β -Actin (Forward): 5' CCCGCGAGTACAACCTTCT 3'
 β -Actin (Reverse): 5' CGTCATCCATGGCGAACT 3'

3. RESULTS

3.1. Histological Examination Results

A nucleus with prominent round or oval shaped nucleolus surrounded by a homogeneously stained cytoplasm was observed in the center of the perikaryon in most neurons in the CA1 region of the hippocampus in the control and sham groups. (Fig. 3-a). It was observed that hippocampal neurons were arranged in a certain order in the sham and control groups.

CA1 neurons of the rat hippocampus in the IR group showed morphological changes consistent with degeneration. Most of the neurons of the IR group showed dark staining because of the condensation of their cytoplasm and nucleus, which is an indicator of degeneration. The amount of CA1 neurons reduced significantly in the IR group. Because the distance between cells increased, the neurons were spaced apart and randomly distributed and showed an irregular order (Fig. 3-b).

It was determined that hippocampal neuron damage decreased, and a statistically significant increase in the number of neurons was observed in the Pol 60 group compared to the IR group. There was no significant difference in neuronal damage and amount of neuron in Pol 30 group (Fig. 3-c and 3-d).

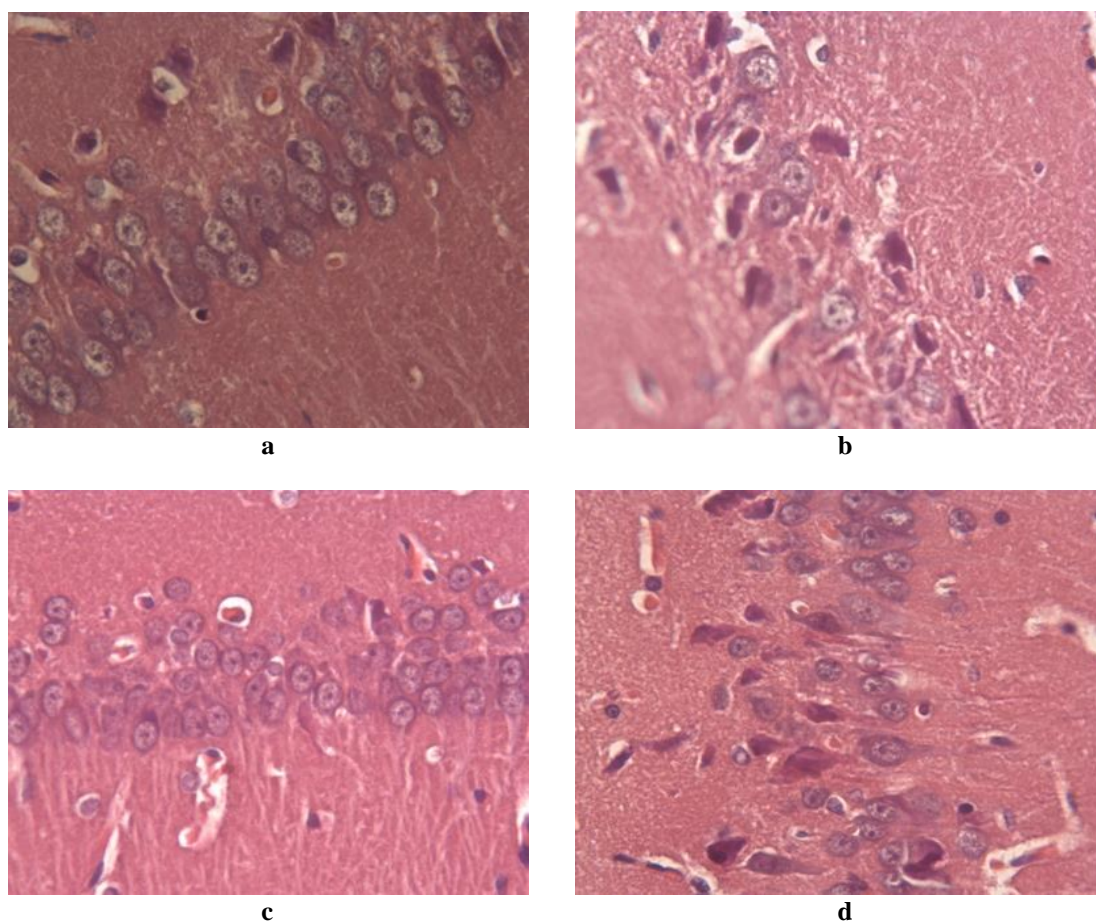


Figure 3. Hippocampal CA1 region in the control and experimental groups, H&E, 40X. **a.** Control group (staining of neurons are homogeneous, large and round-shaped nuclei, prominent nucleoli) , **b.** IR group (dark and shrunken neurons with many pycnotic nuclei, a large distance between neurons due to loss of neurons, irregularly distributed neurons), **c.** Pol 60 group (Only a few damaged neurons were observed). **d.** Pol 30 group (Neurons with multiple hyperchromatic and pycnotic nuclei and also neuron loss was observed).

3.2. Biochemical Analysis Results

Values obtained as a result of biochemical analysis are given in Table 1.

Table 1. Comparison of the biochemical analysis results of the groups.

PARAMETER*	Control (n=8)	Sham (n=8)	IR (n=8)	Pol 30 (n=8)	Pol 60 (n=8)
------------	------------------	---------------	-------------	-----------------	-----------------

CAT (U/mg.protein)	0.98±0.32 ^a	0.81±0.27 ^a	0.93±0.64 ^a	1.09±0.74 ^b	1.12±0.79 ^b
SOD (U/mg.protein)	5.53±0.72 ^a	5.43±0.25 ^a	4.44±1.08 ^b	5.39±0.95 ^a	5.88±0.45 ^a
MDA (nmol/mg.protein)	9.34±0.2 ^a	10.31±0.6 ^a	17.32±0.1 ^b	14.85±0.7 ^c	11.15±0.5 ^d
T.Protein (mg /ml)	88.5±0.2	91.3±0.8	90.8±0.7	78.5±0.6	81.3±0.4

Results are given as mean ± SD.

* : Statistical significance; numbers shown with the same letters on the horizontal plane are not statistically different from each other ($p > 0.05$), while the numbers shown with different letters are statistically significantly different from each other ($p < 0.05$).

There was no significant difference between the control and sham groups in the CAT values. A slight decrease was determined in the IR group in the CAT levels compared to the control, but this value was not significant. The CAT values of Pol 30 and Pol 60 groups increased significantly when compared with control and IR groups. There were no statistically significant differences between the Pol 30 and Pol 60 groups (Fig. 4).

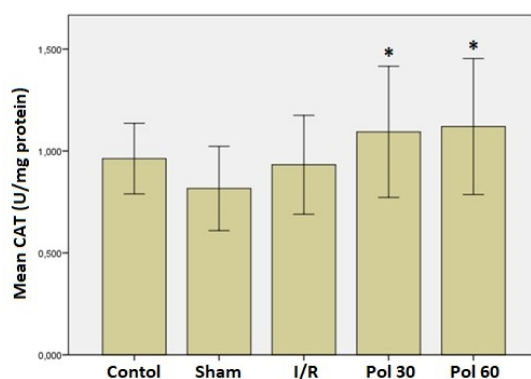


Figure 4. Average CAT levels in brain tissues. (*compared to control $p < 0.05$)

There was no significant difference between the SOD values of the control and sham groups. A significant reduction was detected in the SOD values of the IR group compared to the control. Compared to the IR group, the SOD values of the Pol 30 and Pol 60 groups increased significantly. No significant difference was exhibited between Pol 30 and Pol 60 groups in terms of the SOD values (Fig. 5).

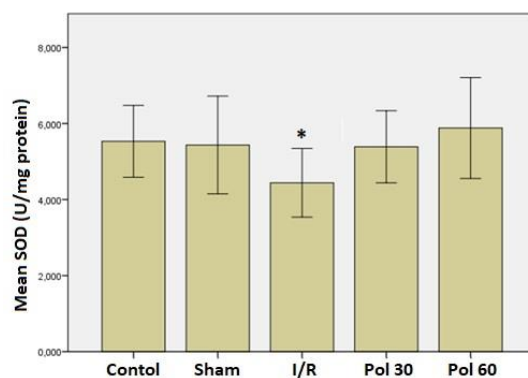


Figure 5. Average SOD levels in brain tissues. (*compared to control $p < 0.05$)

The mean MDA value increased statistically significantly in the IR group compared to the control. The MDA levels of the Pol 30 and Pol 60 groups were significantly decreased when compared to the IR. The decrease in the MDA value of the Pol 60 group was closer to the control group. There was also a statistically significant difference between Pol 30 and Pol 60 groups (Fig. 6).

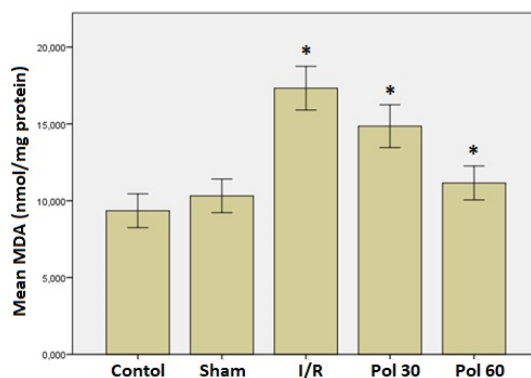


Figure 6. Average MDA levels in brain tissues. (*compared to control $p < 0.05$)

There were no significant differences between the control, sham, and IR groups in total protein values. A significant decrease was observed in the total protein values of the Pol 30 and Pol 60 groups compared to the IR group. There were no significant differences between the Pol 30 and Pol 60 groups in terms of the total protein values.

3.3. Molecular Analysis Results

TNF- α mRNA expression levels of the groups are given in Figure 7. RNA was isolated from brain tissues and TNF- α mRNA expression level was determined by RT-qPCR. According to the results, there were no differences between the control group and the sham group in mRNA expression values

in brain tissue. TNF- α mRNA expression levels significantly increased in the IR group, which was not given polydatin by applying only ischemia/reperfusion, compared to control and sham groups.

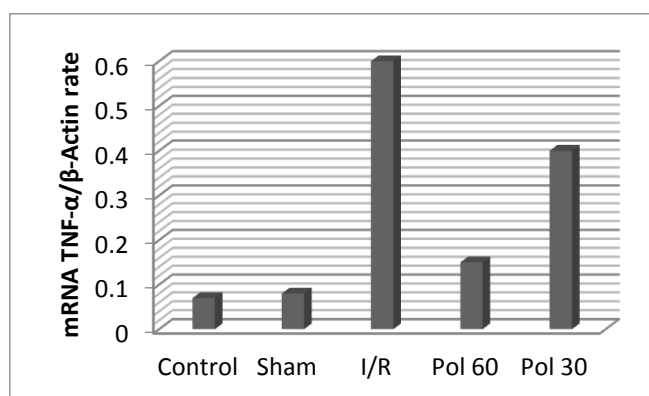


Figure 7. TNF- α mRNA expression levels of the experimental groups.

A significant reduction was observed in the mRNA expression level in the Pol 60 group, in which 60 mg/kg Polydatin was administered before ischemia-reperfusion as a preservative compared to the IR group, and it was determined that it reduced to a value close to the control and sham groups. In the Pol 30 group, the TNF- α mRNA expression value slightly decreased compared to the IR group, but this reduction was not significant.

4. DISCUSSION

In the first few minutes of ischemia, a cytotoxic response occurs, including oxidative stress, proinflammatory response, neuronal death, and neurological injury [47-49]. Therefore, inhibition of the inflammatory response and activation of the antioxidant defense system in the early phase of ischemia are important for reducing ischemic damage [14]. For this reason, this study, aims to examine the protective effects of polydatin, which has a potential antioxidant effect as in many polyphenol compounds, against cerebral ischemia/reperfusion injury. Various animal models of cerebral ischemia have been improved to illustrate the clinical condition of humans as exactly as possible. The anatomy of cerebral vasculature does not differ greatly in rodent and humans, so rat models have often been used in animal experiments on brain ischemia [19].

MDA, SOD, CAT and total protein values are important markers for oxidative stress. MDA is formed as a result of lipid peroxidation and is an important organic compound. It has been shown in previous studies that MDA levels increase significantly after ischemia [50]. In the study of Li et al. [33], in the four – vessels occlusion model of cerebral ischemia, it was reported that the MDA level increased 3-fold. CAT and SOD are antioxidant enzymes. They are protective against the detrimental effects of super oxide radicals. The activity of this enzyme decreases in cerebral ischemia [50]. Hippocampal CAT and SOD levels decreased by 32% and 27%, respectively, in rats that were applied the four-vessel occlusion model [33].

In this study, it was detected that while MDA level rose, SOD and CAT levels fell, and there was no significant change in the total protein level in the IR group rats compared to the control group. It was observed that MDA level reduced significantly in Pol 30 and Pol 60 groups, in which 30 and 60 mg/kg polydatin were administered as a protective. Especially the decrease in the Pol 60 group was closer to the control. The SOD and CAT values of these groups were significantly higher compared to the I / R group. The mean total protein level decreased significantly in the Pol 30 and Pol 60 groups compared to the control and IR groups.

Previous studies support the data obtained in our study. Li et al. [33] applied polydatin to rats for 30 days after cerebral ischemia induced by the four-vessel occlusion method and found that the MDA level decreased by 40%. Also, this decrease varied depending on the concentration. It was observed that polydatin administered at doses of 25mg/kg and 50mg/kg decreased the MDA levels by 49% and 57%, respectively [33]. In addition, in the same study, it was observed that the application of polydatin increased CAT and SOD activities approximately 1,4 times [33]. Ji et al. [14] applied 50 mg/kg polydatin to rats immediately after ischemia created by the cerebral artery occlusion model and found that the levels of SOD1 protein and mRNA expression increased 2,3 times. In another study, it was determined that cell viability increased significantly, MDA level decreased and SOD activity increased with polydatin administration against ischemic damage due to oxygen-glucose deprivation [23]. Similar results were also obtained in a study on the effects of polydatin on learning and memory [33].

These results demonstrate that polydatin can develop cellular antioxidant properties and effectively decrease neuronal cell loss and damaged area to reduce oxidative stress caused by cerebral ischemia. However, it can be said that the protective effect of polydatin against ischemia/reperfusion damage is related to its anti-oxidative activity.

After cerebral ischemia reperfusion, degeneration and tissue losses are observed in neurons because of lack of oxygen to the brain tissue. According to the results of the study of Yaidikar et al. [51], H&E-stained sections of the brain tissues of the group in which ischemia was created with the cerebral artery occlusion model showed many degenerated neurons and morphological changes due to edema. In another study, 10 days after ischemia/reperfusion, cresyl violet staining was performed to the brain tissues. In the brain tissues, concentrated, pyknotic and shrunken neurons were determined in the CA 1 region of the hippocampus [52]. In another study, Janyou et al. [53] observed that neurons in the cortex region of the brains, which were removed 24 hours after ischemia/reperfusion, were composed of a pyknotic nucleus and a vacuole surrounding it. In the study of Wang et al. [54], necrosis, reticular lesions, pyknotic or lost nuclei in neurons, cytoplasmic dissolution, and cellular edema were observed in the brain tissue of mice induced with cerebral ischemia/reperfusion.

The results of our study are also similar to previous studies. In the IR group, hippocampal CA1 neurons showed morphological changes consistent with degeneration. Dark staining and loss of CA 1 neurons were detected in the IR group because of the densification of the cytoplasm and nucleus of the neurons. In addition, the neurons showed a spaced and random order due to the increased intercellular distance. Neuronal injury in the hippocampus decreased and the number of neurons increased statistically significantly, especially in the Pol 60 group compared to the IR group. These

findings show that polydatin, a powerful antioxidant, neutralizes free radicals caused by ischemia/reperfusion, prevents neuronal loss in the brain, and thus prevents the brain from being damaged.

In ischemia, some neuronal cells (microglia cells, neurons, astrocytes, endothelial cells) that secrete inflammatory cytokines are also activated. In this study, we determined the mRNA expression amounts of the TNF- α (tumor necrosis factor) gene, which is one of the inflammation factors, is released from endothelial cells due to the increase of superoxide radicals as a result of ischemia and reperfusion. The results of this study exhibited that the mRNA expression level of the TNF- α gene was significantly higher in the IR group compared to the control. In the Pol 60 group, the mRNA expression level rose to a value close to the control.

Similar results are seen in other studies. In many studies, an increase in TNF- α mRNA expression was reported after cerebral ischemia/reperfusion [28,55,56]. Liu et al. [26] found that polydatin statistically significant decreased the high level of TNF- α and IL - 1 β caused by ischemia/reperfusion in the kidneys. On the other hand, Xu et al. [18] found that TNF- α , IL - 1 β and IL - 6 genes, which rose in serum as a result of oxidative stress after liver and brain injury, decreased with polydatin administration. Li et al. [27] observed that polydatin treatment decreased the amount of mRNA expression of the TNF- α gene, which increased as a result of lung damage. These data show that the effects of polydatin on ameliorating cerebral ischemia/reperfusion damage are achieved by inhibiting TNF- α proinflammatory cytokines.

There are limitations in this study, such as the fact that there is only one drug group and the mechanism of action of the drug used is not clear. In the study, the effects of two different doses of a single drug (polydatin) were compared. Results can be supported by comparison with another drug with proven efficacy. In addition, the protective effect of polydatin against ischemia/reperfusion damage was determined in the study, but the mechanism of action was not studied. Obtained results can be strengthened with immunohistochemical data. Studies on this subject are needed.

5. CONCLUSION

According to the findings of this research, the increase in MDA, decrease in SOD and CAT values, increase in TNF- α gene mRNA expression and histological damage in the brain because of cerebral ischemia/reperfusion in rats were restored to normal levels with 30 and 60 mg/kg polydatin administration as protective before ischemia.

As a result, with the data of this study, it has been detected that especially high-dose polydatin supplementation of 60 mg/kg has a neuroprotective effect against oxidative stress damage caused by cerebral ischemia/reperfusion thanks to its antioxidant potential.

Existing risks can be avoided by using polydatin prophylactically before the ischemia-reperfusion injury occurs in humans. For this purpose, dietary habits can be regulated with foods containing polydatin. It may be possible to reduce thrombolytic risks when supported by an exercise program too.

ACKNOWLEDGEMENTS

This work was supported by the Scientific Research Project Unit of Kütahya Dumlupınar University (No: 2018-07). This study was presented as oral presentation 1. International Health Sciences And Biomedical Congress on January 23-24 2021, Ankara, Turkey.

REFERENCES

- [1] Yang, W., Chen, X., Pan, J., Ge, H., Yin, K., Wu, Z., Li, X., Sha, D., and Xu, Y., (2015), Malibatol A protects against brain injury through reversing mitochondrial dysfunction in experimental stroke, *Neurochemistry International*, 80, 33-40.
- [2] Tang, K.S. and Tan, J.S., (2019), The protective mechanisms of polydatin in cerebral ischemia, *European Journal of Pharmacology*, 842, 133-138.
- [3] Gao, Y., Chen, T., Lei, X., Li, Y., Dai, X., Cao, Y., Ding, Q., Lei, X., Li, T., and Lin, X., (2016), Neuroprotective effects of polydatin against mitochondrial-dependent apoptosis in the rat cerebral cortex following ischemia/reperfusion injury. *Molecular Medicine Reports*, 14(6), 5481-5488.
- [4] Wicha, P., Tocharus, J., Janyou, A., Jittiwat, J., Changtam, C., Suksanrarn, A., and Tocharus, C., (2017), Hexahydrocurcumin protects against cerebral ischemia/reperfusion injury, attenuates inflammation, and improves antioxidant defenses in a rat stroke model, *Plos One*, 12(12), e0189211.
- [5] Bonnefont-Rousselot, D., (2016), Resveratrol and cardiovascular diseases, *Nutrients*, 8(5), 250.
- [6] Du, Q. H., Peng, C., and Zhang, H., (2013), Polydatin: a review of pharmacology and pharmacokinetics, *Pharmaceutical Biology*, 51(11), 1347-1354.
- [7] Kakoti, B.B., Hernandez-Ontiveros, D.G., Kataki, M.S., Shah, K., Pathak, Y., and Panguluri, S.K., (2015), Resveratrol and omega-3 fatty acid: its implications in cardiovascular diseases, *Frontiers in Cardiovascular Medicine*, 2, 38.
- [8] Kitada, M. and Koya, D., (2013), Renal protective effects of resveratrol, *Oxidative Medicine and Cellular Longevity*, Article ID 568093.
- [9] Stefenon, C.A., Bonesi, C.D.M., Marzarotto, V., Barnabé, D., Spinelli, F.R., Webber, V., and Vanderlinde, R., (2014), Phenolic composition and antioxidant activity in sparkling wines: Modulation by the ageing on lees, *Food Chemistry*, 145, 292-299.

- [10] Wang, J., Feng, J., Xu, L., Ma, J., Li, J., Ma, R., Sun, K., Wang, Z., and Zhang, H., (2019), Ionic liquid-based salt-induced liquid-liquid extraction of polyphenols and anthraquinones in *Polygonum cuspidatum*, *Journal of Pharmaceutical and Biomedical Analysis*, 163, 95-104.
- [11] Yan, J., Wang, Y., Wu, H., Sun, Z., Tan, S., Wang, W., Gong, L., Xia, X., and Li, S., (2019), Development of a method for simultaneous determination of two stilbenes and four anthraquinones from *Polygonum cuspidatum* by RP-HPLC, *Journal of AOAC International*, 102(1), 69-74.
- [12] Yang, Z., Cai, Q., Chen, N., Zhou, X., and Hong, J., (2016), Selective separation and identification of metabolite groups of *Polygonum cuspidatum* extract in rat plasma using dispersion solid-phase extraction by magnetic molecularly imprinted polymers coupled with LC/Q-TOF-MS. *RSC Advances*, 6(15), 12193-12204.
- [13] Ban, S.H., Kwon, Y.R., Pandit, S., Lee, Y.S., Yi, H.K., and Jeon, J.G., (2010), Effects of a bio-assay guided fraction from *Polygonum cuspidatum* root on the viability, acid production and glucosyltransferase of mutans streptococci, *Fitoterapia*, 81(1), 30-34.
- [14] Ji, H., Zhang, X., Du, Y., Liu, H., Li, S., and Li, L., (2012), Polydatin modulates inflammation by decreasing NF- κ B activation and oxidative stress by increasing Gli1, Ptch1, SOD1 expression and ameliorates blood-brain barrier permeability for its neuroprotective effect in pMCAO rat brain, *Brain Research Bulletin*, 87(1), 50-59.
- [15] Arslan-Acaroz, D., Zemheri, F., Demirel, H.H., Kucukkurt, I., Ince, S., and Eryavuz, A., (2018), In vivo assessment of polydatin, a natural polyphenol compound, on arsenic-induced free radical overproduction, gene expression, and genotoxicity, *Environmental Science and Pollution Research*, 25(3), 2614-2622.
- [16] Chen, Z., Wei, Q., Hong, G., Chen, D., Liang, J., He, W., and Chen, M. H., (2016), Polydatin induces bone marrow stromal cells migration by activation of ERK1/2, *Biomedicine and Pharmacotherapy*, 82, 49-53.
- [17] Su, D., Cheng, Y., Liu, M., Liu, D., Cui, H., Zhang, B., Zhou, S., Yang, T., and Mei, Q., (2013), Comparison of piceid and resveratrol in antioxidation and antiproliferation activities in vitro, *PLoS One*, 8(1), e54505.
- [18] Xu, L.Q., Xie, Y.L., Gui, S.H., Zhang, X., Mo, Z.Z., Sun, C.Y., Li, C.L., Duo, L.L., Zhang, Z.B., Su, Z.R., and Xie, J.H., (2016a), Polydatin attenuates d-galactose-induced liver and brain damage through its anti-oxidative, anti-inflammatory and anti-apoptotic effects in mice, *Food & Function*, 7(11), 4545-4555.
- [19] Fang, J., Luo, L., Ke, Z., Liu, C., Yin, L., Yao, Y., Feng, Q., Huang, C., Zheng, P., and Fan, S., (2019), Polydatin protects against acute cholestatic liver injury in mice via the inhibition of oxidative stress and endoplasmic reticulum stress, *Journal of Functional Foods*, 55, 175-183.

- [20] Zhao, X.J., Yu, H.W., Yang, Y.Z., Wu, W.Y., Chen, T.Y., Jia, K.K., Kan, L.L., Jiao, R.Q., and Kong, L.D., (2018), Polydatin prevents fructose-induced liver inflammation and lipid deposition through increasing miR-200a to regulate Keap1/Nrf2 pathway, *Redox Biology*, 18, 124-137.
- [21] Xu, G., Kuang, G., Jiang, W., Jiang, R., and Jiang, D., (2016b), Polydatin promotes apoptosis through upregulation the ratio of Bax/Bcl-2 and inhibits proliferation by attenuating the β -catenin signaling in human osteosarcoma cells, *American Journal of Translational Research*, 8(2), 922.
- [22] Hu, T., Fei, Z., Su, H., Xie, R., and Chen, L., (2019), Polydatin inhibits proliferation and promotes apoptosis of doxorubicin-resistant osteosarcoma through LncRNA TUG1 mediated suppression of Akt signalling, *Toxicology and Applied Pharmacology*, 371, 55-62.
- [23] Xu, B., Lin, H.B., Zhou, H., and Xu, J.P., (2010), Protective effect of polydatin on a PC12 cell model of oxygen-glucose deprivation. *Journal of Southern Medical University*, 30(5), 1041-1043.
- [24] Wang, F.Y., Xu, Z.J., Zhang, X.L., Wang, W.T., Ha, M.L., and Wang, Y., (2008), Protective effects of polydatin against lung ischemia/reperfusion injury and the initial exploration for its mechanism, *Chinese Journal of Applied Physiology*, 24(1), 62-65.
- [25] Zhang, L.P., Yang, C.Y., Wang, Y.P., Cui, F., and Zhang, Y., (2008), Protective effect of polydatin against ischemia/reperfusion injury in rat heart, *Acta Physiologica Sinica*, 60(2), 161-168.
- [26] Liu, H.B., Meng, Q.H., Huang, C., Wang, J.B., and Liu, X.W., (2015), Nephroprotective effects of polydatin against ischemia/reperfusion injury: a role for the PI3K/Akt signal pathway, *Oxidative Medicine and Cellular Longevity*, Article ID 362158.
- [27] Li, T., Cai, S., Zeng, Z., Zhang, J., Gao, Y., Wang, X., and Chen, Z., (2014), Protective effect of polydatin against burn-induced lung injury in rats, *Respiratory Care*, 59(9), 1412-1421.
- [28] Wang, W., Tang, L., Li, Y., and Wang, Y., (2015), Biochanin A protects against focal ischemia/reperfusion in rats via inhibition of p-38-mediated inflammatory responses, *Journal of Neurological Science*, 348(1-2), 121-125.
- [29] Li, P., Wang, X., Zhao, M., Song, R., and Zhao, K.S., (2015), Polydatin protects hepatocytes against mitochondrial injury in acute severe hemorrhagic shock via SIRT1-SOD2 pathway, *Expert Opinion on Therapeutic Targets*, 19(7), 997-1010.
- [30] Zeng, Z., Chen, Z., Li, T., Zhang, J., Gao, Y., Xu, S., and Zhao, K.S., (2015a), Polydatin: a new therapeutic agent against multiorgan dysfunction, *Journal of Surgical Research*, 198(1), 192-199.

- [31] Zeng, Z., Chen, Z., Xu, S., Song, R., Yang, H., and Zhao, K.S., (2015b), Polydatin alleviates small intestine injury during hemorrhagic shock as a SIRT1 activator, *Oxidative Medicine and Cellular Longevity*, Article ID 965961.
- [32] Deng, Y.H., Alex, D., Huang, H.Q., Wang, N., Yu, N., Wang, Y.T., and Lee, S.M.Y., (2011), Inhibition of TNF- α - mediated endothelial cell–monocyte cell adhesion and adhesion molecules expression by the resveratrol derivative, trans- 3, 5, 4'-trimethoxystilbene, *Phytotherapy Research*, 25(3), 451-457.
- [33] Li, R.P., Wang, Z.Z., Sun, M.X., Hou, X.L., Sun, Y., Deng, Z.F., and Xiao, K., (2012), Polydatin protects learning and memory impairments in a rat model of vascular dementia, *Phytotherapy Research*, 19(8-9), 677-681.
- [34] White, B.C., Grossman, L.I., and Krause, G.S., Brain injury by global ischemia and reperfusion: A theoretical perspective on membrane damage and repair, *Neurology*. 1993, 43(9), 1656.
- [35] Islekel, H., Islekel, S., Guner, G., and Özdamar, N., (1999), Evaluation of lipid peroxidation, cathepsin L and acid phosphatase activities in experimental brain ischemia-reperfusion, *Brain Research*, 843(1-2), 18-24.
- [36] Roumen, R.M.H., Hendriks, T., Ven-Jongekrijg, J., Nieuwenhuijzen, G.A., Sauerwein, R.W., van der Meer, J.W., and Goris, R.J., (1993), Cytokine patterns in patients after major vascular surgery, hemorrhagic shock, and severe blunt trauma. Relation with subsequent adult respiratory distress syndrome and multiple organ failure, *Annals of Surgery*, 218(6), 769-776.
- [37] Ferran, C., Millan, M.T., Csizmadia, V., Cooper, J.T., Brostjan, C., Bach, B.F., and Wnkler, H., (1995), Inhibition of NF-kappa B by pyrrolidine dithiocarbamate blocks endothelial cell activation, *Biochemical and Biophysical Research Communication*, 214(1), 212–223.
- [38] Draper, H.H. and Hadley, M., (1990), Malondialdehyde determination as index of lipid peroxidation, In *Methods in Enzymology*, Academic Press, Cambridge, Massachusetts, ABD, 186, 421-431.
- [39] Altikat, S., Coban, A., Ciftci, M., and Ozdemir, H., (2006), In vitro effects of some drugs on catalase purified from human skin, *Journal of Enzyme Inhibition and Medicinal Chemistry*, 21(2), 231-234.
- [40] Coban, A., Ciftci, M., Ozdemir, H., and Altikat, S., (2007), Purification and characterization of catalase enzymes from chicken liver and sheep erythrocytes, *Asian Journal of Chemistry*, 19(5), 3941.
- [41] Gumustekin, K., Ciftci, M., Coban, A., Altikat, S., Aktas, O., Gul, M., Timur, H., and Dane, S., (2005), Effects of nicotine and vitamin E on glucose 6-phosphate dehydrogenase activity in

some rat tissues in vivo and in vitro, *Journal of Enzyme Inhibition and Medicinal Chemistry*, 20(5), 497-502.

- [42] Guney, T., Yıldız, B., Altikat, S., Kural, N., and Alatas, O., (2009), Decreased antioxidant capacity and increased oxidative stress in patients with juvenile idiopathic arthritis, *Journal of Pediatric Sciences*, 1.
- [43] Aebi, H.E. (1974), Catalase, *Methods of Enzymatic Analysis*, 2, 673-684.
- [44] Crosti, N., Servidei, T., Bajer, J., and Serra, A., (1987), Modification of the 6-hydroxydopamine technique for the correct determination of superoxide dismutase, *J. Clin. Chem. Clin. Biochem.*, 25, 265-266.
- [45] Heikkilä, R.E. and Cabbat, F., (1976), A sensitive assay for superoxide dismutase based on the autoxidation of 6-hydroxydopamine, *Analytical Biochemistry*, 75(2), 356-362.
- [46] Lowry, O.H., Rosebrough, N.J., Farr, A.L., and Randall, R.J., (1951), Protein measurement with the folin phenol reagent, *J. Biol. Chem.*, 193(1), 265-275.
- [47] Cuzzocrea, S., Riley, D. P., Caputi, A. P., and Salvemini, D., (2001), Antioxidant therapy: a new pharmacological approach in shock, inflammation, and ischemia/reperfusion injury, *Pharmacological Reviews*, 53(1), 135-159.
- [48] Ikeda, K., Negishi, H., and Yamori, Y., (2003), Antioxidant nutrients and hypoxia/ischemia brain injury in rodents, *Toxicology*, 189(1-2), 55-61.
- [49] Simonyi, A., Wang, Q., Miller, R.L., Yusof, M., Shelat, P.B., Sun, A.Y., Sun, G.Y., (2005), Polyphenols in cerebral ischemia, *Molecular Neurobiology*, 31(1), 135-147.
- [50] Miao, Q., Wang, S., Miao, S., Wang, J., Xie, Y., and Yang, Q., (2011), Cardioprotective effect of polydatin against ischemia/reperfusion injury: roles of protein kinase C and mito KATP activation, *Phytomedicine*, 19(1), 8-12.
- [51] Yaidikar, L., Byna, B., and Thakur, S.R., (2014), Neuroprotective effect of punicalagin against cerebral ischemia reperfusion-induced oxidative brain injury in rats, *Journal of Stroke and Cerebrovascular Diseases*, 23(10), 2869-2878.
- [52] Lu, Q., Tucker, D., Dong, Y., Zhao, N., and Zhang, Q., (2016), Neuroprotective and functional improvement effects of methylene blue in global cerebral ischemia, *Molecular Neurobiology*, 53(8), 5344-5355.
- [53] Janyou, A., Wicha, P., Jittiwat, J., Suksamrarn, A., Tocharus, C., and Tocharus, J., (2017), Dihydrocapsaicin attenuates blood brain barrier and cerebral damage in focal cerebral ischemia/reperfusion via oxidative stress and inflammatory, *Scientific Reports*, 7(1), 1-11.

- [54] Wang, D., Yuan, X., Liu, T., Liu, L., Hu, Y., Wang, Z., and Zheng, Q., (2012), Neuroprotective activity of lavender oil on transient focal cerebral ischemia in mice, *Molecules*, 17(8), 9803-9817.
- [55] Bai, L., Shi, W., Liu, J., Zhao, X., Zhang, Y., Zhou, Z., Hou, W., and Chang, T., (2017), Protective effect of pilose antler peptide on cerebral ischemia/reperfusion (I/R) injury through Nrf-2/OH-1/NF- κ B pathway, *International Journal of Biological Macromolecules*, 102, 741-748.
- [56] Han, T., (2013), Effects of solidoside pretreatment on expression of tumor necrosis factor-alpha and permeability of blood brain barrier in rat model of focal cerebral ischemia-reperfusion injury, *Asian Pacific Journal of Tropical Medicine*, 6(2), 156-158.

APPENDIX

**T.C.
KÜTAHYA SAĞLIK BİLİMLERİ ÜNİVERSİTESİ
HAYVAN DENEYLERİ YEREL ETİK KURULU
ARAŞTIRMA BAŞVURUSU ONAYI**

BASVURU BİLGİLERİ	ARAŞTIRMANIN ADI	Serebral İskemi/Reperfüzyon Hasarında Polidatinin Koruyucu Etkileri		
	ARAŞTIRMA YÜRÜTÜCÜSÜ KURUMU	Dr. Öğr. Üyesi Saadet ÇELİKOZLU DPU Altıntaş MYO Genel Biyoloji AD		
	PROJE YÜRÜTÜCÜSÜ KURUMU	Dr. Öğr. Üyesi Saadet ÇELİKOZLU DPU Altıntaş MYO Genel Biyoloji AD		
	YARDIMCI ARAŞTIRICILAR	Dr. Öğr. Üyesi Saadet ÇELİKOZLU Doç. Dr. Sayit ALTIKAT Dr. Öğr. Üyesi Filiz OZYIĞIT Arş. Gör. Dr. Emrah TUMER Doç. Dr. Sibel KOKTURK Uzm. Biyolog Halit ÇELİKOZLU		
	ARAŞTIRMANIN TAHMİNİ SÜRESİ	12 ay		
	KULLANILACAK HAYVAN TURU VE SAYISI	Sprague Dawley (E) – 16 adet		
	DESTEKLEYİCİ KURULUŞ	-		

DEĞERLENDİRİLEN İLGİLİ BELGELER	Belge Adı	Tarihi
	ARAŞTIRMA BAŞVURU FORMU	08.04.2019

KARAR BİLGİLERİ	Karar No : 2019.03.04	Tarih : 17.04.2019
	Yukarıda başvuru bilgileri verilen araştırma projesi gerekeç, amaç ve yöntemler dikkate alınarak görüşüldü ve ilgili belgeler incelendi. Projenin etik açıdan uygun olduğuna, çalışmanın aşağıdaki hususlar dikkate alınarak yürütülmesine ve sorumlu araştırmacıya iletmesine Oy Çoğunluğu ile karar verildi: 1) Projede herhangi bir değişiklik gerektiğinde kurulumuzdan onay alınması, 2) Projede çalışacağı bildirilen araştırmalarda değişiklik olduğunda kurulumuzdan onay alınması, 3) Deneysel hayvanları üzerinde yapılacak girişimin başlangıç ve bitiş tarihinin bildirilmesi, 4) Çalışma süresinde tamamlanamaz ise ek süre talebinde bulunulması, 5) Çalışma tamamlandığında sonuç raporunun gönderilmesi.	

ETİK KURUL BİLGİLERİ

ÜYELER

Unvanı / Adı / Soyadı EK Üyeligi	Uzmanlık Dalı	Kurumu	İlişki (*)	İmza
Doç. Dr. Aynur GÜLCAN Başkan	Mikrobiyoloji ve Klinik Mikrobiyoloji Anabilim Dalı	Tıp Fakültesi	<input type="checkbox"/> E <input checked="" type="checkbox"/> H	
Vet. HEKİM Aydın AKCILAR Üye	Veteriner HEKİM	Tıp Fakültesi DEHYUB	<input type="checkbox"/> E <input checked="" type="checkbox"/> H	
Doç. Dr. Hasan Emre AYDIN Üye	Beyin ve Sinir Cerrahisi Anabilim Dalı	Tıp Fakültesi	<input type="checkbox"/> E <input checked="" type="checkbox"/> H	 Toplantıya katılmadı.
Doç. Dr. Sermet İNAL Üye	Ortopedi ve Travmatoloji Anabilim Dalı	Tıp Fakültesi	<input type="checkbox"/> E <input checked="" type="checkbox"/> H	
Dr. Öğr. Üyesi Sezer AKÇER Üye	Anatomi Anabilim Dalı	Tıp Fakültesi	<input type="checkbox"/> E <input checked="" type="checkbox"/> H	DERSTE
Dr. Öğr. Üyesi Yasemin TEKŞEN Üye	Farmakoloji Anabilim Dalı	Tıp Fakültesi	<input type="checkbox"/> E <input checked="" type="checkbox"/> H	
Dr. Öğr. Üyesi Fikriye Yasemin ÖZATIK Üye	Farmakoloji Anabilim Dalı	Tıp Fakültesi	<input type="checkbox"/> E <input checked="" type="checkbox"/> H	
Vet. HEKİM Ali BILCAN Sivil Üye	Veteriner HEKİM	Kütahya Belediyesi	<input type="checkbox"/> E <input checked="" type="checkbox"/> H	
Mustafa ÖZUNLU Sivil Üye, STK Temsilcisi	Öğretmen	Milli Eğitim Bakanlığı	<input type="checkbox"/> E <input checked="" type="checkbox"/> H	

* Araştırma ile ilişkisi



RESEARCH ARTICLE

**DETECTION OF FETAL ELECTROCARDIOGRAM SIGNALS FROM MATERNAL
ABDOMINAL ECG RECORDINGS**

Ulvi BAŞPINAR^{1*}, Yasemin KÖYLÜ²

^{1*}University of Marmara, Technology Faculty, Electrical-Electronics Engineering, Istanbul,
ubaspinar@marmara.edu.tr, ORCID: 0000-0002-3359-9713

²University of Marmara, Institute of Pure and Applied Science, Electrical-Electronics Engineering Department, Istanbul,
yaseminkoylu@marun.edu.tr, ORCID: 0000-0002-7611-2565

Receive Date: 10.09.2022

Accepted Date: 16.03.2023

ABSTRACT

Fetal electrocardiogram (fECG) is a signal that contains vital information about the health of the fetus throughout pregnancy. During pregnancy, it is important to monitor and analyse this signal because it represents the electrical activity of the developing fetal heart. Early detection of fetal ECG problems during the fetus' development is crucial because it allows early treatment and provides knowledge about diseases that may emerge at a later time. Extraction of fetal ECG from the abdomen ECG signal is valuable in these aspects. In order to extract the fetal ECG from the recorded abdomen ECG signals correctly, it must be handled appropriately. It could be challenging to separate the fetal ECG signal from other physiological artifacts and noises in the mother abdominal signal. In this study, signal processing techniques were used to separate the fetus ECG signal from real abdominal ECG recordings. These methods include Ensemble Empirical Based Denoising, Finite Impulse Response Filter, Independent Component Analysis, and Pan & Tompkins approach. The results show that utilizing only the ICA technique to extract fECG signals is insufficient and that additional algorithms, such as those indicated above, should be used together. The mECG and fECG signals can be successfully extracted using the suggested approach.

Keywords: fECG extraction, mECG and fECG separation, Wearable fECG monitoring.

1. INTRODUCTION

ECG monitoring of the mother and baby is very important for the health of the mother and baby, especially in the last weeks of pregnancy, as it allows the detection of cardiac anomalies and early intervention before the baby is born[1]. Pregnant women must frequently attend the hospital for ECG tests, which are performed with ultrasound-based equipment. Non-invasive ECG measuring techniques have been developed to address these issues. Especially with the widespread use of wearable sensor systems, it will be possible to monitor mother and baby ECG for 24 hours[2, 3]. In non-invasive systems, measurements are made from certain points in the mother's navel[4]. In these measurements, the ECG signals of the mother and the baby are mixed with each other. The detection of fECG has been studied using a variety of signal processing techniques in the literature[5]. The

fundamental approaches to fECG signal processing can be mainly categorised as adaptive and non-adaptive processes [6]. Each technique has benefits and drawbacks of its own. Adaptive methods are based on learning systems and need a clear mECG signal recorded from mother's chest as well as an abdominal ECG signal includes both mECG and fECG signals. Examples of adaptive techniques include least squares algorithm[7], recursive least squares algorithm, adaptive linear neuron-based methods[8] adaptive neuro-fuzzy extraction system, Kalman filter-based methods, nonlinear adaptive techniques, and hybrid neural networks, artificial neural networks, and adaptive neuro-fuzzy extraction systems.

The non-adaptive methods do not need a clear mECG signal recorded from the mother's chest so the signals are measured directly from the abdomen of the pregnant woman. Independent Component Analysis (ICA)[9], Wavelet Transform (WT)[10], Empirical Mode Decomposition (EMD)[11], Singular Value Decomposition (SVD), filtering techniques[6], correlation technique[12], average techniques are among the non-adaptive methods[6]. Despite numerous studies on the subject, there is still a need for practical methods to separate the maternal and fetal ECG signals from each other.

Some of the studies on fECG extraction in the literature are as follows: Liu et al. performed fECG extraction with Independent Component Analysis (ICA), Ensemble Empirical Mode Decomposition (EEMD), Wavelet Shrinkage (WS) based noninvasive fECG separation and an adaptive integrated algorithm for noise reduction. First, they separated the noisy fECG signals from the mixed abdominal ECG data using the ICA technique. Second, the noisy fECG was cleared that was found with partial reconstruction of IMFs. Finally, they used EEMD to decompose the noisy fECG. In the study, four-channel abdominal recordings from Abdominal and Direct Fetal ECG Database[13] were used as test data. Although all WS, EMD-WS and EEMD-WS algorithms were able to effectively reduce noise, they concluded that EEMD-WS outperformed the other three algorithms.

Taralunga et al.[14] proposed a method for fetal ECG extraction from abdominal signals based on ICA and EMD. The performance of the proposed algorithm, called ICA_EMD, was evaluated on both simulated and real data and compared with the results obtained by ICA. They performed the ICA_EMD method in two steps. Firstly, they obtained the ICs with the JADE algorithm, then the EMD was applied to the ICs containing the fECG, and the fetal ECG extraction process was completed. They observed that the proposed ICA_EMD method has a higher performance than the JADE algorithm in both simulated and real data.

In this study, separation of fECG from a mother's abdominal ECG recordings was realized. The steps of the method used in the separation of the fECG from the abdominal ECG(aECG) recordings are given in Figure 1.

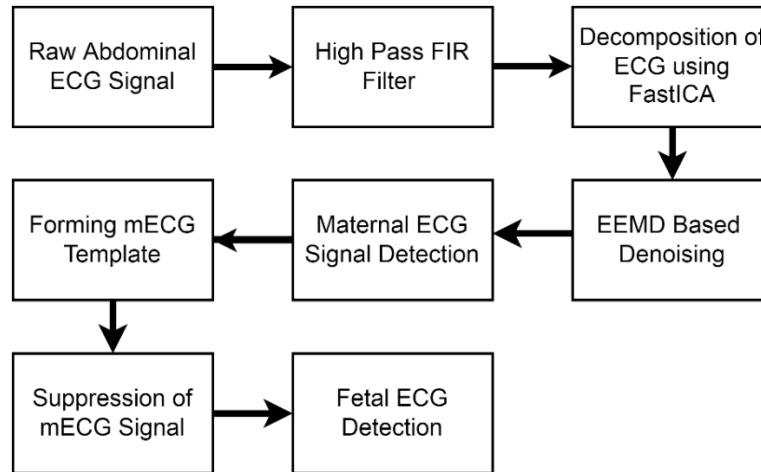


Figure 1. The steps of fECG extraction method from abdominal ECG recordings.

The algorithm has four basic steps. The first step of the algorithm is eliminating DC components in the ECG recordings by using a high pass FIR filter. In the FAST ICA block, the mixed ECG recordings are separated into their independent components. As a third step the EEMD denoising technique is applied to separated components to obtain a more clean maternal ECG. In the last step, the denoised mECG signal is used as a template to suppress of mECG signal from the mixed abdominal ECG signals.

In the article, methods are presented in section II, experimental results and discussions are given at the sections following it.

2. METHODS

2.1. Independent Component Analysis (ICA)

Independent Component Analysis (ICA) is a mathematical technique for finding hidden signals in the observed mixtures of signals and it is primarily used to separate the mixed signals in multi-sensor/source applications[15]. ICA is also one of the popular methods that separate the fECG signal from aECG and it uses the statistical independence of the predicted components and aims to find independent components by maximizing this independence. The definition of independence for ICA can be done in two ways; mutual information is minimized and non-Gaussianity is maximized[15]. The mathematical model of the ICA is given as in Eq. 1, where x is a linear mixture of two or more independent source signals, s is the independent components and A is considered to be the mixing matrix.

$$x = A \cdot s \quad (1)$$

The aim of the model is to find the A and s using x . The matrix A is calculated as a square matrix and the independent components can be found by calculating the inverse of this matrix[15]. When we

multiply both sides of equality in Eq. 1 by the inverse of the mixing matrix, we obtain Eq. 2, where W , is the inverse of the mixing matrix.

$$s = W \cdot x \quad (2)$$

2.1.1. FastICA algorithm

FastICA is a popular and effective algorithm of independent component analysis[16]. It is very useful to separate signal components when the number of observations is less. In order to increase the success of the algorithm, the preprocessing stages such as centering and whitening are applied to the observed mixtures[15].The aim of the centering is to find the general average of the data and subtract it from each element of the data vector[17]. In whitening, data correlation is maximized and the variance of the data vectors acquired using by Eigen Value Decomposition (EVD)[9].

2.2. Ensemble Empirical Mode Decomposition

The Empirical Mode Decomposition (EMD) technique has a data-driven working mechanism[18, 19]. It is a method that works on the analysis of single channel signals and very useful technique for the separation of nonlinear and non-stationary time series[18, 20].

The EMD technique enables the data to be analysed according to the time scale feature of itself without any previous operation and staying in the time domain. It is therefore adaptable and applicable for all types of ECG signals[20]. It divides the signal into components called Intrinsic Mode Functions (IMF) at different time scales [18]. IMFs are non-stationary components in finite and few oscillations resulting from the separation of complex data[19]. In EMD method, the signal is divided into IMFs by a repeated shifting process. Each IMF must comply with the following two conditions:

- First, the number of extremes and the number of zero crossings must be equal in the entire signal recording.
- Secondly, the average value of the envelope defined by the local maxima and the envelope defined by the local minima must be equal to zero in all records[21].

The steps of the EMD algorithm for the raw signal are as follows:

- a) Peak points of the raw signal are determined.
- b) The lower envelope and the upper envelope of the signal are obtained separately.
- c) The average envelope is determined and subtracted from the original signal and the first Intrinsic Mode Function candidate (IMF1) is created. This step is shown in the Eq. 3. Here $s(t)$ represents the raw signal, $m_1(t)$ represents the mean envelope, and $h_1(t)$ represents the first found IMF candidate.

$$h_1(t) = s(t) - m_1(t) \quad (3)$$

If $h_1(t)$ provides the conditions of being IMF, it is accepted as the first IMF obtained in the elimination process. If it does not provide the conditions of being an IMF, steps a) and b) for $h_1(t)$ are repeated until the condition of being IMF fulfilled(Eq. 4).

$$h_{1,1}(t) = h_1(t) - m_{1,1}(t) \quad (4)$$

After the steps are provided iteratively, the IMF after n cycles is shown as in Eq. 5.

$$h_{1,n}(t) = h_{1,n-1}(t) - m_{1,n}(t) \quad (5)$$

d) The first IMF ($c_1(t)$) is removed from the original signal and $r_1(t)$ is now obtained (Eq. 6):

$$r_1(t) = s(t) - c_1(t) \quad (6)$$

e) $r_1(t)$ accepted as the new signal for the second IMF; It is expressed as $c_2(t)$. The above steps are repeated again to get the second residual $r_2(t)$. Now the signal can be expressed as in the following Eq. 7.

$$r_p(t) = r_{p-1}(t) - c_p(t) \quad (7)$$

The original data can be obtained by summing all the IMFs and the last residual signal:

$$s(t) = \sum_{i=1}^K c_i(t) + r_L(t) \quad (8)$$

Here K is the number of IMFs obtained after separation[22].

Although EMD has a large application area, it also has weaknesses. It can cause mode mixing when reconfiguring many of the Intrinsic Mode Functions of the signal[22]. Ensemble Empirical Mode Decomposition(EEMD) is obtained by adding a finite amount of Gaussian white noise to the signal processed with EMD and it is very effective eliminating the mode mixing problem[23].

In EEMD, firstly white noise is added to the original signals to obtain grouped data sets. EMD is then applied to each ensemble dataset until it reaches the final ensemble count. The final value is obtained by averaging the successive components resulting from the batch operation.

The steps of EEMD can be summarized as follow[22]:

1. Add a set of white noise $n(t)$ into the original signal $s(t)$ (Eq. 9) and get the new signal:

$$Y(t) = s(t) + n(t) \quad (9)$$

2. Decompose $Y(t)$ into n IMFs by EMD method(Eq. 10).

$$Y(t) = \sum_{i=1}^n imf_i(t) + r_n(t) \quad (10)$$

3. Add j different white noise sequences to the original signal (Eq. 11) and repeat the steps 1 and 2:

$$Y_j(t) = \sum_{i=1}^n imf_{ij}(t) + r_{nj}(t) \quad (11)$$

4. Calculate the average amount parsed by EEMD with the same IMF value (Eq. 12):

$$Y_j(t) = 1/n(\sum_{i=1}^n imf_{ij}(t) + r_{nj}(t)) \quad (12)$$

5. Add $imf_j(t)$ and the last remainder to obtain the denoised signal (Eq. 13):

$$Y(t) = \sum_{i=1}^n imf_i(t) + r_n(t) \quad (13)$$

2.2.1. EEMD based denoising technique

EEMD based denoising technique steps are as follows:

- Firstly, a region that does not contain information is determined in the signal. Noise thresholds are calculated with this selected region.
- The raw signal is separated into IMFs by the EEMD method.
- Each of the obtained IMF is filtered according to thresholding technique.

In this study, soft thresholding technique was used with universal threshold determination. med_i in Eq. 14 is the median absolute deviation of the IMF_i , ϱ_i indicates the noise level of the IMF_i and t_i in Eq. 15 indicates the threshold value. L is the size of the IMF.

$$\varrho_i = med_i/0.6745 \quad (14)$$

$$t_i = \varrho_i(2 \log(L))^{1/2} \quad (15)$$

2.3. Pan & Tompkins Method

The Pan and Tompkins method is used to detect the QRS complex in the ECG signal and it provides good QRS detection performance when high quality ECG signal data is available[24, 25]. The algorithm has following stages: bandpass filter, derivative, a squaring function, a moving window integration (MWI), thresholding and decision. In bandpass filter stage, the algorithm passes the signal through a low pass and a high pass filter to reduce the artefacts such as muscle noise, power line interference, and lead cable movements[24]. While band-pass filter reduces the effect of noise, it maximizes the QRS energy to a suitable frequency[25]. The derivative process is used to detect the largest sloping QRS complex that suppresses P and T waves of the ECG signal[26]. After differentiation, the signal is squared[27]. The squaring function reduce higher amplitudes of T waves to prevent misdetection[25]. The aim of moving window integration is to get information about the waveform and slope of the R wave[27]. The integrated window is important in this process. The widest integrated window should be used to match a possible QRS complex [26]. After the signal has been preprocessed, the next step is the decision phase. In this step, the decision is given whether the MWI result is a QRS complex or not by using thresholds[25].

3. RESULTS

The steps of the study can be summarized in 5 steps: The first step is applying a high-pass filter, the second step is applying FastICA to the high-pass filtered signals. The third step is applying EEMD based denoising to prepare the signal to the Pan-Tompkins method which is used to obtain the QRS points template of the mother ECG signal. Finally, the template is used to suppress mother ECG signals in mixed ECG signals.

The database, that is used in the study, contains multichannel fetal electrocardiogram recordings measured from 5 pregnant women between 38 and 41 weeks of pregnancy [28]. The recordings include four signals measured from the navel and a direct electrocardiogram signal recorded

simultaneously from the head of the fetal. In the study, Abdomen_1, Abdomen_2, Abdomen_3, Abdomen_4 signals in the r01.edf signal records of a pregnant woman were used. The records are shown in Figure 2. All records have 16-bit resolution, 1 kHz sampling frequency and 10 seconds signal length.

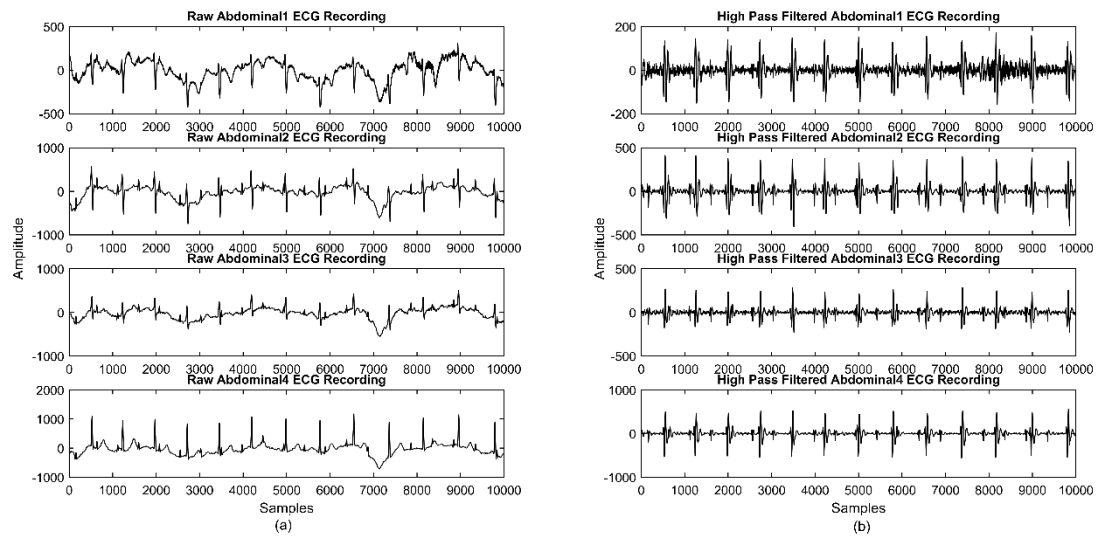


Figure 2. (a) Abdominal recordings used in the study. (b) Recordings of ab-1, ab-2, ab-3, ab-4, filtered through FIR filter.

The raw signals in Figure 2(a) were subjected to a high pass filter with a 5 Hz cut-off frequency as a pre-processing step before to FastICA to remove DC levels. The results of high-pass filtered signals are shown in Figure 2(b).

The abdominal signals that passed through a high-pass FIR filter, were separated into independent components using the FastICA technique. Four abdominal signals without DC components were used as the FastICA input, and the algorithm was directed to find four independent components at the output. Negentropy was employed in FastICA as a non-Gaussianity metric. The output of the FastICA algorithm is given in Figure 3.

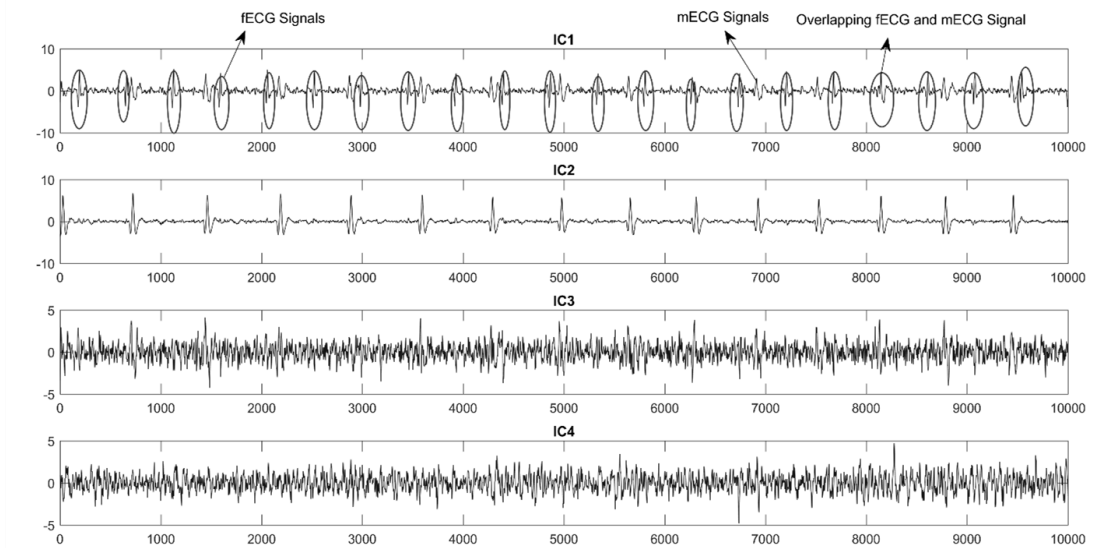


Figure 3. The result of FastICA algorithm: The Independent Components of the ab-1, ab-2, ab-3, ab-4 abdominal signals.

The mECG, fECG, and locations where these two signals overlapped in the IC1 signal can be seen in Figure 3. The IC2 signal is the maternal ECG signal. The majority of the noisy components, as well as the fECG and mECG signals, are present in the IC3 and IC4 signals.

We require the mECG QRS points in order to remove the maternal ECG signal from the mixed ECG data. In the study, the Pan-Tompkins method was used but it needs a high SNR ratio so EEMD based denoising technique was applied to the IC1 and IC2 components to get a cleaner signal. Figure 4 shows the results of the EEMD-based denoising technique on the Independent components.

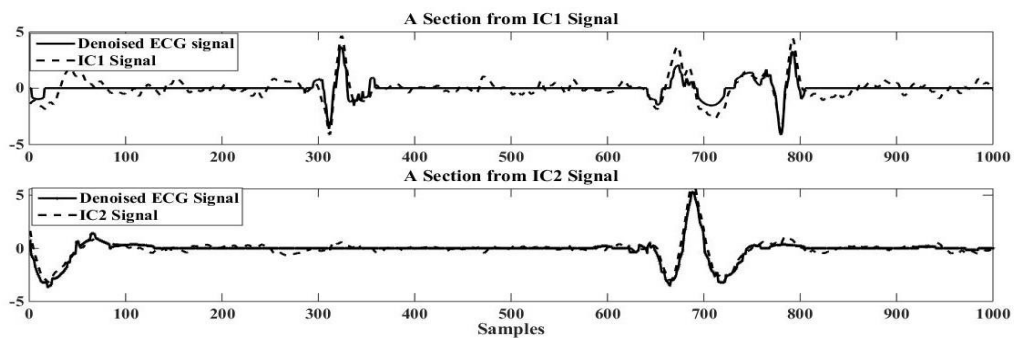


Figure 4. A section from independent components and the results of EEMD based denoising technique.

The denoised IC2 signal was subjected to the Pan & Thompkins algorithm, and the QRS points of the mECG signal were located (Figure 5). Based on the acquired QRS points, a maternal ECG template was generated.

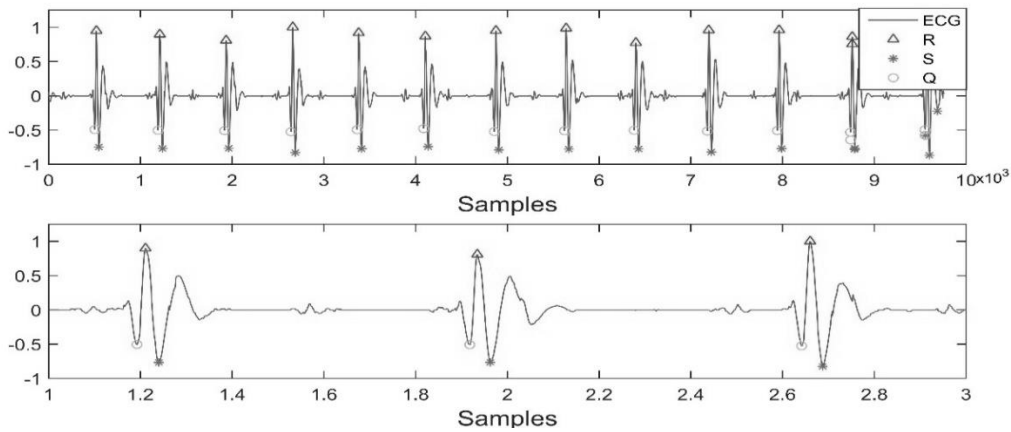


Figure 5. The detected QRS points of denoised IC2 signal using by Pan & Thompkins algorithm.

In Figure 6(a), direct fetal ECG signal, mECG signal and the peak points of fetal ECG detected by our algorithm are plotted on top of each other. As can be seen in Figure 6(a), the algorithm is unable to detect one R point and misdetects one R point in the fECG records. To obtain the fetal ECG signal, the created template was applied to the denoised IC1 data. The result of the masking and detected R points are given in Figure 6(b).

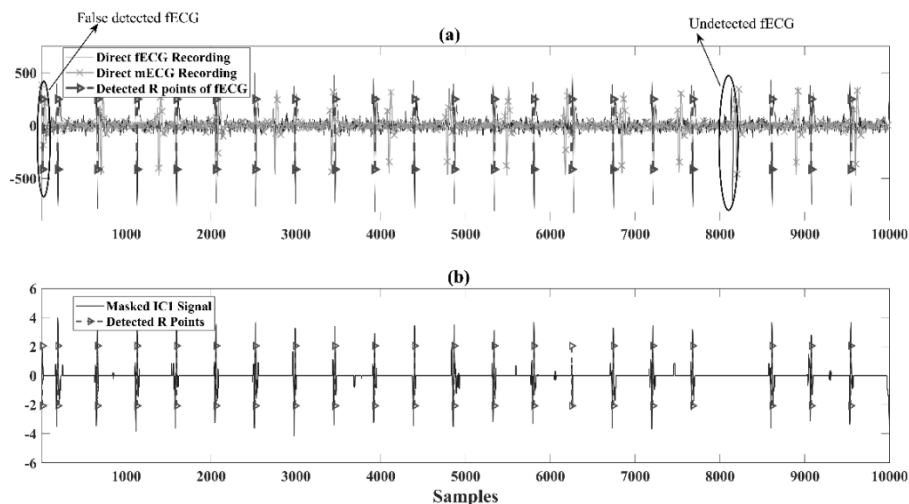


Figure 6. (a) Direct fECG Recording, Direct mECG Recording and Detected R points of fECG detected by our algorithm. **(b)** Masked IC1 signal and detected R points of fECG.

To evaluate the results of the study, we used sensitivity (Se), positive predictive value (PPV) and accuracy (F_1) values of the classification rates. TP , FP and FN values in the formula indicate true positives, false positives, and false negatives, respectively. TP ; true fECG R-peaks, FP ; false fECG R-peaks, FN ; shows undetectable R-peaks. PPV refers to the probability of detecting true fetal ECG R-peaks, while the Se value indicates the ability to detect the R-peak. F_1 indicates the possibility of accurate detection of fetal ECG R-peaks [28].

In Eq. 18, 19 and 20, formulas for Se , PPV and F_1 are given respectively.

$$Se = \frac{TP}{TP+FN} * 100 \quad (18)$$

$$PPV = \frac{TP}{TP+FP} * 100 \quad (19)$$

$$F_1 = 2 \frac{PPV \cdot Se}{PPV+Se} = \frac{2 \cdot TP}{2 \cdot TP+FN+FP} * 100 \quad (20)$$

The studies given in previous sections were made on the R04 records in the database. In Table 1, the detected R peaks of the all records in the database by the proposed method are given.

Table 1. The Results of ECG Signal Extraction Method from aECG Recording.

ECG Data Record No.	ECG Type	Number of R-peaks in ECG Records	Number of detected R-peaks in ECG Records	Percentage of Success (%)
R04	fECG	21	20	95.23
	mECG	15	15	100
R07	fECG	21	19	90.47
	mECG	12	12	100
R08	fECG	21	16	76
	mECG	15	15	100
R10	fECG	20	18	90
	mECG	18	18	100

Performance measures of the proposed method for the Fetal R peak detection are given in Table 2.

Table 2. Performance Measures for Fetal R-peak detection.

ECG Data Record No.	Se(%)	PPV(%)	F ₁ (%)
R04	95.23	95.23	95.23
R07	95	100	97.43
R08	94.11	94.11	94.11
R10	100	94.7	97.29

According to Table 2, the proposed algorithm shows 91.9% average success in the extraction of fECG in recordings R04, R07 and R10. The success rate is low at recording R08 due to much overlapping of mECG and fECG signals. When we compare the results with the study[15] that is used the same data, the proposed method shows a slight increase in separation fECG. In R04 data, fetal R peak detection success is 95.4% while in the other study it is 90.4%. The success rate of R07 and R10 are the same in both studies.

4. CONCLUSION

In this study, it was aimed to separate the fECG signals from the abdominal ECG recordings in order to early detection of anomaly and illness from the Fetal ECG signals. In the study, the abdominal ECG recordings of a pregnant mother was used to test separation techniques. The results show that the FastICA method can recover mECG signals from aECG recordings but it is insufficient to separate fECG signals. Additional techniques such as EEMD and Pan-Tompkins algorithms were used together with FastICA to extract fECG signal from the aECG recordings.

The study proves that aECG recordings are include linear mixtures of fECG and mECG signals as well as nonlinear components of them so the FastICA algorithm is insufficient separating aECG signals. The other conclusion about the study is that the techniques used in this study are unable to detect overlapping mECG and fECG signals. In the future, it is planned to study on the techniques to separate overlapping ECG signals and embedded system solutions for wearable fetal ECG monitoring systems.

ACKNOWLEDGEMENTS

The authors acknowledge that "This study was supported by Marmara University BAPKO (Project Number: ADF-2022-10660)".

REFERENCES

- [1] Verdurmen, K.M., Eijvoogel, N.B., Lempersz, C., Vullings, R., Schroer, C., van Laar, J.O., Oei, S.G. (2016). A systematic review of prenatal screening for congenital heart disease by fetal electrocardiography, *International Journal of Gynecology & Obstetrics*, 135 129-134.
- [2] Yang, Z., Zhou, Q., Lei, L., Zheng, K., Xiang, W. (2016). An IoT-cloud based wearable ECG monitoring system for smart healthcare, *Journal of medical systems*, 40 1-11.
- [3] Spanò, E., Di Pascoli, S., Iannaccone, G. (2016). Low-power wearable ECG monitoring system for multiple-patient remote monitoring, *IEEE Sensors Journal*, 16 5452-5462.
- [4] Martinek, R., Kahankova, R., Nazeran, H., Konecny, J., Jezewski, J., Janku, P., Bilik, P., Zidek, J., Nedoma, J., Fajkus, M. (2017). Non-invasive fetal monitoring: A maternal surface ECG electrode placement-based novel approach for optimization of adaptive filter control parameters using the LMS and RLS algorithms, *Sensors*, 17 1154.

- [5] Sameni, R., Clifford, G.D. (2010). A review of fetal ECG signal processing; issues and promising directions, *The open pacing, electrophysiology & therapy journal*, 3 4.
- [6] Preethi, D., Valarmathi, R. (2018). An Analysis of FIR Filter Algorithms in Fetal Heart Rate Monitoring, 2018 International Conference On Advances in Communication and Computing Technology (ICACCT), IEEE, 265-268.
- [7] Widrow, B., Glover, J.R., McCool, J.M., Kaunitz, J., Williams, C.S., Hearn, R.H., Zeidler, J.R., Dong, J.E., Goodlin, R.C. (1975). Adaptive noise cancelling: Principles and applications, *Proceedings of the IEEE*, 63 1692-1716.
- [8] Kahankova, R., Martinek, R., Mikolášová, M., Jaroš, R. (2018). Adaptive linear neuron for fetal electrocardiogram extraction, IEEE 20th International Conference on e-Health Networking, Applications and Services (Healthcom), IEEE, 2018, pp. 1-5.
- [9] Alkhodari, M., Rashed, A., Alex, M., Yeh, N.-S. (2018) Fetal ECG Extraction Using Independent Components and Characteristics Matching, International Conference on Signal Processing and Information Security (ICSPIS), IEEE, 1-4.
- [10] Cardenas-Lattus, J., Kaschel, H. (2017). Fetal ECG multi-level analysis using daubechies wavelet transform for non-invasive maternal abdominal ECG recordings, 2017 CHILEAN Conference on Electrical, Electronics Engineering, Information and Communication Technologies (CHILECON), IEEE, 1-6.
- [11] Gupta, P., Sharma, K.K., Joshi, S.D. (2016). Fetal heart rate extraction from abdominal electrocardiograms through multivariate empirical mode decomposition, *Computers in biology and medicine*, 68 121-136.
- [12] Hasan, M.A., Reaz, M.B.I., Ibrahimy, M.I. (2011). Fetal electrocardiogram extraction and R-peak detection for fetal heart rate monitoring using artificial neural network and Correlation, *The 2011 International Joint Conference on Neural Networks*, IEEE, 15-20.
- [13] Goldberger, A.L., Amaral, L.A., Glass, L., Hausdorff, J.M., Ivanov, P.C., Mark, R.G., Mietus, J.E., Moody, G.B., Peng, C.-K., Stanley, H.E. (2000). PhysioBank, PhysioToolkit, and PhysioNet: components of a new research resource for complex physiologic signals, *circulation*, 101 e215-e220.
- [14] Taralunga, D.D., Gussi, I., Strungaru, R. (2016). A new method for fetal electrocardiogram denoising using blind source separation and empirical mode decomposition, *Revue Roumaine des Sci Techn, serie Électrotechnique et Énergetique*, 61 94-98.
- [15] Nikam, S., Deosarkar, S. (2016) Fast ICA based technique for non-invasive fetal ECG extraction, 2016 Conference on Advances in Signal Processing (CASP), IEEE, 60-65.
- [16] Hyvärinen, A., Oja, E. (2000). Independent component analysis: algorithms and applications, *Neural networks*, 13 411-430.

- [17] Hassan, N., Ramli, D.A. (2018). A comparative study of blind source separation for bioacoustics sounds based on FastICA, PCA and NMF, *Procedia Computer Science*, 126 363-372.
- [18] Roshini, M., Thanaraj, K.P. (2016). Extraction of Fetal QRS Complex from Abdominal ECG Signals, *International Journal of Computer Trends and Technology (IJCTT)*, 34-1 29-34
- [19] Taralunga, D.D., Gussi, I., Strungaru, R. (2016). A new method for fetal electrocardiogram denoising using blind source separation and empirical mode decomposition, *Revue Roumaine des Sci. Techn., serie Électrotechnique et Énergetique*, 61 94-98.
- [20] Wei, Z., Xiaolong, L., Jin, Z., Xueyun, W., Hongxing, L. (2018). Foetal heart rate estimation by empirical mode decomposition and MUSIC spectrum, *Biomedical Signal Processing and Control*, 42 287-296.
- [21] Jaros, R., Martinek, R., Kahankova, R. (2018). Non-adaptive methods for fetal ECG signal processing: a review and appraisal, *Sensors*, 18 3648.
- [22] Yin, J., Chen, X., Zhang, P., Shao, L., Li, J., Liu, H. (2020). Research on ECG signal denoising by combination of EEMD and NLM, *2020 Chinese Control And Decision Conference (CCDC)*, IEEE, 5033-5038.
- [23] Gong, Y., Wang, Z., Xu, G., Zhang, Z. (2018). A comparative study of groundwater level forecasting using data-driven models based on ensemble empirical mode decomposition, *Water*, 10 730.
- [24] Pavlatos, C., Dimopoulos, A., Manis, G. (2005). Papakonstantinou, G., Hardware implementation of Pan & Tompkins QRS detection algorithm, *IFMBE Proc*, 1727-1983.
- [25] Fariha, M., Ikeura, R., Hayakawa, S., Tsutsumi, S. (2020). Analysis of Pan-Tompkins algorithm performance with noisy ECG signals, *Journal of Physics: Conference Series*, IOP Publishing, 012022.
- [26] Bali, J., Nandi, A., Hiremath, P., Patil, P.G. (2018). Detection of sleep apnea in ECG signal using Pan-Tompkins algorithm and ANN classifiers, *Compusoft*, 7 2852-2861.
- [27] Patel, A.M., Gakare, P.K., Cheeran, A. (2012). Real time ECG feature extraction and arrhythmia detection on a mobile platform, *Int. J. Comput. Appl*, 44 40-45.
- [28] Gini, J.R., Ramachandran, K., Nair, R.H., Anand, P. (2016). Portable fetal ECG extractor from abdECG, *2016 International Conference on Communication and Signal Processing (ICCSP)*, IEEE, 0845-0848.



RESEARCH ARTICLE

A KINETIC STUDY OF THERMOCHEMICALLY BORIDED AISI 316L STAINLESS STEEL

Gökhan BAŞMAN¹, Mustafa Merih ARIKAN^{2,*}, C. Fahir ARISOY³, M. Kelami ŞEŞEN⁴

¹Eti Krom A.Ş., R&D Center, Bingöl Karayolu, 55. Km, Elazığ, gbasman@gmail.com, ORCID: 0000-0001-8835-3641

²*Arkan Engineering and Consultancy, Antalya, meriharikan@yahoo.com, ORCID: 0000-0002-5820-1871

³İstanbul Teknik Üniversitesi, Kimya-Metalurji Fakültesi, Metalurji ve Malzeme Mühendisliği Bölümü, İstanbul, fahir@itu.edu.tr, ORCID: 0000-0003-3399-9271

⁴İstanbul Teknik Üniversitesi, Kimya-Metalurji Fakültesi, Metalurji ve Malzeme Mühendisliği Bölümü, İstanbul, mksesen@itu.edu.tr, ORCID: 0000-0002-8113-6289

Receive Date: 23.03.2022

Accepted Date: 28.03.2023

ABSTRACT

Biomaterials are used in different parts of human body as replacement implants in medical applications. An implant material should have high biocompatibility, corrosion and wear resistance, and suitable mechanical properties in terms of safety and long-service period. There are only a few biocompatible implant materials: AISI316L stainless steel is one of the materials used in this type of applications. They have relatively poor wear resistance. Boriding being a thermochemical diffusion treatment is one of the processes to improve their wear resistance. Borides are formed by introducing boron atoms by diffusion onto a substrate surface and they are non-oxide ceramics and could be very brittle. The growth kinetics of boride layer is analyzed by measuring depth of layers as a function of boriding time within a temperature range. In this study, the effects of Ekabor-2 bath on formation mechanism and properties of boride layer in thermochemical diffusion boriding of AISI316L stainless steel were investigated. Different temperatures and durations were applied in boriding operations and hardness, optical microscopy, XRD, EPMA and SEM studies were performed to detect the properties of boride layers. It was found that thickness of boride layer increased with increasing temperature and time; the basic phase in the boride layer formed was Fe₂B and FeB phase also formed. It was also found that surface hardness values of borided materials increased depending on temperature and time of boriding process; surface hardness values of borided materials are approximately 10 times higher than surface hardness values of non-borided AISI316L stainless steel and formation activation energy of boride layer is 149.3 kJmol⁻¹.

Keywords: *Boriding, AISI 316L Stainless Steel, Diffusion Kinetics, Surface Treatment, Hardness.*

1. INTRODUCTION

Implant materials are internally or externally used in the human body for the cure and repair purposes; this type of materials can be temporary or permanent in the body [1-3]. Biomaterials are used in

different parts of the human body as replacement implants [4-6] and improve the life quality and help increasing the lifetime of human beings. Biomedical implants encompass cardiovascular implantable, neural and orthopedic fixation devices, cochlear and retinal applications, orthopedic prostheses, bone tissue engineering scaffolds and dental implants [7,8]. A metallic implant should possess high biocompatibility, corrosion and wear resistance, and suitable mechanical properties in terms of safety and long service period [9].

There are only a few biocompatible implant materials although the large number of metals and alloys are produced in industry. These materials can be categorized as stainless steels, cobalt-based alloys, titanium-based alloys and the others [5, 10-12].

AISI 316L type stainless steels are used in the applications requiring wear, corrosion and fatigue resistance. 316L stainless steel has a Young Modulus of about 200 GPa, a tensile strength of 500–1000 MPa, and a fracture toughness of $100 \text{ MPa(m)}^{1/2}$ [13] and is used as an implant material to make internal fixation devices and/or prostheses for the amputees due to its good mechanical properties and corrosion resistance, satisfactory biocompatibility and low cost [6,14].

Boriding is one of the processes applied onto the parts made of AISI 316L stainless steels since they have relatively poor wear resistance. A number of surface treatments such as nitriding by ion implantation, pulsed plasma nitriding and plasma immersion ion implantation are also applied to improve their wear resistance without compromising their corrosion resistance [15].

Boriding process is used to increase the hardness, wear, erosion and corrosion resistance on the surfaces of the metals and alloys; and it is also aimed to sustain these properties at elevated temperatures. Boriding process is industrially applied to mostly ferrous-based alloys [16-18]. Boriding is a process in which a boride layer is formed on the surface of the substrate metal by the diffusion of boron atoms at elevated temperatures [15,16,19]. Boriding is also known as the diffusion of boron atoms which will form a compound on the surface. Boriding can be applied to well surface cleaned materials with durations of 1-10 hours at temperatures of 800-1100°C in the various environments such as solid, paste, liquid and gas.

New techniques such as plasma boriding and fluidized bed boriding are also used except for the thermo-chemical boriding methods in the gaseous environment by the technological developments. Non-thermo-chemical physical vapor deposition (PVD), chemical vapor deposition (CVD), plasma-spray and ion deposition are also methods used for boriding [16,20]. Thermo-chemical methods are the most common methods within these techniques. Thermo-chemical boron coating is a method based on the diffusion of boron atoms onto metal as a function of temperature and time.

The most important feature of boriding is that the obtained boride layer has high hardness (1450-5000HV) and high melting temperature. The hardness of the coating layer is permanent up to the lower-critical temperature (650°C) in the ferrous-based materials [21]. The hardness of the boride layers formed on the plain-carbon steels are much higher than the hardness obtained by the cementation and nitration which are traditional hardening methods. Surface hardness values of tool

steels hardened by boriding can reach hardness values of electrolytic hard chromium coating and tungsten carbide.

Boride phase on the surface of material initially grows as nucleus when the iron and ferrous-based materials are borided. Boride layer consists of two different boride layers including (Fe,M)B phase at the outer surface and (Fe,M)₂B phase at the inner part (just above the substrate).

Boride layers in different structures can be obtained by various boriding methods. The structure of boride layers can be either in a smooth form or tooth-shaped morphology depending on the boriding method and the composition of the material to be borided. Determination of some of the layer properties is possible originating from the layer types. Single-phase boride layer (Fe₂B) is preferred in the industry [22]. Post-boriding processes can be applied to the substrate material without affecting the properties of borided layer negatively [20]. It should be taken into consideration that the layer thickness should not be too thick especially on the double-phase layers since brittleness will increase as the layer thickness increase. Boron diffusion into steel becomes more difficult as the content of alloying elements increases [23].

In addition, tooth-shaped boride morphology on the high-alloy steels is denser, more uniform and has a smooth structure. Difficulties arise in the description of the layer thickness and different descriptions are made since the boride layers are in needle or variable form. Layer thickness is given in the literature by comparing the tooth structure to a flat plane and taking the average value of the heights of these teeth according to the plane [16].

Borided steels are characterized by high surface hardness and wear resistance. Another superiority of borided surfaces in terms of wear is that the heat resulting from both working environment and sliding friction does not cause a significant decrease in the hardness and wear resistance of the boride layers [24]. Almost all of the researchers investigating the effects of boriding on the friction coefficient concluded that boriding reduces the friction coefficient [25,26].

Growth kinetics of boride layer is specified by the depth measurement of FeB and Fe₂B layers as a function of boriding time and temperature. There is no simple relationship between surface and interface morphology. Fe₂B columnar structure at the material interface is explained with the growth mechanism from the end. While Fe₂B grows inside the soft material, FeB grows inside the hard Fe₂B matrix and thus different local stresses and interface deteriorations occur. Borides are non-oxide ceramics and mostly brittle.

The effects of Ekabor-2 bath on the formation mechanism and the properties of the boride layer in the boriding by thermo-chemical diffusion method of AISI 316L stainless steel were investigated in this study. Different temperatures and times were applied in boriding operations. Various experiments were carried out after the boriding process to detect the properties of the boride layers.

The character of the boride layer surface was observed by optical microscope; phases formed were detected by X-ray diffraction method; the character of boride layer was detected by electron probe micro analyzer (EPMA) and boride layer morphology was investigated by scanning electron

microscope (SEM) and EPMA. Coating thickness values were measured and furthermore, hardness profile of the borided surface was obtained.

2. EXPERIMENTAL METHOD

Hot rolled and annealed AISI 316L austenitic stainless steel was used in boriding processes. The composition of this steel is given in Table 1. The proper specimens were prepared from the stainless steel sheet for experimental studies.

Table 1. The chemical composition of AISI 316L stainless steel materials used in the experimental studies.

Element	C	Si	Mn	P	S	Cr	Ni	Mo	N
% wt.	0.015	0.45	1.50	0.026	0.028	16.98	10.2	2.07	0.07

Boriding operations were carried out in commercial Ekabor-2 boriding bath under argon atmosphere and small AISI 304 stainless steel containers were used in the boriding. Experiments were performed at 850, 950 and 1050°C for 2, 4 and 6 hours, taking into account the accepted temperatures and times in the literature.

Athmospheric-controlled Heraeus branded electric resistance furnace was used for boriding the specimens. Specimens were air cooled down to room temperature and residues on the specimen surfaces after boriding process were removed by holding the specimens in the boiling water. Then the specimens were exposed to ultrasonic cleaning in the alcohol.

Hardness measurements of boride layer and substrate of borided specimens were carried out by Future Tech FM 700 branded microhardness tester with a Vickers indenter under a load of 0.1 N. Hardness measurements were conducted from the surface to the substrate in certain intervals. Thus the change in the hardness from surface to the substrate was detected depending on the bath composition, boriding temperature and time. Hardness values were measured for all temperatures and times.

Boride layer thickness measurements were carried out using layer thickness detection methods developed for boriding. Computer-controlled Nikon Epiphot 200 branded optical microscope having Clemex image analysis program was used to examine the specimens. The zone from the outer surface to the end part was chosen as layer thickness and the average of 10 measurements were calculated and noted as layer thickness. Equation 1 developed first by Brakman [27] which is a special analysis of Fick's law was utilized for the calculation of diffusion coefficient in the boride structure of boron during the investigation of boride layer thickness in terms of kinetics. There is an exponential relationship between diffusion coefficient (D) which is a measure for displacement trend of boron atoms and temperature (Eq. 1). Diffusion coefficient is a property unique to material and sets the rate of diffusion.

$$d^2 = D t \tag{1}$$

Here; d is layer thickness (cm), D is diffusion coefficient (m^2s^{-1}), t is time (s). Activation energy required for the formation of the coating layer (Q) and Frequency factor (D_0) values were found from the Arrhenius equation (Eq. 2).

$$D = D_0 \exp(-Q/RT) \quad (2)$$

Here, D_0 is frequency factor (m^2s^{-1}), Q is activation energy ($kJmol^{-1}$), R is gas constant ($8.3145 \text{ Jmol}^{-1} \text{ } ^\circ K$), and T is temperature ($^\circ K$).

Activation energy required for the boride layer formation and diffusion coefficient values of boron were found depending on the boride layer thickness of borided specimens after the calculations.

X-ray diffraction method (XRD) was used to detect the phases formed on the surfaces of borided specimens. PHILIPS PW 3710 branded X-ray diffractometer and JADE Materials Data XRD Pattern Processing V5.0.2195(2) Service Pack 2 and ICDD database and $Co \text{ K}\alpha$ ($\lambda = 1.79021 \text{ \AA}$) radiation source and 2θ angles ranging from 10 to 90° were used.

Studies on the Secondary Electron (SE) and Back Scattered Electron (BSE) images, X-ray mapping and detection of the chemical composition of boride layer were made by electron probe micro analyzer (EPMA) instrument. Scanning electron microscope (SEM) was used to investigate the properties of the boride layers. SEM and elemental diffusion spectrometry (EDS) analyses were carried out by JEOL JSM T-330 and JEOL-JSM5410 scanning electron microscopes.

3. RESULTS AND DISCUSSION

Boride layer thicknesses of specimens borided at 850 , 950 and $1050^\circ C$ for 2 , 4 and 6 h were measured and layer thickness values depending on the boriding time were given in Table 2.

Table 2. Layer thickness values depending on boriding temperature and time.

Boriding temperature ($^\circ C$)	Boriding time (h)	Layer thickness (μm)
850 $^\circ C$	2	9.8
	4	16.9
	6	20.1
950 $^\circ C$	2	12.7
	4	24.9
	6	41.4
1050 $^\circ C$	2	23.3
	4	38.1
	6	60.9

Micrographs showing the boride layers of metallographically prepared sections of borided specimens at 850 °C and 1050°C for 6 h were given in Figure 1 (a) and (b) respectively. Boride layer thickness was found to increase with the boriding temperature. Different structures from the surface were observed depending on the boriding temperature and time after boriding process. These are;

- Boride layer zone containing the boride phases in its composition in the form of compact and flat layer,
- Boron-rich transition zone having a grain structure different from the matrix,
- Steel matrix.

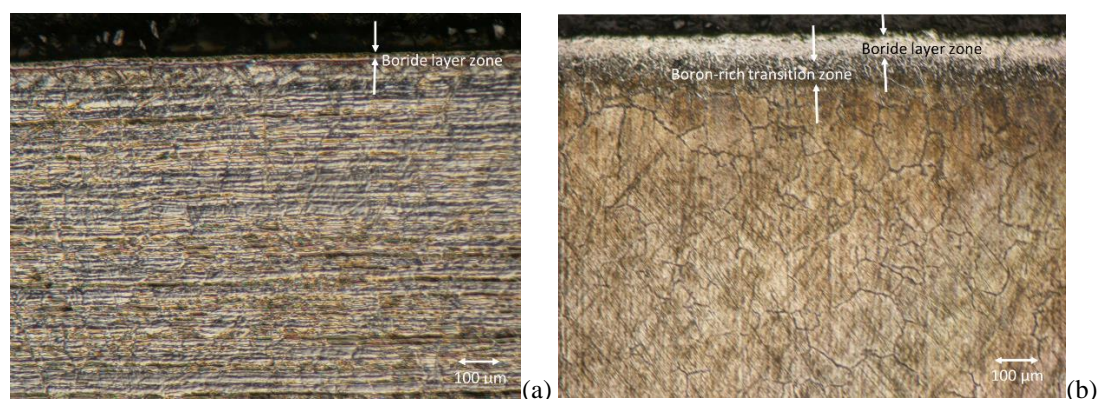


Figure 1. Cross-sectional views of borided specimens at 850°C (a) and 1050°C (b) for 6h.

In Figure 1a, the boron-rich transition zone cannot be seen clearly because the boriding temperature is not very high. It is pointed out in many studies that boride layer formed in the tooth-like form in the pure iron and plain carbon steels [28], and formed in the form of plain-like -not in the form of tooth-like- in the alloyed steels depending on the alloying elements [29-30]. It is seen that the coating thickness obtained for boriding at 850°C for 2 h is 9.8 µm. The highest coating thickness was reached in boriding at 1050°C for 6 h and the obtained coating thickness value was 60.9 µm. It is also seen that similar coating thicknesses were obtained in a boriding study [30] performed on AISI 316L steel with Ekabor-2 (6.2 – 63.5 µm). It is reported that the coating thickness obtained in another study, in which continuous boriding was performed on AISI 316L stainless steel with Ekabor-2 at 900°C for 1 h, was approximately 13 µm [31].

There are theoretically two factors in growth reaction kinetics. These are reaction products diffused on the reaction interface (diffusion-controlled) and a chemical barrier for transportation of the substances reacting on the reaction interface (reaction controlled). Boride layer grows linearly as the treatment time increases in the case of reaction-controlled process; it grows proportional to the square root of the reaction time if the process is diffusional. The increase in the layer thickness depending on the time and temperature is an expected result since boriding process is a diffusional process.

Although boride layer thicknesses formed in the boriding process are homogeneous on all over the specimen surface, some differences are observed in the length of the boride columns. The reason for these differences is the occurrence of boron gradient from the surface being enriched with boron to the substrate [32,33]. Contour diagram showing the boride layer depth depending on the temperature and time is shown in Figure 2. This diagram provides an ease of estimation for tuning the boriding process parameters in the industry.

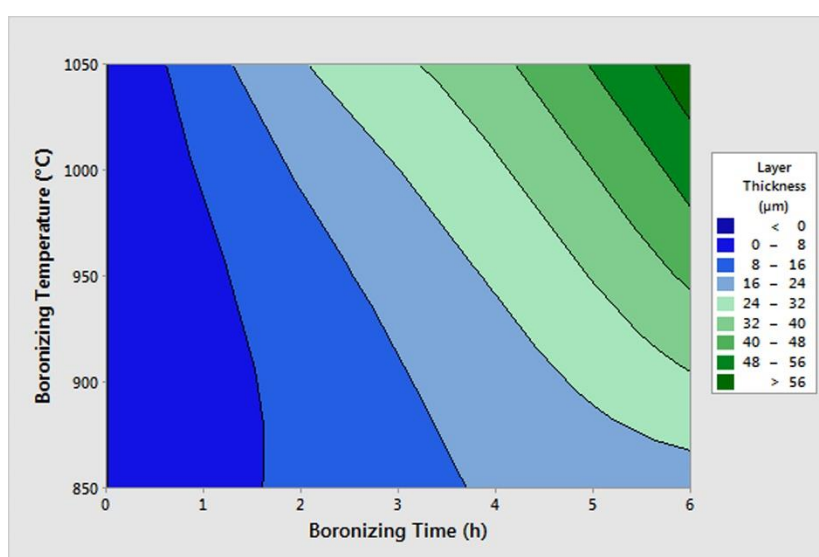


Figure 2. Contour diagram showing the layer thickness depending on the temperature and time.

3.1. Investigation of Boride Layer Thickness in Terms of Kinetics

Diffusion coefficient of boron in the boriding treatment were calculated by Eqs. 1 and 2 (developed by Brakman) utilizing the diagrams belonging to the boride layer thicknesses depending on the boriding time and temperature. Diffusion coefficients were calculated from the slope of d^2-t diagrams shown in Figure 3 and given in Table 3 for the borided specimens.

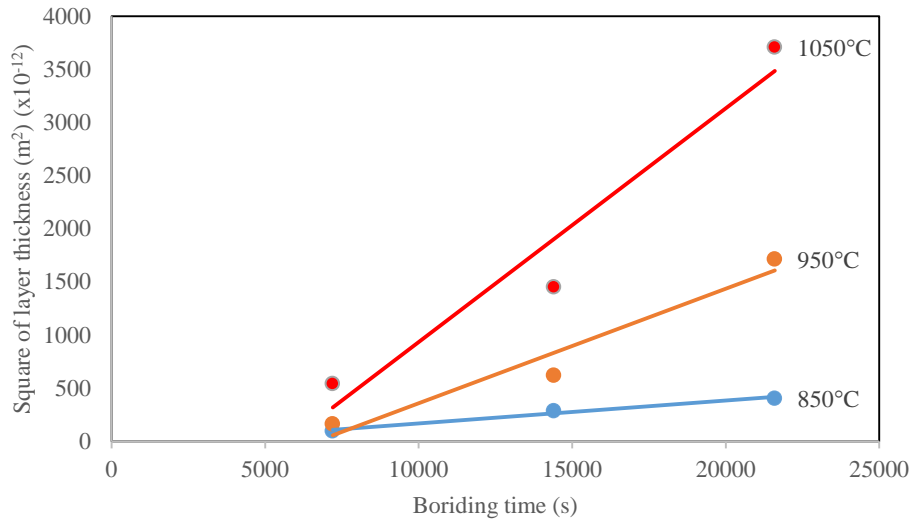


Figure 3. Variation of square of the boride layer thickness with time for different temperatures on the borided specimens ($d^2 - t$ variation).

Table 3. Diffusion coefficients of boron depending on the temperature during boriding treatment.

Temperature (°C)	Diffusion coefficient (m^2s^{-1})
850	2×10^{-14}
950	11×10^{-13}
1050	22×10^{-13}

Activation energy for the occurrence of boride layer was found using the diffusion coefficients and $\ln D - 1/T$ curve was drawn according to the Arrhenius equation and shown in Figure 4. There is an exponential relationship between temperature and the diffusion coefficient (D) which is a measure for the displacement trend of the atoms.

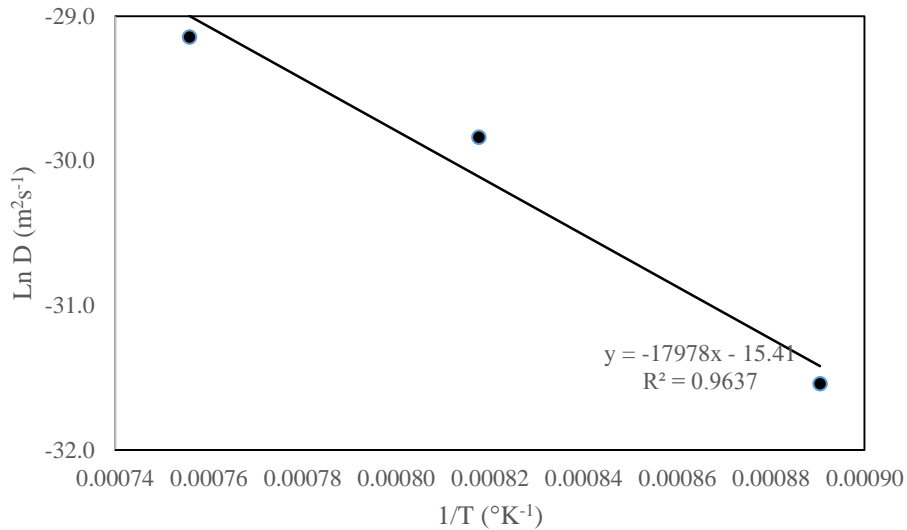


Figure 4. Variation of diffusion coefficient with the inverse of temperature.

Activation energy and frequency factor values of boride layer are given in Table 4. Diffusion coefficient is a unique property for the material and also governs the diffusion rate. Activation energy decreases as the diffusion coefficient increases and thus the diffusion rate increases. Desired layer thicknesses can be estimated practically without performing any experiments for a certain temperature and time after obtaining these kinetic data (Q , and D_0). Practical equations seen below (Eq. 3) were deduced for the calculation of diffusion coefficients from the kinetic data found in this study.

Table 4. Activation energy (Q) and frequency factor (D_0) values of boride layers.

Bath	Q (kJmol ⁻¹)	D_0 (m ² s ⁻¹)
Ekabor-2	149.3	1.96×10^{-7}

Diffusion coefficient of boron for borided AISI 316L steel specimen:

$$D = 1.96 \times 10^{-7} \exp(-17978/T) \quad (3)$$

Bath compositions utilized in the kinetic study are effective on the diffusion coefficient and activation energy values found in this study. Bozkurt and Sundararajan [34,35] point out the effect of boriding media and material composition on the kinetic values found in their studies on the steels. Activation energy results of some boriding studies made by different boriding methods were given in Table 4. Activation energies for the formation and growth of boride layers are consistent with the literature as can be seen from Table 5 [30,31,36-45].

Table 5. Activation energy values in some boriding studies carried out by different boriding methods.

Boriding Method	Material	Conditions (Temperature ; time)	Activation Energy (kJmol ⁻¹)	Hardness (HV)	Ref. No
Salt bath: Ekabor-2	AISI 316L	850,950,1050° C; 2,4,6 h	149.3	1543-1795	-
Salt bath: Ekabor-2	AISI 316L	800,850,900,950°C; 2,4,6 h	244.15	2125 (max)	[30]
Salt bath: Ekabor-2	AISI 316L	900°C; 1 h		26,3 (GPa)	[31]
Salt bath: Ekabor	AISI 316	800,875,950° C; 2,4,6,8 h	199.0	1700	[36]
Salt bath: 65% borax, 15% boric acid, %20 FeSi	AISI 4140	850,900,950° C; 2,4,6,8 h	215.0	1446-1739	[37]
Salt bath: borax and boric acid, FeSi	AISI 5140	850,900,950° C; 2,4,6,8 h	223.5	1198-1739	[38]
Salt bath: borax and boric acid, FeSi	AISI 4340	850,900,950° C; 2,4,6,8 h	233.7	1077-1632	[38]
Vacuum boriding: boron powder (98.3% B, 0.04% C, 1.6% O, 0.01%>Si-Cu-Mg, 0.001>Fe), Activator KBF ₄	Fe-%10 Cr	850,900, 950°C; 1-12 h	147.5 (156.4 FeB ₂)	1180-1300	[39]
Salt bath: Ekabor-2 (90% SiC, 5% B ₄ C, 5% KBF ₄)	AISI 440C	950°C; 2 h		2160	[40]
Salt bath: 60% borax, 20% boric acid, 20% FeSi	AISI 304	800,950°C; 3,5,7 h		2150	[41]
Salt bath: 70% borax, 30% SiC	AISI 316L	850,950,1000° C; 2,4,6 h	174.6		[42]
Salt bath: Ekabor-2	AISI D2 AISI M2	950°C; 1h 1000°C; 1h		2000 2000	[43]
Salt bath: Ekabor-2	ASTM A36	850,900,950, 1000°C 2,4,6, 8 h	161		[44]
Boron powder (Hef-Durferrit)	80/20 Ni-Cr	900,950,975° C; 2,4,6 h	145,9	1052-1350	[45]

3.2. X-Ray Diffraction Results

The results of X-ray diffraction analyses of the phases formed on the boride layers of specimens which were borided at 1050°C for 6 h are given in Figure 5 as an example. It is seen from the X-ray diffraction analysis graphics that FeB phase peaks in addition to Fe₂B phase are present in the layer formed in the borided specimens.

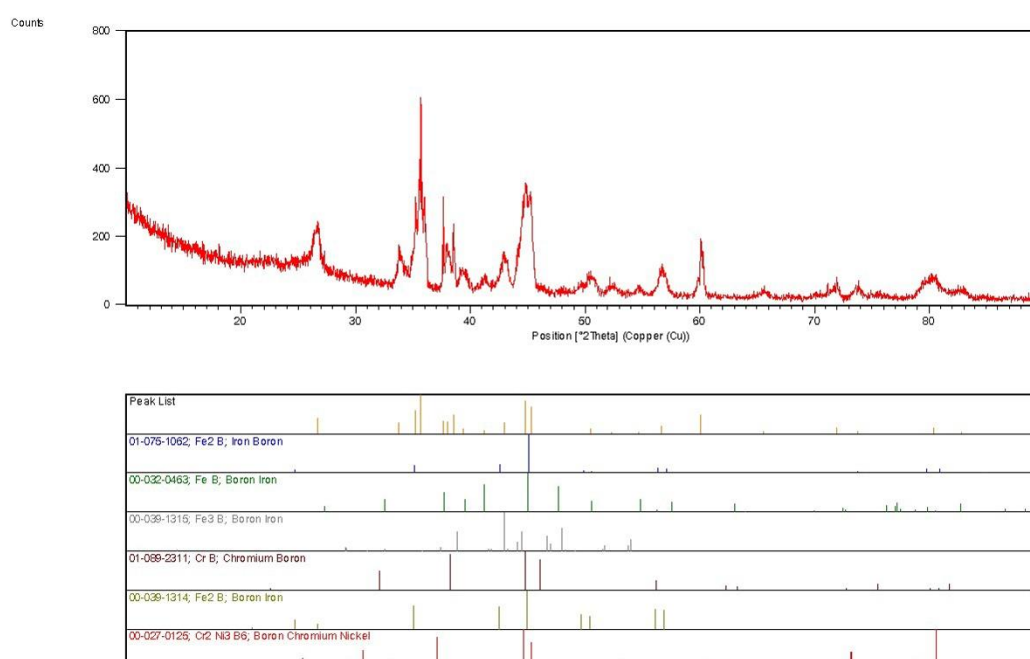


Figure 5. The results of X-ray diffraction analyses of the phases formed on the boride layers of specimens which were borided at 1050°C for 6 h.

SE and BSE images obtained from the EPMA and SEM investigations belonging to the boride layers of borided specimens are given in Figure 6; elemental distribution images obtained from X-ray mapping are given in Figure 7. Boride layer thickness is almost the same on all over the specimen as seen in Figure 6: boride layer formed homogenously on the surface. However, it is observed that there have been differences in the length of boride columns. The differences in the length of columns result from the boron gradient (concentration difference) between boron-enriched surface and substrate [32,33]. Boride layers, layer-substrate transition zone and substrate are obviously observed from the investigation by SEM and EPMA of boride layer morphologies of borided specimens. After the boriding process following structures and zones were observed depending on the boriding temperature and time: i) non-metallic ceramic zone in the form of compact and flat layer containing boride phases,

- ii) metallic transition zone between boride layer and matrix in which the boron concentration decreases from the surface; and this zone is non-homogeneous and poorer than the surface as boron,
- iii) structures in the form of matrix in the original material's structure unaffected by the boriding.

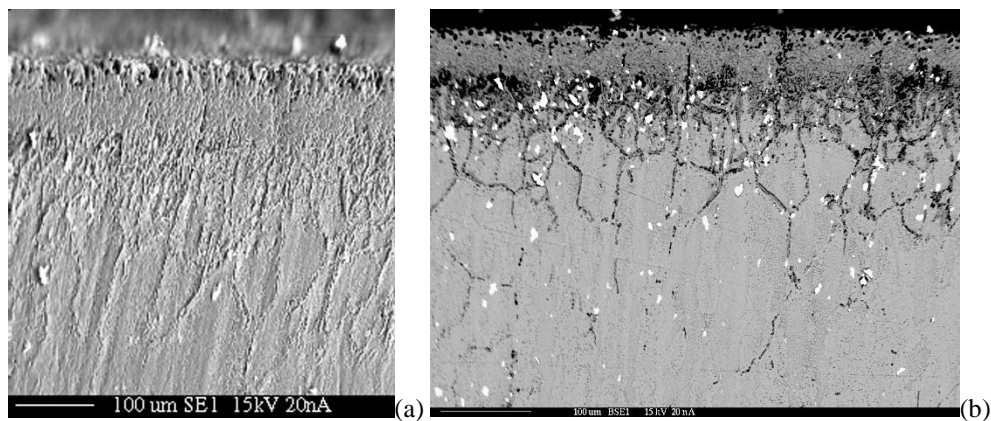


Figure 6. Images of boride layers formed on the AISI 316L stainless steel specimens borided at 1050°C for 6 h: (a) SE image, (b) BSE image.

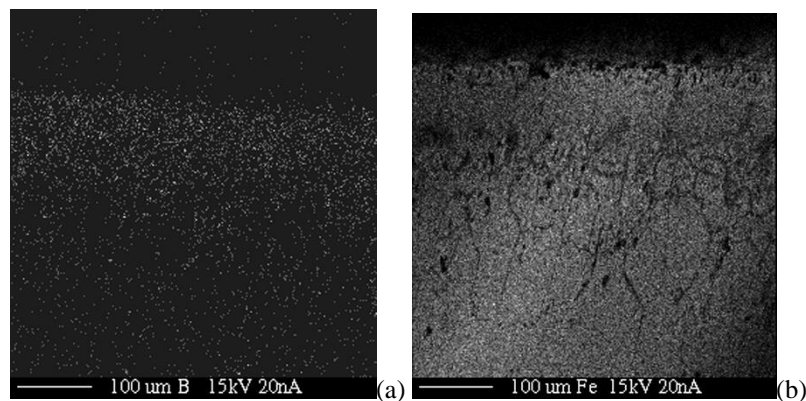


Figure 7. The X-ray mapping images of B and Fe on the surface of boride layers formed on the AISI 316L stainless steel specimens borided at 1050°C for 6 h: (a) B, (b) Fe.

Boride structure was observed to be in the form of a flat layer depending on the Cr, Ni and Mo content of stainless steel. Boride layer forms in tooth-shape structure in the pure iron and plain carbon steels [28]. Boride layer forming depending on the alloying elements in the alloyed steels is in the form of smooth structure more than the tooth-shape structure [29]. Also alloying elements in the investigated AISI 316L stainless steel made boride layer smooth. B content was observed to be 2.085% at the

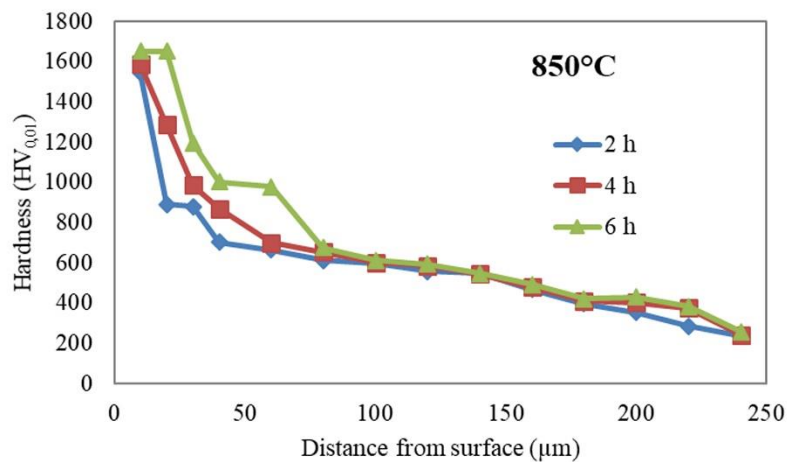
middle zone of the sections of boride layers of specimens borided at 1050°C for 6 h by semi-quantitative analysis method.

3.3. Hardness Results

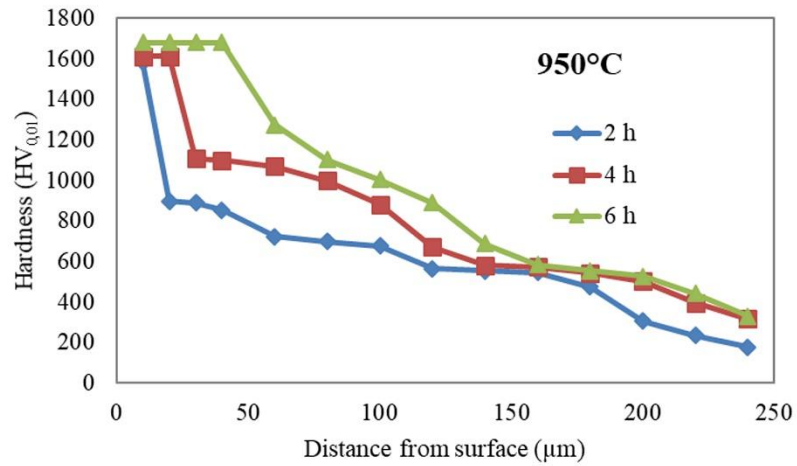
Hardness measurements were carried out on the borided specimens at certain distances from surface to the substrate. By this way, variation of the hardness from surface to substrate was observed depending on the boriding time and temperature. Hardness measurements were performed for all temperature and time conditions.

Hardness distribution of the materials borided at 850, 950, and 1050 °C for 2, 4, 6 h were given in Figure 8. Hardness values gradually decrease in the specimens borided at 850°C for all boriding times depending on the distance from the surface as can be seen from Figure 8 (a). The highest hardness was obtained in the regions near the surface, and being the richest zone in terms of boron. Hardness values were also found to increase with the increasing time. The hardness values seem to keep the high values on the surface toward the interior as the boriding temperature increased especially for the boriding time of 6h. The surface hardness value appears to be maintained up to 60µm at boriding temperature of 1050°C for 6h (Figure 8 (c)).

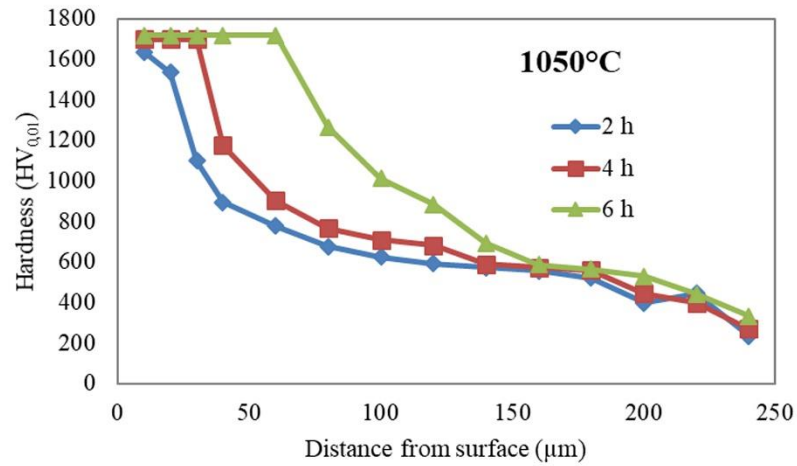
Surface hardness values of borided materials increase depending on the temperature and time. The hardness of non-borided AISI 316L stainless steel specimen is HV170. Surface hardness values of borided materials are 9.1 to 12 times higher than the non-borided material depending on the temperature and time. Taktak [41] has found that surface hardness values of borided AISI 304 stainless steel were 7.4 to 11 times higher depending on the temperature and time than the non-borided one.



(a)



(b)



(c)

Figure 8. Hardness distribution of borided specimens at (a) 850°C, (b) 950°C, (c) 1050°C for 2, 4 and 6 h.

Surface hardness values obtained in this study and some values from the literature are seen in Table 5. Basic phase in the boride layer formed in the boriding is Fe₂B. FeB phase also forms.

4. CONCLUSIONS

The following results were obtained in the studies on boriding the surfaces of AISI 316L stainless steel material with Ekabor-2.

The thickness of boride layer increases with the increasing temperature and time during the boriding process.

Boride layers which form on the surfaces of the specimens are continuous and have a smooth structure. The basic phase in the boride layer formed in the boriding processes of stainless steel is Fe₂B. FeB phase also formed in the boriding with the bath containing Ekabor-2.

Activation energy for the formation and growth of boride layer is 149.319 kJmol⁻¹ in the boriding with the bath containing Ekabor-2 and consistent with the literature.

Surface hardness values of borided materials increase during the boriding process depending on the temperature and time.

ACKNOWLEDGEMENT

The authors acknowledge Yılmaden Holding, Eti Krom A.Ş. R&D Center.

REFERENCES

- [1] Güven, Ş.Y., (2014), Biyouyumluluk ve biyomalzemelerin seçimi. Süleyman Demirel University, Journal of Engineering Sciences and Design, 2(3) SI:BioMechanics, 303-311.
- [2] Güven, Ş.Y. and Delikanli, K., (2006 Nisan), Metalik biyomalzemelerde son gelişmeler. TİMAK-Tasarım İmalat Analiz Kongresi, Balıkesir, 26-28.
- [3] Patel, N.R. and Gohil, P.P., (2012), A review on biomaterials: Scope, applications and human anatomy significance. International Journal of Emerging Technology and Advanced Engineering, 2(4), 91-101.
- [4] Geetha, M., Singh, A.K., Asokamani, R. and Gogia, A.K., (2009), Ti based biomaterials, the ultimate choice for orthopaedic implants - A review. Progress in Materials Science, 54, 397-425.
- [5] Paital, S.R. and Dahotre, N.B., (2009), Calcium phosphate coatings for bio-implant applications: Materials, performance factors, and methodologies. Materials Science and Engineering R, 66, 1-70.

- [6] Talha, M., Behera C.K. and Sinha, O.P., (2013), A review on nickel-free nitrogen containing austenitic stainless steels for biomedical applications. *Materials Science and Engineering C*, 33(7), 3563–3575.
- [7] Arsiwala, A., Desai, P. and Patravale, V., (2014), Recent advances in micro/nanoscale biomedical implants. *Journal of Controlled Release*, 189(10), 25–45.
- [8] Parsapour, A., Khorasani, S.N. and Fathi, M.H., (2012), Effect of surface treatment and metallic coating on corrosion behavior and biocompatibility of surgical 316L stainless steel implant. *Journal of Materials Science and Technology*, 28(2), 125–131.
- [9] Rautray, T.R., Narayanan, R. and Kim, K-H., (2011), Ion implantation of titanium based biomaterials. *Progress in Materials Science*, 56(8), 1137–1177.
- [10] Chen, Q. and Thouas, G.A., (2015), Metallic implant biomaterials. *Materials Science and Engineering R*, 87(1), 1–57.
- [11] Tiwari, S.K., Mishra, T., Gunjan, M.K., Bhattacharyya, A.S., Singh, T.B. and Singh, R., (2007), Development and characterization of sol–gel silica–alumina composite coatings on AISI 316L for implant applications. *Surface & Coatings Technology*, 201, 7582–7588.
- [12] Schwab, H., Prashanth, K.G., Löber, L., Kühn, U. and Eckert, J., (2015), Selective laser melting of Ti-45Nb alloy. *Metals*, 5, 686-694.
- [13] Lemons, J.E., Misch-Dietsh, F. and McCracken, M.S., (2015), Biomaterials for dental implants, In *Dental Implant Prosthetics* (pp. 66-94). Elsevier Inc.
- [14] Öztürk, O., (2009), Microstructural and mechanical characterization of nitrogen ion implanted layer on 316L stainless steel. *Nuclear Instruments and Methods in Physics Researchs Section B: Beam Interactions with Materials and Atoms*, 267(8-9), 1526–1530.
- [15] Başman, G. and Şeşen, M.K., (2011), AISI 316 L tipi paslanmaz çeliğin yüzey özelliğinin borlama ile geliştirilmesi. *İTÜ Dergisi/D Mühendislik*, 10(2), 115-121.
- [16] Sinha, A.K., (1991), Boriding (Boronizing), *ASM Handbook, J. Heat Treatment*, OH, USA, 4, 437-447.
- [17] TMMOB Metalurji Mühendisleri Odası, Bor Raporu, (2003), *Metalurji Dergisi*, 134, 11-72.
- [18] Hocking, M.G., Vasantasree, V. and Sidky, P.S., (1989), *Metallic and ceramic coatings*. John Wiley & Sons Inc., New York, pp. 1-2.

- [19] Yapar, U., Başman, G., Arısoy, C.F., Yeşilçubuk A., and Şeşen, M.K., (2004), The influence of boronizing on mechanical properties of EN-C35E steel, *Key Engineering Materials*, 264-268, 629-632.
- [20] Matuschka, A.G., (1980), *Boronising*. Carl Hanser Verlag, München.
- [21] Graf, A. and Matuschka, W., (1997), *Borieren*. Carl Hanser Verlag, München, Wien, pp.1-87.
- [22] Yapar, U., Arısoy, C.F., Başman, G., Yeşilçubuk S.A. and Şeşen, M.K., (2004), Surface modification of EN-C35E steels by thermochemical boronizing process and its properties, *Key Engineering Materials*, 264-268, 633-636.
- [23] Ficht, W., Trausner, N. and Matuschka, A.G., (1987), *Borieren mit ekabor*, ESK GmbH.
- [24] Eyre, T.S., (1975), Effect of boronising on friction and wear of ferrous metals. *Wear*, 34, 383-397.
- [25] Geoeuriot, P., Thevenot, F., Driver, J.H. and Magnin, T., (1983), Methods for examining brittle layers obtained by a boriding surface treatment (Borudif). *Wear*, 86, 1-10.
- [26] Soydan, Y., (1996), Katı ortamda bor yayınımları ile sertleştirilen çelik yüzeylerinin kuru kayma halinde sürtünme ve aşınma davranışları, Doktora Tezi, İ.T.Ü. Fen Bilimleri Enstitüsü, İstanbul.
- [27] Brakman, C.M., Gommers, A.W.J. and Mittemeijer, E.J., (1989), Boriding of Fe and Fe-C, Fe-Cr, and Fe-Ni Alloys: Boride layer kinetics. *Journal of Materials Research*, 4, 1354-1370.
- [28] Palombarini, G. and Carbucicchio, M., (1984), On the morphology of thermochemically produced Fe₂B/Fe interfaces. *Journal of Materials Science Letters*, 3, 791-794.
- [29] Carbucicchio, M. and Palombarini, G., (1987), Effects of alloying elements on the growth of iron boride coatings. *Journal of Materials Science Letters*, 6, 1147-1149.
- [30] Ayvaz, S.I. and Aydın, I., (2020), Effect of the microwave heating on diffusion kinetics and mechanical properties of borides in AISI 316L. *Transactions of the Indian Institute of Metals*, 73(10):2635-2644.
- [31] Valdes, D.F., Rosa, O.V.D., Castro, G.A.R., Amador, A.M., Lievano, A.L., Ramirez, A.O., (2021), *Surface & Coatings Technology*, 423, 127556, 1-11.
- [32] Başman, G., (2010), AISI 316L tipi paslanmaz çeliğin termokimyasal difüzyon yöntemi ile borlanması, borlama banyosu bileşenlerinin borür tabakası özelliklerine etkisi, Doktora tezi, İ.T.Ü. Fen Bilimleri Enstitüsü, İstanbul.

- [33] Yapar, U., (2003), Düşük ve orta karbonlu çeliklerin termokimyasal borlama ile yüzey özelliklerinin geliştirilmesi, Yüksek Lisans Tezi, İ.T.Ü. Fen Bilimleri Enstitüsü, İstanbul.
- [34] Bozkurt, N., (1984), Bor yayınımla çeliklerde yüzey sertleştirme, Doktora Tezi, İ.T.Ü. Fen Bilimleri Enstitüsü, İstanbul.
- [35] Chen, X.J., Yu, L.G., Khor, K.A. and Sundararajan, G., (2007), The effect of boron-pack refreshment on the boriding of mild steel by the spark plasma sintering (SPS) process. *Surface & Coatings Technology*, 202(13), 2830–2836.
- [36] Ozdemir, O., Omar, M.A., Usta, M., Zeytin, S., Bindal, C. and Üçışık, A.H., (2009), An investigation on boriding kinetics of AISI 316 stainless steel. *Vacuum*, 83, 175–179.
- [37] Şen, Ş., Şen, U. and Bindal, C., (2005), The growth kinetics of borides formed on boronized AISI 4140 Steel. *Vacuum*, 77, 195-202.
- [38] Şen, Ş., Şen, U. and Bindal, C., (2005), An approach to kinetic study of boride steels. *Surface & Coatings technology*, 191, 274-285.
- [39] Dybkov, V.I., Lengauer, W. and Barmak, K., (2005), Formation of boride layers at the Fe-%10Cr alloy-boron interface. *Journal of Alloys and Compounds*, 398(1-2), 113,122.
- [40] Taktak, Ş., (2006), Tribological behavior of borided bearing steels at elevated temperatures. *Surface & Coatings Technology*, 201(6), 2230-2239.
- [41] Taktak, Ş., (2007), Some mechanical properties of borided AISI H13 and 304 steels. *Materials Design*, 28(6), 1836-1843.
- [42] Mebarek, B., Madouri, D., Zanoun, A. and Belaidi, A., (2015), Simulation model of monolayer growth kinetics of Fe₂B phase, *Materiaux and Techniques*, 103(7), 703.
- [43] Ertürk, Ş. and Kayabaşı, O., (2019), Investigation of the cutting performance of cutting tools coated with the thermo-reactive diffusion (TRD) technique. *IEEE Access*, 7, 106824-106838.
- [44] Ortiz-Domínguez, M., Gómez-Vargas, O.A., Ares de Parga, G., Torres-Santiago, G., Velázquez-Mancilla, R., Castellanos-Escamilla, V.A., Mendoza-Camargo, J. and Trujillo-Sánchez, R., (2019), Modeling of the growth kinetics of boride layers in powder-pack borided ASTM A36 steel based on two different approaches. *Advances in Materials Science and Engineering*, 2019-7.
- [45] Ulloa A.C, Trabolsi, P.A.R., Avila, I.P.T., Álvarez, C.O., Rosas, R.T., Velázquez, J.C. and Sánchez, E.H., (2022), Kinetics and mechanical characterization of hard layers obtained by boron diffusion in 80/20 nickel–chromium alloy. *Coatings*, 12, 1387, 1-14.



RESEARCH ARTICLE

THE EFFECT OF LEVOTHYROXINE TREATMENT ON MATERNAL AND PERINATAL OUTCOMES IN PREGNANT WOMEN WITH SUBCLINICAL HYPOTHYROIDISM: A 5-YEAR RETROSPECTIVE STUDY AT A TERTIARY CARE HOSPITAL IN TURKEY

Halil İbrahim ERBIYIK^{1,2}, Rabia Merve PALALIOĞLU^{3*}

¹Uskudar University, Operation Room Services, İstanbul drhalilibrahim@gmail.com, ORCID: 0000-0001-5526-2663

²Dr. Moral Obstetrics and Gynecology Clinic, İstanbul drhalilibrahim@gmail.com, ORCID: 0000-0001-5526-2663,

³University of Health Science Umraniye Training and Research Hospital, Department of Obstetrics and Gynecology, İstanbul drmerbiyik@gmail.com, ORCID: 0000-0003-2717-7925,

Receive Date: 17.02.2023

Accepted Date: 23.03.2023

ABSTRACT

Subclinical hypothyroidism is characterized by elevated thyroid stimulating hormone (TSH) levels with normal free thyroxine (fT4) levels. The aim of this study was to compare obstetric and neonatal outcomes in pregnant women with and without treatment for subclinical hypothyroidism. In this study, maternal and perinatal outcomes were evaluated in a total of 270 pregnant women who were diagnosed with subclinical hypothyroidism as a result of screening performed in three trimesters of pregnancy between 2015 and 2020 and followed up in our clinic, 149 of whom received levothyroxine treatment and 121 of whom did not receive treatment. Further, different cutoff values for TSH were compared. The rates of neonatal intensive care unit (NICU) requirement were not different according to the levothyroxine use status of the patients ($p=0.73$, $p>0.05$). Miscarriage rates did not differ according to levothyroxine use ($p=0,87$, $p>0,05$). TSH, T4 and antithyroid peroxidase levels did not differ according to the maternal use of levothyroxine ($p>0,05$). Birth weight, gestational week at birth, 1- and 5-minute APGAR scores, neonatal TSH and T4 levels did not differ according to the maternal use of levothyroxine ($p>0,05$). Among the adverse maternal and perinatal outcomes, the need for NICU admission and the rates of placental abruption, fetal distress, preterm premature rupture of membranes, preeclampsia, preterm labor, and small for gestational age were not significantly different among the TSH cutoff groups ($p>0,05$). The rate of premature rupture of membranes was higher in the group with TSH levels ≥ 2.5 mIU/L ($p=0.04$). Choosing 2.5 mIU/L as the cutoff value for TSH levels allows early diagnosis of subclinical hypothyroidism with a higher rate in pregnant Turkish women and proactive therapeutic management. Our study provides limited evidence for the success of levothyroxine therapy for adverse obstetric and neonatal outcomes.

Keywords: Adverse pregnancy-fetal outcomes, Levothyroxine, Pregnancy, Screening, Subclinical hypothyroidism, Thyroid hormone replacement.

1. INTRODUCTION

Thyroid diseases are recognized as the second most common endocrinopathies after gestational diabetes mellitus in women of reproductive age. Role of the thyroid hormone is crucial for a healthy pregnancy and fetal development. Maternal thyroid dysfunction may cause various adverse obstetric outcomes, including miscarriage, intrauterine growth restriction, hypertensive disorders, and preterm delivery [1]. Notably, fetal development of the thyroid tissue depends on uteroplacental levels of thyroid hormone. The incidence of subclinical hypothyroidism has been reported to be 2%–3% in pregnant women. Moreover, subclinical hypothyroidism is characterized by high thyroid-stimulating hormone (TSH) levels (2.5–10 mIU/L) and normal free thyroxine (fT4) levels in asymptomatic pregnant women. The fetus is particularly dependent on the mother's thyroid hormone during the first trimester. Thus, antibody tests are recommended for the treatment or follow-up of patients with subclinical hypothyroidism. Anti-TPO positivity can lead to negative consequences for the mother and fetus, and approximately 2-17% of women of reproductive age have anti-thyroid peroxidase (anti-TPO) and anti-thyroglobulin (anti-TG) autoantibodies [2]. Further, the risk of thyroid dysfunction has been increasing in Turkey—an endemic region for iodine deficiency. There is no recommendation by the American College of Obstetricians and Gynecologists (ACOG) that the diagnosis and treatment of maternal subclinical hypothyroidism improves neurocognitive outcomes in children, and thyroid function tests are not recommended during pregnancy [3]. In contrast, the Turkish Society of Endocrinology and Metabolism (TSEM) advocates the initial measurement of TSH levels in all women planning pregnancy and in all pregnant women [4]. TSEM and American Thyroid Association (ATA) recommend that TSH levels should be 0.1–2.5, 0.2–3.0, and 0.3–3.0 mIU/L in the first and third trimester, respectively [2, 4]. Hormone replacement therapy for hypothyroidism involves the oral administration of T4 (levothyroxine). The American Endocrinology Society (ES) [5] and the European Thyroid Association [6] recommend starting this therapy in pregnant women with TSH levels >2.5 mIU/L and >3.0 mIU/L in the first trimester and in the second and third trimesters, respectively. If hypothyroidism is not treated in such cases, it may increase the risk of perinatal morbidity, preterm birth, miscarriage, low birth weight, and mortality [7]. Notably, thyroid screening is not recommended for cases other than pregnancy and infertility because the benefits of the therapy for subclinical hypothyroidism have not been clearly established [8-10]. However, managing subclinical hypothyroidism is important because it can progress to overt hypothyroidism and has negative effects on the cardiovascular system, fertility, quality of life, depression, and cognitive functions. Notably, TSH levels are elevated in 2%–5% of all pregnant women. Generally, TSH levels of >4 mIU/L are considered significant in pregnant women with subclinical hypothyroidism. In patients with TSH levels above the specified cutoff value, treatment planning is recommended if the anti-TPO level is also positive [2]. According to a study that used the cutoff value of 2.5 mIU/L for TSH levels, 25% of the population needed treatment for hypothyroidism; however, when the cutoff value was set at 4 mIU/L, there was a 10-fold decrease in the number of pregnant women receiving therapy [11]. The aim of this study was to compare obstetric and neonatal outcomes in pregnant women with subclinical hypothyroidism who received and did not receive treatment.

2. MATERIALS AND METHODS

This retrospective cross-sectional case-control study was conducted between 2015 and 2020 at the Department of Obstetrics and Gynecology of Health Sciences University Ümraniye Training and Research Hospital. Patients with maternal diseases, such as overt hypothyroidism, autoimmune thyroiditis, hyperthyroidism, thyroid cancer, congenital heart diseases, diabetes mellitus, antiphospholipid antibody syndrome, idiopathic thrombocytopenic purpura, thrombotic thrombocytopenic purpura, other autoimmune-related diseases, multiple pregnancies, and chronic hypertension were excluded from the study. Macrosomia, polyhydramnios, intrauterine fetal death, were excluded from the study. In contrast, a known history of hypothyroidism before pregnancy, levothyroxine users and nonusers and women with pregnancy-related complications, such as preeclampsia, oligohydramnios, SGA, LBW, gestational hypertension, gestational thrombocytopenia, cholestasis, PROM, PPRM, preterm labor, postterm pregnancy were included. A total of 439 pregnant women enrolled for the study; of these, 41 were excluded because they were diagnosed with overt hypothyroidism and autoimmune thyroiditis, and 128 were excluded because they were not followed up at our clinic and their deliveries were performed at an external facility. After implementing the inclusion and exclusion criteria, 270 pregnant women (149 receiving treatment and 121 not receiving treatment) were reviewed and included in the final analysis. The clinical and laboratory data of all pregnant women from all three trimesters diagnosed with subclinical hypothyroidism were collected from the hospital automation system and retrospectively analyzed. Gravida, parity, number of abortions, gestational ages of all patients were recorded. Maternal serum TSH, T4 and anti-TPO levels were recorded. It was recorded whether they were diagnosed with hypothyroidism before pregnancy and whether they used levothyroxine. The gestational weeks when each patient gave birth, fetal weight, type of delivery, indications for cesarean section, gender of the newborns, appearance; pulse; grimace; activity; and respiration 1- and 5-minute (APGAR) scores, neonatal TSH and T4 values were also recorded. Those who received neonatal intensive care unit (NICU) support were determined. Obstetric anamnesis was taken from all pregnant women included in the study. Crown-rump length, last menstruation date were recorded. Preeclampsia, small for gestational age (SGA), low birth weight (LBW), preterm birth, preterm premature rupture of membranes (PPROM) were recorded. The diagnosis of preeclampsia was based on the guideline updated by ACOG in 2019 [12]. Fetal weight below the 10th percentile were termed as SGA. LBW was considered when it was below 2500 g. Births before 37 weeks of gestation were termed as premature births. Rupture of membranes before 37th gestational week was designated as PPRM [13]. Pregnant women with gestational diabetes mellitus [14] who had a positive oral glucose tolerance test were excluded from the study, but pregnant women with placenta previa [15] were included. In our study, the normal ranges for TSH, T4, and anti-TPO levels were considered 0.1–2.5 mIU/L, 0.93–1.71 ng/dl, and <5.60 IU/mL, respectively. Based on the obtained results, TSH levels were classified into three groups: 2.5, 2.5–4, and 3–10 mIU/L. Different cutoff values for TSH levels were then compared between these groups. Subclinical hypothyroidism diagnosis of the patients included in the study was made according to the criteria by the ATA 2011, 2017 and ES 2012 [2, 5]. Previously, the upper limit for TSH value was specified as 2.5 mIU/L for the first trimester in the guidelines. In 2017, the upper limit was revised to 4 mIU/L. Therefore, in our study, both upper limits were used as cutoff values for comparison purposes. Ethical approval was obtained from the Health Sciences University Ümraniye

Training and Research Hospital Ethics Committee (Date: April 14, 2020; confirmation number: B.10.1.TKH.4.34.H.GP.0.01/85). Informed consent was obtained from all the participants included in this cross-sectional retrospective study.

2.1. Statistical Analysis

Descriptive statistics were presented as mean, standard deviation ($\text{Avr} \pm \text{SD}$), confidence interval (95% CI) value for continuous variables. The conformity of the data to the normal distribution was evaluated with the Kolmogorov-Smirnov test. Non-parametric methods were used because the measurement data in the study were not suitable for normal distribution ($p=0.01$) and the numbers within the group were not very high. Mann Whitney U test was used for pairwise comparisons and Kruskal Wallis test for triple comparisons. Chi-square test was used to evaluate the difference in group ratios. Fisher correction was applied if the expected cell value was less than 5%, 20% or more. $p < 0.05$ was accepted as the critical value. The data were analyzed using the SPSS 25.0 (Statistical Packages of Social Sciences) program on the computer.

3. RESULTS

We found that the rate of NICU requirement was not different between levothyroxine users and nonusers ($p=0.73$, $p > 0.05$). In contrast, the rate of diagnosis of hypothyroidism before pregnancy was different between levothyroxine users and nonusers, and the rate of levothyroxine use was higher in patients who were diagnosed with hypothyroidism before pregnancy ($p=0.01$, $p < 0.05$). Notably, the mode of delivery ($p=0.50$, $p > 0.05$) and infant gender ($p=0.31$, $p > 0.05$) did not differ according to levothyroxine use. Taking maternal levothyroxine did not make a difference in all three trimesters ($p=0.09$, $p > 0.05$) (Table 1a). Further, the age of the patients did not differ according to levothyroxine use ($p=0.18$, $p > 0.05$). Gravida ($p=0.02$) and parity ($p=0.01$) were significantly higher among levothyroxine users than among nonusers. The rate of miscarriage did not significantly differ according to the maternal use of levothyroxine ($p=0.87$, $p > 0.05$). Furthermore, TSH, T4, and anti-TPO levels did not differ according to levothyroxine use ($p > 0.05$). Birth weight, gestational week at birth, 1- and 5-minute APGAR scores and neonatal TSH and T4 levels were not found to be different in those who received or did not receive levothyroxine ($p > 0.05$) (Table 1b).

Table 1a: Examination of Patient Characteristics According to Levothyroxine Usage Status.

		Levothyroxine		p
		No (n=121) n (%)	Yes (n=149) n (%)	
NICU need	No	101 (83.5)	122 (81.9)	0.73
	Yes	20 (16.5)	27 (18.1)	
History of hypothyroidism	No	75 (62)	68 (45.6)	0.01*
	Yes	46 (38)	81 (54.4)	
Delivery type	NSD	60 (49.6)	80 (53.7)	0.50
	C/S	61 (50.4)	69 (46.3)	

Gender	Female	48 (39.7)	68 (45.9)	0.31
	Male	73 (60.3)	80 (54.1)	
Gestational ages	1 st Trimester	98 (81)	133 (89.3)	0.09
	2 nd Trimester	19 (15.7)	11 (7.4)	
	3 rd Trimester	4 (3.3)	5 (3.4)	

**Chi-square test was performed *Significant difference at 0.05 level

Table 1b: Analysis of Patient Measurements According to Levothyroxine Usage Status.

	Levothyroxine				p
	No (n=121)		Yes (n=149)		
	Avr±SD	95% CI	Avr±SD	95% CI	
Age	28.44±6.2	27.32±29.55	29.36±5.18	28.52-30.19	0.18
Gravida	2.30±1.56	2.02±2.58	2.71±1.47	2.47-2.95	0.02*
Parity	0.85±1.01	0.67±1.03	1.29±1.08	1.11-1.46	0.01*
Abortus	0.45±0.97	0.28±0.63	0.44±0.92	0.29-0.58	0.87
TSH (mIU/L)	4.4±5.91	3.33±5.46	4.95±4.16	4.28-5.63	0.36
ft4 (ng/dL)	1.56±7.01	0.3±2.82	2.55±14.28	0.24-4.86	0.48
Anti-TPO (IU/mL)	194.03±322.23	94.86±293.19	160.5±275.07	89.44-231.56	0.57
Gestational age at birth	38.28±2.28	37.87±38.69	38.27±2.3	37.9-38.64	0.96
Birth weight	3237.85±595.86	3130.6±3345.1	3197.92±577.34	3104.45-3291.39	0.57
APGAR 1	8.46±1.17	8.25±8.67	8.54±0.97	8.38-8.69	0.57
APGAR 5	9.63±1.09	9.43±9.82	9.69±0.7	9.58-9.8	0.58
Newborn TSH (mIU/L)	4.77±4.19	3.6±5.94	4.86±4.2	3.78-5.95	0.90
Newborn ft4 (ng/dL)	1.21±0.25	1.15±1.28	1.25±0.25	1.19-1.32	0.41

***Kruskall Wallis test ** Mann Whitney U test *Significant difference at 0.05 level

We found that the need for NICU did not differ according to trimesters ($p=0.14$, $p>0.05$). Moreover, the rate of levothyroxine use was not different according to trimesters ($p=0.10$, $p>0.05$). However, the rate of patients diagnosed with hypothyroidism before pregnancy was different among the first, second, and third trimesters, and this rate was the highest in the first trimester ($p=0.01$, $p<0.05$). The mode of delivery ($p=0.89$, $p>0.05$) and infant gender ($p=0.33$, $p>0.05$) did not differ among the trimesters (Table 2a). Moreover, age, gravida, parity, and miscarriage rates were not different among

the trimesters ($p>0.05$). We also found that TSH, T4, and anti-TPO levels were not significantly different among the trimesters ($p>0.05$). No difference were found in terms of birth weight, gestational week at birth, 1- and 5-minute APGAR scores, neonatal TSH and T4 levels in all three trimesters ($p>0.05$) (Table 2b).

Table 2a: Investigation of Patient Characteristics by Gestational Ages.

		Gestational Ages			p
		1 st Trimester (n=231) n (%)	2 nd Trimester (n=30) n (%)	3 rd Trimester (n=9) n (%)	
NICU need	No	195 (84.4)	22 (73.3)	6 (66.7)	0.14
	Yes	36 (15.6)	8 (26.7)	3 (33.3)	
Levothyroxine	No	98 (42.4)	19 (63.3)	4 (44.4)	0.10
	Yes	133 (57.6)	11 (36.7)	5 (55.6)	
History of hypothyroidism	No	104 (45)	30 (100)	9 (100)	0.01*
	Yes	127 (55)	0 (0)	0(0)	
Delivery type	NSD	111 (48.1)	14 (46.7)	5 (55.6)	0.89
	C/S	120 (51.9)	16 (53.3)	4 (44.4)	
Gender	Female	101 (43.9)	13 (43.3)	2 (22.2)	0.33
	Male	129 (56.1)	17 (56.7)	7 (77.8)	

**Chi-square test was performed *Significant difference at 0.05 level

Table 2b: Examination of Patient Measurements According to Gestational Ages.

	Gestational Ages						p
	1 st Trimester (n=231)		2 nd Trimester (n=30)		3 rd Trimester (n=9)		
	Avr±SD	95% CI	Avr±SD	95% CI	Avr±SD	95% CI	
Age	29.17±5.74	28.43-29.92	27.2±4.74	25.43-28.97	28.89±6.13	24.17-33.6	0.20
Gravida	2.57±1.58	2.37-2.78	2.27±1.17	1.83-2.7	2.22±1.2	1.3-3.15	0.49
Parity	1.09±1.08	0.95-1.23	1.17±1.02	0.79-1.55	0.89±1.17	-0.01-1.79	0.79
Abortus	0.49±1.00	0.36-0.62	0.13±0.43	-0.03-0.3	0.22±0.44	-0.12-0.56	0.11
TSH (mIU/L)	4.76±5.14	4.1-5.43	4.56±4.72	2.8-6.32	3.7±1.88	2.26-5.15	0.81
ft4 (ng/dL)	2.29±12.52	0.66-3.91	1.14±1.3	0.65-1.63	0.74±0.14	0.63-0.84	0.82
Anti-TPO (IU/mL)	188.29±311.65	121.47-255.11	110.9±18.039	14.78-207.02	-	-	0.54
Gestational age at birth	38.33±2.08	38.06-38.6	37.87±3.49	36.56-39.17	38.22±2.49	36.31-40.14	0.58

Birth weight	3237.77±56	3164.56-3310.98	3031±724	2760.6-3301.4	3268.33±5	2853.07-3683.6	0.18
APGAR 1	8.55±0.9	8.44-8.67	8.17±1.86	7.47-8.86	8.33±1.32	7.32-9.35	0.15
APGAR 5	9.72±0.64	9.64-9.8	9.3±1.91	8.59-10.01	9.44±1.01	8.67-10.22	0.04
Newborn TSH (mIU/L)	4.89±4.34	4.03-5.75	4.8±2.53	2.15-7.45	3.44±1.93	1.05-5.83	0.75
Newborn fT4 (ng/dL)	1.23±0.24	1.18-1.28	1.35±0.25	1.11-1.58	1.17±0.31	0.67-1.67	0.41

**Kruskall Wallis test *Significant difference at the 0.05 level

The rates of previous cesarean section (p=0.54), fetal distress (FDS) (p=0.23), nonprogressive labor (p=0.67), cephalopelvic disproportion (CPD) (p=0.61), malpresentation (p=0.52), placenta previa (p=0.49), and placental abruption (p=0.44) did not significantly differ according to TSH cutoff levels (Table 3).

Table 3: Cesarean section indications according to different TSH cut-off values.

		TSH cut-off values			P
		2.5 (mIU/L)	2.5-4 (mIU/L)	4-10 (mIU/L)	
		n (%)	n (%)	n (%)	
Previous cesarean section	No	54 (68.4)	55 (67.1)	69 (63.9)	0.54
	Yes	25 (31.6)	27 (32.9)	39 (36.1)	
Fetal distress	No	68 (86.1)	72 (87.8)	98 (90.7)	0.23
	Yes	11 (13.9)	10 (12.2)	10 (9.3)	
Progress failure	No	78 (98.7)	80 (97.6)	107 (99.1)	0.67
	Yes	1 (1.3)	2(2.4)	1 (0.9)	
Cephalopelvic disproportion	No	77 (97.5)	81 (98.8)	106 (98.1)	0.61
	Yes	2 (2.5)	1 (1.2)	2 (1.9)	
Malpresentation	No	76 (96.2)	80 (97.6)	103 (95.4)	0.52
	Yes	3 (3.8)	2 (2.4)	5 (4.6)	
Placenta previa	No	78 (98.7)	80 (97.6)	107 (99.1)	0.49
	Yes	1 (1.3)	2 (2.4)	1(0.9)	
Placental abruption	No	74 (93.7)	78 (95.1)	106 (98.1)	0.44
	Yes	5 (6.3)	4 (4.9)	2 (1.9)	

**Chi-square test was performed *Significant difference at the 0.05 level

The need for NICU (p=0.16) placental abruption (p=0.44), FDS (p=0.23), preeclampsia (p=0.58), PPRM (p=0.33), preterm labor (p=0.18), and SGA/LBW (p=0.19) did not significantly differ

according to TSH cutoff levels. Notably, the rate of PROM was higher in the groups with a TSH level of ≥ 2.5 mIU/L ($p=0.04$, $p<0.05$) (Table 4).

Table 4: Adverse maternal and perinatal outcomes according to different TSH cut-off values.

		TSH cut-off values			p
		2.5 (mIU/L) n (%)	2.5-4 (mIU/L) n (%)	4-10 (mIU/L) n (%)	
NICU need	No	68 (86.1)	66 (80.5)	89 (81.7)	0.16
	Yes	11 (13.9)	16 (19.5)	20 (18.3)	
Placental abruption	No	74 (93.7)	78 (95.1)	106 (98.1)	0.44
	Yes	5 (6.3)	4 (4.9)	2 (1.9)	
Fetal distress	No	68 (86.1)	72 (87.8)	98 (90.7)	0.23
	Yes	11 (13.9)	10 (12.2)	10 (9.3)	
Preeclampsia	No	77(97.5)	80(97.6)	105(97.7)	0.58
	Yes	2(2.5)	2 (2.4)	3(2.8)	
PPROM	No	79 (100)	80 (97.6)	104 (96.3)	0.33
	Yes	0 (0)	2 (2.4)	4 (3.7)	
PROM	No	71 (89.9)	64 (78)	89 (82.4)	0.04*
	Yes	8 (10.1)	18 (22)	19 (17.6)	
Preterm birth	No	77 (97.5)	77 (93.9)	100 (92.6)	0.18
	Yes	2 (2.5)	5 (6.1)	8 (7.4)	
Low birthweight and small-for-gestational age	No	75 (94.9)	81 (98.8)	107 (99.1)	0.19
	Yes	4 (5.1)	1 (1.2)	1 (0.9)	

**Chi-square test was performed *Significant difference at the 0.05 level

4. DISCUSSION

There is still no clear information about the benefit of levothyroxine treatment in pregnant women with subclinical hypothyroidism. Furthermore, the results of the present study are insufficient to make any suggestions for reducing adverse pregnancy outcomes and achieving positive neurocognitive outcomes in children using this therapy. This study investigating the effect of levothyroxine treatment on maternal and perinatal outcomes in pregnant women with subclinical hypothyroidism is one of the first in Turkey. We evaluated the pregnancy outcomes of patients who were followed up and underwent labor at our clinic within the past 5 years and who did or did not receive levothyroxine therapy after the diagnosis of subclinical hypothyroidism.

Since retrospective studies have reported fetal losses and neurodevelopmental disorders in infants born to mothers with subclinical hypothyroidism, lowering TSH levels to reference ranges by administering levothyroxine therapy has become a common practice. There is no study reporting the positive effects of maternal treatment on neuropsychological development in babies of pregnant

women with subclinical hypothyroidism [16]. TSEM reported that levothyroxine therapy reduces obstetric risk in pregnant women with subclinical hypothyroidism who test positive for anti-TPO antibodies. However, the need for this therapy in pregnant women with subclinical hypothyroidism who test negative for these antibodies is controversial owing to conflicting data on obstetric risks [4]. According to ES 2012, this treatment is recommended for all pregnant women with elevated TSH levels, regardless of their antibody status [5].

The cutoff values for TSH are extremely important because decreasing the upper limit of normal for TSH from 5 to 2.5 mIU/L increases the prevalence of subclinical hypothyroidism from 4.6% to 20% [17]. Notably, women with subclinical hypothyroidism have increased risks of complications associated with pregnancy and childbirth. The rate of spontaneous abortion was 17% in women testing positive for anti-TG and anti-TPO antibodies and 8.4% in women testing negative for these antibodies [18]. A previous study evaluated the risks associated with delivery and reported that the incidence of subclinical hypothyroidism was 2.3% in 25,756 pregnant women, and the risk of placental abruption and preterm delivery was two times higher in such patients than in normal women [19]. In addition, it was found that there was an increased risk of miscarriage, low birth weight and growth retardation in pregnant women with undiagnosed and untreated subclinical hypothyroidism.

Some studies have reported varying results related to the benefits of administering levothyroxine therapy for subclinical hypothyroidism. Previous double-blind randomized studies have reported that this therapy improved psychometric evaluation parameters and hypothyroidism symptom scores in patients with a TSH level of >10 mIU/L; however, it did not lead to any changes in patients with subclinical hypothyroidism and TSH levels of <10 mIU/L [20, 21]. Among the poor maternal and perinatal outcomes evaluated in the present study, the need for NICU admission and the rates of placental abruption, FDS, PPRM, preeclampsia, preterm labor, and SGA/LBW did not significantly differ among the groups stratified according to different TSH cutoff levels. However, the rate of PROM was higher in groups with TSH levels of ≥ 2.5 mIU/L. The significance of administering levothyroxine therapy to pregnant women with a TSH level of ≥ 2.5 mIU/L has not been clearly established because it is not possible to predict which pregnant woman will develop PROM.

Regarding the indications for cesarean section according to different TSH cutoff groups, no significant difference was found in terms of previous cesarean section, FDS, nonprogressive labor, CPD, malpresentation, placenta previa, and placental abruption. Notably, our findings do not support the treatment of subclinical hypothyroidism diagnosed during pregnancy.

In a previous study, TSH levels did not increase in untreated pregnant women with subclinical hypothyroidism, but these levels were found to be high in mothers with positive anti-TPO antibody during pregnancy [22]. In our study, TSH, T4, and anti-TPO levels were not different between levothyroxine users and nonusers. Moreover, there was no difference between birth weight, gestational week at birth, 1- and 5-minute APGAR scores and neonatal TSH and T4 levels according to maternal levothyroxine use. In one of the previous studies, it was shown that the risk of miscarriage increased in anti-TPO positive pregnant women [16]. In a study conducted with pregnant women with subclinical hypothyroidism with a TSH level of 2.5-4 mIU/L, the rate of preterm birth was found to be

significantly higher, while fetal weight and gestational week at birth were found to be significantly lower [23]. In addition, in a study of pregnant women with subclinical hypothyroidism and positive anti-TPO antibody, levothyroxine therapy reduced the risk of preterm delivery and amniotic fluid abnormalities [24]. In another study involving the use of levothyroxine, the risks of miscarriage, gestational hypertension, intrauterine growth retardation, low birth weight, and preterm delivery were not significantly higher in women with subclinical hypothyroidism than in women with euthyroidism [25]. Moreover, it has been reported that the treatment of subclinical hypothyroidism with levothyroxine significantly reduces the incidence of preterm delivery, miscarriage, postpartum hemorrhage, and low birth weight [26]. In the present study, gravida and parity were significantly higher in levothyroxine users. However, no difference was found in the rate of miscarriage according to the maternal use of levothyroxine.

In a study of pregnant women at increased risk for cesarean section due to placental abruption, anemia, postpartum hemorrhage, and preterm delivery (3.13-fold increase when TSH level was >3 mIU/L at 16 weeks of gestation), maternal–fetal adverse reactions, such as low birth weight and impaired fetal brain development, were reported [16]. One study showed no statistically significant difference in obstetric and neonatal outcomes between the levothyroxine group and the control group [27]. Additionally, a previous study found no evidence on the benefit of levothyroxine therapy for pregnant women with subclinical hypothyroidism in terms of pregnancy, neonatal, and childhood outcomes [28]. Similarly, in our study, indications for cesarean section did not increase and there were no maternal or neonatal adverse outcomes, except for PROM.

A previous study suggested that levothyroxine improves pregnancy-related outcomes in patients with subclinical hypothyroidism as well as the neurointellectual development of newborns [29]. In contrast, we found no significant difference in NICU requirement, mode of delivery, gestational week at birth, mean age, and infant gender according to the maternal use of levothyroxine.

This study has some limitations. First, the prevalence of hypothyroidism was not determined. Second, the infant neurocognitive status was not assessed prospectively. Third, levothyroxine dose, race, ethnicity, iodine intake, body mass index before pregnancy, and socioeconomic status were not analyzed. Finally, we did not consider the factors influencing TSH levels and time of the day of blood collection during the diagnosis of subclinical hypothyroidism as this was a retrospective study.

This study also has pertinent strengths. First, to the best of our knowledge, this is the first study in Turkey evaluating maternal and perinatal outcomes and comparing patients receiving thyroid hormone replacement therapy with those not receiving the therapy. Second, in contrast to other studies, different cutoff values were evaluated in the present study.

5. CONCLUSION

Subclinical hypothyroidism is believed to cause pregnancy-related complications and adverse obstetric outcomes, such as placental insufficiency; however, there is a lack of solid evidence on this subject. We believe that future studies involving large patient groups in our country, which is an

endemic region for goiter, will provide a better understanding of the subject. In addition to the higher incidence of PROM in pregnant women with a TSH cutoff of ≥ 2.5 mIU/L, the benefit of thyroid hormone replacement therapy for other obstetric complications is questionable. This study did not provide conclusive evidence regarding the benefit of maternal levothyroxine therapy on maternal and fetal outcomes in pregnant women with subclinical hypothyroidism.

ACKNOWLEDGEMENT

Financing has not been used. The authors declare that they have no conflict of interest. Patients signed informed consent for the publication of their data. All procedures comply with the ethical standards of the national research committee and the 1964 Declaration of Helsinki, its later amendments, or comparable ethical standards.

REFERENCES

- [1] Krassas, G. E., Poppe, K., and Glinöer, D. (2010). Thyroid function and human reproductive health. *Endocrine reviews*, 31(5), 702–755.
- [2] Alexander, E. K., Pearce, E. N., Brent, G. A., Brown, R. S., Chen, H., Dosiou, C., Grobman, W. A., Laurberg, P., Lazarus, J. H., Mandel, S. J., Peeters, R. P., and Sullivan, S. (2017). 2017 Guidelines of the American Thyroid Association for the Diagnosis and Management of Thyroid Disease During Pregnancy and the Postpartum. *Thyroid : official journal of the American Thyroid Association*, 27(3), 315–389.
- [3] Practice Bulletin No. 148: Thyroid disease in pregnancy. (2015). *Obstetrics and gynecology*, 125(4), 996–1005.
- [4] Tiroid hastalıkları tanı ve tedavi kılavuzu. (2017). Türkiye Endokrinoloji ve Metabolizma Derneđi. Türkiye Klinikleri Yayın Seri. ISBN: 978- 975-9118-66-2;157.
- [5] De Groot, L., Abalovich, M., Alexander, E. K., Amino, N., Barbour, L., Cobin, R. H., Eastman, C. J., Lazarus, J. H., Luton, D., Mandel, S. J., Mestman, J., Rovet, J., and Sullivan, S. (2012). Management of thyroid dysfunction during pregnancy and postpartum: an Endocrine Society clinical practice guideline. *The Journal of clinical endocrinology and metabolism*, 97(8), 2543–2565.
- [6] Lazarus, J., Brown, R. S., Daumerie, C., Hubalewska-Dydejczyk, A., Negro, R., and Vaidya, B. (2014). 2014 European thyroid association guidelines for the management of subclinical hypothyroidism in pregnancy and in children. *European thyroid journal*, 3(2), 76–94.
- [7] Stagnaro-Green A. (2011). Overt hyperthyroidism and hypothyroidism during pregnancy. *Clinical obstetrics and gynecology*, 54(3), 478–487.

- [8] Oglak, S. C., and Obut, M. (2021). Subclinical hypothyroidism of unexplained infertility patients does not affect intrauterine insemination success: A case-control study. *Annals of Medical Research*, 28(7), 1346–1350.
- [9] Garber, J. R., Cobin, R. H., Gharib, H., Hennessey, J. V., Klein, I., Mechanick, J. I., Pessah-Pollack, R., Singer, P. A., Woeber, K. A., and American Association of Clinical Endocrinologists and American Thyroid Association Taskforce on Hypothyroidism in Adults (2012). Clinical practice guidelines for hypothyroidism in adults: cosponsored by the American Association of Clinical Endocrinologists and the American Thyroid Association. *Endocrine practice : official journal of the American College of Endocrinology and the American Association of Clinical Endocrinologists*, 18(6), 988–1028.
- [10] Ruge, J. B., Bougatsos, C., and Chou, R. (2015). Screening and treatment of thyroid dysfunction: an evidence review for the U.S. Preventive Services Task Force. *Annals of internal medicine*, 162(1), 35–45.
- [11] Karcaaltincaba, D., Ozek, M. A., Ocal, N., Calis, P., Inan, M. A., and Bayram, M. (2020). Prevalences of subclinical and overt hypothyroidism with universal screening in early pregnancy. *Archives of gynecology and obstetrics*, 301(3), 681–686.
- [12] ACOG Practice Bulletin No. 202: Gestational Hypertension and Preeclampsia. (2019). *Obstetrics and gynecology*, 133(1), 1.
- [13] Ölmez, F., Oğlak, S. C., and Can, E. (2022). The Implication of Aquaporin-9 in the Pathogenesis of Preterm Premature Rupture of Membranes. *Zeitschrift für Geburtshilfe und Neonatologie*, 226(4), 233–239.
- [14] Oğlak, S. C., Yavuz, A., Olmez, F., Gedik Özköse, Z., and Süzen Çaypınar, S. (2022). The reduced serum concentrations of β -arrestin-1 and β -arrestin-2 in pregnancies complicated with gestational diabetes mellitus. *The journal of maternal-fetal & neonatal medicine : the official journal of the European Association of Perinatal Medicine, the Federation of Asia and Oceania Perinatal Societies, the International Society of Perinatal Obstetricians*, 35(25), 10017–10024.
- [15] Oğlak, S. C., Ölmez, F., and Tunç, Ş. (2022). Evaluation of Antepartum Factors for Predicting the Risk of Emergency Cesarean Delivery in Pregnancies Complicated With Placenta Previa. *The Ochsner journal*, 22(2), 146–153.
- [16] Casey, B. M., Thom, E. A., Peaceman, A. M., Varner, M. W., Sorokin, Y., Hirtz, D. G., Reddy, U. M., Wapner, R. J., Thorp, J. M., Jr, Saade, G., Tita, A. T., Rouse, D. J., Sibai, B., Iams, J. D., Mercer, B. M., Tolosa, J., Caritis, S. N., VanDorsten, J. P., and Eunice Kennedy Shriver National Institute of Child Health and Human Development Maternal–Fetal Medicine Units Network (2017). Treatment of Subclinical Hypothyroidism or Hypothyroxinemia in Pregnancy. *The New England journal of medicine*, 376(9), 815–825.

- [17] Hollowell, J. G., Staehling, N. W., Flanders, W. D., Hannon, W. H., Gunter, E. W., Spencer, C. A., and Braverman, L. E. (2002). Serum TSH, T(4), and thyroid antibodies in the United States population (1988 to 1994): National Health and Nutrition Examination Survey (NHANES III). *The Journal of clinical endocrinology and metabolism*, 87(2), 489–499.
- [18] Stagnaro-Green, A., Roman, S. H., Cobin, R. H., el-Harazy, E., Alvarez-Marfany, M., and Davies, T. F. (1990). Detection of at-risk pregnancy by means of highly sensitive assays for thyroid autoantibodies. *JAMA*, 264(11), 1422–1425.
- [19] Casey, B. M., Dashe, J. S., Wells, C. E., McIntire, D. D., Byrd, W., Leveno, K. J., and Cunningham, F. G. (2005). Subclinical hypothyroidism and pregnancy outcomes. *Obstetrics and gynecology*, 105(2), 239–245.
- [20] Jaeschke, R., Guyatt, G., Gerstein, H., Patterson, C., Molloy, W., Cook, D., Harper, S., Griffith, L., and Carbotte, R. (1996). Does treatment with L-thyroxine influence health status in middle-aged and older adults with subclinical hypothyroidism?. *Journal of general internal medicine*, 11(12), 744–749.
- [21] Mooradian A. D. (2011). Subclinical hypothyroidism in the elderly: to treat or not to treat?. *American journal of therapeutics*, 18(6), 477–486.
- [22] Mir, F., Chiti, H., and Mazloomzadeh, S. (2022). Short-Term Adverse Pregnancy Outcomes in Women with Subclinical Hypothyroidism: A Comparative Approach of Iranian and American Guidelines. *Journal of thyroid research*, 2022, 9315250.
- [23] Simten, G. E., and Cingillioğlu, B. (2022). Effects of subclinical hypothyroidism on maternal and obstetric outcomes during pregnancy. *The European Research Journal*, 8, 247–255.
- [24] Luo, J., and Yuan, J. (2022). Effects of Levothyroxine Therapy on Pregnancy and Neonatal Outcomes in Subclinical Hypothyroidism. *International journal of general medicine*, 15, 6811–6820.
- [25] Dash, S. C., Sahoo, N., Rout, U., Mishra, S. P., Swain, J., and Mazumder, A. G. (2022). Outcomes With Levothyroxine Treatment in Early Pregnancy With Subclinical Hypothyroidism. *Cureus*, 14(5), e24984.
- [26] Geng, X., Chen, Y., Wang, W., Ma, J., Wu, W., Li, N., and Sun, C. (2022). Systematic review and meta-analysis of the efficacy and pregnancy outcomes of levothyroxine sodium tablet administration in pregnant women complicated with hypothyroidism. *Annals of palliative medicine*, 11(4), 1441–1452.
- [27] Yamamoto, J. M., Benham, J. L., Nerenberg, K. A., and Donovan, L. E. (2018). Impact of levothyroxine therapy on obstetric, neonatal and childhood outcomes in women with subclinical

hypothyroidism diagnosed in pregnancy: a systematic review and meta-analysis of randomised controlled trials. *BMJ open*, 8(9), e022837.

[28] Jiao, X. F., Zhang, M., Chen, J., Wei, Q., Zeng, L., and Liu, D. (2022). The impact of levothyroxine therapy on the pregnancy, neonatal and childhood outcomes of subclinical hypothyroidism during pregnancy: An updated systematic review, meta-analysis and trial sequential analysis. *Frontiers in endocrinology*, 13, 964084.

[29] Qian, X., Sun, Y., and Xu, X. (2022). Effect of Levothyroxine Sodium Tablets on Pregnancy Outcome and Offspring Development Quotient of SCH during Pregnancy. *Journal of healthcare engineering*, 2022, 9001881.



RESEARCH ARTICLE

**AN EFFICIENT CALIBRATION PROCESS FOR THE PREDICTION OF ROCK
STRENGTH THROUGH MACHINE LEARNING ALGORITHMS**

Şaziye Özge DİNÇ GÖĞÜŞ¹

^{1*}Istanbul Technical University, Geological Engineering, Istanbul, dincgogus@itu.edu.tr, ORCID: 0000-0003-3227-309X

Receive Date: 20.01.2023

Accepted Date: 23.03.2023

ABSTRACT

Numerical models based on the discrete element method (DEM) have been widely used to predict the mechanical behaviors of rocks in rock engineering applications. Nevertheless, calibration of the model parameters is done by running numerous simulations and this time-consuming simulation process precludes the numerical platforms to be used as a practical tool in such applications. This study aims to accelerate the calibration process of the micro-parameters of three-dimensional (3D) numerical models built based on DEM and facilitate the generation of an efficient database by using machine learning algorithms in the prediction of rock strength. Namely, these algorithms are linear regression (LR), decision tree (DT) regression, and random forest (RF) regression. The appropriate methodology for predicting the uniaxial compressive strengths (UCS) of certain rock types was investigated using a dataset consisting of micro-parameters of 87 DEM-based rock models, generated through an open-source code, Yade. The performance of such methods was evaluated by using metrics including R-squared score (R^2), mean squared error (MSE), root mean squared error (RMSE), and mean absolute error (MAE), and then their statistical discrepancies were analyzed. The most accurate prediction of UCS was obtained in the LR method and the lowest percentage of performance was derived from the RF algorithms. LR method provides the results efficiently during calibration of the micro-parameters of a DEM-based rock model.

Keywords: *Rock strength, Discrete element method, Numerical model calibration, Machine learning.*

1. INTRODUCTION

Determining the failure and deformation processes of rocks under applied stresses has paramount importance in rock engineering. While laboratory and analytical methods are used conventionally to investigate this process, recently numerical modeling methods have also been commonly used as an alternative/supporting and effective technique to these methods. In particular, for discontinuous media such as in rocks, numerical models based on the discrete element method (DEM) are mainly preferred because of their advantage in reflecting each structural element (e.g. cracks, joints, faults, layers, etc.) formed by rock behaviors. Therefore, deformation and damage processes examined through numerical modeling, provide useful insights into understanding the extent and magnitude of rock failure

characteristics [1-13]. On the other hand, the generation of a numerical model as a representative of the real rock domain depends on the accurate and reliable calibration of the model parameters. The calibration is done according to the fundamental macro mechanical parameters (i.e uniaxial compressive strength, UCS; tensile strength UTS, Young modulus, E and Poisson's ratio, ν) of the rocks obtained by laboratory experiments. As a result, in order to rely on precise calibration, numerous simulations are sometimes required to be run, and each simulation cycle can turn into a very time-consuming workload depending on the resolution of the generated model.

Machine learning (ML), one of today's artificial intelligence technologies, has become an established technique to produce objective and sensitive results within the most efficient timeframe for the problems encountered in energy & mining industries, as well as agriculture, finance, education, and many other fields. This technology facilitates targeted decision-making or forecasting by focusing on building systems that learn and improve performances based on the data type. Therefore, various machine learning methods have been developed according to the specific application topic, the purpose of the study, and the type of database. The most well-known and widely used methods for numerical datasets (e.g. integer, float, etc.) are artificial neural networks (ANN), linear regression (LR), decision trees (DT), Naive Bayes (NB), K-nearest neighbors (KNN), and random forest (RF) algorithms. Specifically, ANN has been considered in many studies that aim to predict one of the most critical parameters in rock engineering, for instance, the UCS value for revealing the effects of various rock properties [14- 26]. Furthermore, these studies [14-26] emphasize the important role of laboratory and field measurements and observations regarding rock failure characteristics.

Nevertheless, machine learning attempts on constituting efficient datasets and receiving quick responses from numerical modeling in rock deformation which is a robust tool for considering the scale effect, have rarely been used [27, 28, 29]. More specifically, machine learning studies focusing on the improvement of the calibration process of the DEM-based model parameters to achieve more productive and cost-efficient predictions for the rock strength and failure/deformation behaviors are very limited [28, 29]. For instance, Waqas [28], used machine learning techniques to provide a faster computational time in the discrete analysis of rock properties. However, the results may not be easily evaluated because of using only two metrics to measure the performance of the applied machine learning method. More recently, considering several statistical metrics to test the accuracy of the performances of the predictive models, Fathipour-Azar [29] estimated the UCS values of DEM-based models through machine learning approaches. UCS values were predicted according to two micro-shear properties, cohesion and internal friction angle of discrete elements' contacts. These attempts made by Fathipour-Azar [29] proposed a rapid calibration process through the utilized methods whose robustness might further be increased by using more input parameters.

In this study, LR, DT, and RF methods of machine learning technology were applied to the micro-parameters of three-dimensional (3D) numerical rock models based on DEM by considering the time, storage space, and optimization of the data processing, and thereupon, rock strength (UCS) values were predicted. The dataset has 87 rows and 7 columns consisting of 6 micro-parameters and UCS values that were derived from the numerical models assigned in accordance with these parameters. As the most common split ratio, 80% of the dataset goes into the training set and 20% of the dataset goes into the testing set. The performances of the methods were evaluated through the coefficient of

determination (R^2), mean squared error (MSE), mean absolute error (MAE), and root mean squared error (RMSE) metrics. The results present findings that contribute to the users acquiring data much faster in rock engineering applications where the DEM modeling technique is used.

2. METHODOLOGY

2.1. 3D-DEM Rock Model

The numerical rock models used in this study were generated using a 3D open-source DEM code, Yade [30]. It is fundamentally based on the bounded particle model (BPM) which was first proposed by Potyondy and Cundall [3] and then modified by Scholtès and Donzé [9] to be used in the DEM platform. A rock material is a structure/assembly consisting of bonded, rigid, and spherical particles of different sizes (Figure 1a). Particles are also called discrete elements (DEs) and these elements are bonded together (Figure 1b) in an interaction ratio (γ_{int}) based on the elastic-brittle contact law (Eq.1). This ratio is determined before the numerical model is generated.

$$D_{eq} \leq \gamma_{int} * (R_x + R_y) \quad (1)$$

Here, γ_{int} is the parameter that controls the initial number of interacting bonds (N). D_{eq} is the initial distance between the particles x and y with radii of R_x and R_y , respectively. This parameter as irrespective of the number of particles in the rock model is assigned before the simulation starts. It represents the average number of bonds per particle (N). Therefore, the rigidity of rock is controlled by decreasing or increasing the γ_{int} (or N) value according to the ratio of UCS to UTS of relevant rock material. For instance, for modeling a relatively weak rock material, γ_{int} is selected to be close to 1 which shows poor interlocking among the particles. Moreover, the greater γ_{int} values ($\gamma_{int} > 1$) indicate a rock with a higher UCS/UTS ratio and a more rigid domain (see Scholtès and Donzé [9] for more details).

Interaction forces between particles are subdivided into two components such as normal (F_n) and shear (F_s) forces (Figure 1c). Along the normal axis, F_n is calculated;

$$F_n = k_n * u_n \quad (2)$$

with k_n , the normal stiffness computed as a function of an equivalent elastic modulus Y (in Pa) (Eq. 3), and u_n is the normal relative displacement.

$$k_n = 2Y * \frac{R_x * R_y}{R_x + R_y} \quad (3)$$

Under compression, F_n can increase indefinitely while under tension, F_n increases up to a threshold value, $F_{n,max} = t * A_{int}$. Here, t is the interparticle tensile strength (in Pa), and A_{int} is the surface area that depends on the particle sizes ($A_{int} = \pi * [\min(R_x; R_y)]^2$). When $F_n \geq F_{n,max}$, the bond breaks, and a mode I (tensile) crack forms at the bond location.

F_s as the driving force along the shear axis is computed incrementally from the equation of $F_s = F_{s, t-\Delta t} + k_s \cdot \Delta u_s$. k_s is the shear stiffness obtained from $k_s = P \cdot k_n$ (Figure 1b). P is a model constant and it varies between 0 and 1. Δu_s is the relative incremental displacement and $F_{s, t-\Delta t}$ is the shear force at the previous timestep. So, the maximum admissible shear force, $F_{s, \max}$ is determined by Mohr-Coulomb criteria such as;

$$F_{s, \max} = c \cdot A_{\text{int}} + F_n \cdot \tan(\varphi) \quad (4)$$

where c is the interparticle cohesion (in Pa) and φ is the interparticle friction angle (in °). When $F_s \geq F_{s, \max}$, the bond breaks and a mode II (shear) crack forms at the bond location.

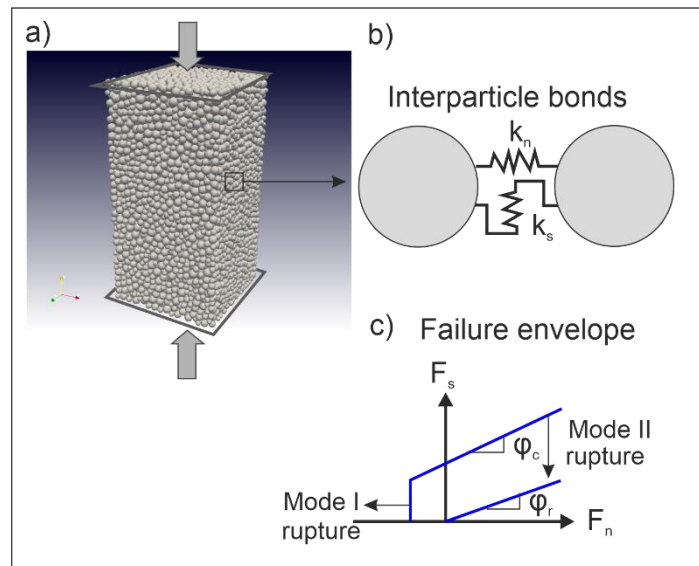


Figure 1. a) Configuration of 3D-DEM model sample (based on BPM technique) under UCS test simulation, b) Interparticle bonds, c) Interaction forces between the particles and rock failure mechanisms (modified from Scholtès and Donzé [9]).

It is worth noting that similar to the laboratory experiments, all simulations here were carried out under quasi-static conditions. Moreover, a global viscous damping ratio, chosen as 0.4 was used to reduce the kinetic energy during the simulations.

The parameters (Y , P , t , c , φ , and N) mentioned above are the micro-parameters of a 3D numerical DEM model and calibrated according to the macro mechanical strength parameters (UCS, UTS) and deformation parameters (E , Young modulus, and ν , Poisson's ratio) by performing a series of laboratory test simulations. The calibration process is repeated until the model represents accurately the stress-strain behaviors and mechanical properties of the real rock. Therefore, this process may take

longer and it requires many iterations and simulations. The type of simulation (tensile strength test, uniaxial compressive strength test, triaxial compressive strength test, etc.) is selected according to the parameter to be calibrated. For example, t as the tensile strength of the particles controls the UTS value and is derived from the UTS test simulation [12]. Furthermore, the calibration of some model parameters is done by running various test simulations. For example, c affects the UCS value while Y directly controls the E value of the rock material. P as the ratio of k_s to k_n has an influence on ν value of the rock. To calibrate these three macro-parameters, both uniaxial and triaxial compressive strength test simulations are required to run. ϕ controls the slope of the rock failure envelope and is determined directly in the triaxial compressive test simulations. As is different from others, the N parameter is assigned according to the UCS/UTS ratio of the real rock before the simulation starts. The details of the effects and roles of each micro-parameter on macro mechanical properties can also be followed in Dinç Göğüş [31].

Similar to other numerical rock modeling techniques, the duration of the calibration of a numerical DEM model is primarily dependent on the resolution of the generated model. For the sake of clarity and reducing complexity, all rock models here were built in $1 \times 2 \times 1$ model unit sizes and they consist of 10,000 particles to obtain the results to be irrespective of the model resolution.

The dataset used in the study has 87 rows and 7 columns consisting of 6 micro-parameters (Y , P , t , c , ϕ , and N) with different values as well as the UCS values (as the peak/maximum stress that the model can resist) of the 3D-DEM model samples formed by such parameters (Figure 2). The parameters belong to 6 different rock types, from the weak to the strong rock material: claystone, ignimbrite, marble, andesite, diabase, and granite.

The details of the machine learning methods on the dataset are given in the following section.

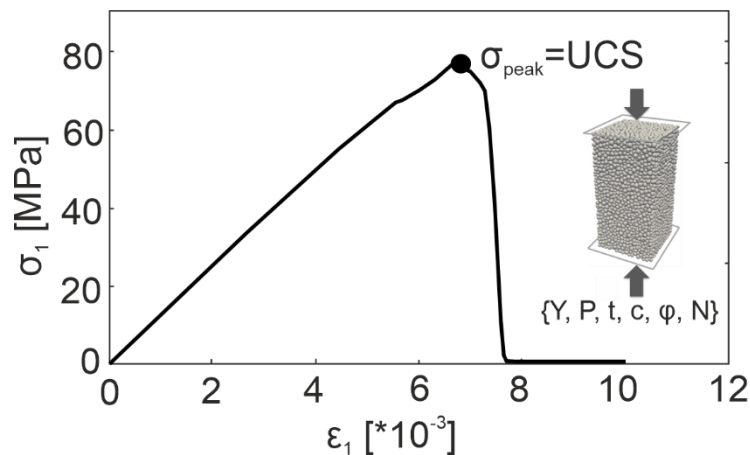


Figure 2. Under the uniaxial loading condition, the stress-strain response of a 3D-DEM model sample formed by 6 micro-parameters.

2.2. Machine Learning Methods

Machine learning, which teaches the existing data or information to the machine and extracts a function from this information is a subfield of artificial intelligence systems. The term machine learning was first introduced to the literature by Arthur Samuel an IBM employee, in 1959, and has been implemented in geotechnical and rock mechanical applications since the 1990s. The operation of the system, in which training data sets are used to obtain the targeted results and the user does not need to control the model, is based on the principle of using a known input dataset (training data). Further, the corresponding outputs are used to produce the most appropriate outputs for the new data (test data) that the algorithm has never seen before. (Figure 3). The flow chart of the machine learning process is presented in Figure 3. In this study, 20% of the total data is used for testing, and the remaining 80% is applied for training.

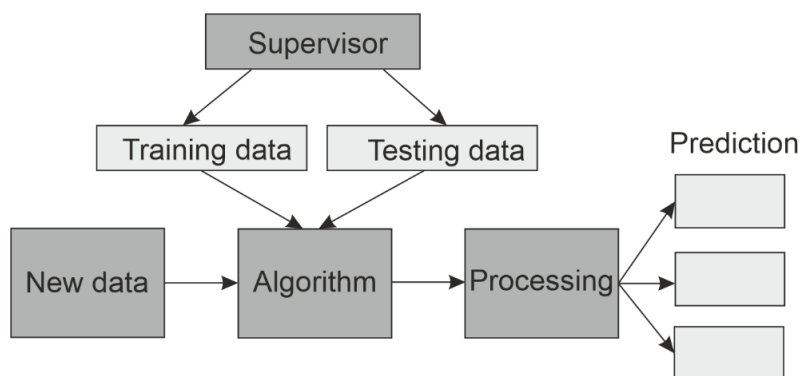


Figure 3. The general flow chart of the machine learning process.

The process of applying machine learning methods to the dataset consists of 3 stages. The first step is data preparation, called data preprocessing, transforming the data and making it suitable for models. All data in this study is numerical (e.g. integer, float, etc.), and there is no missing data or data with a value of 0 (zero). The second stage consists of model selection, and in the third stage, the model is trained/developed and the first-order parameters that affect the predictions are determined. The quantiles of the micro-parameters and the UCS values are presented in Table 1 and the UCS values range from 17.8 to 111 MPa, presenting different rock types.

Table 1. Quantities of micro-parameters and estimated UCS parameter.

Parameter	Ave	Std	Min	%25	%50	%75	Max
N (-)	9.92	1.03	8.00	9.00	10.00	11.00	12.00
Y (GPa)	11.99	2.45	9.00	10.00	12.00	14.00	17.00
φ (°)	2.48	2.55	1.00	1.00	1.00	5.00	15.00
P (-)	0.43	0.05	0.30	0.40	0.40	0.50	0.50
t (MPa)	7.50	2.36	4.00	5.00	7.00	9.00	13.00
c (MPa)	77.69	29.23	25.00	59.00	74.00	90.00	180.00

UCS (MPa) 57.24 24.05 17.80 38.50 47.00 83.25 111.00

*N: coordination number, Y: equivalent elastic modulus, ϕ : friction angle of particles, P: stiffness ratio, t: tensile strength of particles, c: cohesion of particles, and UCS: uniaxial compressive rock strength

LR (linear regression), DT (decision tree regression), and RF (random forest regression) methods were chosen respectively from the machine learning methods to predict the UCS values of the DEM model samples. LR is a well-known method for continuous and linear variables in the supervised machine learning technique. A linear curve is obtained by using one or more independent variables that accurately predict the value of the dependent variable (Figure 4a). The coefficient of the equation of this curve gives information about the reliability of the prediction. Since it uses a formulation that is relatively more practical to interpret, it is mostly preferred in statistical studies in various fields.

The second method, DT, used in classification and regression problems, consists of tree-structured algorithms. Since the target variable in this study is continuous (numerical), the algorithms are called DT regression trees here. A dataset is divided into smaller subsets as forming decision and leaf nodes according to feature and target (Figure 4b). It is worth noting that since DT regression is not continuous like other regression models but is discrete, it can produce the same results for the targeted predictions in a certain range.

The third method of the study, RF, is a regression method based on the principle of generating a random forest using more than one DT algorithm (Figure 4c). In other words, the average value of all DT predictions gives the result of RF. Because it uses DT algorithms, it is discrete and therefore can also produce the same results for the targeted predictions in a certain interval that care must be taken.

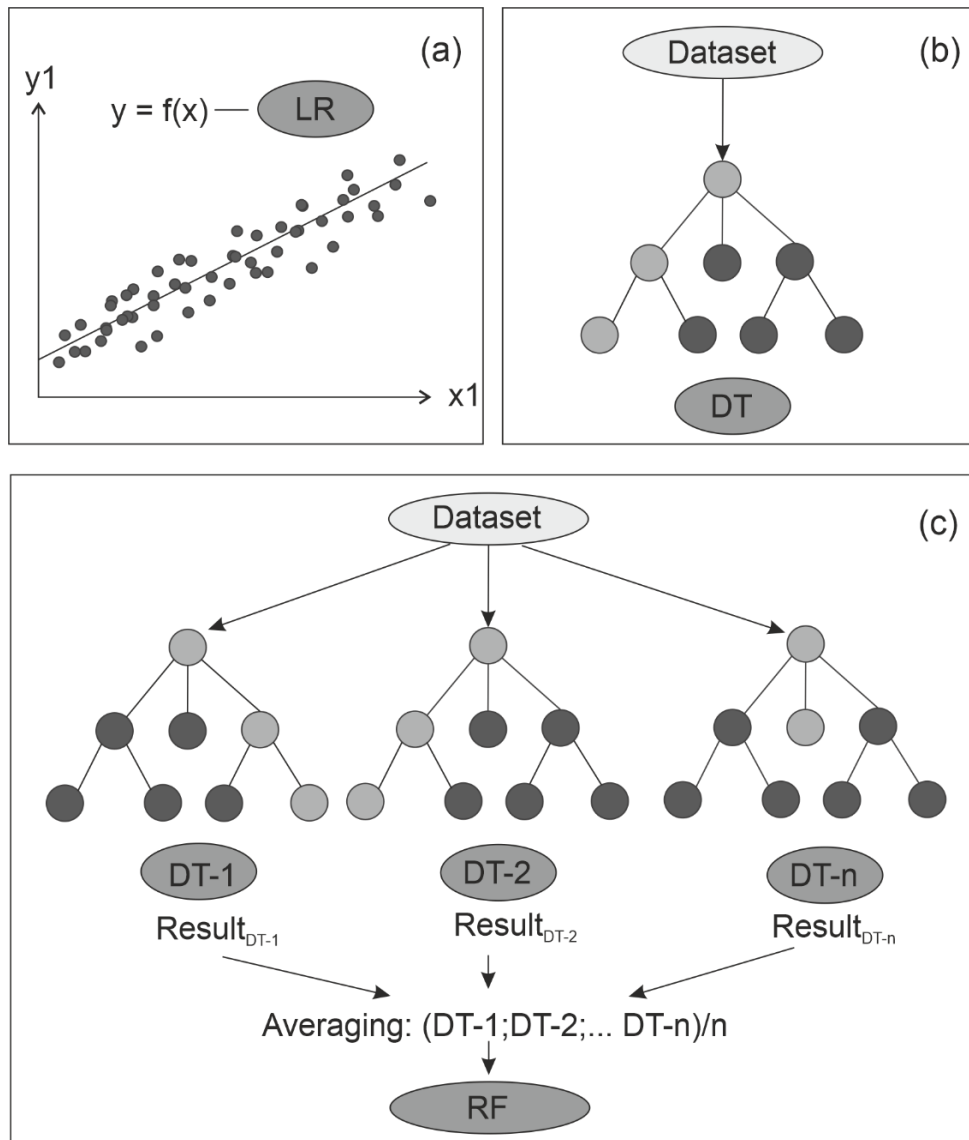


Figure 4. Configurations of the used machine learning methods a) LR (linear regression) b) DT (decision tree regression) and c) RF (random forest regression).

The coefficient of determination (R^2), mean squared error (MSE), mean absolute error (MAE), and root mean squared error (RMSE) metrics were used to evaluate the performance of the methods presented above. R^2 is a statistical measure of how close the model result is to the regression line, and

it is specifically used in the LR method (Eq. 5). In other words, if the R^2 value is close to 1, the data is close to the linear line. R^2 is calculated such that;

$$R^2 = 1 - \frac{\sum(y_i - y_i')^2}{\sum(y_i - y_{io})^2} \quad (5)$$

where y_i , y_{io} , y_i' are the actual, mean, and predicted values, respectively.

The second metric, MSE, is the mean square error, which measures the average squared difference between the y_i' and the y_i values and is derived from Eq. 6.

$$MSE = \frac{1}{N} \sum_{i=1}^N (y_i - y_i')^2 \quad (6)$$

The lower the MSE value the more accurate the model is. In other words, a value close to zero represents better quality of the predictor (regression model). However, since errors are squared when using this metric, exaggerated results can be produced in case of large deviations in the data.

RMSE is a square root of value gathered from the MSE function, shown in Eq. 7. It is used when the MSE is too large to be compared. The RMSE value can range from 0 to ∞ .

$$RMSE = \sqrt{\frac{\sum_{i=1}^N (y_i - y_i')^2}{N}} \quad (7)$$

It indicates how dense the data is around the line that best fits the data.

As the last metric used here, MAE measures the absolute difference between the y_i' and y_i values. Similar to MSE, the closer MAE is to 0, the more accurate the model is. In particular, MAE values of less than 10% show that the prediction models have high accuracy. It is calculated from Eq. 8 and is one of the most preferred metrics besides RMSE in the evaluation of model performances in regression methods.

$$MAE = \frac{1}{N} \sum_{i=1}^N |y_i - y_i'| \quad (8)$$

3. RESULTS AND DISCUSSION

Three different machine learning methods (LR, DT, and RF) described above were applied to estimate the UCS values of rocks obtained from 3D-DEM numerical models and the performances of the methods were evaluated according to R^2 , MSE, RMSE, and MAE metrics (Table 2). The results showed that the highest performance estimation was obtained from the LR method for all metrics. Especially based on the MSE results, the LR method provides better estimation/prediction than that of other methods. However, considering the relationship between the actual and predicted UCS values, regardless of the metrics, it is observed that all three methods' results are close to each other (Figure 5).

Table 2. Performance of the machine learning methods in UCS prediction according to the R^2 , MSE, RMSE, and MAE metrics.

Method	R^2	MSE	RMSE	MAE
LR	0.981	8.487	2.913	2.289
KA	0.895	41.221	6.420	5.398
RO	0.849	80.844	8.991	6.655

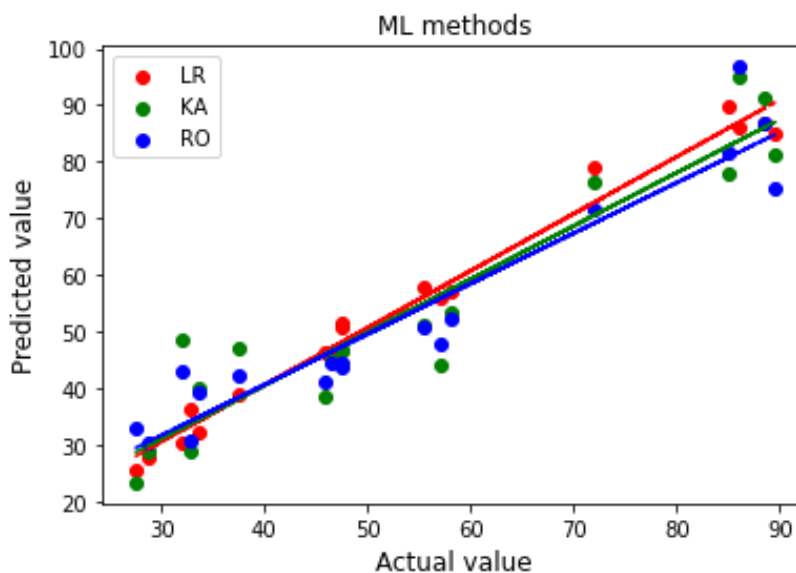


Figure 5. The relationship between the actual and estimated UCS values according to the LR, DT, and RF methods.

Doğan and Doğan [32] pointed out that since the R^2 metric estimates the combined distribution against the individual distributions of the observed and predicted variables, a model with systematically over- or under-estimates can produce R^2 values close to 1, even if all of the predicted values are incorrect. Therefore, three more metrics (MSE, RMSE, MAE) were considered in this study, since it is not sufficient to test a model's performance only with the R^2 value. Furthermore, it is highlighted in the literature that the mean error can produce misleading results in the performance evaluations of the methods in which the RMSE is considered [33]. It is noted that because the criteria based on the sum of squares of error are generally considered uncertain indicators, such as mean deviation, mean error, and mean variability, it can cause misinterpretations of the predictions [32]. Although it is suggested that MAE is generally a better criterion for such interpretations [33], one can

clearly realize that the use of these metrics strongly depends on the content, property, and usage area of the data.

Besides the comparison of the performance of machine learning methods in estimating the numerical UCS value, the most effective micro-parameters on this estimation were also determined. For this purpose, the feature/parameter selection process was applied to the dataset. In fact, this process is generally used in studies where too many variables are taken for estimation/prediction, and a faster and less complex model is created by eliminating the variables that have very little influence on the results. Because of the few numbers of parameters used in this study, there was no need to eliminate any variable (parameter). The UCS prediction was done by using all 6 micro-parameters.

Therefore here, the feature selection methodology was applied to reveal which micro-parameters play the most effective role in the prediction of the UCS value. For this purpose, a criterion called mutual information (MI), which measures the non-linear relation between random variables in probability and information theories, was used [34, 35]. It is the measure of how much knowledge one can acquire of a significant variable by knowing the value of another variable.

For two discrete variables x and y whose joint probability distribution is $P(x,y)$, the mutual information between them $MI(X;Y)$ is calculated such that;

$$MI(X; Y) = \sum_{x \in X} \sum_{y \in Y} p(x,y) \log\left(\frac{p(x,y)}{p(x) \cdot p(y)}\right) \quad (9)$$

MI ranges from 0 to 1. MI values that are close to 1 indicate relatively more effective parameters over the estimated/predicted feature (parameter) (Figure 6). As expected, MI results show that Y (equivalent elastic modulus), t (micro-tensile strength), and c (micro-cohesion) parameters play a more effective role on the UCS value than the others.

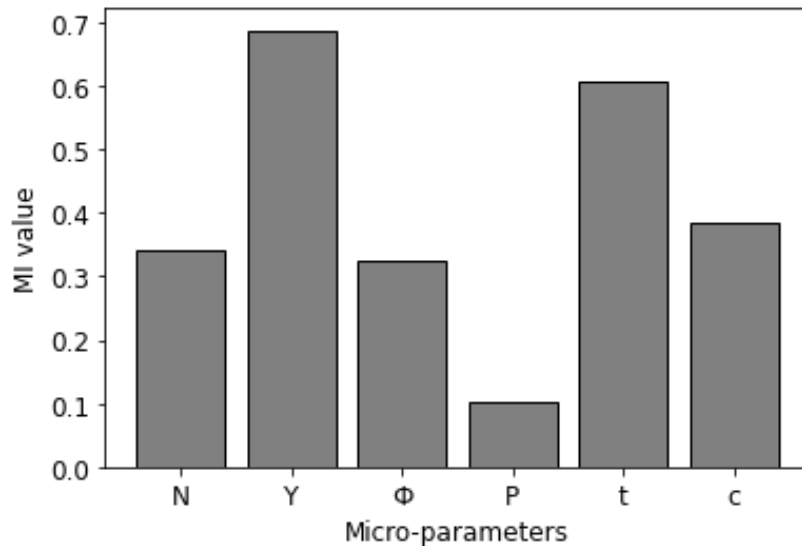


Figure 6. The most effective parameters in UCS prediction according to MI evaluation.

Although the metric results show that the applied machine learning methods produce good performances as well as predictions close to each other, the highest performance is obtained from the LR method. For this reason, the LR method was applied to the DEM model samples by assigning values for 6 micro-parameters and then the UCS value was predicted for validation. For instance, for the values of $N=9$, $Y=12$ GPa, $\varphi=1^\circ$, $P=0.4$, $t=6$ MPa, and $c=60$ MPa, the LR method gives the UCS value as 32.1 MPa, close to the calculated one. In general, this process took approximately about 36 minutes with a 3-core processor speed, whereas the estimation of the UCS value with the LR method took only a few seconds after running the script. Therefore, machine learning approaches can be used as reliable and practical tools in the calibration problems of particle-based DEM models that were also pointed out by Fathipour-Azar [29].

In the calibration of the numerical UCS value according to the real UCS value of a rock, the method suggested here provides extremely fast information in which values or at least ranges of the parameters should be selected before the simulation starts. This insight provides the user significant amount of time, especially in engineering applications where the high model resolution needs to be configured.

4. CONCLUSIONS

DEM-based numerical models provide important information for predicting the failure and deformation behaviors of rocks that host engineering structures. The reliability of this information is precisely based on the accuracy of the model generated. Therefore, the calibration process is critical to

implicitly represent the mechanical characteristics of real rock. This process sometimes takes an extremely long time, depending on the model resolution as well as the experience of the user.

In this study, the UCS values of 3D-DEM models calibrated with 6 micro-parameters were predicted by using machine learning methods, which became widely used in the field of rock mechanics recently. In the present research, LR, DT, and RF methods were tested in terms of their robustness, and the highest estimation performance for R^2 , MSE, RMSE, and MAE metrics was obtained from the LR method. Furthermore, the most effective parameters on the UCS value were determined as Y , c , and t micro-parameters with the feature selection methodology. The results show that machine learning methods can be used effectively in shortening and facilitating the calibration time of a 3D numerical DEM model and producing reliable results for the calibration process of micro-parameters of the model domain.

ACKNOWLEDGEMENT

The author declares that there is no conflict of interest.

REFERENCES

- [1] Potyondy, D.O., Cundall, P.A., Lee, C.A. (1996). Modelling rock using bonded assemblies of circular particles. 2nd North American Rock Mechanics Symposium; 1996 Montreal Canada, 1937–1944.
- [2] Hazzard, J.F., Young, R.P., Maxwell, S.C. (2000). Micromechanical modeling of cracking and failure in brittle rocks. *Journal of Geophysical Research*, 105(7), 16683–16697.
- [3] Potyondy, D.O., Cundall, P.A. (2004). A bonded-particle model for rock. *International Journal of Rock Mechanics and Mining Sciences*, 41 (8):1329–1364.
- [4] Al-Busaidi, A., Hazzard, J.F., Young, R.P. (2005). Distinct element modeling of hydraulically fractured Lac du Bonnet granite. *Journal of Geophysical Research-Atmospheres*, 110 (6), doi: 10.1029/2004JB003297.
- [5] Cho, N., Martin, C.D., Sego, D.C. (2007). A clumped particle model for rock. *International Journal of Rock Mechanics and Mining Sciences*, 44, 997–1010.
- [6] Wang, Y., Tonon, F. (2009). Modeling Lac du Bonnet granite using a discrete element model. *International Journal of Rock Mechanics and Mining Sciences*, 46, 1124–1135.
- [7] Plassiard, J.P., Belheine, N., Donzé, F.V. (2009). A spherical discrete element model: calibration procedure and incremental response. *Granular Matter*, doi: 10.1007/s10035-009-0130-x.

- [8] Potyondy, D.O. (2012). A flat-jointed bonded-particle material for hard rock. In: Proceedings of the 46th US rock mechanics/geomechanics symposium, American Rock Mechanics Association, Chicago, USA.
- [9] Scholtès, L., Donzé, F.V. (2013). A DEM model for soft and hard rocks: role of grain interlocking on strength. *Journal of the Mechanics and Physics of Solids*, 61, 352–369.
- [10] Ding., X., Zhang, L. (2014). A new contact model to improve the simulated ratio of unconfined compressive strength to tensile strength in bonded particle models. *International Journal Rock Mechanics Mining Science*, 69, 111–119.
- [11] Dinç, Ö., Scholtès, L. (2018). Discrete analysis of damage and shear banding in argillaceous rocks. *Rock Mechanics Rock Engineering*, 51(5), 1521–1538.
- [12] Dinç Göğüş, Ö. (2020). 3D discrete analysis of damage evolution of hard rock under tension. *Arabian Journal of Geosciences* 13: 661, <https://doi.org/10.1007/s12517-020-05684-1>.
- [13] Dinç Göğüş Ö., Avşar, E. (2022). Stress levels of precursory strain localization subsequent to the crack damage threshold in brittle rock. *Plos One*, 17(11): e0276214. <https://doi.org/10.1371/journal.pone.0276214>.
- [14] Meulenkamp, F., Alvarez Grima, M. (1999). Application of neural networks for the prediction of the unconfined compressive strength (UCS) from Equotip hardness. *International Journal of Rock Mechanics and Mining Sciences*, 36:29–39.
- [15] Singh, T.N., Dubey, R.K. (2000). A study of transmission velocity of primary wave (P-Wave) in coal measures sandstone. *Journal of Scientific & Industrial Research India*, 59:482–486.
- [16] Kahraman, S., Alber, M. (2006). Estimating the unconfined compressive strength and elastic modulus of a fault breccia mixture of weak rocks and strong matrix. *International Journal of Rock Mechanics and Mining Sciences*, 43:1277–1287.
- [17] Çobanoğlu, I., Çelik, S.B. (2008). Estimation of uniaxial compressive strength from point load strength, Schmidt hardness and P-wave velocity. *Bulletin of Engineering Geology and the Environment*, 67:491–498.
- [18] Zorlu, K., Gökçeoğlu, C., Oçakoğlu, F., Nefeslioğlu, H.A., Açıklın, S. (2008). Prediction of unconfined compressive strength of sandstones using petrography-based models. *Engineering Geology*, 96:141–158.
- [19] Yılmaz, I., Yüksek, A.G. (2008). An example of artificial neural network (ANN) application for indirect estimation of rock parameters. *Rock Mechanics and Rock Engineering*, 41(5):781–795.

- [20] Sarkar, K., Tiwary, A., Singh, T.N. (2010). Estimation of strength parameters of rock using artificial neural networks. *Bulletin of Engineering Geology and the Environment*, 69:599–606.
- [21] Kahraman, S., Alber, M., Fener, M., Günaydın, O. (2010). The usability of Cerchar abrasivity index for the prediction of UCS and E of Misis Fault Breccia: regression and artificial neural networks. *Expert Systems with Applications*, 37(12): 8750-8756.
- [22] Çevik, A., Sezer, E.A., Cabalar, A.F., Gökçeoğlu, C. (2011). Modeling of the unconfined compressive strength of some clay-bearing rocks using neural network. *Applied Soft Computing*, 11:2587–2594.
- [23] Yağız, S., Sezer, E.A., Gökçeoğlu, C. (2011). Artificial neural networks and nonlinear regression techniques to assess the influence of slake durability cycles on the prediction of uniaxial compressive strength and modulus of elasticity for carbonate rocks. *International Journal for Numerical and Analytical Methods in Geomechanics*, 36, 1636–1650. doi:10. 1002/nag.1066.
- [24] Ceryan, N., Okkan, O., Kesimal, A. (2012). Application of Generalized Regression Neural Networks in Predicting the Unconfined Compressive Strength of Carbonate Rocks. *Rock Mechanics and Rock Engineering*, 45:1055–1072.
- [25] Liu, Z. B., Shao, J. F., Xu, W. Y., Wu, Q. (2015). Indirect estimation of unconfined compressive strength of carbonate rocks using extreme learning machine. *Acta Geotechnica*, 10, 651–663.
- [26] Mahmoodzadeh, A., Mohammadi, M., Salim, S., Farid Hama Ali, H., Hashim Ibrahim, H., Nariman Abdulhamid, S., Nejati, H.R., Rashidi, S. (2022). Machine learning techniques to predict rock strength parameters. *Rock Mechanics and Rock Engineering*, 55 (3), 1721–1741.
- [27] Wang, Y., Zhang, X., and Liu, X. (2021). Machine learning approaches to rock fracture mechanics problems: Mode-I fracture toughness determination. *Engineering Fracture Mechanics*, 253, doi:10.1016/j.engfracmech.2021.107890.
- [28] Waqas, M. (2018). Discrete element and artificial intelligence modeling of rock properties and formation failure in advance of shovel excavation. Ph.D. Thesis, Mining Engineering, Missouri University of Science and Technology, 254.
- [29] Fathipour-Azar, H. (2022). Machine learning-assisted distinct element model calibration: ANFIS, SVM, GPR, and MARS approaches. *Acta Geotechnica*, 17:1207–1217.
- [30] Šmilauer, V. et al. (2015). Yade Documentation 2nd edition. doi:10.5281/zenodo.34073. <http://yade-dem.org>.
- [31] Dinç Göğüş, Ö. (2021). Mikro Parametrelerin Makro Mekanik Kaya Davranışı Üzerindeki Etkisi: Ayrık Elemanlar Yöntemiyle Model Kalibrasyonu. *Jeoloji Mühendisliği Dergisi*, 45: 67-82.

- [32] Doğan, İ., Doğan, N. (2020). Model Performans Kriterlerinin Kronolojisine ve Metodolojik Yönlerine Genel Bir Bakış: Bir Gözden Geçirme. An Overview of Chronology and Methodological Aspects of Model Performance Criteria: A Review. *Türkiye Klinikleri Journal of Biostatistics*, 12(1):114-25.
- [33] [Willmott, C.J., Matsuura, K. (2005). Advantages of the mean absolute error (MAE) over the root mean square error (RMSE) in assessing average model performance. *Climate Research*, 30(1):79-82.
- [34] Cover, T.M., Thomas, J.A. (1991). *Elements of information theory*. John Wiley & Sons, New York, NY, 774.
- [35] Battiti, R. (1994) Using mutual information for selecting features in supervised neural net learning. *IEEE Transactions on Neural Networks*, 5(4):537-50.



RESEARCH ARTICLE

**CHEMICAL AND MINERALOGICAL ANALYSES OF THE LATE NEOLITHIC
CERAMICS FROM ŞAH VALLEY (SINGUBER), TURKEY**

Murat BAYAZIT^{1*}, Esra KAYNAK², Nilgün COŞKUN³

^{1*}Batman University, Faculty of Fine Arts, Department of Ceramics, Batı Raman Campus, Batman, m.bayazit@hotmail.com,
ORCID: 0000-0003-1453-249X

²Batman University, Received M.Sc. at Department of Archaeometry, Institute of Science, esrakaynakk@hotmail.com,
ORCID: 0000-0002-1070-957X

³Hatay Mustafa Kemal University, Faculty of Letters, Department of Archaeology, Hatay, nilguncoskun@yahoo.com, ORCID:
0000-0003-0848-9413

Receive Date: 18.11.2022

Accepted Date: 23.03.2023

ABSTRACT

Numerous settlements have been identified during the surveys in Şırnak province (Turkey) since the beginning of the 19th century. The potsherds found in the central of such settlements have been thought to be affected by Mesopotamian culture, and the ones from the hillside of the Şah Valley were considered as the most eastern examples of the Hassuna Samara culture. This study presents the results regarding one of the first detailed archaeometric investigations carried out for the Late Neolithic ceramic findings unearthed from Şah Valley (Şırnak province, Turkey). The ceramics were initially characterized by means of portable X-ray fluorescence (p-XRF) and X-ray diffraction (XRD) in order to enlighten the chemical and mineralogical features of the samples, respectively. The results indicated use of calcareous raw material sources and a low firing temperature range (ca. 700-800°C). The potsherds were also investigated through petrography which showed the presence of quartz, opaque minerals, plagioclase and biotite as the minerals, and clay, claystone and marl rock contents as the rock types for the samples, in general. Fourier transformed infrared (FTIR) spectroscopy was additionally applied for the potsherds. This complementary technique provided information about the vibrations of the chemical bands in the ceramics which displayed the characteristic bond vibrations of decisive minerals in the ceramic fabrics, such as calcite, clay minerals and quartz. Considering the whole archaeometric data, it can be deduced that the Neolithic ceramics of the Şah Valley have been subjected to low firing temperatures which could be assigned to a basic production procedure presumably claiming daily-use wares.

Keywords: *Materials characterization, Archaeometry, Late Neolithic, Ceramics, Şah Valley.*

1. INTRODUCTION

When the archaeological excavations are examined in general, the most numerous finds among the materials unearthed are the ceramics. The word "ceramic" is derived from the Greek word "Keramos"

meaning "burnt material" and is defined as the material obtained as a result of shaping the compositions of inorganic materials after they gain a certain plasticity, drying and firing them until they reach sufficient hardness and strength. The main raw materials of the ceramic are clay, quartz and feldspars. In general, ceramic materials obtained as a result of shaping the soil with water and baking it with fire to obtain the ultimate product have been used by people for many different purposes throughout the history. Thus, ancient ceramic materials are of great importance in terms of history of humanity, and therefore archaeology. Especially in the last century archaeometric studies, which include engineering and science (as well as archaeology, art history), have recently become widespread and are used to reveal the characteristic features of ancient artifacts (e.g. ceramics, metal, glass, tile etc.) [1-4].

Ceramics, which started with the terracotta products of the Neolithic Period between 8000-5500 BC and showed a continuous development in parallel with the way of life of human beings from the beginning of the ceramic period in Anatolia, have constantly renewed and developed themselves. With the industrial revolution, ceramic materials showed themselves in various fields such as automotive, space crafts, sanitary wares, wearable technologies, which require an advanced technology. According to today's archaeological data, the Neolithic Period, dated approximately between 10000 BC and 6000 BC, is one of the most important eras in human history, since the Neolithic Period is an indication of the transition to settled life and the foundation of today's life [5-7].

The southeastern Anatolia region is geographically located between the southern part of the southeast Taurus Mountains in Anatolia and the border of Syria and Iraq. Southeastern Anatolia region is the widest part of the area called "Fertile Crescent" (Mediterranean in the west, Zagros Mountains in the east, Southeast Taurus Mountains in the north and Arabian Desert in the south). This strategic area, where different civilizations intersect, was frequently used by caravans trading between Mesopotamia, Syria and Anatolia, by nomads doing animal husbandry and also by societies organizing expeditions. Şırnak, located at the northeastern end of the Fertile Crescent, is surrounded by Namaz Mountain, which is connected to the southeast Taurus Mountains (from the north), Gabar Mountain (from the west), and Cudi Mountain (from the southeast). Şırnak and its surroundings appear as a crossroads in the Neolithic Period [8-11].

The earliest painted pottery cultures of Northern Mesopotamia are traced in the period called Hassuna Samarra or Late Neolithic-4, which dates back to about 8000 years ago. These painted potteries were named after the centers where they were found for the first time. The pottery, all of which are hand-formed, may be light brown, cream, beige paste, mostly unslipped, and contain sand, plant and sometimes grit tempered. Their surfaces are generally lightly burnished and smoothed. This type of pottery was found in Salat Mosque and Hakemi Use, among the excavations carried out in the Upper Tigris Valley, in the easternmost part of the Southeast Anatolian Region [12,13].

Within the scope of this study, a research was conducted including the archaeometric characterization of 30 ceramic samples dated to the Neolithic Period, which are the easternmost examples of Hassuna Samarra culture in the slope settlement of Şah Valley (Şırnak) (Figure 1) [8], and thus, it is aimed to contribute to the existing literature. The ceramic group, which is the subject of this study, was found in the settlement determined during the Şırnak Province Center, Güçlükönak, Uludere and

Beytüşşebap Districts Survey conducted by the team headed by Nilgün Coşkun (Hatay Mustafa Kemal University) with the permission of Ministry of Culture and Tourism, Turkey. The ceramic findings were analyzed by means of portable X-ray fluorescence (p-XRF), X-ray diffraction (XRD), optical microscope (petrography) and Fourier transformed infrared (FTIR) spectroscopy, which are frequently employed for ceramic findings.

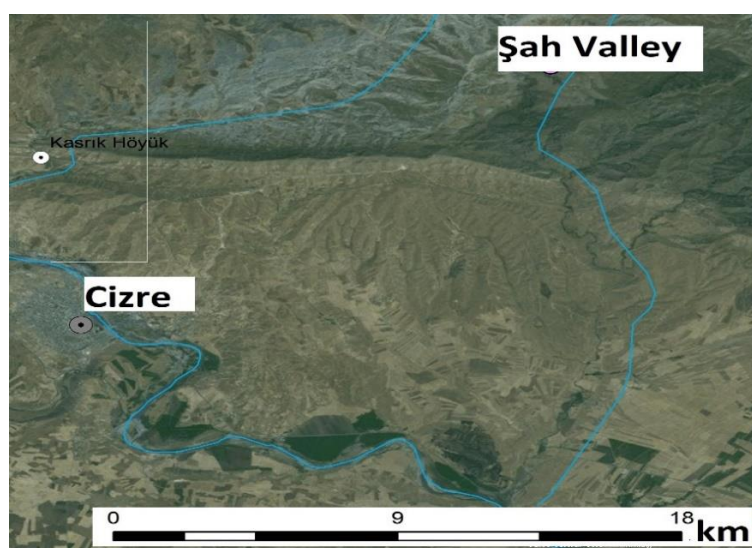


Figure 1. Location of Şah Valley [8].

2. EXPERIMENTAL

2.1. Sampling

30 potsherds representing the Neolithic ceramics of Şah Valley were selected among the amorphous potsherds (considering form, color, etc.) by Assoc. Prof. Dr. Nilgün (Masatcıoğlu) Coşkun, the scientific advisor of "Sırnak Province Center, Güçlükonak, Uludere and Beytüşşebap Districts Survey" (Şırnak İli Merkez, Güçlükonak, Uludere ve Beytüşşebap İlçeleri Yüzey Araştırması, in Turkish). Some of the representative samples are given in Figure 2 (sample code abbreviation is **SV**, Şah Valley).

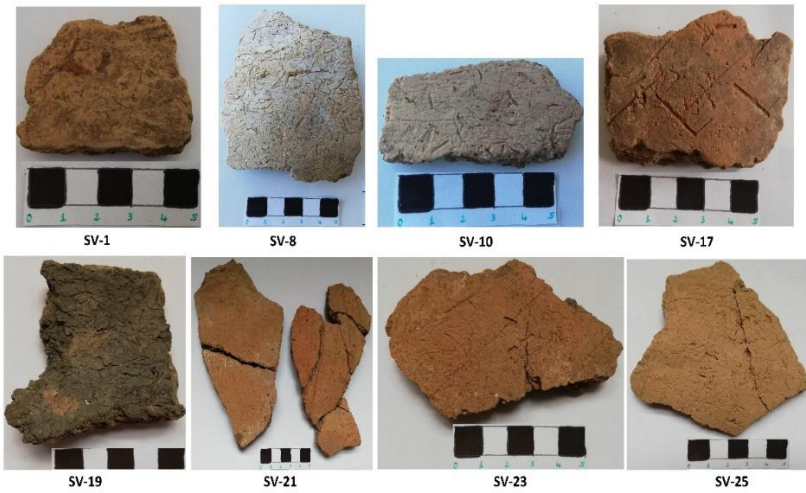
































Figure 2. Some of the representative Neolithic ceramics analyzed in the study.

Table 1. L, a, b values and Equivalent colors of the potsherds.

Sample	L	a	b	Equivalent color
SV-1	40.82	4.26	17.40	
SV-2	48.39	7.79	27.81	
SV-3	37.91	15.33	24.01	
SV-4	27.38	5.17	21.83	
SV-5	40.22	6.79	19.65	
SV-6	46.38	12.79	25.87	
SV-7	33.59	14.94	28.34	
SV-8	29.24	10.89	18.32	
SV-9	43.49	9.74	23.03	
SV-10	49.08	12.20	27.19	
SV-11	42.07	10.77	21.13	
SV-12	36.54	12.13	20.23	
SV-13	43.32	5.87	20.31	
SV-14	44.85	8.59	23.08	
SV-15	42.39	10.20	23.90	
SV-16	37.78	5.60	16.86	
SV-17	37.42	7.25	21.26	
SV-18	38.27	10.58	21.93	
SV-19	20.05	10.36	20.70	
SV-20	38.87	6.42	19.60	
SV-21	31.38	7.28	19.22	
SV-22	42.45	-1.55	18.90	
SV-23	42.66	8.20	21.27	
SV-24	45.89	15.41	28.20	
SV-25	35.42	6.11	20.34	
SV-26	28.35	12.37	19.68	
SV-27	44.74	15.73	27.25	
SV-28	45.28	11.62	27.82	
SV-29	32.49	12.91	22.12	
SV-30	50.09	9.71	29.58	
<i>Mean</i>	<i>39.23</i>	<i>9.52</i>	<i>22.56</i>	

L: White/black (0/100), a: green (0/-60) and red (0/+60), b: blue (b: 0/-60) and yellow (0/+60).

Ceramic samples were kept in distilled water for 24-48 hours considering the contamination status. These impurities were softened and separated from the sample surface. Visible impurities were removed from the surface with the help of a scalpel and the samples were ground into powder in a porcelain mortar in order to use in XRD and FTIR. Bulk samples were used in p-XRF and petrography. After the cleaning process, the equivalent colors of the ceramics were determined. For this purpose, CIA L, a, b values (Commission Internationale de L'Eclairage color system) in ceramics were determined with the ColorQA Pro System III program with a portable colorimeter (Table 1).

2.2. Analyses

In the present study, the chemical compositions of 30 samples were examined with the INNOVX model OLYMPUSX portable XRF device. Analyzes were performed in GeoChem mode. The elements that can be scanned in the first scattering (40 kV) in the analyzes made in the Geochem mode of the device are Zn, Pt, W, Au, Br, Pb, Bi, Rb, Hg, As, V, Cr, Fe, Mn Co, Ni, Cd, Sn, Sb, Ti Cu, Se, U, Sr, Y, Zr, Th, Nb, Mo, Ag. Elements within the scanning limit in the second scattering (10 kV) are Ca, Si, Mg, Al, P, Mn, K, S, Ti. Portable XRF was used as a non-destructive technique.

XRD analysis was used to detect the minerals in the ceramics and was performed with a Rigaku/Miniflex-2 XRD device. The goniometric speed was 2°/min and the scanning range was 5-50 2-theta, which is the range in which soil minerals can be detected. The anode in the device was CuK α (1.541871 Å) and analyzes were carried out under 35 kV voltage and 15 mA current. Powder samples were used in XRD analysis and no acidification was applied.

FTIR was employed as a complementary technique in the research. The analyses were carried out on the sample powders using a Perkin Elmer FTIR device. The spectra were taken between the wavenumbers of 650-4000 cm⁻¹. The assignment of the bands for the minerals are made in the range of 650-1800 cm⁻¹ (the fingerprint region for the ceramics). The results were interpreted comparatively with the band values in the available literature. The petrographic analyzes of ceramics were performed with a DMLP model Leica Research Polarizing optical microscope. A Leica DFC280 digital camera was used to capture the images during the analyses. The camera has x25 magnification and works with both single and double nicol. A Leica Qwin digital imaging system was used to evaluate the images obtained for the ceramics. Point Counting method was applied in the determination of mineral/rock contents in the samples.

3. RESULTS AND DISCUSSION

3.1. Portable XRF results

The oxides detected in p-XRF analysis for the ceramics are given in Table 2, and variation of the oxides are given in Figure 3.

The high amount of CaO (27.83 wt. % on average) determined for the ceramics indicated that carbonates (i.e. calcite) were included in the raw materials used in production. The high values of CaO ratio also suggested that the amount of clay minerals in the raw material(s) was low. The amount of Al₂O₃ determined in the ceramics (8.22 wt. % on average) supports this interpretation. It was seen that

the amount of SiO₂ in the ceramics was also relatively low (41.29 wt. % on average). These results indicated that the starting raw material of the ceramics would have a calcareous character. Taking into account the moderate and/or relatively high amounts of K₂O, it can be deduced that potassium would have originated from the clay and/or feldspathic materials (K-feldspar or plagioclases). The low Al₂O₃ content in the samples, on the other hand, indicated that the potassium oxide might have come mostly from feldspar or plagioclase. The ceramics with high MgO content were thought to possess dolomite which was presumably present as a carbonate raw material in addition to calcite [14,15].

Table 2. The oxides detected in ceramics by p-XRF.

Code	CaO	SiO ₂	Fe ₂ O ₃	MgO	Al ₂ O ₃	K ₂ O ₅	P ₂ O ₅	TiO ₂	MnO	Cr ₂ O ₃
SV- 1	30.92	41.05	11.88	-	8.70	4.63	2.08	0.94	0.14	-
SV- 2	28.95	40.56	13.52	5.08	7.61	2.29	1.34	0.74	0.08	0.14
SV- 3	40.39	29.85	9.90	8.76	6.03	2.28	1.87	0.63	0.09	-
SV- 4	35.20	37.51	10.98	3.88	7.17	3.15	1.64	0.74	0.17	-
SV- 5	17.50	48.79	13.95	-	10.97	4.93	2.48	1.18	0.20	-
SV- 6	17.57	49.58	14.10	-	10.94	4.97	1.97	1.07	0.20	-
SV- 7	30.30	38.76	11.84	8	7.18	1.91	1.37	0.63	0.08	-
SV- 8	30.35	40.74	12.73	3.50	7.14	3.18	1.98	0.8	0.15	-
SV- 9	43.14	33.04	8.92	3.64	7.32	2.23	1.22	0.64	0.06	-
SV- 10	31.69	39.16	10.84	-	8.23	4.25	2.04	0.81	0.15	-
SV- 11	33.47	37.72	10.66	3.41	7.90	3.88	2.18	0.77	0.15	-
SV- 12	43.02	32.22	9.26	3.80	7.51	2.29	1.41	0.67	0.08	-
SV- 13	30.95	37.96	12.34	7.93	6.74	1.72	1.34	0.65	0.08	-
SV- 14	25.64	40.30	12.28	8.69	7.84	2.21	1.67	0.77	0.21	0.15
SV- 15	31.94	38.07	11.91	7.38	6.75	1.82	1.25	0.66	0.09	-
SV- 16	19.01	47.52	14.50	-	10.25	4.82	1.91	1.20	0.22	-
SV- 17	14.60	48.14	15.38	7.91	8.17	3.35	1.74	0.82	0.14	-
SV- 18	14.92	48.91	15.50	3.38	9.67	4.54	2.33	1.22	0.22	-
SV- 19	13.80	52.08	15.45	-	11.42	4.33	2.36	1.19	0.09	-
SV- 20	28.16	40.39	12.36	5.68	7.01	2.87	1.83	0.76	0.15	0.15
SV- 21	15.35	47.39	15.32	7.46	8.39	3.12	1.87	0.85	0.18	-
SV- 22	38.73	33.90	11.68	3.76	6.28	3.54	1.43	0.67	0.08	-
SV- 23	21.25	45.42	12.73	3.76	9.97	4.28	1.85	0.95	0.26	-
SV- 24	30.63	39.96	12.15	-	8.54	5.15	2.24	0.90	0.09	-
SV- 25	32.70	38.81	11.02	3.15	7.95	3.74	1.98	0.88	0.16	-
SV- 26	34.40	37.28	11.01	3.40	7.80	3.74	1.84	0.84	0.16	-
SV- 27	16.41	45.90	14.01	9.60	8.29	2.62	1.71	0.78	0.17	-
SV- 28	39.14	37.05	10.70	-	7.37	3.38	1.74	0.80	0.14	-
SV- 29	15.56	50.51	14.23	-	10.81	5.08	2.11	1.13	0.09	-
SV- 30	29.26	40.41	13.33	5.17	6.89	2.94	1.50	0.73	0.09	-
Mean	27.83	41.29	12.48	5.58	8.22	3.44	1.80	0.84	0.13	0.14

(-): not determined or below the detection limit (not included in the mean value).

It was predicted that the element that have provided the red and brown hues to the body was mainly iron, since no other colorant elements were not determined in the portable XRF analysis. As is known, iron oxides can give various colors in different firing atmospheres. Iron is oxidized in oxidizing firing atmosphere and turns into hematite resulting in reddish tones, whereas it is reduced in reducing firing atmosphere and turns into magnetite resulting in black tones [16].

The ceramics with black-gray tones of paste between two red-brown surfaces, or with layers that can be clearly distinguished as red and black inside and outside are referred as "sandwich structure" in the literature. The emergence of this type of structure mainly depends on the raw material and the firing conditions, and could be also due to addition of organic materials. In the present study, elongated and irregular voids were clearly observed on most of the ceramic surfaces, which were predicted to be formed as a result of removal of organic materials (e.g. straw, grass). Such additives could have been used as temper materials in order to strengthen the ceramic body. It could be deduced that organic additives would have been used in addition to iron content for the potsherds having sandwich structure in the present study [17].

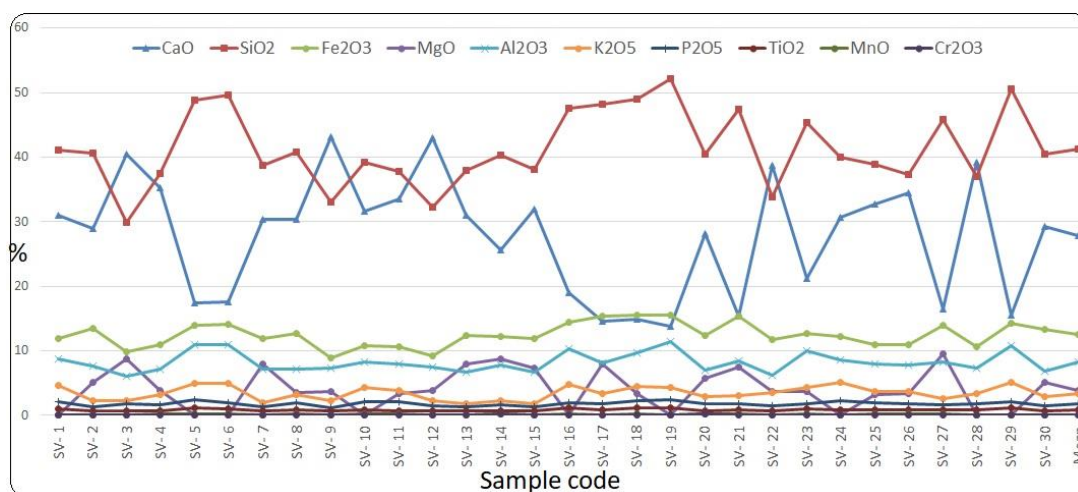


Figure 3. The variation of oxides in the samples.

The ceramics were classified through the hierarchical clustering analysis using SPSS 17.0. statistical program. The clustering analysis was initially applied considering the amounts of CaO, SiO₂, Al₂O₃, Fe₂O₃, K₂O and TiO₂ (Figure 4a). Then, only CaO, SiO₂ and Al₂O₃ (having relatively higher ratios in p-XRF) were taken into account for the same analysis (Figure 4b). Absence of any significant difference between two dendrogram indicated that the starting raw materials used in the production of the ceramics mainly contain calcium, silica and alumina. It was observed that the ceramics were divided into two main groups in the clustering analysis performed through the oxide contents. The groups are as the followings;

Group-1: SV-5, SV-6, SV-16, SV-17, SV-18, SV-19, SV-21, SV-23, SV-27, SV-29 (CaO: 13.80-21.25 wt. %).

Group-2: SV-1, SV-2, SV-3, SV-4, SV-7, SV-8, SV-9, SV-10, SV-11, SV-12, SV-13, SV-14, SV-15, SV-20, SV-22, SV-24, SV-25, SV-26, SV-28, SV-30 (CaO: 25.64-43.14 wt. %).

As can be seen, the CaO content was decisive in the separation of ceramics into groups. Ceramics with the content of CaO between 13.80% and 21.25% formed the first group, and the ceramics with the content of CaO between 25.64% and 43.14% formed the second group. In any case, since the use of calcareous raw materials comes to the fore, it was foreseen that a similar or the same source, but varying in carbonate raw material content would have been used in ceramic production, in general. In a way, this may indicate the possibility that the potters would have made random choices in the use of raw materials.

Table 3. Trace elements detected in ceramics by p-XRF (ppm).

Code	Sr	Ni	Zn	Zr	Cu	Rb	Y	Nb	As	Pb	S	Br	Cr	Sb	Th	Mo
SV-1	496	169	154	97	76	39	27	22	18	12	-	-	485	-	-	-
SV-2	311	416	129	68	61	15	20	20	18	-	-	-	-	-	-	-
SV-3	408	241	138	63	54	14	15	11	-	-	221	2	407	-	-	-
SV-4	674	294	164	63	52	26	20	-	-	-	-	-	562	-	-	-
SV-5	272	230	139	151	71	60	30	30	14	20	-	-	407	-	-	-
SV-6	215	194	122	171	79	62	31	21	15	13	-	-	374	-	-	-
SV-7	425	423	141	56	61	17	20	-	-	-	-	-	719	-	-	-
SV-8	494	389	165	72	50	29	30	23	14	-	-	-	710	-	-	-
SV-9	472	172	105	65	52	21	11	-	-	-	-	-	638	-	-	-
SV-10	535	194	147	94	62	40	26	19	20	-	-	-	343	-	-	-
SV-11	577	191	144	84	74	33	26	15	19	12	-	-	343	83	-	-
SV-12	466	187	102	102	45	23	17	-	-	14	-	2	333	-	-	-
SV-13	416	440	114	47	74	15	18	13	-	-	-	-	719	-	-	-
SV-14	179	377	128	77	44	17	18	19	-	-	-	-	-	-	-	-
SV-15	520	405	125	50	65	16	19	13	-	-	-	-	567	-	-	-
SV-16	221	236	121	155	41	66	37	26	16	22	-	-	281	-	32	-
SV-17	325	518	196	74	96	30	29	25	23	-	-	-	769	-	-	-
SV-18	259	344	193	140	70	60	35	26	17	12	-	2	428	-	-	9
SV-19	199	239	147	186	47	67	35	30	20	18	-	-	677	-	-	-
SV-20	455	358	160	73	65	26	28	19	-	-	-	-	-	-	-	-
SV-21	342	588	166	79	85	28	27	19	24	-	-	-	926	-	-	-
SV-22	346	249	103	49	68	19	14	15	18	-	-	-	567	-	-	-
SV-23	399	272	172	114	76	46	31	18	14	-	-	-	396	-	-	-
SV-24	398	172	132	111	47	39	28	16	14	14	-	2	395	-	-	-
SV-25	554	243	147	97	79	36	30	22	16	14	-	-	409	-	-	-
SV-26	540	159	140	89	58	34	28	12	18	-	-	-	415	-	-	-
SV-27	392	612	197	74	96	23	26	15	13	12	-	1	795	-	-	-
SV-28	632	231	162	77	70	33	24	16	11	-	-	2	373	-	-	-
SV-29	241	222	130	176	65	71	34	27	14	18	-	2	312	-	-	-
SV-30	440	454	141	59	58	19	18	17	9	-	-	2	698	-	-	-

(-): not determined or below the detection limit.

The trace elements detected in p-XRF analysis for the ceramics are given in Table 3, and the variations of dominant ones are given in Figure 5. A classification was also made through the trace elements considering both all the trace elements (Figure 6a) and the elements (Sr, Zn, Rb, Y, Cu, Zr, Ni, Cr) excluding the ones that are not present in some samples or are below the detection limit (Figure 6b). In the classification made in terms of the oxide contents, ceramics were divided into two groups and the most decisive oxide in that grouping was CaO which indicated that calcareous raw materials were used in ceramics, but the raw material(s) varied on carbonate contents. Although it was observed that there was a relative compatibility between the classifications made through the trace elements and oxide contents, it was determined that some of the samples have replaced within the groups. This situation supported the prediction that a single source would have not been utilized in the use of raw materials.

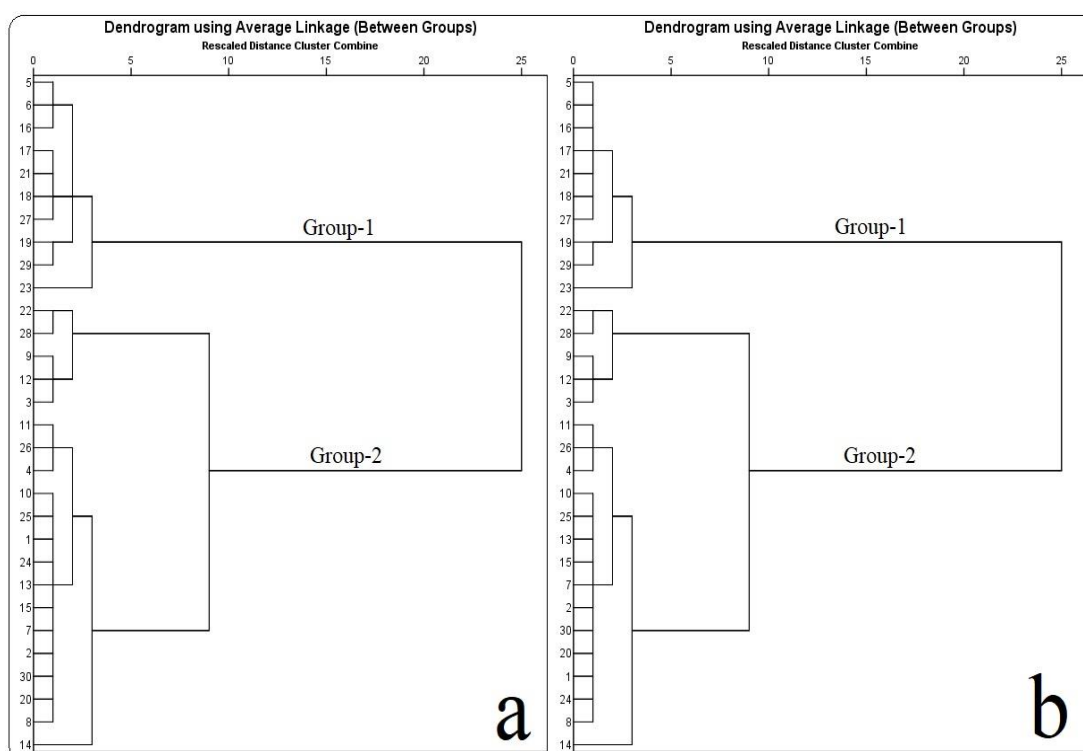


Figure 4. Dendrograms showing the classification made by considering (a) CaO, SiO₂, Al₂O₃, Fe₂O₃, K₂O and TiO₂, (b) CaO, SiO₂ and Al₂O₃.

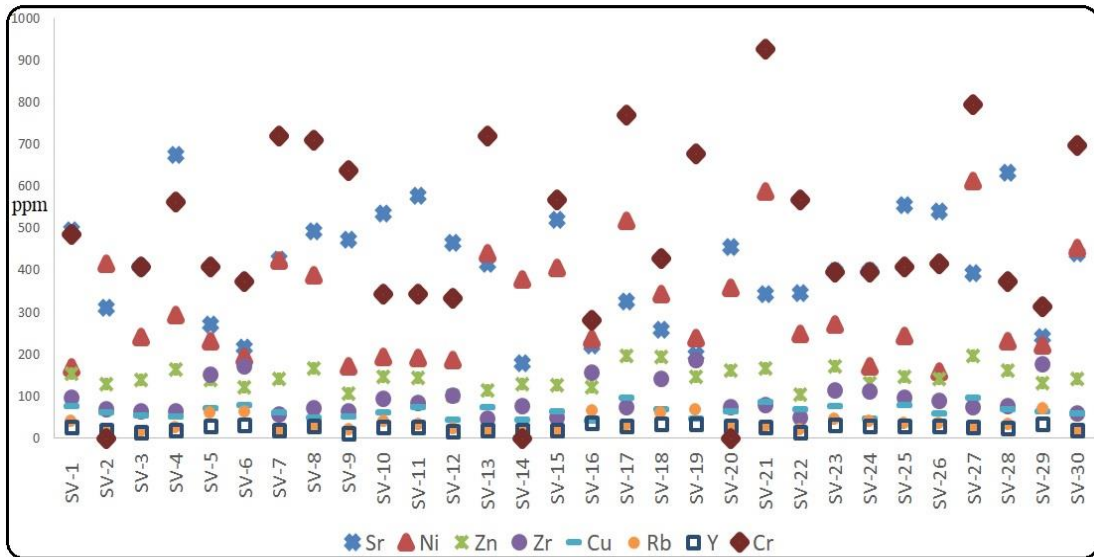


Figure 5. The variation of trace elements dominant in the samples.

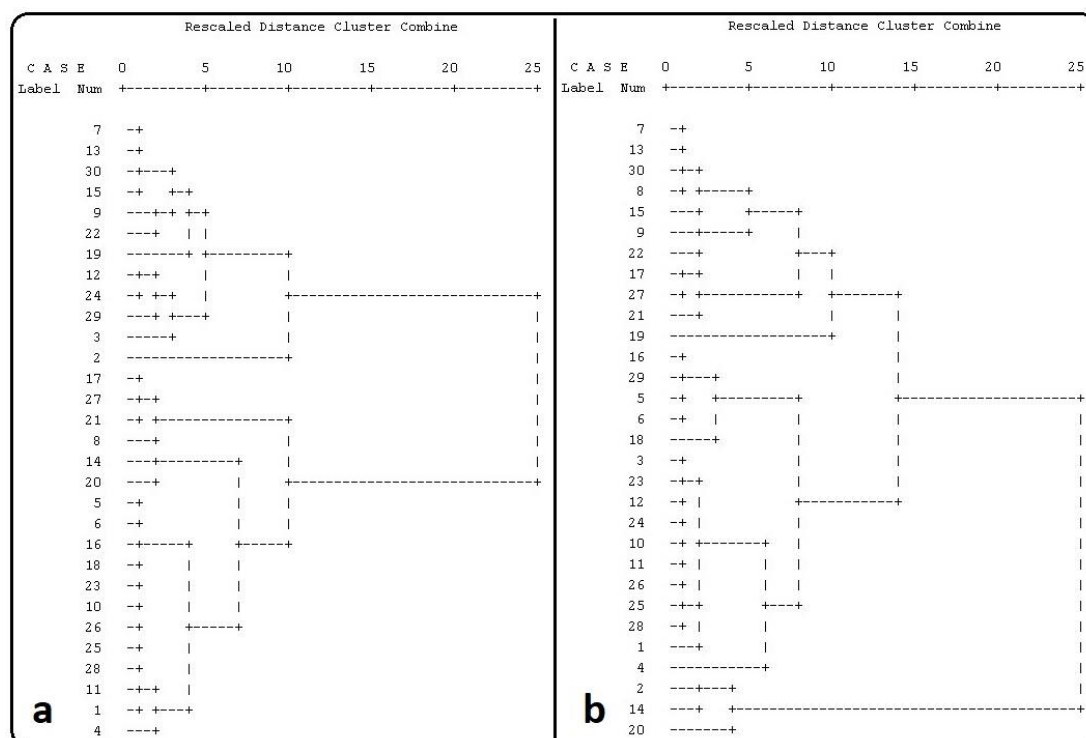


Figure 6. Dendrograms showing the classification made by considering (a) all trace elements identified, (b) Sr, Zn, Rb, Y, Cu, Zr, Ni, Cr.

3.2. XRD Results

XRD patterns of representative samples are given in Figure 7. Quartz, calcite, clay minerals, feldspar and plagioclase were detected for the whole set, while gehlenite and pyroxene were seen in few samples (Table 4). The mineralogical assemblages suggested a calcareous raw material source, and the neo-formations occasionally identified in some of the potsherds indicated a relatively higher firing temperature for such samples. Ceramics in which calcite was determined as the major mineral are SV-1, SV-2, SV-3, SV-4, SV-7, SV-9, SV-10, SV-11, SV-12, SV-13, SV-14, SV-15, SV-20, SV-22, SV-23, SV-24, SV-25, SV-26, SV-28, SV-30. Ceramic samples in which calcite was determined at lower intensities than quartz are SV-5, SV-6, SV-8, SV-16, SV-17, SV-18, SV-19, SV-21, SV-27, SV-29.

The firing temperature ranges of the ceramics were determined considering the decomposition and formation reactions of the minerals. Clay minerals tend to structurally decompose with the increasing temperature. The removal of hydroxyl groups in clay minerals can be seen around 700°C, and structural degradation around 900°C. Afterwards, the clay minerals turn into an amorphous phase and/or form new phases at higher temperatures. The structural decomposition of calcite begins ca.

700°C which might last at around 800-850°C, and the maximum temperature of calcite decomposition would vary depending on the grain size, abundance of calcite and/or the firing conditions (heating rate, firing atmosphere etc.). Dolomite decomposes at lower temperatures than calcite (i.e. ~600-700°C). Following the decomposition reactions, new phases are formed with the increasing temperature in the matrix. These are generally gehlenite (carbonated raw material + clay; ca. 800-850°C) from the melilite group and augite or diopside (carbonated raw material + quartz; ca. 850-900°C) from the pyroxene minerals [18-21].

Considering the temperature ranges of the decomposition and formation reactions of the minerals mentioned above, the evident presence of calcite in the ceramic matrix indicated that such samples were not exposed to very high temperatures (i.e. 900-1000°C). Therefore, it was predicted that the firing temperature did not exceed 800°C for the ceramics in which calcite was dominantly determined. The clay minerals detected in all samples indicated that the firing temperature of the ceramics did not exceed 900°C, while the high-temperature minerals detected in some samples pointed out that these ceramics may have been exposed to a temperature around 800-850°C, although not as high as 900°C. Even though it has been demonstrated that the high temperature minerals distinguished some of the ceramics from others (in terms of the firing temperature), the environmental conditions to which the ceramics were exposed during the firing cycle should also be taken into account. The fact that high temperature minerals generally have intensities below 50 cps on XRD patterns (except SV-2) reveals that it should not be forgotten that such minerals may be formed as a result of exposure of some ceramics to high heating rates during the firing, which would propose an uneven firing process [18-21].

Table 4. XRD results of the potsherds.

Sample	Mineral/phase
SV-1	Quartz, Calcite, Clay Mineral, Feldspar, Plagioclase
SV-2	Quartz, Calcite, Clay Mineral, Feldspar, Plagioclase, Gehlenite
SV-3	Quartz, Calcite, Clay Mineral, Feldspar, Plagioclase
SV-4	Quartz, Calcite, Clay Mineral, Feldspar, Plagioclase
SV-5	Quartz, Calcite, Clay Mineral, Feldspar, Plagioclase
SV-6	Quartz, Calcite, Clay Mineral, Feldspar, Plagioclase
SV-7	Quartz, Calcite, Clay Mineral, Feldspar, Plagioclase
SV-8	Quartz, Calcite, Clay Mineral, Feldspar, Plagioclase, Gehlenite
SV-9	Quartz, Calcite, Clay Mineral, Feldspar, Plagioclase
SV-10	Quartz, Calcite, Clay Mineral, Feldspar, Plagioclase
SV-11	Quartz, Calcite, Clay Mineral, Feldspar, Plagioclase
SV-12	Quartz, Calcite, Clay Mineral, Feldspar, Plagioclase
SV-13	Quartz, Calcite, Clay Mineral, Feldspar, Plagioclase
SV-14	Quartz, Calcite, Clay Mineral, Feldspar, Plagioclase, Gehlenite
SV-15	Quartz, Calcite, Clay Mineral, Feldspar, Plagioclase
SV-16	Quartz, Calcite, Clay Mineral, Feldspar, Plagioclase, Pyroxene, Gehlenite
SV-17	Quartz, Calcite, Clay Mineral, Feldspar, Plagioclase
SV-18	Quartz, Calcite, Clay Mineral, Feldspar, Plagioclase, Pyroxene, Gehlenite
SV-19	Quartz, Calcite, Clay Mineral, Feldspar, Plagioclase, Gehlenite
SV-20	Quartz, Calcite, Clay Mineral, Feldspar, Plagioclase
SV-21	Quartz, Calcite, Clay Mineral, Feldspar, Plagioclase
SV-22	Quartz, Calcite, Clay Mineral, Feldspar, Plagioclase, Gehlenite
SV-23	Quartz, Calcite, Clay Mineral, Feldspar, Plagioclase
SV-24	Quartz, Calcite, Clay Mineral, Feldspar, Plagioclase, Gehlenite
SV-25	Quartz, Calcite, Clay Mineral, Feldspar, Plagioclase
SV-26	Quartz, Calcite, Clay Mineral, Feldspar, Plagioclase
SV-27	Quartz, Calcite, Clay Mineral, Feldspar, Plagioclase
SV-28	Quartz, Calcite, Clay Mineral, Feldspar, Plagioclase
SV-29	Quartz, Calcite, Clay Mineral, Feldspar, Plagioclase
SV-30	Quartz, Calcite, Clay Mineral, Feldspar, Plagioclase

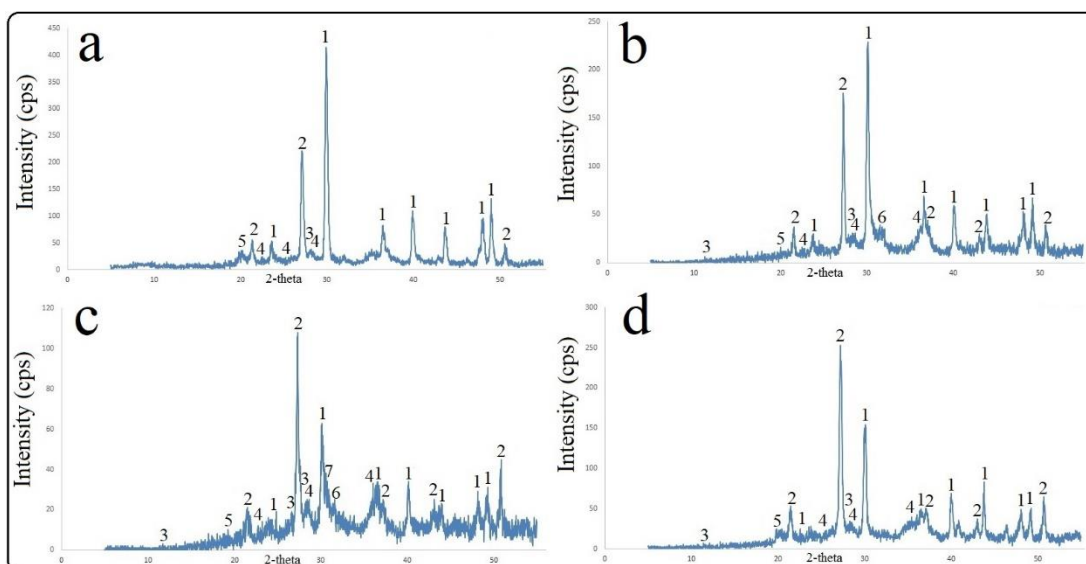


Figure 7. XRD patterns of representative samples (a) SV-4, (b) SV-14, (c) SV-16, (d) SV-21 (1: Calcite, 2: Quartz, 3: Feldspar, 4: Plagioclase, 5: Clay mineral, 6: Gehlenite, 7: Pyroxene).

3.3. Petrography results

Quartz and plagioclase were detected for the whole set, and opaque minerals, biotite and pyroxene minerals were seen in most of the samples (Table 5). In addition to the chert content detected in all samples, clay, claystone, marl (clay rich in calcium carbonate) and argillized dacite (volcanic rock with a composition between andesite and rhyolite) were occasionally determined in the sample set. The groups formed as a result of the petrographic analysis are as follows (please see Table 5);

Gr1: SV-17, SV-28

Gr2: SV-7, SV-10, SV-16, SV-27

Gr3: SV-11, SV-13, SV-15, SV-25, SV-26, SV-29

Gr4: SV-1, SV-5, SV-6, SV-18, SV-19, SV-30

Gr5: SV-2, SV-3, SV-4, SV-9, SV-12, SV-14, SV-24

Gr6: SV-8, SV-20, SV-21, SV-22, SV-23

Table 5. Petrography results of the ceramics.

Groups	Porosity (% in vol.)	MTA* (% in vol.)	Rock/Mineral**	Aggregate***	Rock Origin
Gr1	15	45	Q,Ch,Pl,Op,G (%2)	Very fine	Claystone
Gr2	12	29	Q,C,Ch,Pl,Op	Medium	Marl
Gr3	12	22	Q,Ch,Pl,Op,G (%1)	Fine	Clay
Gr4	12	20	Q,Ch,Pl,Bi,Py,Op,D,G (%1)	Coarse	Argillized Dacite
Gr5	15	10	Q,Ch,Pl,Bi,Py,G (%2)	Very fine	Claystone
Gr6	14	22	Q,Ch,Pl,Bi,Py,Op	Fine	Claystone

(*) MTA: Matrix Total Aggregate,

(**) Bi: Biotite, C: Calcite, Ch: Chert, D: Dacite, Op: Opaque Minerals, Pl: Plagioclase, Py: Pyroxene, Q: Quartz, G: Grog (brick particles)

(***) Fine / Medium / Coarse Aggregate (mm): <0,5 / 0,5-1,0 / >1,0

In addition to the minerals and rock types identified in the ceramic pastes, the grog content was also revealed for some of the samples. Ceramics containing grog 1 % (in volume) are SV-1, SV-5, SV-6, SV-11, SV-13, SV-15, SV-18, SV-19, SV-25, SV-26, SV-29, SV-30. Ceramics containing grog 2 % (in volume) are SV-2, SV-3, SV-4, SV-9, SV-12, SV-14, SV-17, SV-24 SV-28. As is seen, most of the ceramics contain grog, which is thought to be preferred as a temper material in order to strengthen the ceramic body [19,22]. Grog content can be specified as ground ceramic or brick pieces, as well as the temper raw materials used in the form of clay lumps, and these types of materials could be subsequently added to the raw material and prevent the ceramic body from deforming due to water loss during the drying or firing process [19,22]. The grog content was also occasionally observed in microphotographs of the ceramics (SV-5, SV-9, SV-12, SV-14) (Figure 7). Elongated or sometimes irregularly shaped gaps, which are evident in the macro observations of the ceramics and were thought to be most likely formed as a result of the burning away of the organic materials (vegetable remains, straw, grass, etc.) during firing, were also encountered in micro-photographs (e.g. SV-2, SV-3, SV-7, SV-10, SV-19, SV-20, SV-30) (Figure 8).

In an archaeometric study for Çatalhöyük Neolithic ceramics [23], another parameter was mentioned in the use of herbal additives such as straw, which increase the binding property of clay during drying. It has been stated that the use of such easily combustible materials in the production of clay-based products can help to reach higher temperatures in a shorter time during firing. In the mentioned study, it was stated that the small (or trace) amount of gehlenite and aluminum diopside detected in the ceramic bodies were also an indicator of that prediction [23].

In the current study, the high temperature minerals determined for some of the ceramics in XRD analysis and the voids determined in the thin section analysis suggested that combustible organic additives could have increased the sensible temperature of such ceramics, and may have boosted the heating rate, as Akça et al., 2009 [23] pointed out.

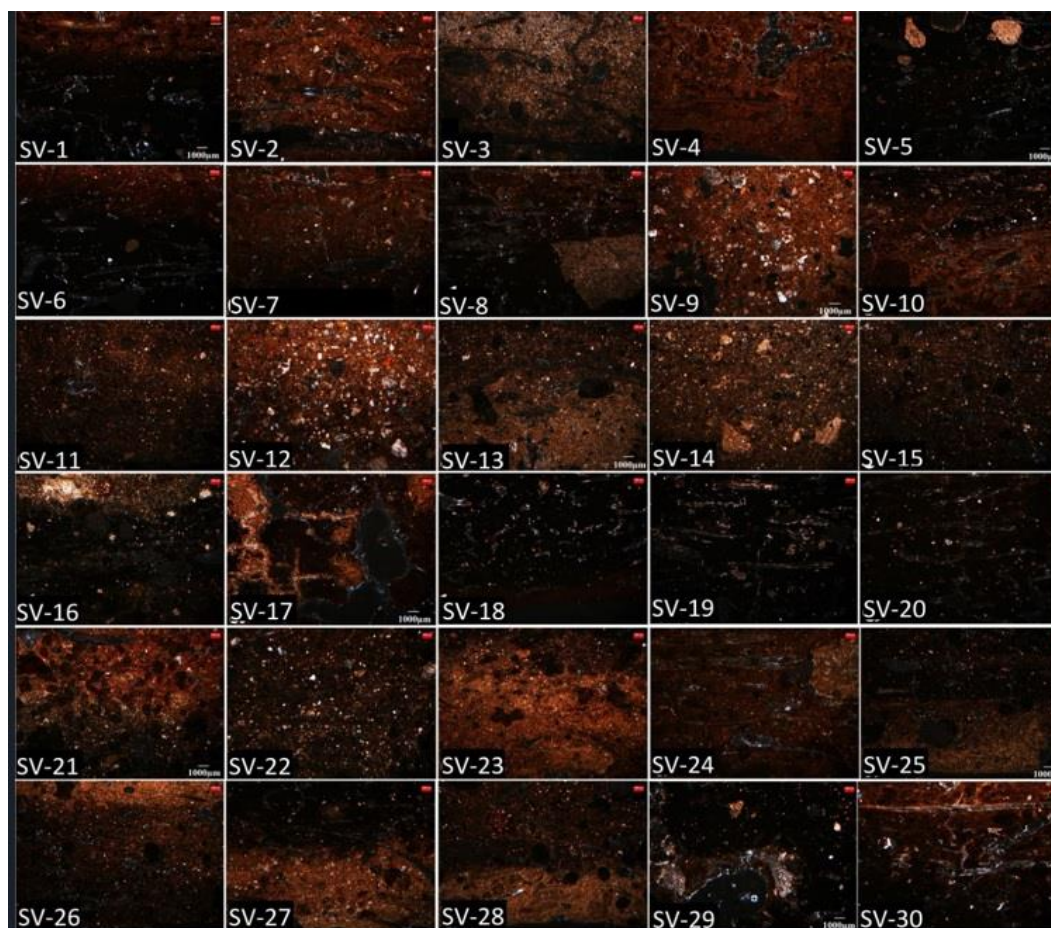


Figure 8. Microphotographs of the ceramics.

3.4. FTIR results

FTIR analysis was carried out between $650\text{-}4000\text{ cm}^{-1}$ (Figure 9), but the results were interpreted considering the range of $650\text{-}1800\text{ cm}^{-1}$ (the fingerprint region for the ceramics). Thus, only the bands between $650\text{-}1800\text{ cm}^{-1}$ are given in this section (all the raw results of FTIR are not given here). When the band values in the FTIR spectra were examined (Table 6), it was observed that these values were generally in harmony with the mineralogical content determined in the XRD analysis.

It was predicted that calcite, which dominantly appeared in the XRD analysis, showed peaks in the ranges of $1412\text{-}1439\text{ cm}^{-1}$, $871\text{-}877\text{ cm}^{-1}$ and $709\text{-}716\text{ cm}^{-1}$ in the FTIR spectra. Apart from these band values, calcite was also revealed with the bands in the range of $1440\text{-}1458\text{ cm}^{-1}$. It was thought

that the reason for the shift of the band values from 1412 cm⁻¹ to 1458 cm⁻¹ could be secondary calcite formed in the ceramic body due to the burial conditions [19,24].

Table 6. Bands detected in FTIR analysis and the possible minerals assigned.

SV	Band value (cm ⁻¹)	Minerals assigned* [16, 24-34]
1	1797/1647/1430/874/798/712/691/670	C/OH/C/C,Pr,Do/Q/C/Q/Fs,P
2	1795/1636/1427/1158/873/798/779/712/667	C/OH/C/Q,Fs,P/C,Pr,Do/Q/Q/C/Fs,P
3	1795/1642/1412/872/798/778/712	C/OH/C/C,Pr,Do/Q/Q/C
4	1797/1643/1425/1003/873/798/779/712	C/OH/C/K,I,Fs,P/C,Pr,Do/Q/Q/C
5	1643/1429/875/819/796/775/716/693/672/655	OH/C/C,Pr,Do/Ch,I/Q/Q/C/Q/Fs,P/Fs,P
6	1648/1437/871/798/779/709/690/658	OH/C/C,Pr,Do/Q/Q/C/Q/Fs,P
7	1458/1166/1093/894/873/836/824/796/773/711/693/665	C/Q,G,Fs/Fs,P/I/C,Pr,Do/Ar,Do,S/Ch/Q/Q/C/Q/Fs,P
8	1797/1671/1426/1161/1016/797/773/711/688/651	C/OH/C/Q,Fs,P/K,Fs,P/Q/Q/C/Q/Fs,P
9	1797/1641/1427/1163/873/798/779/712/691	C/OH/C/Q,Fs,P/C,Pr,Do/Q/Q/C/Q
10	1652/1436/1158/1091/915/875/798/779/714/691	OH/C/Q,G,Fs/Fs,P/K,Pr,C,Pr,Do/Q/Q/C/Q
11	1428/1161/874/798/775/712/690	C/Q,G,Fs/C,Pr,Do/Q/Q/C/Q
12	1795/1435/1166/873/800/777/712/697	C/C/Q,G,Fs/C,Pr,Do/Q,K/Q/C/Q
13	1435/1163/1002/873/799/777/712	C/Q,G,Fs/K,I,Fs,P/C,Pr,Do/Q,K/Q/C
14	1441/1019/877/831/794/773/709/690/651	C/K,Fs,P/C,Pr,Do/Ar,Do,S/Q/Q/C/Q/Fs,P
15	1797/1650/1428/1163/873/799/779/712	C/OH/C/Q,G,Fs/C,Pr,Do/Q,K/Q/C
16	1643/1433/1009/874/793/775/709/690	OH/C/K,I,Fs,P/C,Pr,Do/Q,K/Q/C/Q
17	1641/1428/1165/1006/874/798/779/711/691	OH/C/Q,G,Fs/K,I,Fs,P/C,Pr,Do/Q,K/Q/C/Q
18	1424/1166/1002/873/798/777/711/693/662	C/Q,G,Fs/K,I,Fs,P/C,Pr,Do/Q,K/Q/C/Q/Fs,P
19	1654/1442/1001/875/789/772/742/695	OH/C/K,I,Fs,P/C,Pr,Do/Q,K/Q/Fs,P/Q
20	1795/1643/1434/1019/877/797/775/712/691	C/OH/C/K,Fs,P/C,Pr,Do/Q,K/Q/C/Q
21	1640/1440/1163/1004/874/798/777/712	OH/C/Q,G,Fs/K,I,Fs,P/C,Pr,Do/Q,K/Q/C
22	1795/1645/1428/1002/875/798/775/712/693	C/OH/C/K,Fs,P/C,Pr,Do/Q,K/Q/C/Q
23	1643/1438/1163/874/796/779/711/691	OH/C/Q,G,Fs/C,Pr,Do/Q,K/Q/C/Q
24	1799/1645/1428/1009/874/796/777/711/693	C/OH/C/K,Fs,P/C,Pr,Do/Q,K/Q/C/Q
25	1443/1016/875/798/777/711/691	C/K,Fs,P/C,Pr,Do/Q,K/Q/C/Q
26	1797/1641/1428/1006/873/798/779/712/691	C/OH/C/K,Fs,P/C,Pr,Do/Q,K/Q/C/Q
27	1643/1458/1439/1156/1102/1013/875/798/775/711/693/655	OH/C/C/Q,G,Fs/P,Pr/K,I,Fs,P/C,Pr,Do/Q,K/Q/C/Q/Fs,P
28	1793/1441/1166/1013/874/798/775/712/693/674	C/C/Q,G,Fs/K,I,Fs,P/C,Pr,Do/Q,K/Q/C/Q/Pr
29	1452/1008/873/798/773/737/712/691	C/K,Fs,P/C,Pr,Do/Q,K/Q/Fs,P,M/C/Q
30	1797/1645/1428/1159/1076/1002/873/798/777/712/693/667	C/OH/C/Q,G,Fs/Q,Pr,M/K,Fs,P/C,Pr,Do/Q,K/Q/C/Q/Fs,P

* A: Aragonite, C: Calcite, Ch: Chlorite, Do: Dolomite, Fs: Feldspar, G: Gypsum, I: Illite,

K: Kaolinite, M: Muscovite, OH: H-O-H stretches, P: Plagioclase, Pr: Pyroxene, S: Sanidine

The band values in the range of 1000-1019 cm^{-1} were attributed to the clay minerals, while the bands in the range of 1158-1166 cm^{-1} , 794-800 cm^{-1} , 772-779 cm^{-1} and 688-697 cm^{-1} indicated the existence of quartz. It should not be ignored that the bands in the range of 1158-1166 cm^{-1} pointing to quartz may be also indicative of feldspar/plagioclase minerals. This type of band overlapping is likely to be encountered in FTIR spectra. The band values of 1636-1647 cm^{-1} , 1650-1654 cm^{-1} and 1671 cm^{-1} were assigned to OH⁻ vibrations (H-O-H stretches) which suggested the presence of hygroscopic water in ceramic paste [16, 24-34].

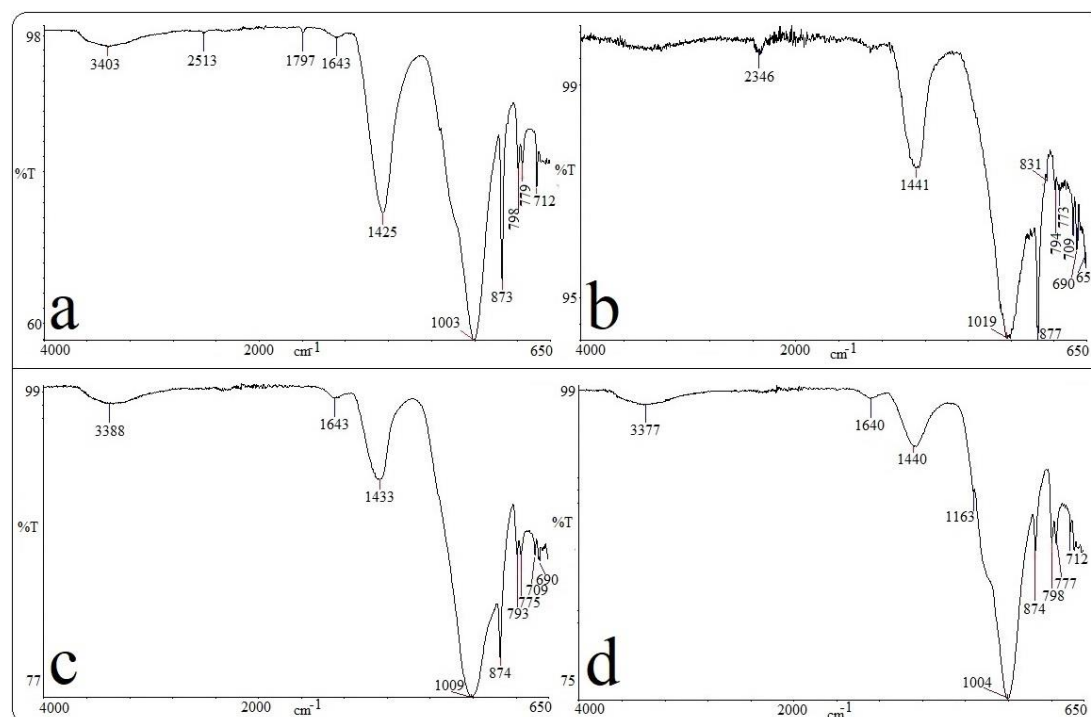


Figure 9. FTIR spectra of representative samples (a) SV-4, (b) SV-14, (c) SV-16, (d) SV-21.

4. CONCLUSIONS

The pottery recovered from the Şah Valley hillside settlement represents the easternmost examples of Hassuna Samarra, and this research has focused on Neolithic ceramic findings belonging to that culture. The chemical composition and mineralogical assemblage of the samples indicated to use of calcareous raw materials. The geological structure rich in carbonated raw materials in and around the province of Şırnak indicates that the high CaO content is likely of regional origin [35-39]. In XRF analysis, it was determined that iron was the main element in formation of the reddish colors in

ceramic bodies. The elongated and irregular voids, which were clearly observed on most of the ceramic surfaces and were predicted to be formed as a result of the removal of organic materials by burning, suggested that organic materials would be as effective as iron in formation of sandwich structure. The voids on the potsherds can also be caused by wheel construction or partial loss of calcite. Considering the fact that the potsherds belong to the Neolithic Period, use of wheel could be ignored and partial loss of calcite may be evaluated as a valid parameter in occurrence of the gaps, in addition to the probable presence of organic additives [40].

In the hierarchical clustering analysis performed through the statistical program SPSS (considering the chemical composition of the ceramics), it was revealed that the starting raw materials used in the production of ceramics generally contain calcium, magnesium, silica and alumina. In the statistical analyses, ceramics were divided into two groups and CaO was decisive in the formation of these groups. The results indicated that sources varying in carbonated raw material contents would have been used in ceramic production, in general. In the clustering analysis carried out with the trace elements, the displacement of some samples between the former groups (created depending on the main oxides) indicated that more than one source would have been used in preparation of the starting materials.

Taking into account the temperatures of decomposition and formation reactions of the minerals, it was revealed that the ceramics were mostly fired at temperatures not exceeding 800°C. In FTIR analysis, which was applied as a complementary technique in the study, the data were compatible with the XRD patterns. In petrography analysis, which was another method of determining the mineral content, quartz and plagioclase were detected for the whole set, and opaque minerals (hematite, magnetite, etc.), biotite and pyroxene minerals were detected in most of the samples. Grog, which was thought to be preferred as a temper material in most of the ceramics, has been detected and it was predicted that this content might have been subsequently added to the paste to prevent the ceramic from deforming due to water loss during the drying and firing processes.

Six groups were revealed in petrographic investigation which re-assorted the potsherds unlike the first grouping made in XRF analysis. It was also seen that the potsherds possessing calcite at lower intensities than quartz in XRD were mostly in compatible with Group-1 emerged in XRF analysis (except SV-23), while the potsherds having calcite as the dominant mineral in XRD were mostly compatible with Group-2 revealed in XRF analysis (except SV-8). These results suggested that the chemical and mineralogical contents were coherent and there would have been more than one raw material source which may indicate use of different clay batches by the potters. Such prediction would also point out there could be different pottery ateliers, instead of a single production center.

Within this research, a detailed archaeometric database is created for the Neolithic ceramics of Şah Valley. It is thought that the results of this work would be directive for the further studies on Neolithic ceramics in Anatolia. In addition to this research, provenance studies can be carried out using clay samples supplied from the region.

ACKNOWLEDGEMENTS

We gratefully thank Assoc. Prof. Dr. Ali Akın Akyol (Ankara Hacı Bayram Veli University), Prof. Dr. Yusuf Kağan Kadioğlu and Assist. Prof. Dr. Kıymet Deniz (Ankara University, Earth Sciences Application and Research Center; YEBİM), Assoc. Prof. Dr. Sema Tetiker and Assoc. Prof. Dr. Mahmut Aydın (Batman University), and Gülşen Albuz Geren (Ankara Hacı Bayram Veli University, Materials Research and Conservation Laboratory; MAKLAB) for their support in application of the analytical techniques. We also thank the laboratories for preparation of the samples and application of the analyses; Dicle University Science and Technology Application and Research Center, Batman University Central Research Laboratory, Ankara University Earth Sciences Application and Research Center, Ankara Hacı Bayram Veli University Materials Research and Conservation Laboratory. This paper covers the data of the master thesis submitted by Esra Kaynak to the Department of Archaeometry at the Institute of Science, Batman University (2019).

REFERENCES

- [1] Eramo, G., Laviano, R., Muntoni, I. M. and Volpe, G. (2004). Late Roman cooking pottery from the Tavoliere area (Southern Italy): raw materials and technological aspects. *Journal of Cultural Heritage*, 5(2), 157-165.
- [2] Arcasoy, A. (1983). *Seramik Teknolojisi*, Marmara Üniversitesi Yayınları, İstanbul.
- [3] Bayazit, M., Adsan, M., Genç, E. (2020). Application of spectroscopic, microscopic and thermal techniques in archaeometric investigation of painted pottery from Kuriki (Turkey). *Ceramics International*, 46, 3695-3707.
- [4] Bayazit, M. and Akyol, A.A. (2015). Medeniyetler arasındaki etkileşim köprüsü: seramik (arkeometrik yaklaşım), 9. Uluslararası Eskişehir Pişmiş Toprak Sempozyumu, 5-20 Eylül 2015, Eskişehir, 69-78.
- [5] Bayram, G. (2018). Güneydoğu Anadolu'nun Neolitik Çağ totemleri ve ritüel nesnelere. *AMISOS*, 3(4), 67-89.
- [6] Özüşen, B. and Yıldız, Z. (2012). Buzul Çağı'ndan İlk Çağ'a Tüketimin Tarihi. *Süleyman Demirel Üniversitesi Vizyoner Dergisi*, 4(7), 1-16.
- [7] Efecan, S. (2011). Geç Neolitik Döneme ait Hacılar Kazılarında Bulunmuş Terracota Figürlerin Çağdaş Yorumlarla Biçimlendirilmesi, Yüksek Lisans Tezi, Arkeoseramik Anasanat Dalı, Güzel Sanatlar Enstitüsü, Süleyman Demirel Üniversitesi.
- [8] Coşkun, N., Ayman, İ., Yumruk, Ş. and Aşkar, İ.T. (2019). 2017 Yılı Şırnak İli Merkez, Güçlükonak, Uludere ve Beytüşşebap İlçeleri Yüzey Araştırması, 36. Araştırma Sonuçları Toplantısı (7-11 Mayıs 2018, Çanakkale), Ankara, 175-194.

- [9] Erinç S. (1980). Kültürel çevre bilim açısından Güneydoğu Anadolu. In H. Çambel and R.J. Braidwood (Eds.), *Güneydoğu Anadolu Tarihöncesi Araştırmaları*, İÜ Edebiyat Fakültesi, İstanbul, pp. 65-72.
- [10] Çelik, B. (2010). Şırmak ve çevresinin obsidyen ticaretinde yeri ve önemi. *Anadolu / Anatolia* 36, 1-11.
- [11] Yakar, J. (2007). *Anadolu'nun Etnoarkeolojisi: Tunç ve demir çağlarında kırsal kesimin sosyo-ekonomik yapısı* (çev. S.H. Riegel, ed. B. Avunç), Homer Kitabevi.
- [12] Tekin, H. (2015). Yukarı Mezopotamya'nın ilk boyalı çanak-çömlekleri: Hassuna, Samarra ve Halaf: yeni yorumlar ve yaklaşımlar. Bölüm 1: Hassuna ve Samarra. *OLBA*, 23, 1-57.
- [13] Tekin, H. (2017). *Tarihöncesinde Mezopotamya: Yeni yaklaşımlar, yeni yorumlar ve yeni kronoloji*, Bilgin Kültür Sanat Yayınları, Ankara, 476 p.
- [14] Bayazit, M. (2018). Archaeometric study of possible Ninevite-5 pottery from upper Tigris region using SEM-EDS, PEDXRF, and OM. *X-Ray Spectrometry*, 47, 92-104.
- [15] Kibaroğlu, M. (2005). Sedimentary geochemical approach to the provenance of the noncalciferous north Mesopotamian Metallic Ware. *Archeometriai Muhely*, 2, 48-51.
- [16] İssi, A. (2012). Estimation of ancient firing technique by the characterization of semi-fused Hellenistic potsherds from Harabebezikan/Turkey. *Ceramics International*, 38 (3), 2375-2380.
- [17] Bong, W.S.K., Matsumura, K. and Nakai, I. (2008). Firing technologies and raw materials of typical early and middle Bronze Age pottery from Kaman-Kalehöyük: a statistical and chemical analysis. *Anatol. Archaeol. Stud.*, 17, 295-311.
- [18] Cultrone, G., Rodriguez-Navarro, C., Sebastian, E., Cazalla, O. and De La Torre, M.J. (2001). Carbonate and silicate phase reactions during ceramic firing. *Eur. J. Miner.* (13), 621-634.
- [19] Fabbri, B., Gualtieri, S. and Shoval, S. (2014). The presence of calcite in archeological ceramics. *J. Eur. Ceram. Soc.*, 34, 1899-1911.
- [20] Broekmans, T., Adriaens, A. and Pantos, E. (2004). Analytical investigations of cooking pottery from Tell Beydar (ne-Syria). *Nuclear Instruments & Methods in Physics Research Section B*, 226, 92-97.
- [21] Shoval, S., Gaft, M., Beck, P. and Kirsh, Y. (1993). The thermal behavior of limestone and monocrySTALLINE calcite tempers during firing and their use in ancient vessels. *J. Therm. Anal.*, 40, 263-73.

- [22] Rice P.M. (1987). Pottery analysis: A sourcebook, University of Chicago Press, Chicago, 584p.
- [23] Akça, E., Kapur, S., Özdöl, S., Hodder, I., Poblome, J., Arocena, J., Kelling, G. and Bedestenci, Ç. (2009). Clues of production for the Neolithic Çatalhöyük (central Anatolia) pottery. *Scientific Research and Essays*, 4(6), 612-625.
- [24] Mazzocchin, G.A., Agnoli, F. and Colpo, I. (2003). Investigation of roman age pigments found on pottery fragments. *Analytica Chimica Acta* (478), 147-161.
- [25] Gadsden, J.A. (1975). *Infrared Spectra of Minerals and Related Inorganic Compounds*, Butterworth & Co Publishers, London, 277 p.
- [26] Iglesias, J.E. and Serna, C.J. (1985). The IR spectra of hematite-type compounds with different particle shapes. *Miner. Petrogr. Acta*, 29A, 363-370.
- [27] Palanivel, R. and Velraj, G. (2007). FTIR and FT-Raman spectroscopic studies of fired clay artifacts recently excavated in Tamilnadu, India. *Indian Journal of Pure and Applied Physics*, 45, 501-508.
- [28] Faust, G.T. (1953). Huntite, $Mg_3Ca(CO_3)_4$, a New Mineral. *American Mineralogist*, 38, 4-24.
- [29] Farmer, V.C. (1974). *Infrared Spectra of Minerals*, Ed. Mineralogical Society, London, 539 p.
- [30] Ion, R.M., Dumitriu, I., Fierascu, R.C., Ion, M.L., Pop, S.F., Radovici, C., Bunghez, R.I. and Niculescu, V.I.R. (2011). Thermal and mineralogical investigations of historical ceramic, A case study. *J Therm Anal Calorim*, 104, 487-493.
- [31] De Benedetto, G.E, Laviano, R., Sabbatini, L. and Zambonin, P.G. (2002). Infrared spectroscopy in the mineralogical characterization of ancient pottery. *Journal of Cultural Heritage*, 3, 177-186.
- [32] Ellid, M.S., Murayed, Y.S., Zoto, M.S., Music, S. and Popovi, S. (2003). Chemical reduction of hematite with starch. *Journal of Radioanalytical and Nuclear Chemistry*, 258 (2), 299-305.
- [33] <http://rruff.info/> (Access date 30.05.2019).
- [34] Maravelaki-Kalaitzaki, P. and Kallithrakas-Kontos, N. (2003). Pigment and terracotta analyses of Hellenistic figurines in Crete. *Analytica Chimica Acta* 497, 209-225
- [35] Maden Tetkik ve Arama Genel Müdürlüğü. “İl Maden Haritaları-Şırnak”, 29.04.2019, <http://www.mta.gov.tr/v3.0/sayfalar/hizmetler/maden-haritalari/Sirnak.pdf>
- [36] Maden Tetkik ve Arama Genel Müdürlüğü. “İl Maden Haritaları-Mardin”, 29.04.2019, <http://www.mta.gov.tr/v3.0/sayfalar/hizmetler/maden-haritalari/mardin.pdf>

- [37] Maden Tetkik ve Arama Genel Müdürlüğü. “İl Maden Haritaları-Batman”, 29.04.2019, <http://www.mta.gov.tr/v3.0/sayfalar/hizmetler/maden-haritalari/batman.pdf>
- [38] Maden Tetkik ve Arama Genel Müdürlüğü. “İl Maden Haritaları-Van”, 29.04.2019, <http://www.mta.gov.tr/v3.0/sayfalar/hizmetler/maden-haritalari/Van.pdf>
- [39] Maden Tetkik ve Arama Genel Müdürlüğü. “İl Maden Haritaları-Hakkari”, 29.04.2019, <http://www.mta.gov.tr/v3.0/sayfalar/hizmetler/maden-haritalari/hakkari.pdf>
- [40] Semiz, B., Duman, B. (2017). Tripolis’te bulunan Geç antik Çağ Unguentariumları’nın Arkeometrik yönden değerlendirilmesi, Tripolis ad Maeandrum I, Tripolis arařtırmaları (Ed.: Duman, B.), Ege Yayınları, 165-180.



RESEARCH ARTICLE

**BRAIN TUMOR DETECTION AND BRAIN TUMOR AREA CALCULATION WITH
MATLAB**

Burak KAPUSIZ^{1*}, Yusuf UZUN², Sabri KOÇER³, Özgür DÜNDAR⁴

^{1*}Necmettin Erbakan University, Institute of Science, Department of Mechatronics Engineering, Konya,
burak_kapusuz@hotmail.com, ORCID: 0000-0003-1592-0240

² Necmettin Erbakan University, Faculty of Seydisehir Ahmet Cengiz Engineering, Department of Computer
Engineering, Konya, yuzun@erbakan.edu.tr, ORCID: 0000-0002-7061-8784

³Necmettin Erbakan University, Engineering Faculty, Department of Computer Engineering, Konya, skocer@erbakan.edu.tr,
ORCID: 0000-0002-4849-747X

⁴Necmettin Erbakan University, Faculty of Aeronautics and Astronautics, Department of Space and Satellite Engineering,
Konya, ozdundar@erbakan.edu.tr, ORCID: 0000-0002-4142-4446

Receive Date: 09.07.2022

Accepted Date: 23.03.2023

ABSTRACT

Brain tumors that impair the functionality of the person in daily life occur for many different reasons. Treatment of a brain tumor depends on accurately identifying the type, location, size and boundaries of the tumor. Magnetic Resonance Imaging (MRI) technique is used to diagnose the disease. However, this method cannot detect tumors below a certain size due to its nature. The aim of this study is to calculate the area of the tumor region through the successful method after determining which of the Fuzzy C-Means (FCM), Herbaceous Method, Region Growing and Self-Organizing Maps (SOM) methods are more successful in the analysis of MR images. The threshold values of the algorithms used, the number of clusters and the similarity coefficients of jaccard and dice were determined one by one by changing the index codes in the software. The highest similarity index was found in the K-means 10 cluster numbered segmentation in all trials. In general, K-means and Very Grassy Threshold gave very close results. In this context, advanced imaging technique was used by separating the MR image; Tumor spots and brain fluids were detected. Fuzzy C Mean (FCM) was found to be the best method during detection. Brain fluid pushes segmentations used in area calculations to miscalculate. For this reason, while calculating the tumor area, the brain fluids that appear in white spots are completed by point filling. Then, after the tumor zone was identified, the area of this region was used to produce the volume of the region by using Watershed, Graph-Cut and Active Counter segments. It is aimed to determine the number of tumors in which the tumor is in the detection area.

Keywords: *Image processing, Magnetic Resonance Imaging, Glioma, Image Segmentation.*

1. INTRODUCTION

The brain, as one of the vital organs of the body, responsible for the task of managing the body as well as for many processes such as controlling the body's organs, maintaining logic functions, providing learning, memory and emotion in the context of remembering and forgetting. A brain tumor is a mass formed by cells that proliferate and grow uncontrollably in the brain [1]. Brain tumors that impair the functionality of the person in daily life occur for many different reasons.

While methods such as radiotherapy and chemotherapy are used in addition to surgical methods for the treatment of brain tumors, Magnetic Resonance Imaging (MRI) technique is used for the diagnosis of the disease. The most appropriate treatment for brain tumors depends on the physician's precise determination of the tumor type, its location, size, and frame [2]. However, this method cannot detect tumors below a certain size due to its nature. Therefore, there is a need for the use of Computer Aided Diagnostic Systems in the diagnosis of diseases such as tumors.

Computer aided diagnostic systems are actually based on artificial neural networks in the field of artificial intelligence within the principle of machine learning. Artificial neural networks have the ability to make machine decisions on the basis of classification, clustering, pattern recognition, estimation and optimization. YSA learns the problem given from the examples and decides using the information obtained when it encounters the examples that have never been seen before. The most important feature of the YSAs is that it can make inferences for different situations by using the experience gained by learning from information. YSAs consist of two stages: training and testing. In the first step, YSA is trained with training data. The network is then tested using test data to evaluate the performance of the trained YSA. The most important and laborious part of the method is the educational process of the network, which includes the presence of the most suitable values for weights in network architecture, which is a challenging optimization problem. [3,4]

Computer Aided Diagnostic Systems are mainly studied under the headings of image recognition, image segmentation and image analysis. Image is the process of perceiving and describing concretely where and what objects are in the world. This covers the points that we can perceive within the volume in which the image is located [5]. Image recognition is the ability of a computer-integrated device to detect features of objects contained in a digital material, such as an image. Image segmentation is the process of dividing an image into meaningful regions according to a specific application area. These meaningful regions should not overlap with each other and should show continuity within themselves according to a defining feature. These regions that emerge as a result of segmentation are called segments. Therefore, improving segmentation is of great importance for automatic vision [6].

Grayness level, texture feature, color information, striation and continuity can be taken as determining features in image segmentation. If RGB (Red_Green_Blue) color is taken, the process is repeated three times. However, the gray level can provide enough information for an image [7]. The segmentation process is used in every area of the automatic view. Yaman et al., the gray level images of the passengers waiting at the station in the Ankara High Speed Rail System, detected by the

cameras used for security purposes in the system, were transferred to the computer environment, and then the objects were separated from the background by image segmentation processes.

The images of the separated objects were clarified by image enhancement methods and the number of passengers in the station was determined from the image histogram [8]. Image analysis, on the other hand, are the methods in which the threshold values of the methods are examined by using the Fuzzy C-Means (FCM), Herbaceous Method, Region Growing and Self-Organizing Maps (SOM) methods. The explanations about these methods are discussed in detail in the next sections of the study. The aim of this study is to calculate the area of the tumor region through the successful method after determining which of the Fuzzy C Means (FCM), Herbaceous Method, Region Growing and Self-Organizing Maps (SOM) methods are more successful in the analysis of MR images.

In the area calculation, it was determined that the area where the tumor and brain fluids appeared as white dots. Brain fluid pushes segmentations used in tumor area calculations to miscalculate. For this reason, while calculating the tumor region, the brain fluids appearing as white dots were completed by point filling. Moreover, after the tumor region was detected, the area of this region was determined spatially using Watershed, Graph-Cut and Active Counter segmentations. It is aimed to determine the stage of the tumor by using the detected area.

2. MATERIALS AND METHODS

In this study, MR images were first collected for examination. Collected MR images were collected on the basis of image quality in T1 and T2 sequences. An image database was created with the collected MR images [9]. In this database, a database was created using 40 MR images of 40 different patients, 20 males and 20 females. MR images can be taken in DICOM format. After the captured format, two-dimensional images were converted into data sets.

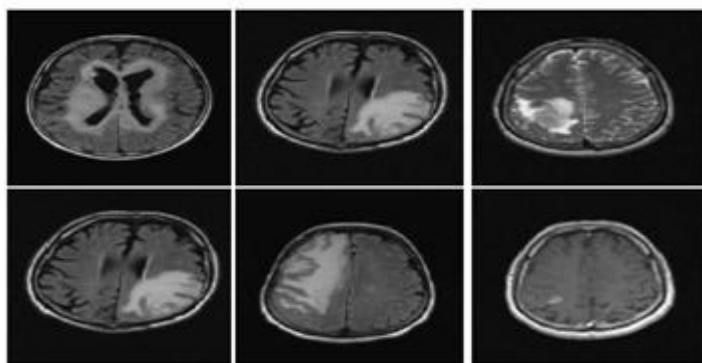


Figure 1. Brain mri images.

Image segmentation methods, one of the image processing methods, should be used in order to detect

the tumor region in the obtained MR images. Among these methods, Fuzzy C-Means (FCM), Herbaceous Method, Region Growing and Self-Organizing Maps (SOM) were used separately to determine the best image section and the result was compared.

2.1. Fuzzy C-Means (FCM)

The Fuzzy C-Means (FCM) algorithm was introduced by Dunn in 1973 and was developed by Bezdek in 1981 [10]. This method is frequently used in image processing, clustering and segmentation [11]. FCM, a widely used algorithm for image segmentation, uses an objective function based on a weighted similarity criterion between the pixels in the image and each segment center forming the image. It performs segmentation by dividing the resulting image into two or more clusters. The fuzzy c-mean formula is as in Eq. 1.

$$W_m(U, V) = \sum_{k=1}^n \sum_{i=1}^c (u_{ik})^m (d_{ik})^2 \quad (1)$$

Here, the fuzzy membership value of the k.ci pixel in the i.ci clump indicates the distance of the perpendicular k.ci pixel from the i.ci clump center.

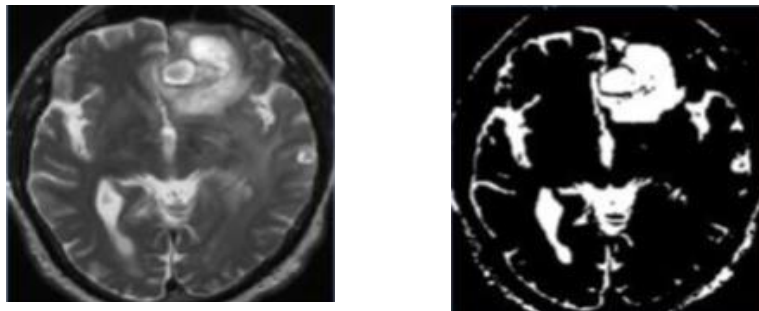


Figure 2. Fuzzy c mean mr image segmentation.

2.2. Region Growing

Region Augmentation Method is an approach used in image segmentation in which a corner is included in a region class if no corner is detected as a result of the evaluation of a pixel with neighboring pixels [12]. This process is iteratively executed for each border in the region. The method first starts by selecting a seed pixel point on a specific region of the image. Then, the region is enlarged by testing the similarity of neighboring pixels to the selected seed pixel in terms of color, intensity and brightness. The first pixel/pixel group is determined manually or automatically on the image. By calculating a similarity value between the initial seed pixel and the new/candidate pixel, if the new pixel is smaller than this similarity value, it is included in the region.

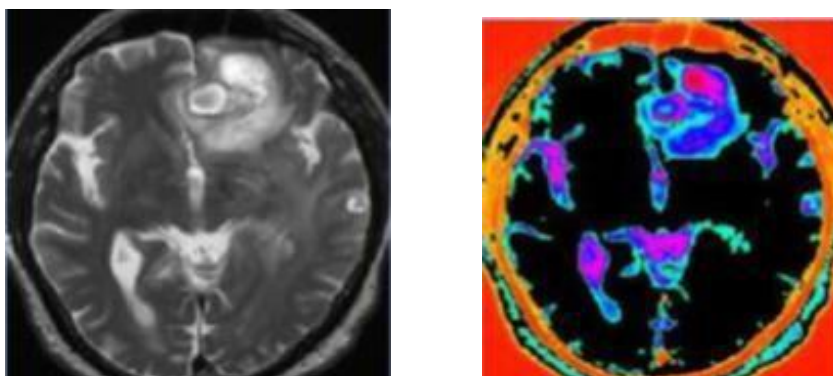


Figure 3. Region magnification mr image segmentation.

2.3. Self-Organizing Maps (SOM)

Self-Organizing Maps (SOM) are a special form of artificial neural networks and an unsupervised learning method developed by Kohonen [13]. It is frequently preferred in applications such as image segmentation, classification and clustering [14]. In its basis, there is a process of converting very large inputs to small-sized inputs, and size reduction is applied. This application takes place in 2 stages. In the 1st stage, competitive learning is carried out and the system is self-training. In the second stage, mapping is done to reduce the incoming input and the output is transferred to the system with correct mapping.

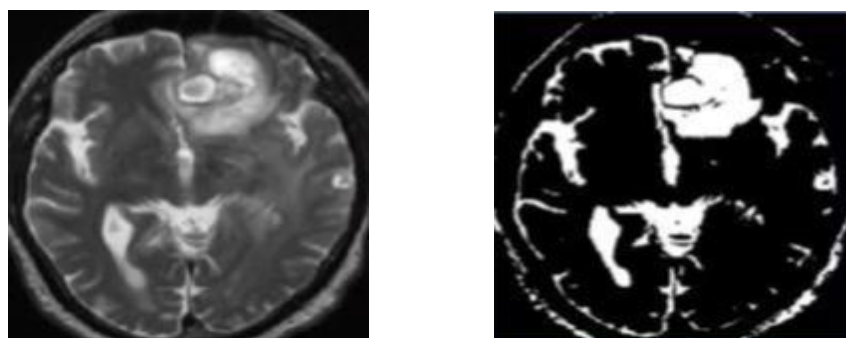


Figure 4. Som mr image segmentation.

2.4. Herbaceous Method

Herbaceous Method is one of the image segmentation methods applied on gray levels. Herbaceous Method is very effective on the images that have a bimodal histogram. However, it is difficult to segment an image that has overlapped regions [15]. In this method, it is assumed that the image consists of two parts. Part 1 contains the background colors of the image, and part 2 contains the foreground colors of the image. Then, the threshold value of the background and foreground colors is

calculated and their variance value is revealed. The threshold value that ensures the variance value to take the lowest value is selected. According to the selected threshold value, the image is converted to a binary image and image segmentation is completed. In this method, a histogram of colors is used.

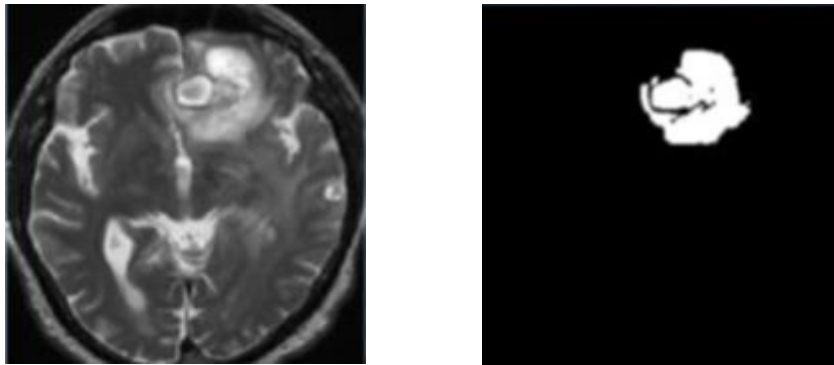


Figure 5. Herbaceous method mr image segmentation.

3. EXPERIMENTAL STUDIES AND EVALUATION

In order to perform thresholding, the image must be read by the algorithm and the histogram must be obtained. With the histogram, the lower and upper borders of the image must be established [16]. The algorithm used generates the threshold values randomly between the determined limits. The threshold values created must be sequential. After the threshold value calculations were made, the fitness values of the functions were determined. The solution archive set is created by combining the applied solution values until the function fitness values are determined. An iterative loop is created to construct the algorithm steps.

In the loop, the algorithm updates the threshold values for an optimum segmentation and executes the algorithm, and a balanced solution set is created. It can choose between expert solutions using algorithms. Four methods used to separate the images obtained from MR images and to find the tumor region were examined, and as a result of the examinations, using the Fuzzy C Mean (FCM) method for the detection of the tumor region was found to be more successful in the detection of the tumor region. Two parts that needed improvement in this study drew attention. First, as a result of the Fuzzy C Mean (FCM) method used, the tumor areas and the parts where the brain fluid remains are shown in white in the final image. The method is unable to separate the brain fluid from the tumor region while separating it. Secondly, tumor stages cannot be determined since the calculation of the size of the tumor area cannot be made with the Fuzzy C Mean (FCM) method. However, if the cross-sectional area of the tumor area could be utilized, the determination of tumor stages would be easier. For this reason, in this study, basically these methods were tried to be developed.

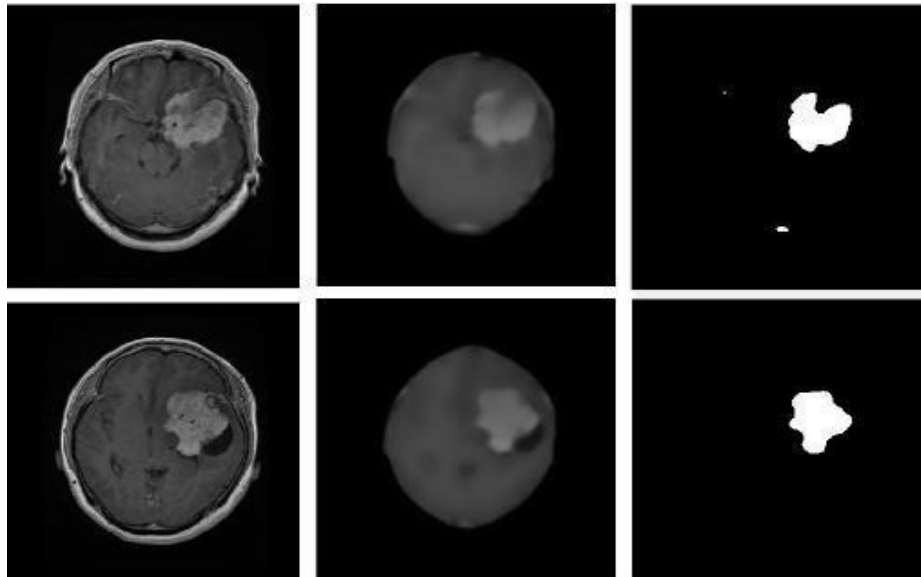


Figure 6. Brain tumor and brain fluid imaging by methods.

Threshold values, cluster numbers and similarity coefficients of jaccard and dice values of Single threshold, Multiple Herbaceous threshold, K-means, Fuzzy C-means segmentations were determined one by one by changing the index codes in the software and these were tabulated. These index values are needed to extract brain fluid from the brain tumor area.

Table 1. Threshold values and similarity indices of the methods.

	Threshold Value	Jaccard	Dice	
Single Threshold	1 (233)	0.8549	0.9217	
	1 (245)	0.8406	0.9134	
	Number of Thresholds	Number of Clusters	Jaccard	Dice
Very Grassy Threshold	7	8	0.8395	0.9128
	4	5	0.8067	0.8930
	10	11	0.8549	0.9217
	Number of Clusters	Jaccard	Dice	
K-means	6	0.8534	0.9209	
	8	0.8551	0.9219	
	10	0.8580	0.9236	
	Number of Clusters	Jaccard	Dice	

Fuzzy C-means	0.79	0.82	0.79
----------------------	------	------	------

In all trials, the highest similarity index was found in the K-means ten cluster numbered segmentation. In general, K-means and Very Grassy Threshold gave very close results. As an algorithm, it has a simple algorithm. It separates our tumor image into ten clusters according to their color in my best algorithm. In the prepared algorithm, the tumor image is in cluster no. An algorithm that removes other clusters was designed and only tumor image was obtained.

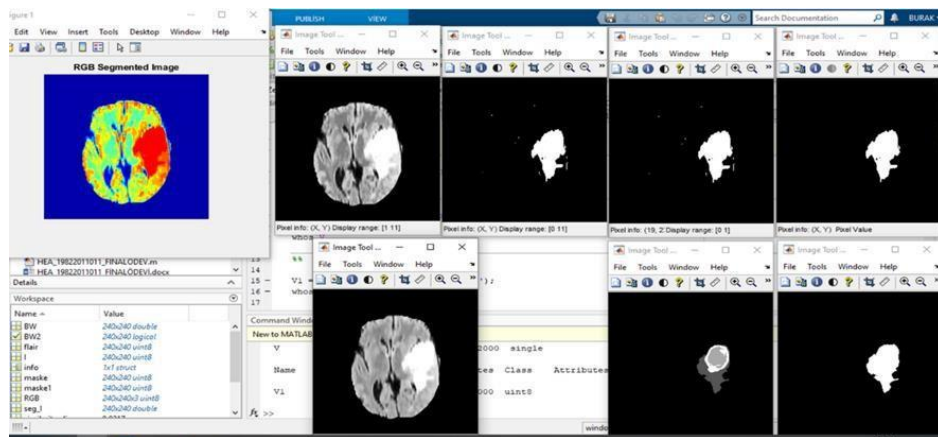


Figure 7. Detection of tumor area in mr images.

Tumor areas with brain fluid are shown in white. The white parts shown as dots in this study show the brain fluid. Finally, a tumor image was obtained by using an algorithm to fill in unwanted small spots.

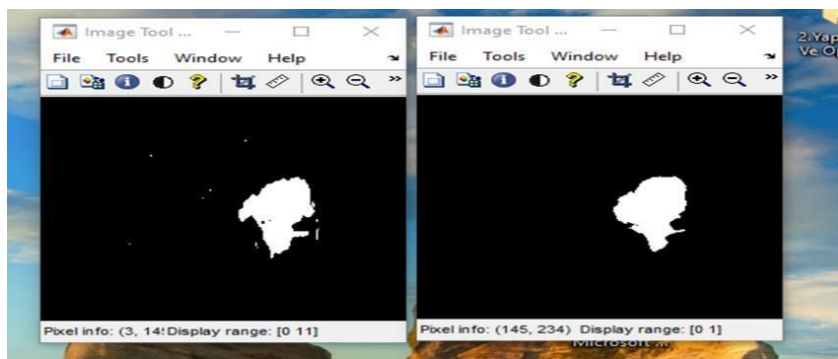


Figure 8. Algorithm for separating brain fluid from the tumor area.

Table 2. Tumor area calculation algorithms.

	Required Remarks Parameter Values	Jaccard	Dice
watershed	840 from the cluster 579.	0.8339	0.9094
graph-cut	254 from the cluster 238.	0.7834	0.8785
active counter	30 iteration	0.4863	0.6544

The image in the area, centroid and rectangle after the Watershed segmentation is as follows;

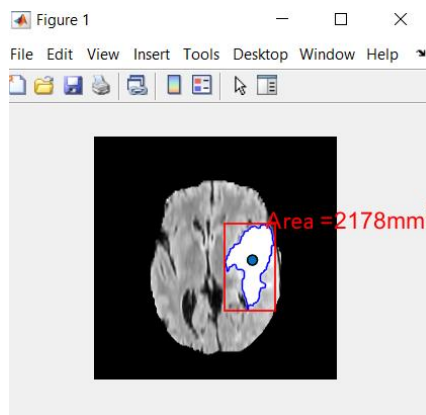


Figure 9. Watershed segmentation area.

The image in the area, centroid and rectangle after Graph-cut segmentation is as follows;

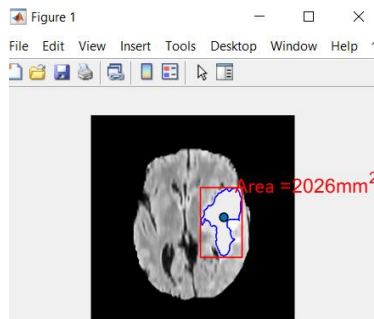


Figure 10. Graph-cut segmentation area.

Active counter codes are taken from the official site of MATLAB. The mask was adjusted around the tumor area and the number of iterations was found by experimenting.

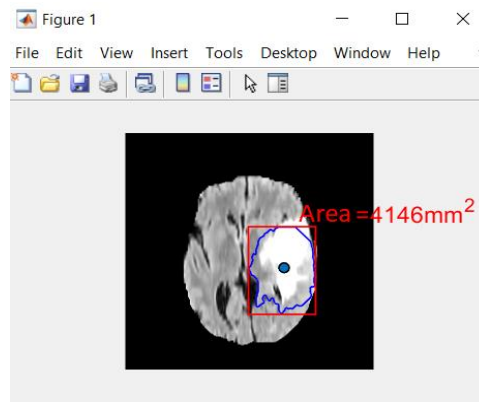


Figure 11. Active counter segmentation area.

Then, the accuracy rate was found with the best tumor image masked with jaccard and dice. After these procedures, the features of the shape of the tumor in which it is best found in the image were taken and the surrounding area was drawn. Then the smallest rectangle that will surround it is drawn and the center point is marked. The area of the tumor image was found to be mm², and they were all plotted and printed on the first plain tumor image.

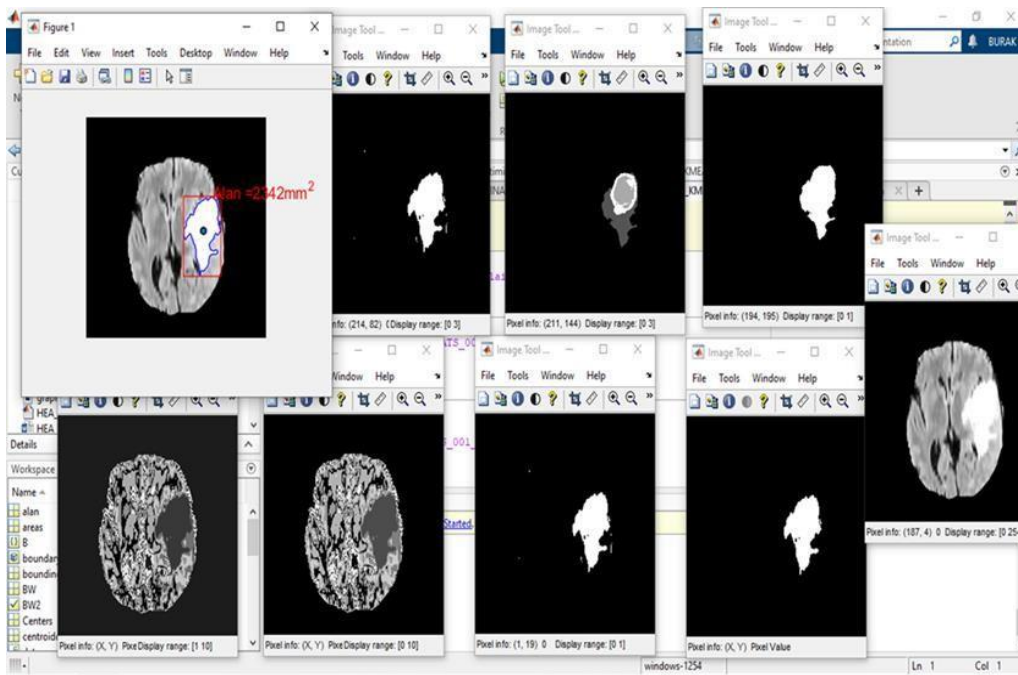


Figure 12. Process steps of brain tumor.

4. CONCLUSION

It has been determined that there are some deficiencies in the Herbaceous Method and FCM methods when their software is examined. One of them is that the brain fluids enter the white color area as in the tumor region, so the algorithm detects the brain fluid as a tumor, this deficiency will cause doctors to be wrong in determining the tumor stage and will cause wrong calculations as it will shift the central point in tumor area calculations. An algorithm that removes other clusters was designed and only tumor image was obtained. Finally, a tumor image was obtained by using an algorithm to fill in unwanted small spots.

The other point that is seen as a deficiency is that the tumor area cannot be calculated after the brain fluid is distinguished. In this regard, three segmentations were used. The accuracy rate was found by finding jaccard and dice values from watershed, graph-cut, and active counter segmentations. After these procedures, the tumor was drawn around by taking the features of the shape that he found best in the image. Then the smallest rectangle that will surround it is drawn and the center point is marked.

The area of the tumor image was found to be mm^2 , and they were all plotted and printed on the first plain tumor image. It has been shown that the developed software can be used as a tool for physicians to determine the location of the tumor at the brain tumor point, how much the tumor has spread, how

much area it has, and what stage the tumor has reached. As a future development, training time can be shortened by adding new models to feature extraction.

5. DISCUSSION

In this study, in order to detect the brain tumor area on MR images, the Fuzzy C-Means (FCM), Herbaceous Method, Region Growing and Self-Organizing Maps (SOM) methods were used and the threshold values of the methods were examined and the best method that distinguishes the brain tumor from the other parts of the brain. method was tried to be determined. Herbaceous and FCM methods differentiate tumors more successfully than the other two methods (region augmentation and SOM).

ACKNOWLEDGEMENT

I would like to express my endless thanks to my esteemed advisor Asst. Prof. Yusuf UZUN, who shared his valuable information in the realization of this study, and to my dear wife, Bilgehan İYİĞÖREN KAPUSIZ, who did not spare me a moment of help throughout my study, who faced all the difficulties with me during my study and supported me at every stage of my life.

REFERENCES

- [1] Şimşek, A. B. and Dicle, A. (2013), Primer beyin tümörü: klinik özellikler, tedavi ve bakım, Dokuz Eylül Üniversitesi Hemşirelik Yüksekokulu Elektronik Dergisi, 6 (2), 102-113.
- [2] Dandıl, E, Çakıroğlu, M. and Elşi, Z. (2015), Computer-aided diagnosis of malign nad benign brain tumors on mr images, Advances in Intelligent Systems and Computing, 3(11), 155-166.
- [3] Tümer, E. A., Edebalı, S. and Gülcü, Ş. (2020), Modeling of removal of chromium (vi) from aqueous solutions using artificial neural network, Iranian Journal of Chemistry and Chemical Engineering, 39(1), 163-175. Doi: 10.30492/ijcce.2020.33257.
- [4] Gülcü, Ş. (2022), An improved animal migration optimization algorithm to train the feed-forward artificial neural networks, Arabian Journal for Science and Engineering, 47(2022), 9557-9581. Doi: 10.1007/s13369-021-06286-z.
- [5] Castelman, R.K. (1994), Digital image processing, 1st Eddition, Prentice Hall, Englwood Cliffs, New Jersey, USA.
- [6] Bulut, M. and İstanbullu, A. (2004), Bulanık c-ortalama (fcm) algoritmasına dayalı yeni görüntü bölütleme sisteminin geliştirilmesi, Teknoloji, 7(3), 361-367.
- [7] Pal, R.N. and Pal, S. K. (1993), A review on image segmentation techniques, Pattern Recognition, 26(9),1277-1294.

- [8] Yaman, K., Sarucan, A., Atak, M. and Aktürk, N. (2001), Dinamik çizelgeleme için görüntü işleme ve arama modelleri yardımıyla veri hazırlama, Gazi Üniversitesi Mühendislik Mimarlık Fakültesi Dergisi, 16(1), 19-40.
- [9] <https://paperswithcode.com/dataset/brats-2018-1>. (Erişim Tarihi: Şubat, 2022).
- [10] Aslantaş, A, Dandıl, E and Çakiroğlu, M, (2014), Detection of bone metastases using fcm and edge detection algorithm, International Journal of Information and Electronics Engineering, 4(6), 423-427.
- [11] http://home.dei.polimi.it/matteucc/Clustering/tutorial_html/cmeans.html. (Erişim Tarihi: Aralık, 2021).
- [12] Kamdi, S. and Krishna, R.K. (2008), Image segmentation and region growing algorithm, International Journal of Computer Technology and Electronics Engineering (IJCTEE), 2(1), 13-25.
- [13] [13] Kohonen, T. (2001), Self-Organizing Maps, 3rd Edition, Springer.
- [14] Dandıl, E, Çakiroglu, M, Eksi, Z, Ozkan, M, Kurt, O.K. and Canan, A. (2014), Artificial neural network- based classification system for lung nodules on computed tomography scans, In Soft Computing and Pattern Recognition (SoCPaR), 6th International Conference of IEEE, 382-386.
- [15] Karakoyun, M., Gülcü, Ş. and Kodaz, H. (2021), D-MOSG: Discrete multi-objective shuffled gray wolf optimizer for multi-level image thresholding, Engineering Science and Technology, An International Journal, 24(2021), 1455-1466.
- [16] Darga, S., Evirgen, H., Çakiroğlu, M. and Dandıl, E. (2014), BT görüntüleri üzerinde pankreasın bölge büyütme yöntemi ile yarı otomatik segmentasyonu, International Conference and Exhibition on Electronic, Computer and Automation Technologies (ICEECAT 14), May 9-11, Konya, Turkey, 55- 58.



RESEARCH ARTICLE

ANTIMICROBIAL ACTIVITY of (*E*)-3-(4-SULFAMOYLPHENYL CARBAMOYL)
ACRYLIC ACID DERIVATIVES

Halil İLKİMEN^{1*}, Cengiz YENİKAYA², Aysel GÜLBANDILAR³

^{1*}Kütahya Dumlupınar University, Faculty of Art and Sciences, Department of Chemistry, Kutahya,
halil.ilkimen@dpu.edu.tr, ORCID: 0000-0003-1747-159X,

²Kütahya Dumlupınar University, Faculty of Art and Sciences, Department of Chemistry, Kutahya,
cengiz.yenikaya@dpu.edu.tr, ORCID: 0000-0002-5867-9146

³Eskişehir Osmangazi University, Faculty of Agricultural Engineering, Department of Food Engineering, Eskişehir,
aysel.gulbandilar@ogu.edu.tr, ORCID: 0000-0001-9075-9923

Receive Date: 06.06.2022

Accepted Date: 28.03.2023

ABSTRACT

In this study, proton transfer salts {(Hap)⁺(samal)⁻ (**4**) and (HBI)⁺(samal)⁻ (**5**)} were synthesized from the reaction of (*E*)-3-(4-sulfamoylphenylcarbamoyle)acrylic acid (Hsamal, **1**) with 1*H*-benzimidazole (BI, **3**) or 2-aminopyridine (ap, **2**), metal complexes of **1** {Fe(II) {[Fe(samal)(H₂O)₂][Fe(OH)₃(H₂O)] (**6**) and [(H₂O)(OH)₂Fe(samal)Fe(H₂O)₂] (**7**)}, Co(II) {[Co(samal)(H₂O)₂] (**8**)}, Ni(II) {[Ni(samal)₂(H₂O)₂] (**9**)} and Cu(II) {[Cu(samal)₂(H₂O)₂] (**10**)}, of **4** {Ni(II) {[Ni(samal)(OH)₂(ap)(H₂O)₂] (**11**)}, Cu(II) {[Cu(samal)(OH)(ap)₂] (**12**)} and of **5** {Co(II) {[Co(samal)(OH)₂(BI)₂] (**13**)}, Ni(II) {[Ni(samal)(OH)₂(BI)₂] (**14**)} and Cu(II) {[Cu(samal)(OH)₂(BI)₂] (**15**)} by the methods found in the literature. Antimicrobial activities of **1-15** and metal salts {iron(II) sulfate heptahydrate (**16**), cobalt(II) acetate tetrahydrate (**17**), nickel(II) acetate tetrahydrate (**18**) and copper(II) acetate dihydrate (**19**)} against *Enterococcus faecalis* (ATCC 29212) (Gram positive), *Pseudomonas aeruginosa* (ATCC 27853), *Bacillus subtilis* (wild type), *Staphylococcus aureus* (NRRL B-767), *Listeria monocytogenes* (ATCC 7644), *Escherichia coli* (ATCC 25922) (Gram negative) and *Candida albicans* (ATCC 14053) (yeast) microorganisms has been tested. The MIC (Minimum Inhibitory Concentration) values of **1-19** were compared with those of reference antimicrobial compounds Vancomycin, Cefepime, Levofloxacin and Fluconazole. Compounds with the best activity are **12** (15.60 µg/mL) for *C. albicans*, **1** and **2** (31.25 µg/mL) for *B. subtilis*, **13** (31.25 µg/mL) for *E. faecalis*, **13** (15.60 µg/mL) for *S. aureus*, **4** and **12** (15.60 µg/mL) for *E. Coli*, **3** and **8-12** (31.25 µg/mL) for *L. monocytogenes*, and **8** (31.25 µg/mL) for *P. aeruginosa*.

Keywords: 3-(4-sulfamoylphenylcarbamoyle)acrylic acid, 2-Aminopyridine, Salt, Metal Complexes, Antimicrobial activity

1. INTRODUCTION

Proton transfer reactions are unique among numerous chemical processes in which a proton is transferred from one binding site to another, either intermolecularly or intramolecularly. These only involve the transport of a nucleus without any auxiliary electrons. Such reactions can occur without serious disorder in the bonding electrons and without introducing repulsive forces between the non-bonding electrons [1]. Proton transfer is one of the most fundamental processes that plays an important role in many biochemical and chemical reactions [2,3]. Recently, research on proton transfer has been mainly focused on catalytic reactions [4], crystal engineering [5,6], energetic materials [7-9], organic ferroelectrics [10,11], hydrogen storage [12-15], nonlinear optical materials [16,17] and pharmaceutical industry [18,19]. Proton transfer is also known as an important step in many biochemical processes [20-24]. Aromatic/aliphatic carboxylic acids and aromatic/aliphatic bases are generally used in the synthesis of proton transfer salts. In these reactions, the proton of the acid is transferred by the base to form compounds with (+) and (-) charges. These compounds are water-soluble compounds [25].

The biological activity of (*E*)-3-(4-sulfamoylphenylcarbamoyl) acrylic acid (**1**) derivatives are known such as antimicrobial activity [26], dielectric properties [27], anti-inflammatory [28] and antiglaucoma [29,30]. In the literature, proton transfer salts of **1** with 2-aminopyridine [30], 1*H*-benzimidazole [30], 3-aminopyridine, 2-amino-4/5/6-methylpyridines [31] and Ni(II), Co(II), Cu(II) and Fe(II) metal complexes of **1** have been synthesized.

Nowadays, it becomes useless because bacteria that cause diseases gain resistance to the chemicals used in the treatment of diseases. Therefore, there is a need for new chemicals obtained in an effective and inexpensive way to eliminate microorganisms harmful to human health [32-36]. Finding that the compounds obtained in this study have antimicrobial activity against bacteria and yeasts will shed light on future studies. It is obvious that proton transfer salts obtained from 3-(4-sulfamoylphenylcarbamoyl) acrylic acid and its derivatives with antifungal and antibacterial activity and other organic ligands will show similar properties in co-crystal and mixed ligand metal complexes [26-30].

In this study, proton transfer salts **4** and **5** were synthesized from the reaction of 3-(4-sulfamoylphenylcarbamoyl) acrylic acid (**1**) with 2-aminopyridine (**2**) or 1*H*-benzimidazole (**3**), simple metal complexes (**6-10**) of **1** and metal complexes (**11-15**) of salts by the methods found in the literature. Antimicrobial activities of **1-15** and metal salts (**16-19**) against *E. faecalis* (Gram +), *B. subtilis* (wild type), *L. monocytogenes*, *E. coli*, *P. aeruginosa*, *S. aureus* (Gram -) and *C. albicans* (yeast) microorganisms has been tested. The MIC values of the **1-19** were compared with those of control compounds Vancomycin, Cefepime, Levofloxacin and Fluconazole.

2. EXPERIMENTAL

2.1. Materials and Methods

This study, maleic anhydride, sulphanilamide, 2-aminopyridine, 1*H*-benzimidazole, iron(II) sulfate heptahydrate, cobalt(II) acetate tetrahydrate, nickel(II) acetate tetrahydrate and copper(II) acetate dihydrate were obtained from Sigma Aldrich.

2.2. Synthesis of 4-15.

The compounds (**4-15**) were synthesized and characterized by methods found in the literature [30, 31]. The structures of **1-15** are given in Figure 1.

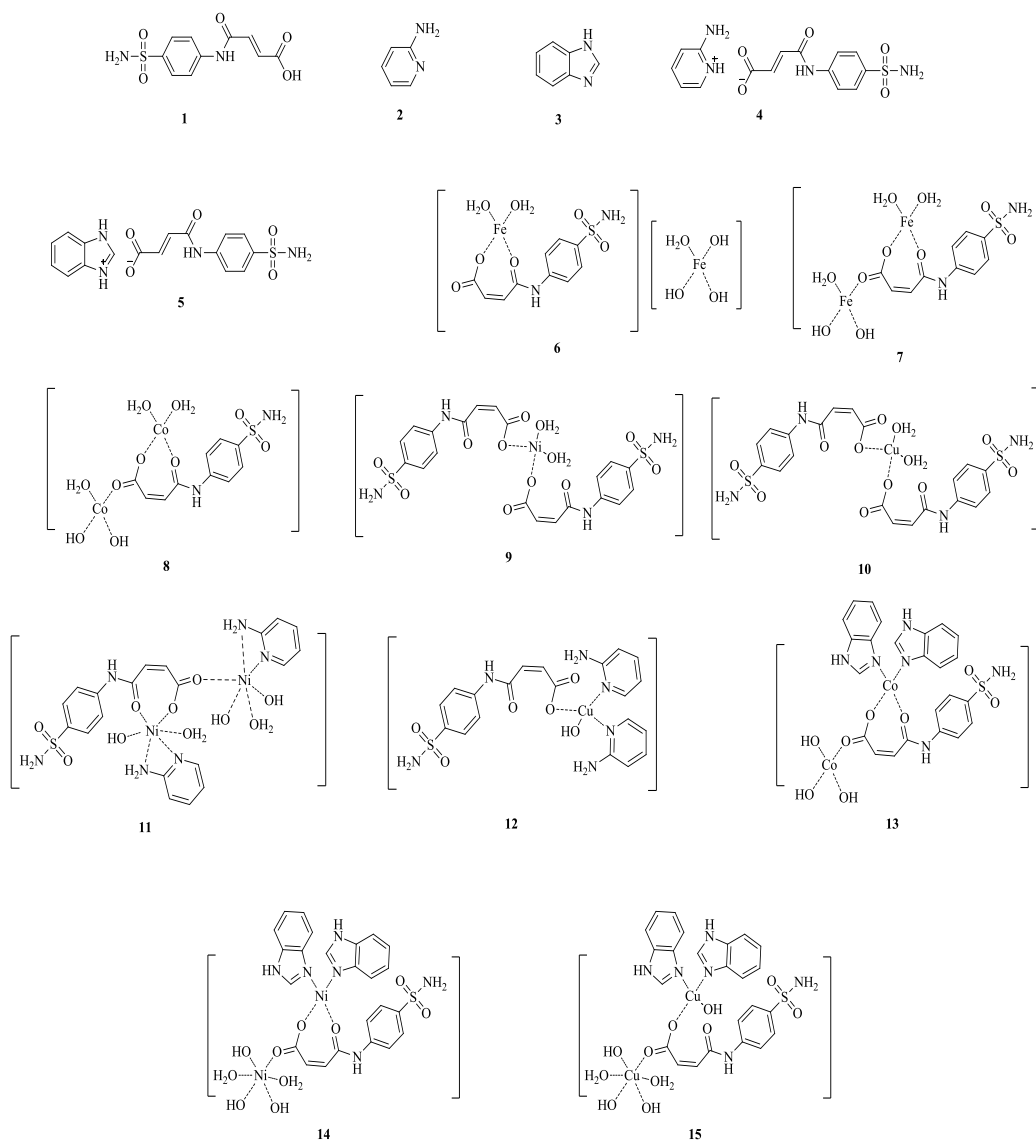


Figure 1. Structures of 1-15.

2.3. Antimicrobial Assay

E. coli (ATCC 25922) and *E. faecalis* (ATCC 29212) has been obtained from Eskişehir Osmangazi University, Faculty of Medicine and *S. aureus* (NRRL B-767), *B. subtilis*, *P. aeruginosa* (ATCC 27853), *L. monocytogenes* (ATCC 7644) and *C. albicans* (ATCC 14053) from Eskişehir Technical

University, Biology Department. Microdilution susceptibility test was used to evaluate the antimicrobial activities of **1-19**.

2.3.1. Microorganism

Microbroth dilution susceptibility test was used for antimicrobial analysis of the compounds [37]. MHB medium was prepared as single and double force. The **1-19** and reference antimicrobial compounds (4 mg) were dissolved in 2 mL of DMSO solution. The fungal and bacterial species used were incubated overnight on single-strength MHB medium and their fresh cultures were prepared. Suspensions of the cultures were prepared, and cell densities were adjusted to 0.5 Mc Farland tube turbidity { 1.0×10^8 CFU/mL} [38,39].

3. RESULTS AND DISCUSSION

3.1. Antifungal and Antibacterial Activities of Compounds

In this work, antifungal and antibacterial activity of all compounds (**1-19**) were tested by microdilution method. MIC values of **1-19** are given in Table 1. **1-19** were observed to have antibacterial and antifungal activity properties. The antifungal and antibacterial activity results obtained are in agreement with similar studies in the literature [26,27,40-43].

Against *C. albicans* yeast species, the compounds **12** (15.60 $\mu\text{g/mL}$), **7** and **13-15** (31.25 $\mu\text{g/mL}$) showed a higher effect than the control compound Fluconazole (62.50 $\mu\text{g/mL}$) while other compounds (except **5**, **8**, **16**, and **19**) had similar effects with Fluconazole. The compounds **5**, **8**, **16**, and **19** (125.00 $\mu\text{g/mL}$) showed less activity than Fluconazole.

Against *E. faecalis* bacteria, compound **13** was more effective than Vancomycin and Levofloxacin while the other compounds (except **3**, **8**, and **10**) had similar effects with Vancomycin and Levofloxacin (62.50 $\mu\text{g/mL}$). The compounds **3**, **8**, and **10** (125.00 $\mu\text{g/mL}$) showed less activity than Vancomycin and Levofloxacin. The compound **13** (31.25 $\mu\text{g/mL}$) had similar effects with Cefepime while other compounds showed less activity (62.50-125.00 $\mu\text{g/mL}$) than Cefepime.

Against *B. subtilis* bacteria, all compounds were found to have higher activity than the Vancomycin. It was determined that compounds **1** and **2** (31.25 $\mu\text{g/mL}$) had the highest activity against bacteria. The compounds **1** and **2** were more effective than Levofloxacin and Cefepime while the other compounds (except **10**) had similar effects with Levofloxacin and Cefepime. The compound **10** (125.00 $\mu\text{g/mL}$) showed less activity than Levofloxacin and Cefepime.

Against *S. aureus* bacteria, the compounds **1**, **2**, **4-9**, **12**, and **15-18** were determined to have similar effects (62.50 $\mu\text{g/mL}$) with Cefepime while the compounds **3**, **10**, and **11** showed less activity (125.00 $\mu\text{g/mL}$) than Cefepime. The others compound **13** (15.60 $\mu\text{g/mL}$), **14**, and **19** (32.25 $\mu\text{g/mL}$) were more effective than Cefepime. The **14** and **19** (31.25 $\mu\text{g/mL}$) were determined to have similar effects with Levofloxacin and Vancomycin while other compounds showed less activity (62.50-125.00 $\mu\text{g/mL}$) than Vancomycin and Levofloxacin.

Against *E. coli* bacteria, compounds **4** and **12** (15.60 µg/mL) had higher activity than all control compounds. Compounds **1, 2, 5, 11, 15,** and **16** (31.25 µg/mL) for Vancomycin and Levofloxacin and **3, 6, 9, 10, 13, 14,** and **17-19** (62.50 µg/mL) for Cefepime have similar effects with control compounds.

Against *L. monocytogens*, all compounds had higher activity than Vancomycin. The **3** and **8-12** were determined to have similar effects (31.25 µg/mL) with Levofloxacin and Cefepime while the other compounds showed less activity than Levofloxacin and Cefepime.

Against *P. aeruginosa* bacteria, the compound **8** showed a higher effect (15.60 µg/mL) than the control compounds. The compounds **1-5, 7, 10,** and **13-19** were determined to have similar effects (62.50 µg/mL) with Vancomycin while the compound **11** showed similar activity (31.25 µg/mL) than Levofloxacin and Cefepime. The compounds **6** and **9** showed less activity (125.00 µg/mL) than all the control compounds.

Table 1. Antibacterial and antifungal activity values (µg/mL) of compounds

Compound	<i>C. albicans</i>	<i>B. subtilis</i>	<i>E. faecalis</i>	<i>S. aureus</i>	<i>E. coli</i>	<i>L. monocytogens</i>	<i>P. aeruginosa</i>
Cefepime	Not tested	62.50	31.25	62.50	62.50	31.25	31.25
Vancomycin	Not tested	250	62.50	31.25	31.25	125.00	62.50
Levofloxacin	Not tested	62.50	62.50	31.25	31.25	31.25	31.25
Fluconazole	62.50	Not tested	Not tested	Not tested	Not tested	Not tested	Not tested
1	62.50	31.25	62.50	62.50	31.25	62.50	62.50
2	62.50	31.25	62.50	62.50	31.25	62.50	62.50
3	62.50	62.50	125.00	125.00	62.50	31.25	62.50
4	62.50	62.50	62.50	62.50	15.60	62.50	62.50
5	125.00	62.50	62.50	62.50	31.25	62.50	62.50
6	62.50	62.50	62.50	62.50	62.50	62.50	125.00
7	31.25	62.50	62.50	62.50	125.00	62.50	62.50
8	125.00	62.50	125.00	62.50	125.00	31.25	15.60
9	62.50	62.50	62.50	62.50	62.50	31.25	125.00
10	62.50	125.00	125.00	125.00	62.50	31.25	62.50
11	62.50	62.50	62.50	125.00	31.25	31.25	31.25
12	15.60	62.50	62.50	62.50	15.60	31.25	62.50
13	31.25	62.50	31.25	15.60	62.50	62.50	62.50
14	31.25	62.50	62.50	31.25	62.50	62.50	62.50
15	31.25	62.50	62.50	62.50	31.25	62.50	62.50
16	125.00	62.50	62.50	62.50	31.25	62.50	62.50
17	62.50	62.50	62.50	62.50	62.50	62.50	62.50
18	62.50	62.50	62.50	62.50	62.50	62.50	62.50

19	125.00	62.50	62.50	31.25	62.50	62.50	62.50
-----------	--------	-------	-------	-------	-------	-------	-------

4. CONCLUSIONS

All compounds (**1-19**) showed antimicrobial activity against *S. aureus*, *E. faecalis*, *B. subtilis*, *E. coli*, *C. albicans*, *L. monocytogenes* and *P. aeruginosa* microorganisms. **1-19** with the best activity are **12** (15.60 µg/mL) for *C. albicans*, **1** and **2** (31.25 µg/mL) for *B. subtilis*, **13** (31.25 µg/mL) for *E. faecalis*, **13** (15.60 µg/mL) for *S. aureus*, **4** and **12** (15.60 µg/mL) for *E. Coli*, **3** and **8-12** (31.25 µg/mL) for *L. monocytogenes* and **8** (15.60 µg/mL) for *P. aeruginosa*. In general, metal complexes showed better activity results than proton transfer salts and starting materials.

ACKNOWLEDGEMENT

This work was supported by Kütahya Dumlupınar University Research Foundation (Grant No: 2013/36 and 2019/12) and was carried out at the Chemistry Department of same University.

REFERENCES

- [1] Gupta, S. K. S., (2016). Proton transfer reactions in apolar aprotic solvents. *Journal of Physical Organic Chemistry*, 29, 251–264.
- [2] Armentano, D., De Munno, G., Mastropietro, T. F., Julve, M., and Lloret, F. (2005). Intermolecular proton transfer in solid phase, a rare example of crystal-to-crystal transformation from hydroxo-to oxo-bridged iron (III) molecule-based magnet. *Journal of the American Chemical Society*, 127, 10778–10779.
- [3] Root, M. J., and MacKinnon, R. (1994). Two identical noninteracting sites in an ion channel revealed by proton transfer. *Science*, 265, 1852–1856.
- [4] Gerlits, O., Wymore, T., Das, A., Shen, C. H., Parks, J. M., Smith, J. C., Weiss, K. L., Keen, D. A., Blakeley, M. P., Louis, J. M., Langan, P., Weber, I. T., and Kovalevsky, A. (2016). Long-range electrostatics-induced two-proton transfer captured by neutron crystallography in an enzyme catalytic site. *Angewandte Chemie International Edition*, 55, 4924–4927.
- [5] Moghimi, A. Alizadeh, R., Shokrollahi, A., Aghabozorg, H., Shamsipur, M., and Shokravi, A. (2003). First anionic 1,10-phenanthroline-2,9-dicarboxylate containing metal complex obtained from a novel 1,1 proton-transfer compound, Synthesis, characterization, crystal structure, and solution studies. *Inorganic Chemistry*, 42, 1616–1624.
- [6] Nichols, D. A., Hargis, J. C., Sanishvili, R., Jaishankar, P., Defrees, K., Smith, E. W., Wang, K. K., Prati, F., Renslo, A. R., Woodcock, H. L., and Chen, Y. (2015). Ligand-induced proton transfer and low-barrier hydrogen bond revealed by x-ray crystallography. *Journal of the American Chemical Society*, 137, 8086–8095.

- [7] Shimizu, G. K, Taylor, J. M., and Kim, S. (2013). Proton conduction with metal-organic frameworks. *Science*, 341, 354–355.
- [8] Yoon, M., Suh, K., Natarajan, S., and Kim, K. (2013). Proton conduction in metal–organic frameworks and related modularly built porous solids. *Angewandte Chemie International Edition*, 52, 2688–2700.
- [9] Bolton, O., and Matzger, A. J. (2011). Improved stability and smart-material functionality realized in an energetic cocrystal. *Angewandte Chemie International Edition*, 50, 896–8963.
- [10] Horiuchi, S., and Tokura, Y. (2008). Organic ferroelectrics. *Nature Materials*, 7, 357–366.
- [11] Horiuchi, S., Kumai, R., and Tokura, Y. (2007). A supramolecular ferroelectric realized by collective proton transfer. *Angewandte Chemie International Edition*, 46, 3497–3501.
- [12] Lototsky, M. V., Tolj, I., Davids, M. W., Klochko, Y. V., Parsons, A., Swanepoel, D., Ehlers, R., Louw, G., Westhuizen, B., Smith, F., Pollet, B. G., Sita, C., and Linkov, V. (2016). Metal hydride hydrogen storage and supply systems for electric forklift with low-temperature proton exchange membrane fuel cell power module. *International Journal of Hydrogen Energy*, 41, 13831–13842.
- [13] Adamson A., Guillemin J.C., and Burk P. (2015). Proton transfer reactions of hydrazine-boranes. *Journal of Physical Organic Chemistry*, 28, 244–249.
- [14] Spry, D. B., and Fayer, M. D. (2009). Proton transfer and proton concentrations in protonated Nafion fuel cell membranes. *The Journal of Physical Chemistry B*, 113, 10210–10221.
- [15] Cochlin, D. (2014). Graphene’s promise for proton transfer in fuel cell membranes. *Fuel Cells Bulletin*, 2014, 12-12.
- [16] Asselberghs, I., Zhao, Y., Clays, K., Persoons, A., Comito, A., and Rubin, Y. (2002). Reversible switching of molecular second-order nonlinear optical polarizability through proton-transfer. *Chemical Physics Letters*, 364, 279–283.
- [17] Jayanalina, T., Rajarajan, G., Boopathi, K., and Sreevani, K. (2015). Synthesis, growth, structural, optical and thermal properties of a new organic nonlinear optical crystal, 2-amino-5-chloropyridinium-*L*-tartarate. *Journal of Crystal Growth*, 426, 9–14.
- [18] Bica, K., Shamshina, J., Hough, W. L., MacFarlane, D. R., and Rogers, R. D. (2011). Liquid forms of pharmaceutical co-crystals, exploring the boundaries of salt formation. *Chemical Communications*, 47, 2267–2269.
- [19] Steed, J. W. (2013). The role of co-crystals in pharmaceutical design. *Trends in Pharmacological Sciences*, 34, 185–193.

- [20] Chen, K. (2000). Atomically defined mechanism for proton transfer to a buried redox centre in a protein. *Nature*, 405, 814–817.
- [21] Chen, K. Y., Lai, C. H., Hsu, C. C., Ho, M. L., Lee, G. H., and Chou, P. T. (2007). Ortho green fluorescence protein synthetic chromophore; excited-state intramolecular proton transfer via a seven-membered-ring hydrogen-bonding system. *Journal of the American Chemical Society*, 129, 4534–4535.
- [22] Luecke, H., Richter, H. T., and Lanyi, J. K. (1998). Proton transfer pathways in bacteriorhodopsin at 2.3 angstrom resolution. *Science*, 280, 1934–1937.
- [23] Heberle, J., Riesle, J., Thiedemann, G., Oesterhelt, D., and Dencher, N. A. (1994). Proton migration along the membrane surface and retarded surface to bulk transfer. *Nature*, 370, 379–382.
- [24] Dellago, C., and Hummer, G. (2006). Kinetics and mechanism of proton transport across membrane nanopores. *Physical Review Letters*, 97, 245901.
- [25] Aghabozorg, H., Sadrkhanlou, E., Shokrollahi, A., Ghaedi, M., and Shamsipur, M. (2009). Synthesis, characterization, crystal structures, and solution studies of Ni(II), Cu(II) and Zn(II) complexes obtained from pyridine-2,6-dicarboxylic acid and 2,9-dimethyl-1,10-phenanthroline, *Journal of the Iranian Chemical Society*. 6(1), 55-70.
- [26] Bapna, S., Hiran, B. L., and Jain, S. (2015). Antimicrobial evaluation of maleimide monomers, homopolymers and copolymers containing azo, sulfonamide and thiazole groups. *Journal of Advances In Chemistry*, 11(1), 3404-3415.
- [27] Erol, I. (2022). Synthesis and characterization of novel sulfonamide functionalized maleimide polymers, Conventional kinetic analysis, antimicrobial activity and dielectric properties. *Journal of Molecular Structure*, 1255, 132362.
- [28] Jan, M. S., Ahmad, S., Hussain, F., Ahmad, A., Mahmood, F., Rashid, U., Abid, O. R., Ullah, F., Ayaz, M., and Sadiq, A. (2020). Design, synthesis, in-vitro, in-vivo and in-silico studies of pyrrolidine-2,5-dione derivatives as multitarget anti-inflammatory agents. *European Journal of Medicinal Chemistry*, 186, 111863.
- [29] Oktay, K., Kose, L. P., Sendil, K., Gultekin M. S., Gulcin, I., and Supuran, C. T. (2016). The synthesis of (Z)-4-oxo-4-(arylamino)but-2-enoic acids derivatives and determination of their inhibition properties against human carbonic anhydrase I and II isoenzymes. *Journal of Enzyme Inhibition and Medicinal Chemistry*, 31(6). 939-945.
- [30] Yenikaya, C., İlkimen, H., Demirel, M. M., Ceyhan, B., Bulbul, M., and Tunca, E. (2016). Preparation of two maleic acid sulfonamide salts and their copper(II) complexes and antiglaucoma activity studies, *Journal of the Brazilian Chemical Society*, 27(10). 1706-1714.

- [31] İlkimen, H., and Yenikaya, C. (2022). Synthesis and characterization of proton salts of aminopyridine derivatives and (*E*)-3-(4-sulfamoylphenylcarbamoyl)acrylic acid. *Sinop University Journal of Science*, 7(1), 57-70.
- [32] Parekh, J., and Chanda, S. (2007). Antibacterial and phytochemical studies on twelve species of Indian medicinal plants, *African Journal of Biomedical Research*, 10, 175-181.
- [33] Palaniappan, K., and Holley, R. A. (2010). Use of natural antimicrobials to increase antibiotic susceptibility of drug resistant bacteria. *International Journal of Food Microbiology*, 140, 164-168.
- [34] Kumar, A. S., Venkateshwaran, K., Vanitha, J., Saravanan, V. S., Ganesh, M., Vasudevan, M., and Sivakumar, T. (2008). Synergistic activity of methanolic extract of *Thespesia populnea* (Malvaceae) flowers with oxytetracycline. *Bangladesh Journal of Pharmacology*, 4, 13-16.
- [35] Uymaz, B. (2010). Probiotics and Their Use. *Pamukkale University Journal of Engineering Sciences*, 16(1), 95-104.
- [36] Topal, M., Şenel, G. U., Topal, E. I. A., Öbek, E. (2015). Antibiotics and usage areas. *Journal of Erciyes University Institute of Science and Technology*, 3(3), 121-127.
- [37] Khan, R., Dogan, Ö., and Güven, K. (2020). N-Substituted aziridine-2-phosphonic acids and their antibacterial activities. *Organic Communications*, 13(2), 51-56.
- [38] Kaplancıklı, Z. A., Turan-Zitouni, G., Özdemir, A., and Güven K. (2004). Synthesis and study of antibacterial and antifungal activities of novel 2-[[[(benzoxazole/benzimidazole2yl)sulfanyl] acetyl amino]thiazoles. *Archives of Pharmacal Research*, 27(11), 1081-1085.
- [39] Kaplancıklı, Z. A., Turan-Zitouni, G., Özdemir, A., Revial, G., and Güven K. (2007). Synthesis and antimicrobial activity of some thiazolyl-pyrazoline derivatives. *Phosphorus, Sulfur, and Silicon and the Related Elements*, 182(4), 749-764.
- [40] İlkimen, H., Yenikaya, C., Gülbandılar, A., and Sarı M. (2016). Synthesis and characterization of a novel proton salt of 2-amino-6-nitrobenzothiazole with 2,6-pyridinedicarboxylic acid and its metal complexes and their antimicrobial and antifungal activity studies. *Journal of Molecular Structure*, 1120, 25-33.
- [41] İlkimen, H., Türken, N., and Gülbandılar, A. (2021). Synthesis, characterization, antimicrobial and antifungal activity of studies of two novel aminopyridine-sulfamoylbenzoic acid salts and their Cu(II) complexes. *Journal of the Iranian Chemical Society*, 18, 1941–1946.
- [42] İlkimen, H., Salün, S. G., Gülbandılar, A., and Sarı, M. (2022). The new salt of 2-amino-3-methylpyridine with dipicolinic acid and its metal complexes: Synthesis, characterization and antimicrobial activity studies. *Journal of Molecular Structure*, 1270, 133961.

- [43] Büyükkıdan, N., İlkimen, H., Bozyel, S., Sarı, M., and Gülbandılar, A. (2023). The syntheses, structural and biological studies of Co(II) complexes of 1,2-bis(pyridin-4-yl)ethane with 2-aminobenzene-1,4-disulfonic acid and 2,6-pyridinedicarboxylic acid. *Journal of Molecular Structure*, 1275, 134586.



RESEARCH ARTICLE

INVESTIGATION OF SOME UNIVARIATE NORMALITY TESTS IN TERMS OF TYPE-I ERRORS AND TEST POWER

Sevda KORKMAZ¹, Yıldırım DEMİR^{2*}

¹ Van Yüzüncü Yıl University, Institute of Science, Department of Statistics, Van, tekirdagsevda@gmail.com,
ORCID: 0000-0001-8247-4645

² Van Yüzüncü Yıl University, Faculty of Economics and Administrative Sciences, Department of Statistics, Van,
ydemir@yyu.edu.tr, ORCID: 0000-0002-6350-8122

Receive Date: 22.12.2022

Accepted Date: 27.03.2023

ABSTRACT

In this study, Shapiro-Wilk, Kolmogorov-Smirnov, Skewness, Kurtosis, Lilliefors, Jargue-Bera and D'Agostino -Pearson tests, which are univariate normality tests, were compared in point of type-I error and power performances. For comparisons, samples were created in various distributions and sample volumes by simulation technique, and the probability of type-I error was taken as 0.05 in comparisons. Thus, it is aimed to determine the best test to check whether the normality condition is met in univariate data. As a result of the comparison, it was determined that the Jargue-Bera test gave better results than the other tests in point of type-I error probability. In addition, when the normality tests examined in all distributions were taken into account and compared, it was concluded that the Shapiro-Wilk gives better results than other tests in general for normal and non-normal distributions, and that D'Agostino -Pearson, Skewness and Jargue-Bera tests were also stronger than the other tests. In addition, it was determined that the increase in sample sizes increased power of the test. In conclusion, it can be said that in addition to the distribution pattern, type-I error probability and sample size are also very important factors for test power.

Keywords: *Univariate normality tests, Type-I error, Power of test*

1. INTRODUCTION

In order to apply statistical analysis correctly, it is necessary to know the dataset distribution. In cases where the assumptions of the normal distribution are met, one of the assumptions of the parametric statistical tests is also met. For this reason, it should be determined whether the data of the sample studied show a normal distribution. Because the expected benefits from the tests to be used are related to whether the normality assumption is fulfilled. For this reason, the assumption of normality should be checked before the data are analyzed in order for the results obtained by statistical methods to reflect the real situation [1]. Normality tests are basically divided into two as univariate and multivariate.

To ascertain whether the data exhibit normal distribution, numerous univariate normality tests have been created and extensively studied. To ascertain whether the data has a normal distribution, numerous normality tests are employed. Researchers use these tests to determine whether the data come from a normal distribution [2]. However, it has been an important issue to know which of these tests can be used as the most effective method for the control of the normality prerequisite. For this reason, univariate normality tests should be compared in terms of type-I error and test power under different experimental conditions, and the performances of these tests should be measured under the same conditions. Which of these tests used has the higher power and whichever gives the same level of type-I error at the end of the experiment, the test in question should be preferred in testing whether the assumption of normality is met [3].

In this study, Shapiro-Wilk (SW), Kolmogorov-Smirnov (KS), Skewness, Kurtosis, D'Agostino-Pearson (DP), Lilliefors and Jargue-Bera (JB) tests, which are univariate normality tests, are compared in terms of power performance and type-I error. In order to make the said comparisons, normal, symmetrical and different curvature sample distributions were created in different sample sizes with the simulation technique, and the tests were compared using these data sets. In the comparisons made, the probability of type-I error was taken as 0.05 and the tests were compared according to 10000 simulation results using the Python programming language. Comparisons were made by taking sample sizes of 10, 20, 25, 30, 40, 50, 70, 100, 150. Thus, the effects of different sample sizes on the tests are also observed. As a result, before the statistical calculations of the univariate data, the normality test was selected by taking into account the sample size of the available data to check whether the normality prerequisite was met.

The aim of this study is to compare some univariate normality tests in terms of type I error and test power in data sets with different sample sizes and distributions.

2. MATERIAL AND METHOD

It is known that the Monte Carlo technique provides excellent dimensional control and has good power in generating data [4]. For this reason, this technique is used in the simulation study for the comparison of the tests. Since the simulation results for the sample and alternative distributions vary at different levels, the data are derived according to different sample sizes and distributions [2]. Thus, the effects of sample size and data distribution on the tests are observed.

Kurtosis, Skewness, SW, KS, DP, Lilliefors and JB tests, which are univariate normality tests, were compared in terms of type-I error and power performances. In the comparisons performed, the type-I error value was taken as 0.05. Data were derived from a normally distributed population with 50 mean and 5 standard deviations, taking into account different sample sizes. Each normality test statistic was calculated for all 10000 samples created by simulation, and the rejection numbers of the basic hypothesis were counted for each test and then these numbers were converted to %. In addition, different skewness (α_3) and kurtosis (α_4) values and type-I error rates were examined.

In order to compare the power of the specified univariate normality tests, non-normal Chi-Square, Uniform, t and Beta distributions were also used in addition to the normal distribution.

2.1. Type-I Error, Type-II Error and Power of Test

Basic idea of statistical hypothesis testing is to decide whether a sample of data comes from a population, assuming true a formulated hypothesis about the population.

When a sample is not typical of the population, generalizing from it to the whole population might result in inaccurate conclusions and interpretations. Rejecting an actually true hypothesis leads to a type-I error, and not rejecting an actually false hypothesis leads to a type-II error. Type-I (α) and type-II (β) errors can never be completely prevented, however by boosting sample numbers, error levels can be decreased. Because the larger the sample size, the better the population is represented and the less the difference between the population and the sample [5]. The α and β values are not independent of each other, and there is an inverse proportion between them. Since the increase in the sample size reduces the sampling error, both errors are minimized [6].

If the H_0 hypothesis is not true, H_0 rejecting is a correct decision. The rejection of the false H_0 hypothesis is defined as the power of the test ($1-\beta$), and the power of a test increases as the sample size increases [7].

2.2. Distribution Models

A probability distribution describes how the values of a random variable are distributed. Random variables in distributions are divided into two as continuous and discrete distributions in terms of the values they take. If the random variables have a probability of being in a certain interval and being continuous, the distribution is called continuous distribution. There are many continuous statistical distributions. Normal, chi-square, beta, t and uniform distribution are among these distributions [8].

2.2.1. Normal distribution

Of all distributions, the normal distribution is the most well-known and often utilized. The normal distribution, a hypothetical symmetrical distribution used for comparison, is actually a family of distributions and has the following properties.

In the standard normal distribution, the mode, mean and median are equal and curve symmetrical.

The total area under the curve is equal to 1.

The curve is bell-shaped.

The data are largely close to the mean. The data decreases with distance from the mean in both directions.

Almost all data (99.7%) fall within a range of ± 3 standard deviations from the mean [9].

The normal distribution depends on the mean and standard deviation, and the normal distribution is calculated by Eq. 1. For a sample of size n , with standard deviation σ and the population mean μ .

$$f(x) = \frac{1}{\sigma\sqrt{2\pi}} e^{-\frac{(x-\mu)^2}{2\sigma^2}} \quad (1)$$

The standard deviation serves as a measure for dispersion; the higher this value, the more spread out the curve. The mean, otherwise, is a measure of central tendency and determines the position of the normal distribution curve that it divides into two [9].

2.2.2. Chi-Square distribution

A chi-square random variable is defined as the sum of the squares of independently distributed standard normal random variables, describing the additive property of independent chi-square random variables [10].

Where x is a random variable and n is the degrees-of-freedom of the distribution, the Chi-Square Distribution's Probability Density Function is defined by Eq. 2 and the Cumulative Probability Density Function by Eq. 3 [11].

$$f(x) = \begin{cases} \frac{1}{\Gamma(\frac{n}{2})2^{n/2}} x^{\frac{n}{2}-1} e^{-x/2} & 0 < x < \infty \\ 0 & x \leq 0 \end{cases} \quad (2)$$

$$F(x) = \int_0^x \frac{1}{\Gamma(\frac{n}{2})2^{n/2}} x^{\frac{n}{2}-1} e^{-x/2} dx = 1 - \sum_{k=0}^{n-1} \frac{e^{-2x} 2^k x^k}{k!}, x > 0 \quad (3)$$

The sum of the squares of the values of the n -unit sample, independently selected from any main population with a normal distribution with a variance of 1 and an arithmetic mean of 0, expresses the chi-square distribution. Chi-square indicates a continuous value greater than or equal to zero.

For small degrees of freedom, the distribution is skewed to the right, and for large degrees of freedom, the distribution approaches a normal curve.

The chi-square tests whether the observed frequencies according to H_0 approach the calculated expected frequencies, and in general, the test statistic is calculated with Eq. 4.

$$\chi^2 = \sum_{i=1}^k \frac{(O_i - B_i)^2}{B_i} \quad (4)$$

Here O_i , is the observed frequencies and B_i , is the expected frequencies [12].

2.2.3. Beta distribution

The beta density function is a two parameter continuous density function defined in the range $0 \leq x \leq 1$. If x , which is a random variable, has a beta probability density distribution with the parameters α and β , the density function of x is given by Eq. 5.

$$f(x) = \begin{cases} \frac{x^{\alpha-1}(1-x)^{\beta-1}}{B(\alpha,\beta)}, & 0 \leq x \leq 1 \\ 0, & \text{Other cases} \end{cases} \quad (5)$$

Here, the value of $B(\alpha, \beta)$ represents the gamma function (Γ) and is calculated with Eq. 6 [13].

$$B(\alpha, \beta) = \int_0^1 x^{\alpha-1}(1-x)^{\beta-1} dx = \frac{\Gamma(\alpha)\Gamma(\beta)}{\Gamma(\alpha+\beta)} \quad (6)$$

2.2.4. t distribution

One of the key characteristics of the t distribution, which has many uses in mathematical statistics, is that the distribution approaches the normal distribution as sample sizes approach infinity [14]. For a given sample size or degree-of-freedom, the set of all t values measured from each possible random sample gives the t-distribution. The parameters μ and σ are meaningful descriptive measures that locate the center and describe the spread associated with a random variable x.

The test statistic for the n -size t distribution with sample mean \bar{x} , standard deviation s, population mean μ is given with Eq. 7 [15].

$$t = \frac{\bar{x}-\mu}{\frac{s}{\sqrt{n}}} \quad (7)$$

2.2.5. Uniform distribution

The simplest form of continuous probability distribution is uniform probability distribution. If the random variable x takes every value with the same probability in a given interval, the distribution is uniform. The uniform distribution, which takes values in a certain range, is defined by the parameters a and b. It can be said that a random variable x has a uniform probability distribution in the range [a, b], with a minimum and b maximum value [16]. Thus, the probability density function of x is represented by Eq. 8 and the cumulative distribution function by Eq. 9.

$$f(x) = \begin{cases} \frac{1}{(b-a)} & a \leq x \leq b \\ 0 & \text{Other cases} \end{cases} \quad (8)$$

$$F(x) = \int_{-\infty}^x \frac{1}{b-a} dx = \begin{cases} 0, & x < a \\ \frac{x-a}{b-a} & a \leq x < b \\ 1, & x \geq b \end{cases} \quad (9)$$

The expected values for the mean and variance of a random uniform variable are calculated with Eq. 10 and Eq. 11.

$$E(X) = \int_a^b x \frac{1}{b-a} dx = \frac{1}{b-a} \left(\frac{x^2}{2} \Big|_a^b \right) \Rightarrow \mu = \frac{b+a}{2} \quad (10)$$

$$Var(X) = E(X^2) - (E(X))^2 = \frac{1}{3}(b^2 + ab + a^2) - \frac{(a+b)^2}{4} = \frac{(b-a)^2}{12} \quad (11)$$

In addition to being used to create random numbers from other distributions, the uniform distribution can also be used as a "first guess" if just the random variable x 's range between a and b is known. Additionally, a uniform distribution can be used to describe the probability behavior of such a phenomenon in real-world problems with smooth behavior within a particular range [15].

2.3. Univariate Normality Tests

The majority of frequently employed statistical techniques are predicated on the idea that the data are normally distributed. In order to obtain more reliable and accurate results from the studies, it is important to determine whether the normalcy assumption is provided [17]. Normality assumption can be checked in two ways, graphical and analytical methods. While graphical methods for normality test show the distribution of data with various graphs, analytical methods include many different statistical test solution methods using mathematical models [18].

As a result of all statistical tests, a probability (p) value of the test statistics is calculated. The p value in statistical analysis determines whether a test becomes significant. A p -value over the significance level in one study implies that the data set is normally distributed, and the higher the value, the more sensitive the statistic utilized in comparison to the other studies [18]. In general, hypotheses regarding tests are established as follows.

H_0 : The sample is drawn from a population with a normal distribution.

H_1 : The sample is not drawn from a normally distributed population.

2.3.1. Shapiro-Wilk test

The test was proposed by Shapiro and Wilk (1965) for testing the assumption of normal distribution. By dividing the square of an appropriate linear component of the sample rank statistics by the sum of squares, the SW test statistic is calculated [19]. SW test statistic is calculated with Eq. 12.

$$SW = \frac{(a'x)^2}{(n-1)s^2} = \frac{(\sum_{i=1}^n a_i x_i)^2}{\sum_{i=1}^n (x_i - \bar{x})^2} \quad (12)$$

Here, it is denoted by $a' = (a_1, a_2, \dots, a_n) = \frac{m'V^{-1}}{(m'V^{-1}V^{-1}m)^{1/2}}$. While $V = V_{ij}$ represents the $n \times n$ dimensional covariance matrix, $m' = (m_1, m_2, \dots, m_n)$ represents the vector of expected values of n rank statistics in the standard normal distribution $N(0,1)$. In addition, $x_i = (x_1, x_2, \dots, x_n)$ gives the arithmetic mean of the observations, \bar{x} gives the values of the observations ordered from the smallest to the largest of an n dimensional random sample with a normal distribution with a mean of 0 and a variance of 1 [19].

2.3.2. Skewness test

Skewness is used to determine the goodness of fit of the data by referring to a particular type of distribution. The skewness test is a measure that reflects the degree to which a distribution is asymmetrical. Distributions with long tails to the right are called positive curves and distributions with long tails to the left are called negative curves. The third moment of a distribution about the mean gives the measure of the skewness [20]. Accordingly, the skewness measure is calculated with Eq. 13.

$$m_3 = \frac{\sum_{i=1}^n (X_i - \bar{X})^3}{n} \quad (13)$$

Since m_3 is a third order value, the unitless statistics g_1 is generally used to indicate the curvature. g_1 is an estimator of the population parameter γ_1 and is calculated with Eq. 14. S is the sample standard deviation.

$$g_1 = \frac{m_3}{S^3} \quad (14)$$

When the skewness value is between -3 and +3, the distribution is symmetrical, and when this value is 0, the symmetrical distribution approaches a perfect distribution. If the value of g_1 is greater than 0, the distribution is skewed to the right, and less than 0 causes the distribution to be skewed to the left. Although the normal distribution is symmetrical, not all symmetrical distributions show normal distribution [20].

2.3.3. Kurtosis test

Kurtosis is often defined as a measure that reflects the degree to which a distribution reaches its peak. In other words, kurtosis gives information about the height of a distribution according to the standard deviation value, and the most important reason for measuring kurtosis is to determine whether the data are derived from a population with a normal distribution. Kurtosis is generally considered within the framework of three general categories: mesokurtic, leptokurtic, and platikurtic, all of which have representative frequency distributions. For normal distributions, the Kurtosis is called mesokurtic, if the Kurtosis is very high, it is called leptokurtic, and if it tends to be much broader, it is called platikurtic [20]. The kurtosis is calculated using certain quantitative values in the distribution, and the most effective kurtosis measure is obtained with the fourth moment relative to the mean. Thus, the kurtosis value, which is the fourth moment with respect to the mean, is calculated by Eq. 15.

$$m_4 = \frac{\sum_{i=1}^n (X_i - \bar{X})^4}{n} \quad (15)$$

Since the calculated value for m_4 is of the fourth order, the unitless statistics g_2 , which is an estimator of the population parameter γ_2 , is used to indicate the kurtosis and is calculated with Eq.16.

$$g_2 = \frac{m_4}{S^4} \quad (16)$$

When a distribution has a mesokurtic (normal) distribution, the value of g_2 equals 0. If the value of g_2 is significantly greater than 0, it creates a leptokurtic distribution and a small value creates a platikurtic distribution [20].

2.3.4. D'Agostino-Pearson test

D'Agostino and Pearson [21], D'Agostino [22] and Zar [23] demonstrated that the D'Agostino-Pearson test, proposed by D'Agostino and Pearson in 1973, is a very effective method for assessing fit to normal distribution. The D'Agostino-Pearson test statistic is based on the sum of the squares of the kurtosis and Skewness test statistics values and is calculated with Eq. 17 [20]. Here, $Z(\sqrt{b_1})$ shows the skewness test statistical value, while $Z(b_2)$ shows the kurtosis test statistical value. The hypotheses regarding the D'Agostino-Pearson test are established as follows.

H_0 : Sample distribution conforms to normal distribution

H_1 : Sample distribution is not suitable for normal distribution

$$\chi^2 = Z(\sqrt{b_1})^2 + Z(b_2)^2 \quad (17)$$

The D'Agostino-Pearson test is based on the χ^2 statistic, as it has a two-degrees-of-freedom chi-square ($\chi^2_{(2)}$) distribution. Thus, when $\chi^2 > \chi^2_{\alpha,2}$, the H_0 hypothesis is rejected [20].

2.3.5. Jarque-Bera test

Jarque-Bera test, which was proposed by Jarque and Bera in 1980 for testing normality in univariate data, is based on skewness and kurtosis tests. The Jarque-Bera test statistic is calculated using the skewness and kurtosis coefficients obtained from a (x_1, x_2, \dots, x_n) dataset assumed to be normally distribution [24]. If $\{x_1, x_2, \dots, x_n\}$ is assumed to be a randomly drawn sample from an independent population, the j th trigonometric moment with respect to the mean is calculated by Eq.18.

$$m_j = \frac{1}{n} \sum_{i=1}^n (x_i - \bar{x})^j \quad j = 2, 3 \quad (18)$$

Here; Since \bar{x} is the sample mean, $\hat{\sigma}^2$ can be written as m_2 . Thus, the skewness and kurtosis statistics are calculated with the JB test statistic Eq. 19, to be $\sqrt{b_1} = \frac{m_3}{\hat{\sigma}^3}$ and $b_2 = \frac{m_4}{\hat{\sigma}^4}$ respectively.

$$JB = n \left[\frac{(\sqrt{b_1})^2}{6} + \frac{(b_2-3)^2}{24} \right] \quad (19)$$

The JB test statistic has an asymptotic chi-square distribution with two degrees-of-freedom ($\chi^2_{(2)}$) under the assumption of normality [24].

2.3.6. Kolmogorov-Smirnov test

The Kolmogorov-Smirnov test was first proposed by Kolmogorov in 1933 as an alternative to the chi-square fit test and was revised by Smirnov in 1939. This test is based on the largest absolute difference between the expected and cumulative distribution functions [25]. In order to calculate the

values of the cumulative distribution function, the observation values of the sample are ordered from the smallest to the largest, as $x_1 < x_2 < \dots < x_n$. Then, Z values and their cumulative probabilities are calculated for these observation values. Thus, Kolmogorov-Smirnov (KS) test statistic for n ordered data is calculated with Eq. 20.

$$D = \max|F_o(X) - F_e(X)| \tag{20}$$

Here, $F_o(X)$ shows the observed cumulative frequency value of the variable X, while $F_e(X)$ shows the expected cumulative frequency value of the variable X.

2.3.7. Lilliefors test

Lilliefors test, which is a modification of the Kolmogorov-Smirnov goodness-of-fit test, is one of the best tests developed by Lilliefors (1967) and Van Soest (1967) and used to test the assumption of normality [26; 27]. In cases where the sample mean and variance are unknown and must be estimated from the population, Lilliefors table values obtained by Monte Carlo calculations are used to test whether this sample is drawn from a normal population [28].

This test of normality is stronger than other tests under many non-normal circumstances, according to Lilliefors (1967). In addition, according to Dagnelie (1968), an analytical formula can be used to estimate the critical values provided by Lilliefors [29]. This formula eliminates the risk of error when entering table values and facilitates the software of computer programs [26]. The observed distribution function of the n dimensional x_1, x_2, \dots, x_n random sample is $S_n(x)$ for each value of x and is defined by Eq. 21.

$$S(x) = \begin{cases} 0 & x < x_1 \\ \frac{i}{n} & x_{(i+1)} \\ 0 & x \geq x_n \end{cases} \quad i = 1, 2, \dots, (n - 1) \tag{21}$$

The vertical distance between the distribution function $S(x)$ and the theoretical distribution function $F(x)$ is denoted by D. The size of the differences in D results, which represents sampling errors, is used as a measure of conformity to the normal distribution [30].

$$D = \max. |S(x_i) - F(x_i)| \tag{22}$$

3. RESULTS

3.1. Comparison of Tests in terms of Type-I Error

In this study, 7 of the univariate normal distribution tests were examined and the performances of these tests were determined with data sets owner different sample sizes obtained by simulation. Analysis results for Type-I error values are given in Table 1.

In Table 1, when error values are taken as 0.05, it is seen that type-I error probabilities of test statistics are generally close to 5%. For all sample sizes, JB is the test with the lowest probability of type-I

error, that is, the probability of rejecting the H_0 hypothesis, regarding that these samples are drawn from a normally distributed population.

Table 1. Type-I error values for different sample sizes in normal distribution.

α	n	DP	Kurtosis	Skewness	SW	KS	Lilliefors	JB
0.05	10	5.77	4.38	5.04	5.03	5.14	5.06	0.91
	20	5.58	4.48	4.99	5.23	4.99	5.09	2.43
	25	5.69	4.72	5.06	4.87	5.28	5.12	2.78
	30	5.76	5.13	5.08	5.07	4.56	5.08	3.10
	40	5.99	5.17	5.05	5.24	5.70	5.45	3.61
	50	5.80	5.37	5.00	5.10	5.08	4.99	3.71
	70	5.02	5.08	4.92	4.89	5.25	3.74	3.60
	100	5.44	5.29	5.17	4.93	4.83	4.96	4.23
	150	5.41	5.58	4.81	4.95	4.81	4.48	4.44

In all sample sizes, it is determined that the type-I error probabilities of the JB test are less than 5% and has lower values than the other six tests. As the sample size increases, the probability of type-I error in the JB test also increases. When the sample size is $n \leq 25$, the JB test is followed by the kurtosis test, the KS test when it is 30 and 100, the skewness test when it is 40, and the Lilliefors test when it is 50, 70 and 150. In general, it can be said that type-I error values in the skewness test do not change much with the sample size and are generally around 5%.

Type-I error probabilities of DP test range from 5% to 6%, and highest type-I error probability is found to be 5.99% when $n = 40$. In addition, among these 7 tests, the highest probability of type-I error is obtained from the DP test for all sample sizes except $n = 70$ and 150. Type-I error probabilities in the KS, SW, and Lilliefors tests are generally around 5%, and the highest probability of type-I error in these three tests is obtained when the sample size is 40, and is found to be 5.70%, 5.24%, and 5.45%, respectively. In addition, the lowest probability value among these three tests, when $n = 70$, belongs to the Lilliefors test with a value of 3.74%, and this value is very close to the type-I error probability of the JB test for the same sample size.

The tests are compared in terms of type-I error rates the different skewness, kurtosis and in the sample sizes and the results are given in Table 2.

Table 2. Type-I error rate values for different skewness, kurtosis and sample sizes.

α	n	DP	Kurtosis	Skewness	SW	KS	Lilliefors	JB
$\alpha_3 = 0$ $\alpha_4 = 1$	10	5.72	3.66	5.24	4.94	4.72	4.67	1.01
	20	5.44	4.32	4.88	4.73	4.87	4.56	2.26
	25	5.49	4.48	4.76	4.76	4.68	4.62	2.81
	30	6.05	5.25	5.39	5.32	5.32	5.57	3.20
	40	5.71	4.94	4.93	5.00	4.72	5.04	3.32

	50	5.96	5.34	5.16	5.25	4.81	5.07	4.18
	70	5.58	5.35	4.97	4.94	5.20	3.22	3.75
	100	5.36	5.20	4.67	4.87	5.07	4.42	4.01
	150	5.53	5.36	5.16	5.02	5.34	2.96	4.65
$\alpha_3 = 0.05$ $\alpha_4 = 2.8$	10	5.68	3.82	5.07	4.81	4.82	4.62	0.86
	20	5.96	5.08	5.24	5.12	4.81	5.15	2.48
	25	6.32	5.45	5.48	5.57	5.21	4.74	3.23
	30	5.69	5.10	5.04	5.12	4.99	5.12	3.13
	40	5.54	5.29	4.77	4.99	4.93	4.95	3.17
	50	5.83	5.35	5.10	4.98	5.10	5.10	3.82
	70	6.37	5.58	5.49	5.08	4.80	3.52	4.34
	100	5.46	5.30	5.18	4.83	5.11	4.95	4.02
	150	5.45	4.92	5.19	5.07	5.16	3.13	4.42
$\alpha_3 = 0.05$ $\alpha_4 = 3.2$	10	5.90	3.91	5.09	4.85	5.11	5.04	0.83
	20	5.70	4.78	5.29	5.17	5.44	5.27	2.49
	25	5.40	4.74	5.02	4.93	5.10	5.08	2.65
	30	5.80	4.91	4.97	5.23	4.98	5.38	3.19
	40	5.71	5.18	5.04	5.24	5.01	5.24	3.44
	50	5.67	5.28	4.69	5.15	4.90	4.98	3.57
	70	5.57	5.60	4.75	5.31	4.95	3.30	4.00
	100	5.38	5.11	4.86	5.05	4.73	4.94	4.13
	150	5.48	5.19	5.11	5.24	5.69	3.46	4.33
$\alpha_3 = -0.05$ $\alpha_4 = 2.8$	10	6.04	4.21	5.28	4.96	4.96	4.84	0.83
	20	5.67	4.64	5.25	4.99	4.83	5.01	2.53
	25	5.59	4.67	4.57	4.78	5.31	4.93	2.43
	30	6.06	5.35	5.02	4.96	4.75	4.96	3.24
	40	6.05	5.43	5.15	5.25	5.30	4.96	3.71
	50	5.61	5.42	5.01	5.05	5.46	4.58	3.62
	70	5.92	5.75	4.85	5.11	5.23	3.24	4.04
	100	5.58	5.10	4.99	4.71	4.73	4.97	4.10
	150	5.26	5.23	4.87	5.14	4.76	3.25	4.44
$\alpha_3 = -0.05$ $\alpha_4 = 3.2$	10	6.42	4.32	5.75	5.05	4.73	5.45	0.75
	20	5.37	4.27	4.96	5.08	5.20	5.29	2.32
	25	5.40	4.40	4.98	4.8	4.88	5.26	2.63
	30	5.82	5.26	5.13	5.26	5.20	5.05	3.12
	40	5.50	5.35	5.06	5.04	5.07	5.14	3.47
	50	5.42	5.19	4.95	4.64	4.74	4.75	3.84
	70	5.93	5.78	5.22	5.27	4.90	3.30	4.15
	100	5.43	5.40	4.76	5.00	5.00	5.19	4.21
	150	5.31	5.35	4.76	4.75	4.92	3.46	4.08

When Table 2 is examined, it is observed that although the skewness and kurtosis values are changed, the normal distribution tests show similar behaviors to those in Table 1 in terms of type-I error rates and do not show significant differences from Table 1.

3.2. Comparison of Methods in terms of Power of Test

In order to compare the performance of the 7 tests in terms of power, data sets suitable for chi-square, beta, t and uniform distribution are generated and comparisons are made on these data sets.

Using chi-square distributions with various degrees of freedom, the comparison of univariate normality tests is looked at in terms of test power. Because the chi-square distribution approaches the normal as the degree of freedom grows [31]. Thus, the power values obtain from data sets with univariate 1 and 5 degrees of freedom (df) chi-square distributions in different sample sizes are given in Table 3.

When Table 3 is examined, it is seen that the test powers approach 100% with the increase in sample size in all samples drawn from a population with 1 degree of freedom chi-square distribution. It is seen that the SW test is stronger than the other tests in all sample sizes, the JB test is weaker when $n = 10$ and the kurtosis test is weaker when $n > 10$ than the other tests. The highest power value (99.99%) is reached when $n = 40$ with the SW test. When the sample size is $n \geq 25$, it was determined that the power performances of all the tests except the kurtosis were higher than 84%.

Table 3. Power values of the tests in the chi-square distribution (%).

$\alpha: 0.05$	n	DP	Kurtosis	Skewness	SW	KS	Lilliefors	JB
df=1	10	49.63	34.43	56.32	73.36	54.47	53.6	27.34
	20	80.78	55.26	89.49	98.29	86.29	88.27	71.89
	25	89.97	63.66	95.38	99.74	94.65	95.51	84.36
	30	94.14	70.23	98.07	99.93	99.88	98.12	92.15
	40	98.80	80.14	99.73	99.99	99.93	99.85	98.27
	50	99.88	86.89	99.97	99.99	99.99	99.99	99.79
	70	99.99	94.54	99.99	99.99	99.99	99.99	99.99
	100	99.99	98.56	99.99	99.99	99.99	99.99	99.99
df=5	150	99.99	99.87	99.99	99.99	99.99	99.99	99.99
	10	18.93	12.69	19.92	20.19	14.34	14.68	6.32
	20	35.59	21.15	41.32	45.15	24.19	28.11	24.99
	25	42.17	23.64	50.08	54.46	35.67	32.47	35.52
	30	48.46	26.19	58.78	64.30	37.91	32.21	39.99
	40	61.33	31.65	73.61	79.35	48.88	48.43	55.00
	50	72.77	36.67	83.75	89.26	59.82	59.73	68.43
	70	88.03	45.42	94.68	97.63	65.52	69.72	86.37
100	97.73	56.13	98.93	98.93	89.87	88.83	96.97	
150	99.96	69.02	99.96	99.99	97.79	96.57	99.95	

According to the results of the 5-degrees-of-freedom Chi-square distribution, it is observed that the test powers increased with the increase in sample size. In addition, it is determined that the SW test is more powerful than the other tests in all sample sizes. In general, the most powerful test after the SW test is the skewness test, followed by the DP test. The JB test is the weakest test when the sample size is 10, and the kurtosis test is the weakest for other sample sizes. In the same sample size, it can be said

that the SW test and the skewness test give closer values to each other. In addition, a parallelism is observed between the power values of the KS test and the Lilliefors test.

In Table 4, the power values of the normality tests used in data sets with different sample sizes (2, 5) and (1, 1) parameter Beta distributions are given.

Beta distribution with 1 and 1 parameters has a flat and symmetrical distribution with Kurtosis and skewness values, while beta distribution with 2 and 5 parameters has an asymmetric and vertical distribution [31]. In this study, the power performances of univariate normality tests are also examined in beta distributions at the specified parameter values. According to the results of beta distribution with 2 and 5 parameters given in Table 4, the SW test is more powerful than other tests in all sample sizes. When $n = 10$, KS is the strongest test after the SW test, while the SW test and SW are followed by the skewness test in other sample sizes. It is observed that the weakest test is the JB test when $n < 40$, and the kurtosis test for larger sample sizes. Also, after $n \geq 50$, the sample size hardly affect the power of the kurtosis test.

According to the results of 1 and 1 parameter beta distribution, it is seen that $n = 10$ the first two strongest tests are SW and kurtosis, respectively, and the strongest test is kurtosis when there is $n > 10$. The second strongest test following the kurtosis test is SW when $n < 30$ and DP when $n \geq 30$. At small sample sizes ($n \leq 50$) JB is the weakest test, while at larger sample sizes, especially when is $n \geq 100$, a huge improvement in the power of JB is seen and so, skewness becomes the weakest test. Also, when $n = 150$ the power performances of the kurtosis, DP, JB and SW tests approach 100%.

Table 4. Power values of normality tests in beta distributions (%).

$\alpha: 0.05$	n	DP	Kurtosis	Skewness	SW	KS	Lilliefors	JB
Beta (2.5)	10	7.99	5.47	7.91	8.98	8.16	7.64	1.54
	20	11.51	7.84	13.25	16.93	12.21	11.92	5.17
	25	13.51	8.86	16.31	21.46	13.45	13.66	6.27
	30	15.71	9.20	20.59	27.30	14.67	16.01	8.31
	40	19.29	9.84	26.48	38.08	19.18	20.60	11.32
	50	24.64	11.19	34.90	50.24	23.25	26.01	16.05
	70	37.24	11.63	50.75	71.23	43.58	30.14	27.15
	100	61.14	11.71	70.15	89.22	50.73	49.45	50.83
150	89.99	11.15	89.82	98.93	67.09	62.37	85.40	
Beta (1.1)	10	2.78	6.92	2.12	7.92	2.03	5.89	0.25
	20	14.78	29.36	0.72	19.83	5.02	9.64	0.10
	25	27.23	44.35	0.50	28.61	29.60	11.79	0.03
	30	39.36	56.86	0.32	37.99	33.31	14.41	0.01
	40	63.18	76.88	0.28	57.58	46.95	19.09	0.01
	50	80.76	88.91	0.25	75.52	57.70	26.39	0.01
	70	95.87	97.88	0.18	93.66	70.88	30.86	3.64
	100	99.78	99.91	0.23	99.65	85.14	58.65	56.60

150 99.99 99.99 0.15 99.99 93.94 75.08 98.64

As the degrees of freedom increase in the t distribution, the type-I errors get very large values and the distribution approaches the standard normal distribution [32]. In this study, power performances of univariate normality tests are also investigated with two different degrees of freedom t distributions. Power performances of normality tests for various sample sizes in t distributions with 10 and 5 degrees of freedom are given in Table 5.

According to the results of the 10-degrees-of-freedom t distribution given in Table 5, normality tests for all sample sizes perform quite poorly because the $t_{\alpha;10}$ distribution has a symmetrical and vertical distribution. When $n < 150$, the DP test gives the best results in terms of power performance. When the sample size is $n < 40$, the skewness test gives the best results after DP. The JB test, which performed poorly at first and even showed the worst performance when $n = 10$, generally gives the best results after DP when $n \geq 40$, and becomes the best test when $n \geq 150$. In addition, when $n > 10$, the worst performance belongs to Lilliefors and KS tests, respectively, and the power performances of these two tests were found to be very close to each other. Thus, it can be said that the kurtosis, DP and JB tests, which are the moment tests that can test the steepness, generally have better performances than the other tests.

Considering the inclination and kurtosis values of the 5-degrees-of-freedom t distribution, its $t_{\alpha;5}$ distribution is symmetrical and vertical. When the 5-degrees-of-freedom t distribution is examined, it is seen that all test statistics have weak power performances in all sample sizes. However, as the sample sizes increased, significant improvements occurred in the JB, kurtosis, DP and SW tests, albeit insufficiently, compared to the other tests, but even at high sample sizes ($n < 150$), the estimated test statistical power values remained below 70%. When $n \geq 150$, the most powerful tests are JB, kurtosis, DP and SW, respectively, the powers of these tests exceeded 71%. When $n < 70$, DP is the strongest test, and when $n \geq 70$, the most powerful test is the JB test. Although the weakest test varies according to the sample size, it is seen that the JB test is the weakest test when $n = 10$, and the KS test is generally the weakest in other sample sizes.

Table 5. Power values of the tests in t distribution (%).

$\alpha: 0.05$	n	DP	Kurtosis	Skewness	SW	KS	Lilliefors	JB
df=10	10	9.72	6.37	8.74	7.26	6.12	6.61	1.94
	20	12.58	9.65	11.20	9.70	7.32	6.86	7.66
	25	13.86	10.71	12.42	10.68	7.63	7.90	9.60
	30	15.57	12.07	13.64	11.72	7.98	7.68	11.83
	40	16.99	13.69	14.29	13.54	8.73	8.15	14.66
	50	19.41	16.14	15.74	15.63	8.81	8.60	17.73
	70	23.29	20.06	17.79	18.98	9.57	6.91	22.89
	100	26.91	24.73	18.80	22.63	10.81	10.20	20.21
150	34.08	33.70	21.30	22.91	11.63	9.52	37.59	
df=5	10	14.67	10.23	13.47	11.03	9.23	9.43	4.43
	20	23.18	18.88	20.79	19.08	10.46	13.46	16.63

25	26.73	22.01	23.69	22.21	13.11	14.44	21.27
30	29.68	25.01	25.15	24.97	13.86	16.23	25.35
40	35.34	31.01	28.99	30.55	16.98	18.69	32.90
50	39.24	36.46	30.80	34.80	20.66	21.25	38.70
70	49.02	46.76	36.38	45.37	23.57	21.75	50.30
100	60.35	60.12	40.52	56.33	32.77	33.37	63.27
150	73.74	75.37	44.58	71.23	43.26	38.15	77.69

The distribution of the data drawn from the uniform distribution has a symmetrical feature. The power performances of the tests at different sample sizes in uniform distribution are given in Table 6.

When Table 6 is examined, it is seen that the strongest test is skewness except for the case of $n = 10$, the second strongest test is SW in small sample sizes ($n < 30$), DP in larger sample sizes ($n \geq 30$). When $n = 150$, it is seen that the powers of the kurtosis, DP and SW tests approach 100%. In addition, the power of the JB test, which has the weakest power when $n < 70$, approached 100% in large sample sizes ($n = 150$). Again, although the skewness test performed very poorly and there is a slight improvement, not with the increase in the sample volumes, there is a decline in the test performance.

Table 6. Powers of normality tests in uniform distribution (%).

α	n	DP	Kurtosis	Skewness	SW	KS	Lilliefors	JB
0.05	10	2.83	7.47	1.97	8.67	5.65	6.36	0.21
	20	15.51	29.98	0.65	20.24	6.98	9.78	0.06
	25	27.22	43.90	0.36	28.78	9.67	12.2	0.02
	30	40.28	57.18	0.41	38.53	12.81	14.79	0.05
	40	62.82	76.78	0.39	57.80	19.09	20.96	0.02
	50	79.74	88.46	0.23	74.95	21.23	26.29	0.03
	70	95.81	98.13	0.19	94.00	39.08	30.95	3.60
	100	99.70	99.86	0.08	94.31	55.24	59.06	56.5
150	99.99	99.99	0.09	99.99	80.57	75.78	98.65	

4. DISCUSSION AND CONCLUSION

In this study, it is determined that the best results in terms of type-I error in different sample sizes are given by the JB test. The same results are obtained for normal distributions in the studies conducted by [33] and [3]. It is determined from the simulation results that the most powerful test for normal distributions is the skewness test by [2]. [34] is determined that the JB test is not a strong test in the chi-square distribution, similar results are obtained for $n=10$ in this study, and the kurtosis test is the weakest test for larger sample sizes. In this study, the lowest test power is obtained from the t distributions, especially the 10 degrees of freedom t distribution. [35] is stated that all tests have low power in the beta (2, 5) distribution and [33] in the t distribution. In this study, it is observed that SW is a strong test in general in non-normal distributions and the test power increased as the sample size increased. Similarly, [1] and [2] suggest SW for non-normally distributed distributions; [25], on the

other hand, states that although SW has low power in small sample sizes in normal and non-normal distributions, it is generally a powerful test.

[36] are compared the results of nine statistical procedures for normality assessment. They are stated that the SW test is more sensitive than many alternative tests used to test normality in small samples ($n < 20$). [37] compares some tests with the SW test at different distributions and sample sizes and tested their power performance for normality. it is stated that the Anderson-Darling (AD) test has a power close to the SW test and can be used as an alternative. [38] compared univariate normality tests using 20, 50, and 100 sample sizes in different distributions in terms of type-I error and test power, and found that the AD test is more powerful than the KS test. [39] compared the KS, SW, AD, and Lilliefors tests for test power. It is observed that the SW test is the strongest test of normality in normal and non-normal distributions, followed by the AD, Lilliefors and KS tests, respectively. In addition, it has been determined that these four tests have low power performance in small-sized samples.

With the Monte Carlo simulation study, univariate normality tests are examined in terms of type-I error value in samples taken from a normally distributed population. When the test results according to $\alpha = 0.05$ are compared, the JB test type-I error value remains well below 5%, and the type-I error value increases with the sample size, reaching a maximum of 4.44%. Type-I error probabilities of skewness, kurtosis, KS, SW, and Lilliefors tests ranged from 4.5-5.5% with small deviations, and generally close to 5%. However, although the DP test has high power values in general, type-I error rates could not maintain the 5% level and all values of type-I error rates are found to be between 5% and 6%, usually close to 6%. Type-I error probabilities of the kurtosis test, although they are slightly low at the beginning, increased slightly with the increase in the sample size, reaching over 5%. On the contrary, in the Lilliefors test, while type-I error probabilities are above 5% at the beginning, type-I error probabilities decreases to around 4.5% as the sample size increased.

In a 1-degree-of-freedom chi-square distribution, the power performances of the other tests except the kurtosis test exceed 80% when the sample size is at least 25, and this performance approaches 100% when the sample sizes are enlarged. Power performances above 80% for the other tests except the kurtosis test in the chi-square distribution with 5 degrees of freedom are obtained only when the sample size is 100. In chi-square distributions with 1 and 5 degrees of freedom, increasing the sample size increases the power performances of the normality tests, while increasing the degrees of freedom decreases the power performances of the normality tests.

It is seen that the power performances of the normality tests are low in small sample sizes in the 2 and 5 parameter beta distribution. So much so that when $n = 100$, only the SW test is over 80%, and when $n = 150$, the power performances of the DP, skewness, SW and JB tests are over 80%. It has been observed that the power performances of the kurtosis test do not change much with the sample sizes and perform very poorly. In the 1 and 1 parameter beta distribution, as the sample size increases, the test powers also increase. However, when $n = 50$, it is seen that the powers of only the DP and kurtosis tests exceed 80% and the skewness test performs very poorly in general. In general, the power performances of the normality tests in the 2 and 5 parameter beta distribution are much better than the power performances obtained from the 1 and 1 parameter beta distribution. In addition, it is observed

that the kurtosis test in the 2 and 5 parameter beta distribution and the skewness test in the 1 and 1 parameter beta distribution gave very bad results.

It is determined that the test powers in the 5-degrees-of-freedom t distribution are weak in all sample sizes and there is a certain improvement in the power values of all tests with the increase in sample sizes. The power values of the tests in the t-distribution with 10 degrees of freedom are quite weak in all sample sizes. The highest power values are obtained with the JB test, such that the JB reached a maximum with value of 77.69 in the 5-degrees-of-freedom distribution and 37.59 in the 10 degrees-of-freedom distribution.

When $n \leq 70$ in the uniform distribution, the power performance of the JB test and the skewness test in other sample sizes are quite low. When $n \leq 50$, only the power of the DP and kurtosis tests are exceeded 80%. The JB test, which performs very poorly in small sample sizes, reaches a very high power of 98.65% when $n=150$.

When the DP, kurtosis, skewness and JB tests from the moment tests are compared, it is seen that the skewness and SW tests are stronger than the other moment tests in non-normal distributions such as $\chi^2_{(1)}$, $\chi^2_{(5)}$ and beta (2, 5). In addition, it is observed that the DP test is more powerful than the JB test, and the JB, which gives bad results in small sample sizes, gives very good results in large sample sizes. In beta distributions, it is observed that the kurtosis and skewness tests are highly affected by the distribution parameters.

When the normality tests examined in this study are taken into account and compared in all distributions, it is determined that SW gave better results than other tests for normal and non-normal distributions, and DP, skewness and JB tests are also strong. In addition, it can be said that the increase in sample size increases the test power, and as a result, the sample size is an important parameter for the power of the test as well as the distribution pattern. Moreover, it was determined that SW test gave good results in all distributions, JB could be used as an alternative to SW in large sample sizes, and normality tests gave poor results in 5 and 10 degrees of freedom t distributions.

Thus, the study is capable of helping the selection of appropriate univariate normality tests to obtain more reliable results by considering the sample distribution and size in future studies.

ACKNOWLEDGEMENT

The author declares that there are no conflict of interests.

REFERENCES

- [1] Noughabi, H. A., and Arghami, N. R. (2009). Monte carlo comparison of seven normality tests. *Journal of Statistical Computation and Simulation*, 81, 965-972.

- [2] Adefisoye, J., Golam Kibria, B., and George, F. (2016). Performances of several univariate tests of normality: An empirical study. *Journal of Biometrics & Biostatistics*, 7, 1-8.
- [3] Özer, A. (2007). Comparison of normality tests. Unpublished Master's Thesis, University of Ankara, Ankara.
- [4] Dufour, J. M., Farhat, A., Gardiol, L., and Khalaf, L. (1998). Simulation-based finite sample normality tests in linear regressions. *Econometrics Journal*, 1, 154-173.
- [5] Banerjee, A., Chitnis, U. B., Jadhav, S. L., Bhawalkar, J. S., and Chaudhury, S. (2009). Hypothesis testing, type I and type II errors. *Industrial Psychiatry Journal*, 18, 127-131.
- [6] Eygü, H. (2020). Çözümlü güncel örneklerle olasılık ve istatistik. Ankara: Nobel Yayınları. ss.251-252.
- [7] Elsayir, H. A. (2018). Factors determining the power of a statistical test for the difference between means and proportions. *American Journal of Mathematics and Statistics*, 8, 171-178.
- [8] Ugar, H. (1999). Functions of random variables and applications to probability distributions. Unpublished Master's Thesis, University of Istanbul, Istanbul.
- [9] Gordon, S. (2006). The normal distribution. Produced by UPS, Sydney.
- [10] Lancaster, H. O., and Seneta, E. (2005). Chi-square distribution, p. armitage and t. Colton in *Encyclopedia of Biostatistics*, Wiley, Chichester.
- [11] Karagöz, Y. (2003). Demonstration of relationship between exponential and chi-square distributions with random numbers produced by simulation. *C.Ü. İktisadi ve İdari Bilimler Dergisi*, 4(1), 197-209 .
- [12] Dündar, D. (1987). Hipotez testi ve ki-kare ile bir uygulama. *İstanbul Üniversitesi İktisat Fakültesi Mecmuası*, 45, 196-212.
- [13] Wackerly, D. D., Mendenhall, W., and Scheaffer, R. L. (2008). *Mathematical statistics with applications*. Cengage Learning, USA.
- [14] Koepf, W., and Masjed-Jamei, M. (2006). A generalization of student's t-distribution from the viewpoint of special functions. *Integral Transforms and Special Functions*, 17, 863-875.
- [15] Ramachandran, K. M., and Tsokos, C. P. (2009). *Mathematical statistics with applications*. Academic Press, USA.
- [16] Saraçoğlu, Ö. (2002). Düşük akım hidrolojisi ve akdeniz bölgesi'nde uygulanması. Unpublished Master's Thesis, University of Istanbul, Istanbul.

- [17] Cain, M. K., Zhang, Z., and Yuan, K. (2016). Univariate and multivariate skewness and kurtosis for measuring nonnormality: Prevalence, influence and estimation. *Behavior Research Methods*, 49, 1716-1735.
- [18] Nosakhare, U. H., and Bright, A. F. (2017). Statistical analysis of strength of w/s test of normality against non-normal distribution using monte carlo simulation. *American Journal of Theoretical and Applied Statistics*, 6, 62-65.
- [19] Shapiro, S. S., and Wilk, M. B. (1965). An analysis of variance test for normality (complete samples). *Biometrika*, 52, 591-611.
- [20] Sheskin, D. J. (2000). *Handbook of parametric and nonparametric statistical procedures*. Chapman & Hall/CRC, USA.
- [21] D'Agostino, R. B., and Pearson, E.,S. (1973). Tests for departure from normality. empirical results for the distributions of b_2 and $\sqrt{b_1}$. *Biometrika*, 60, 613-622.
- [22] D'Agostino, R. B. (1986). In *tests of the normal distribution, rb d'agostino and ma stephens, goodness of fit techniques*. Marcel Dekker, Inc, New York.
- [23] Zar, J.H. (1999). *Biostatistical analysis*. Prentice Hall, New Jersey.
- [24] Dong, L. B., and Giles, D. E. A. (2004). An empirical likelihood ratio test for normality. *Communications in Statistics-Simulation and Computation*, 36, 197-215.
- [25] Razali, N. M., and Yap, B. W. (2010). Power comparisons of some selected normality tests. *Proceedings of the Regional Conference on Statistical Sciences, July 2010, Selangor, Malaysia*. 126-138.
- [26] Abdi, H., and Molin, P. (2007). *Lilliefors test of normality*, N.J. Salkind, *Encyclopedia of measurement and statistics*. SAGE Publications, Inc, California.
- [27] Soest, J. V. (1967). Some experimental results concerning tests of normality. *Statistica Neerlandica*, 21, 91-97.
- [28] Lilliefors, H. W. (1967). On the kolmogorov-smirnov test for normality with mean and variance unknown. *Journal of the American Statistical Association*, 62, 399-402.
- [29] Dagnelie, P. (1968). A propos de l'emploi du test de Kolmogorov-Smirnov comme test de normalité. *Biométrie-Praximétrie*, 9, 3-13.
- [30] Genceli, M. (2007). Kolmogorov-smirnov, lilliefors and shapiro-wilk tests for normality. *Sigma Journal of Engineering and Natural Sciences*, 25, 306-328.

- [31] Akçadağ, H. İ. (2013). Tek değişkenli ve çok değişkenli bazı normallik testlerinin karşılaştırılması, Yayınlanmamış Doktora Tezi, Selçuk Üniversitesi Fen Bilimleri Enstitüsü, Konya.
- [32] Keskin, S. (2002). Varyansların homojenliğini test etmede kullanılan bazı yöntemlerin 1. tip hata ve testin gücü bakımından irdelenmesi, Yayınlanmamış Doktora Tezi, Ankara Üniversitesi Fen Bilimleri Enstitüsü, Ankara.
- [33] Öztuna, D., Elhan, A. H., and Tuccar, E. (2006). Investigation of four different normality tests in terms of type 1 error rate and power under different distributions. *Tübitak Academic Journals*, 36, 171-176.
- [34] Thadewald, T., and Büning, H. (2007). Jarque-bera test and its competitors for testing normality-a power comparison. *Journal of Applied Statistics*, 34, 87-105.
- [35] Mendeş, M., and Pala A. (2003). Type I error rate and power of three normality tests. *Pakistan Journal of Information and Technology*, 2, 135-139.
- [36] Shapiro, S. S., Wilk, M. B., and Chen, H. J. (1968). A comparative study of various tests for normality. *Journal of the American Statistical Association*, 63, 1343-1372.
- [37] Stephens, M. A. (1974). EDF statistics for goodness of fit and some comparisons. *Journal of the America Statistical Association*, 69, 730-737.
- [38] Seier, E. (2002). Comparison of tests for univariate normality. site file:///C:/Users/ASUS/Downloads/Comparison_of_tests_of_univariate_normality.pdf. Access Date: 20.12.2021.
- [39] Razali, N. M., and Yap, B. W. (2011). Power comparisons of shapiro-wilk, kolmogorov-smirnov, lilliefors and anderson-darling tests. *Journal of Statistical Modeling and Analytics*, 2, 21-33.



RESEARCH ARTICLE

INVESTIGATION OF THE STRAIN RATE SENSITIVITY OF Mg-6Sn AND Mg-6Sn-3Y ALLOYS

Güven YARKADAŞ^{1*}

^{1*}Mersin University, Faculty of Engineering, Department of Metallurgical and Materials Engineering, Mersin, guvenyarkadas@mersin.edu.tr, ORCID: 0000-0002-4592-2768

Receive Date:03.11.2022

Accepted Date: 28.03.2023

ABSTRACT

This study reports the influence of the addition of Yttrium (wt.3%) on strain-rate sensitivity of Mg-6Sn alloy. The Mg-6Sn and Mg-6Sn-3Y alloys were made by using high pressure die-cast. The microstructural and X-ray diffraction results exhibited that the Sn_3Y_5 and MgSnY intermetallic phases were formed with addition of Y to the Mg-6Sn alloy. Furthermore, the grain structure of the Mg-6Sn alloy was changed from dendritic to globular with addition of Y. The strain-rate sensitivity value of the Mg-6Sn-3Y alloy is found higher than that of the Mg-6Sn alloy for all strain value. This result was attributed to the formation of new intermetallics (Sn_3Y_5 and MgSnY) and microstructure morphology (from dendritic structure to globular).

Keywords: Mg-Sn alloy, high pressure die casting, yttrium, strain-rate sensitivity

1. INTRODUCTION

The strain-rate sensitivity (SRS) is very vital parameter for pure Mg and its alloys, which have the hexagonal close-packed structure apart from some Mg-Li alloys. It is well known for homogeneous deformation that it needs to at least five independent slip systems. However, many Mg alloys have only two available independent basal slip systems at low temperatures. Therefore, it can be said that they have limited ductility or formability when compared with aluminum alloys and steel [1-5]. The magnesium alloys are the best candidate for structural and automotive applications because of their lower density than that of other metallic components like steel and aluminum. However, the Mg alloys have some disadvantages (such as formability, mechanical properties and corrosion resistance), which are still not improved adequately. The ductility is one of the disadvantages for pure Mg and Mg alloys. Hence, the SRS of commercial Mg alloys has been investigated by many researchers to obtain information about tensile ductility and the deformation mechanisms [6-9]. For instance, Wang et. al. [10] displayed that the SRS of rolled Mg-3Al-3Sn alloy depends on the alloy' grain size and reported that the SRS increases with the improvement of grain size. At another study, the SRS of pure magnesium, Mg-1Al and Mg-1.4 Gd alloys was investigated by Stanford et. al. [11] and they found

that while the Mg-1Al alloy's SRS was 30% lower than that of pure Mg and the SRS of Mg-1.4Gd alloy was similar to pure Mg. Ang et. al. [12] published article about the SRS of magnesium alloys containing aluminum. It is reported that when the Al content in Mg alloys is increase, the strain-rate sensitivity is decreased and furthermore, twinning has important effect in deformation of magnesium-aluminium based alloys.

As seen above that, a lot of studies concerned with the strain-rate sensitivity were performed on magnesium-aluminium based alloys. In the last decade, if it is considered that the findings about Mg-Sn binary alloy systems, these alloys could be an alternative to Mg-Al binary alloys due to their better mechanical properties [13-17]. However, the Mg-Sn alloys' SRS has not studied adequately. Therefore, this study investigated the SRS of Mg-Sn and yttrium-added Mg-Sn alloys. The tensile behavior of the alloys was investigated over a wide strain rate range 10^0 - 10^{-4} s⁻¹.

2. MATERIAL AND METHOD

2.1. Experimental Details

Magnesium ingot, high purity tin granules and Mg-30 wt.%Y were used to prepare Mg-xSn and Mg-xSn-yY alloys (x=6 and y=3 wt.%), whose composition is listed in Table 1. The alloys were obtained using an induction furnace in a SiC crucible under a mixture gas (99% CO₂ +1% SF₆) to prevent oxidation. Firstly, pure Mg was melted at 750°C, after melting, and then Mg-30Y master alloy and pure tin were added. Both alloys were kept at 750°C for 600 s to ensure chemical reaction, then the oxidized layer on the melt was cleaned. After this stage, the prepared alloys were solidified at 250°C by a high pressure die casting machine in a mold designed to produce 4 tensile samples and metallographic samples.

Table 1. Chemical composition of Mg-Sn-Y alloy using X-ray fluorescence (Bruker S8Tiger) analysis.

Sample	Magnesium (Mg) (wt.%)	Tin (Sn) (wt.%)	Yttrium (wt.%)
Mg-6Sn	93.37	6.07	-
Mg-6Sn-3Y	90.58	5.98	3.08

Metallographic specimens were chemically etched with (20 ml CH₃ COOH, 60 ml ethylene glycol, 1 ml HNO₃ and 19 ml distilled water) acetic glycol after polishing and investigated by an optical and a scanning electron microscopy (SEM). X-ray (with a Cu K α radiation (wave length 0.15418 nm) at 40 kV and 40 mA) patterns were characterized.

The alloys' tensile properties were tested via a RAAGEN tensile test machine with a strain rate of 10^0 , 10^{-1} , 10^{-2} , 10^{-3} and 10^{-4} s⁻¹. The alloy's tensile results are the average value of three tests under each condition.

3. RESULTS

3.1. Microstructural characterization

Fig. 1 depicts the X-RD results of the Mg-6Sn and Mg-6Sn-3Y alloys. The resulted patterns show that both α -Mg and Mg_2Sn intermetallic phases exists in both alloys. Furthermore, the peak of Sn_3Y_5 and MgSnY intermetallic phases was found with addition of Y element.

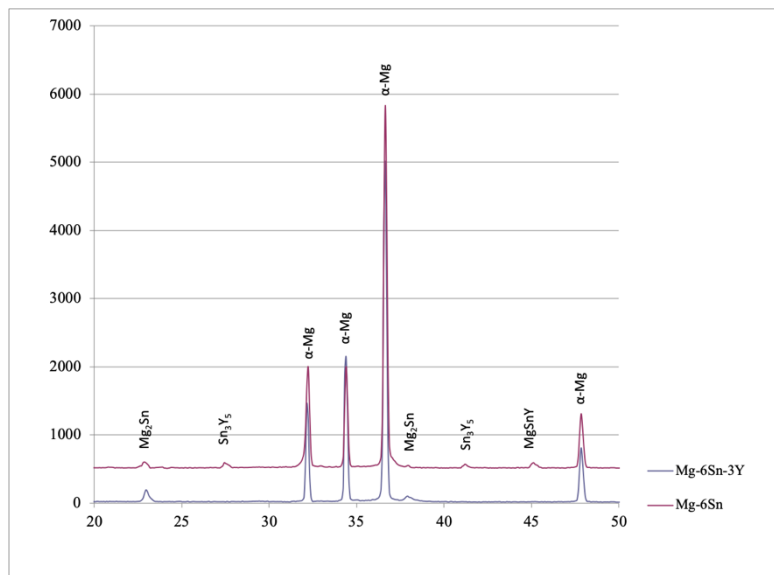
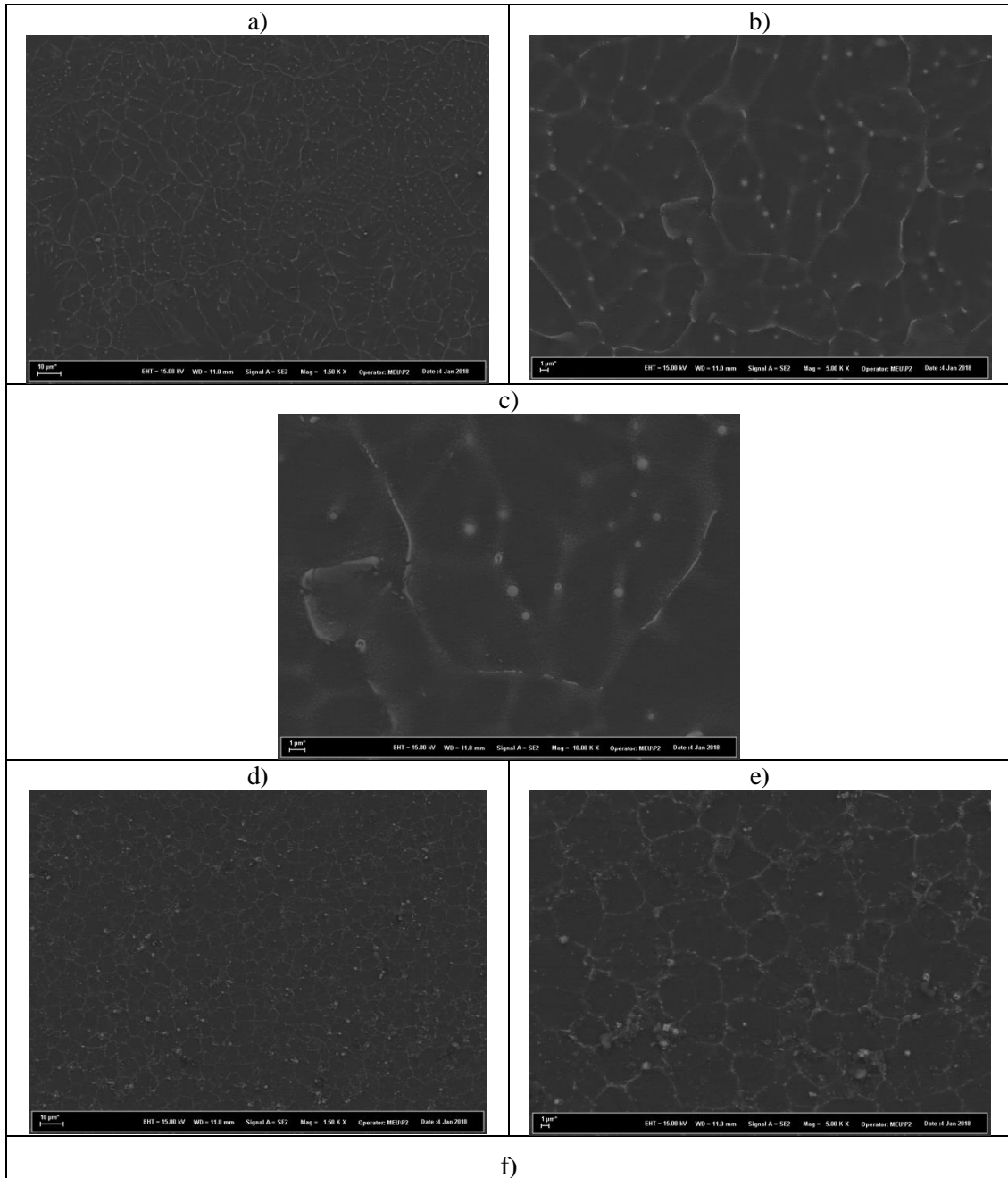


Figure 1. The X-RD results of the Mg-6Sn and Mg-6Sn-3Y alloys.

Fig. 2 shows the general microstructure of the Mg-6Sn (Fig. 2 a, b and c) and Mg-6Sn-3Y (Fig. 2 d, e and f) alloys. Microstructure images exhibit that the dendritic structured grains are dominant in the Mg-6Sn alloy. According to the phase diagram of Mg-Y binary alloy[18], there is limited solid solubility of Y in the magnesium matrix. Hence, Y atoms are pushed to the edge of the liquid /solid interface, which restricts the growing of grains and promotes new seed formation in the melt during solidification. Hence, the microstructural morphology of the Mg-6Sn alloy was changed from dendritic to globular with addition of Y.



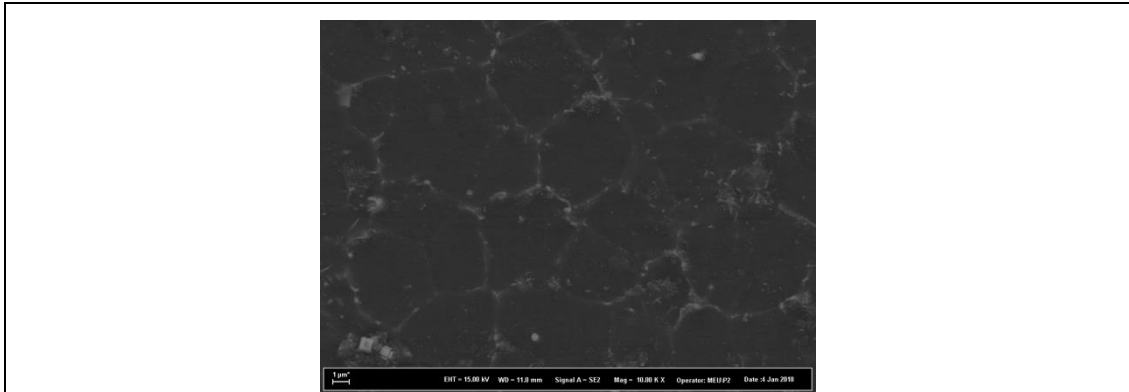
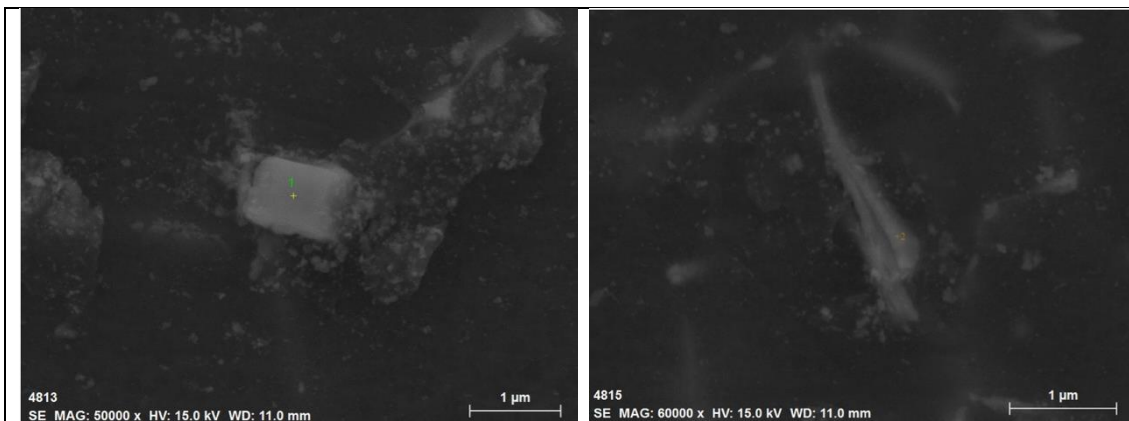


Figure 2. The SEM microstructure of experimental alloys; (a), (b) and (c) Mg-6Sn, (e), (f) and (g) Mg-6Sn-3Y.

Muthuraja et. al [19] have been thermodynamically computed the phase diagram of magnesium-yttrium-tin ternary alloy systems. They mentioned the presence of the Sn_3Y_5 and MgSnY intermetallic phases in Mg-3Sn-15Y alloy. The EDS measurement of the Mg-6Sn-3Y alloy is shown in Fig. 3. Considering the atomic ratio of Sn to Y, the spot 1 could be identified as MgSnY ternary intermetallic phase. Since spot 2 contains a higher amount of Y than the spot 1, it was thought that the spot 2 was Sn_3Y_5 intermetallic phase.



Spot No:	Chemical compositions, (at.%)			Atomic ratio	
	Sn	Y	Mg	Mg/Sn	Sn/Y
1	28.19	29.52	42.29	1.5	0.95

2	11.03	14.98	73.99	5.94	0.73
---	-------	-------	-------	------	------

Figure 3. The EDS measurement of the Mg-6Sn-3Y alloy.

3.2. Tensile properties

Fig. 4 exhibits tensile test curves at different strain rates ranging from 10^{-4} to 10^0 s⁻¹ for the Mg-6Sn and Mg-6Sn-3Y alloy, respectively. Table 2 depicts mechanical properties of the Mg-6Sn and Mg-6Sn-3Y alloys at different strain rate. It can be seen from Fig. 4 a and b the test curves of the both alloys that the yield strength value was decreased with declining strain rate, while the elongation of alloys increased with declining strain rate. Furthermore, the alloys' tensile strength was reduced with decreasing strain rate.

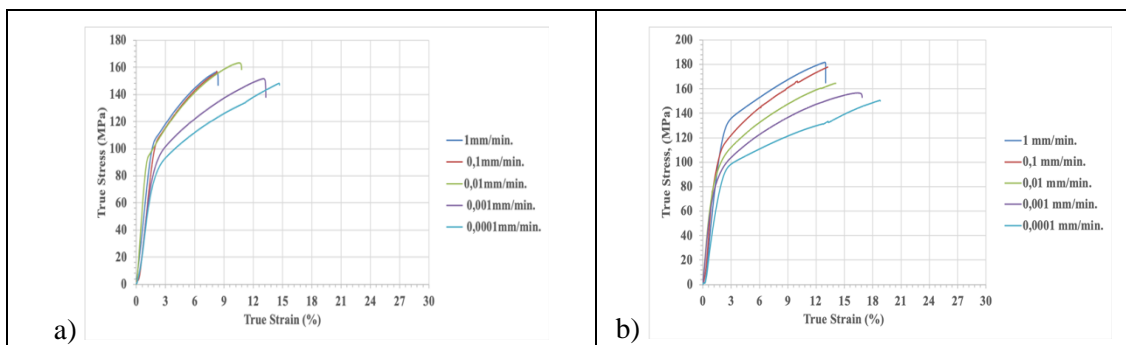


Figure 4. Stress-Strain curves of experimental alloys at different strain rate.

Table 2. The Alloys's yield, tensile and elongation to failure results at various strain rates.

Strain rate, (s ⁻¹)	Yield strength, (MPa)		Tensile strength, (MPa)		Elongation to Failure, (%)	
	Mg-6Sn	Mg-6Sn-3Y	Mg-6Sn	Mg-6Sn-3Y	Mg-6Sn	Mg-6Sn-3Y
10 ⁰	108	137	156	186	8,32	13,01
10 ⁻¹	106	115	154	178	8,47	13,26
10 ⁻²	96	111	152	164	10,72	13,96
10 ⁻³	94	102	149	157	13,21	16,92
10 ⁻⁴	84	96	146	153	14,53	18,81

3.3. Strain rate sensitivity (SRS)

The stress- strain curves can be used for describing the SRS exponent (m), which is determined by the following equation [8, 10, 20-21].

$$m = \frac{\ln(\frac{\sigma_1}{\sigma_2})}{\ln(\frac{\dot{\epsilon}_1}{\dot{\epsilon}_2})} \quad (1)$$

where σ is the true flow stress at a given true strain rate $\dot{\epsilon}$ under constant temperature and strain (ϵ). Fig. 5 shows variations of strain-rate sensitivity with true strain. It can be said that from Fig.5 strain-rate sensitivity rises with strain in both of the experimental alloys. Also, the Mg-6Sn-3Y alloy's SRS is found higher than that of the Mg-6Sn alloy for all strain value.

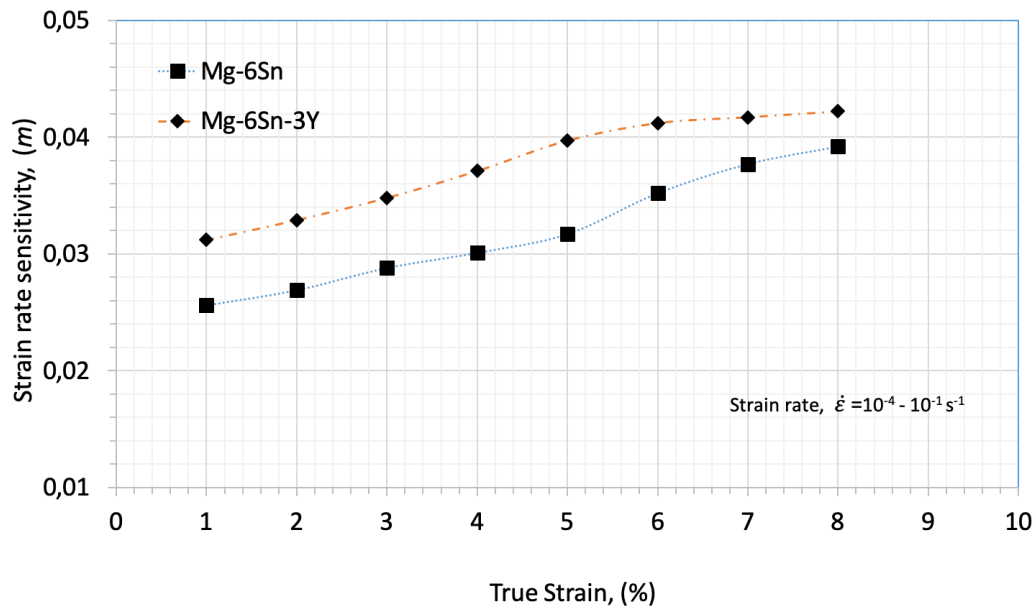


Figure 5. Variations of strain-rate sensitivity with true strain, $\dot{\epsilon} = 10^{-4} - 10^{-1} \text{ s}^{-1}$.

3.4. Fracture

Fracture morphology of Mg polycrystalline alloys apart from some Mg-Li based alloys is generally quasi-cleavage fracture or brittle through cleavage because of their h.c.p. crystal structure. The major plastic deformation mode occurs via dislocation slips on prismatic and basal planes as well as deformation twinning [3, 10, 22-24]. Fig. 6 exhibits the fractured surfaces of the Mg-6Sn (Fig. 6 a and b) and Mg-6Sn-3Y (Fig. 6 d and c) alloys at the lowest and highest strain rates. Largely, it was observed from Fig. 6 (a) and (b) that quasi-cleavage, tearing edges and dimples can be detected on the fractured surface of the main and Y content alloys. Furthermore, it can be said that more uniform dimples, which are much larger and deeper, can be observed on the Mg-6Sn-3Y fractured surface compared to that of the Mg-6Sn alloy. This result proved that the Mg-6Sn-3Y alloy displays a more ductile behavior.

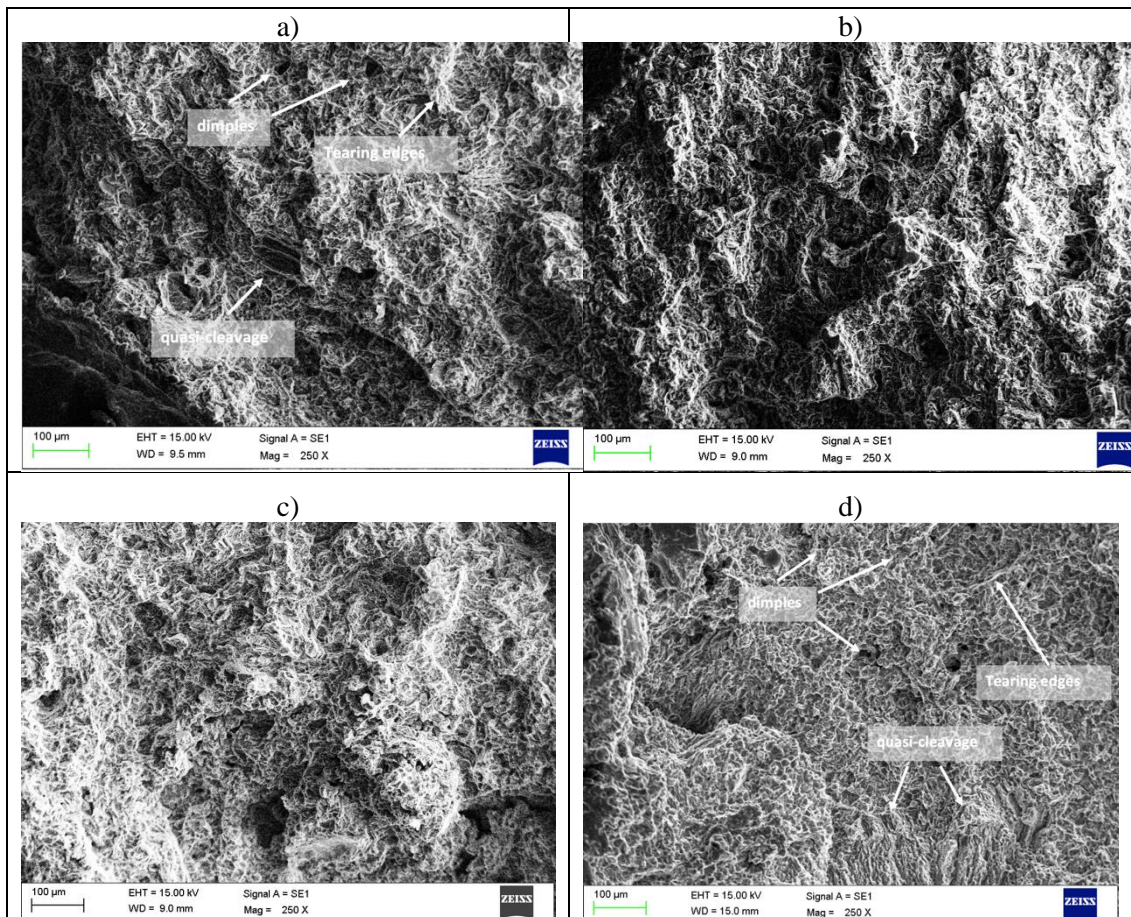


Figure 6. The fracture surfaces of (a) and (b) the Mg-6Sn and (c) and (d) Mg-6Sn-3Y alloys at the lowest and highest strain rates.

4. DISCUSSIONS

Obtained results showed that the Mg-6Sn-3Y alloy exhibited more plastic deformation behavior than Mg-6Sn alloy for all strain rates (Fig. 4). Furthermore, the strain rate sensitivity value of Y including alloy is higher than Mg-6Sn alloy for all strain rates (Fig. 5). The underlying cause in the Mg-6Sn-3Y alloy is probably the formation of new intermetallics (Sn_3Y_5 and MgSnY) and microstructure morphology (from dendritic structure to globular). Because, it is thought that the microstructural modifications were increased the density of dislocations, and the twins of deformation in the α -Mg grains. Additional newly formed twin boundaries from deformation twins probably play an important

role for barriers to mobility of dislocations and stock the pile-up of dislocation, which could provide huge resistance to the more dislocation movement.

5. CONCLUSIONS

The conclusions as follows;

1. The α -Mg and Mg₂Sn intermetallic phases have found in both alloys. Moreover, the new Sn₃Y₅ and MgSnY phases were observed with the addition to Y.
2. The microstructure of Mg-6Sn alloy was changed from dendritic to globular with the addition of alloying element Y.
3. The main fracture mechanisms of the both alloys were the quasi-cleavage, tearing edges and dimples for both the alloys. In addition to this, the fractured surfaces of the Mg-6Sn-3Y alloy at high and low strain rates have more uniform dimples. It means that the Mg-6Sn-3Y alloy exhibits a more ductile behavior.

The strain rate sensitivity value of Y including alloy is higher than that of Mg-6Sn alloy for all strain. The underlying cause in the Mg-6Sn-3Y alloy is probably the formation of new inter-metallics and microstructure morphology (from dendritic structure to globular).

ACKNOWLEDGEMENT

There is no funding body the author could acknowledge.

REFERENCES

- [1] Yang, H.P., Fu, M.W., To, S., Wang, G.C., (2016), Investigation on the maximum strain rate sensitivity (*m*) superplastic deformation of Mg-Li based alloy Mater. and Design 112, 151-159. <http://dx.doi.org/10.1016/j.matdes.2016.09.066>
- [2] Nan, X.L., Wang, H.Y., Wu, Z.Q., Xue, E.S., Zang, L., Jiang, Q.C., (2013), Effect of *c/a* ratio on Schmid Factors in Hexagonal close-packed metals, Scrip. Mater. 68, 530-533. <http://dx.doi.org/10.1016/j.scriptamat.2012.12.006>
- [3] Pekköleryüz, K. U. Kainer, A.A. Kaya, first ed., Woodhead Publishing Limited, Philadelphia, (2013).
- [4] Friedrich, B. Mordike, Springer, Verlag Berlin Heilderberg (2006).
- [5] Sandlöbes, S., Zaeferrer, S., Schestakow, I., S. Yi, Gonzalez-Martinez, R., (2011), On the role of non-basal deformation mechanisms for the ductility of Mg and Mg-Y alloys Acta Mater. 59, 429-439. Doi:10.1016/j.actamat.2010.08.031.

- [6] Han, G., H.K. Park, H.K. Kim, T.S. (2012), Local and global deformation behaviour in rolled pure magnesium sheets at room temperature under different strain rates Mater. Sci. and Eng. A 762, 138110. <https://doi.org/10.1016/j.msea.2019.138110>
- [7] Valle, J.A., Rauno O.A., (2006), Influence of the grain size on the strain rate sensitivity in an Mg-Al-Zn alloy at moderate temperatures, Scrip. Mater. 55, 775-778. Doi:10.1016/j.scriptamat.2006.07.013
- [8] Matsunaga, T., H. Somekawa, H. Hongo, Tabuchi M., (2015), Deformation mechanism transition with strain rate in Mg-3Al-1Zn alloy, Mater. Sci. and Eng. A 647, 212-215. <http://dx.doi.org/10.1016/j.msea.2015.09.029>.
- [9] Song, W.Q., Beggs P., Easton M., (2009), Compressive strain-rate sensitivity of magnesium-aluminum die casting alloys, Mater. Des. 30. 642-648. Doi:10.1016/j.matdes.2008.05.050.
- [10] Wang, H.Y., E.S. Xue, X.L. Nan, T. Yue, Y.P. Wang, Q.C. Jiang,(2013), Influence of grain size on strain rate sensitivity in rolled Mg-3Al-3Sn alloy at room temperature Scrip. Mater. 68, 229-232. <http://dx.doi.org/10.1016/j.scriptamat.2012.10.019>.
- [11] Stanford, N., I. Sabirov, G. Sha, A. Fontaine, S.P. Ringer, M.R. Barnett, (2010), Effect of Al and Gd solutes on the strain rate sensitivity of Mg alloys, Metal. and Trans., 41, 734-743. doi: 10.1007/s11661-009-0107-8
- [12] Ang, H.Q., Zhu S., Abbott T., D. Qiu, Easton M., (2017), Strain-rate sensitivity of die-cast magnesium-aluminium based alloys Mater. Sci. and Eng. A. 699, 239-246. <http://dx.doi.org/10.1016/j.msea.2017.05.093>.
- [13] Yarkadaş, G., C. Kumruoğlu, H. Şevik, (2018), The effect of Cerium addition on microstructure and mechanical properties of high pressure die cast Mg-5Sn alloy, Mater. Charc.136, 152-156. <https://doi.org/10.1016/j.matchar.2017.11.057>.
- [14] Liu, H., Y. Chen, Y. Tang, S. Wei, G. Niu, (2007), The microstructure, tensile properties, and creep behavior of as-cast Mg-(1-10)%Sn alloys J. Alloys and Comp. 440, 343-351. Doi:10.1016/j.jallcom.2006.09.024.
- [15] Zhou, Y., P. Wu, Y. Yang, D. Gao, P. Feng, C. Gao, H. Wu, Y. Liu, H. Bian, C. Shuai, (2006), The microstructure, mechanical properties and degradation behaviour of laser-melted Mg-Sn alloys, J. Alloys and Comp. 687, 109-114. <http://dx.doi.org/10.1016/j.jallcom.2016.06.068>.
- [16] Nayyeri, G., R. Mahmudi, (2010), Effects of Sb additions on the microstructure and impression creep behavior of a cast Mg-5Sn alloy J. Mater. Sci. and Eng. A. 527, 669-678. Doi:10.1016/j.msea.2009.08.056.

- [17] Qing, W., C. Yungui, X. Sufen, Z. Xiaoping, T. Yongbai, W. Shanghai, Z. Yuanghua, ,(2010), Study on microstructure and mechanical properties of as-cast Mg-Sn-Nd alloy, *J. of Rare Earth.* 28, 790-793. doi:10.1016/S1002-0721(09)60202-7.
- [18] ASM handbook, Alloy Phase Diagrams, Volume 3, p. 1111.
- [19] Muthuraja, C., A. Akalya, R. Ahmed, J. Nampoothiri, I. Balasundar, K.R., (2017), Experimental investigation and thermodynamic calculation of the phase equilibria in the Mg-rich region of Mg-Sn-Y alloy, *J. of All. and Comp.* 695, 3559-3572. <http://dx.doi.org/10.1016/j.jallcom.2016.11.413>.
- [20] Chun, Y.B., C.H.J. Davies, (2011), Twinning-induced negative strain rate sensitivity in wrought Mg alloy AZ31 *Mater. Sci. and Eng. A* 528, 5713-5722. Doi:10.1016/j.msea.2011.04.059.
- [21] Karimi, E., A. Hanzaki, M. Pishbin, H. Abedi, P. Changizian. (2013), Instantaneous strain rate sensitivity of wrought Mg alloys *Mater. Design* 49, 173-180. <http://dx.doi.org/10.1016/j.matdes.2013.01.068>
- [22] Somekawa, H., A. Singh, R. Sahara, T. (2018), Excellent room temperature deformability in high strain rate, *Sci. Rep.* 656, 198-208. Doi:10.1038/s41598-017-19124-w.
- [23] Lü, Y., Q. Wang, X. Zeng, W. Ding, C. Zhai, Y. Zhu, (2000), Effect of grain size distribution and texture on the cold extrusion behavior and mechanical properties of AZ31 Mg alloy, *Materials Science and Engineering: A*, 528 (9), 3428-3434.
- [24] Wang, H., P. Wu, S. Kurukuri, M. J. Worswick, Y. Peng, D. Tang, D. Li, (2008), Strain rate sensitivities of deformation mechanisms in magnesium alloys. *International Journal of Plasticity*, 107, 207-222. <https://doi.org/10.1016/j.ijplas.2018.04.005>.



RESEARCH ARTICLE

**DESIGN AND ANALYSIS OF MULTI-BAND COMPACT MICROSTRIP ANTENNA IN
GSM1900/WLAN/WiMAX/DSRC/X-BAND FREQUENCY BANDS FOR VEHICLE
APPLICATIONS**

Husnu YALDUZ^{1,*}, Hüseyin ÇİZMECİ²

¹ Hitit University, Vocational School Of Technical Sciences, Çorum, husnuyalduz@hitit.edu.tr, ORCID: 0000-0001-9776-3896

² Hitit University, Vocational School Of Technical Sciences, Çorum, huseyincizmecci@hitit.edu.tr,
ORCID: 0000-0003-4093-9592

Receive Date: 08.11.2022

Accepted Date: 28.03.2023

ABSTRACT

This study focuses the design and analysis of a compact, multi-band microstrip patch antenna for wireless communications operations. The design antenna exhibits distinct quad resonance frequency bands I from 1.879 GHz to 1.986 GHz, II from 3.1 GHz to 3.87 GHz, and III from 4.97 GHz to 6.515 GHz, IV from 7.26 GHz to 8.6 GHz, which covers GSM 1.900 GHz, WLAN (5.2/5.8 GHz), DSRC 5.9 GHz and WiMAX (3.5/5.5 GHz) bands. In addition, it can also support the X-band from 7.26 to 8.6 GHz. The antenna is designed on an inexpensive substrate of FR4 with dimensions of 36(L) × 25(W) mm² and consists of two branches of curved strips for a quad-band response. The antenna is designed and analyzed using electromagnetic 3D computer simulation software. The designed antenna can provide advantages in GSM/WLAN/WiMAX/DSRC/X-band satellite applications for vehicle communication with four resonant frequency bands, nearly omnidirectional radiation characteristics, and acceptable gain.

Keywords: *Microstrip antenna, multi-band antenna, WLAN, WiMAX, DSRC Band, Vehicle communication*

1. INTRODUCTION

Recently, wireless communication technology has shown tremendous improvement. This technology, which brings great convenience to people's activities, has ensured that it is adopted in almost every aspect of human life. With this technology, we can connect almost any device today without cables. On the other hand, developments in computing, cloud computing, and the internet of things (IoT) are paving the way for automation and intelligence in everyday work. Because of this progress, interest in intelligent transportation systems (ITS) and vehicle communication is increasing. Wireless communication, sensing capabilities, and advanced computing play a vital role in ITS [1–4].

Modern automobile (vehicle) technology has become a sector that has recently shown increasing interest in various wireless communication systems to improve both traffic flow and traffic safety [5]. With wireless vehicle communications in the ITS, many new functions, such as traffic alerts, road emergency alerts, and safety alerts, can be easily realized. Thus, drivers and other users can share real-time information to prevent potential traffic hazards and increase traffic efficiency [6].

The antenna plays a crucial role at the front end of wireless systems and is an important component of in-vehicle communication systems. In recent years, Monopole, Microstrip Patch, On-Glass, Bonded Foil, and Fractal Antennas have been among the commonly used antenna technologies for in-vehicle communication. However, the microstrip patch antenna is more popular than other in-vehicle communication technology. It is widely used due to its unobtrusive low profile, lightweight, flat structure, and ease of integration into components such as the vehicle bumper, fender, roof, or the back of the trunk lid [3, 7].

An ITS uses GPS, WLAN, WiMAX, Dedicated short-range communication (DSRC), etc., to transmit traffic information over short distances. It should cover different wireless communication standards, such as Multi-band antennas that have the potential to connect numerous professional forms in a single device [8]. In this case, it is most suitable if the antenna is multi-band operable [9]. Multi-band, low-profile, low-cost antennas that combine multiple antennas in a system are of great interest in the ITS. To create multi-band resonance, techniques such as creating slots in the antenna patch and ground plane, adding fractals of various shapes, and parasitic loading are commonly used [8,10,11]. In the literature, dual-band [1,12,13] and multi-band [14–16] antennas operating in WLAN, WiMAX, DSRC, and other communication bands have been studied for vehicle communication. DSRC is a standard wireless technology and operates in the 5.9 GHz (5.850 - 5.925 GHz) frequency band to enable vehicle-to-vehicle (V2V) and vehicle-to-infrastructure (V2I) cooperation in ITS. [17,18].

In this study, a quad-band low-profile microstrip patch antenna with a simple geometric architecture is proposed for vehicle communication applications. The antenna covers the GSM 1.900 GHz, WiMAX3.5/5.5 GHz, WLAN 5.2/5.8 GHz, DSRC 5.9 GHz and X-band satellite frequency bands. WLAN applies to high-speed low-energy internet access in the vehicle, and with DSRC vehicle communication, it can provide the driver with some advantages, such as accident prevention on the roads. This article is organized into four sections. Detailed geometric structure and antenna design are presented in section 2. The simulated reflection coefficient and radiation pattern results are discussed and presented in section 3, and concluding explanations of this article are given in section 4.

2. ANTENNA DESIGN

This study aims to propose a microstrip antenna operating in multiple frequency bands for vehicle communication applications. In addition, the antenna must have an omnidirectional radiation pattern and good impedance matching that supports vehicle-to-vehicle and vehicle-to-roadside communications. Figure 1 shows the geometry and parametric configuration dimensions of the proposed quad-band antenna for GSM, WiMAX, WLAN, DSRC, and X-band bands operation. The antenna is designed on an inexpensive FR4 substrate with a thickness of 1.57 mm, a relative permittivity of 4.4, a loss tangent of 0.02, and a compact size of 36×25 mm². The conductor layers are

realized using a thick copper material of 0.017 mm ($T_{cop}=1$ Oz). As shown in Figure 1a, the top side of the FR4 substrate consists of the two branches of curved strip radiating element and a 50Ω microstrip inset feed line for good impedance matching at the selected bands. The width of feed line is set at 3.08 mm. As shown in Figure 1b, a rectangular partial ground plane is printed on the bottom layer of the substrate for omnidirectional radiation. In addition, a small slot ($W_{gs} \times L_{gs}$) was created in the ground plane for good impedance matching. The antenna structure was designed and analyzed using 3D commercial electromagnetic simulation software (CST). Table 1 summarizes the detailed dimensions of the proposed design. The final all design parameters of the antenna structure are showed in Table 1 (units are in mm).

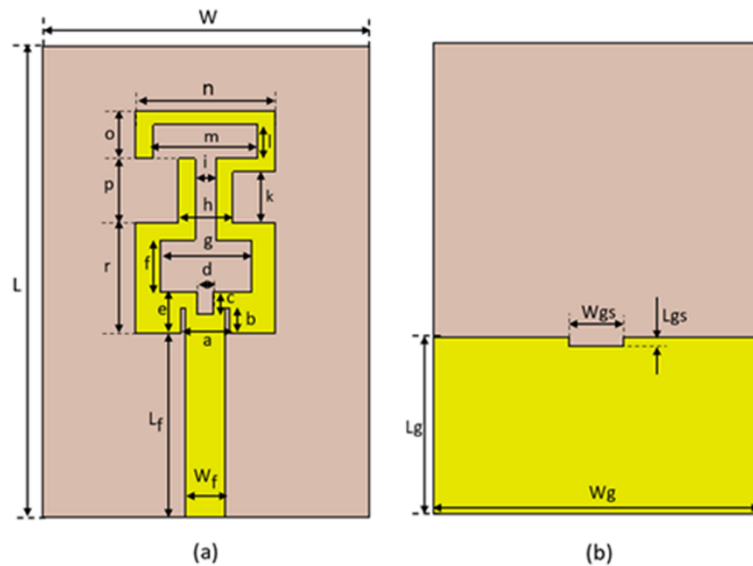


Figure 1. Proposed multi-band antenna. (a) Top architecture (b) Bottom architecture.

Table 1. The design parameters of the proposed antenna (mm).

W	L	W_f	L_f	a	b	c	d
25	36	3.08	14	3.68	2	1.7	1.2
e	f	g	h	i	k	l	m
3.2	4	7	4.2	1.6	3.9	2.6	8
n	o	p	r	W_g	L_g	W_{gs}	L_{gs}
10.7	3.7	4.9	8.5	25	13.5	4.2	0.65

3. SIMULATION RESULTS AND ANALYSIS

The reflection coefficient (S_{11}), radiation patterns, gain and radiation efficiency performance parameters of the antenna were simulated and analyzed. Figure 2 shows the frequency versus reflection coefficient (S-parameter) curve calculated via simulation. Based on $S_{11} \leq -10$ dB criteria, the calculated S_{11} shows that Antenna realizes four resonances at 1.936 GHz, 3.425 GHz, 5.89 GHz, and 7.8 GHz, with the corresponding frequency bands of 1.879–1.986 GHz, 3.10–3.87 GHz, 4.97–6.515 GHz, and 7.26–8.6 GHz. Results S_{11} indicate that the first resonance frequency at 1.936 GHz operates in the GSM 1.900 GHz (1.850-1.990 GHz) band, and its bandwidth is near the GSM band (For $S_{11} \leq -6$ dB criteria, it covers GSM 1.900 GHz band). The second resonance frequency at 3.43 GHz covers the WiMAX 3.5 GHz (3.30-3.80 GHz) band. The third resonance frequency at 5.9 GHz cover the WLAN 5.2 GHz/5.8 GHz (5.15-5.35, and 5.725-5.85 GHz), WiMAX 5.5 GHz (5.25-5.85 GHz), DSRC 5.9 GHz (5.850-5.925 GHz) bands. The fourth resonance frequency at 7.8 GHz operates in the X-band.

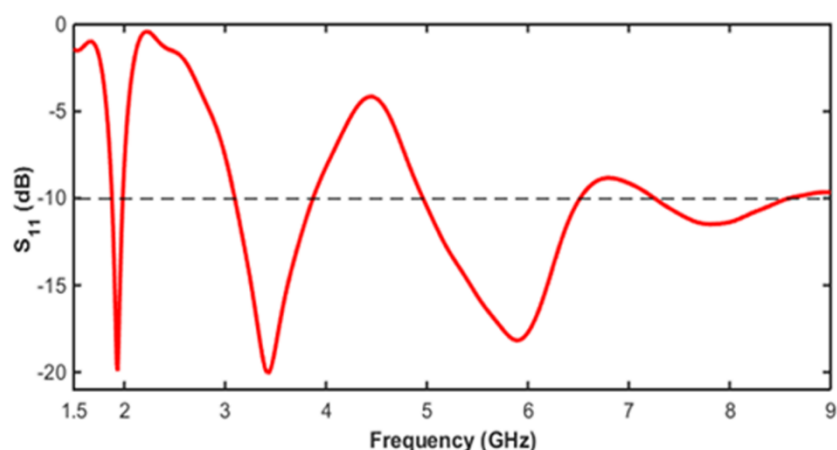


Figure 2. The simulated frequency versus reflection coefficient (S-parameter) curve.

The surface current distributions of the antenna calculated in the simulation at 1.936 GHz, 3.43 GHz, 5.9 GHz and 7.8 GHz are illustrated in Figure 3. The larger one indicates surface current distributions in red, and the smaller one in blue. As can be seen from the results, the current distributions of the frequencies are different from each other. For the lowest frequency band at 1.936GHz, it is seen that the surface currents are more concentrated on the long arm patch radiator and some parts of the short patch (Figure 1a). However, on the higher resonant frequency bands, generally decreasing density of surface currents is observed. As shown in Figure 3b, the current at 3.43 GHz frequency is concentrated on the short arm of the patch, especially on the vertical conductor between the horizontal conductors, and there is also partial current density on the microstrip feed line close to the patch. As seen in Figures 3c and 3d, current densities are close to homogeneous on the microstrip feed line and patches. The current density at 5.9 GHz is slightly more concentrated on the upper horizontal

conductor of the long arm of the patch and the microstrip feedline than in the other parts of the antenna.

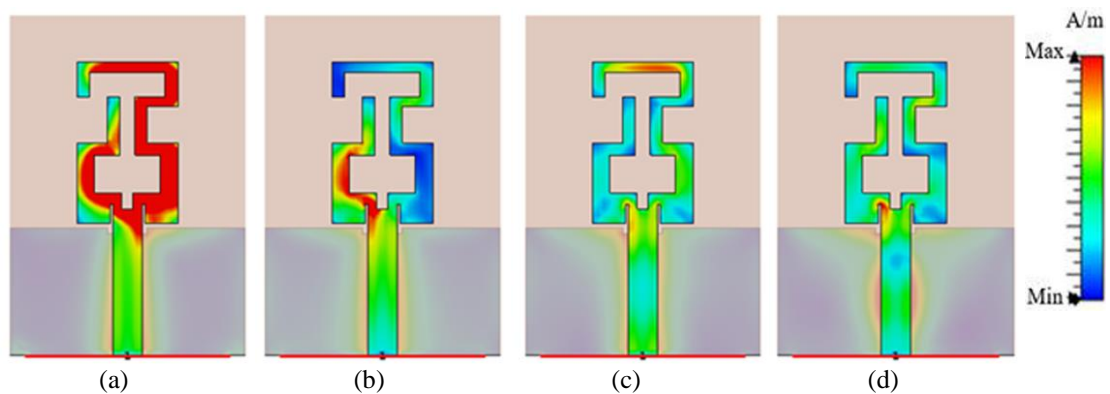


Figure 3. Simulated surface current distributions for different operating frequency bands of the antenna. (a) 1.936 GHz (b) 3.43 GHz (c) 5.9 GHz (d) 7.8 GHz.

Figure 4 illustrates the simulated far-field radiation patterns for the antenna in the polar coordinate system at 1.936 GHz, 3.43 GHz, 5.9 GHz, and 7.8 GHz maximum resonance frequencies. The solid and dash lines are $\phi=0^\circ$ and $\phi=90^\circ$, respectively. As illustrated in Figure 4, the antenna exhibits omnidirectional radiation nearly dipole-like radiation patterns at 1.936 GHz, 3.43 GHz (Figure 4a and 4b) and very close to omnidirectional at 5.9 GHz and 7.8 GHz (Figure 4c and 4d). It can be seen that the radiation patterns are somewhat distorted towards the upper resonance frequencies. This may be due to the asymmetrical patch of the proposed antenna and the excitation of higher-order resonance modes. However, it still has an omnidirectional radiation pattern acceptable for vehicle applications. An antenna with an omnidirectional radiation pattern is highly preferred in wireless vehicle communication systems since it provides signal communication from all directions.

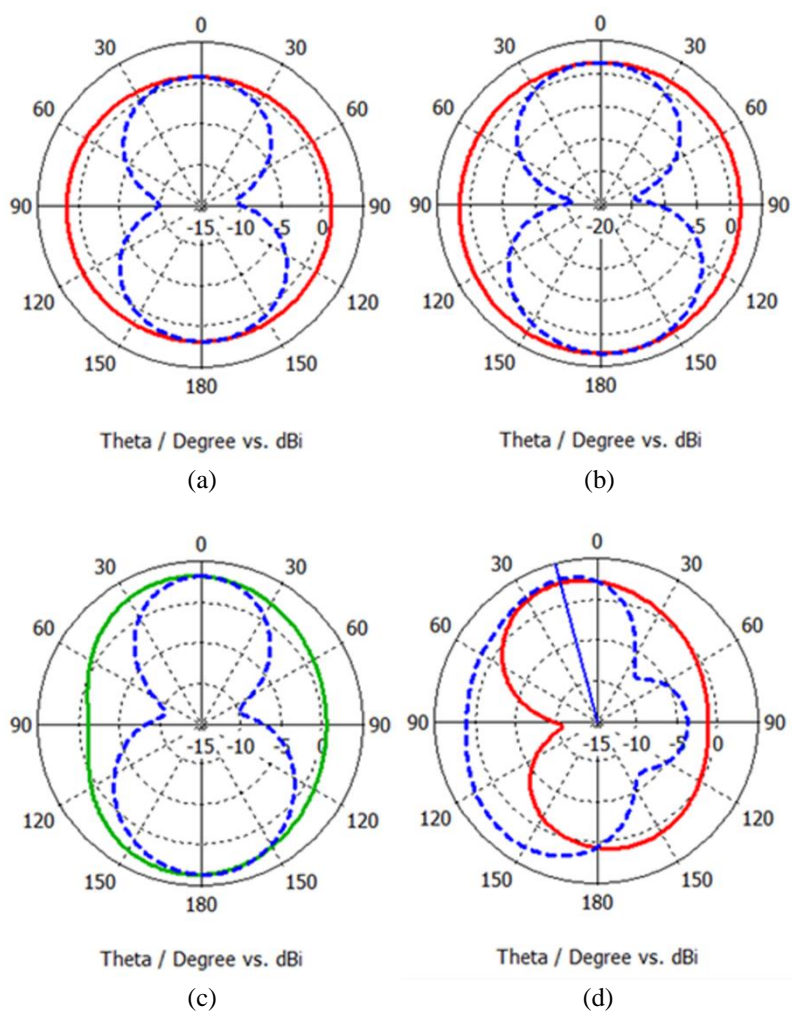


Figure 4. Simulated far-field directivity radiation pattern (— Phi:0°, - - - Phi:90°) of quad band antenna at(a) 1.936 GHz, (b) 3.43 GHz, (c) 5.9 GHz, and (d) 7.8 GHz.

Figure 5 illustrates the variation of the simulated gain with the frequency of the quad-band compact printed antenna for all operating quad-frequency bands. The simulated maximum gains variation of the antenna are -0.16–0.61 dBi, 1.76–2.16 dBi, 1.87–2.6 dBi, and 2.5–3.3 dBi in 1.879–1.986 GHz, 3.10–3.87 GHz, and 4.97–6.515 GHz, respectively. In addition, the gains at operating frequencies of 1.936 GHz, 3.43 GHz, 5.2 GHz, 5.5 GHz, 5.8 GHz, 5.9 GHz, and 7.8 GHz are about 0.34 dBi, 1.97 dBi, 2.05 dBi, 2.30 dBi, 2.50 dBi, 2.55 dBi, and 2.74 dBi, respectively. The reason why the gain is low or negative is because the antenna ground plane and dimensions are small in terms of electrical size (λ) as wavelength in free space. There is a similar situation in the literature [25][26]. In fact, these

antennas in the literature[25][26] are lower and have negative gain. For example, in [25] the antenna gains are -6 dBi, -4 dBi, 2.5 dBi, 5 dBi and 4 dBi at 1.5 GHz, 3 GHz, 5.5 GHz, 9.5 GHz and 11 GHz, respectively. This proposed antenna exhibits acceptable gains at GSM 1900 GHz, WiMAX 3.5/5.5 GHz, WLAN 5.2/5.8 GHz, DSRC 5.9 GHz, and X-band satellite (7.26 - 8.6 GHz) operating bands, which makes it suitable for practical vehicle applications.

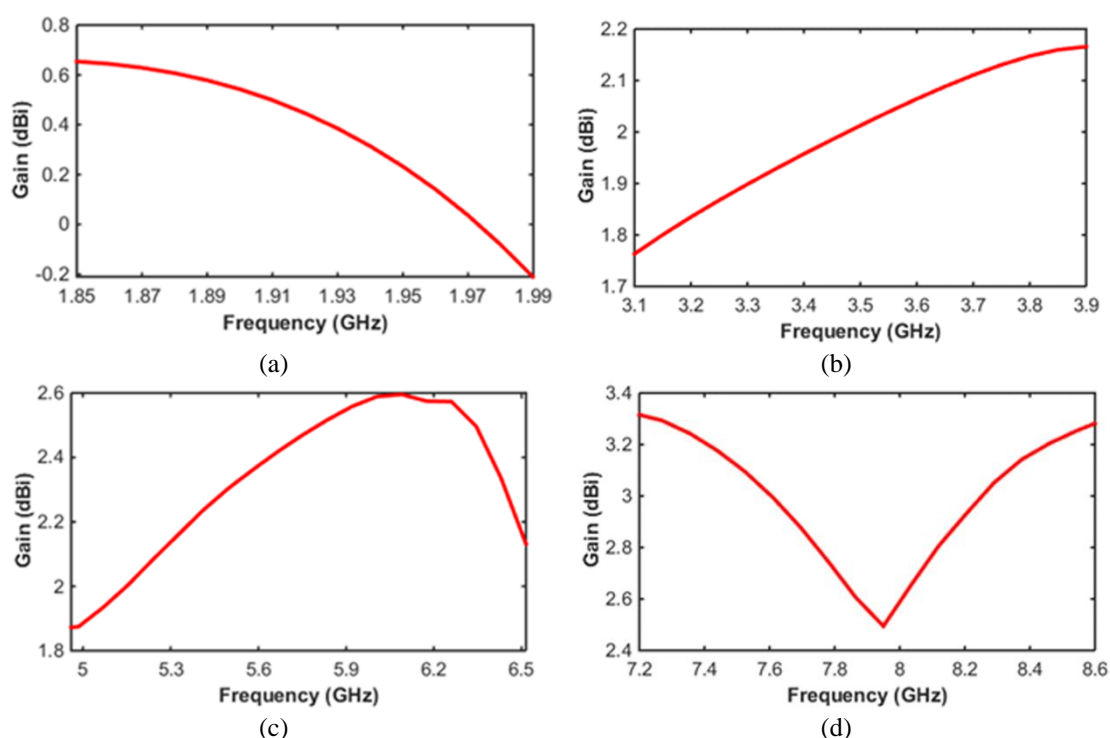


Figure 5. Simulated gain of quad band antenna at (a) GSM 1.900 GHz, (b) WiMAX 3.5 GHz, (c) WLAN 5.2/5.8 GHz, WiMAX 5.5 GHz, and DSRC 5.9 GHz, (d) X-Band 7.26 - 8.6 GHz.

Figure 6 illustrates the variation of the simulated radiation efficiency result for the antenna. The radiation efficiencies are about 60%, 82%, 77%, and 72% at the lower, second, third and higher frequency bands, respectively. According to these results, the antenna radiation efficiency is at a suitable level for vehicle communication applications.

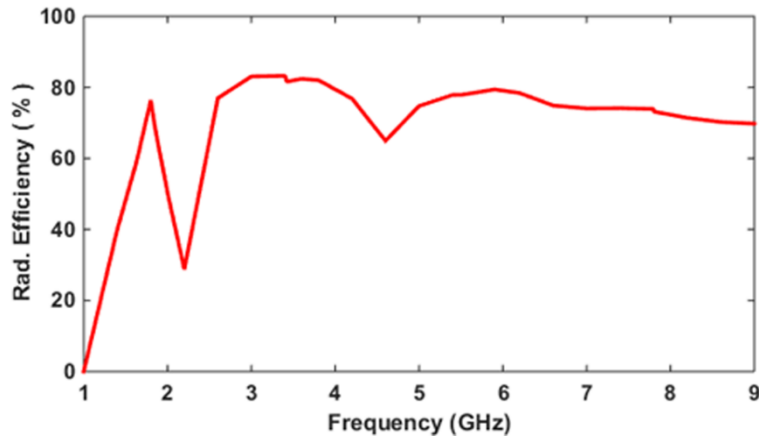


Figure 6. Simulated radiation efficiency variation with the frequency of quad band antenna.

A performance comparison between the design antenna and the multi-band reference antennas in the literature for size, number of operating frequency bands, and gain characteristics are given in Table 2. The design presented in the table seems to be very advantageous compared to other reference antennas in terms of electrical size (λ) as wavelength in free space and operation frequency band numbers. Only reference[20] is equal to the recommended antenna, but its size and gain are smaller than recommended. In addition, in terms of gain, the proposed antenna is higher than the ref [19-22, 24] antennas and is close to the gain of the reference[23] antenna. From Table 2, it is evident that the quad-band antenna provides decent gains in a simple structure with a small size for vehicle communication in GSM 1.900 GHz, WiMAX 3.5/5.5 GHz, WLAN 5.2/5.8 GHz, DSRC 5.9 GHz, and X-band applications.

Table 2. Performance comparison of dimensions, resonant frequency, number of bands and gain.

Ref.	Antenna Dimensions (mm/ λ)	Resonant Frequency (GHz)	Num. of Band	Gain (dBi)	Applications
[19]	$45.5 \times 20.8 \times 1.6$ FR4 $0.388 \lambda \times 0.177 \lambda \times 0.013 \lambda$	2.20 – 2.92 3.22 – 4.39 5.08 – 6.79	Tri Band	2.15 2.42 1.08	WLAN, WiMAX
[20]	$30 \times 24.8 \times 1.6$ FR4 $0.309\lambda \times 0.255\lambda \times 0.016\lambda$	3.04 – 3.15 5.44 – 5.72 6.76 – 7.72 9.42 – 9.98	Quad band	1.35 1.0 1.07 1.75	WiMAX, Satellite TV, and X-Band
[21]	$35 \times 30 \times 1.6$ FR4 $0.29\lambda \times 0.254\lambda \times 0.013\lambda$	2.41 – 2.56 3.12 – 3.18	Dual band	1.05 1.09	WLAN, WiMAX

[22]	$50 \times 40 \times 1.6$ FR4 $0.395\lambda \times 0.316\lambda \times 0.012\lambda$	1.85 – 2.90 4.90 – 5.50	Dual band	2.3 3	3G, 4G, WLAN, and Bluetooth
[23]	$36 \times 39 \times 1.6$ FR4 $0.294 \lambda \times 0.318 \lambda \times 0.013 \lambda$	2.35 – 2.52 3.20 – 4.16 5.13 – 5.87	Tri band	1.14 – 1.69 2.41 – 2.79 2.68 – 4.02	WLAN WiMAX
[24]	$56 \times 56 \times 1.6$ FR4 $0.35\lambda \times 0.35\lambda \times 0.01 \lambda$	1.75 – 2.0 3.01 – 4.18	Dual band	1.5 2.05	GSM and 5G (sub-6- GHz)
Our Design	$36 \times 25 \times 1.6$ FR4 $0.232 \lambda \times 0.161 \lambda \times 0.01 \lambda$	1.879 – 0.986 3.100 – 3.87 4.970 – 6.515 7.260 – 8.60	Quad band	-0.16 – 0.61 1.76 – 2.16 1.87 – 2.6 2.50 – 3.3	GSM, WLAN, WiMAX, DSRC and X- bands

4. CONCLUSIONS

This article proposes a microstrip fed planar multi-band antenna for vehicular communication applications. The antenna has two branches of curved strips shaped radiator for multi-band response and is designed on an FR4 dielectric with dimensions of $36 \times 25 \times 1.6$ mm³. The antenna is designed and optimized through the 3D electromagnetic simulation software program, and the antenna reflection coefficient, directivity, and gain parameters simulation results are presented successfully. The proposed design antenna offers four resonance frequency bands from 1.879 to 1.986, 3.10 to 3.86 GHz, 4.97-6.515GHz and 7.26-8.60 GHz, cover many applications like GSM1900, WLAN, WiMAX, DSRC and X-bands. These bands have acceptable gains and nearly omnidirectional radiation properties for vehicle applications and many other applications. In addition, since the antenna is simple and small size design, it can be easily produced with an electronic printed circuit technique and can be easily integrated into different parts of the vehicle. With these advantages, the design is thought to offer good performance for modern multi-band wireless vehicle communication system applications.

ACKNOWLEDGEMENT

The authors declare that they have no conflict of interest.

REFERENCES

- [1] Tripathi, S., Pathak, N. P. and Parida, M., (2018), Dual-band dual-beam microstrip patch antenna for intelligent transportation systems application, In 2018 5th IEEE Uttar Pradesh Section International Conference on Electrical, Electronics and Computer Engineering (UPCON), IEEE 2-4 November, 2018, 1–5.

- [2] Malathy, E.M., Praveen Joe, I.R. and Ajitha, P., (2021), Miniaturized dual-band metamaterial-loaded antenna for heterogeneous vehicular communication networks, *IETE Journal of Research*, 1-10.
- [3] Prasojo, J. and Sarno, R., (2020), Hexagonal patch microstrip antenna with parasitic element for vehicle communication, In: *2020 International Seminar on Application for Technology of Information and Communication (iSemantic)*, IEEE 2020, 340–345.
- [4] Hakanoglu, B.G., Koc, B., Sen, O., Yalduz ,H. and Turkmen, M., (2021), Stub loaded patch antenna and a novel method for miniaturization at sub 6 GHz 5G and Wi-Fi frequencies, *Advances in Electrical and Computer Engineering*, 21, 23–32.
- [5] Santos, M.V., Faria, S.M.M. and Fernandes, T.R., (2021), A simple slot Antenna for vehicle to infrastructure communication using 802.11 p, In: *2021 Telecoms Conference (ConfTELE)*, IEEE 2021, 1–5.
- [6] Wen, L., Gao, S., Luo, Q., Hu, W. and Yin, Y., (2020), Wideband dual circularly polarized antenna for intelligent transport systems, *IEEE Transactions on Vehicular Technology*, 69, 5193–5202.
- [7] Zabri, S.N., Salleh, N.M., Abu, M. and Mohamad, S.Y., (2017), Study of a flexible antenna for intelligent transport system application, In: *2017 IEEE Asia Pacific Microwave Conference (APMC)*, IEEE 2017, 1357–1360.
- [8] Mahendran, K., Gayathri, R. and Sudarsan, H., (2021), Design of multi band triangular microstrip patch antenna with triangular split ring resonator for S band, C band and X band applications. *Microprocessors and Microsystems*, 80, 103400.
- [9] Anilkumar, T., Madhav, B.T.P., Rao, M.V. and Nadh, B.P., (2020), Bandwidth reconfigurable antenna on a liquid crystal polymer substrate for automotive communication applications, *AEU-International Journal of Electronics and Communications*, 117, 153096.
- [10] Sarwar, S.M., Chowdhury, M.F.F. and Das, H.S., (2019), A dual band shark sin integrated vehicle antenna for 5G and Wi-Max applications, In: *2019 IEEE International Conference on Telecommunications and Photonics (ICTP)*, IEEE 2019, 1–4.
- [11] Rao, T.R., (2017), Design and performance analysis of a penta-band spiral antenna for vehicular communications, *Wireless Personal Communications*, 96, 3421–3434.
- [12] Joshi, M.P. and Gond, V.J., (2019), Design and analysis of microstrip patch antenna for WLAN and vehicular communication, *Progress In Electromagnetics Research C*, 97, 163–176.

- [13] Gao, S., Ge, L., Zhang, D. and Qin, W., (2018), Low-profile dual-band stacked microstrip monopolar patch antenna for WLAN and car-to-car communications, *IEEE Access*, 6, 69575–69581.
- [14] Madhav, B.T.P., Anilkumar, T. and Kotamraju, S.K., (2018), Transparent and conformal wheel-shaped fractal antenna for vehicular communication applications, *AEU-International Journal of Electronics and Communications*, 91, 1–10.
- [15] Kishore, N., Prakash, A. and Tripathi, V.S., (2016), A multi-band microstrip patch antenna with defected ground structure for its applications, *Microwave and optical technology letters*, 58, 2814–2818.
- [16] Agarwal, S. and Sharma, A., (2020), A miniaturized wideband antenna for vehicular communication, wimax, and wlan applications, In: 2020 International Conference on Radar, Antenna, Microwave, Electronics, and Telecommunications (ICRAMET), IEEE 2020, 151–154.
- [17] Varum, T., Matos, J.N., Pinho, P. and Oliveira, A., (2012), Printed antenna for DSRC systems with omnidirectional circular polarization, In: 2012 15th International IEEE Conference on Intelligent Transportation Systems, IEEE 2012, 475–478.
- [18] Patanvariya, D.G. and Chatterjee, A., (2019), Design of two-element circularly polarized bubbled antenna for vehicular communication, In: 2019 IEEE 16th India Council International Conference (INDICON), IEEE 2019, 1–4.
- [19] Tangthong, N., Moeikham, P. and Akatimagool, S., (2016), A compact multi band CPW-Fed monopole antenna using L-shaped and straight slots, In: 2016 13th International Conference on Electrical Engineering/Electronics, Computer, Telecommunications and Information Technology (ECTI-CON), IEEE 2016, 1–4.
- [20] Ali, T., Aw, M.S. and Biradar, R.C., (2018), A fractal quad-band antenna loaded with L-shaped slot and metamaterial for wireless applications, *International Journal of Microwave and Wireless Technologies*, 10, 826–834.
- [21] Singh, G., Kanaujia, B.K., Pandey, V.K., Gangwar, D. and Kumar, S., (2019), Design of compact dual-band patch antenna loaded with D-shaped complementary split ring resonator, *Journal of Electromagnetic Waves and Applications*, 33, 2096–2111.
- [22] Ran, X., Yu, Z., Xie, T., Li, Y., Wang, X. and Huang, P., (2020), A novel dual-band binary branch fractal bionic antenna for mobile terminals, *International Journal of Antennas and Propagation*, 2020, Article ID 6109093.
- [23] Wang, S., Kong, F., Li, K. and Du, L., (2021), A planar triple-band monopole antenna loaded with an arc-shaped defected ground plane for WLAN/WiMAX applications, *International Journal of Microwave and Wireless Technologies*, 13, 381-389.

- [24] Patel, U., Upadhyaya, T., Desai, A., Pandey, R. and Pandya, K., (2022), Dual-band compact split-ring resonator-shaped fractal antenna with defected ground plane for sub-6-GHz 5G and global system for mobile communication applications, *International Journal of Communication Systems*, 35, e5105.
- [25] Bod, M., Hassani, H.R. and Taheri, M.S., (2012), Compact UWB printed slot antenna with extra bluetooth, GSM, and GPS bands, *IEEE Antennas and Wireless Propagation Letters*, 11, 531-534.
- [26] Li, H., Zhou, Y., Mou, X., Ji, Z., Yu, H. and Wang, L., (2014), Miniature four-band CPW-fed antenna for RFID/WiMAX/WLAN applications, *IEEE Antennas and Wireless Propagation Letters*, 13, 1684-1688.



RESEARCH ARTICLE

DETECTION OF PNEUMONIA FROM X-RAY IMAGES USING DEEP LEARNING TECHNIQUES

Halit BAKIR^{1*}, Semih OKTAY², Timuçin Emre TABARU^{3,4,5}

^{1*}Computer Engineering Department, Sivas University of Science and Technology, Sivas, halit.bakir@sivas.edu.tr,
ORCID: 0000-0003-3327-2822

²Sivas University of Science and Technology, Defense Technologies Department, Sivas, oktaysemih@outlook.com,
ORCID: 0000-0002-7426-5584

³Department of Electrical-Electronic Engineering, Sivas University of Science and Technology, Sivas, etabaru@sivas.edu.tr,
ORCID: 0000-0002-1373-3620

⁴UNAM-Institute of Materials Science and Nanotechnology, Bilkent University, Ankara 06800, Turkey

⁵Department of Clinical Engineering Research and Application Center, Erciyes University, Kayseri 38039, Turkey

Receive Date: 15.12.2022

Accepted Date: 28.03.2023

ABSTRACT

X-ray images is one of the most common utilities used by health care specialists for detecting healthy problems in patients' chest. In this work, deep learning techniques have been adopted for diagnosing and detecting of lung diseases. First, an experimental study has been conducted for selecting the best artificial neural network ANN model that can be used for lung X-Ray image classification. The obtained best model has been used for classifying the lung X-Ray images into three classes (Multi class classification) namely bacterial pneumonia, viral pneumonia, and healthy lung. After that, three well-known CNN architectures, namely ResNet, Inception, and MobileNet have been adopted and used as a feature extractor for the selected best ANN model. Moreover, the above-mentioned ANN model (both with and without the features extraction phase) has been used for classifying the lung X-Ray images as healthy and pneumonia lungs (Binary classification). As a result of the study, the proposed ANN model with ResNet feature extraction phase gave the highest classification accuracy rate of 81.67% when multi-class classification has been conducted on the lung X-Ray dataset. On the other hand, the proposed ANN model with MobileNet feature extraction phase gave the highest accuracy rate of 95.67% when a binary classification has been conducted on the X-Ray image dataset.

Keywords: *X-Ray, Artificial Neural Networks, Pneumonia; Pre-Trained Models, Deep Learning.*

1. INTRODUCTION

Today, X-Ray images are an effective tool used in the health sector for detecting many health problems. One of the most important advantages of X-ray images is that it helps to analyse the lungs by imaging pneumonia in them. The COVID-19 epidemic, which has exploded in recent years, has

shown that one of undoubtedly the most important issues in this field is the detection of the disease earlier and at a lower cost. However, it is difficult to detect pneumonia on X-Ray images, as well as to decide whether the detected pneumonia is bacterial or viral. It is a problematic situation that takes a long time for radiologists and remains in the middle of great hesitations about making the correct diagnosis. On X-Ray images, the part of the pneumonia is usually not conspicuously visible when viewed. It may even resemble images of other diagnoses and may overlap at some points. At the same time, it may appear as benign abnormalities that do not damage the lungs on the images, leading to a misdiagnosis. However, what is desired in the health sector is to make the most accurate diagnosis in a fast time. Deep learning techniques that emerged with the development of technology have been included in our lives and have become applicable in almost every sector. Deep learning is a machine learning technique that is effectively used in many problems and applications these days. In other words, deep learning is a branch of machine learning used in multiple domains such as natural language processing, computer vision, and voice recognition. The most striking feature of deep learning compared to previously used techniques is that it does not explicitly require a feature extraction step. The deep learning model receives unprocessed input to determine which parts of the model are valuable and will affect the result. Then it maps the predicted output to the desired output. Features are automatically extracted by the deep learning model without any manual intervention from the outside. Although the deep learning models that have been used and created recently within this technology require high levels of processing performance, this situation is no longer considered a problem with the increase in processor power in the 21st century. Deep learning models are a combination of traditional neural networks with an increasing number of hidden layers. Deep learning techniques can automatically reveal image features that contain the image's most distinctive information. There is no human intervention or manual feature determination in the extraction of features in these types of architectures. These techniques have recently been widely used in image recognition and image classification processes [5]. Deep learning techniques have been used to serve disease detection purposes as well. Multiple models have been proposed using this technology and adopted in various domains and obtained aver high results. In fact, these methods have become able to reduce the workload of radiologists and doctors working in the health sector and early detect the type of disease accurately. In this context, the use of deep learning techniques to detect and classify the disease from chest X-Ray images can be shown as an important development in terms of service to human health. Many research, articles, and applications have been conducted on this subject, and the detection accuracy results have increased and the detection time have decreased day by day. However, deep learning methods are still considered as an area for improvement as they give different accuracy results depending on the dataset and hyperparameters used in the models. Therefore, different methods, models and hyperparameters can be adjusted experimentally, and the best results can be obtained by performing performance analyse.

2. RELATED WORKS

In Ayan et al.'s study, two well-known CNN architectures, namely Xception and VGG16, have been used for classifying lung X-Ray images as normal and pneumonia cases [1]. At the same time, the performance of both architectures has been compared using different metrics. As a result of the research, it has been stated that the Xception architecture was better at detecting pneumonia cases, while the VGG16 architecture was more successful in detecting normal cases. Rajpurkar et al. [2], a

deep CNN model called CheXNet has been proposed to detect pneumonia from lung X-Ray images. It is stated that the proposed model is trained with one of the largest publicly available datasets, called ChestX-Ray14. As a result, it was observed that the CheXNet model obtained F1 score, exceeding the average radiologist's performance. In [3], [4], a dataset composed of 5856 computer tomography (CT) images and X-ray images has been used. The dataset includes 4273 pneumonia images and 1583 healthy images. Multiple well-known CNN architectures namely VGG16, Inception_V3, VGG19, Inception_ResNet_V2, DenseNet201, MobileNet_V2, Resnet50, and Xception were adopted to classify the used dataset's images. As a result of the study, while CNN architectures such as MobileNet_V2, Resnet50, and Inception_Resnet_V2 showed high performance, VGG16, VGG19, Inception_V3, Xception, and DenseNet201 CNN architectures were partially successful. The model that gave the highest accuracy rate was Resnet50 with an accuracy of 96.61%. In [4], 6 different models have been created for the detection of pneumonia from X-ray images. Two of these models consist of two and three convolution layers and have been named model 1 and model 2 in the study, while the others are the pre-trained VGG16, ResNet50, VGG19, and Inception-v3 models. At the end of the study, performance comparisons of these models have been conducted, and in the results, the model 1 and model 2 obtained a validation accuracy reached 85.26% and 92.31%, respectively. The accuracy of the other models i.e. VGG16, ResNet50, VGG19, and Inception-v3 were 87.28%, 77.56%, 88.46%, and 70.99%, respectively. In the study of Kamrul et al. [5], a VGG16 CNN architecture has been used to detect a viral infection called COVID-19. It has been stated that, this architecture can detect pneumonia with a high accuracy reached 91.69% and sensitivity of 95.92%. In [6], a two-class classification model has been proposed to detect pneumonia. Instead of using different trained architectures as in other studies, it has been shown that creating a CNN network from scratch gives an effective accuracy result. The results obtained from the proposed model showed that the test accuracy was 95.31%, and the validation accuracy was 93.73%. In [7], four different models' architectures have been compared to design a model that gives better results than the models in the literature. Two of these models are the pre-trained i.e. ResNet152V2 and MobileNetV2 models, while one of the other two models is a CNN-based model and the remaining model is the LSTM-CNN-based model. As a result of the research, the most successful results have been obtained using the ResNet152V2 with 99.22% of accuracy, 99.43% of Precision and 99.44% of F1 score rate. Also, it has been stated that approximately 91% of successful results have been obtained from the other adopted models. In [8], it has been aimed to define a model to identify and localize the pneumonia from the chest X-Ray images. The proposed model is based on Mask-RCNN, a deep neural network that combines global and local features for pixel-by-pixel segmentation. It was observed that the presence of pneumonia was not evident in the images, and the distinction between the two conditions was rather vague. In addition, it has been inferred that the larger image may be more useful for deeper information. However, it is stated that the computational cost will also increase exponentially when dealing with large image. Finally, data augmentation, dropout and L2 regularization techniques have been used in order to prevent the overfitting problem. In [9], it has been aimed to propose a model that could classify the data set consisting of four different X-Ray image classes, including coronavirus X-Ray images. To this end, seven CNN architectures namely VGG16, DenseNet201, VGG19, Inception_ResNet_V2, Resnet50, Inception_V3, and MobileNet_V2 have been adopted and compared in order to find the best model. It has been concluded that the Inception_ResNet_V2 model gave a better result than the other models with an accuracy rate of 92.18%. In [10], a CNN-based model called CVDNet model has been proposed for faster detection of patients with COVID-19 virus

from a dataset containing X-Ray images of viral pneumonia, COVID-19, and healthy people. The proposed CVDNet model has been trained using a small dataset containing 2905 X-Ray images, and the model's accuracy rate was 96.69%. In [11], five CNN architectures, namely ResNet50, ResNet152, ResNet101, Inception_ResNetV2, and InceptionV3 have been tested to select the best model for detecting COVID-19 cases from three X-Ray datasets. By investigating the results of the study, it is seen that the ResNet50 pre-trained architecture gives the highest accuracy among the tested five architectures for the used three different datasets. In [12], a model that can detect and classify COVID-19 cases has been proposed. In the proposed model, an CNN-based architecture called DarkCovidNet, inspired by the DarkNet architecture, has been adopted. Less layers and filters have been used in the proposed architecture compared to the original DarkNet architecture. It has been stated that the proposed architecture was able to perform multi-class and binary classification tasks with an accuracy of 87.02% and 98.08%, respectively. In [13], the use of ResNet model variants were proposed for differentiating COVID-19 pneumonia from bacterial, other viral pneumonia, and healthy cases in X-Ray. First, X-Ray images have been classified into three different classes using the ResNet50 architecture: healthy cases, bacterial and viral pneumonia. Later, all cases classified as viral pneumonia have been differentiated as COVID-19 induced pneumonia and other viral pneumonia using the ResNet101 architecture. As a result of the research, a success rate of 93.01% has been achieved in the first stage of the model, while a very high success rate of 97.22% has been obtained in the second stage. In [14], two different deep learning and machine learning-based models have been proposed for conducting multi-class and binary classification over the used the used X-Ray image dataset. Also, SMOTE algorithm, which is one of the oversampling methods used to make the image distribution in the classes equal and to overcome the imbalance data problems, has been used for balancing the dataset. Some metrics such as accuracy, precision, recall, and F1 score were used to evaluate the proposed model. As a result, a 95% of accuracy rate for binary classification has been achieved from the proposed two models. For multiclass classification, the average values for precision, recall and F1 score of the CNN and Ensemble models were 80%, 78%, 78% and 77%, 75%, and 75%, respectively. Nayak et al. [15] proposed a deep learning-assisted automatic COVID-19 detecting method using lung X-Ray images. They used eight different pre-trained CNN network models and compared the accuracy results of the models to find the best result. Some well-known CNN pre-trained models such as SqueezeNet, ResNet, GoogleNet, etc. have been adopted for conducting classification tasks in the study. As a result of the research, ResNet-34 outperformed other architectures with 98.33% of accuracy. In the study of Apostolopoulos et al., [16] a dataset composed of 3905 X-ray images has been used. First, the images have been divided into 2 classes namely COVID-19 and non-COVID-19, then, the same dataset has been divided into seven classes namely COVID-19, enema, effusion, emphysema, fibrosis, pneumonia, and normal. After that, MobileNet v2 model has been used as a feature extractor, and three different experimental studies have been carried out. As a result, the highest accuracy rate was 99.18% which obtained by applying binary classification, and 87.66% obtained by conducting multi-class classification. In the study of Bhardwaj et al. [17], chest X-ray image dataset includes 2161 COVID-19, 2022 pneumonia, and 5863 healthy people has been used. A pre-processing phase has been conducted including image normalization and contrast enhancement for improving the quality of the images. The authors adopted multiple well-known CNN architectures for classifying the images in the dataset. As a result of the experiments, high accuracy rates reached 98.33% obtained by applying binary classification and 92.36% obtained by conducting multi-classification have been observed. In [18], some CNN pre-trained model has

been adopted as a feature extraction phase for a deep learning model used for diagnosis of cataract disease in the eye.

To our literature review, all studies conducted till now have used pre-trained models to diagnose chest diseases from X-Ray images. Classical neural networks (ANN) have not been tested for this issue in any of the reviewed previous studies. Therefore, in this work, an artificial neural network model were proposed and adopted to detect chest diseases based on X-ray images. Also, some pre-trained CNN models were used as feature extractor for the proposed ANN model to improve its results. Particularly, this work contains the following contributions:

- An artificial neural network model was proposed for classifying the lung images as a binary and multi-class classification.
- Multiple experiments have been conducted in order to select the best structure for the proposed ANN model.
- Three well-known CNN architectures, including ResNet, Inception, and MobileNet, have been adopted to be used as a feature extractor for the proposed ANN model.
- The proposed ANN architecture has been tested in terms both of binary and multi-class classification and the classification accuracy reached 81.67% and 95.67% for multi-class classification and binary classification respectively.

3. MATERIAL AND METHOD

3.1. Used Dataset

In this study, chest X-Ray images obtained from the popular database Kaggle's "Chest X-Ray Images (Pneumonia) with new class" radiography database [19] has been used. This dataset contains three different classes of chest X-Ray images including people with bacterial pneumonia, people with viral pneumonia (pneumonia), and healthy (normal) people. There is a total of 4479 lung X-Ray images in the dataset including 1493 bacterial pneumonia images, 1493 viral pneumonia images, and 1493 normal images. The dataset has been divided into 80% as a training dataset, 10% as a validation dataset, and 10% as a testing dataset. Figure 1 shows some sample images from the used dataset.

3.2. Method

In this study, performance analysis for deep learning techniques has been performed and different models have been tested in order to select the best model that can classify chest X-Ray images as viral pneumonia, bacterial pneumonia, or healthy with high performance and as low computational overhead as possible. An artificial neural network model has been proposed to classify chest X-Ray images in the used dataset. In addition, three pre-trained CNN models, namely ResNet, Inception, and MobileNet, have been used as a feature extractor to improve the results of the proposed ANN model.

3.2.1. Artificial neural network (ANN)

Artificial neural networks are systems consisting of processing elements connected to each other with different weight coefficients, which have been proposed to mimic the information exchange between the nerve cells in the human nervous system. Feed forward-back propagation ANN model is the most used method among the artificial neural network (ANN) techniques, where, this model can work with the logic of backward propagation of errors. Generally, ANN models are composed of five main

components namely an input layer, weight coefficients, activation function, hidden layers, and output layer. A neural network contains three-layer is shown schematically in Figure 2 [20].

3.2.2. Convolutional neural network

Convolutional neural network (CNN) is a type of NN that is commonly applied in computer vision [21] and natural language processing [22] domains. Generally, CNN can contains three different type of layers, namely input layer, one or more hidden layer, and finally an output layer. The hidden layer section can contain five different layer types including convolutional layers, activation function layers, pool layers, fully connected layers and normalization layers. The convolution operation conducted using multiple filters can be used for extracting features (feature map) from the dataset, which can be used as input for the next layers. The Pooling layer, also known as down-sampling layer, is used to reduce the size of feature maps such that the total computational time of the model can be reduced. MaxPooling and average pooling are the most popular used pooling operations. If we compare it with other classification algorithms and look at its advantages, CNN requires much less pre-processing and can give more successful results as the number of samples in the training dataset increases.

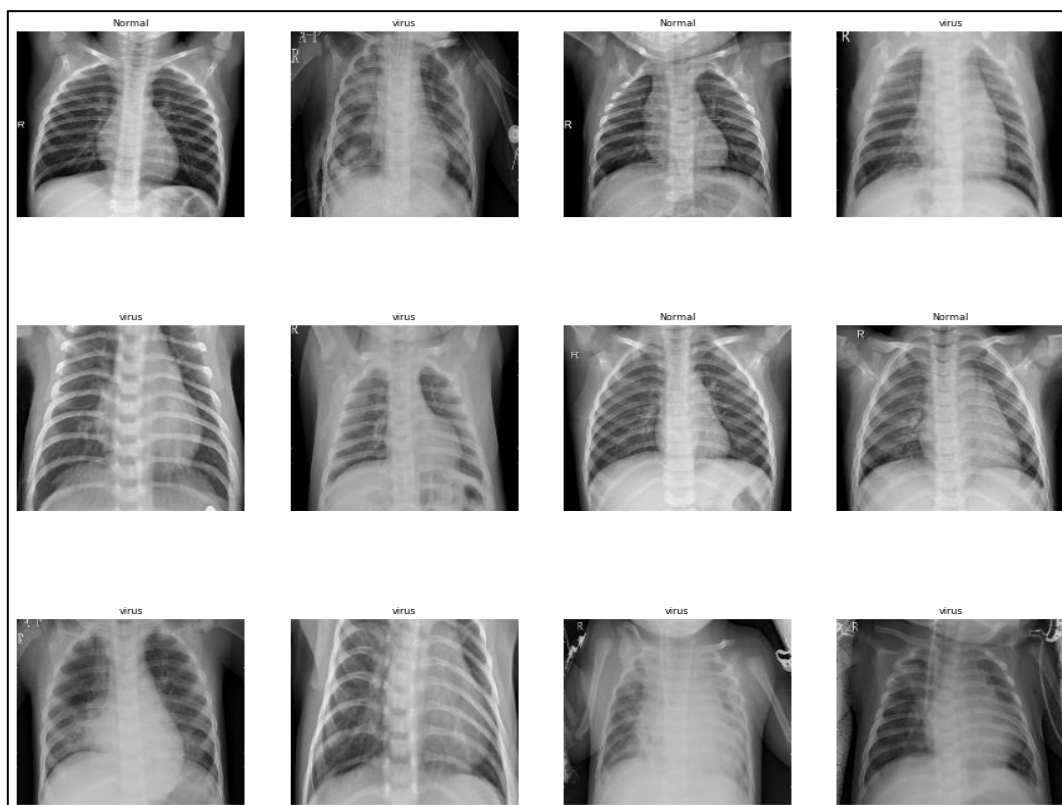


Figure 1. Some examples of X-Ray images used.

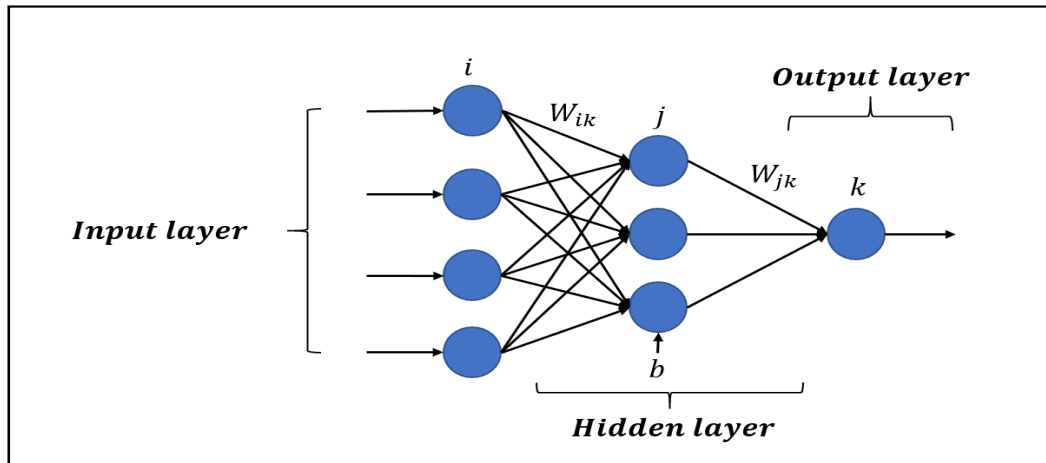


Figure 2. General representation of artificial neural network.

3.2.3. ResNet model

ResNet 2015 [23], short for Residual Network, is a CNN architecture introduced to solve the most complex problems. Some additional layers have been proposed and added in order to improve the performance of the deep neural networks. Particularly, skip connection has been proposed in order to skip un-useful or not used layers in order to train a very deep structure without any overfitting problem. The reason behind adding more layers is for those layers to learn more and more complex features. Figure 3 shows the difference between the block used in the ResNet architecture and the block used in the normal CNN architecture.

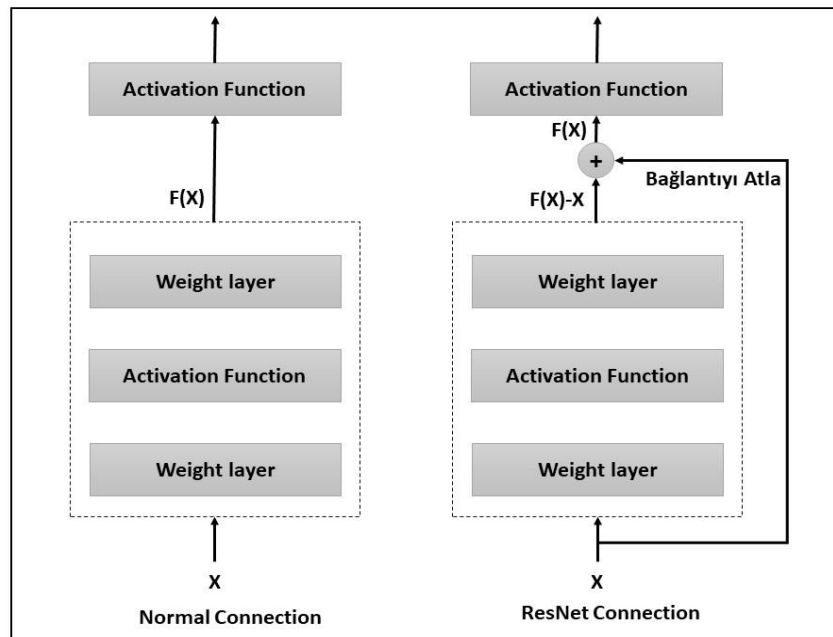


Figure 3. The difference between the block used in the ResNet architecture and the block used in the normal CNN architecture.

3.2.4. Inception net

Inception Network was once considered a cutting-edge deep learning architecture to solve image recognition and detection problems and was proposed in the 2014 article titled as "Going deeper with convolutions" [24]. The article proposes a new type of architecture called GoogleNet or Inception Network. It is basically a CNN architecture with a depth of 27 initial layers or filter blocks. Each initial layer is composed of a combination of convolutional layers (i.e. a layer containing a various filter sizes) with a single output vector that forms the input of the next layers. Figure 4 shows the filter logic used in the Inception architecture.

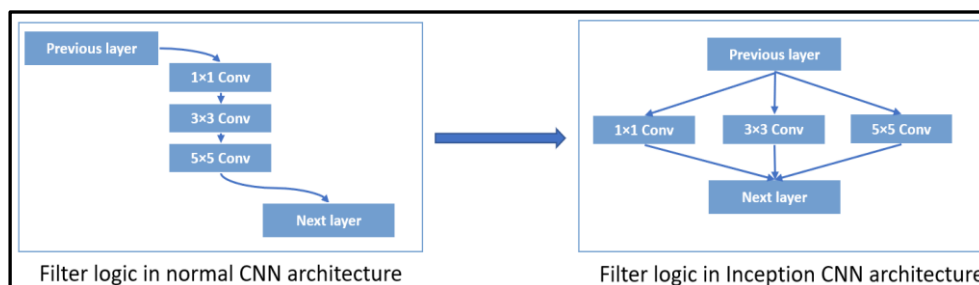


Figure 4. Filter logic used in the Inception architecture.

3.2.5. MobileNet model

MobileNet V3 is a combination of hardware-aware architectures initially proposed to be used in limited resource platforms such as mobile phones but it got more popular, and it is used in almost all platforms nowadays [25]. MobileNet architecture is based on different types of convolutional layers different from the classical one called Depthwise Separable convolution. The convolutional layers used in the MobileNet structure are composed of two steps namely Depthwise convolution and Pointwise convolution. Figure 5 shows the difference between the convolution operation used in the MobileNet architecture and the normal convolution operation.

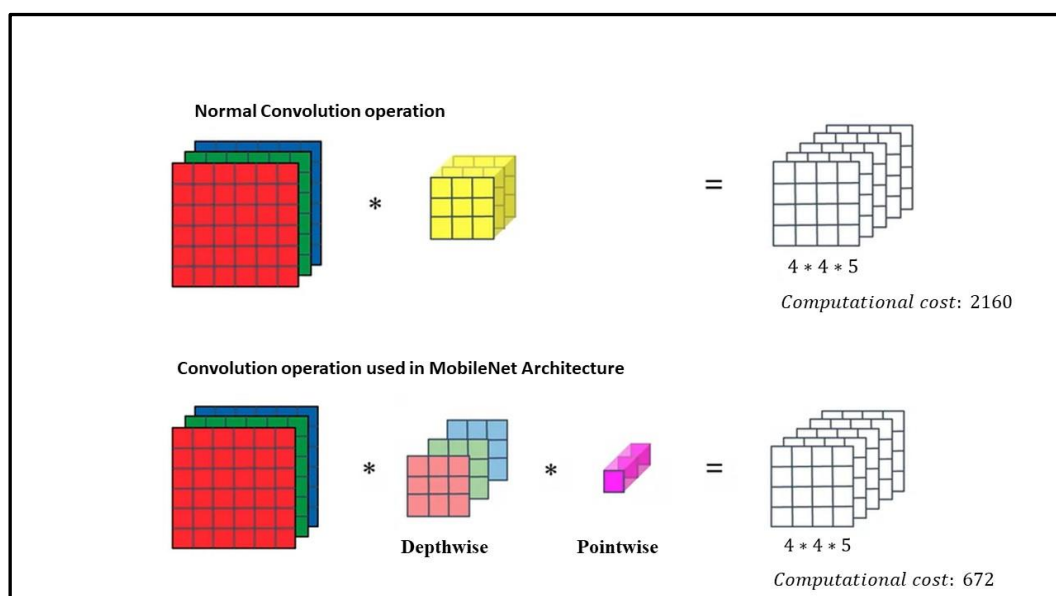


Figure 5. The difference between the convolution operation used in the MobileNet architecture and the normal convolution operation.

3.2.6. Proposed model

In this study, multiple neural network architectures, multiple CNN architectures and pre-trained CNN models have been tested and multiple experiments have been conducted, it has been observed that the neural network architecture can give better results for this problem. Therefore, in this study, a classical artificial neural network-based model has been adopted, and multiple pre-trained CNN models have been tested as a feature extraction phase for the proposed ANN model. First, we started with a shallow neural network architecture. Afterward, the number of layers used in the model and other hyperparameters have been changed and the model that gave the best result has been selected. Particularly, different values for regularization techniques such as L1 and L3, kernel initializers, activation functions, loss functions, batch normalization have been applied and tested in order to increase the performance and reduce the overfitting problem. In addition to this, all other

hyperparameters have been manipulated with different values, and at the end, the model that gave the most suitable and the best results for the research problem has been selected.

First, the images in the dataset have been resized to 180 x 180 size before being used for training the proposed ANN model. Then, the pixel values in the image have been normalized to be between 0 and 1. Afterward, the used dataset has been divided into 80% for training, 10% for testing, and 10% for validating the proposed model. In the next step, the two values for "batch size" has been tested i.e. 32 and 64, but when the batch size was 64, the model gave a better result, so the batch size of 64 has been used. Also, the data samples in each batch have been configured to be randomly selected when entered into the model. The same logic has been applied to the validation dataset. Therefore, the model was validated using different data samples in each epoch. This means that the model is trained using different data and validated using different data in each epoch. This prevents the model from falling into overfitting to some extent. In the experiments conducted to obtain the best performance, it was aimed to determine the number of layers that gave the best performance and the number of neurons in each layer. As a result of multiple experiments, when we reached a neural network model consisting of 7 layers as in Table 1, the best results have been obtained.

The "ReLU" activation function has been used in the hidden layers and the "softmax" activation function has been used in the output layer since the addressed problem is multi-class classification problem. "Adam" has been used as an optimizer and the "learning rate" value has been selected as 0.001 after trying a range of values. Moreover, "sparse categorical crossentropy" has been used as a loss function. Also, "he_uniform" has been used as a kernel initializer to optimize the performance of the model.

Table 1. Structure of the proposed ANN model.

Layers Number	Neurons Number
1	512
2	256
3	128
4	128
5	64
6	32
7	3

After selecting the best hyperparameter values of the ANN model that gives the best results, it is suggested to use some well-known pre-trained CNN architectures as a feature extraction phase to further improve the results of the proposed model. In particular, three well-known pre-trained architectures, namely ResNet, Inception, and MobileNet, have been tested. Figure 6 shows the final version of the proposed model.

4. EXPERIMENTAL RESULTS

The models proposed in this study has been implemented using Jupyter notebook and python programming language on a laptop with Intel(R) Core (TM) i7-9750H CPU @ 2.60GHz 2.59 GHz processor, NVIDIA GeForce GTX 1650 graphics card and 8 GB of memory. Multiple Python libraries such as Tensorflow, Tensorflow_hub, and Keras have been adopted to implement the proposed model.

First of all, some pre-processing operations have been applied to the images in the dataset, for example, all the images in the dataset have been resized to 180×180 and their pixel values have been rescaled to be between 0 and 1. We have conducted multiple experiments to select the best model that can achieve this task with the best score. For example, a different number of dense layers such as 2, 3, 4, 5, and 6 have been tested, and it is concluded that the model with 6 layers can give the best results. Also, we have tested 32, 64, 128,256, and 512 values for the number of units in each dense layer, 32 and 64 values for batch size, and 0.1, 0.01, and 0.001 values for the learning rate, uniform, normal, glorot_uniform, he_normal, he_uniform values for the weight initializer, and tanh and relu for the activation function used in the model's layers. As mentioned previously mentioned the model gave the best results contains six dense layers with relu activation function and he_uniform weight initializer in each layer.

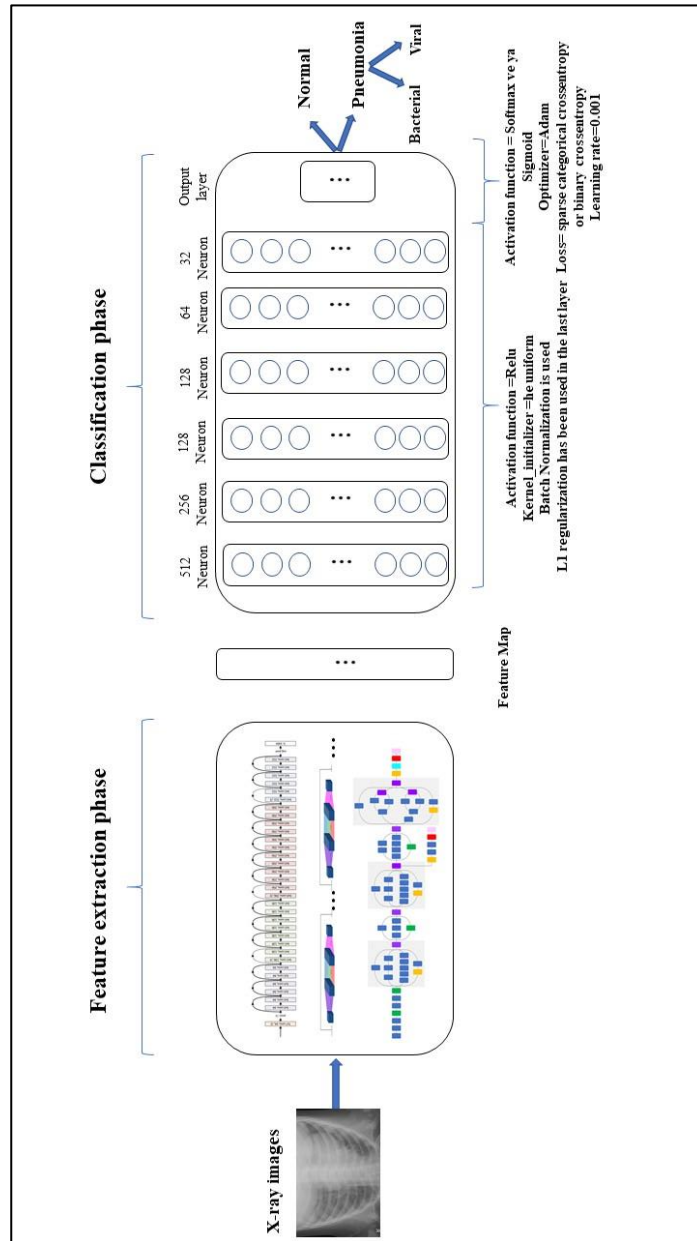


Figure 6. The proposed neural network model.

Also, we choose to use the Adam optimizer with a learning rate of 0.001 and 50 epochs to be used during training of the ANN model. Furthermore, the softmax or Sigmoid activation function has been adopted in the output layer for conducting the classification task depending on whether the task is a binary or multi-class classification. As a result of various trials, it has been observed that the model was exposed to a certain level of overfitting as shown clearly in the top section of figure 7. a. It can be noted from the figure that while the training loss decreased in accordance with the epoch number, it was not the case for the validation loss, where the validation loss increased with the increase in the epoch number. Also, we can note from the bottom section in figure 7. a, that while the training accuracy of the model increased in accordance with the increase in the number of epochs the validation accuracy was almost constant. No doubt it can be said that there is an overfitting problem in the model. So, various regularization techniques have been tested to overcome this problem. First, the "Batch Normalization" regularization technique has been applied between each hidden layer, but sufficient results could not be obtained. Afterward, the "dropout" technique has been applied, but this technique had a negative effect on the model's performance. At the same time, since the loss value of the model got close to zero after a certain number of epochs, the training of the model slowed down and almost stopped. In order to solve this problem, the "L1" regularization technique has been tested. When we look at the results after the application of L1 regularization, we noted that the accuracy rates obtained from the experiments performed on the test dataset improved as can be seen in Table 2. Also, figure 7. a show the changes in the loss and accuracy values during training and validating of the model before using the L1 regularization technique. It can be clearly seen from the figure that while the training loss decreases as the epoch progresses, the validation loss increases as the epoch progresses. Figure 7.b shows the changes in the loss and accuracy values during training and validating the model after using the L1 regularization technique. It can be observed from Figure 7.b that this problem has disappeared to a good extent. Particularly, by looking at the figure we can observe that each of the training loss and the validation loss decreased in accordance with the increase in epoch number. Also, the training accuracy and validation accuracy increased in accordance with the increase in the number of epochs. So, we could mitigate the overfitting problem to some extent. The highest accuracy rate obtained by applying the pure artificial neural network model for multi-class classification was 78.33%.

After, that we proposed using some well-known CNN architectures as a feature extraction phase to improve the results of the proposed neural network model. To this end, three pre-trained CNN models, namely ResNet, Inception, and MobileNet, have been used. The feature maps extracted using these models have been used to train the proposed neural network model.

First, the ResNet model were used as a feature extractor for the proposed ANN model. Since this model does not face the problem of overfitting like other CNN architectures, thanks to its skip connection logic, the "L1" regularization technique has not been applied. After training this model, the accuracy rate on the test dataset reached 81.67%. Then, the Inception structure were used as a feature extractor for the proposed neural network model. It has been seen that the accuracy rate of the trained model on the test dataset dropped down to 75% and negatively affected the original model.

Finally, the MobileNet architecture were used as a feature extractor for the proposed artificial neural network model. In this experiment, the performance of the model reached 78.67% and a slight improvement has been noted over the original model's performance.

As can be seen in Table 3, the ResNet-ANN model obtained the best accuracy value between the applied four scenarios, i.e. pure ANN model, Inception-ANN model, MobileNet-ANN model, and ResNet-ANN model. Also, the Precision, Recall, and f1 score values of the proposed ResNet-ANN model are shown in Table 4.

However, when we look at the results, the expected success has not been achieved even in the ResNet-ANN model, which gave the best results. So, we investigated the confusion matrix and the classification reports of the proposed models. As can be seen from the classification reports illustrated in Table 4 and the confusion matrix illustrated in Figure 8, the normal class has been detected with very high accuracy, and it was noticed that the highest error rate occurred between bacterial and viral classes. This is because the images in bacterial pneumonia and viral pneumonia classes have so many common features and similarities. Normally, these two classes have been considered as a single class in the previous studies in the literature [26]–[28]. Also, the high number of correctly classified images in the healthy class and the high number of misclassifications in other classes (which can be observed from the confusion matrix) support this situation. For example, 26 chest images from the first class (with Bacterial pneumonia class) have been wrongly perceived as second class (Viral pneumonia class), and 18 chest images from the second class have been wrongly perceived as first class. Also, by looking at the classification report, we can note that the Precision, Recall, and Accuracy metrics in the zeroth class (normal chest images) were very high, while these metrics were low for the other two classes. Therefore, we decided to test the performance of the proposed models after combining the two abnormal classes to be one class (applying binary classification for classifying the X-ray images as diseased and healthy).

Table 2. The effect of L1 regularization technique on the proposed ANN model.

L1 Regularization Technique	Accuracy Rate (%)
NONE	76,33
ACTIVE	78,33

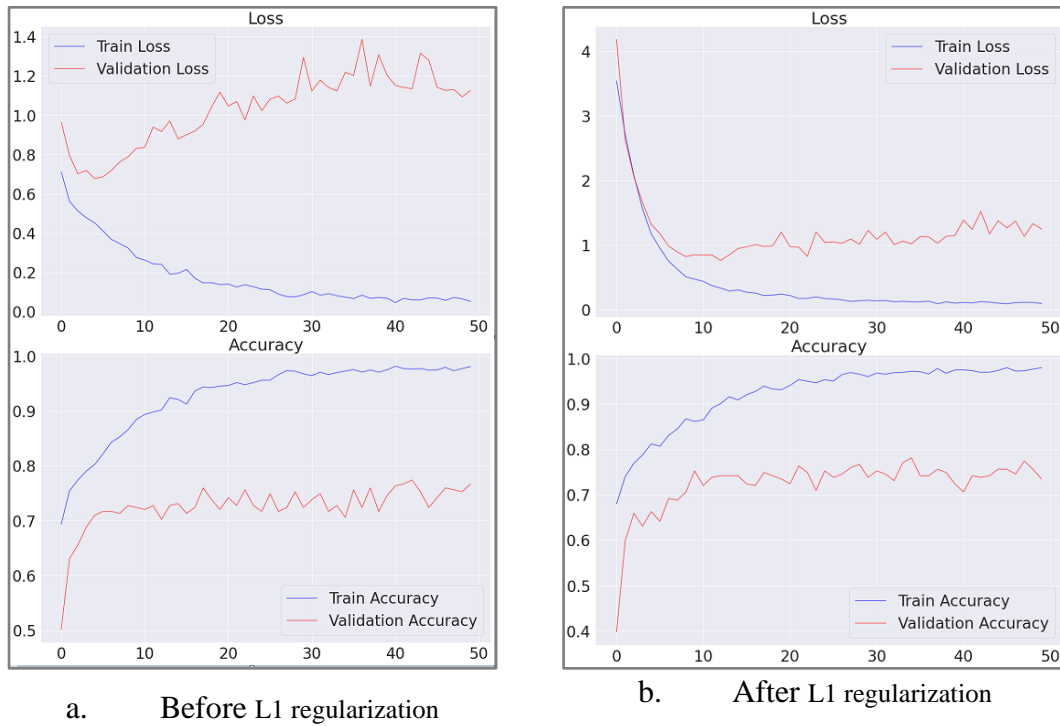


Figure 7. Loss and accuracy curves of the training and validation values of the model before and after the use of the L1 regularization.

Table 3. Comparison of the proposed models' results in multi-class classification.

Used Model	Accuracy Rate (%)
Artificial Neural Networks (ANN)	78,33
ResNet-ANN	81,67
Inception-ANN	75
MobileNet-ANN	78,67

Table 4. Classification report of the ResNet-ANN model used for multi-class classification.

Class	Precision	Recall	F1-Score
0	91	99	95
1	79	70	74
2	75	76	75

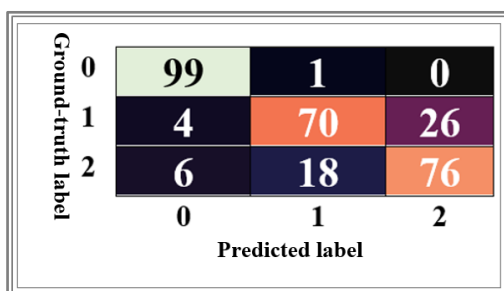


Figure 8. The confusion matrix of the ResNet-ANN model used for multi-class classification.

After that, we proposed using the same proposed architectures i.e. pure ANN model, Inception-ANN model, MobileNet-ANN, and ResNet-ANN model for conducting binary classification. To this end, we changed the output layer in the model i.e. Softmax layer into Sigmoid layer, and the "sparse_categorical_crossentropy" loss function into "binary_crossentropy".

When the results obtained after conducting the binary classification process have been investigated it is observed that great success has been achieved by all the proposed architectures. In this case study, the proposed MobileNet-ANN model has achieved the best results with a classification accuracy of 95.67%.

Also, the classification report and confusion matrix of the MobileNet-ANN model, which gives the highest result in the binary classification dataset, are shown in Table 6 and Figure 9. As seen in the classification report and confusion matrix, the misclassification between the classes is very low. Particularly, the F1 scores of the proposed MobileNet-ANN architecture reached 97 and 94% for pneumonia and normal classes respectively. Also, it can be concluded from the confusion matrix that only 4 data samples from the normal class and 9 samples from the pneumonia class have been wrongly predicted by the model.

Table 5. Comparison between the results of the proposed models when they were used for binary classification.

Used Model	Accuracy Rate (%)
Artificial Neural Networks (ANN)	92,67
ResNet-ANN	94,33
Inception-ANN	94,33
MobileNet-ANN	95,67

Table 6. Classification report of the MobileNet-ANN model used for binary classification.

Class	Precision	Recall	F1-Score
0	91	96	94
1	98	95	97

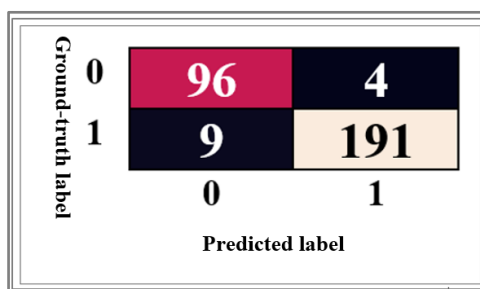


Figure 9. The confusion matrix of the MobileNet-ANN model used for binary classification.

5. COMPARISON STUDY

In this section, the results obtained using the proposed ANN model have been compared with some well-known and pre-trained CNN models. Particularly, in order to prove the efficiency of the proposed model, the pre-trained models that we used as the feature extraction phase in our model, namely ResNet, MobileNet, and Inception, have been tested as End-to-End models. In other words, the used pre-trained ResNet, MobileNet, and Inception models have been tested in terms of classifying X-ray images into two classes as standalone models. In addition, the results obtained in this work have been compared with the results of some previously conducted studies. using similar datasets. Table 7 shows the conducted comparison study. Also, figure 10 illustrates a comparison between the proposed models in terms of the obtained classification accuracy.

Table 7. Comparison of the obtained results.

Study	Year	Used Model	Classification Accuracy
DARICI et al. [14]	2020	CNN model	95%
Kaushik et al. [23]	2020	CNN model	92.31%
Mabrouk et al. [24]	2022	Ensemble CNN model	93.91%
Sharma et al. [25]	2020	CNN model	90.68%
Tested End-to-End MobileNet	-	Pre-trained MobileNet	88.33%
Tested End-to-End ResNet	-	Pre-trained ResNet	91.33%
Tested End-to-End Inception V3	-	Pre-trained Inception V3	91.33%
ResNet-ANN	-	Pre-trained ResNet + ANN	94,33
Inception-ANN	-	Pre-trained Inception V3 + ANN	94,33
MobileNet-ANN	-	Pre-trained MobileNet + ANN	95,67

6. DISCUSSION AND CONCLUSION

Lung X-Ray images can be used as a first-line procedure to detect and classify healthy persons, patients with viral pneumonia, and patients with bacterial pneumonia. At the same time, the similarity between the features of the lung X-Ray images with viral pneumonia and the image with bacterial pneumonia makes it difficult for radiologists and physicians to diagnose the disease. In this study, an artificial neural network-based model has been proposed to diagnose pneumonia lung images. The proposed ANN model has been built empirically so that a range of values for each hyperparameter has been tested and the structure that can give the best results has been chosen. To this end, multiple values have been tested for multiple hyperparameters including the number of dense layers, the unit number in each layer, activation functions, the weight initializer that should be used in each layer, the batch size used during fed the data to the model, and the learning rate that should be used for training the model. First, the proposed ANN model has been tested as an end-to-end model in order to evaluate its efficiency in detecting pneumonia from X-ray images. This model has been named as Pure ANN model. After that, we proposed to use some well-known CNN architectures as a feature extraction phase to improve the performance of the proposed pure ANN model. To this end, three different pre-trained CNN architectures namely ResNet, Inception, and MobileNet, have been adopted as a feature extraction phase for the proposed pure ANN model. Therefore, four different deep learning models, namely pure ANN, ResNet-ANN, MobileNet-ANN, and Inception-ANN, have been proposed for detecting pneumonia from X-Ray images. The proposed four models have been used in two different scenarios. In the first scenario, the proposed models have been adopted for classifying the lung X-ray images into three classes (multi-class classification) namely normal lung, lung with viral pneumonia, and lung with bacterial pneumonia. In the second scenario, the proposed models have been adopted for classifying the X-ray images as pneumonia-free lung (or normal lung) and lung with pneumonia. As a result, it was concluded that the deep learning techniques can reliably distinguish lung X-Ray images of patients with bacterial and viral pneumonia from lung X-Ray images of other healthy people. In fact, the deep learning model that gives the best results has been obtained by hybridizing the MobileNet well-known model with a fine-tuned ANN model, and its accuracy rate reached 95.67%, as seen in Figure 10. However, since the X-Ray images of patients with viral and bacterial pneumonia are very similar, all the models used were partially successful in distinguishing between the viral and bacterial pneumonia images. Particularly, when the X-ray images have been classified into three classes using the proposed model the ResNet-ANN gave the best results with an accuracy rate of 81.67%. At the end of the conducted study, and as proof of concepts for the efficiency of the proposed models, we tested the used three pre-trained models as end-to-end models and the obtained results have been compared with the results obtained when the same models have been used as feature extractor for the proposed ANN model. We concluded that it is more efficient to use these models as aid models for some other models rather than using them as end-to-end models, where their accuracy did not exceed 91.33% compared to 94.33 and 95.67% that was obtained by using these models as a feature extraction phase for the proposed model. Therefore, it can be concluded that this model can be used as X-Ray image-based diseases detector in order to ease the work of health sector specialists.

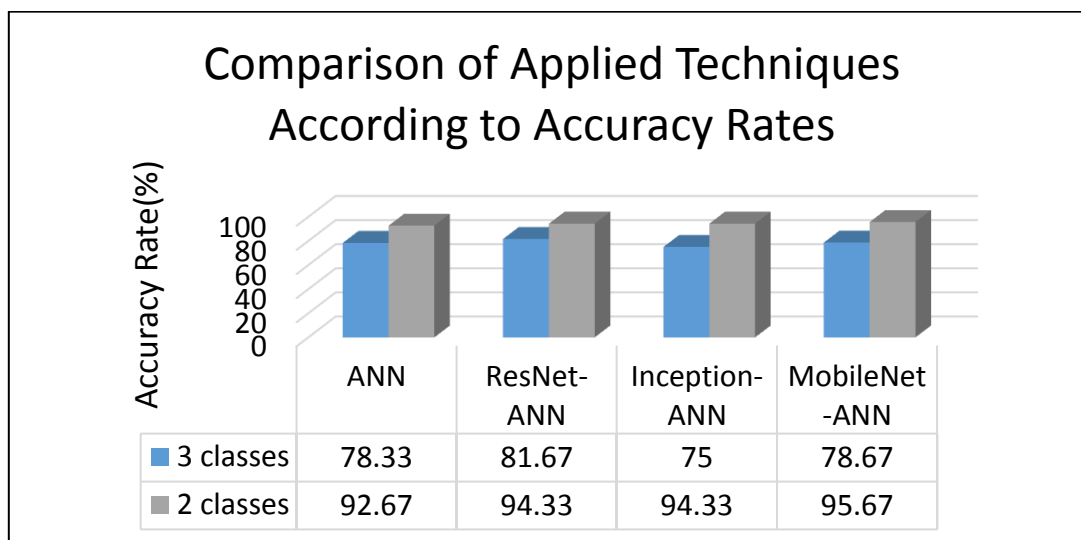


Figure 10. Comparison of proposed models According to Accuracy Rates.

In future studies, deeper and more fine-tuned structures can be conducted using a better level of processor capabilities and larger datasets. In addition, hyperparameters in the model can be fine-tuned using optimization methods such as Grid Search and Bayesian optimization algorithms. Also, the deep learning techniques such as well-known CNN architectures, ANN structures, and maybe auto-encoder structures can be tuned and used as a feature extractors for classical machine learning algorithms.

ACKNOWLEDGEMENT

The authors would like to thank Google Colaboratory for allowing to run the model effectively on the cloud and for free.

REFERANCES

- [1] Ayan, R. and Ünver, H. M., (2019), “Diagnosis of pneumonia from chest X-ray images using deep learning,” in 2019 Scientific Meeting on Electrical-Electronics & Biomedical Engineering and Computer Science (EBBT), pp. 1–5.
- [2] Rajpurkar et al., (2017), “Chexnet: Radiologist-level pneumonia detection on chest x-rays with deep learning,” arXiv preprint arXiv:1711.05225.
- [3] El Asnaoui, K.,Chawki, Y. and Idri, A., (2021), “Automated methods for detection and classification pneumonia based on x-ray images using deep learning,” in Artificial intelligence and blockchain for future cybersecurity applications, Springer, pp. 257–284.

- [4] Jain, R., Nagrath, R., Kataria, G., Kaushik, V. S. and Hemanth, D. J., (2020), "Pneumonia detection in chest X-ray images using convolutional neural networks and transfer learning," *Measurement*, vol. 165, p. 108046.
- [5] Hasan et al., (2021), "Deep learning approaches for detecting pneumonia in COVID-19 patients by analyzing chest X-ray images," *Math Probl Eng*, vol. 2021, pp. 1–8.
- [6] Stephen, O., Sain, M., Maduh, U. J. and Jeong, D-U., (2019), "An efficient deep learning approach to pneumonia classification in healthcare," *J Healthc Eng*, vol. 2019.
- [7] Elshennawy, N.M. and Ibrahim, D. M., (2020), "Deep-pneumonia framework using deep learning models based on chest X-ray images," *Diagnostics*, vol. 10, no. 9, p. 649.
- [8] Jaiswal, A. K., Tiwari, P., Kumar, S., Gupta, D., Khanna, A. and Rodrigues, J. J. P. C., (2019) "Identifying pneumonia in chest X-rays: A deep learning approach," *Measurement*, vol. 145, pp. 511–518.
- [9] El Asnaoui, K. and Chawki, Y., (2021), "Using X-ray images and deep learning for automated detection of coronavirus disease," *J Biomol Struct Dyn*, vol. 39, no. 10, pp. 3615–3626.
- [10] Ouchicha, C., Ammor, O. and Meknassi, M., (2020), "CVDNet: A novel deep learning architecture for detection of coronavirus (Covid-19) from chest x-ray images," *Chaos Solitons Fractals*, vol. 140, p. 110245.
- [11] Narin, A., Kaya, C., and Pamuk, Z., (2021), "Automatic detection of coronavirus disease (covid-19) using x-ray images and deep convolutional neural networks," *Pattern Analysis and Applications*, vol. 24, pp. 1207–1220.
- [12] Ozturk, T., Talo, M., Yildirim, E. A., Baloglu, U. B., Yildirim, O. and Acharya, U. R., (2020), "Automated detection of COVID-19 cases using deep neural networks with X-ray images," *Comput Biol Med*, vol. 121, p. 103792.
- [13] Jain, G., Mittal, D., Thakur, D. and Mittal, M. K., (2020), "A deep learning approach to detect Covid-19 coronavirus with X-Ray images," *Biocybern Biomed Eng*, vol. 40, no. 4, pp. 1391–1405.
- [14] Darici, M. B., Dokur, Z. and Olmez, T., (2020) "Pneumonia detection and classification using deep learning on chest x-ray images," *International Journal of Intelligent Systems and Applications in Engineering*, vol. 8, no. 4, pp. 177–183.
- [15] Nayak, S. R., Nayak, D. R., Sinha, U., Arora, V. and Pachori, R. B., (2021), "Application of deep learning techniques for detection of COVID-19 cases using chest X-ray images: A comprehensive study," *Biomed Signal Process Control*, vol. 64, p. 102365.

- [16] Apostolopoulos, I. D., Aznaouridis, S. I. and Tzani, M. A., (2020), “Extracting possibly representative COVID-19 biomarkers from X-ray images with deep learning approach and image data related to pulmonary diseases,” *J Med Biol Eng*, vol. 40, pp. 462–469.
- [17] Bhardwaj P. and Kaur, A., (2021), “A novel and efficient deep learning approach for COVID-19 detection using X-ray imaging modality,” *Int J Imaging Syst Technol*, vol. 31, no. 4, pp. 1775–1791.
- [18] Bakır, H. and Yılmaz, Ş., “Using Transfer Learning Technique as a Feature Extraction Phase for Diagnosis of Cataract Disease in the Eye,” *International Journal of Sivas University of Science and Technology*, vol. 1, no. 1, pp. 17–33.
- [19] Kermany et al., (2018), “Identifying medical diagnoses and treatable diseases by image-based deep learning,” *Cell*, vol. 172, no. 5, pp. 1122–1131.
- [20] Khobragade, S., Tiwari, A., Patil, C. Y., and Narke, V., (2016), “Automatic detection of major lung diseases using chest radiographs and classification by feed-forward artificial neural network,” in *2016 IEEE 1st international conference on power electronics, intelligent control and energy systems (ICPEICES)*, pp. 1–5.
- [21] Hassaballah M., and Awad, A. I., (2020), *Deep learning in computer vision: principles and applications*. CRC Press.
- [22] Otter, D. W., Medina, J. R. and Kalita, J. K., (2020), “A survey of the usages of deep learning for natural language processing,” *IEEE Trans Neural Netw Learn Syst*, vol. 32, no. 2, pp. 604–624.
- [23] He, K., Zhang, X., Ren, S. and Sun, J., (2016) “Deep residual learning for image recognition,” in *Proceedings of the IEEE conference on computer vision and pattern recognition*, pp. 770–778.
- [24] Szegedy et al., (2015), “Going deeper with convolutions,” in *Proceedings of the IEEE conference on computer vision and pattern recognition*, pp. 1–9.
- [25] Howard et al., (2019), “Searching for mobilenetv3,” in *Proceedings of the IEEE/CVF international conference on computer vision*, pp. 1314–1324.
- [26] Sirish Kaushik, V., Nayyar, A., Kataria, G. and Jain, R., (2020), “Pneumonia detection using convolutional neural networks (CNNs),” in *Proceedings of First International Conference on Computing, Communications, and Cyber-Security (IC4S 2019)*, pp. 471–483.
- [27] Sharma, H. , Jain, J. S., Bansal, P., and Gupta, S., (2020), “Feature extraction and classification of chest x-ray images using cnn to detect pneumonia,” in *2020 10th International Conference on Cloud Computing, Data Science & Engineering (Confluence)*, pp. 227–231.

- [28] Al Mubarak, A. F., Dominique, J. A. M. and Thias, A. H., (2019), "Pneumonia detection with deep convolutional architecture," in 2019 International conference of artificial intelligence and information technology (ICAIIIT), pp. 486–489.



RESEARCH ARTICLE

ECOLOGICAL EVALUATION OF UNCOMMON HEAVY METALS CONTAMINATION IN THE SOILS OF THE CENTRAL PROVINCE OF UŞAK, WESTERN TURKIYE

Ümit YILDIZ^{1*}

¹Black Hills Natural Science Field Station, South Dakota Mines, Geology & Geological Engineering, 57701, Rapid City, USA.
E-posta: umit.yildiz@sdsmt.edu, ORCID: 0000-0002-3843-7203

Receive Date: 04.03.2023

Accepted Date: 28.03.2023

ABSTRACT

This study aimed to evaluate the concentrations of the uncommon heavy metals (Ag, Bi, Co, Sb, Th, Tl, U, and V) in 90 soil samples obtained from both urban and agricultural lands near Uşak, western Turkiye to investigate dimensions of the existing ecological pollution using geoaccumulation and enrichment factor indices, and to identify their potential pollutants. The concentration values for the selected elements ranged from 0.01 to 0.46 mg/kg for silver (Ag); 0.07 to 0.72 mg/kg for bismuth (Bi); 7.9 to 55.8 mg/kg for cobalt (Co); 0.12 to 27.99 mg/kg antimony (Sb); 3.4 to 17.7 mg/kg for thorium (Th); 0.04 to 0.5 mg/kg for thallium (Tl); 0.3 to 7.3 mg/kg for uranium (U); and 18 to 72 mg/kg for vanadium (V). Igeo values of Ag showed moderate to heavy contamination in the city center of Uşak province. Igeo values of Bi and Sb in the west part of the study area indicated extremely contaminated soils. EF values for Bi and Sb also showed significant enrichment in the soils in the western portion of the study area which further validates that the potential sources for Bi and Sb heavy metals contaminations might be anthropogenic.

Keywords: *Uncommon heavy metals contamination, Geoaccumulation index, Enrichment Factor, Bismuth, Antimony.*

1. INTRODUCTION

Rapid industrialization and population growth, especially in developing countries, have started to be inevitable problems related to environmental pollution by heavy metals contamination which is one of the biggest issues facing the world today. Heavy metals are generally defined as metals or metalloids with a density higher than 5 g/cm³ [1-2]. It has been observed by numerous scholars that toxic elements (e.g., heavy metals) infiltrate humans and animals via the skin, the digestive system, or respiration. [3-4]. Toxic heavy metals have been proven to pose a major threat to human and animal health because of their capacity to affect DNA and disrupt the functioning of enzymes and protein molecules [5]. Although the heavy metals enter the organism easily, they are not so easily expelled from the metabolism and accumulate in the organism over time. Most of the health problems due to heavy metals accumulation in the human metabolism are chronic diseases or cancers that require

advanced diagnosis and treatment [6]. The heavy metals accumulation in soils occurs mostly at the surface or depths close to the surface. Almost all of the heavy metals are adsorbed by clay minerals in the soil or turn into stable forms by forming organic compounds in the soil. The heavy metal concentration in the soil decreases with depth [7], thus physicochemical properties of the soils play a major role during ecological assessment efforts. Heavy metals contamination in the soil occurs usually due to agricultural activities, waste disposal, industrial activities and effluents, mining and smelting, corrosion of metallic materials, motor vehicle exhaust, and electronic and biomedical waste (Figure 1). Environmental pollution caused by the accumulation of common heavy metals (As, Al, Cd, Cr, Cu, Hg, Pb, Ni, and Zn) and their anthropogenic sources in soils has been extensively studied before. However, the ecotoxicity of uncommon heavy metals (Ag, Bi, Co, Sb, Th, Tl, U, and V) in soils is currently underestimated and needs to be researched in order to better understand their impact on the environment [8]. This is due to the fact that their pollution is far less prevalent than that of common heavy metals. The purpose of this study is: (1) to analyze the concentrations of the selected uncommon heavy metals (Ag, Bi, Co, Sb, Th, Tl, U, and V) by obtaining chemical data from 90 samples collected from both urban and agricultural soils within the municipal boundaries of Uşak province, Türkiye; (2) to examine the extent of the current ecological pollution using a variety of geostatistical techniques, and (3) to identify their potential pollutants.

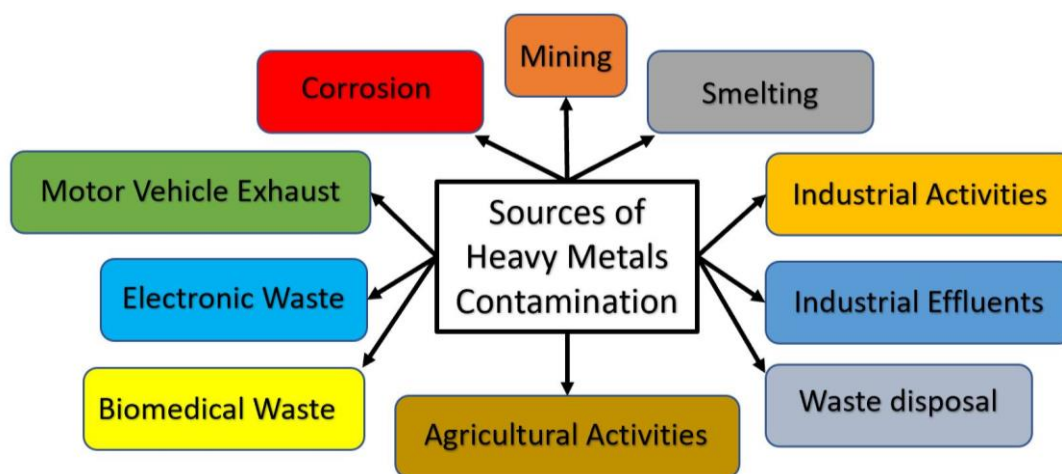


Figure 1. The image shows common anthropogenic pollutant sources of heavy metals contamination in soils.

2. STUDY AREA

The research site is situated in the central province of Uşak, a small city located in western Türkiye (Figure 2). Uşak province has a land area of around 5,341 km² and its total population is approximately 375,000 according to the 2021 census [9]. The climate in Uşak alternates between a continental climate, where the temperature differences between the seasons are large, and a Mediterranean climate, where summers are hot and mostly dry, and winters are generally mild. The

annual average temperature in Uşak is 12°C and the annual precipitation varies between 430 mm and 700 mm.

Uşak province has a long history of industrialization. Türkiye’s first factory processing sugar was established in 1926 in Uşak, consequently, the first electricity in Türkiye was utilized at this establishment. Uşak province received its share of the rapid industrialization, along with other provinces in Türkiye. Due to the city's strategic location along the E-96 major highway connecting Ankara and İzmir, its accessibility to international ports, and the availability of a rail transit system, industrialization has become inevitable for the city. In 1988, a mixed-organized industrial zone was established for leather tanning, and the organized industrial zone began its operations in 1994. As of 2022, the city of Uşak is home to 625 businesses, both large and small, that are currently engaged in a variety of industries, including the manufacturing of ceramics, ferrous metals, chemical paints, solid waste incineration, leather tanning, and textile. Furthermore, the population of the central province of Uşak is around 256,000, and the number of registered vehicles exceeds 149,000 [9].

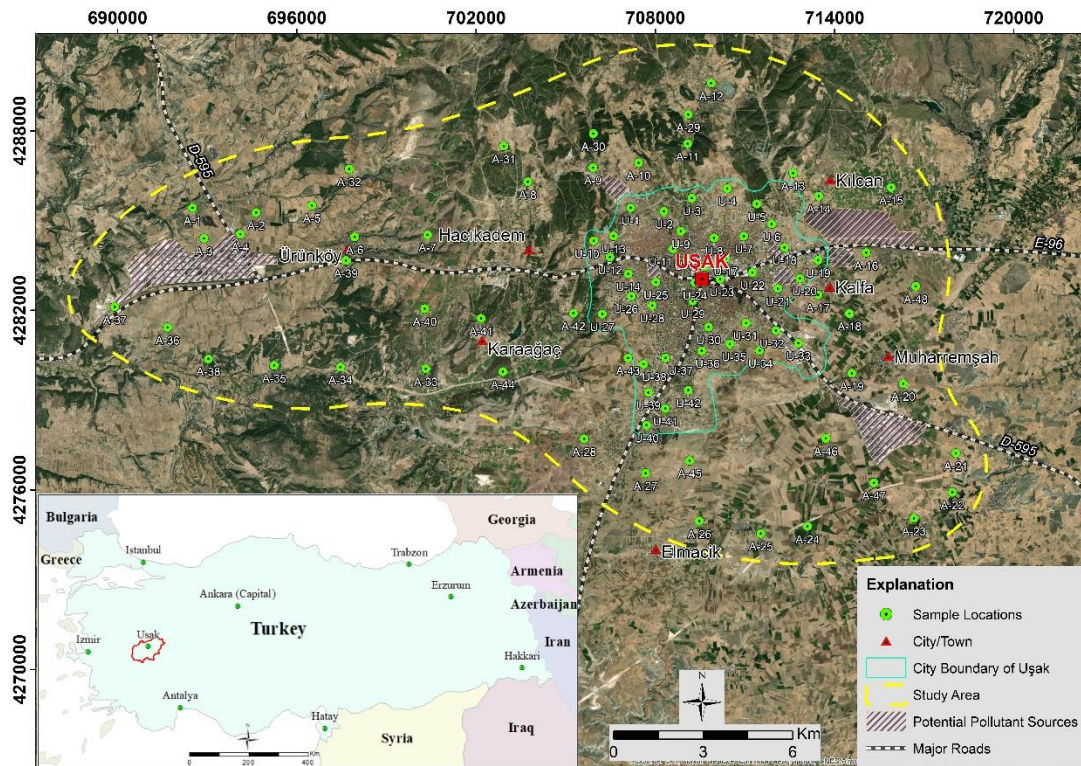


Figure 2. The study area and the soil sampling points are shown in two maps.

2.1. Regional Geologic Settings

Paleozoic age metamorphic rocks (gneiss, schist, and marble) of the Menderes Massif form the oldest tectonostratigraphic units in Uşak [10] (Figure 3). The Jurassic Kızılcaşöğüt Formation unconformably overlays the Menderes Massif, which is composed of metasandstone, metasiltstone, and slightly dolomitized limestones. A mélangé, considered to have formed in an accretionary complex, was emplaced on the Kızılcaşöğüt Formation in Late Cretaceous. Tertiary volcanic activities further shaped the geology of the region (Beydağ and Karaboldere formations). The Uşak region was affected by the western extensional province in the Lower Miocene. As a result, structural basins were formed during Neogene. Lacustrine argillaceous limestones (Ulubey Formation) were deposited in these basins during the Pliocene, and with the drying of these lakes during the Quaternary Period, terrestrial sediments were deposited in both alluvial and fluvial environments.

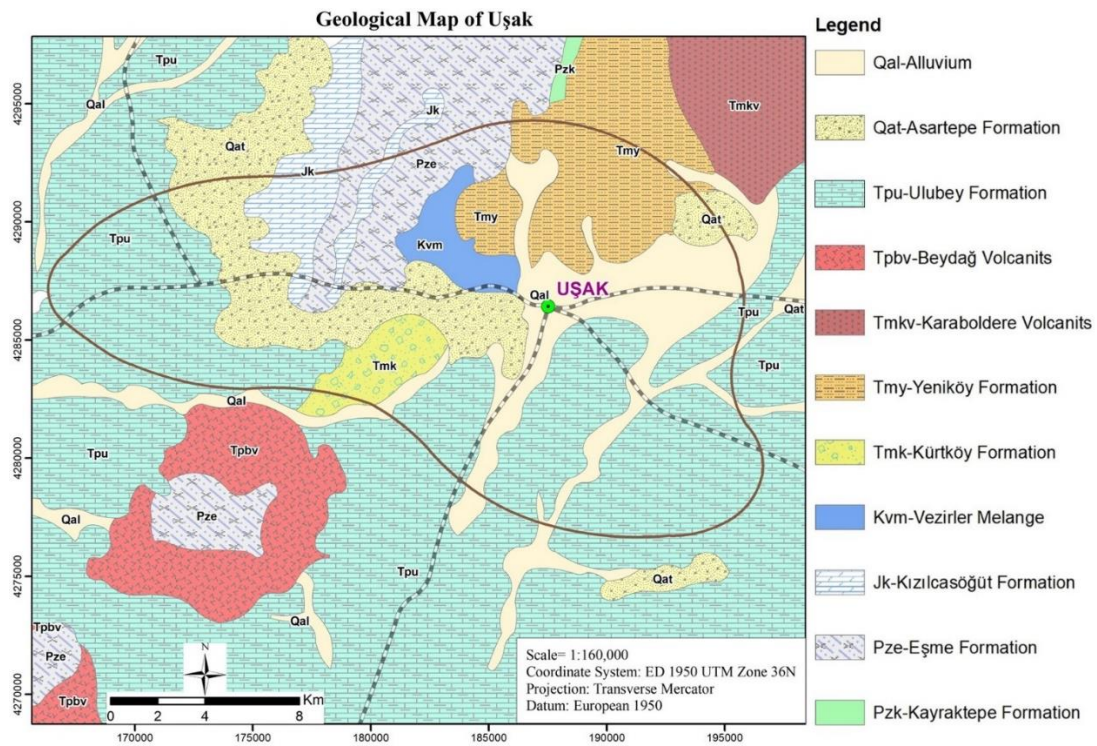


Figure 3. Geologic map of Uşak showing major formations [10].

3. MATERIALS AND METHODS

3.1. Analytical Methods

90 soil samples were taken both from urban and agricultural lands of the central province of Uşak considering the locations of potential pollutant sources. The research site covers an area of

approximately 340 km² (Figure 2). Soil samples were collected in September 2021. Unique object IDs were assigned for both urban (U-1, U-2.....) and agricultural (A-1, A-2.....) soil samples. Plastic shovels were used for sampling and approximately one-kilogram soil sample was taken from 0-20 cm depth. The samples were kept until further analysis in gallon-size sealable plastic bags. In situ pH measurements were also made by using a portable Hanna pH meter. Each sampling site's geographic location was documented using a handheld Garmin E-trex unit. The coordinate system was set up using European Datum 1950 and Zone 35 North of the Universal Transverse Mercator (UTM). All of the soil samples taken from the study area were dried at room temperature for 5 days in a laboratory environment. Then soil specimens were passed through an 80-mesh sieve to obtain a grain size of 180 µm, which is ideal for chemical analysis of soil samples [11-12]. The dissolution process of the samples was carried out in Aqua Regia solution (HCl+HNO₃+H₂O) of 0.5 g dried and powdered soil sample at 95°C for an hour. This technique is frequently used in the chemical analysis of soils because it is one of the closest solubilization methods to the total concentrations [13]. Concentration measurements of selected uncommon heavy metals (Ag, Bi, Co, Sb, Th, Tl, U, and V) from the solutions were made by ACME (Canada) laboratories using AQ250-Ultratrace ICP-MS method. Later, the same method was used to analyze four blank soil pulps. For the purposes of quality assurance and control, the analytical procedures were tested using the standardized reference materials DS11 and STD OREAS262. In order to determine ecologic pollution levels in soils; geoaccumulation and enrichment factor parameters were utilized. Data from the analysis were then transferred to a personal computer for additional assessments. All geostatistical operations and map productions were performed using ArcMap software [14].

3.2. Data Analysis

3.2.1. Geoaccumulation index

The geoaccumulation index (I_{geo}) is employed to examine the level of metal pollution in the soil by comparing the existing element values with the values before industrialization. The I_{geo} was first introduced by Müller [15] and is currently used by many researchers for the assessment of soil pollution [16-17-18-19-20-21]. The following equation can be used to calculate geoaccumulation (Eq.1):

$$I_{geo} = \log_2\left(\frac{C_n}{1.5 \times B_n}\right) \quad (1)$$

where C_n is the value of the metal concentration in the soil sample; B_n is the mean value of n metal in soil [22]; 1.5 is the base value matrix corresponding to correlation factor values. Müller [15] divided geoaccumulation index values into 7 different pollution categories:

Category	Value	Soil quality
i	$I_{geo} \leq 0$	Unpolluted
ii	$0 < I_{geo} < 1$	Unpolluted to moderately polluted
iii	$1 < I_{geo} < 2$	Moderately polluted
iv	$2 < I_{geo} < 3$	Moderately to heavily polluted
v	$3 < I_{geo} < 4$	Heavily polluted
vi	$4 < I_{geo} < 5$	Heavily to extremely polluted

vii 5<Igeo Extremely polluted

3.2.2. Enrichment factor

The enrichment factor (EF) is a method that is widely used to identify and compare the rate and degree of soil pollution associated with heavy metals [23]. The EF is determined by normalizing the amount of a measured element to the reference value of the same element. The reference element is characterized by the fact that its concentration in the soil does not change and it has a very low chemical reaction [24-25]. Mn, Al, Fe, Zn, Ti, and Sc are the reference elements that are most commonly utilized [25-26-27-28-29-30]. During this research, Mn was employed as the normalizing reference element. For EF calculations, Mielke's [22] composition of the Earth's crust was used for reference values of all studied elements (Ag: 0.075 mg/kg; Bi: 0.0085 mg/kg; Co:25 mg/kg; Sb:0.2 mg/kg; Th: 9.6 mg/kg; Tl: 0.85 mg/kg; U: 2.7 mg/kg; V: 120 mg/kg). The EF can be calculated with Eq. 2:

$$EF = \frac{\left(\frac{C_n}{C_{ref}}\right) \text{ sample}}{\left(\frac{B_n}{B_{ref}}\right) \text{ background}} \quad (2)$$

where C_n is the quantity of the studied element in the soil sample, C_{ref} is the quantity of the reference element in the studied sample, and B_n is the quantity of the examined element in the reference environment whereas B_{ref} is the quantity of the reference element in the environment that serves as the reference [21, 22, 25]. Sutherland [30] divided EF values into 5 classes:

Class	EF value	EF category
i	EF < 2	Minimal enrichment
ii	EF = 2–5	Moderate enrichment
iii	EF = 5–20	Significant enrichment
iv	EF = 20–40	Very high enrichment
v	EF > 40	Extremely high enrichment

4. RESULTS

Descriptive statistical results of the analyses of 90 soil samples taken from the central province of Uşak are presented in Table 1. Heavy metals concentrations obtained from 90 soil samples were used to investigate potential ecological pollution within the study area. Igeo values are given in Table 2, and EF values are presented in Table 3.

4.1. Concentrations of Heavy Metals

The uncommon heavy metals concentration values for the selected elements ranged from 0.01 to 0.46 mg/kg (average: 0.04 mg/kg) for silver (Ag); 0.07 to 0.72 mg/kg (average: 0.25 mg/kg) for bismuth (Bi); 7.9 to 55.8 mg/kg (average: 23.5) for cobalt (Co); 0.12 to 27.99 mg/kg (average: 1.04 mg/kg) for antimony (Sb); 3.4 to 17.7 mg/kg (average: 8.3 mg/kg) for thorium (Th); 0.04 and 0.5 mg/kg (average: 0.26 mg/kg) for thallium (Tl); 0.3 to 7.3 mg/kg (average: 0.9 mg/kg) for uranium (U); and 18 to 72

mg/kg (average: 35.7 mg/kg) for vanadium (V). Soil Quality Standards of Türkiye (SQST) set the maximum allowable limits for cobalt, thallium, and uranium as 20 mg/kg, 5 mg/kg, and 1 mg/kg respectively [31]. Maximum permissible concentrations in soils [8] for Ag, Bi, Sb, Th, and V are 3.1 mg/kg, 6.6 mg/kg, 3.2 mg/kg, 28.5 mg/kg, and 296 mg/kg respectively. This study shows the mean concentration values of Co exceed the SQST's limit, however, Ag, Bi, Sb, Th, Tl, U, and V values appear to be in a normal range. In addition, the mean concentration values of the studied heavy metals were compared to mean concentration values from various locations in the world [32, 33, 34, 35]. According to the findings of this study, none of the mean heavy metal concentrations exceeded the results obtained from other locations in the world (Table 1). The pH of the soil samples in the central province of the Uşak varied between 7.4 and 8.5, with a mean value of 8.0, indicating alkaline-type soils. Generally, prevailing winds blow from east to west.

Table 1. Heavy metals concentrations (mg/kg) and descriptive statistics of soil samples of Uşak.

	pH	Ag	Bi	Co	Sb	Th	Tl	U	V
Mean	8.03	0.04	0.25	23.54	1.04	8.36	0.26	0.93	35.71
Median	8.04	0.03	0.24	22.85	0.59	7.50	0.25	0.70	35.00
Min	7.42	0.01	0.07	7.90	0.12	3.40	0.04	0.30	18.00
Max	8.51	0.46	0.72	55.80	27.99	17.70	0.53	7.30	72.00
Skewness	-0.52	5.46	1.71	1.32	8.62	0.77	0.53	5.34	0.78
Kurtosis	1.21	35.79	4.83	2.78	78.33	-0.20	0.01	37.69	0.84
St. Dev.	0.19	0.06	0.11	8.69	2.97	3.42	0.10	0.84	10.86
Other studies (mean)	-	3.71	2.14	30	3.5	9	0.3	2	43

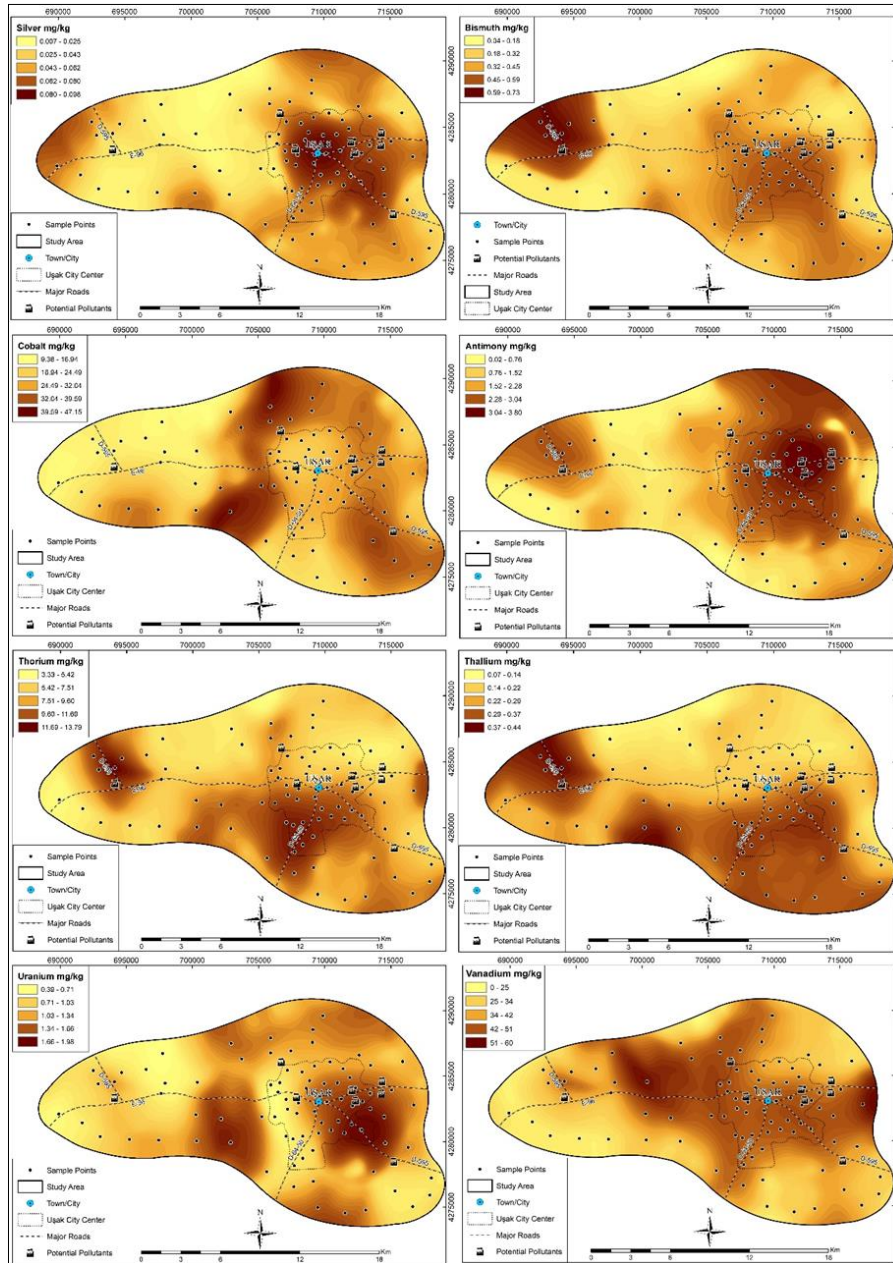


Figure 5. Spatial distribution maps show the fluctuations in the selected uncommon heavy metal concentrations.

Furthermore, ArcMap's kriging interpolation algorithm was utilized to produce distribution maps for each heavy metal concentration (Figure 5). The Ag concentration map shows elevated values in the city center. The concentration map for Bi indicates accumulation in the northwest part of the Uşak. The Co map shows higher concentration values surrounding the city center in every direction except due south. The northeast and northwest regions of the study area, as well as the city center, show elevated values on the Sb concentration map. The Th map shows that the study region has high values in the west and south. The Tl map mimics the Th map and shows elevated concentration values in the west and the south. A map for the U concentrations shows higher values in the east part of the city as well as the south and south-central part of the study area. The V map indicates accumulation within the city center and south-central portion of the research site. The obviously elevated concentration values of Bi, Tl, Th, and Sb in the west are directly correlative with the location of the largest industrial zone in the Uşak (Figure 5).

4.2. Geoaccumulation Index (Igeo) Values

A statistical summary of the Igeo values of the selected uncommon heavy metals in 90 specimens from the central province of Uşak is shown in Table 2. Igeo maps created for the selected uncommon heavy metals are also presented in Figure 6. Igeo values for Tl and V show no contamination within the study area which may indicate the concentration values at this location is due to geogenic sources. At certain locations, Igeo values for Co, Th, and U indicate uncontaminated to moderately contaminated soils. Igeo values of Ag suggest moderate to heavy contamination in the city center of Uşak province. Bi and Sb Igeo values show extremely contaminated soils in the west, around the large industrial zone, and in the city center of Uşak (Figure 6).

Table 2. Statistical summary of the geoaccumulation index (Igeo) values for the selected uncommon heavy metals within the study area.

	$I_{geo}(Ag)$	$I_{geo}(Bi)$	$I_{geo}(Co)$	$I_{geo}(Sb)$	$I_{geo}(Th)$	$I_{geo}(Tl)$	$I_{geo}(U)$	$I_{geo}(V)$
Mean	-1.78	4.19	-0.76	0.91	-0.90	-2.43	-2.39	-2.40
Median	-1.79	4.20	-0.71	0.98	-0.94	-2.38	-2.53	-2.36
Min	-3.81	2.46	-2.25	-1.32	-2.08	-4.99	-3.75	-3.32
Max	2.04	5.82	0.57	6.54	0.30	-1.27	0.85	-1.32
Skewness	0.94	-0.14	0.01	1.15	0.11	-0.84	1.12	-0.01
Kurtosis	2.46	0.83	0.54	4.07	-0.88	2.22	2.58	-0.39
St. Dev.	0.99	0.61	0.51	1.24	0.58	0.61	0.78	0.43

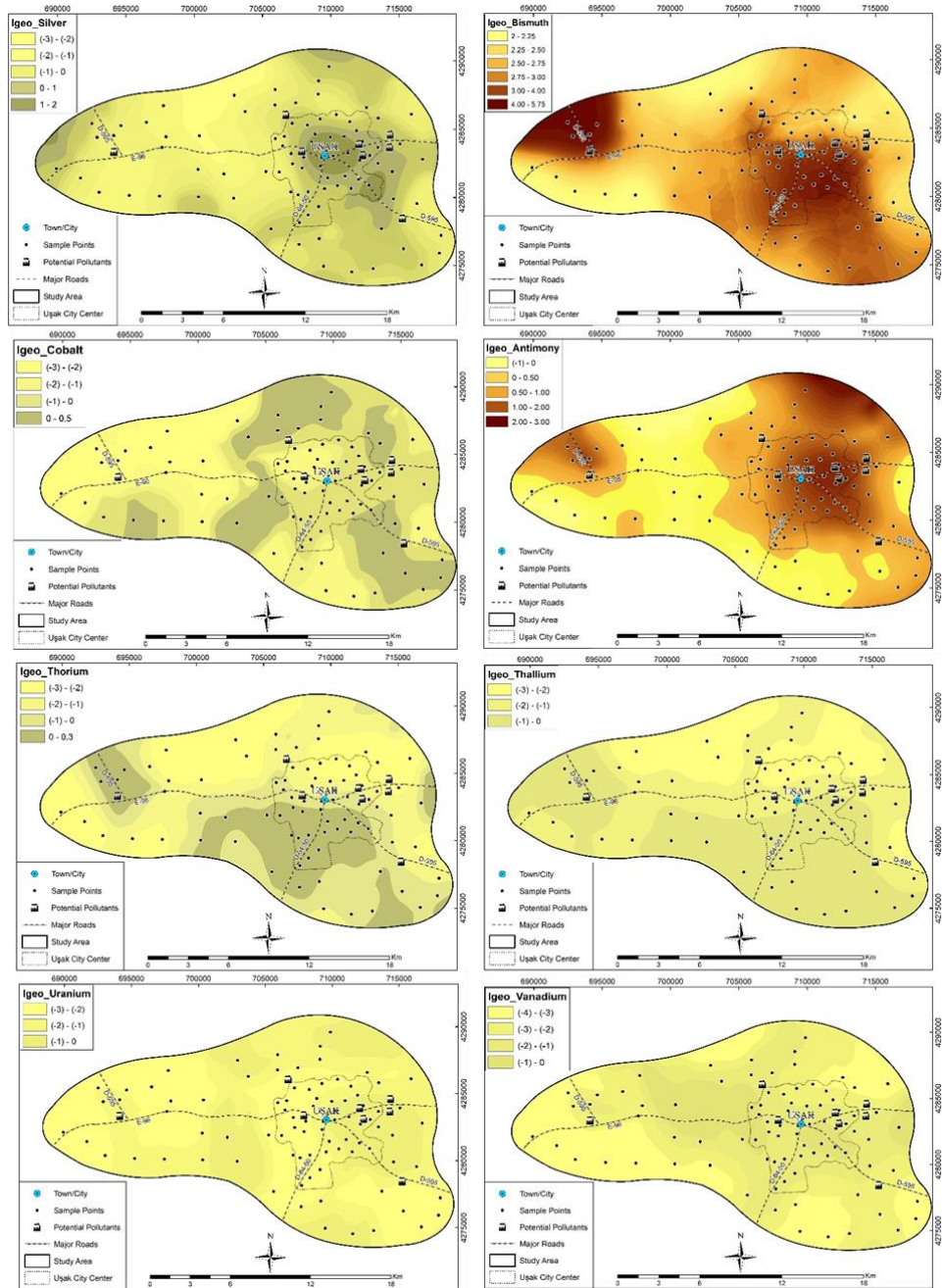


Figure 6. Maps showing the Igeo values for the uncommon heavy metals within the study area.

4.3. Enrichment Factor (EF) Values

A statistical summary of the enrichment factor (EF) values of the uncommon heavy metals in 90 soil samples from the central province of Uşak is presented in Table 3. The following are the mean EF values, listed from highest to lowest: Bi (51.62) is followed by Sb (8.82), Co (1.58), Th (1.53), Ag (1.01), U (0.65), Tl (0.52), and V (0.52). EF values for Ag, Co, Th, Tl, U, and V indicate minimal heavy metals enrichment in the research site. In addition, maps were created for the EF values and are presented in Figure 7. EF values for Sb suggest significant enrichment, especially in the northeast and northwest parts of the research site, and extremely high enrichment within the city center. EF values for Bi indicate significant enrichment in the city center and extremely high enrichment in the south-central and west parts of the study area (Figure 7). According to Yan et al., [36], both natural and anthropogenic sources can release Sb and Bi into the environment. In comparison to geogenic sources, anthropogenic activities such as smelting, fuel burning, waste incineration, the production of plastics and textiles, and motor vehicle brake wear have a significant impact on elevating Sb and Bi concentrations in soils [37, 38, 39]. Presence of the city's largest industrial site in the west where elevated EF values of Sb and Bi suggests that industrial activities might be the potential sources of the pollution. Domestic waste, corrosion, and industrial activities in the city center might also be the source for the significant enrichment of these two substances (Sb and Bi).

Table 3. Statistical summary of the EF values for the selected uncommon heavy metals within the study area.

	EF(Ag)	EF(Bi)	EF(Co)	EF(Sb)	EF(Th)	EF(Tl)	EF(U)	EF(V)
Mean	1.01	51.62	1.58	8.82	1.53	0.52	0.65	0.52
Median	0.72	44.58	1.41	4.49	1.37	0.47	0.41	0.47
Min	0.15	12.01	0.50	1.20	0.42	0.06	0.13	0.15
Max	11.70	214.50	5.99	242.61	11.30	3.05	7.46	3.28
Skewness	5.96	3.31	3.88	8.66	6.75	5.47	5.96	6.50
Kurtosis	42.10	14.36	22.32	78.88	55.97	41.31	42.28	51.70
St. Dev.	1.39	30.14	0.66	25.73	1.17	0.32	0.88	0.34

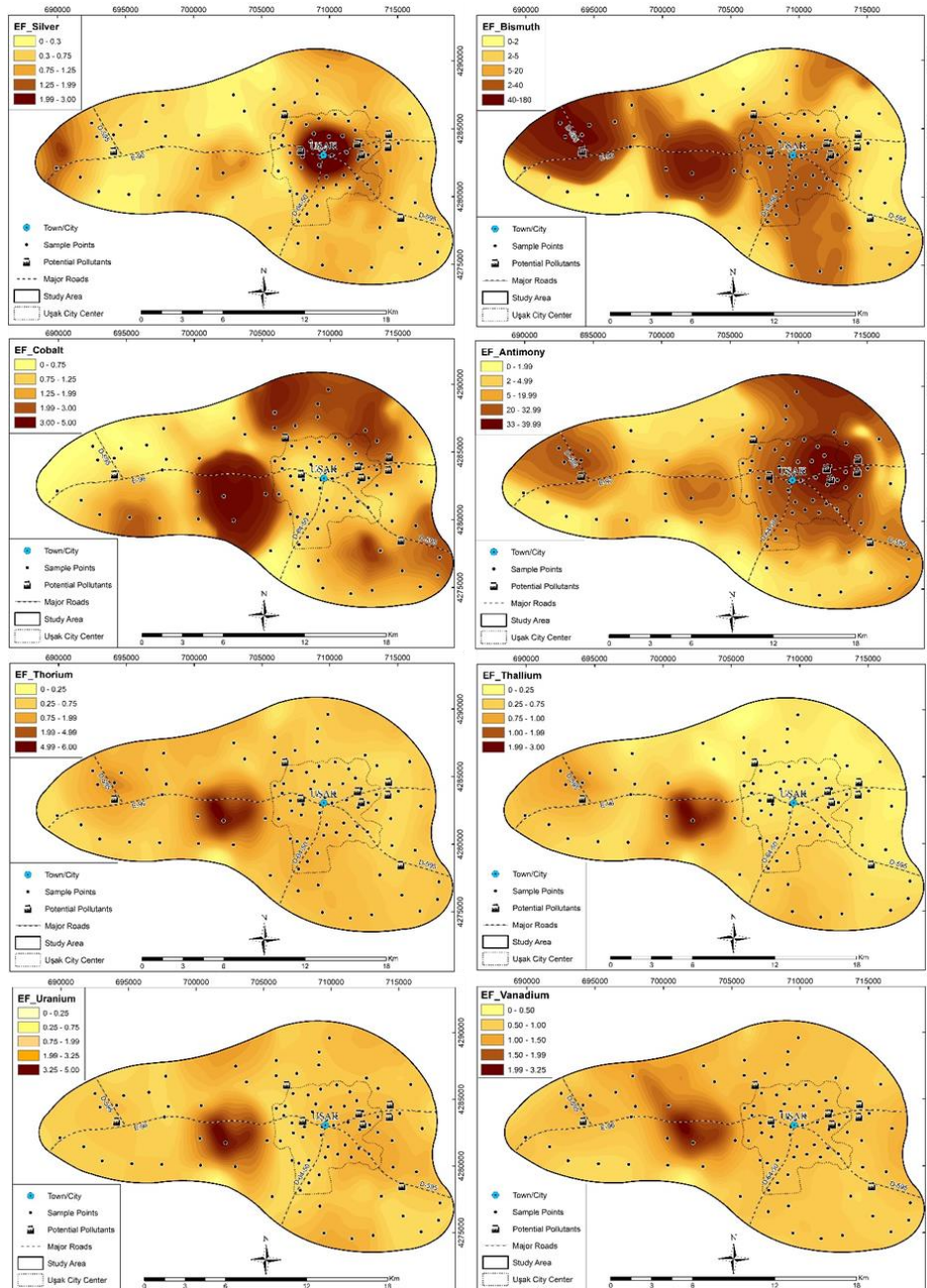


Figure 7. Maps illustrate the variations of the EF values for each heavy metal within the study area.

5. DISCUSSIONS AND CONCLUSIONS

During this research, chemical data from 90 soil samples collected from both urban and agricultural lands of the central province of Uşak was examined to identify ecological pollution and the potential pollutant sources. Igeo and EF indices were utilized to examine the existing ecologic risks both in the urban and agricultural soils of the Uşak. In addition, maps for the heavy metal concentrations, Igeo values, and EF values were generated to observe their spatial distributions within the study area. This study suggests that except for Co, the mean concentration values of Ag, Bi, Sb, Th, Tl, U, and V appear to be in a normal range. Igeo values of Ag showed contamination in the city center that ranges from moderate to heavy, potential pollutant source for the Ag contamination in the city center was interpreted to be due to domestic waste. Igeo values of Bi and Sb in the west part of the study area indicated extremely contaminated soils. These elevated Igeo values appeared to be in the soils around the Uşak Organized Industrial Zone (UOIZ) which might suggest that industrial activities such as paint manufacturing and waste disposal and burning are potential pollutants. Spatial distribution maps of EF values for Bi and Sb also showed significant enrichment in the soils around the UOIZ which further validates that the potential sources for Bi and Sb heavy metals contaminations might be the industrial activities at this specific location.

Finally, the soils of the central province of Uşak have shown pollution associated with the selected uncommon heavy metals. For future research, it is recommended to take more frequent samples by expanding the coverage of the research site. Based on the findings of this study, uncommon heavy metals can also cause soil pollution. It is therefore recommended that uncommon metals should be included in future environmental studies.

ACKNOWLEDGMENT

This study was funded by Dumlupınar University with the project number BAP/2021-28. This article was presented as an oral presentation at the 5th International Congress of Engineering Sciences and Multidisciplinary Approaches held in Istanbul between 25-26 February 2023 with remote access and the abstract was published in the congress proceedings abstract book with the following title "ECOLOGICAL EVALUATION OF UNCOMMON HEAVY METALS CONTAMINATION IN THE SOILS OF THE CENTRAL PROVINCE OF UŞAK, WESTERN TURKIYE".

REFERENCES

- [1] Duffus, J. H. (2002). Heavy metals a meaningless term (IUPAC Technical Report). Pure and applied chemistry, 74(5), 793-807.
- [2] Kahvecioğlu, Ö., Kartal, G., Güven, A., and Timur, S. (2009). Metallerin çevresel etkileri. Metalurji Dergisi, 136(1), 47-53.

- [3] Ljung, K., Selinus, O., and Otabbong, E. (2006). Metals in soils of children's urban environments in the small northern European city of Uppsala. *Science of the Total Environment*, 366(2-3), 749-759.
- [4] Nieć, J., Baranowska, R., Dziubanek, G., and Rogala, D. (2013). Children's exposure to heavy metals in the soils of playgrounds, sports fields, sandpits and kindergarten grounds in the region of Upper Silesia. *Journal of Ecology and Health*, 17(2), 55-62.
- [5] Witkowska, D., Slowik, J., and Chilicka, K. (2021). Heavy Metals and Human Health: Possible Exposure Pathways and the Competition for Protein Binding Sites. *Molecules*, 26(19), 6060.
- [6] Özboilat, G., and Tuli, A. (2016). Ağır Metal Toksisitesinin İnsan Sağlığına Etkileri. *Arşiv Kaynak Tarama Dergisi*, 25(4), 502-521.
- [7] Tok, H. H. (1997). Çevre kirliliği. *Anadolu Matbaa Ambalaj San Tic Ltd Şti, İstanbul*, p:266-283.
- [8] Kolesnikov, S., Minnikova, T., Kazeev, K., Akimenko, Y., and Evstegneeva, N. (2022). Assessment of the ecotoxicity of pollution by potentially toxic elements by biological indicators of haplic chernozem of Southern Russia (Rostov region). *Water, Air and Soil Pollution*, 233(1), 18.
- [9] TÜİK. (2021). Turkish Statistical Institute, Road Motor Vehicles News Bulletin-Oct-No: 45712.
- [10] Ercan, T., Dincel, A., Metin, S., Türkecan, A., and Günay, E. (1978). Geology of the Neogene basins in Uşak region. *Bulletin of the Geological Society of Turkey*, 21(1), 97-106.
- [11] Rose A. W., Hawkes H. E., and Webb J. S. (1991). Volatiles and airborne particulates. *Geochemistry in Mineral Exploration*, 2nd edition. Academic Press, 501-503.
- [12] Thomson, I. (1986). Exploration geochemistry: design and interpretation of soil surveys. *Reviews of Economic Geology*, 3(1), 1-18.
- [13] Chen, M., and Ma, L.Q. (2001). Comparison of three aqua regia digestion methods for twenty Florida soils. *American Society of Soil Science Journal*, 65(1), 491-499.
- [14] ESRI. (2019). ArcGIS Desktop: Release 10.7.1: Environmental Systems Research Institute, Redlands, CA.
- [15] Müller, G. (1969). Index of geoaccumulation in sediments of the Rhine River. *Geojournal*, 2(1), 108-118.

- [16] Miko, S., Peh, Z., Bukovec, D., Prohic, E., and Kastmüller, Z. (2000). Geochemical baseline mapping and Pb pollution assessment of soils in the karst in Western Croatia. *Natura Croatica*, 9 (1), 41-59.
- [17] Loska, K., Wiechula, D., Barska, B., Cebula, E., and Chojnecka, A. (2003). Assessment of arsenic enrichment of cultivated soils in Southern Poland. *Polish Journal of Environmental Studies*, 12(2), 187-192.
- [18] Sengupta, S., Chatterjee, T., Ghosh, P. B., and Saha, T. (2010). Heavy metal accumulation in agricultural soils around a coal-fired thermal power plant (Farakka) in India. *Journal of Environmental Science and Engineering*, 52(4), 299-306.
- [19] Chung, S., and Chon, H.T. (2014). Assessment of the level of mercury contamination from some anthropogenic sources in Ulaanbaatar, Mongolia. *Journal of Geochemical Exploration*, 147(1), 237-244.
- [20] Vural, A. (2014). Toprak ve Akasya Ağacı Sürgünlerindeki İz/Ağır Metal Dağılımı, Gümüşhane-Türkiye. *Maden Tetkik ve Arama Dergisi*, 148(1), 85-106.
- [21] Yıldız, U., and Ozkul, C. (2022). Spatial distribution and ecological risk assessment of heavy metals contamination of urban soils within Uşak, western Türkiye. *International Journal of Environmental Analytical Chemistry*, <https://doi.org/10.1080/03067319.2022.2154661>.
- [22] Mielke, J. E. (1979). Composition of the Earth's crust and distribution of the elements. *Review of Research on Modern Problems in Geochemistry*, 13-37.
- [23] Buat-Menard, P., and Chesselet, R. (1979). Variable influence of the atmospheric flux on the trace metal chemistry of oceanic suspended matter. *Earth and Planetary Science Letters*, 42(3), 399-411.
- [24] Barbieri, M. (2016). The Importance of Enrichment Factor (EF) and Geoaccumulation Index (Igeo) to Evaluate the Soil Contamination. *Journal of Geology and Geophysics*, 5(1), 1-4.
- [25] Özkul, C. (2016). Heavy metal contamination in soils around the Tunçbilek thermal power plant (Kütahya, Turkey). *Environmental Monitoring and Assessment*, 188(5), 1-12.
- [26] Quevauviller, P., Lavigne, R., and Cortez, L. (1989). Impact of industrial and mine drainage wastes on the heavy metal distribution in the drainage basin and estuary of the Sado River (Portugal). *Environmental Pollution*, 59(4), 267-286.
- [27] Pacyna, J. M., and Winchester, J. W. (1990). Contamination of the global environment as observed in the Arctic. *Global and Planetary Change*, 2(1-2), 149-157.

- [28] Schiff, K. C., and Weisberg, S.B. (1999). Iron as a reference element for determining trace metal enrichment in Southern California coastal shelf sediments. *Marine Environmental Research*, 48(2), 161-176.
- [29] Reimann, C., and de Caritat, P. (2000). Intrinsic flaws of element enrichment factors (EFs) in environmental geochemistry. *Environmental Science and Technology*, 34(1), 5084–91.
- [30] Sutherland, R. A. (2000). Bed sediment-associated trace metals in an urban stream, Oahu, Hawaii. *Environmental Geology*, 39(1), 611–27.
- [31] Resmi Gazete. (2005). Toprak Kirliliğinin Kontrolü Yönetmeliği. Çevre ve Ormancılık Bakanlığı, Türkiye. No: 25831, 31.05.2005.
- [32] Coşkun, M., Steinnes, E., Frontasyeva, M. V., Sjobakk, T. E., and Demkina, S. (2006). Heavy metal pollution of surface soil in the Thrace region, Turkey. *Environmental Monitoring and Assessment*, 119(1), 545-556.
- [33] Vodyanitskii, Y. N. (2012). Standards for the contents of heavy metals and metalloids in soils. *Eurasian Soil Science*, 45(1), 321-328.
- [34] Timofeev, I., Kosheleva, N., and Kasimov, N. (2018). Contamination of soils by potentially toxic elements in the impact zone of tungsten- molybdenum ore mine in the Baikal region: A survey and risk assessment. *Science of the Total Environment*, 642(1), 63-76.
- [35] Adnan, M., Xiao, B., Xiao, P., Zhao, P., Li, R., and Bibi, S. (2022). Research progress on heavy metals pollution in the soil of smelting sites in China. *Toxics*, 10(5), 231.
- [36] Yan, G., Mao, L., Jiang, B., Chen, X., Gao, Y., Chen, C., Li, F., and Chen, L. (2020). The source apportionment, pollution characteristic and mobility of Sb in roadside soils affected by traffic and industrial activities. *Journal of Hazardous Materials*, 384(1), 121-352.
- [37] Tian, H., Zhou, J., Zhu, C., Zhao, D., Gao, J., Hao, J., He, M., Liu, K., Wang, K., and Hua, S. (2014). A comprehensive global inventory of atmospheric antimony emissions from anthropogenic activities, 1995–2010. *Environmental Science and Technology*, 48(17), 10235-10241.
- [38] Herath, I., Vithanage, M., and Bundschuh, J. (2017). Antimony as a global dilemma: Geochemistry, mobility, fate and transport. *Environmental Pollution*, 223(1), 545-559.
- [39] He, M., Wang, N., Long, X., Zhang, C., Ma, C., Zhong, Q., Wang, A., Wang, Y., Pervaiz, A., and Shan, J. (2019). Antimony speciation in the environment: Recent advances in understanding the biogeochemical processes and ecological effects. *Journal of Environmental Sciences*, 75(1), 14-39.



REVIEW ARTICLE

BIOSENSORS: TYPES, APPLICATIONS, AND FUTURE ADVANTAGES

Aleyna GUNDOĞDU¹, Gizem GAZOĞLU², Elif KAHRAMAN³, Esmâ YILDIZ⁴, Gizem CANDIR⁵,
Duygu YALCIN⁶, Atakan KOC⁷, Fatih SEN^{8*}

¹Sen Research Group, Department of Biochemistry, Kütahya Dumlupınar University, Kutahya,
aleyna.gundogdu@ogr.dpu.edu.tr, ORCID: 0000-0003-3045-9181

²Sen Research Group, Department of Biochemistry, Kütahya Dumlupınar University, Kutahya, gizem.gazoglu@ogr.dpu.edu.tr,
ORCID: 0000-0002-0335-1792

³Sen Research Group, Department of Biochemistry, Kütahya Dumlupınar University, Kutahya, elif.kahraman2@ogr.dpu.edu.tr,
ORCID: 0000-0003-1304-4638

⁴Sen Research Group, Department of Biochemistry, Kütahya Dumlupınar University, Kutahya, esma.yildiz@ogr.dpu.edu.tr,
ORCID: 0000-0002-7326-781X

⁵Sen Research Group, Department of Biochemistry, Kütahya Dumlupınar University, Kutahya, gizem.candir@ogr.dpu.edu.tr,
ORCID: 0000-0002-6231-7922

⁶Sen Research Group, Department of Biochemistry, Kütahya Dumlupınar University, Kutahya, duygu.yalcin@ogr.dpu.edu.tr,
ORCID: 0000-0003-3978-0668

⁷Sen Research Group, Department of Biochemistry, Kütahya Dumlupınar University, Kutahya, atakan.koc@ogr.dpu.edu.tr,
ORCID: 0000-0001-5159-1398

⁸Sen Research Group, Department of Biochemistry, Kütahya Dumlupınar University, Kutahya, fatihsen1980@gmail.com,
ORCID: 0000-0001-6843-9026

Receive Date: 20.12.2022

Accepted Date: 16.03.2023

ABSTRACT

With the developing technology and increasing population, nanotechnology has started to be used in all areas of life. The use of biosensors, which have an important place in the field of nanotechnology, is increasing day by day. Biosensors can be defined as biological devices that help us interpret the analyte concentration in a sample by converting it into measurable signals. Advantageously, it has both speed and high precision. There are many types of biosensors used in many fields. These; enzymatic, nucleic acid, electrochemical and optical biosensors. All of them can have different components and uses. Biosensors are used especially in early diagnosis of diseases, environment and agriculture, pharmaceutical industry, defense industry and food industry. For example, biosensors are used in the treatment of oncological diseases using electrochemical impedance spectroscopy, in the determination of pesticides, which is one of the environmental pollutants, in the potentiometric analysis of glutamate, in the detection of chemical warfare agents and toxic substances. In addition, it is expected that the usage areas of biosensors will become widespread in the future, and they will be used more widely in the early diagnosis of diseases. At this point, the use of biosensors has increased worldwide and has attracted the attention of scientists. In this study, classification of biosensors, application areas, characterization, studies on biosensors, technologies developed and applied for the future are mentioned.

Keywords: *Biosensor, Biosensor Types, Biosensor Applications, Biosensor Characterization, Biosensor Advantages.*

1. INTRODUCTION

Nanotechnology plays an important role in the use of devices in the processing of materials with dimensions less than 10 nanometers [1]. The suffix nano in the word nanotechnology derives from the Greek word "dwarf" and combines with the word technology to form nanotechnology [2]. The word nanotechnology was first used by Japanese researcher Norio Taguchi in 1974, approximately 50 years ago [3]. After the 2000s, nanotechnology has shown rapid developments in the field of biosensors and the use of biosensors has become widespread at this point [4]. Sensors can be used in all areas of technology now and have features that can be used in many devices. For example, there are sensors in the use of many large or small devices such as computers, refrigerators, and television remotes [5]. Sensors are devices that help detect physical and electrical changes such as pressure, temperature, humidity, motion, and force used to detect the content in a sample [3,6]. In a sensor, features such as sensitivity, selectivity, high resolution, repeatability, and response time are sought [5,7]. Biosensors can detect even low concentrations of certain pathogens and chemicals of various shapes or sizes [8]. The importance of size and shape for the analyte to recognize the substrate is shown in Figure 1.

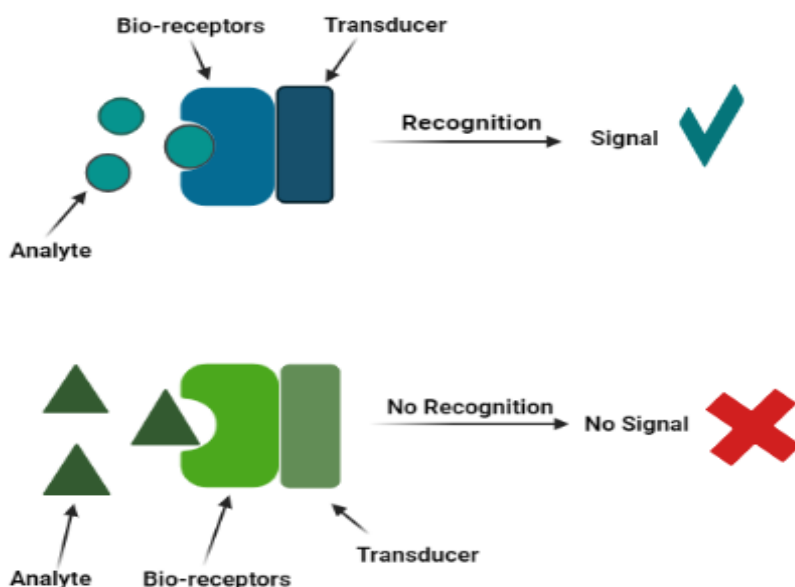


Figure 1. Importance of size and shape for the analyte to recognize the substrate [9].

The sensors consist of 3 main parts. These are defined as a receiver, converters, and reading systems [10,11]. In addition, a biosensor generally consists of the analyte, bioreceptor, transducer, electronics, and display parts [12], and biosensor components are shown in Figure 2. The analyte identifies the components as the detected substance, is detected by receptors, and converted into electrical signals [13]. A bioreceptor can be defined as a molecule or element that can detect the target substrate. Examples of these are DNA, RNA, enzymes, and antibodies [14,15]. Enzymes are one of the most widely used types of bioreceptors in the field of biosensors. They come first because they are natural proteins and can convert the substrate [16] molecule into a product without being consumed because

of the reaction [11]. They are also highly selective, sensitive, and fast compared to other chemical reactions [17]. The transducer is very important for a biosensor. Devices that convert the detection or recognition event into a signal by establishing a connection in the presence of a chemical or a target [18,19]. Energy conversion is called signaling [12,20]. Transducers can be classified as optical, thermal, electronic, gravimetric, and electrochemical [15]. Electronic systems are intermediate devices that transform the signals produced by the converter into a larger signal and transfer it to the screen [21,22]. On the other hand, the screen is the digital medium provided for reading and interpreting digital, graphical, and tabular signals [12].

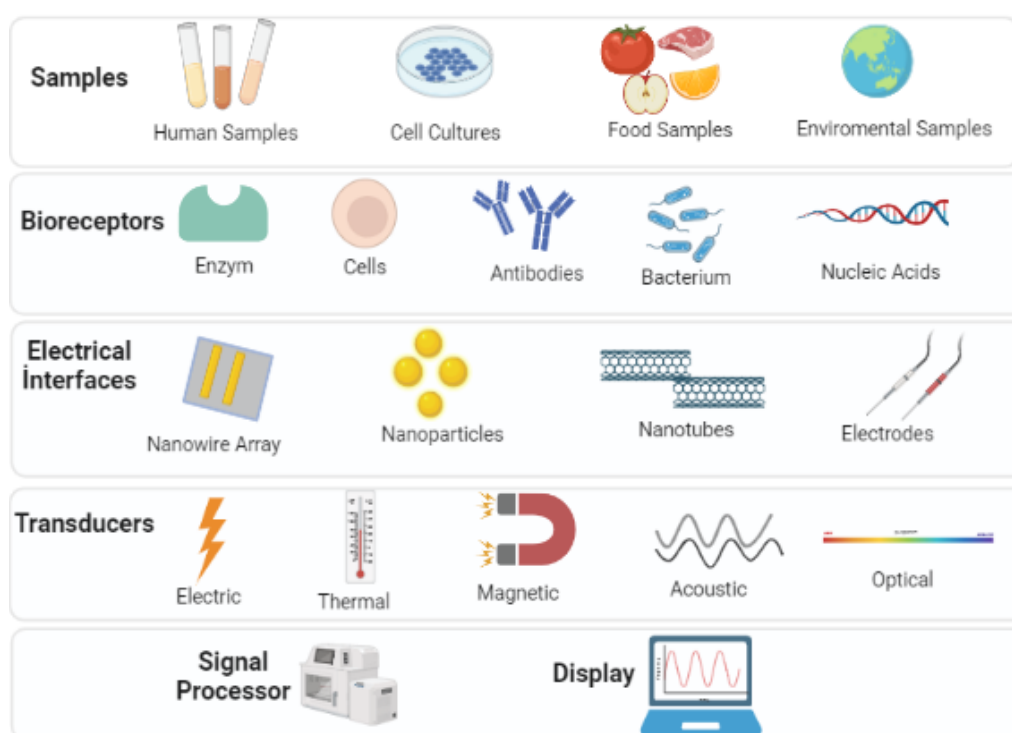


Figure 2. Components of a biosensor [23].

Some biosensor enhancements are being made for future work [24]. The first is to develop a sensitive biosensor [25]. A sensitive biosensor not only measures the analyte concentration; It also changes its configuration to improve its sensitivity, selectivity, and performance [26]. The second work is to develop a hybrid biosensor. The goal here is to develop a type of biosensor that combines engineering, and biological materials to create a more sensitive sensor [27]. The third is to develop in-body biosensors. The aim here is to develop nano electronic brain and body sensors that can be injected intravenously and implanted into the body to continuously monitor and record physiological variables [22,28].

In addition, nanomaterials have an important place in the creation of biosensors and in making them usable in application areas. These materials allow biosensors to work more efficiently. For example, in a study for the determination of ferritin, it was observed that using graphene as a nanomaterial maximized activity [29]. In addition, graphene appears to be used in different applications such as DNA damage detection [30]. At the same time, nanomaterials; are dopamine, ascorbic acid, uric acid, glucose, toxic substances, etc. It is seen that it is used extensively in biosensor applications by being used in many material determinations [31,32]. At this point, many studies and research are carried out today [33]. This review mentions many important issues such as biosensor types, working principles, application areas, characterization methods of biosensors, studies on biosensors, and future advantages.

2. TYPES OF BIOSENSORS

Today, because of developments in biological and nanoscience applications, biosensors are gaining more efficient performance features and developing by integrating innovations in many subjects. Biosensors are generally called bioanalytical devices, which are developed with the knowledge of various scientific fields such as physics, chemistry, biochemistry, biology, and engineering, using multidisciplinary methods, together with biological molecules, with the selectivity properties of systems and electronic technical process capabilities [34]. The diversity of biosensors enables them to be used and developed in many areas. At the same time, many analytes and receptors can be used in the creation of biosensors. For example, carbohydrates and nucleic acids are also used in different fields such as gene ring analyzes and cell surface characterizations. Biosensor classification takes place depending on the relationship that develops between transmission and measurement systems. For example, classified by bioreceptor domain (antibody/antigen interaction, nucleic acid interaction, cellular interaction, enzymatic interactions, biomimetic material interactions) or transducer type (electrochemical measurements, optical measurements, mass sensitivity measurements) [34]. Transducers are structures that measure the biological reactions elicited by the receptors and convert them into a physical signal. Detection of physical and chemical change is measured after the recognition of the analyte and transferred to digital signals. Transducer selection is made by considering biochemical reactions. Devices in the structure of biosensors (transducers) that convert one form of energy into another form of energy, electrochemical (with voltammetry, amperometry, capacitive, potentiometric, conductive, impedance ones), optical (chemical luminescence, surface plasmon resonance, absorption, fluorescence, biological luminescence, optical fiber) ones exhibit piezoelectric (surface sound wave, quartz crystal microbalance) magnetic and calorimetric properties [35]. Biosensors are classified under two main headings according to their working principles, physical transducers, and biocomponents.

2.1. Classification of Biosensors by Biocomponent

Among the various designs of biosensors, biocomponents such as nucleic acids, enzymes, antibodies, microorganisms, tissue, and organelles are used [36]. At the same time, the transducing elements are divided into three groups. These are electrochemical biosensors, optical and mass-based, respectively. The classes mentioned are explained below. [37–39].The classification of biosensors is shown in Figure 3.

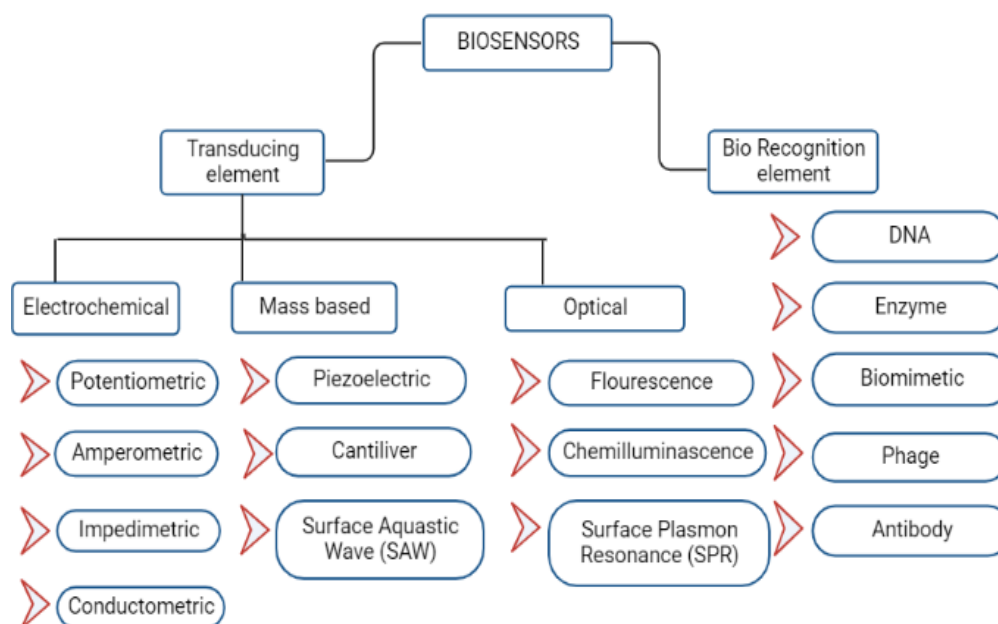


Figure 3. Classification of biosensors [40].

2.2. Enzyme Biosensors

Enzyme biosensors are one of the main sensors in which enzymes are used as biocomponents ed by comparing them with each other [41][42][43]. Enzymes are generally protein biomolecules with catalytic functions. During the catalytic reaction, by forming an enzyme-substrate complex, the product formed because of the reaction provides signals that can be indirectly measured by the biosensor [44]. Many enzyme-based biosensors use oxidoreductases as enzymes [45]. After the invention of the enzyme electrode, enzyme-based biosensors have attracted increasing attention due to a variety of potential applications [43]. The concept of an enzyme-based biosensor is generally based on placing the enzyme near the sensor surface. In enzymatic-based biosensors, the concentration of the substrate is determined by the enzymatic reactions on the sensor surface. It occurs through two reaction processes, enzymatic conversion in the substrate and diffusion in the enzyme layer of the product [45]. According to these two reactions, enzyme-based biosensors; It is an important technique used in the quantitative and qualitative analysis of various target analytes in the environment, biomedicine, food quality control, agriculture, and pharmaceutical industries. In addition, there are 4 types of enzyme-based biosensors used commercially and practically. These; are lactate (intensive care, food, biotechnology, sports medicine), glucose (food science, diagnosis, and treatment of diabetes, food science, biotechnology) glutamate/glutamine (food, biotechnology), and urea (clinical applications) [46,47]. Since enzymes show stability in properties such as temperature, pH, and ionic strength, their use in biosensors is limited. Therefore, while designing enzyme-based biosensors, it is tried to provide a suitable environment for enzymes to continue their activities. Enzyme-based biosensors generally consist of three components: biological recognition element, transducer, and signal processing signals. When these components are connected; the enzyme functions as recognition and is immobilized in the matrix on the transducer surface to maintain enzyme activity. The presence

of certain analytes is determined by measuring factors such as detection principle, proton concentration (H^+), gas release or uptake (CO_2 , NH_3 , etc.), and light emission. The transducer then converts these changes into relevant measurable signals (electrical, thermal, or optical signals) that are used to identify the presence of relevant analytes.

2.3. Microbial Biosensors

They are biosensors in which microorganisms are used as biocomponents in biosensor design. Microorganisms as biological sensors have extensive advantages in chemical substance detection. Also, enzymes that are most used in the production of biosensors are structures with high sensitivity. Purification processes for enzymes are costly, tedious, and time-consuming. Microorganisms offer an ideal alternative to these problems [48]. In addition, the use of microorganisms also has disadvantages. Since the cell membrane structure creates a diffusion barrier, suitable biosensors cannot be prepared for molecules and macromolecules that cannot pass through the membrane [49]. Compared to enzyme sensors, the response time of microbial biosensors and the time to return to the basic signal point after use are quite long. Contamination and decreased activity during immobilization are among the most important problems.

2.4. Nucleic Acid Biosensors

In the use of biosensors, they are biosensors in which nucleic acids are used as biocomponents. Research on the use of various nucleic acids as a recognition surface area in biosensors designed for quantitative and qualitative analysis of DNA in this type of biosensor has become the focus of attention [50], [51], [52]. Biosensors with nucleic acid recognition surfaces can be used for various purposes such as revealing the interaction mechanism of the analyte (drugs, carcinogens, etc.) interacting with this surface, quantifying the studied substance, and monitoring hybridization events in some regions of the DNA base sequence [53].

2.5. Immunosensors

They are biosensors in which antibodies are used as a biocomponent in biosensor design. Glycoproteins produced by the immune system are called antibodies. This biosensor is prepared based on antibody-antigen interaction [54]. It is important to be able to directly examine antibody-antigen interactions. There are various immunosensors to study this interaction. One of them is impedimetric immunosensors [55]. Apart from this, immobilized antigens in different formats of electrochemical immunosensors are important in the effective use of antibodies [56].

2.6. Lactate Biosensors

Lactate is an essential key metabolite in the anaerobic metabolism pathway. Since the energy demand of the tissues is not sufficient with aerobic respiration, an increase in lactate concentration in anaerobic metabolism occurs [45], [57]. Lactic acid has mirror images, and they are divided into two L (+) and D (-). In mammalian metabolism, L (+) lactate is an intermediate, and D (-) lactate is generally produced by microorganisms, algae, and plants; but its use by humans is limited. Some microorganisms, for example, lactic acid bacteria form in both mirror images as a racemic mixture [58], [65]. It is widely used in electrochemical biosensors due to its low cost, excellent sensitivity, ease of use, and high selectivity, which are the most important factors in the determination of lactic acid. Among the enzyme-based lactate biosensors, the most widely used biosensors are lactate oxidase (LOD) and lactate dehydrogenase (LDH) based biosensors, due to the ease of enzymatic reactions and design. [59][60] [61].

3. CLASSIFICATION OF BIOSENSORS BY CONVERSION MEANS

Biosensors can be divided into three groups as conversion tools. These; It is an electrochemical biosensor, mass-based biosensors, and optical biosensors. In general, general information about electrochemical biosensors is given later in this review. In addition, the thermal biosensor, which is the subtitle of the electrochemical biosensor, and the piezoelectricity, which is one of the mass-based biosensors, are explained [62].

3.1. Electrochemical Biosensors

Electrochemical biosensors find a wide range of applications in terms of being portable, highly sensitive, simple, short-response, selective, inexpensive, and specific. Elements widely used in the design of electrochemical biosensors; electrodes made of silver, gold, carbon, or platinum [63]. Electrochemical biosensors are obtained because of the conversion of chemical change into electrical signals in proportion to its concentration [64]. As seen in Figure 4, in the electrochemical biosensor, the biological component recognizes the analyte, resulting in a binding event that produces an electrical signal that is monitored by a transducer proportional to its analytical concentration. Some of these sensor devices have reached the commercial stage and are frequently used in clinical, industrial, environmental, and agricultural applications [65]. Electrochemical biosensors play an important role in the transition of diagnostic devices to the present day. These various electrical devices are highly suitable for connecting to compact analyzers to provide diagnostic information simply, quickly, and cost-effectively. The remarkable properties of electrochemical devices show great promise for increasing the monitoring efficiency in cancer diagnosis and treatment [66].

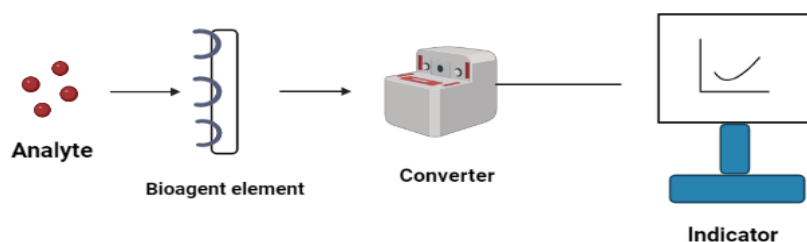


Figure 4. The general structure of electrochemical biosensors [67].

It can be defined as the current released by the electrochemical oxidation or reduction of an electroactive species. The resulting current is directly related to the concentration of electroactive species or the rate of mass production or consumption within the adjacent biocatalytic layer [68]. Potentiometry is generally based on measuring the potential difference between the working electrode and the reference electrode. The analyte concentration is one of the factors affecting the obtained potential difference. Among the transducer recognition elements can be an ion-selective electrode (ISE), an electrochemical sensor based on thin films, or selective membranes [69]. The most used potentiometric devices are pH electrodes, as well as (F, CN⁻, Ca⁺², K⁺, Na⁺, NH⁴⁺) or gas (CO₂, NH₃) selective electrodes [70]. Conductometric biosensors are used to determine the air humidity and the concentration of certain gases. The advantages of conductometric biosensors are that they do not use reference electrodes during analysis, operate at low voltage, and are insensitive to light. Conductometric biosensors have less application area than other sensors [71].

3.2. Optical Biosensors

It has been developed by taking advantage of the absorption of light, refraction of light, the reflection of light, scattering of light, or brightness of light as a transducer type. In optical biosensor studies, the reference electrode is not used [72]. Today, optical biosensors, which are powerful detection and analysis devices in optical biosensors, have wide application areas in biomedical research, national security, environmental monitoring, medical products, and war. They can perform multiple and remote sensing in a single device. In addition, they are not affected by electromagnetic interference [73]. Among the advantages of optical biosensors, are signal or magnetic interference to be more resistant, fast, and high information content. Optical transducers: can detect changes such as light scattering, refractive index, absorbance, chemiluminescence, and fluorescence/phosphorescence [74]. In general, detection protocols can be divided into two, these are fluorescent-based and label-free detection. In fluorescence-based detection, both the target molecule and the bio-identifying molecular dyes are labeled with a fluorescent label. In label-free detection, target molecules are not affected in any way, and besides, they cannot be changed, they are determined only in their natural forms. This type of determination is not only easy and inexpensive but also facilitates the quantitative and kinetic measurement of molecular interactions [73],[74]. As an optical technique, surface plasmon resonance (SPR) is the technique used in the field of chemical sensing. SRP, which can be applied for biomolecular interaction analysis, is a phenomenon that occurs during the optical illumination of the metal surface [75].

3.3. Piezoelectric Biosensors

As a piezoelectric effect mechanism, it means that it generates a voltage because of a stretched surface. As a result of the change in the voltage sent to the surface of a piezoelectric material, oscillation or mechanical stress occurs and this change is proportional to the mass. There are many application areas in the design of analytical sensors [75]. Biosensors with piezoelectric transducers are also used to measure changes in viscosity, mass, or density on the sensor surface [76]. The piezoelectric crystal, which is used to take advantage of the piezoelectric effect, is coated with high-selectivity compounds with biological materials with enzymes or antibodies [77]. Piezoelectric transducers are used practically in immune applications, and in the fields of immune identification. Among the advantages of using this type of converter are it has tag-free identification, real-time tracking, and ease of use. However, the lack of sensitivity and specific features need to be eliminated. Also, piezoelectric biosensors have calibration and format problems [78][79].

3.4. Thermal Biosensors

Thermometric measurements are concerned with the measurement of heat absorbed during a biochemical reaction. Thermal biosensors take advantage of the fundamental properties of biological reactions such as heat absorption and heat release [58]. Thermal biosensors have been developed by combining a biomaterial, also called a calorimetric biosensor, with a physical transducer such as a thermometer. The use of thermal-based calorimetric biosensors is used to measure various conditions such as clinical monitoring, anhydrous environment measurements, and enzyme activity measurements by following the temperature changes [80]. In addition, thermal transducers have also been used in the determination of antibody-antigen interactions, and this technique is called the Thermometric Elisa Test. However, expensive instrumentation is among the disadvantages of this technique .

4. APPLICATION AREAS OF BIOSENSORS

The first biosensor is L.C. It was used by Clark in 1950 to measure the amount of glucose in the blood [81]. Today, studies on biosensors continue to gain importance considering the results obtained in recent years [59]. Because the working discipline of biosensors has a wide range. In general, the amount of glucose is used for the detection of drugs, viruses, diseases, etc. Its use continues to be widespread in many application areas [60]. In addition to these, it also operates in areas such as medicine, food, pharmacy, quality control, industry, animal husbandry, environmental pollution, waste control, and military applications [61]. In addition to these, the possible application areas of biosensors are as follows. Bacterial and viral diagnosis, Process control, Industrial wastewater control, Toxic gas analysis in mines and enterprises, Biomedical, Field agriculture, Vineyard-garden agriculture, Veterinary, etc. Although 25 biosensors have been used commercially so far, biosensors have been prepared for many more different substances. Although this number is not clear, it is known as more than 180 [82]. From these applications, biosensors have been used by utilizing silver nanoparticles in bacterial viral diagnosis [83]Figure 5 shows the application areas of biosensors.

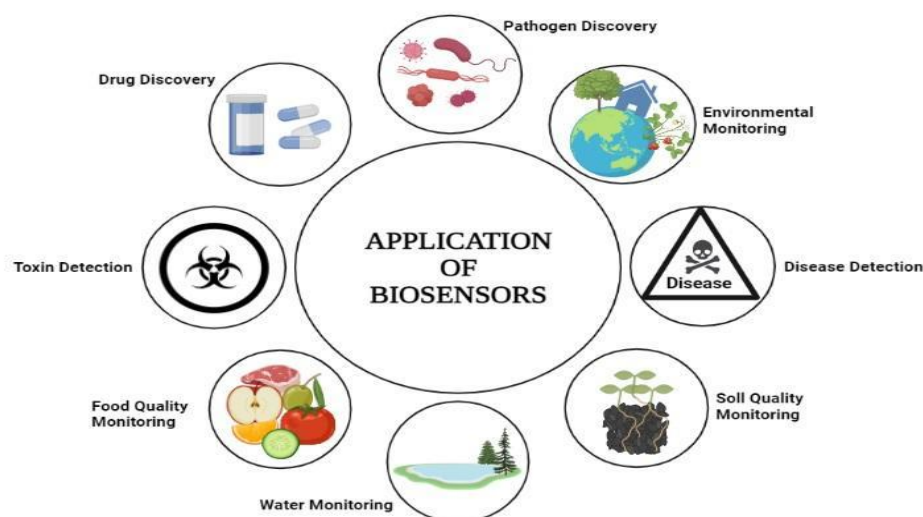


Figure 5. Application Areas of Biosensors [84].

4.1. Use of Biosensors in Medicine

Biosensors with high reaction specificity characteristics are suitable for use in the medical field [85]. Biosensors are most used in the medical field as an application. For example, in blood, it is used in many biological determinations. The glucose oxidase biosensor is known as the first produced and most used commercial biosensor in this field. The glucose oxidase biosensor is manufactured for diabetics and its use is becoming widespread as it is possible and easy to use at home [61]. In addition, it is noteworthy that biological products such as urea and sugar in the body are monitored, and microbial agents are detected and used in the monitoring of cancers [59]. The determination of the increased PSA level in prostate cancer, which is common in men, is an example of the use of biosensors in this area [86]. Another type of biosensor that is most often used is the enzyme sensor.

Because high sensitivity in measurements, ease of installation, and application, are the excess of commercially suitable transducer types. [69], [72]. Microbial sensors are not used in biosensors in the medical field. Because these sensors work with biological fluids, these liquids, on the other hand, form the environment that allows microorganisms to reproduce [85]. There are also diagnostic areas that are of vital importance. These; in the measurement of toxic gas and atmospheric gas, the diagnosis of infectious diseases spreading in a certain area, the detection of dangerous substances and high-dose drugs in the body, in determining the density of continuously used drugs in the blood, it is used in intensive care units and to determine the instantaneous drug density in the blood before critical surgeries [61]. In the medical field, when it comes to drugs, biocompatibility is the sought-after and most important parameter [82,87].

4.2. Use in the Field of Agriculture and Environmental Protection

Biosensors are also used in the diagnosis of pesticides, bad odors, artificial fertilizers, and plant-animal diseases in the field of agriculture. It is known that it is also used to understand the level of heavy metals and pesticides in soil and groundwater, and to determine the occurrence of soil diseases that cannot be resolved. Another use is the rapid detection of plant diseases, especially bacteria and viruses, and used in agriculture and dairy technology. It is a reliable and fast option for the determination of lactose in milk [86]. Especially in cities, its use in the control of environmental pollution and quality monitoring, and its use in the control of microorganisms and toxins is observed. At the same time, it is used in the measurement of organic impurities in water in [85]. Chemical analyzes and eco-toxicological tests are usually used to clean nature that has been polluted for various reasons. However, these tests take a long time due to some steps. At this point, by applying biosensors, chemical information is obtained without processing the sample completely, and the process is accelerated and shortened [88].

4.3. Use in the Field of Food

Biosensors are used in determining food quality, determining basic nutritional components in foods, determining parameters such as aroma and freshness in the detection of mutagens, allergens, and mycotoxins, residue analysis of agricultural drugs, and determining the level of additives in food, etc. it shows usage in many fields [86]. It is also used to determine the physical properties of foods, the chemical components found in foods, and the amount of harmful microorganisms [89].

4.4. Use in the Defense Industry

Biological weapons are the weapons that cause the greatest danger of mass destruction. In biological attacks, it is very important to determine the danger in advance and develop methods to deal with possible problems. The use of biosensors is the most preferred method at this point. The reason for the preference is that biosensors provide fast, reliable, and accurate results [85]. Biological weapons are a way that can be used against the state, as they can create a wide fuss and trouble for terrorists [88]. According to studies conducted in previous years, calculating the cost of damage that will occur in a biological attack on the United States is an example of the use of biosensors in this area [86]. Due to the recent increase in bioterrorism and the spread of diseases, biosensors have been used to identify infectious agents. These agents are various bacteria, viruses, fungi, protein poisons, etc. since it causes the reproduction of structures, biosensors come into play in their detection [88].

4.5. Its Use in the Medical Field and Drug Research

In studies aimed at monitoring chemical substances, it is necessary not only to detect carcinogenic and toxic substances but also to bioassays that can determine the bioavailability of these substances.

Biosensors meet this requirement [88]. There is more than one type of biosensor usage in drug determination. Electrochemical and optical biosensors are some of them. Optical biosensors take advantage of the selectivity arising from drug-protein and antigen-antibody interactions. In this way, it is used in complex drug analysis and in the determination of physiological parameters [88,89].

4.6. Why is Nanotechnology Used in Biosensors?

Nanotechnology, since it works with smaller-sized structures, it facilitates the provision of high precision. At the same time, the processing capabilities of biosensors increase when small particles are transferred. In this way, it shortens the analysis time of small molecules with complex structures. If the value obtained is high when the surface area is proportional to the volume, its selectivity increases. The energy required in the studies is low and there is no diffusion problem. In this way, the long life of the biosensors is ensured. It ensures the conclusion of the study without damaging the cells in the studies [90].

4.7. Biosensors and Biochip

In addition to the application areas of biosensors, biosensors and biochips have been developed in the field of nanomedicine and have been implemented to shorten the diagnostic time [69]. Recently, laboratories on the chip have been established and studies have been carried out on microsystems. With this improved technology, it is possible to examine all genomes on a chip whose interactions between many genes have been determined and these chips are described as miniaturized DNA biosensors [82]. Another example is glucose nano biosensors prepared with high sensitivity non-enzymatic using different metals. Another example is glucose nano biosensors prepared with high sensitivity non-enzymatically using different metals [91]

5. CHARACTERIZATION OF BIOSENSORS

Characterization methods serve the purpose of determining the behavior and characteristics of equipment [92]. After the immobilization values and working conditions of biosensors are adjusted, characterization studies are started because of various stages [93]. Characterization Work Steps: these can be listed as linear measurement range, repeatability, reproducibility electrochemical impedance characterization, and real sample trials [41].

5.1. Linear Measurement Range

After the working possibilities of the developed biosensor and the adjustment of the bioactive layer components, biosensors are prepared under minimum conditions [94]. A standard graph is obtained by determining the values of the various concentrations of the substance to be studied. The range in which linear increase is observed in graphic interpretation is determined as the measurement range [95].

5.2. Repeatability

In the optimum conditions revealed in the repeatability tests of the analysis results made with the biosensors created, new measurements are taken with the biosensor prepared in the concentration of many substances, for example, tributyltin. Repeatability is observed by calculating the variation coefficients and standard deviations of the values taken [94]. As a result of the measurements made, it is determined whether the standard deviation and variation coefficients calculated, and the biosensors are reusable [95]. The variation coefficient must be less than 5% to prove that the biosensor system is workable [58].

5.3. Reproducibility

Reproducibility trials are carried out to determine how different the results obtained during the preparation stages of biosensors are from each other. To determine the result of this, standard graphs are created by preparing a certain number of biosensors with the same composition under the same conditions. Linear determination ranges and R^2 values of these graphs are interpreted [1]. The suffix nano in the word nanotec

5.4. Electrochemical Impedance Characterization (EIS)

This characterization method is carried out using EIS. This structure is a way to detect the surface sensitivities, and electrical resistance of systems, as well as differences in their quantity [93]. Recently, it has been frequently preferred both in the observation of specific interactions of biomolecules and in the preparation stages of biosensors and quantitative analysis. EIS is an important and very helpful tool in illuminating surface morphology with imaging techniques [96].

5.5. Real Sample Trials

Biosensor systems produced because of the studies carried out are applied to real examples. As a result of this application, it provides commentary on whether the manufacturability and analysis repeatability of the biosensor assembly exists and the use of its properties in later studies [41].

5.6. The Used Techniques in Characterization Most

In characterization, Transmission Electron Microscope (TEM) is used to determine the properties of materials. X-ray Photoelectron Spectroscopy (XPS), Atomic Force Microscope (AFM), Scanning Tunneling Microscope (STM), X-Ray Diffraction (XRD), Water Contact Angle, and Environmental Scanning Electron Microscope (ESEM) analyses are frequently preferred. It is important to study the physical and chemical properties of materials. During the research, surface chemical analysis and surface hydrophobicity of the modified paper obtained in studies such as surface morphology, ESEM, XPS, water contact opener, and Washburn test are used to analyze the intracellular behavior of channels [92].

5.7. ESEM

Environmental scanning electron microscopy is called ESEM. ESEM has many features. these; the ability to condense and vaporize liquids are properties associated with the condensation, evaporation, and transport of water in carbon nanotubes [97]. ESEM is also used to view insulating samples without the need for prior sample preparation [98]. ESEM is a versatile device and is used in detailed material characterization. It is a very preferred powerful device due to its high sensitivity, resolution, and focuses features [99]. The first use of ESEM was used in 1960 as a tool for device studies and the importance of semiconductor materials. Today, it is used in many areas of science and technology. With the production of X-ray detectors, ESEM is making great progress [100]. ESEM is also used for imaging insulating samples without the need for prior sample preparation [98] ESEM has many features. These; the ability to condense and evaporate liquids are properties associated with condensation, evaporation, and transport of water in carbon nanotubes.

5.8. TEM

TEM is a characterization device used together with different techniques. It makes micro-examinations and illuminates the crystal structure. Attention is paid to the fine size of the substances

to be analyzed in TEM characterization. The desired ideal fineness is sized samples with less than 50 nm [56].

5.9. XPS

The XPS device has high sensitivity. Thanks to this feature, it helps us learn about the content and structure of the materials [101]. It is a method of surface analysis. At the same time, information is obtained about the oxidation step and molecular structure of the elements with this method. This information is associated with the stimulation of electrons on the surface by the X-ray method and the photoelectric event.

5.10. AFM

Thanks to the AFM, surface images are obtained directly without the need for preliminary preparation. At the same time, surface roughness gives parameters numerically. Its nanometer-sized surfaces allow displaying its structure in three dimensions and high resolution [82].

5.11. Water Contact Angle

The angle formed between solid and liquid surfaces is called the angle of contact. The magnitude of this angle is related to adhesion and cohesion forces. This angle increases if the cohesion force is greater than the adhesion force. Surfaces with a contact angle less than 90° are known as hydrophilic, and those larger than 90° are known as hydrophobic surfaces [85].

5.12. STM

STM is used to examine the surfaces of samples that need to be investigated in atomic dimensions. STMs have many advantages because they are low-cost and small in size. The disadvantage is that it works at a low speed [100].

5.13. XRD

This method is used in powder and large-scale samples other than thin films. It works on the principle that the X-ray beam sent on the sample shows scattering and breaking at different angles. The purpose of use of this characterization method is to illuminate the chemical composition, and atomic and molecular structure of the crystal [86].

6. STUDIES ON THE BIOSENSOR

Nowadays, biosensors; It has begun to be researched and applied in many fields such as medicine, animal husbandry, agriculture, quality control, and military applications [102,103]. For this reason, scientists turned to biosensors, tools that provide cheap, small, fast, and sensitive data.[103]. If we look specifically at the studies on these sensors today, virus detection can be made using biosensors [88]. Electrochemiluminescence essence-based biosensors, which are strong in biosensing, were used to detect viruses [89]. In addition, affinity sensors, immunosensors, and genome sensors are used. According to another study besides virus testing, cancer detection can now be done with biosensors [90]. According to the studies of X. Wei et al., optical biosensors are used to detect cancer. The reason for using optical biosensors here is that it facilitates the diagnosis of cancer-causing substances such as deoxyribonucleic acid (DNA) proteins and tumor cells. In addition, another biosensor used as a cancer biomarker is the surface plasmon resonance biosensor [92]. Surface plasmon resonance biosensors, on the other hand, are preferred because of their high selectivity, and safety and are included in research topics [93] As noted in every article or review, biosensors have many uses. At the

same time, studies and research continue for the development of biosensors. At this point, it is foreseen that faster and more sensitive determination can be made in the future.

7. FUTURE ADVANTAGES OF BIOSENSORS

Biosensors are the general name for tools developed to study the dynamic changes of biomolecules and bio-functions. Today, its use has become widespread in many fields. However, biosensors are tools developed in many fields that will be used not only for today's studies but also in the future [104]. In the future, there will be many applications with the following advantages of biosensor technology. These advantages are illustrated in Figure 6.

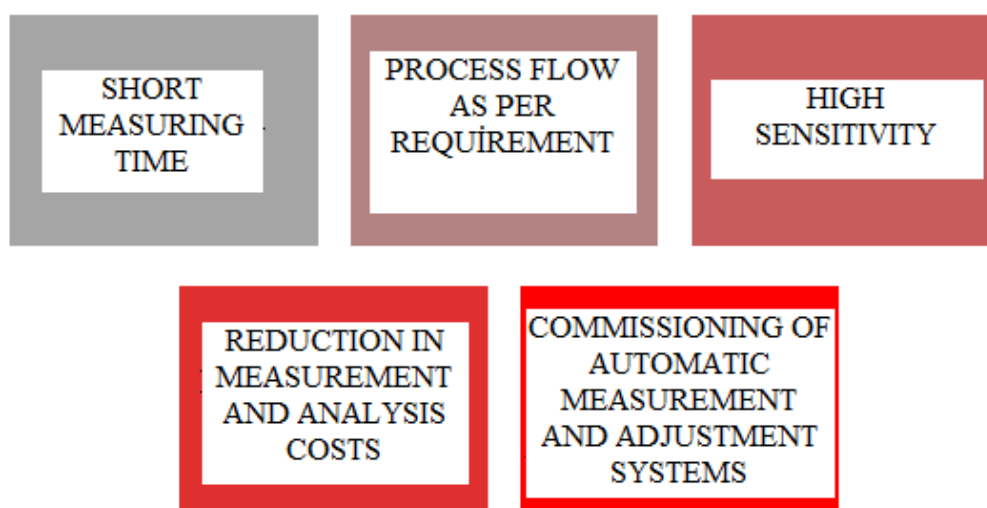


Figure 6. Biosensor usage advantages [101].

In addition, biosensors are promising biosensors because they give reliable results, provide practical and short-term results, are reusable, can be mass produced in a low-cost disposable way, give specific and reliable results, and do not require special experience during the use of these species. It clearly shows that there are sensors with the development of biochip technology, the application areas of biosensors will gain importance and increase their weight day by day [105]. Nanotechnology has also opened the horizons of biosensors and has given an advantage to various applications of biosensors in the future [101].

7.1. Future Advantages of Biosensors over Nanotechnology

The importance of nanotechnology will be understood more clearly as innovations and studies increase. Nanotechnology is revolutionary in many fields for the future. It is thought that biosensors, which are currently produced in the field of nanotechnology, will be developed, and will provide convenience and use in many areas in the future. Wall paints, germicidal filters, fungi, and bacteria-killing socks, and some of them in medicine can be given as examples [106]. At the same time, combining biosensors with nanotechnology will allow the development of faster and more sensitive methods in the future. We cannot have information about which viral or pathogenic microbial

outbreaks await us in the future, but by improving the technologies we have, we can develop early methods of combating the problems that may occur in the future. For example, artificial intelligence and new detection methods, which can be used jointly with biosensors, provide convenience to prevent the uncontrolled spread of diseases and to keep them under control [107].

7.2. The Future Advantage of Biosensors in Healthcare

Biosensors are very common in medicine and have a very important place. The use of biosensors in the healthcare field is quite wide. For example, it detects glucose in blood and urine very quickly. It is used to monitor cholesterol levels and to evaluate muscle fatigue with acetylcholine electrodes. At the same time, it is thought that it will be of great benefit in elucidating structures such as antigen-antibody in the future [101]. Biosensors will facilitate detection in the early diagnosis and treatment of cancer in the future. Studies have been started for these applications, and the developed nano-devices are in the feasibility stage. Remote monitoring will be performed in patients without obvious signs of cancer. Thanks to this monitoring, the disease will be diagnosed at the earliest stage and intervention will be carried out [104]. Accordingly, in the future, biosensors in the form of chip applications can be used instead of expensive optical-based biosensors, offering point-of-care testing technology to cancer patients who hope for early diagnosis [105]. It is predicted that it will be soon to adjust and control the proportions of drugs in the body. Artificial pancreas studies are an example of this. It is the in vivo determination of low-concentration substances and short-lived hormones such as nitric oxide and superoxide [101]. In addition, the effects of drugs on the receptor, monitoring of bioprocesses at the nucleic acid level, and transmitter-receptor interaction are examples of important future studies of biosensors. Sequence recognition levels used in biosensor design will add new dimensions to known electrochemical levels and will play an important role in doctor-controlled analyzes in the future. Biosensors in which DNA is preferred as the recognition surface are called DNA biosensors [104]. The biosensors used today are larger and contain materials used only for in vitro diagnostics. Therefore, its sensitivity is low, and it is late to produce results. The emergence of bio-nanomaterials shows promise for the rapid detection of diseases and biomolecules due to their small size, large surface area, and intact stability. The amount of biocompatibility developed for these structures continues to increase day by day [108]. In the next 10 years, diagnostic devices that will be created with the development of biosensors will be put into use and the realization of thousands of measurements will become much faster and cheaper. The most widely used clinical diagnostic application will be the analysis of blood proteins, and the use of these devices is promising not only for the current period but also for the long term [110]. Nano diagnostics currently under development will help reduce test wait times soon [106]. In line with these considerations, it is expected that the urine results of people with infectious diseases come to the hospital, reach the doctors and a prescription is created quickly, thus reducing the cost of the process by shortening the patient's waiting time for results [108]. Considering the general characteristics of biosensors, project studies have been designed for convenience in the future. One of these works is the Japanese Nanorobot.

7.3. Japanese Nanorobot

The purpose of the development of this robot is to facilitate medical diagnosis and surgery. It is aimed for the robot to be in a size that can even fit inside a human hair and to be able to communicate with the special communication system to be created in this way. Today, project studies are carried out on nano-sized nanorobot technologies that will provide damaged organ repair by giving human blood. With the innovative developments in technology, robots that will assist doctors during surgery, as well as nurses and medical robots that will assist caregivers by taking over their duties, represent an example of the convenience that biosensors will create in the future. With the help of nanotubes

moving with blood in the brain vessels, diagnosis and treatment can be done without problems, the blockages in the capillaries can be removed, and the paralysis caused by the lack of neural communication will be cured with artificial capillaries produced with nanotechnology [109]. Considering the extremely rapid development of biosensors, it is thought that the expected future will not be too distant [104].

7.4. Future Challenges of Biosensors

While biosensors have future advantages, they also have some challenges. For example, SPR biosensors have many advantages like other types of biosensors. However, working with smaller analytes other than large analytes is much more difficult. Because small analytes give small reactions. Therefore, SPR biosensors are disadvantaged for small analytes. This challenge will be overcome in the future if SPR biosensors are developed [110]. Another example is the contribution of microbial-based biosensors to many fields. However, there may be problems in terms of human values. The study by Ma et al. suggests that while microbial-based biosensors are an advantage for genetic modification, they may be a disadvantage for humans [111]. Better explanations on this subject are needed for further use of microbial-based biosensors in the future. According to another study, some features should be considered when using biosensors in production control. At this point, the sensors must be able to keep their activity constant and care must be taken as the activation of the sensor biomaterial is adversely affected at extreme temperatures [112]. In this context, biosensors can be difficult to use. In addition, biosensors in the ecology and food industry are not very well developed. At this point, there are deficiencies in the application areas. In the future, if these difficulties of biosensors are overcome, they will be preferred more in production control [112].

8. CONCLUSION

With the literature research carried out within the scope of the study, it has been seen that biosensors produce solutions to various problems according to their usage areas and this process progresses further as technology develops. In addition, biosensors provided the opportunity to work with different receptors by processing different samples. At the same time, it stands out in every field with its sensitivity, fast results, and detection of very small molecules. In addition, the use of enzymes and antibodies as receptors has become widespread. This is because they can convert the substrate into a product without being consumed by the reaction. It is seen that such biosensors have been developed more in the field of medicine, in line with research. At the same time, it is known that sensor studies for faster and earlier diagnosis of cancer diseases continue in the medical field. At this point, studies on the development of Nanodiagnosics, that is, early diagnosis tests, continue. In addition, the effects and usage areas of biosensors on transducer elements (electrochemical, gravimetric, optical, etc.) are changing by dividing them into different classes. For example, electrochemical biosensors are known for being inexpensive and responsive. They are mostly used in agriculture, environment, and industrial areas. Optical biosensors continue to evolve in medical products and biomedical research and come to the fore in SPR (surface plasmon resonance) studies. In addition, studies have shown that the selection of nanomaterials is very important for the acceptors and converter elements. In the literature; for sensor applications; nanomaterials; It has been seen that the sensor helps to obtain more selective, more sensitive, faster results and studies have been carried out for more cost-effective production. At this point, it is seen that especially carbon-based materials attract a lot of attention by researchers for sensor applications. For the characterization of these materials obtained for sensor application, ESEM, XPS, XRD etc. are often used. techniques are used. The most important feature of the environmental scanning electron microscope is its high sensitivity and its use for detailed material

characterization. X-ray photoelectron spectroscopy is a very important characterization method in terms of obtaining information about material content and structure. The data obtained, it is expected that biosensors will come to the fore in the fields of medicine, food, agriculture, and environment and have a promising future in many fields. In addition, it is predicted that biosensors, which are easy to use in every field, will be an important factor in solving many problems in the future. At this point, it is thought that biosensor studies should be increased.

ACKNOWLEDGMENT

No support has been received.

REFERENCES

- [1] Mamalis, A.G., (2007)., Recent advances in nanotechnology, *Journal of Materials Processing Technology*, 181, 52–58.
- [2] Banotra, M., Kumar, A., Sharma, B.C., Nandan, B., Verma, A., Kumar, R., Gupta, V., Bhagat, S., (2017), Prospectus of use of nanotechnology in agriculture-a review article, *International Journal of Current Microbiology and Applied Sciences*, Int.J. Curr.Microbiol.App.Sci, 6, 1541–1551.
- [3] Vashist, S.K., Venkatesh, A. G., Mitsakakis, K., Czilwik, G., Roth, G., von Stetten, F., Zengerle, R., (2012), Nanotechnology-based biosensors and diagnostics: technology push versus industrial/healthcare requirements, *BioNanoScience*, 2, 115–126.
- [4] Jianrong, C., Yuqing, M., Nongyue, H., Xiaohua, W., and Sijiao, L., (2004), Nanotechnology and biosensors, *Biotechnology Advances*, 22, 505–518.
- [5] Bagriyanik, D.B., (2011)., Potansiyometrik esaslı glutamin biyosensörü tasarlanması ve karakterizasyonu, Master Thesis, Graduate School of Natural and Applied Sciences, İstanbul, 88pp.
- [6] Altungeyik, Y. (2014)., Biyolojik uygulamalar için direnç sensörleri, Master Thesis, Department of Physics, Kirikkale University, Kirikkale, 63pp.
- [7] Mustafa, D. and Sezgintürk, K., (2013)., Bir meme kanseri biyomarkeri olan her 3 analizi için biyosensör sisteminin geliştirilmesi, Master Thesis, Graduate School of Natural and Applied Sciences, Namik Kemal University, Tekirdag, 64pp.
- [8] Purohit, B., Vernekar, P.R., Shetti, N.P., and Chandra, P., (2020), Biosensor nanoengineering: design, operation, and implementation for biomolecular analysis, *Sensors International*, 1, 100040.
- [9] Liu, H., Ge, J., Ma, E., and Yang, L., (2019), Advanced biomaterials for biosensor and theranostics. *Biomaterials in Translational Medicine: A Biomaterials Approach*, 213–255.

- [10] Huang, X., Zhu, Y., and Kianfar, E., (2021), Nano biosensors: properties, applications and electrochemical techniques, *Journal of Materials Research and Technology*, 12, 1649–1672.
- [11] Karunakaran, C., Rajkumar, R., and Bhargava, K., (2015), Introduction to biosensors. *Biosensors and Bioelectronics*, 1–68.
- [12] Naresh, V. and Lee, N., (2021), A review on biosensors and recent development of nanostructured materials-enabled biosensors, *Sensors*, 21, 1109.
- [13] Canver M.İ., (2018), Enzimatik tabanlı bakteriyel biyosensör, Master Thesis, Department of Bioengineering, Hacattepe University, Ankara, 49pp.
- [14] Cırak, T., (2014), Biyolojik moleküllerin tayinine yönelik kantilever bazlı biyosensör sisteminin geliştirilmesi, PhD Thesis, Hacattepe University, Ankara, 184pp.
- [15] Özcan, L., (2008), Polipirol iletken polimerinin biyosensör olarak kullanımı, PhD Thesis, Department of Chemistry, Anadolu University, Eskişehir, 114pp.
- [16] Atan, Ç., (2013), ZnO nanorod temelli glukoz biyosensörü hazırlanması ve kan serumunda glukoz tayininde kullanılması. Master Thesis, Graduate School of Natural and Applied Sciences, Yıldız Technical University, İstanbul, 93pp.
- [17] Boz, B., Paylan, İ.C., Kızmaz, M.Z., and Erkan, S., (2017), Biyosensörler ve tarım alanında kullanımı, *Dergi Park Akademik*, 13, 141–148.
- [18] Papadakis, G., Skandalis, N., Dimopoulou, A., Glynos, P., and Gizeli, E., (2017), Biyosensörler ve tarım alanında kullanımı, *Journal of Agricultural Machinery Science*, 13, 141–148.
- [19] Tüylek, Z., (2021), Nanoteknoloji uygulamalarında hayatımıza yansımalar, *Eurasian Journal of Biological and Chemical Sciences*, 4, 69–79.
- [20] Yılmaz, T. (2021). Gıda ürünlerinde mikrobiyal bozulmaya neden olan *Pseudomonas* spp bakterisinin yüzey plazmon rezonans (SPR) temelli biyosensör kullanılarak belirlenmesi, Master Thesis, Department of Bioengineering, Hacattepe University, Ankara, 111pp.
- [21] Tabanlı, M., Biyosensörü, P., İzlenmesi, S.T., and Çakar, B., (2018), Mikrobiyal ped biyosensörü ile su toksitesi izlenmesi, *Bitlis Eren Üniversitesi Fen Bilimleri Dergisi*, 7, 484–491.
- [22] Tüylek, Z., (2019), Nanotıp alanında kullanılan sistemler, *Archives Medical Review Journal*, 28, 119–129.
- [23] Baryeh, K., Takalkar, S., Lund, M., and Liu, G., (2017), Introduction to medical biosensors for point of care applications, *Medical Biosensors for Point of Care (POC) Applications*, 3–25.
- [24] Sıtkı, M., Üniversitesi, K., and Bölümü, F., (2019), Nanoteknolojinin insan sağlığına faydalı ve zararlı yönleri, *Ordu University Journal of Science and Technology*, 9, 136–148.

- [25] Türkmen, H., (2013), Tiyofenin elektrokimyasal polimerizasyonu karakterizasyonu ve biyosensör olarak geliştirilmesi, Master Thesis, Department of Chemistry, Graduate School of Natural and Applied Sciences, Nevsehir Hacıbektaşveli University, Nevsehir, 62pp.
- [26] Canturk, E., (2013), Amino asitlere duyarlı biyosensörlerin hazırlanması ve çalışma şartlarının belirlenmesi, Master Thesis, Graduate School of Natural and Applied Sciences, Department of Chemistry, Gazi Osman Paşa University, Tokat, .
- [27] Yun, Y. H., Dong, Z., Shanov, V., Heineman, W.R., Halsall, H. B., Bhattacharya, A., Conforti, L., Narayan, R. K., Ball, W. S., Schulz, M. J., (2007), Nanotube electrodes and biosensors, *Nano Today*, 2, 30–37.
- [28] Tuylek, Z., (2021), Biyolojik Sistemlerde gelecekteki nano / biyosensör ürünlerine hazırlık, *Uluslararası Biyosistem Mühendisliği Dergisi*, 2, 17–39.
- [29] Koyun, H.N., (2022), Ferritin tayini için grafen alan etkili biyosensör tasarımı geliştirilmesi, Graduate School of Natural and Applied Sciences, Pamukkale University, Denizli, 87pp.
- [30] Wu, X., Mu, F., Wang, Y., and Zhao, H., (2018), Graphene and graphene-based nanomaterials for dna detection: a review, *Molecules*, 23, 2050.
- [31] Savk, A., Özdil, B., Demirkan, B., Nas, M. S., Calimli, M. H., Alma, M. H., Inamuddin., Asiri, A. M., Sen, F., (2019), Multiwalled carbon nanotube-based nanosensor for ultrasensitive detection of uric acid, dopamine, and ascorbic acid, *Materials Science and Engineering*, 248–254.
- [32] Arikan, K., Burhan, H., Sahin, E., and Sen, F., (2022), A sensitive, fast, selective, and reusable enzyme-free glucose sensor based on monodisperse AuNi alloy nanoparticles on activated carbon support, *Chemosphere*, 291, 132718.
- [33] Lai, X., Liu, Q., Wei, X., Wang, W., Zhou, G., and Han, G., (2013), A survey of body sensor networks, *Sensors*, 13, 5406–5447.
- [34] Istek, M.M., Bulca, S., (2021), Gıda kontaminantlarının analizine yönelik elektrokimyasal biyosensör, *Mehmet Akif Ersoy University, Fen Bilimleri Enstitüsü Dergisi*, 12, 532 – 544.
- [35] Gutés, A., Céspedes, F., Alegret, S., and del Valle, M., (2005), Determination of phenolic compounds by a polyphenol oxidase amperometric biosensor and artificial neural network analysis. *Biosensors and Bioelectronics*, 20 (8 SPEC. ISS.), 1668–1673.
- [36] Mehrotra, P., (2016), Biosensors and their applications – a review, *Journal of Oral Biology and Craniofacial Research*, 6 153–159.
- [37] Shukla, S.K., Govender, P.P., and Tiwari, A., (2016), *Polymeric micellar structures for biosensor technology*, 1st ed. Elsevier Inc.

- [38] Huang, R., He, N., and Li, Z., (2018), Recent progresses in DNA nanostructure-based biosensors for detection of tumor markers, *Biosensors and Bioelectronics*, 109, 27–34.
- [39] Damborský, P., Švitel, J., and Katrlík, J., (2016), Optical biosensors. *Essays in Biochemistry*, 60, 91–100.
- [40] Thévenot, D.R., Toth, K., Durst, R.A., and Wilson, G.S., (2001), Electrochemical biosensors: recommended definitions and classification. International Union Of Pure And Applied Chemistry: Physical Chemistry Division, Commission I.7 (Biophysical Chemistry), Analytical Chemistry Division, Commission V.5 (Electroanalytical. *Biosensors and Bioelectronics*, 16, 121–131.
- [41] Najeeb, M.A., Ahmad, Z., Shakoor, R.A., Mohamed, A.M.A., and Kahraman, R., (2017), A novel classification of prostate specific antigen (PSA) biosensors based on transducing elements. *Talanta*, 168 52–61.
- [42] Clark, L.C. and Lyons, C., (1962), Electrode systems for continuous monitoring in cardiovascular surgery, *Annals of the New York Academy of Sciences*, 102, 29–45.
- [43] Nguyen, H.H., Lee, S.H., Lee, U.J., Fermin, C.D., and Kim, M., (2019), Immobilized enzymes in biosensor applications, *Materials*, 12, 1–34.
- [44] Rathee, K., Dhull, V., Dhull, R., and Singh, S., (2016), Biosensors based on electrochemical lactate detection: a comprehensive review, *Biochemistry and Biophysics Reports*, 5, 35–54.
- [45] Zhao, Z., Lei, W., Zhang, X., Wang, B., and Jiang, H., (2010), ZnO-based amperometric enzyme biosensors, *Sensors*, 10, 1216–1231.
- [46] Wilson, G.S. and Hu, Y., (2000), Enzyme-based biosensors for in vivo measurements, *Chemical Reviews*, 100, 2693–2704.
- [47] Keskin, M., and Arslan, F., (2020), Biyosensörler, *Gazi Üniversitesi Fen Fakültesi Dergisi*, 1, 51–60.
- [48] Tanaka, M. and Sackmann, E., (2005), Polymer-supported membranes as models of the cell surface, *Nature*, 437, 656–663.
- [49] Paleček, E., (1988), New trends in electrochemical analysis of nucleic acids, *Journal of Electroanalytical Chemistry*, 254, 179–194.
- [50] Jelen, F., Erdem, A., and Paleček, E., (2002), Cyclic voltammetry of echinomycin and its interaction with double-stranded and single-stranded DNA adsorbed at the electrode, *Bioelectrochemistry*, 55, 165–167.
- [51] Erdem, A. and Ozsoz, M., (2002), Electrochemical DNA biosensors based on DNA-drug interactions, *Electroanalysis*, 14, 965–974.

- [52] Karadeniz, H., Alparslan, L., Erdem, A., and Karasulu, E., (2007), Electrochemical investigation of interaction between mitomycin C and DNA in a novel drug-delivery system, *Journal of Pharmaceutical and Biomedical Analysis*, 45, 322–326.
- [53] Hartwell, S.K. and Grudpan, K., (2010), Flow based immuno/bioassay and trends in micro-immuno/biosensors, *Microchimica Acta*, 169, 201–220.
- [54] Prodromidis, M.I., (2010), Impedimetric immunosensors- a review, *Electrochimica Acta*, 55, 4227–4233.
- [55] Ricci, F., Adornetto, G., and Palleschi, G., (2012), A review of experimental aspects of electrochemical immunosensors, *Electrochimica Acta*, 84, 74–83.
- [56] Rassaei, L., Olthuis, W., Tsujimura, S., Sudhölter, E.J.R., and van den Berg, A., (2014), Lactate biosensors: current status and outlook. *Analytical and Bioanalytical Chemistry*, 406, 123–137.
- [57] Ramanathan, K. and Danielsson, B., (2001), Principles and applications of thermal biosensors, *Biosensors and Bioelectronics*, 16, 417–423.
- [58] Ibupoto, Z.H., Shah, S.M.U.A., Khun, K., and Willander, M., (2012), Electrochemical L-lactic acid sensor based on immobilized ZnO nanorods with lactate oxidase, *Sensors*, 12, 2456–2466.
- [59] Sun, C., Wang, D., Zhang, M., Ni, Y., Shen, X., Song, Y., Geng, Z., Xu, W., Liu, F., Mao, C., (2015), Novel l-lactic acid biosensors based on conducting polypyrrole-block copolymer nanoparticles. *Analyst*, 140, 797–802.
- [60] Pérez, S., Sánchez, S., and Fàbregas, E., (2012), Enzymatic strategies to construct l-lactate biosensors based on polysulfone/carbon nanotubes membranes, *Electroanalysis*, 24, 967–974.
- [61] Bekmezci, M., Bayat, R., Erduran, V., and Sen, F., (2022), Biofunctionalization of functionalized nanomaterials for electrochemical sensors, *Functionalized Nanomaterial-Based Electrochemical Sensor, Principles, Fabrication Methods, and Applications*, 55–69.
- [62] Şavk, A., Aydın, H., Cellat, K., and Şen, F., (2020), A novel high performance non-enzymatic electrochemical glucose biosensor based on activated carbon-supported Pt-Ni nanocomposite, *Journal of Molecular Liquids*, 300, 112355.
- [63] Heineman, W.R., Anderson, C.W., and Halsall, H.B., (1979), Immunoassay by differential pulse polarography, *Science*, 204, 865–866.
- [64] Ronkainen, N.J., Halsall, H.B., and Heineman, W.R., (2010), Electrochemical biosensors, *Chemical Society Reviews*, 39, 1747–1763.
- [65] Wang, J., (2006), Electrochemical biosensors: towards point-of-care cancer diagnostics, *Biosensors and Bioelectronics*, 21, 1887–1892.

- [66] Dhull, V., Gahlaut, A., Dilbaghi, N., and Hooda, V., (2013), Acetylcholinesterase biosensors for electrochemical detection of organophosphorus compounds: a review, *Biochemistry Research International*, 1–18.
- [67] Pizzariello, A., Stredanský, M., Stredanská, S., and Miertuš, S., (2001), Urea biosensor based on amperometric pH-sensing with hematein as a pH-sensitive redox mediator, *Talanta*, 54, 763–772.
- [68] Thévenot, D.R., Toth, K., Durst, R.A., and Wilson, G.S., (2001), Electrochemical biosensors: recommended definitions and classification, *Biosensors and Bioelectronics*, 16, 121–131.
- [69] Buck, R.P. and Lindner, E., (1994), Recommendations for nomenclature of ion-selective electrodes (IUPAC recommendations), *Pure and Applied Chemistry*, 66, 2527–2536.
- [70] Soldatkin, O. O., Kucherenko, I. S., Pyeshkova, V. M., Kukla, A. L., Jaffrezic-Renault, N., El'skaya, A. V., Dzyadevych, S. V., Soldatkin, A. P., (2012), Novel conductometric biosensor based on three-enzyme system for selective determination of heavy metal ions, *Bioelectrochemistry*. 83, 25–30.
- [71] Chen, C. and Wang, J., (2020), Optical biosensors: an exhaustive and comprehensive review, *Analyst*, 145, 1605–1628.
- [72] Fan, X., White, I.M., Shopova, S.I., Zhu, H., Suter, J.D., and Sun, Y., (2008), Sensitive optical biosensors for unlabeled targets: A review, *Analytica Chimica Acta*, 620, 8–26.
- [73] Velasco-Garcia, M.N., (2009), Optical biosensors for probing at the cellular level: A review of recent progress and future prospects, *Seminars in Cell and Developmental Biology*, 20, 27–33.
- [74] Homola, J., Yee, S.S., and Myszka, D., (2008), Surface plasmon resonance biosensors, *Optical Biosensors*, 185–242.
- [75] Pohanka, M., (2018), Overview of piezoelectric biosensors, immunosensors and DNA sensors and their applications, *Materials*, 11, 448.
- [76] Tothill, I.E., (2001), Biosensors developments and potential applications in the agricultural diagnosis sector. *Computers and Electronics in Agriculture*, 30, 205–218.
- [77] Ozoglu, Ö., Unal L, M.A., and Gunes, E., (2017), Biyosensörler: gıda ve sağlık alanında laktat biyosensörleri, *Türk Yasam Bilimleri Dergisi*, 2, 180–193.
- [78] Mello, L.D. and Kubota, L.T., (2002), Review of the use of biosensors as analytical tools in the food and drink industries, *Food Chemistry*, 77, 237–256.
- [79] Marrazza, G., (2014), Piezoelectric biosensors for organophosphate and carbamate pesticides: A review, *Biosensors*, 4, 301–317.
- [80] Yakovleva, M., Bhand, S., and Danielsson, B., (2013), The enzyme thermistor-a realistic biosensor concept. A critical review, *Analytica Chimica Acta*, 766 1–12.

- [81] Oksuz, O., Sezginturk, M.K., (2013), Nabiltem personelinin enstrümental uzmanlıklarının iyileştirilmesinin ve laboratuvar bünyesinde gerçekleştirilen analiz hizmetlerinin kalitesinin ve güvenilirliğinin artırılmasının araştırılması, *J Conserv Dent*, 16.
- [82] Atar, H. and Colgecen, H., (2021), Gümüş nanopartiküllerinin biyosentezi ve biyosensör materyali olarak kullanımı, *Commagene Journal of Biology*, 5, 214-225.
- [83] Singh, S., Kumar, V., Dhanjal, S., Datta, S., Prasad, R., Singh, J., Singh, S., Kumar, V., Dhanjal, D. S., Singh, J., Datta, S., Prasad, R., (2020), Biological biosensors for monitoring and diagnosis, *SpringerLink*, 317–335.
- [84] Cengiz O., (2010), Temas açısı ölçüm cihazı tasarımı. Master Thesis, Graduate School of Natural and Applied Sciences, Istanbul Technical University, Istanbul, 83pp.
- [85] Dođan, B. and Öztürk, M.M., (2019), Ni-Ti akıllı alaşım ince filmin sıcaklığa bađlı x-ray kırınımı ile karakterizasyonu ve faz dönüşümü tespiti, *Bilecik Şeyh Edebali Üniversitesi Fen Bilimleri Dergisi*, 6, 1-11.
- [86] Ronkainen, N.J., Halsall, H.B., and Heineman, W.R., (2010), Electrochemical biosensors, *Chemical Society Reviews*, 39, 1747–1763.
- [87] Sobhanie, E., Salehnia, F., Xu, G., Hamidipannah, Y., Arshian, S., Firoozbakhthian, A., Hosseini, M., Ganjali, M. R., Hanif, S., (2022), Recent trends and advancements in electrochemiluminescence biosensors for human virus detection, *TrAC Trends in Analytical Chemistry*, 157, 116727.
- [88] Drobysh, M., Ramanaviciene, A., Viter, R., Chen, C. F., Samukaite-Bubniene, U., Ratautaite, V., Ramanavicius, A., (2022), Biosensors for the determination of sars-cov-2 virus and diagnosis of covid-19 infection, *International Journal of Molecular Sciences*, 23, 666.
- [89] Kaur, B., Kumar, S., and Kaushik, B.K., (2022), Recent advancements in optical biosensors for cancer detection, *Biosensors and Bioelectronics*, 197, 113805.
- [90] Arikan, K., Burhan, H., Bayat, R., and Sen, F., (2022), Glucose nano biosensor with non-enzymatic excellent sensitivity prepared with nickel–cobalt nanocomposites on f-MWCNT, *Chemosphere*, 291 132720.
- [91] Wei, X., Yin, M., Zhang, L., Lin, H., Wang, J., Xie, W., Xu, D., (2022), Surface plasmon resonance (SPR) biosensor for detection of mycotoxins: A review, *Journal of Immunological Methods*, 510, 113349.
- [92] Mi, F., Hu, C., Wang, Y., Wang, L., Peng, F., Geng, P. F., Guan, M., (2022), Recent advancements in microfluidic chip biosensor detection of foodborne pathogenic bacteria: a review, *Analytical and Bioanalytical Chemistry*, 414, 2883–2902.

- [93] Azzouz, A., Hejji, L., Kim, K. H., Kukkar, D., Souhail, B., Bhardwaj, N., Brown, R. J.C., Zhang, W., (2022), Advances in surface plasmon resonance–based biosensor technologies for cancer biomarker detection, *Biosensors and Bioelectronics*, 197, 113767.
- [94] Mahmoudpour, M., Ezzati Nazhad Dolatabadi, J., Torbati, M., Pirpour Tazehkand, A., Homayouni-Rad, A., and de la Guardia, M., (2019), Nanomaterials and new biorecognition molecules based surface plasmon resonance biosensors for mycotoxin detection, *Biosensors and Bioelectronics*, 143,111603.
- [95] Ribeiro, S.C., Fernandes, R., Moreira, F.T.C., and Sales, M.G.F., (2022), Potentiometric biosensor based on artificial antibodies for an alzheimer biomarker detection. *Applied Sciences*, 12, 3625.
- [96] Bankole, O.E., Verma, D.K., Chávez González, M.L., Ceferino, J.G., Sandoval-Cortés, J., and Aguilar, C.N., (2022), Recent trends and technical advancements in biosensors and their emerging applications in food and bioscience, *Food Bioscience*, 47, 101695.
- [97] Rossi, M.P., Ye, H., Gogotsi, Y., Babu, S., Ndungu, P., and Bradley, J.-C., (2004), Environmental scanning electron microscopy study of water in carbon nanopipes, *Nano Letters*, 4, 989–993.
- [98] Donald, A.M., (2003), The use of environmental scanning electron microscopy for imaging wet and insulating materials, *Nature Materials*, 2, 511–516.
- [99] Turkcan., C., (2021), Giyilebilir doku elektronigi, *Beykent Üniversitesi Fen ve Mühendislik Bilimleri Dergisi*, 14, 27–34.
- [100] Voss, A., Schroeder, R., Schulz, S., Haueisen, J., Vogler, S., Horn, P., Stallmach, A., Reuken, P., (2022), Detection of liver dysfunction using a wearable electronic nose system based on semiconductor metal oxide sensors, *Biosensors*, 12, 70.
- [101] Kokbas, U., Kayrin, L., and Tuli, A., (2013), Biyosensörler ve tıpta kullanım alanları, *Arşiv Kaynak Tarama Dergisi*, 22, 499–513.
- [102]Çelebier, İ., (2022), Kanser tanısında kullanılmak üzere yeni nesil kolorimetrik biyosensörlerin geliştirilmesi, PhD Thesis, Department of Biology, Hacettepe University, Ankara, 95pp.
- [103]Tuylek, Z., (2017), Biyosensörler ve nanoteknolojik etkileşim, *Bitlis Eren Üniversitesi Fen Bilimleri Dergisi*, 6, 71–80.
- [104]Tuylek, Z. (2021), Biyolojik sistemlerde gelecekteki nano / biyosensör ürünlerine hazırlık, *Biyosistem Mühendisliği Dergisi*, 17–39.
- [105]Yüksel, M., (2012), Protein algılamasına yönelik nano-biyosensörlerin yeni malzeme ve tekniklerle geliştirilmesi, PhD Thesis, Graduate School of Natural and Applied Sciences, Department of Physics, Kırıkkale University, Kırıkkale, 82pp.

- [106] Tuylek, Z., (2019), Nanotıp alanında kullanılan sistemler, Arşiv Kaynak Tarama Dergisi, 119–129.
- [107] Karakaş, T.B., (2021), Biosensors designed for rapid detection of sars-cov-2, Dergipark, 4, 491–506.
- [108] Göktürk, I., (2018), Nanobiyosensörler: hastalık teşhisi için gelecek vaat ediyor mu? Bioreg Bilim, 34–40.
- [109] Tüylek, Z., (2021), Nano-medicine and the new treatment methods, Review Article, Eurasian Journal Of Health Sciences, 4, 121–131.
- [110] Abid, S. A., Ahmed Muneer, A., Al-Kadmy, I. M.S., Sattar, A. A., Beshbishy, A.M., Batiha, G.E.S., Hetta, H.F., (2021), Biosensors as a future diagnostic approach for COVID-19. Life Sciences, 273 119117.
- [111] Ma, Z., Meliana, C., Munawaroh, H. S. H., Karaman, C., Karimi-Maleh, H., Low, S. S., Show, P. L., (2022), Recent advances in the analytical strategies of microbial biosensor for detection of pollutants, Chemosphere, 306, 135515.
- [112] Dzyadevych, S. v., Arkhypova, V.N., Soldatkin, A.P., El'skaya, A. v., Martelet, C., and Jaffrezic-Renault, N., (2008), Amperometric enzyme biosensors: past, present and future, IRBM. 29, 171–180.